Universidade de Lisboa

Faculdade de Farmácia

Reversing Multidrug Resistance (MDR) in Cancer Cells by Targeting P-glycoprotein (P-gp)— Insights into the Mechanism of MDR Reversal from *in silico* P-gp Modeling

Ricardo José Diogo Grácio Ferreira

Orientadores: Professora Doutora Maria José Umbelino Ferreira

Doutor Daniel José Viegas Antunes dos Santos

Tese especialmente elaborada para obtenção do grau de Doutor em Farmácia, especialidade de Química Farmacêutica e Terapêutica.

2017

Universidade de Lisboa

Faculdade de Farmácia

Reversing Multidrug Resistance (MDR) in Cancer Cells by Targeting P-glycoprotein (P-gp)— Insights into the Mechanism of MDR Reversal from *in silico* P-gp Modeling

Ricardo José Diogo Grácio Ferreira

Orientadores: Professora Doutora Maria José Umbelino Ferreira
Doutor Daniel José Viegas Antunes dos Santos

Tese especialmente elaborada para obtenção do grau de Doutor em Farmácia, especialidade de Química Farmacêutica e Terapêutica.

Jurí

Presidente: Doutora Matilde da Luz dos Santos Duque da Fonseca e Castro, Professora Catedrática e Diretora da Faculdade de Farmácia da Universidade de Lisboa;
Vogais:
- Doutora Maria Emília da Silva Pereira de Sousa, Professora Auxiliar, Faculdade de Farmácia da Universidade do Porto;
- Doutora Ana Maria Ferreira da Costa Lourenço, Professora Auxiliar, Faculdade de Ciências e Tecnologia da Universidade Nova de Lisboa;
- Doutor António Manuel Simões Garrão Albuquerque Baptista, Investigador Principal, Instituto de Tecnologia Química e Biológica da Universidade Nova de Lisboa;
- Doutor Miguel Ângelo dos Santos Machuqueiro, Professor Auxiliar Convidado, Faculdade de Ciências da Universidade de Lisboa;
- Doutora Maria José Umbelino Ferreira, Professora Associada com Agregação, Faculdade de Farmácia da Universidade de Lisboa, Orientadora.
- Doutora Noélia Maria da Silva Dias Duarte, Professora Auxiliar, Faculdade de Farmácia da Universidade de Lisboa;
- Doutora Maria Manuel Duque Vieira Marques dos Santos, Investigadora, Faculdade de Farmácia da Universidade de Lisboa;

Tese financiada pela *Fundação para a Ciência e Tecnologia* (FCT) através da B.D. nº SFRH/BD/84285/2012

2017

This thesis was conducted at the
Natural Products Chemistry group, Research Institute for Medicines (iMed.ULisboa), Faculty of Pharmacy, Universidade de Lisboa

The financial support was provided by Fundação para a Ciência e Tecnologia (FCT), Portugal *(Ph.D Grant SFRH/BD/84285/2012; and project PTDC/QEQ-MED/0905/2012).*

Bis vincit qui se vincit in victoria

"He conquers twice who conquers himself when he is victorious"

Publilius Syrus, 1st century BC

Abstract

Multidrug resistance (MDR) in cancer is one of the major impairments in the success of chemotherapy. The main objective of this work was the identification and optimization of MDR reversers, derived from *Euphorbia* species, and to gain insights on the drug efflux mechanism by P-gp.

The phytochemical study of *Euphorbia pedroi* yielded four new diterpenes, two macrocyclic lathyranes (**9**, **12**), one jatrophane (**10**) and an unprecedented rearranged tigliane (**13**). While **9** is characterized by a rare double α,β-unsaturated ketone system, **13** has a new skeleton that may result from a pinacol rearrangement as proposed in a possible biogenetic pathway. Furthermore, a new spiroterpenoid (**6**) was also isolated, together with several known terpenoids (**1**-**5, 7, 8, 14**-**16**) and flavonoids (**17**-**18**).

Molecular derivatization of compounds **15** and **17** yielded two set of new derivatives (**19**-**24** and **25**-**71**, respectively). In this way, reaction of **15** with hydroxylamine hydrochloride gave compound **19** that was further acylated with acyl anhydrides (**20**) and chlorides (**21**-**24**). Flavanone derivatives were obtained through three main approaches. Firstly, the methylation of naringenin (**17**) yielded compounds **46** and **47**. Following, while hydrazones (**25**-**28**, **48**-**53**) and carbohydrazides (**37**, **38**, **40**-**42**, **54**-**63**) were obtained from compounds **17**, **46** and **47**, azines (**29**-**36**) were prepared by the reaction of **28** with aldehydes. A thiosemicarbazone derivative (**39**) was also prepared from **17**. Other flavanone derivatives were additionally synthesized through a Mannich-type reaction (**43**-**45**) or by alkylation of compound **47** with epichlorohydrin (**64**, **65**) followed by the reaction with amines, indole or thiophenol to yield **66**-**71**. The chemical structures of all compounds were deduced from physical and spectroscopic data (IR, MS, 1D- and 2D-NMR experiments).

The P-gp-mediated MDR reversal activity of compounds was evaluated by combining transport and chemosensitivity assays, in mouse lymphoma L5178Y-MDR (**1**-**71**) and Colo320 (**1**-**18**) cell models. While **6** showed high modulation activity even at 0.2 μM, compound **9** combined a good P-gp modulatory activity with a strong cytotoxic effect in both cell lines. When compared to the parent compound (**15**), the derivatives **20** and **22** and **23** were stronger efflux modulators towards the L5178Y-MDR cells. Most of the flavanone derivatives (**25**-**71**) were also more active than the parent compound (**17**) in L5178Y-MDR cells, being the most significant results observed for propanolamines **66**-**69,** where compound **69** was found to be a strong P-gp modulator even at 2.0 μM.

When in combination with doxorubicin, the natural compounds **6**, **9**, **10**, **12** and **13** synergistically enhanced the cytotoxic effects of the drug. Strong synergistic effects were also observed for the derivatives **22** and **69**.

The ability of compounds **25**-**45** to modulate drug efflux by MRP1 and BCRP was also assessed, using human MRP1- and BCRP-transfected cell models. For this set of compounds, a second P-gp-transfected cell model was used. Azines (**29**-**36**) displayed significant activity towards BCRP while hydrazides (**38**-**42**) showed a good selectivity profile for MRP1. Oppositely, derivatives **35** and **36** displayed a good activity profile in both efflux pumps, when tested at 20 μM. Based on these results, new structure-activity relationships (SAR) for the

selective BCRP and MRP1 inhibitors were obtained, unveiling which structural features could be directly correlated with the observed biological activity.

The efflux mechanism of P-gp was studied by means of molecular dynamics and docking studies. The 'linker' polypeptide sequence was found to be important to absorb stronger motions and acting as a 'damper' between both NBDs, stabilizing the cytosolic portion of the transporter. Following, based on a previously refined P-gp structure, three distinct drug-binding sites could be identified and characterized, in a good agreement with published experimental data. Together with a new classification scheme, cross interactions between the substrate/modulator and each halve of P-gp were identified as an important mechanism in efflux modulation. Drug transit from bulk water into the DBP was also characterized as an overall free-energy downhill process, with no activation energy required for crossing the gate found between transmembrane helices 10 and 12. Furthermore, from the analysis on drug adsorption to the cytoplasmic domains in P-gp substrates and modulators were show to have different free energies of adsorption in both lipid/water and protein/ water interfaces and important differences in drug–protein interactions, protein dynamics and membrane biophysical characteristics were observed between non-substrates, substrates and modulators.

Keywords: Euphorbiaceae; *Euphorbia pedroi*; terpenoids; macrocyclic diterpenes; MDR reversal; P-glycoprotein; *ent*-abietanes; flavanones; molecular dynamics; docking; drug-binding sites; drug permeation; efflux mechanism.

Resumo

A resistência a múltiplos fármacos (MDR) no cancro configura-se como um dos principais problemas que atualmente comprometem o sucesso dos regimes de quimioterapia. Dos mecanismos celulares envolvidos na MDR, um dos mais importantes consiste no aumento do efluxo de citotóxicos ou de sequestração intracelular devido à sobre-expressão de transportadores da família ABC, nomeadamente a glicoproteína-P (P-gp), a proteína associada à multirresistência 1 (MRP1) e a proteína de resistência do cancro da mama (BCRP). Envolvidas em fenómenos normais de destoxificação celular, estas bombas de efluxo encontram-se igualmente implicadas na redução da concentração intracelular de fármacos anti-tumorais, transportando-os contra o seu gradiente de concentração, através da utilização da energia gerada pela ligação e hidrólise do ATP.

Apesar das três gerações de moduladores da P-gp já desenvolvidas, nenhum modulador foi clinicamente eficaz na reversão da MDR quando em coadministração com fármacos citotóxicos. No entanto, e uma vez que a procura de fármacos capazes de reverter a MDR continua a ser uma das abordagens mais promissoras, novas moléculas isoladas de fontes naturais são atualmente consideradas como uma possível quarta geração de moduladores de bombas de efluxo, atuando como reversores da MDR em células tumorais. Assim, um dos objetivos principais deste trabalho foi a identificação e otimização de novos reversores da MDR, isolados a partir da espécie *Euphorbia pedroi* ou obtidos através de derivatização química de compostos isolados em grandes quantidades.

O estudo fitoquímico da *E. pedroi* permitiu o isolamento de quatro novos diterpenos, dois latiranos (**9**, **12**), um jatrofano (**10**) e um tigliano rearranjado com um esqueleto novo (**13**). Enquanto a pedrodiona A (**9**) é caracterizada pela presença de dois sistemas α,β-insaturados, o pedrolido (**13**) apresenta um rearranjo de pinacol em C-6/C-7 incomum. Foi também isolado um esteroide novo designado por spiropedroxodiol (**6**), contendo um esqueleto *spiro* raro, conjuntamente com vários terpenoides (**1**-**5**, **7**, **8**, **14**-**16**) e flavonoides conhecidos (**17**-**18**).

Por forma a otimizar as propriedades moduladoras do helioscopinolido E (**15**) e da naringenina (**17**), foram preparados dois conjuntos de compostos com o núcleo do *ent*-abietano (**19**-**24**) e da flavanona (**25**-**71**) através da derivatição molecular de vários grupos funcionais. Enquanto que no primeiro caso a reação do composto **15** com hidroxilamina deu origem à oxima **19** (C=N-OH) e posteriormente aos compostos **20**-**24** por acilação com anidridos ou cloretos de ácido, os derivados do núcleo da flavanona foram obtidos através de três abordagens distintas. Inicialmente, a metilação dos hidroxilos da naringenina (**17**) nas posições C-7 e C-4' originou a sakuranetina (**47**) e a 4'-metoxisakuranetina (**48**). Em seguida, enquanto que as hidrazonas **25**-**28**, **48**-**53** (C=N-NH-R) e as carbohidrazidas **37**, **38**, **40**-**42**, **54**-**63** (C=N-NH-CO-R) foram preparadas a partir dos compostos **17**, **46** e **47**, as azinas **29**-**36** (C=N-N=CH-R) foram sintetizadas através da reação do composto **28** (C=N-NH_2) com aldeídos. Foi também sintetizada uma tiosemicarbazona (**39**) através da reação da naringenina (**17**) com a *N*,*N*-dimetiltio-semicarbazida. Foram ainda preparados outros derivados do núcleo da flavanona i) através de uma reação de Mannich nas posições C-6 e C-8 (**43**-**45**) e ii) através da alquilação do hidroxilo da posição C-4' da sakuranetina (**47**) com epiclorohidrina (**64**, **65**) seguida da reação com aminas, indole ou tiofenol para originar as correspondentes propanolaminas (**66**-

69) e os compostos **70**-**71**. As estruturas químicas dos compostos foram deduzidas a partir dos seus dados físicos e espectroscópicos (IR, MS, 1D e 2D-RMN).

A capacidade de reversão de MDR dos compostos foi avaliada através da combinação de ensaios funcionais com ensaios de quimiossensibilidade, utilizando como modelos as células de linfoma de rato L5178Y-MDR (**1**-**71**) e células Colo320 humanas (**1**-**18**). Enquanto que o spiropedroxodiol (**6**) demonstrou possuir uma elevada capacidade para modular o efluxo mesmo em concentrações submicromolares (0.2 μM), a atividade expressa pela pedrodiona A (**8**) combinou uma boa atividade na reversão de MDR com uma elevada citotoxicidade nas linhas celulares L5178Y-MDR (FAR 19.13, IC_{50} 0.259 ± 1.05 μM) e Colo320 (FAR 1.52, IC_{50} 0.822 ± 1.05 μM).

Relativamente aos derivados obtidos a partir do composto **15**, a acilação da oxima do heliscopinolido E (**19**) aumentou a capacidade moduladora do efluxo nas células de linfoma de rato na maioria dos compostos sintetizados. Nos derivados da naringenina (**17**), a metilação de hidroxilos fenólicos em conjunto com i) a substituição do grupo carbonilo na posição C-4 por hidrazonas (**25**-**28**, **48**-**53**), azinas (**29**-**36**) ou carbohidrazidas (**37**-**42**, **54**-**63**) aumentou a atividade de reversão de MDR dos compostos a 20 μM. Verificou-se também que a alquilação do hidroxilo na posição C-4' para gerar as correspondentes propanolaminas (**64**-**71**) aumentou substancialmente as suas propriedades anti-MDR (**66**-**69**) a concentrações mais baixas (2.0 μM). Adicionalmente, e quando testados em combinação com a doxorubicina, todos os compostos testados (**6**, **10**, **12**, **13**, **22**, **69**) exceto o **9** (efeito aditivo) e o **60** (antagonismo) potenciaram a atividade citotóxica quando em co-administração com o fármaco antitumoral.

Os efeitos dos derivados **25**-**45** da flavanona (**1**7) foram igualmente avaliados noutros transportadores ABC frequentemente sobre-expressos em células tumorais, como a proteína de resistência do cancro da mama (BCRP) e a proteína associada à multirresistência 1 (MRP1). Adicionalmente, estes compostos foram também testados numa linha celular alternativa, igualmente transfetada com o gene da P-gp (NIH/3T3). Assim, enquanto que as hidrazonas (**25**-**36**) demonstraram uma maior seletividade para a BCRP, os derivados de hidrazidas (**37**, **38, 40**-**42**) foram seletivos para a MRP1. No entanto, importa referir que os compostos **35**, **36** e **39** (uma tiosemicarbazona) demonstraram possuir uma atividade apreciável como modulador de efluxo em ambas as bombas MRP1 e BCRP (a 20 μM). Finalmente, e tendo como base os resultados acima descritos, foram desenvolvidas novas relações estrutura-atividade (SAR) em que a posição espacial do substituinte foi identificada como um dos principais fatores para a atividade registada na MRP1 e BCRP. Por fim, este estudo providenciou pela primeira vez um racional para o desenvolvimento de novos moduladores para a P-gp, BCRP e MRP1 a partir do núcleo da flavanona.

A publicação da estrutura cristalográfica da P-gp murina, em 2009, colmatou uma importante falha no estudo das bombas de efluxo e permitiu um crescimento exponencial de estudos estruturais, visando um maior conhecimento sobre o mecanismo de efluxo pela P-gp. Desta forma, e para evitar os problemas subjacentes ao desenvolvimento das primeiras três gerações de moduladores da MDR em que a estrutura do transportador não era conhecida, importa saber os principais passos pelos quais ocorre o efluxo de substratos e alguns detalhes específicos adicionais acerca do mecanismo de efluxo da P-gp.

Assim, foi estudado o mecanismo de efluxo pela P-gp através de dinâmica e *docking* molecular. A estrutura polipeptídica em falta ("linker") foi determinada como essencial para a estabilização dos domínios citoplasmáticos da P-gp, atuando por forma a absorver fortes oscilações estruturais. Com base na estrutura previamente refinada da P-gp, foram identificados e caracterizados de acordo com dados experimentais publicados, três locais de ligação distintos, dois de ligação a substratos e um de ligação a moduladores. Através da publicação de um novo esquema de classificação, as interações cruzadas entre o modulador e cada domínio da P-gp (N- e C-terminais) foram identificadas como um mecanismo importante na modulação de efluxo. O processo biofísico pelo qual moléculas são capazes de permear a membrana a partir do citoplasma e a sua entrada na cavidade interna da P-gp foi também caracterizado como um processo energeticamente favorável, desprovido de barreiras energéticas, mesmo durante a passagem através das hélices transmembranares 10 e 12. Do mesmo modo, substratos e moduladores revelaram ter diferentes energias livres de adsorção em cada uma das interfaces (lípidos/água e proteína/água), tendo sido igualmente registadas diferenças importantes nas interações fármaco-proteína, nos processos dinâmicos do transportador e nas características biofísicas da membrana quando em contacto com não-substratos, substratos e moduladores.

Palavras-chave: Euphorbiaceae; *Euphorbia pedroi*; diterpenos macrocíclicos; reversão da multirresistência; Glicoproteína-P; *ent*-abietano; flavanona; dinâmica molecular; docking; locais de ligação a substratos; permeação; mecanismo de efluxo.

Related publications

From this thesis, several publications and communications in scientific meetings were produced.

Papers

Ferreira RJ, Ferreira MJU, dos Santos DJVA (**2013**) Molecular docking characterizes substrate-binding sites and efflux modulation mechanisms within P-glycoprotein. *J Chem Inf Model* **53** 1747–1760. (doi:10.1021/ci400195v);

Ferreira RJ, Ferreira MJU, dos Santos DJVA (**2013**) Assessing the Stabilization of P-Glycoprotein's Nucleotide-Binding Domains by the Linker, Using Molecular Dynamics. *Mol Inf* **32**, 529–540 (doi:10.1002/minf.201200175);

Ferreira RJ, Ferreira MJU, dos Santos DJVA (**2015**) Do Drugs Have Access to the P-Glycoprotein Drug-Binding Pocket through Gates? *J Chem Theory Comput* **11**, 4525–4529 (doi:10.1021/acs.jctc.5b00652);

Ferreira RJ, Ferreira MJU, dos Santos DJVA (**2015**) Do adsorbed drugs onto P-glycoprotein influence its efflux capability? *Phys Chem Chem Phys* **17**, 22023–22034 (doi:10.1039/C5CP03216D);

Ferreira RJ, dos Santos DJVA, Ferreira MJU (**2015**) P-glycoprotein and membrane roles in multidrug resistance. *Future Med Chem* **7**, 929–946 (doi:10.4155/fmc.15.36);

Ferreira RJ, Ferreira MJU, dos Santos DJVA (**2015**) Reversing cancer multidrug resistance: insights into the efflux by ABC transports from *in silico* studies. *WIREs Comput Mol Sci* **5**, 27–55 (doi:10.1002/wcms.1196);

Ferreira RJ, Bonito CA, Ferreira MJU, dos Santos DJVA (**2017**) About P-glycoprotein: a new drugable domain is emerging from structural data. *WIREs Comput Mol Sci* **7**, e1316 (doi:10.1002/wcms.1316);

Oral communications

Ferreira RJ, Ferreira MJU, dos Santos DJVA (**2013**) An unified view on P-glycoprotein transporter: Insights on structural features and efflux modulation mechanisms from molecular dynamics and docking studies, 6th Theoretical Biophysics Symposium (Theobio2013), Gothemburg, Sweden, June 24th-27th;

Ferreira RJ, Ferreira MJU, dos Santos DJVA (**2013**) On the Importance of the Linker Sequence to the P-glycoprotein's Structural Stability and Substrate Recognition, 5th iMed.ULisboa Post-Graduate Students Meeting, Lisboa, Portugal, June 18th;

Ferreira RJ, Ferreira MJU, dos Santos DJVA (**2014**) P-Glycoprotein/Membrane Role on Multidrug Resistance: Insights from *in silico* studies, XXIII International Symposium on Medicinal Chemistry (EFMC-ISMC 2014), Lisboa, Portugal, September 7th-11th;

Ferreira RJ, Ferreira MJU, dos Santos DVJA (**2015**) Insights on drug adsorption, membrane permeation and P-glycoprotein efflux by means of Molecular Dynamics simulations. 7th International Theoretical Biophysics Symposium (TheoBio2015), Cagliary, Italy, June 8th-12th;

Ferreira RJ, Baptista R, dos Santos DJVA, Fernandes MX, Ferreira MJU (**2015**) Wrapping it all around: in silico approaches to improve the MDR-reversal properties of the macrocyclic diterpenic core. 11º Encontro Nacional de Química Orgânica e 4º Encontro Nacional de Química Medicinal (11ENQO/4ENQT), Porto, Portugal, September 1st - 3rd;

Ferreira RJ, Ferreira MJU, dos Santos DJVA (**2015**) *In silico* Contributions on Drug Adsorption, Membrane Permeation and P-glycoprotein Efflux Mechanism. III EJIBCE - Encontro de Jovens Investigadores de Biologia Computacional Estrutural, Coimbra, Portugal, December 18th;

Ferreira RJ, Khonkarn R, Baubichon-Cortay H dos Santos DJVA, Falson P, Ferreira MJU (**2016**) Overcoming Multidrug Resistance: search for ABC transporters modulators and insights on drug efflux mechanism, 8th iMed.ULisboa Post-Graduate Students Meeting & 1st i3DU Meeting, Lisboa, Portugal, July 14th-15th;

Ferreira RJ, Bonito CA, Ferreira MJU, dos Santos DJVA (**2016**) Decoding the human P-glycoprotein efflux mechanism II: Insights on substrate binding and signal transmission, 12º Encontro Nacional de Química-Física/1º Simpósio de Química Computacional, Évora, Portugal, June 22nd-24th;

Ferreira RJ, Moreno A, Baubichon-Cortay H, dos Santos DJVA, Falson P, Ferreira MJU (**2017**) Flavanones as a source for new ABC transporters efflux modulators, 9th iMed.ULisboa Post-Graduate Students Meeting & 2nd i3DU Meeting, Lisboa, Portugal, July 13th-14th;

Poster communications

Ferreira RJ, Ferreira MJU, dos Santos DJVA (**2013**) Towards more potent Jolkinol D derivatives: how can docking studies guide chemical derivatization?, 10º Encontro Nacional de Química Orgânica, Lisboa, Portugal, September 4-6;

Ferreira RJ, Ferreira MJU, dos Santos DJVA (**2013**) Free Energy Studies adressing P-glycoprotein Multidrug Resistance Phenomena, EJIBCE - Encontro de Jovens Investigadores de Biologia Computacional Estrutural, Porto, Portugal, December 20th;

Ferreira RJ, Ferreira MJU, dos Santos DJVA (**2014**) An *in silico* Approach Towards Drug Interaction with P-Glycoprotein and Lipid Bilayer on Multidrug Resistance, ESMEC 2014 – European School of Medicinal Chemistry, Urbino, Italy, June 29th – July 4th – *Best Poster Prize*;

Ferreira RJ, Mónico A, Ferreira MJU (**2014**) Phytochemical characterization of terpenoids from *Euphorbia pedroi*, 6th iMed.ULisboa Post-Graduate Students Meeting, Lisboa, Portugal, June 2nd;

Ferreira RJ, Ferreira MJU, dos Santos DJVA (**2014**) Towards a Rational Optimization of the Macrocyclic Diterpenic Core: An *in silico* prediction Method to Guide Chemical Derivatization, 6th iMed.ULisboa Post-Graduate Students Meeting, Lisboa, Portugal, June 2nd;

Ferreira RJ, Ferreira MJU, dos Santos DJVA (**2014**) P-Glycoprotein/Membrane Role on Multidrug Resistance: Insights from *in silico* studies, 1st EFMC Young Medicinal Chemist Symposium (EFMC-YMCS 2014), Lisboa, Portugal, September 12th;

Ferreira RJ, Ferreira MJU, dos Santos DJVA (**2014**) Insights on P-Glycoprotein and Membrane Function upon Drug Adsorption, II EJIBCE - Encontro de Jovens Investigadores de Biologia Computacional Estrutural, Coimbra, Portugal, December 18th-19th;

Ferreira RJ, Ferreira M-JU, dos Santos DJVA (**2015**) Hints on macrocyclic diterpenic core derivatization by an optimized in silico method. XXIV Encontro Nacional da Sociedade Portuguesa de Química (XXIV ENSPQ), Coimbra, Portugal, July 1st-3rd;

Ferreira RJ, Ferreira MJU, dos Santos DJVA (**2015**) Key Findings on Drug Transit and the P-glycoprotein, XXIV Encontro Nacional da Sociedade Portuguesa de Química (XXIV ENSPQ), Coimbra, Portugal, July 1st-3rd;

Ferreira RJ, Baptista R, Ferreira MJU, dos Santos DJVA (**2015**) An in silico method towards macrocyclic diterpenic core derivatization, 7th iMed.ULisboa Post-Graduate Students Meeting, Lisboa, Portugal, July 15th-16th;

Ferreira RJ, Baptista R, dos Santos DJVA, Fernandes MX, Ferreira MJU (**2016**) Structure-activity Relationships for the Multidrug-Resistance (MDR) reversal capabilities of a small library of diterpenic derivatives, COST Action CM1407, 1st Training School, Belgrade, Serbia, September 24th-26th;

Ferreira RJ, Ferreira MJU, dos Santos DJVA (**2016**) Molecular Dynamics studies on the ABCG transporter family, EJIBCE 2016 - Encontro de Jovens Investigadores de Biologia Computacional Estrutural, Lisboa, Portugal, December 21st.

Ferreira RJ, dos Santos DJVA, Ferreira MJU (**2017**) Reversing multidrug resistance (MDR) in cancel cells by targeting P-glycoprotein, 1º Encontro do Colégio da Química da Universidade de Lisboa, Lisboa, Portugal, July 20th-21st;

Acknowledgements

I want to express my sincere gratitude to Prof. Dr. Maria José U. Ferreira and Dr. Daniel J.V.A. dos Santos for all the time that they have invested in myself and on this project. Even in the most difficult times, the vision of the world of natural products through the eyes of Prof. Maria José always provided me a strong motivation to tackle any difficulties. Moreover, I must also acknowledge that, by believing in me since 2010 when I first entered her group as a BI fellow, Prof. Maria José contributed decisively for the strong background that I've acquired over the past years. To Dr. Daniel dos Santos, I must acknowledge the endless hours he spent on teaching me how to do "real science". He shared with me his vision and knowledge in computational chemistry with such a commitment that I've rarely seen. To both, my endless gratitude!

I must also thank to all that made this work possible: to Prof. Dr. Joseph Molnár and especially to Dr. Gabriella Spengler from the department of Medical Microbiology, University of Szeged, Hungary, for accepting me in Szeged while teaching me the mesmerizing world of biological assays; to Dr. Imre Ocsovszki, of the FACS Laboratory at the Department of Biochemistry, for the prompt availability of the flow cytometry results; to Dr. Teresa Vasconcelos from Instituto Superior de Agronomia de Lisboa, for the identification of plant material; and to Dr. Rita Ventura, Bioorganic Chemistry at ITQB for providing access to the polarimeter for the optical rotation measurements. I also acknowledge Dr. Carlos Cordeiro for providing data from the FTICR-MS at Faculdade de Ciências da Universidade de Lisboa, to Dr. José Ascenso for the support while using the 500 MHz NMR services at Instituto Superior Técnico and to Dr. Lina Santos for the ESI-MS data at the Faculdade de Fármacia da Universidade de Lisboa.

To all my laboratory colleagues a very warm acknowledgement for all the time spent among distillations, isolations, reactions, TLCs and silica columns. These were Mariana Reis, Angela Paterna, Susana Henriques, Nora Jellenz, Carolina Chaves and David Cardoso, but also Cristina Silva, João Gomes and Jorge Silva that shared the lab in good and bad moments. To the "people next door", Rita Capela for the never-ending fellowship and João Lavrado for the NMR emergency support. I cannot forget my colleagues from the A.3.9 computational room, namely Susana Lucas, Marta Carrasco, Romina Guedes, Rafael Baptista, Cátia Bonito but also the new entrepreneurs Patrícia, Sofia, Rita and Filipa that will (hopefully) continue the good work!

Szeged was wonderful, especially in Winter. Thank you Mário for the initial tour guide, all the lunches and laboratory assistance, Annamária for the valuable experience in dealing with 96-well plates and Anikó for the backoffice support.

Last but not the least, my family… all that I've ever done had you as my most supreme inspiration. To my wife Cátia for the patience, perseverance and endless support (which was finally recognized!), to my daughter Leonor for all the joy. Carolina e João, my parents, I could not ask for better ones! To Alexandre e Helena, thank you for everything since I've moved to Lisboa. Cristina (the sister I've never had) and Tony, thank you for all the fun!

Table of Contents

Abstract **vii**

Resumo **ix**

Related Publications **xiii**

Acknowledgements **xvii**

Table of Contents **xix**

Figures Index **xxvii**

Schemes Index **xxxiii**

Tables Index **xxxiii**

Abbreviations **xxxvii**

Chapter 1 – Introduction

1. Multidrug resistance in cancer **3**

1.1. Resistance mechanisms **4**

1.2. ABC Transporters and Multidrug Resistance **5**

1.2.1. Insights on MDR-related ABC Transporters 5

1.2.2. MDR modulation by innovative strategies: past, present and beyond 8

1.3. Natural products as a new generation of MDR modulators **11**

1.3.1. Diterpenes from *Euphorbia* species 12

1.3.2. MDR reversal and cytotoxic activities of diterpenic scaffolds 16

1.3.2.1. Jatrophanes 16

1.3.2.2. Lathyranes 19

1.3.2.3. Premyrsinanes, myrsinanes and euphoractins 20

1.3.2.4. Other diterpenes 22

1.3.3. Triterpenes and flavonoids in multidrug resistance 24

1.4. Computational studies as useful tools for understanding ABC efflux Transporters **27**

1.4.1. Ligand-based studies on P-glycoprotein substrates and modulators 27

1.4.1.1. Structure-activity relationship (SAR) studies 28

1.4.1.2. SAR and QSAR studies on diterpenic compounds 29

1.4.2. Structure-based studies on ABC transporters: unveiling its efflux mechanism 31

1.4.2.1. Molecular docking 32

1.4.2.2. Molecular dynamics studies 34

Chapter 2 - Objectives

2. Objectives **41**

Chapter 3 - Phytochemical research on *Euphorbia pedroi.* Results and Discussion

3. Structure elucidation of isolated compounds **45**

3.1. Lathyrane-type macrocyclic diterpenes **46**

3.1.1. Pedrodione A, 15β-acetoxy-3β-hydroxylathyra-6(17),12*E*-dien-5,14-dione 46

3.1.2. Pedrodiol, 15β-acetoxy-6(17),12*E*-dien-3β,5α-dihydroxy-lathyra-14-one 50

3.1.3. Piscatoriol A, 15β-acetoxy-6*Z*,12*E*-dien-3β,5α-dihydroxylathyra-14-one 53

3.1.4. Jolkinol D, 15β-acetoxy-3β-hydroxylathyra-5*E*,12*E*-dien-14-one 54

3.1.5. Jolkinol D epoxide, 15β-acetoxy-3β-hydroxylathyra-5,6-epoxi-12*E*-en-14-one 55

3.2. Jatrophane-type macrocyclic diterpenes **57**

3.2.1. Pedrodione B, 3β,5α,15β-triacetoxyjatropha-6(17),12*E*-dien-9,14-dione 57

3.3. Diterpenes with a policyclic scaffold **61**

3.3.1. Pedrolide 61

3.3.2. *ent*-13*R*-hydroxy-3,14-dioxo-16-atisene 65

3.3.3. Helioscopinolide B 67

3.3.4. Helioscopinolide E 69

3.3.5. Preparation of helioscopinolide E oxime derivatives 69

3.4. Steroids 72

3.4.1. Spiropedroxodiol, 3,7-dihydroxy-7(8→9)*abeo*-ergosta-24(28)-en-8-one 72

3.4.2. 7,11-dioxo-obtusifoliol, 3β-hydroxy-4α,14α-dimethyl-5α-ergosta-8,24(28)-dien-7,11-dione 75

3.4.3. β-sitostenone, (24*R*)-stigmast-4-ene-3-one 77

3.5. Tetracyclic and pentacyclic triterpenes 78

3.5.1. Oleanolic acid, 3β-hydroxyolean-12-en-28-oic acid 78

3.5.2. Cycloart-25-en-3β,24-diol 79

3.5.3. Cycloart-23-en-3β,25-diol 79

3.6. Flavonoids 81

3.6.1. Naringenin and Quercetin 81

3.6.2. Preparation of naringenin derivatives 81

Chapter 4 – Biological Studies. Results and Discussion

4. Evaluation of the MDR reversal activity 91

4.1. Anti-proliferative and cytotoxic activity of compounds 1-16 91

4.2. Modulation of P-glycoprotein efflux by compounds 1-16 96

4.3. Anti-proliferative and cytotoxic activity of *ent*-abietane and flavonoid derivatives 98

4.3.1. MDR reversal activities of helioscopinolide E derivatives 99

4.3.1.1. Anti-proliferative and cytotoxic activities of compounds 19-24 99

4.3.1.2. Modulation of rhodamine-123 efflux by compounds 19-24 99

4.3.2. MDR reversal activities of naringenin derivatives 103

4.3.2.1. Anti-proliferative and cytotoxic activities of naringenin derivatives 103

4.3.2.2. MDR reversal activities of compounds **25-63** 104

4.3.3. MDR reversal activities of OH-4'-alkylated naringenin derivatives 106

4.3.3.1. Anti-proliferative and cytotoxic activities of compounds **64-71** 106

4.3.3.2. MDR reversal activities of compounds **64-71** 107

4.4. Drug combination assays 109

4.5. MDR reversal activities of compounds 25-45 in other cell lines 110

4.5.1. Cytotoxicity assays of compounds **25-45** in P-gp, MRP1 and BCRP 110

4.5.2. Fluorescent dye efflux inhibition in P-gp, MRP1 and BCRP 111

4.5.3. Structure-activity relationship studies (SAR) on MRP1 and BCRP efflux modulators 114

Chapter 5 - *In silico* studies on P-glycoprotein efflux mechanism. Results and Discussion

5. *In silico* studies of ABC efflux pumps 121

5.1. The "linker" (residues 627-684) function in P-glycoprotein 122

5.1.1. Structural and functional analysis of the "linker" 123

5.1.2. Detailed "linker" contact analysis 126

5.1.2.1. Lower segment (residues 648-652) 126

5.1.2.2. Middle coil (residues 666-672) 127

5.1.2.3. Upper loop (residues 673-690) 129

5.2. Identification and characterization of the drug-binding sites 131

5.2.1. Identification of drug-binding sites 131

5.2.2. Characterization of the drug-binding sites 135

5.2.3. Development of a classification scheme for substrates and modulators 139

5.2.4. Classification of P-glycoprotein substrates 142

5.2.4.1. Non-substrates (A) 142

5.2.4.2. Transported substrates (B) 143

5.2.4.3. Non-transported substrates (C) 143

5.2.4.4. Modulators (D) 144

5.2.4.5. Intersections between main groups A-D 145

5.2.4.6. Probes 146

5.2.4.7. Lipids 147

5.3. Studies on drug permeation into the drug-binding pocket 147

5.4. Role of drug adsorption at the surface of P-glycoprotein and at the membrane interface 153

5.4.1. Free-energy calculations 154

5.4.2. Protein interaction profiles 157

5.4.3. Internal cavity volumes 160

5.4.4. Membrane biophysics 162

Chapter 6 - Conclusions

6. Conclusions 169

Chapter 7 – Material and Methods

7. Material and Methods 177

7.1.1. Chemistry 177

7.1.1.1. General experimental procedures 177

7.1.2. Phytochemical study of *Euphorbia pedroi* 178

7.1.2.1. Plant material 178

7.1.2.2. Extraction and isolation 178

7.1.2.3. Study of fraction D 179

7.1.2.4. Study of fractions E and F 181

7.1.2.5. Study of fraction G 191

7.2. Generation of a small library of helioscopinolide E derivatives 194

7.2.1. Synthesis of helioscopinolide E oxime 194

7.2.2. General procedure for helioscopinolide E oxime derivatives 195

7.3. Generation of a small library of naringenin derivatives 198

7.3.1. General preparation of naringenin hydrazones 199

7.3.1.1. Reaction between naringenin and hydrazines 199

7.3.1.2. Preparation of naringenin hydrazone (**28**) 200

7.3.1.3. Preparation of compounds **29**-**36** 200

7.3.2. General preparation of naringenin carbohydrazides (**37**-**42**) 206

7.3.3. Synthesis of naringenin derivatives (**43**-**45**) by a Mannich-type coupling reaction 210

7.3.4. Methylation of naringenin (**17**) with dimethylsulphate 212

7.3.5. Synthesis of sakuranetin and 4'-methoxysakuranetin derivatives (**48**-**63**) 213

7.3.6. Synthesis of nitrogen-containing OH-4'-alkyl sakuranetin derivatives 224

7.3.6.1. Reaction of sakuranetin with epichlorohydrin 224

7.3.6.2. General preparation of compounds **66**-**71** 225

7.4. Biological Studies 230

7.4.1. Reversal of multidrug-resistance mediated by P-glycoprotein 230

7.4.1.1. Cell lines and cultures 230

7.4.1.2. Antiproliferative and cytotoxicity assays 231

7.4.1.3. Rhodamine-123 accumulation assay 232

7.4.1.4. Drug combination assay 232

7.4.2. Reversal of drug resistance mediated by P-gp, MRP1 and BCRP in other cell lines 233

7.4.2.1. Cell lines and cultures 233

7.4.2.2. Cytotoxicity assays 233

7.4.2.3. Inhibition tests of MDR pumps mediated drug efflux 234

7.5. Computational Studies **235**

7.5.1. Molecular Dynamics (MD) studies 235

7.5.1.1. Initial structures 235

7.5.1.2. Simulation parameters 235

7.5.1.3. Steered Molecular Dynamics (sMD) 236

7.5.1.4. Adsorption runs 237

7.5.2. Data analysis 237

7.5.2.1. General analysis 237

7.5.2.2. Umbrella sampling 238

7.5.2.3. Adsorption runs 238

7.5.3. Molecular docking studies 240

7.5.3.1. Docking studies 240

7.5.3.2. Identification of drug-binding pockets 240

7.5.3.3. Pocket assignments 241

References **242**

Figures Index

Figure 1.1.	Schematic diagram of resistance to drugs (adapted from Gottesman, 2002).	3
Figure 1.2.	Models currently accepted for MDR onset, the cancer stem cell (CSC) and environmental-mediated drug resistance (EMDR) models (adapted from Zahreddine & Borden, 2013; Meads et al., 2009; Greenow & Clarke, 2012).	4
Figure 1.3.	(A) Crystallographic structure of P-gp, (left), MRP1 (middle) and ABCG2 (right) ABC transporters; (B), membrane topology models of P-gp, BCRP and MRP1 transporters. Images were obtained in MOE from the crystallographic structures 4Q9H, 5UJ9 and 5DO7, respectively, available in Protein Data Bank	7
Figure 1.4.	Timeline for MDR modulation strategies.	9
Figure 1.5.	Molecules from the three generations of P-gp inhibitors.	10
Figure 1.6.	Diterpenic scaffolds isolated from *Euphorbia* species.	13
Figure 1.7.	(A) Enzymatic steps of the MVA and MEP pathways (green contour refers to plastids); (B), Biosynthetic pathway for several intermediates involved in the diterpenic scaffold synthesis, from IPP and DMAPP (adapted from Tholl, 2015; Zografos, 2016).	14
Figure 1.8.	Biosynthesis of casbene, postulated biosynthesis of some complex members of deterpenoids and examples for the tigliane, ingenane and daphnane scaffolds (adapted from Zografos, 2016).	15
Figure 1.9.	Biosynthesis of abietanes, and *ent*-kaurane diterpenes (adapted from Zografos, 2016).	16
Figure 1.10.	Diterpenes with a jatrophane scaffold.	17
Figure 1.11.	Diterpenes with a jatrophane scaffold.	18
Figure 1.12.	Diterpenes with a lathyrane scaffold.	19
Figure 1.13.	Diterpenes with a lathyrane scaffold.	20
Figure 1.14.	(A) Proposed biosynthesis of myrsinanes and euphoractins from epoxilathyranes (adapted from Shi et al., 2008).	21

Figure 1.15.	Diterpenes with premyrsinane and euphoractin scaffolds.	21
Figure 1.16.	Examples of premyrsinanes and euphoractins.	22
Figure 1.17.	Examples of diterpenes with other reported scaffolds.	23
Figure 1.18.	Chemical classification and core structures of triterpenes (Yan et al., 2014).	24
Figure 1.19.	Triterpenes with cycloartane and cucurbitane scaffolds.	25
Figure 1.20.	Chemical classifications and core structures of flavonoids (adapted from Eid et al., 2015).	26
Figure 1.21.	Representation of the reserpine-derived pharmacophore (adapted from Pearce et al., 1989; Zamora et al., 1988).	28
Figure 1.22.	(A) Proposed 4-point pharmacophore (distances, angles, and dihedrals are represented); (B) Lowest RMSD conformations and alignment diagram for verapamil (yellow), tariquidar (purple), vinblastine (green) and latilagascene E (blue), in agreement with the developed pharmacophore (adapted from Ferreira et al., 2011).	29
Figure 1.23.	(A) Structure-activity relationship (SAR) of jatrophane diterpenes on P-gp inhibition; (B), Pharmacophoric hypothesis for epoxylathyrane derivatives. Green and yellow contours identify areas where steric bulk is positively or negatively correlated with biological activity. Red/blue contours identify areas where positively charged/hydrogen bond donor or negatively charged/hydrogen bond acceptor substituents are positively correlated with biological activity (adapted from Zhu et al., 2016; Baptista et al., 2016).	31
Figure 1.24.	(A) Docking studies on several diterpenoids in murine P-gp model; (B), Binding mode of 5-(1-Naphthylacetyloxy)-lathyra-6(17),12-dien-3,15-diol-14-one in a human homology P-gp model; (C), Binding pose of 9,15-Fiacetoxy-3,7-dibenzoyloxy-1,13,14-trihydroxyjatropha-5*E*-ene within a human homology P-gp model (adapted from Reis et al., 2012; Jiao et al., 2015; Zhu et al., 2016)	33

Figure 1.25. Normal motion patterns displayed by the ABC transporter P-glycoprotein (A) in the absence of substrates and (B) in the presence of a substrate at the TM 10-12 portal (adapted from Ferreira et al., 2012). 35

Figure 1.26. Proposed model for the ATP catalytic cycle, according the Constant Contact model for both ATP-binding competent NBDs. The ATP-binding pocket is formed by Walker A motifs of NBD1 (WA1) and NBD2 (WA2) with the signature motifs of the opposite NBD2 (S2) and NBD1 (S1). Pore opening/closing refers to the outward-facing P-gp, dashed lines to the known crystallographic structures (green, inward-facing; blue, outward-facing) (adapted from Ferreira et al., 2015). 36

Figure 3.1. Key COSY and HMBC correlations for pedrodione A (**8**). ^{1}H spin systems (A-B) and respective connections by main heteronuclear $^{2}J_{C\text{-}H}$ and $^{3}J_{C\text{-}H}$ correlations. 47

Figure 3.2. Energy minimized structure for pedrodione A (**9**). Minimization was made in MOE software using the AMBER10:EHT force field, according to the semi-empiric Hamiltonian PM3 (available in MOPAC). 49

Figure 3.3. Key COSY and HMBC correlations for pedrodiol (**12**). ^{1}H spin systems (A-B) and respective connections by main heteronuclear $^{2}J_{C\text{-}H}$ and $^{3}J_{C\text{-}H}$ correlations 51

Figure 3.4. Energy minimized structure for pedrodiol (**12**). Minimization was made in MOE software using the AMBER10:EHT force field, according to the semi-empiric Hamiltonian PM3 (available in MOPAC). 53

Figure 3.5. Key COSY and HMBC correlations for pedrodione B (**10**). ^{1}H spin systems (A-B-C) and respective connections by main heteronuclear $^{2}J_{C\text{-}H}$ and $^{3}J_{C\text{-}H}$ HMBC correlations. 58

Figure 3.6. Key NOESY correlations for pedrodione B (**10**). The energy minimized structure was obtained in MOE software using the AMBER10:EHT force field, according to the semi-empiric Hamiltonian PM3 (available in MOPAC). 60

Figure 3.7. Key COSY, HMBC and NOESY correlations for pedrolide (**13**). ^{1}H spin systems (A-B-C) and respective connections by main heteronuclear $^{2}J_{C\text{-}H}$ and $^{3}J_{C\text{-}H}$ HMBC correlations. 63

Figure 3.8. Possible biogenetic pathway for **13** from the known compound euphodendriane A. 64

Figure 3.9. Energy minimized structure for pedrolide (**13**). Minimization was made in MOE software using the AMBER10:EHT force field, according to the semi-empiric Hamiltonian PM3 (available in MOPAC). 65

Figure 3.10. Key COSY and HMBC correlations for spiropedroxodiol (**6**). ^{1}H spin systems (A-B) and respective connections by main heteronuclear $^{2}J_{C\text{-}H}$ and $^{3}J_{C\text{-}H}$ HMBC correlations. 73

Figure 3.11. Energy minimized structure for spiropedroxodiol (**6**). Minimization was made in MOE software using the AMBER10:EHT force field, according to the semi-empiric Hamiltonian PM3 (available in MOPAC). 74

Figure 4.1. Rare macrocyclic lathyrane-type diterpenes with two α,β-conjugated ketone systems at C-5 and C-14. 96

Figure 4.2. Flow cytometry histograms on R123 accumulation assay for spiropedroxodiol (**6**) at 0.2, 2.0 and 20 μM in chemo-resistant L5178Y-MDR and parental L5178Y-PAR (left) and human adenocarcinoma resistant Colo320 and parental Colo205 (right) cell lines. 98

Figure 4.3. (A) pKa distribution chart for both nitrogen-containing groups and (B) top-ranked docking pose of compound **69** in the internal drug-binding of the refined murine P-gp model. 109

Figure 4.4. Inhibition percentage for MRP1 and BCRP (20 μM). Control (C) refers to verapamil (5 μM, MRP1) and Ko143 (1 μM, BCRP) and were used to determine the fluorescence linked to 100% of inhibition. 113

Figure 4.5. Pharmacophoric hypothesis for A) BCRP and B) MRP1 specific modulators. Measurement of distances, angles and dihedrals on the developed pharmacophores are also depicted. 115

Figure 4.6. Docking poses for the most active compounds in BCRP (A) and MRP1 (B). Reference inhibitors as fumitremorgin C (FMC) and Reversan (RVS) were docked for comparison purposes Drug-binding sites are drawn as molecular surfaces (green, hydrophobic; pink, polar). 117

Figure 5.1. Linker's secondary structure after the 100 ns production run, showing the two α-helices, the N-terminal Ala627 and C-terminal Ala684 residues (Ferreira et al., 2013a) 122

Figure 5.2. (A) Root Mean Square Fluctuations (RMSF) of the α-carbon for the P-gp domains, in the absence (black) or presence (red) of linker, on a POPC membrane (Ferreira et al., 2012); (B) RMSF for linker residues (α-carbons) from the 100 ns run, with the protein-protein contact residues identified by PredictProtein server (Ferreira et al., 2013a). A scheme of the secondary structure is displayed at the top, with α-helices in red, β-sheets in yellow and coils as a black line. 124

Figure 5.3. Best ranked docking poses for verapamil (green), Rhodamine-123 (yellow) and Hoechst 33342 (pink), allowing the M-site (green arrow) and R-site (blue arrow) assignments. Phosphate (red) and nitrogen (blue) atoms of lipid headgroups are also represented to assess the relative position of the lipid membrane (Ferreira et al., 2013b). 132

Figure 5.4. Best ranked docking poses for LDS-751 (green), daunorubicin (yellow) and doxorubicin (pink). The R-site is identified by a blue arrow. Phosphate (red) and nitrogen (blue) atoms of lipid headgroups are also represented to assess the relative position of the lipid membrane (Ferreira et al., 2013b). 133

Figure 5.5. Docking poses for etoposide (green), vinblastine (yellow) and actinomycin D (pink). H-site is identified by a red arrow. Phosphate (red) and nitrogen (blue) atoms of lipid headgroups are also represented to assess the relative position of the lipid membrane (Ferreira et al., 2013b). 134

Figure 5.6. Graphical representation of the Molecular Surface (MS— green, hydrophobic and pink, polar) and Electrostatic Map (EM— blue, electron donor; grey, neutral and red, electron acceptor) for the identified drug-binding sites (Ferreira et al., 2013b). 138

Figure 5.7. Classification scheme for P-gp substrates and modulators (Ferreira et al., 2013b). 141

Figure 5.8. Chemical structures of colchicine (substrate) and tariquidar (modulator) (Ferreira et al., 2015c). 148

Figure 5.9. Potential of mean force (PMF) energetic profile for colchicine and tariquidar translocation from the membrane into the drug binding pocket. The grey shading represents the average radius of the TM helices at the entrance gate ($\xi = 0$) (Ferreira et al., 2015c). 149

Figure 5.10. Potential of mean force (PMF) energetic profile for colchicine and tariquidar permeation from bulk water into the hydrophobic membrane core in the absence of P-gp. The grey shading represents an estimation of the headgroup thickness in the POPC membrane (Ferreira et al., 2015c). 152

Figure 5.11. Chemical structures of the molecules used in the molecular dynamics simulations, with pKa of the ionizable groups, log*P* and log*D* (Ferreira et al., 2015d). 154

Figure 5.12. Free energies of adsorption (mean ± SE) for the different classes at protein-water or membrane-water interface. Statistical significance was determined by comparing the different classes with multiple t-tests ($p < 0.05$) (Ferreira et al., 2015d). 156

Figure 5.13. Spatial distribution maps for the different classes. A. Front view; B, Back view. Isosurfaces represent a probability greater than 50% of molecules to be in that region. Phosphate groups are also represented to assess lipid-water interface boundaries (Ferreira et al., 2015d) 159

Figure 5.14. Normalized internal cavity volume distributions for the *apo* structure and the different classes (Ferreira et al., 2015d) 161

Figure 5.15. Area per lipid (ΔA_L ± SE) and thickness (ΔD_{HH} ± SE) variations for each class (Ferreira et al., 2015d). 162

Figure 5.16. Changes in the residual hydrophobic exposure energy penalty ($\Delta\Delta G_{res}$) for each class compared with the apo system (under parenthesis in kBT units). TMD1, N-terminal transmembrane domain; TMD2, C-terminal transmembrane domain. Residue exposure for helix 6 in TMD1 was undetermined (no exposed residues to the bilayer). 164

Schemes Index

Scheme 3.1.	Preparation of helioscopinolide E (**15**) derivatives (20-24).	70
Scheme 3.2.	Preparation of hydrazones (**25**-**28**, **46**-**51**).	83
Scheme 3.3.	Preparation of azines (**29**-**36**).	84
Scheme 3.4.	Preparation of carbohydrazides (**37**, **38**, **40**-**42**, **54**-**63**).	85
Scheme 3.5.	Preparation of thiosemicarbazone (**39**) and Mannich-type (**43**-**45**) naringenin derivatives.	86
Scheme 3.6.	Preparation of 4'-OH alkylated sakuranetin derivatives (**64**-**71**).	87
Scheme 7.1.	Study of *Euphorbia pedroi*: extraction, isolation procedures and identified compounds from fractions D-G	179

Tables Index

Table 3.1.	^{1}H-, ^{13}C-NMR and DEPT spectra [$CDCl_3$, δ (ppm), J (Hz)] of pedrodione A (**9**).	48
Table 3.2.	^{1}H-, ^{13}C-NMR and DEPT [$CDCl_3$, δ (ppm), J (Hz)] data of pedrodiol (**12**) and piscatoriol A (**11**).	52
Table 3.3.	^{1}H- and ^{13}C-NMR [$CDCl_3$, δ (ppm), J (Hz)] spectra of jolkinol D (**7**) and jolkinol D epoxide (**8**).	56
Table 3.4.	^{1}H-, ^{13}C-NMR and DEPT [$CDCl_3$, δ (ppm), J (Hz)] data for pedrodione B (**10**).	59
Table 3.5.	^{1}H-, ^{13}C-NMR and DEPT [$CDCl_3$, δ (ppm), J (Hz)] data for pedrolide (**13**).	62
Table 3.6.	^{1}H-, ^{13}C-NMR and DEPT [$CDCl_3$, δ (ppm), J (Hz)] spectra for compound **16**.	66
Table 3.7.	^{1}H- and ^{13}C-NMR [$CDCl_3$, δ (ppm), J (Hz)] spectra for helioscopinolide B (**14**) and helioscopinolide E (**15**).	68
Table 3.8.	^{1}H-NMR [$CDCl_3$, δ (ppm), J (Hz)] spectra for *ent*-abietane derivatives **19**-**24**.	71

Table 3.9.	^{13}C-NMR [$CDCl_3$, δ (ppm)] data for *ent*-abietane derivatives **19**-**24**.	71
Table 3.10.	^{1}H-, ^{13}C-NMR and DEPT [$CDCl_3$, δ (ppm), J (Hz)] data of spiropedroxodiol (**6**).	74
Table 3.11.	^{1}H-, ^{13}C-NMR and DEPT [$CDCl_3$, δ (ppm), J (Hz)] spectroscopic data of 7,11-dioxo-obtusifoliol (**5**).	76
Table 3.12.	^{1}H-, ^{13}C-NMR and DEPT data [$CDCl_3$, δ (ppm), J (Hz)] for β-sitostenone (**1**).	77
Table 3.13.	^{1}H-, ^{13}C-NMR and DEPT data [$CDCl_3$, δ (ppm), J (Hz)] of oleanolic acid (**2**).	78
Table 3.14.	^{1}H- and ^{13}C-NMR [$CDCl_3$, δ (ppm), J (Hz)] data of cycloart-25-en-3β,24-diol (**3**) and cycloart-23-en-3β,25-diol (**4**).	80
Table 3.15.	^{1}H- and ^{13}C-NMR [$CDCl_3$, δ (ppm), J (Hz)] data of compounds **17** and **18**.	82
Table 4.1.	Anti-proliferative activity of compounds **1**-**16** on mouse T-lymphoma (L5178Y-PAR and L5178Y-MDR) cells.	92
Table 4.2.	Anti-proliferative activity of compounds **1**-**16** on human adenocarcinoma (Colo205 and Colo320) cells.	93
Table 4.3.	Cytotoxic activity (μM ± SD) of compounds **1**-**16** on mouse T-lymphoma (L5178Y-PAR and L5178Y-MDR) and mouse embryonic fibroblast (NIH/3T3) cells.	94
Table 4.4.	Cytotoxic activity (μM ± SD) of compounds **1**-**16** on human adenocarcinoma (Colo205 and Colo320) and human embryonic fibroblast (MRC-5) cells.	95
Table 4.5.	Effect of isolated compounds on P-gp mediated R123 efflux, in *MDR1*-transfected mouse T-lymphoma (L5178Y-MDR) cells.	97
Table 4.6.	Cytotoxic activity of helioscopinolide E (**15**) derivatives (**19**-**24**) on mouse T-lymphoma (L5178Y-PAR and L5178Y-MDR) cells.	100
Table 4.7.	Anti-proliferative activity of helioscopinolide E (**15**) derivatives (**19**-**24**) on mouse T-lymphoma (L5178Y-PAR and L5178Y-MDR) cells.	101

Table 4.8. Effect of helioscopinolide E (**15**) derivatives (**19**-**24**) on P-gp mediated R123 efflux, in *MDR1*-transfected mouse T-lymphoma (L5178Y-MDR) cells. 102

Table 4.9. Effect on anti-proliferative activity by methylation of the hydroxyls at position C-7 and C-4' for naringenin (**17**), sakuranetin (**46**), 4'-methoxysakuranetin (**47**) and the correspondent hydrazone (**28**, **48**, **49**). 104

Table 4.10. Effect on cytotoxic activity by methylation of the hydroxyls at position C-7 and C-4' for derivatives bearing a benzoyloxy (**41**, **60**, **61**) and 3-indolacetyl (**40**, **62**, **63**) substituent. 104

Table 4.11. Effect of naringenin derivatives (**25**-**31**, **37**-**63**) on P-gp mediated R123 efflux, in *MDR1*-transfected murine T-lymphoma (L5178Y-MDR) cells. 105

Table 4.12. Cytotoxic and anti-proliferative activity of naringenin derivatives (**64**-**71**) on mouse T-lymphoma (L5178Y-PAR and L5178Y-MDR) cells. 107

Table 4.13. Effect of naringenin derivatives (**64**-**71**) on P-gp mediated R123 efflux, in *MDR1*-transfected murine T-lymphoma (L5178Y-MDR) cells. 108

Table 4.14. Interaction type between compounds **6**, **9**, **11**, **13**, **22**, **60** and **69** with doxorubicin in L5178Y-MDR cells. 110

Table 4.15. Cytotoxic activity of naringenin (**17**) and derivatives **25**-**45** on *ABCC1*- (BHK21), *ABCB1*- (NIH/3T3), *ABCG2*-transfected (HEK293) and parental cell lines. 112

Table 4.16. Distribution percentages of the detected molecules for MRP1 and BCRP. 116

Table 5.1. Physical properties of the hydrogen bonds between PP1 and NBD2 (τ, lifetime of bond formation; ΔG, HB formation energy; $\langle N_{HB} \rangle$, average number of HB) (van der Spoel et al., 2006). 127

Table 5.2. Physical properties of the hydrogen bonds between PP2 and NBD2 (τ, lifetime of bond formation; ΔG, HB formation energy; $\langle N_{HB} \rangle$, average number of HB). 129

Table 5.3. Physical properties of the hydrogen bonds between PP3 and NBD2 (τ, lifetime of bond formation; ΔG, HB formation energy; $\langle N_{HB} \rangle$, average number of HB). 130

Table 5.4. Mapped residues for each drug-binding site. 136

Table 5.5. Contacts and hydrogen-bond statistics for each class of molecules. 157

Table 5.6. Comparison between neutral and charged molecules on protein adsorption. 159

Table 5.7. Membrane deformation energy penalty (ΔG_{def}). 164

Table 7.1. Fractions obtained from the EtOAc soluble fraction of *Euphorbia pedroi.* 178

Abbreviations

$[\alpha]_D^{20}$	Specific rotation
$[M]^+$	Molecular ion
$[M + H]^+$	Protonated molecular ion
$[M + Na]^+$	Sodium adduct ion
$^2J_{C\text{-}H}$	C-H coupling constant through two bonds
$^3J_{C\text{-}H}$	C-H coupling constant through three bonds
5-HT_{2A}	5-hydroxytriptamine receptor 2A
A_L	Area per lipid
Acetone-D_6	Deuterated acetone
ABC	ATP-binding cassete
ABCP	ABC placental
ACN	Acetonitrile
ADT1	*Arabidopsis thaliana* alcohol dehydrogenase 1
Ar, ARO	Aromatic
ATP	Adenosine triphosphate
bd	Broad duplet
bs	Broad singlet
bt	Broad triplet
BtuCD	Vitamin B12 import system permease protein
BCRP	Breast cancer resistance protein
BSA	Bovine serum albumin
cAM	Calcein-AM
c	Concentration
CmABCB1	*Cyanidioschyzon merolae* ABCB1
CI	Combination index
COSY	Correlation spectrometry
CRAC	Cholesterol-recognition aminoacid consensus
CRISP-Cas9	Clustered regularly interspaced short palindromic repeats – Cas9 endonuclease system
CSC	Cancer stem cells
CTLA4	Cytotoxic T-lymphocyte-associated protein 4
d	Doublet
DBP	Drug-binding pocket
DBS	Drug-binding sites
dd	Doublet of doublets
ddd	Doublet of doublet of doublets
DEPT	Distorsionless enhancement by polarization
D_{HH}	Membrane thickness
DMAPP	Dimethylallyl diphosphate
DMPC	Dimiristoyl-*sn*-glycero-3-phosphocholine
DMS	Dimethylsulphate
DMSO	Dimethylsulfoxide

DMSO-D_6	Deuterated dimethylsulfoxide
DoU	Degree of unsaturation
dq	Doublet of quartets
dt	Doublet of triplets
DXP	1-deoxy-D-xylulose 5-phosphate
ED_{50}	Half maximal effective dose
EDTA	Ethylenediamine tetraacetic acid
EM	Electrostatic map
EMDR	Environmental-mediated drug resistance
ESI-TOF-HRMS	Electrospray ionization time-of-flight high resolution mass spectrometry
ESI-MS	Electrospray ionization mass spectrometry
EtOAC	Ethyl acetate
Ex	Exclusion volumes
EI	Efficiency index
FAR	Fluorescence activity ratio
FL-1	Mean fluorescence intensity
FSC	Forward scatter
GGPP	Geranylgeranyldiphosphate
GSH	Glutathione
GYR	Radius of gyration
h	Heptuplet
H33342	Hoechst 33342
HBA/AC	Hydrogen-bond acceptor
HBD/DO	Hydrogen-bond donor
HMBC	Heteronuclear multiple bond correlation
HMQC	Heteronuclear multiple quantum correlation
HPLC	High performance liquid chromatography
HYD	Hydrophobic
IC_{50}	Half maximal inhibitory concentration
ICH	Intracellular helix
IPP	Isopentenyl diphosphate
IR	Infrared
J	Coupling constant
kJ	Kilojoules
K	Kelvin
log*D*	Distribution coefficient
log*P*	Octanol-water partition coefficient
LA	Lipinsky number of acceptors
LTC_4	Leukotriene C_4
m	Multiplet
m/z	Ratio of mass to charge
MalK	Maltose/maltodextrin import ATP-binding protein
Me	Methyl
MD	Molecular dynamics
MDR	Multidrug resistance

MM/PBSA	Molecular mechanics/Poisson Boltzman surface area continuum solvation
MEP	Methylerythritol phosphate
MMFF94x	Merck molecular force field 94x
MRP1	Multidrug resistance protein 1
MS	Molecular surface
MTT	3-(4,5-dimethylthiazol-2-yl)-2,5-diphenltetrazolium bromide
MTX	Methotrexate
MVA	Mevalonic acid
MW	Molecular weight
MX	Mitoxantrone
MXR	Mitoxantrone resistance protein
ns	Nanosecond
NADPH	Nicotinamide adenine dinucleotide phosphate
NBD	Nucleotide-binding domain
NMR	Nuclear magnetic resonance
NOE	Nuclear Overhauser effect
NOESY	Nuclear Overhauser enhancement spectroscopy
OAc	Acetoxy
OD	Optical density
pKa	Acid dissociation constant
ppm	Parts per million
p_i	Positional probability
P_i	Normalized probability density
P(V)	Probability volume distribution
P-gp	P-glycoprotein
PAR	Parental
PBC	Periodic boundary conditions
PBS	Phosphate buffer saline
PCA	Principal component analysis
PM3	Semi-empirical parametric method 3
PMF	Potential of mean force
POL	Polar
POPC	1-palmitoyl-2-oleoyl-*sn*-glycero-3-phosphocholine
qd	Quartet of doublets
QSAR	Quantitative structure-activity relationships
R123	Rhodamine-123
RMSD	Root mean square deviation
RMSF	Root mean square fluctuation
RR	Relative resistance
RT-PCR	Real time - Polymerase chain reaction
SAR	Structure-activity relationships
SAS	Solvent accessible area
SBS	Substrate-binding sites
SDS	Sodium dodecyl sulphate
Sav1866	*Staphylococcus aureus* multidrug ABC transporter

SD	Standard deviation
SE	Standard error
SipA	*Salmonella enterica* type III secretion effector
SSC	Side scatter
t	Triplet
td	Triplet of doublets
TLC	Thin-layer chromatography
TM	Transmembrane
TMD	Transmembrane domain
TMH	Transmembrane helix
δ	Chemical shift
Δ	Unsaturated bond
ΔG	Free energy
ΔG_{ads}	Free energy of adsorption
ΔG_{def}	Membrane deformation energy penalty
ΔG_{res}	Residual hydrophobic exposure energy penalty
δ_C	Carbon chemical shift
δ_H	Proton chemical shift
µM	Micromolar
υ_{max}	Maximum wave number
ξ	Reaction coordinate

Chapter 1

Introduction

1. Multidrug resistance in cancer

Fighting cancer has become one of the most important tasks for the healthcare systems worldwide. However, and despite all efforts in early detection and treatment, cancer incidence is expected to increase 59% until 2030 (over 300.000 new cases each year), from which 66% are predicted to decease during the course of the disease (Ferlay et al., 2015).

Although the survival rate of cancer patients is mostly determined by the location and type of cancer, early detection along with current chemotherapeutic regimens provide an effective response in cancer treatment (Hiom, 2015). Nonetheless, from the several factors that can compromise the success of chemotherapy, resistance to anticancer drugs is becoming one of the most reported topics in chemotherapy failures. It is known that cancer cell resistance to cytotoxic drugs may be inherited, already existing prior to the treatment, or acquired through selective pressure over the tumor cells during the initial rounds of treatment, from which only resistant cells survive. However, other factors as pharmaceutical (poor absorption, rapid metabolism or increased excretion), host-related (changes in the host-tumor microenvironment) or tumor-related (absence of cell surface receptors and/or transporters, drug sequestration and alteration/mutation of specific targets) also contribute for the cellular resistance to the pharmacological action of anticancer drugs (**Figure 1.1**) (Baguley, 2010; Gillet and Gottesman, 2010; Gottesman, 2002; Zahreddine and Borden, 2013).

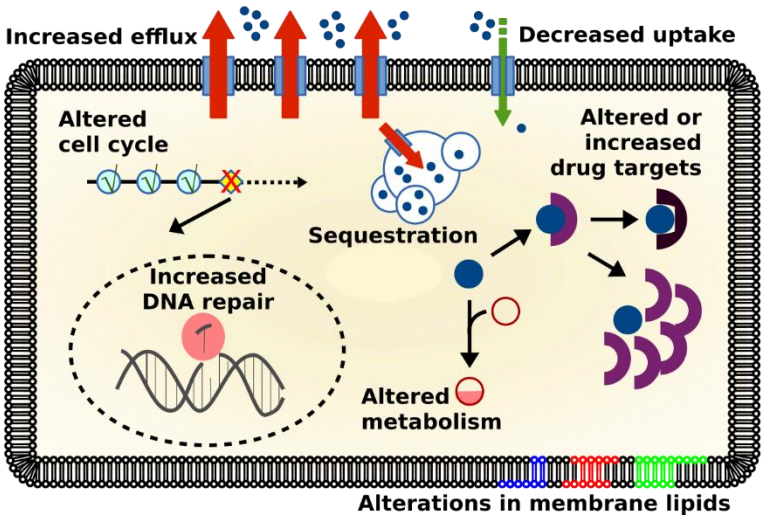

Figure 1.1. Schematic diagram of resistance to drugs (adapted from Gottesman, 2002).

Frequently, such selective pressure also induces the tumor to express one or more resistance mechanisms that, when comprising functionally and/or structurally unrelated drugs,

defines the Multidrug Resistant (MDR) phenotype. As an attempt to explain how cancer cells can develop a MDR phenotype while normal cells do not, two of the currently undergoing theories are the cancer stem cell (CSC) and the environmental-mediated drug resistance (EMDR) models. While the first one claim that small populations of cells already possess tumor-initiating properties with distinct sensibilities to the available chemotherapeutic treatments (Greenow and Clarke, 2012; Nguyen et al., 2012; Zahreddine and Borden, 2013), in the second one, cancer cells are able to interact with the surrounding environment and enter into a quiescent or dormant state to avoid chemotherapy, until being able to acquire a more permanent phenotype (**Figure 1.2**) (Housman et al., 2014; Meads et al., 2009).

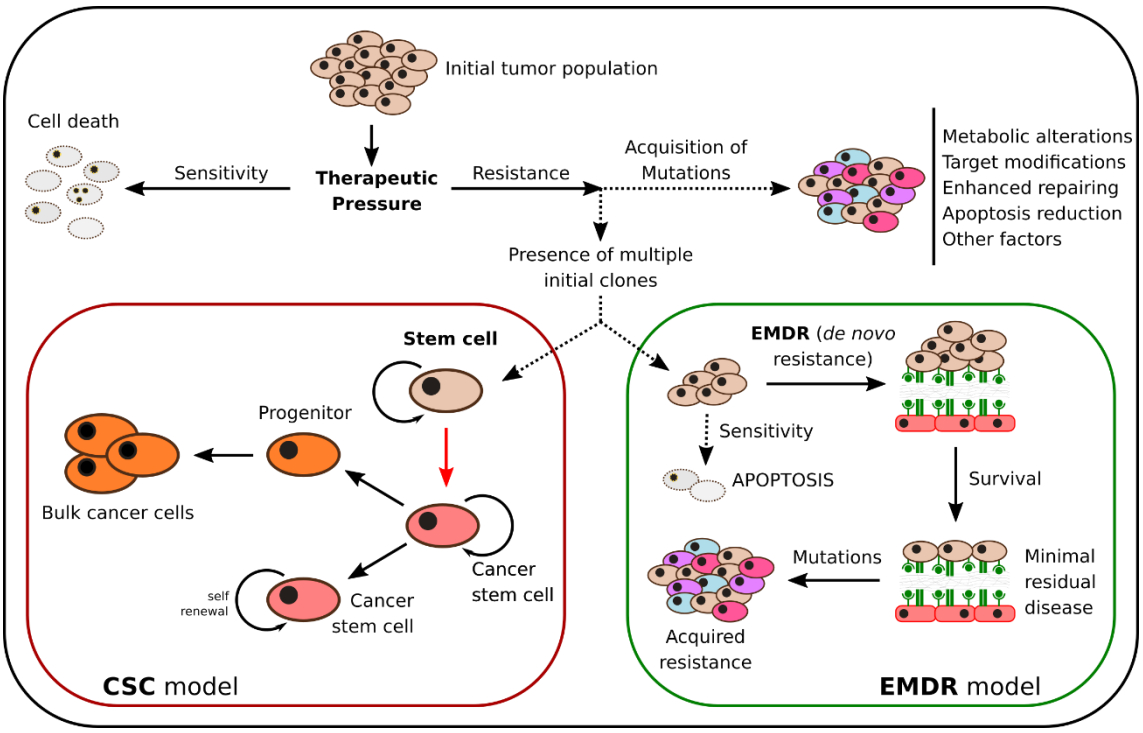

Figure 1.2. Models currently accepted for MDR onset, the cancer stem cell (CSC) and environmental-mediated drug resistance (EMDR) models (adapted from Zahreddine & Borden, 2013; Meads et al., 2009; Greenow & Clarke, 2012).

1.1. Resistance mechanisms

In both CSC or EMDR models, the molecular mechanisms by which cancer cells become resistant to chemotherapy can be classified in 'atypical' (or non-classical) or 'typical' (classical) depending on the MDR phenotype. In 'atypical' MDR, cancer cells often display alterations in the drugs' cellular targets or metabolic pathways. To that matter, increased resistance to apoptosis induction or in DNA repairing mechanisms, suppression or exacerbation of cellular

targets and drug inactivation can not only potentiate the survival of cancer cells but also induce changes in the microenvironment surrounding the tumor, leading to pH, oxygen or nutrient imbalances that compromise the effect of a given drug (Baguley, 2010; Callaghan et al., 2012; Gillet and Gottesman, 2010). Hence, while the lack of oxygen (hypoxia) in the cancer cells and/or surrounding tissues can compromise the cytotoxicity of drugs depending on the production of reactive oxygen species (as for anthracyclines), changes in the surrounding pH can also affect drug permeation of pH-sensitive drugs as *vinca* alkaloids (vinblastine and vincristine).

Oppositely, 'typical' MDR occurs when tumor resistance to anticancer drugs is mainly mediated through the over-expression of surface efflux pumps, belonging to the ATP-binding cassette (ABC) transporters, able to decrease the cytoplasmic concentration of the drug through an ATP-dependent mechanism and against its concentration gradient either by pumping drugs out of the cell or by promoting drug sequestration inside intracellular lysosomes (Seebacher et al., 2016; Yamagishi et al., 2013). Moreover, other studies demonstrated that, associated with the over-expression of ABC transporters at the cell surface, cancer cells also express these transporters at the Golgi apparatus (Gong et al., 2003), mitochondria (Fantappiè et al., 2015) and perinuclear regions (Rajagopal, 2003) and thus also contributing for the global MDR phenotype.

1.2. ABC transporters and multidrug resistance

Although with limitations, the initial studies where P-glycoprotein (P-gp, ABCB1) was found as a contributor for MDR provided the first evidences that over-expression of efflux pumps is, in fact, one of the major contributors for drug resistance in all human cancers (Gottesman and Pastan, 2015). In fact, not only P-gp (Juliano and Ling, 1976) but also the Multidrug Resistance Protein 1 (MRP1, ABCC1) (Leier et al., 1994), Breast Cancer Resistance Protein (BCRP, ABCG2) (Allikmets et al., 1998; Doyle et al., 1998; Miyake et al., 1999) and, more recently, ABCB5 in malignant melanomas (Chartrain et al., 2012; Frank et al., 2005) were found to be determinant for tumor resistance to chemotherapeutic regimens.

1.2.1. Insights on MDR-related ABC transporters

ABC transporters are ubiquitary to all organisms and are characterized by the presence of at least one *signature* (LSGGQ) motif, highly conserved among species. In the human genome,

49 ABC members are known (although only 48 seem to be functional) and can be involved not only in MDR but also in cystic fibrosis (cystic fibrosis transmembrane conductance regulator, ABCC7), intra-hepatic cholestasis (ABCB4, ABCB11), Stargardt's disease (ABCA4) and adrenoleukodystrophies (ABCD1), among others (Tarling et al., 2013). A functional transporter must comprise a minimum of two halves with two domains each: one embedded in the lipid bilayer and the other located at the cytoplasmic side of the membrane (**Figures 1.3A** and **1.3B**). Moreover, while the substrate-binding site was found to be located at the transmembrane domains (TMDs), the nucleotide-binding domains (NBDs) provide the necessary energy for drug translocation by binding and hydrolyzing adenosine triphosphate (ATP) (Callaghan et al., 2012; Dawson and Locher, 2006; Locher, 2009; Rosenberg et al., 2005). In mammals, ABC transporters exist as full- or half-transporters: whereas in full-transporters, as P-gp, both halves are linked together by a flexible polypeptide chain ('linker') that was proved to be essential for drug recognition and activity (Hrycyna et al., 1998; Sato et al., 2009), half-transporters must be assembled as hetero (ABCG5/ABCG8) (Graf et al., 2003) or homodimers (ABCG2) (**Figure 1.3A**), although other higher forms of oligomerization cannot be excluded (Wong et al., 2016; Xu et al., 2004).

While one of the most frequent TMD configuration comprises a 12-helix bundle in a 2 x 6 arrangement that can increase up to 2 x 10 helices (as in BtuCD, the B12 vitamin uptake transporter), NBDs are organized in a head-to-tail manner that upon NBD dimerization form the ATP-binding cavity at the NBD-NBD interface. At this site, the conserved Walker A (G*xx*G*x*GKS/T, where *x* is any aminoacid) and Walker B (*aaaa*DE, where *a* is any hydrophobic residue) motifs in one NBD together with the *signature* of the opposing NBD are the main responsible for binding to ATP (Callaghan et al., 2012; Ford et al., 2009; Locher, 2009). Thus, substrate binding together with ATP hydrolysis are thought to trigger conformational changes by which efflux pumps actively transport substrates that concentrate inside the cell membrane back to the interstitial lumen, according to the hydrophobic 'vacuum cleaner' model (Ferreira et al., 2015a; Higgins and Gottesman, 1992; Raviv et al., 1990).

One of the most studied ABC transporters in cancer is P-gp, an efflux pump able to transport numerous substrates as β-amyloid peptides (Kuhnke et al., 2007; Lam et al., 2001; van Assema et al., 2012), phospholipids (Eckford and Sharom, 2005; Higgins and Gottesman, 1992; Orlowski et al., 2006), steroids (Clay et al., 2015; Garrigues et al., 2002) and hormones (Kwon et al., 1996; Shapiro et al., 2001) but also structurally unrelated compounds as anticancer

drugs. Physiologically, P-gp is found at the apical surface of kidney proximal tubule cells, canalicular membrane of hepatocytes, villous intestinal cells and blood-tissue barriers as the brain, placenta and testis, where it is thought to participate in cellular detoxification pathways (Borges-Walmsley et al., 2003; Sharom, 2011). Together with MRP1 and BCRP, P-gp is considered to have a central role in MDR.

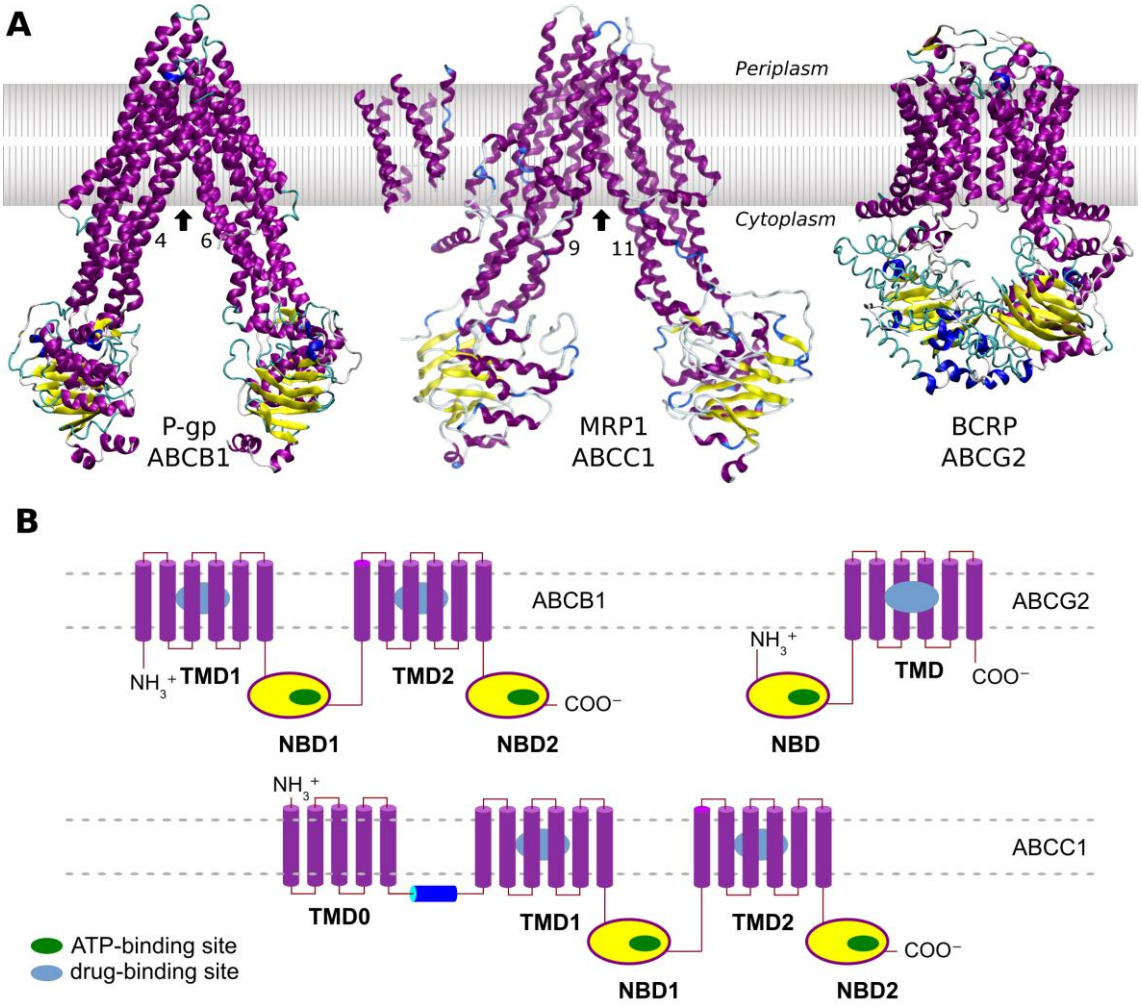

Figure 1.3. (A) Crystallographic structure of P-gp, (left), MRP1 (middle) and BCRP (right) ABC transporters, with the indication of hypothetical "entrance gates" (black arrow); (B), membrane topology models of P-gp, BCRP and MRP1 transporters, with indication of drug- and ATP-binding sites. Images were obtained from PDB ID: 4Q9H, 5UJ9 and 5NJ3, respectively, available in Protein Data Bank.

Regarding the other transporters, MRP1 was initially identified in a H69AR cell line resistant to multiple cytotoxic compounds where no P-gp expression could be detected (Cole et al., 1992), but now its occurrence in hematological malignancies (acute myeloblastic and acute lymphoblastic leukemia), solid cancers (non-small cell lung, prostate and some breast cancers) and neuroblastomas identified MRP1 as a poor indicator for the therapeutic response and

clinical outcome. This protein is localized in basolateral membranes of polarized cells and, although sharing some degree of substrate overlapping with P-gp, its endogenous substrates are known to be negatively charged molecules alone or conjugated with glutathione (GSH), glucuronide, or sulfate groups (Cole, 2014a, 2014b). BCRP, also known as mitoxantrone resistance protein (MXR) (Miyake et al., 1999) or ABCP transporter (Allikmets et al., 1998), is a half-transporter identified for the first time on a MCF-7/AdrVp breast cancer cell line showing 900-fold resistance to doxorubicin when compared with parental cells, while having normal glutathione levels and no P-gp expression (Doyle et al., 1998). It is a functionally obligated homodimer that is mainly expressed in the gastrointestinal tract, placenta, blood–brain barrier and stem cells, acting as a first line of defense against toxicity (Mo and Zhang, 2012). In cancer, is more often found in hematopoietic and solid tumors. More recently, another member of the ABCB family, ABCB5, was also found to be intimately related with increased resistance to anthracyclines and taxanes (Frank et al., 2005; Kawanobe et al., 2012; Keniya et al., 2014) not only in melanomas but also in malignant melanoma-initiating stem cells (Murphy et al., 2014). Therefore, impairing the activity of such transporters in cancer cells is considered to be an attractive strategy to increase the success rates of chemotherapeutical regimens. Accordingly, in 2012 the Food and Drug Administration published new industry guidelines in which "all investigational drugs should be evaluated *in vitro* to determine whether they are a potential substrate of P-gp or BCRP" and that "evaluation of investigational drugs as inhibitors for these transporters should be conducted" (FDA, 2012).

1.2.2. MDR modulation by innovative strategies: past, present and beyond

Since the discovery that non-cytotoxic verapamil concentrations were able to revert resistance to vincristine in P388 leukemia cells (Tsuruo et al., 1981) that targeting P-gp with small molecules has been seen as a promising approach for reversing MDR (**Figure 1.4**). Toward that end, three generations of MDR modulators were developed so far (**Figure 1.5**). The *first generation* included compounds with distinct pharmacological actions as calcium channel blockers (Tsuruo et al., 1981), immunomodulators (Twentyman et al., 1987) or antiarrhythmic drugs (Tsuruo et al., 1984). However, their low affinities towards P-gp and its toxicity due to the high concentrations needed *in vivo* led to the development of similar analogues without intrinsic activity.

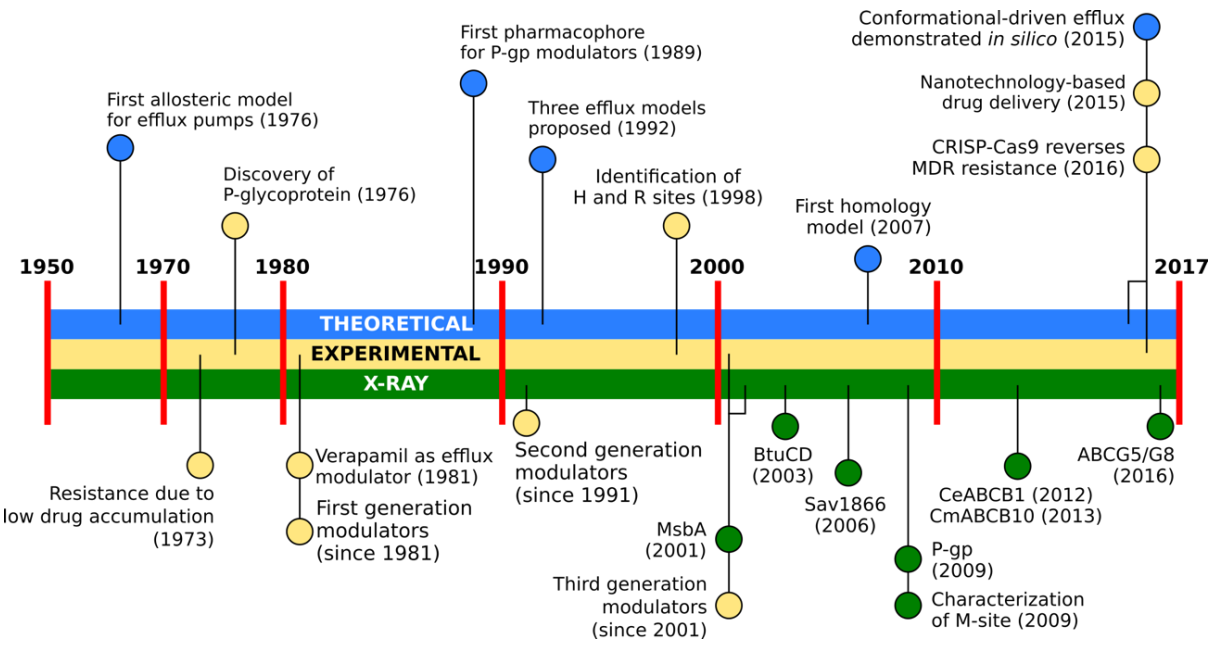

Figure 1.4. Timeline for MDR modulation strategies.

Compounds as dexniguldipine (Reymann et al., 1993), dexverapamil (Höllt et al., 1992), valspodar (Twentyman and Bleehen, 1991) or biricodar (Peck et al., 2001) are included in the *second generation* of MDR modulators (**Figure 1.5**), and although more selective, no further studies were performed due to major toxic side effects and alterations in drugs pharmacokinetic profiles (Palmeira et al., 2012b). The *third generation*, however, relied on quantitative structure-activity relationships (QSAR) and high throughput screening/combinatorial chemistry to increase the selectivity and potency of P-gp modulators up to the nanomolar range (Hyafil et al., 1993). Compounds as tariquidar (Martin et al., 1999), laniquidar (van Zuylen et al., 2000), zosuquidar (Dantzig et al., 1996) and elacridar (Hyafil et al., 1993) are within the most potent MDR modulators with no relevant toxicity towards cytochrome P450 enzymes, but also failed to provide good *in vivo* results when co-administered with cytotoxic drugs. Nowadays, the development of small molecules for MDR modulation is still undergoing, either by the development of new MDR modulators (Emmert et al., 2014; Gao et al., 2016; Krawczyk et al., 2015; Li et al., 2015; Zhang et al., 2016), by specifically targeting the ATP-binding site (Brewer et al., 2014; Follit et al., 2015) or by targeting allosteric sites at the NBDs (Kim et al., 2010; Shahraki et al., 2017).

At present, some of the most recent approaches to circumvent MDR relies on nanotechnology and advanced drug delivery systems able to carry drugs, nucleic acids or drug-conjugates directly into the cells without interference of efflux pumps.

First generation P-gp modulators

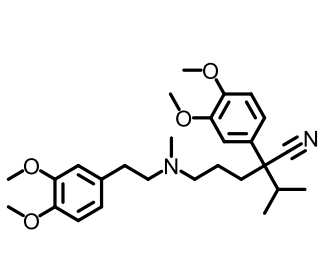

verapamil

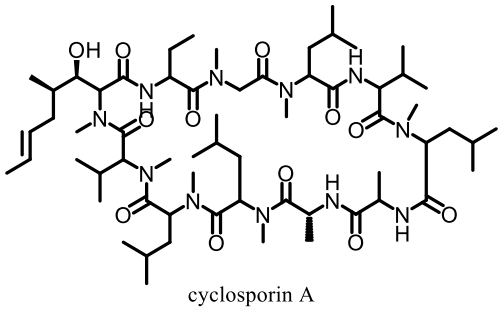

cyclosporin A

Second generation P-gp modulators

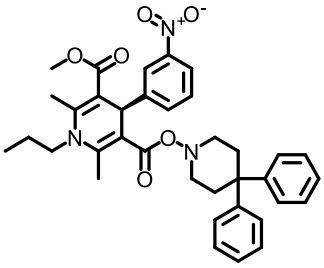

dexniguldipine

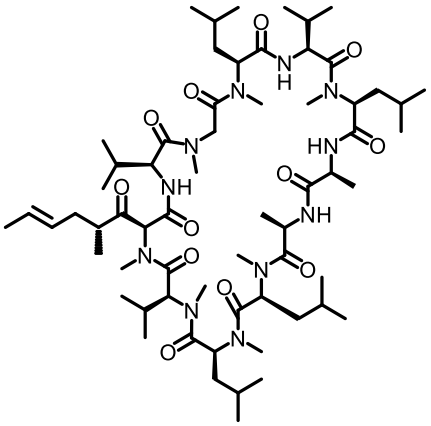

valspodar

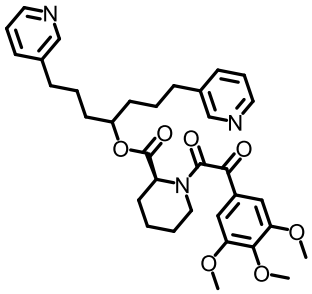

biricodar

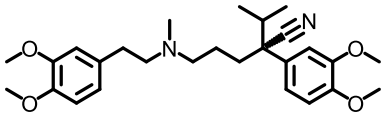

dexverapamil

Third generation P-gp modulators

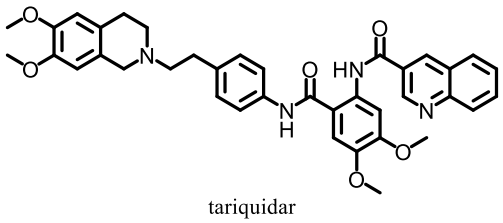

tariquidar

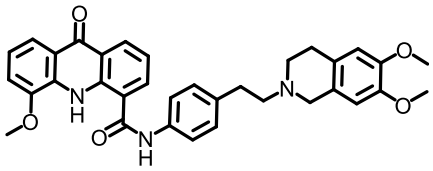

elacridar

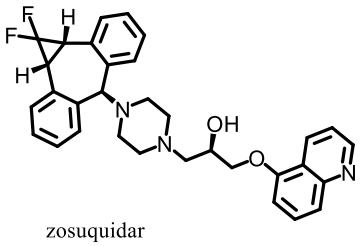

zosuquidar

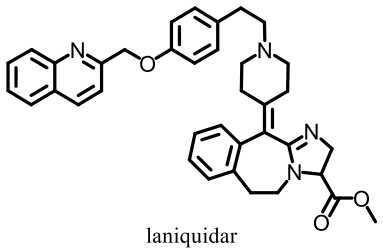

laniquidar

Figure 1.5. Molecules from the three generations of P-gp inhibitors.

Rhodamine-123 accumulation within MDR cells was greatly increased using poly(dichloro-phosphazene) as a drug carrier (Qiu et al., 2012) or by encapsulating them in sphingomyelin-rich liposomes (Zembruski et al., 2013), lipid-functionalized dextran-based nanosystems (Kobayashi et al., 2013), micellar systems with endolysosomal escape properties (Qiu et al., 2014) or multifunctional DNA nanoflowers (Mei et al., 2015). These systems can be used with the drug alone or, additionally, be used to deliver *second* and *third generation* modulators (Singh and Lamprecht, 2014) or siRNAs (Chen et al., 2014; Kobayashi et al., 2013) together with the cytotoxic drug to decrease the required dosages and overall toxicity. Quite interestingly, the usage of gold nanoparticles carrying SipA, a *Salmonella enterica* type III secretion effector, was also used to modulate MDR by decreasing P-gp expression, both in *in vitro* and *in vivo* experiments (Mercado-Lubo et al., 2016).

New technologies, however, are emerging as powerful techniques that can be used in a near future against efflux-related MDR cancers. The recent publication of another crystallographic structure unveiled the development of a new specific and highly potent P-gp modulator, aCAP, tailored as a cyclic peptide that clamped a eukaryotic P-gp homologue (Cm*ABCB1*) in its inward-facing state, as shown by the inhibition of both basal and rhodamine-6G stimulated ATPase activity (Kodan et al., 2014). Interestingly, network analyses of gene expression data between chemotherapy responsive versus non-responsive tumors is also becoming a suitable technique to identify synergisms between drugs that can improve the effectiveness of chemotherapy, a method already proved valid for AB1-HA mesothelioma tumors expressing the CTLA4 cytotoxic T lymphocyte antigen (Lesterhuis et al., 2015). Other approaches may also include the production of reactive oxygen species by specialized photodynamic therapy (Cen et al., 2016; Yu et al., 2016), targeting specific immunoglobulins in order to reduce P-gp expression (Somno et al., 2016) or the utilization of advanced genomic editing techniques as CRISP-Cas9 to knockdown P-gp expression in highly resistant tumors (Simoff et al., 2016; Yang et al., 2016), in order to re-sensitize them to chemotherapy.

1.3. Natural products as a new generation of MDR modulators

In traditional medicine, plants and plant extracts are commonly used to treat all sorts of diseases, from the common cold up to warts, skin affections, infections or cancer (Wink, 2010). As such, many compounds were first isolated from natural sources and used to develop drugs that could be specifically used in some diseases, from which salicylic acid, morphine and quinine are

classical examples. For the treatment of cancer, hemi-synthetic derivatives etoposide and teniposide (podophyllotoxin, *Podophyllum peltatum*), paclitaxel (*Taxus brevifolia*) or vinblastine/vincristine (*Catharanthus roseus*) are some of the most important anticancer drugs currently in use (Wink, 2010). Similarly, plants are also important sources for the isolation of novel scaffolds for reversing MDR. Reserpine, an indole alkaloid, was one of the first naturally-occurring compounds that was found to modulate MDR in human leukemic multidrug resistant (CEM/VLB_{100}) cell, allowing for the first time the identification of structural features directly correlated with efflux modulation (Pearce et al., 1989; Zamora et al., 1988). Since reserpine, many other compounds as lignans, flavonoids, alkaloids and terpenoids were found to also modulate P-gp efflux (Beck et al., 1988; Conseil et al., 1998; Ferreira et al., 2014; Palmeira et al., 2012a; Zeino et al., 2015). The following sections will focus on terpenoids as MDR reversers.

1.3.1. Diterpenes from *Euphorbia* species

The *Euphorbia* genus (Euphorbiaceae) are characterized by not only by its worldwide distribution but also by its morphological variability. Subdivided in four major subgeneric groups through extensive phylogenetic studies, *Euphorbia* species are found as herbs, shrubs or cactus-like forms, in which a wide variety of secondary metabolites have been identified due to traditional usage of plant extracts as laxative, anticancer, antibacterial and antiviral activities (Ernst et al., 2015; King et al., 2014; Vasas and Hohmann, 2014). Herein, multidrug resistance reversal activities described for *Euphorbia* species are mostly due to the presence of diterpenes, a large family of compounds in which these species are particularly abundant. Until now, more than 650 diterpenes have been isolated form this genus and, quite interestingly, many of the identified scaffolds could only be found in this particular genus (Shi et al., 2008; Vasas and Hohmann, 2014).

The most common diterpenic scaffolds found in the *Euphorbia* genus are the casbane, daphnane, tigliane, ingenane, jatrophane, lathyrane, paraliane, pepluane, myrsinane, premyrsinane and cyclomyrsinane. Nonetheless, other scaffolds as rosane, *ent*-abietane, atisane and *ent*-kaurane have also been isolated from these plants (Shi et al., 2008; Vasas and Hohmann, 2014) and it cannot be excluded that unknown scaffolds may still exist in unstudied species within this genus (**Figure 1.6**).

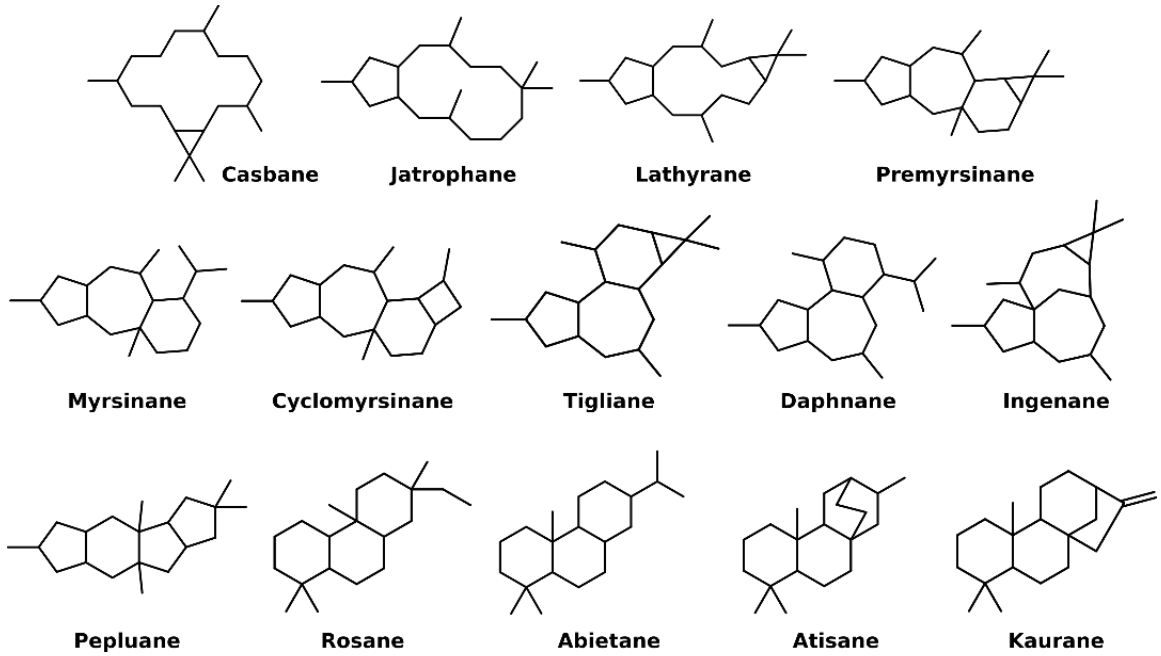

Figure 1.6. Diterpenic scaffolds isolated from *Euphorbia* species.

Diterpenes are a subset of a larger family, the terpenoids (also named isoprenoids), derived from C_5 isoprenic units arranged in head-to-tail in order to create monoterpenes (C_{10}), sesquiterpenes (C_{15}), diterpenes (C_{20}), sesterterpenes (C_{25}), triterpenes (C_{30}), sesquarterpenes (C_{35}, still not found in the *Euphorbia* genus) (Sato, 2013) and tetraterpenes (C_{40}). The basic isoprenoid units, dimethylallyl diphosphate (DMAPP) and isopentenyl diphosphate (IPP), are originated from two independent metabolic pathways: the mevalonic acid (MVA) and the methylerythritol phosphate (MEP) pathways, the latter also known as the 1-deoxy-D-xylulose 5-phosphate (DXP) pathway (**Figure 1.7**). As MVA is more prevalent in the cytosol, sesquiterpenes and triterpenes are herein synthetized while the remaining ones are originated mainly in the plastids, where the MEP pathway is predominant (**Figure 1.7A**). Following, IPP isomerization by IPP isomerase yields DMAPP, a substrate used by prenyltransferases for chain elongation through a head-to-tail manner until the formation of geranylgeranyldiphosphate (C_{20}, GGPP), the main precursors in diterpenoid metabolism. The final cyclization step is catalyzed by several enzymes as casbene, taxadiene, *ent*-copalyl diphosphate and abietane synthases identified so far (**Figure 1.7B**) (Barriault, 2016; Tholl, 2015).

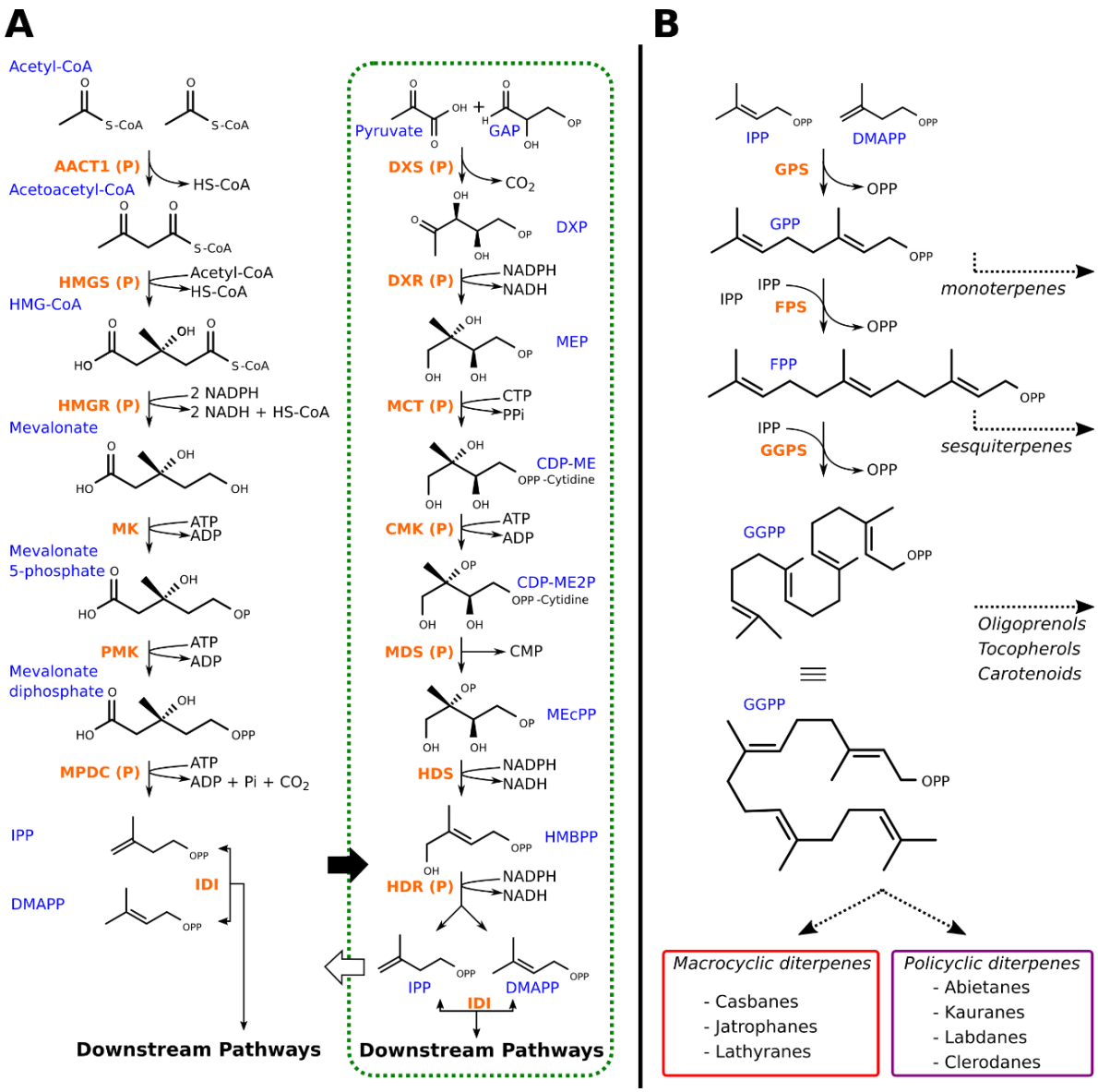

Figure 1.7. (A) Enzymatic steps of the MVA and MEP pathways (green contour refers to plastids); (B) Biosynthetic pathway for several intermediates involved in the diterpenic scaffold synthesis, from IPP and DMAPP (adapted from Tholl, 2015; Zografos, 2016).

In all diterpenes derived from casbene (jatrophanes, lathyranes, tiglianes, daphnanes and ingenanes), the ionization of GGPP due to OPP loss is catalyzed by the casbene synthase, generating a 14-membered ring system that by a loss of a proton and subsequent formation of a cyclopropane ring yields 1*S*,3*R*-casbene. Recent studies identified that region specific oxidations on the casbene scaffold are indeed performed by two cytochrome P450 from the CYP71 clan (CYP71D445 and CYP7126A27 at positions 9 and 5, respectively) and that, together with an alcohol dehydrogenase (ADT1), a 6-hydroxy-5,9-diketocasbene could act as

an intermediate leading to the subsequent rearrangements and cyclization towards macrocyclic and polycyclic diterpenoids (**Figure 1.8**) (King et al., 2016; Luo et al., 2016).

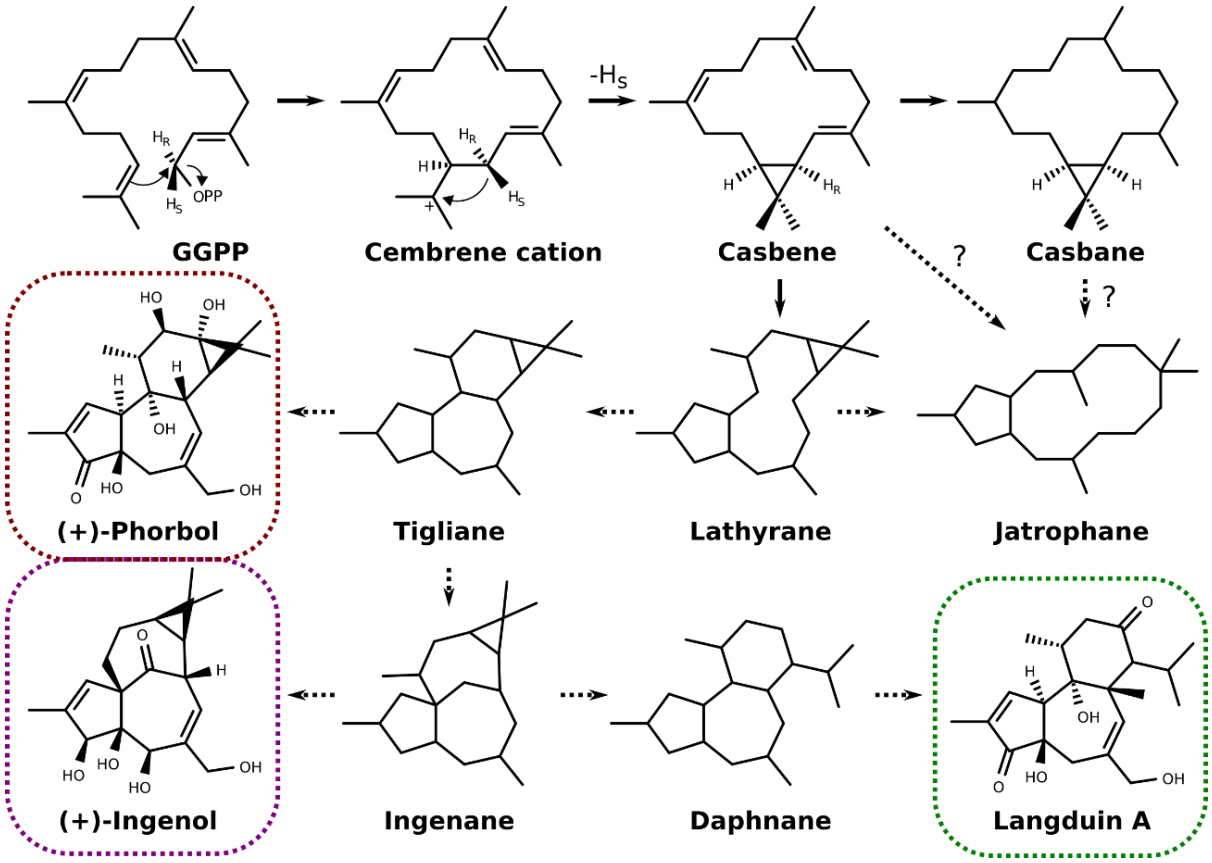

Figure 1.8. Biosynthesis of casbene, postulated biosynthesis of some complex members of deterpenoids and examples for the tigliane, ingenane and daphnane scaffolds (adapted from Zografos, 2016).

Similarly, it is also known that i) in the presence of abietadiene synthase, a proton-triggered cyclization cascade yields the formation of a copalyl diphosphate intermediate, with the loss of OPP inducing a C_{13}-C_{17} cyclization followed by a methyl shift between C_{13} and C_{14} to render the abietane scaffold and ii) GGPP also undergoes a similar cyclization cascade followed by a C_9-C_{15} σ bond formation, a C_{12}-C_{14} methyl shift and by the loss of a proton to yield *ent*-kaur-16-ene as the final product, in this case catalyzed by *ent*-kaurene syntases A and B (**Figure 1.9**) (Zografos, 2016). At last, as many diterpenes are frequently isolated as polyesters, the BAHD acyltransferases superfamily are the enzymes thought to mediate the acylation process in the *Euphorbia* genus (BAHD is named according to the first letter of each of the first four characterized enzymes of this family: Benzylalcohol *O*-acetyltransferase, BEAT; *O*-hydroxycinnamoyltransferase, AHCT; *N*-hydroxycinnamoyl/benzoyltransferase, HCBT; and deacetylvindoline 4-*O*-acetyltransferase, DAT) (King et al., 2014).

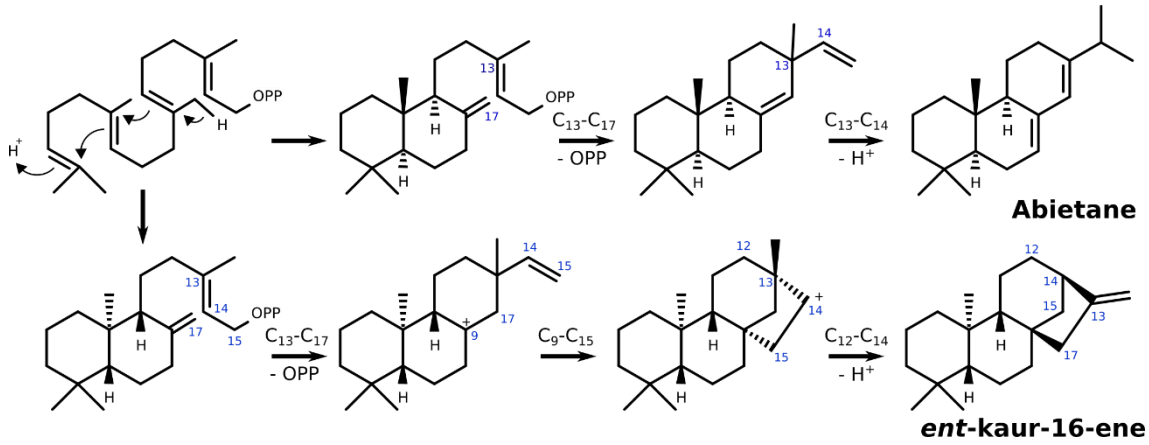

Figure 1.9. Biosynthesis of abietanes, and *ent*-kaurane diterpenes (adapted from Zografos, 2016).

1.3.2. MDR reversal and cytotoxic activities of diterpenic scaffolds

Concerning the identification of novel diterpenes from *Euphorbia* species, several comprehensive reviews were recently published (Ferreira et al., 2014; Vasas and Hohmann, 2014). Thus, in the following section the most recently isolated structures of novel diterpenic compounds, together with their activities (2014-2017), are presented in additional detail.

1.3.2.1. Jatrophanes

Jatrophanes and lathyranes are two of the scaffolds more frequently isolated from *Euphorbia* that have shown significant potencies in reversing MDR due to P-gp overexpression. Jatrophanes are thought to be formed either from the cembrene cation or, alternatively, by ring opening from a casbene precursor (Evans and Taylor, 1983). They are characterized by a 5:12 fused ring system and a variable oxidation pattern, in which the position of the double bonds and acylation pattern of oxygen functions renders them an unusual structural variability. In the following figures (**1.10** and **1.11**), examples of the most recently described jatrophane-type diterpenes from *Euphorbia cissiparias*, *E. welwitschi* and *E. tithymaloides* are presented, together with the reported activities as MDR reversal agents.

E. cyparissias

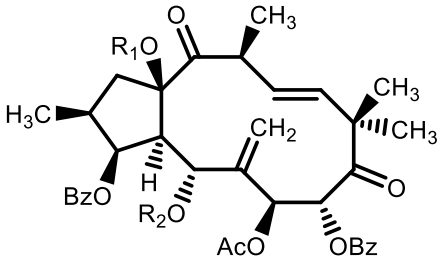

I.1. R_1 = Ac, R_2 = H
I.2. R_1 = H, R_2 = Ac

MDR reversal activity (Lanzotti et al., 2015):

Weak P-gp inhibition for **I.1** (8.55 ± 3.21 μM) and **I.2** (8.72 ± 3.45 μM)

Significant concentration-dependent cytotoxic activity has been observed for both **I.1** and **I.2** in A2780 ADR cells.

E. welwitschii

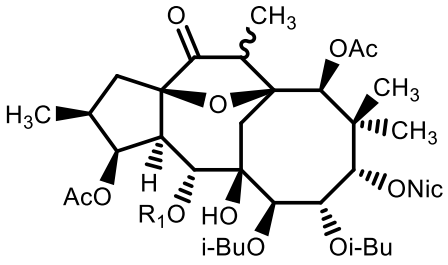

I.3. R_1 = Ac; 20α
I.4. R_1 = H; 20β

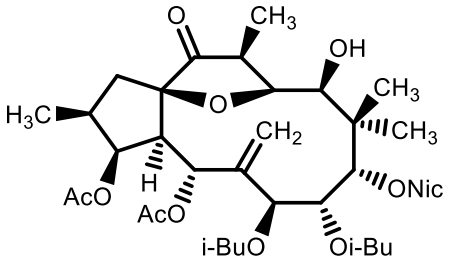

I.5.

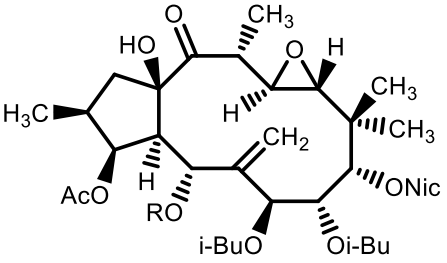

I.6.

MDR reversal activity (Reis et al., 2016):

Antiproliferative activity in EPG85-257RDB:
I.5. IC_{50} = 17.2 ± 1.6 μM, RR = 0.6
I.6. IC_{50} = 3.6 ± 0.3 μM, RR = 0.1

Antiproliferative activity in EPP85-181RN:
I.6. IC_{50} = 21.3 ± 2.5 μM, RR = 0.7

Antiproliferative activity in EPP85-181RNB:
I.6. IC_{50} = 18.2 ± 3.1 μM, RR = 0.6

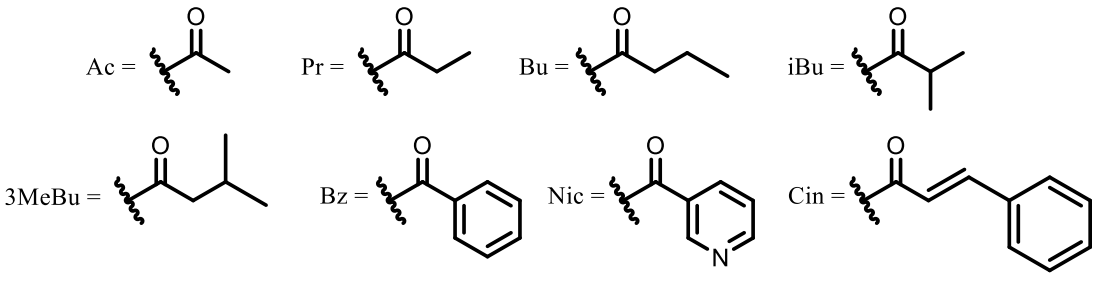

Figure 1.10. Diterpenes with a jatrophane scaffold.

E. tithymaloides

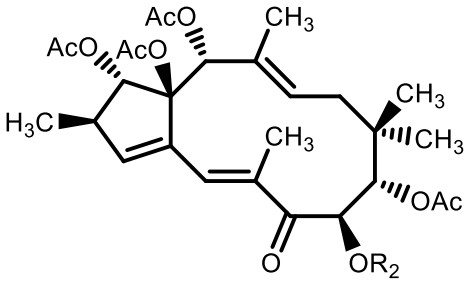

I.7.

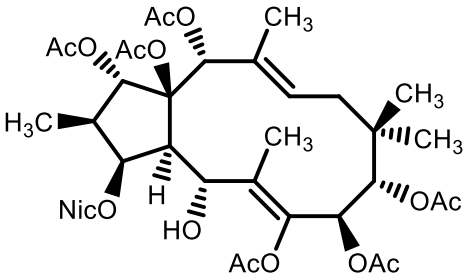

I.8.

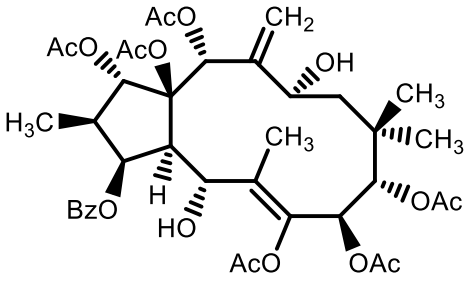

I.9.

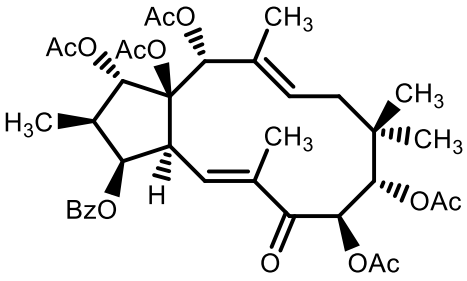

I.10.

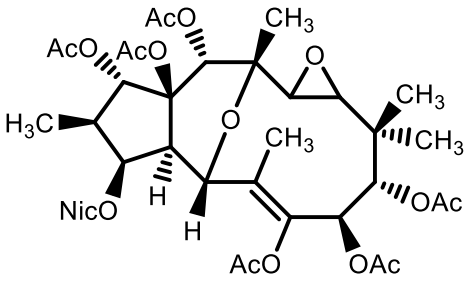

I.11.

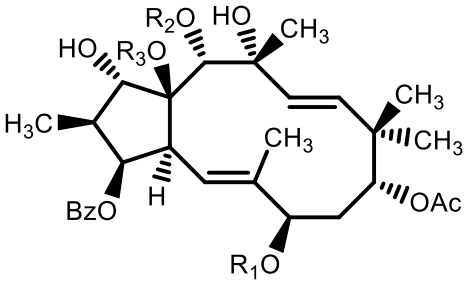

I.12. $R_1 = R_3 = Ac$, $R_2 = H$
I.13. $R_1 = H$, $R_2 = Bz$, $R_3 = Ac$
I.14. R_1 Bz, $R_2 = R_3 = H$

MDR reversal activity (Zhu et al., 2016):

I.10 - I.14, more potent inhibitors of R123 efflux inhibition that of tariquidar at 10 μM;
I.10 - I.14, dose-dependent and greater activity than that of verapamil at equal concentrations;
I.10, comparable effect on R123 efflux inhibition that of tariquidar at 1 μM;

Figure 1.11. Diterpenes with a jatrophane scaffold.

1.3.2.2. Lathyranes

Lathyranes are similar to jatrophanes in their structural variability and oxidation pattern but, as the cyclopropane unit in casbene precursor is maintained, they are characterized by a tricyclic 5:11:3 fused ring system in which positions 9 and 11 are usually non-oxidized. Lathyranes often display variable MDR reversal activities when compared with jatrophanes, which can be related to a less degree of structural flexibility due to the presence of the highly-constrained cyclopropane unit. Below (**Figures 1.12** and **1.13**) are examples of recently described lathyranes.

E. boetica

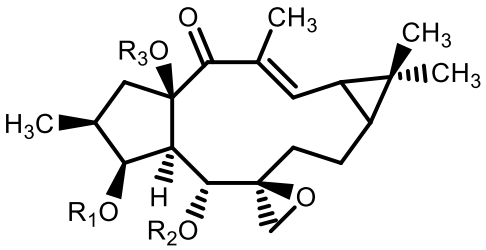

I.15. $R_1 = R_2 = R_3 = Ac$
I.16. R_1 = 3-MeBu, $R_2 = R_3 = Ac$
I.17. R_1 = Pr, $R_2 = R_3 = Ac$
I.18. R_1 = Bu, $R_2 = R_3 = Ac$
I.19. R_1 = Bz, $R_2 = R_3 = Ac$

MDR reversal activity (Vieira et al., 2014):

No significant intrinsic cytotoxicity in L5178Y cells:
MDR: $IC_{50} > 40$ μM
PAR: $IC_{50} > 30$ μM

I.18 was a strong R123 efflux modulators at 2.0 μM;
I.19 found to be a very strong modulator at 2.0 μM;

E. piscatoria

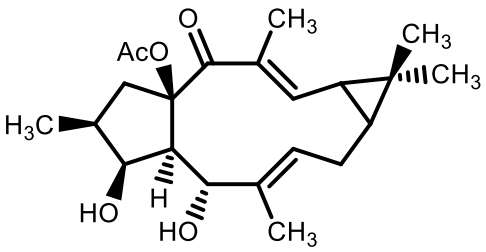

I.20

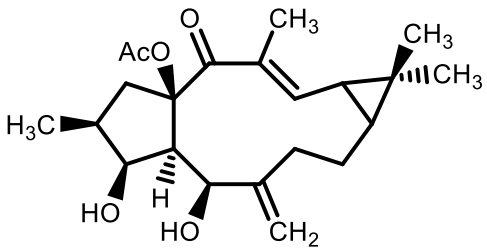

I.21

Drug combination assay (Reis et al., 2014):

I.20 (synergism) and **I.21** (strong synergism) with doxorubicin in L5178Y-MDR mouse cells.

Figure 1.12. Diterpenes with a lathyrane scaffold.

E. macrorrhiza

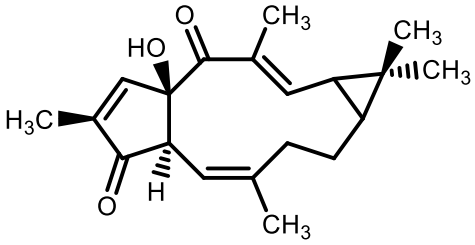

I.22

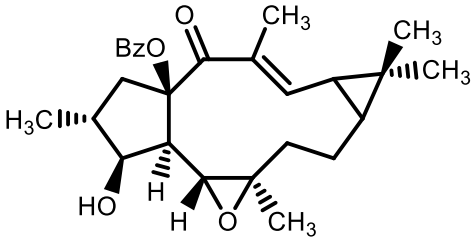

I.23

MDR reversal activity (Gao et al., 2016):

I.23 found to be a very strong P-gp-mediated drug efflux in KBv200 cell line, with no significant citotoxicity against KB or KBv200 cell lines;
I.23 potentiates the cytotoxic action of navelbine against KBv200 cells.

E. soongarica

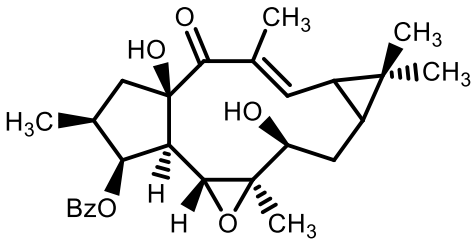

I.24

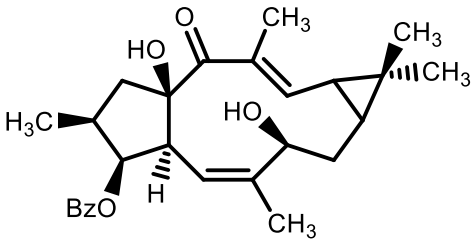

I.25

MDR reversal activity (Gao et al., 2017):

I.24 and **I.25** do not inhibit P-gp-mediated drug efflux in KBv200 cells;
I.25 showed moderate citotoxicity in KB (21.4 μM) and KBv200 (20.6 μM) cell lines;

Figure 1.13. Diterpenes with a lathyrane scaffold.

1.3.2.3. Premyrsinanes, myrsinanes and euphoractins

The known three types of myrsinane diterpenoids (myrsinanes, premyrsinanes and cyclomyrsinanes), are derived from epoxylathyranes and are characterized by a 5/7/6 common scaffold (**Figures 1.14, 1.15 and 1.16**). While the opening the 5,6-epoxide moiety followed by the formation of a 6/12 carbon bridge originates the premyrsinane skeleton, the latter are synthetized through i) the protonation of an hydroxymethyl moiety, which leads to a dehydration step followed by the cyclopropane ring opening (myrsinanes) or ii) by a

nucleophilic attack of a water molecule followed by a C-C bond migration, to originate a cyclobutane ring (cyclomyrsinanes). Similarly, euphoractins are closely related with myrsinanes and also derive from epoxylathyranes, but in this case the 5/6/7/3 fused ring system results from epoxy opening, followed by a 6,13 carbon bridge together with an addition of oxygen in position 12 (**Figure 1.14A**) (Shi et al., 2008). Some examples of premyrsinanes and euphoractins isolated from *Euphorbia macrorrhiza*, *E. prolifera* and *E. soongarica* are depicted in **Figure 1.15** and **Figure 1.16**.

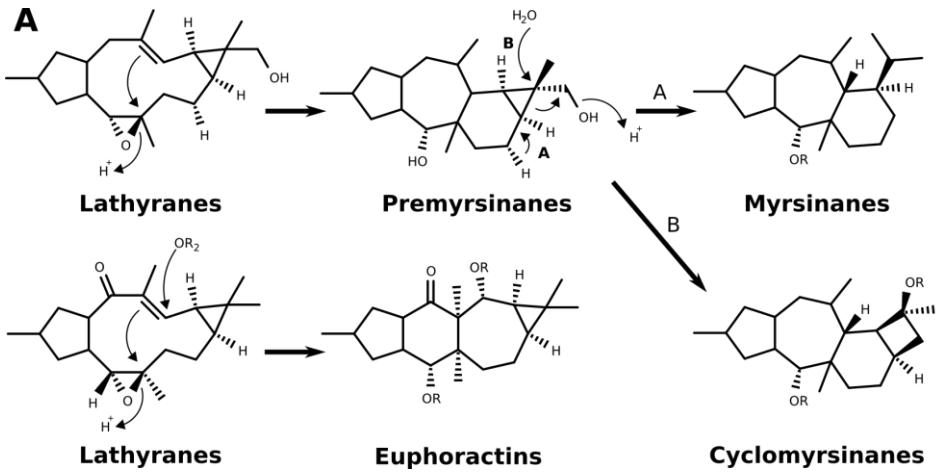

Figure 1.14. (A) Proposed biosynthesis of myrsinanes and euphoractins from epoxylathyranes (adapted from Shi et al., 2008).

E. macrorrhiza

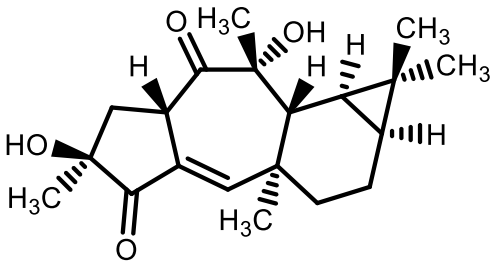

I.26

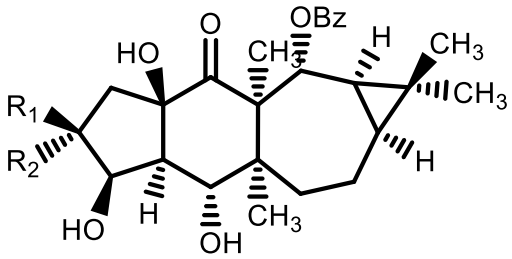

I.27. $R_1 = H$, $R_2 = CH_3$
I.28. $R_1 = CH_3$, $R_2 = H$

MDR reversal activity (Gao et al., 2016):

Moderate MDR reversal activities in KBv200 cell line for **I.27** and **I.28**;
Weak cytotoxic activity (IC_{50}, 20 - 30 μM) for **I.27** and **I.28**.

Figure 1.15. Diterpenes with premyrsinane and euphoractin scaffolds.

E. prolifera

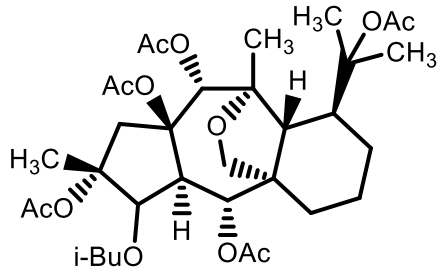

I.29

MDR reversal activity (Chen et al., 2016):

I.29 inhibit P-gp mediated fluorescent dye export in a concentration-dependent manner (0.39 - 50 μM);
I.29 at non-cytotoxic concentrations decreased the IC_{50} of daunorubicin, vincristine and topotecan in MCF7-Adr cells.

E. soongarica

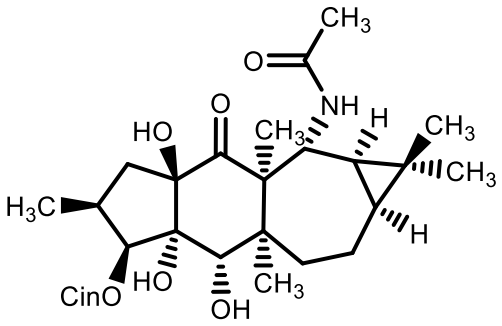

I.30

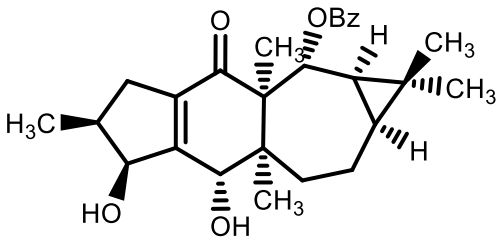

I.31

MDR reversal activity (Gao et al., 2017):

I.30 and **I.31** showed moderate P-gp mediated drug efflux inhibition properties (at 10 μM);
I.31 was moderately cytotoxic for KB (13.5 μM) and KBv200 (16.1 μM) cell lines.

Figure 1.16. Examples of premyrsinanes and euphoractins.

1.3.2.4. Other diterpenes

Although the above scaffolds have proven to be the most active ones in P-gp efflux modulation, there are reports on the MDR reversal activity of diterpenes with different scaffolds. To that matter, cembrenes, kauranes or atisanes are the most commonly isolated, although other types as jatropholane-type diterpenes (Duarte and Ferreira, 2007; Gao and Aisa, 2017), rearranged jatrophanes (Madureira et al., 2006, 2004) or diterpenic lactones (Fei et al., 2016) were also identified. Some of the latest described diterpenes (2016-2017) from *Euphorbia macrorhiza*, *E. fischeriana*, *E. stracheyi*, *E. soongarica* and *E. kansui* are presented in **Figure 1.17**.

E. macrorrhiza

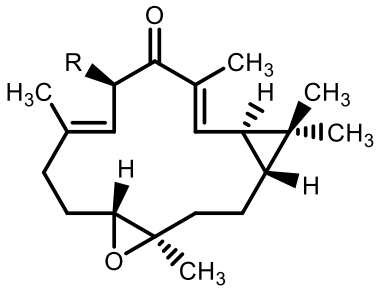

I.28. R = H
I.29. R = OH

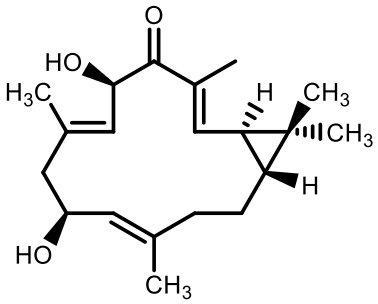

I.30

MDR reversal activity (Gao et al., 2016):

Weak P-gp efflux modulators in KBv200 cell line; weak cytotoxic activity (IC_{50}, 20 - 30 μM) for **I.28**.

E. fisheriana

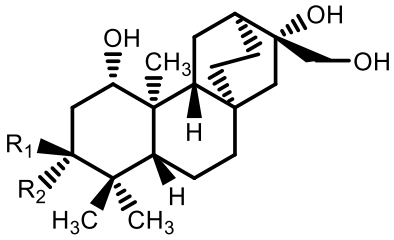

I.31, R_1 = H, R_2 = OH
I.32, R_1 = OH, R_2 = H

Citotoxicity (Wang et al., 2016):

I.31 and **I.32** with IC_{50} levels of 23.21 and 15.42 μM in human MCF-7 cell line;

E. stracheyi

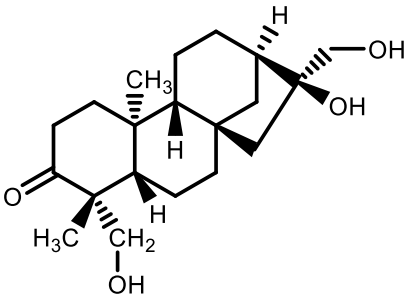

I.33

Citotoxicity (Liu et al., 2017):

No inhibitory effect (IC_{50} > 40 μM)against A-549, SMMC-7721, HL-60, MCF-7 and SW-480 cell lines;

E. soongarica

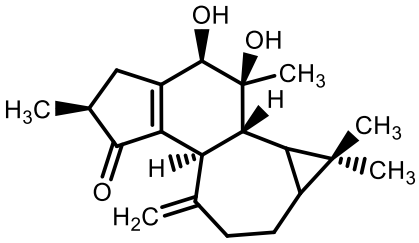

I.34

MDR reversal activity (Gao et al., 2017):

Absence of P-gp inhibition in human KBv200 cell line;

E. kansui

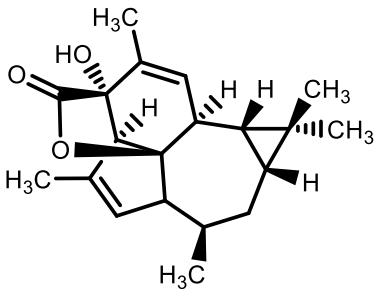

I.35

Citotoxicity (Liu et al., 2017):

Similar cytotoxicity as etoposide in HeLa and NCI-446 cell lines;

Figure 1.17. Examples of diterpenes with other reported scaffolds.

1.3.3. Triterpenes and flavonoids in multidrug resistance

Other scaffolds were also identified as MDR reversal agents, with the large majority acting as P-gp efflux modulators. Triterpenes (**Figure 1.18**) are synthesized from isopentenyl pyrophosphate, with a 30-carbon squalene acting as intermediate in cyclization reactions by members of the oxidosqualene cyclase family (Yan et al., 2014).

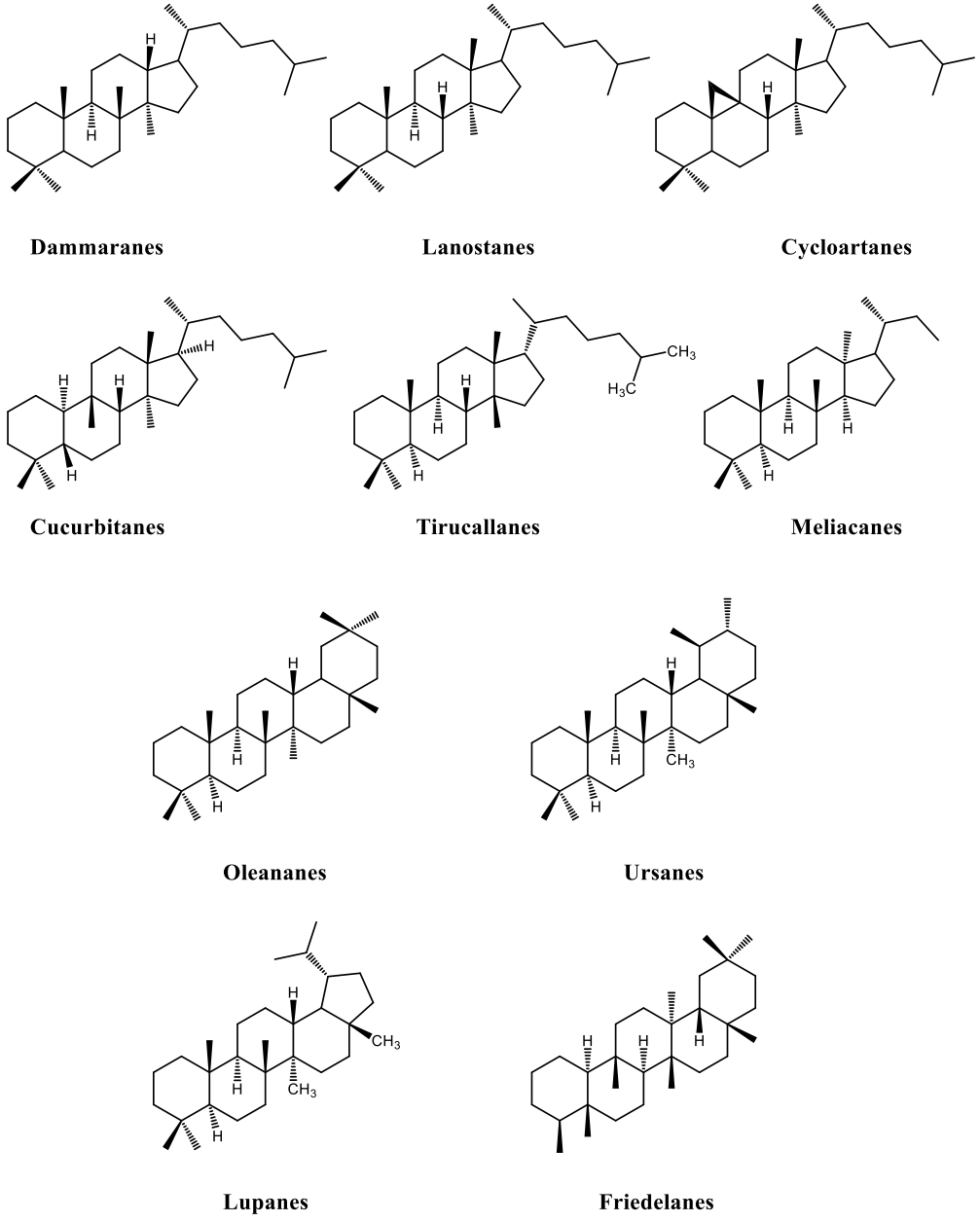

Figure 1.18. Chemical classifications and core structures of triterpenes (adapted from Yan et al., 2014).

As for to diterpenes, triterpenes are also considered as potential anticancer agents due to their chemopreventive and antigenotoxic effects. It has been reported that triterpenes possess,

besides their ability to inhibit efflux pumps, other effects as pro-apoptotic, anti-proliferative, anti-angiogenesis and gene expression modulation. As MDR reversers, while pentacyclic triterpenes demonstrated to be cytotoxic in leukemia cell lines with little or none P-gp modulation activity, cycloartanes and cucurbitanes (**Figure 1.18**) showed to be strong P-gp efflux modulators in MDR1-expressing cell lines (Ferreira et al., 2014; Yan et al., 2014). To that matter, some of the most recently described triterpenes (2016-2017) together with their reported activities as MDR reversal agents are presented in **Figure 1.19**.

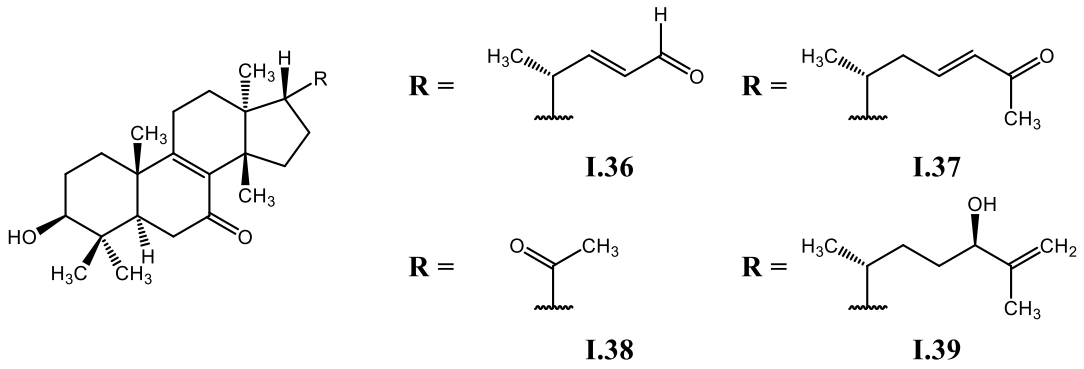

MDR reversal ability (Gao et al., 2017):

I.36 and **I.37** as weak P-gp efflux modulators, **I.39** with potent P-gp modulating potential;
I.39 potentiated navelbine citotoxicity, in a dose-dependent manner in KBv200 cells.

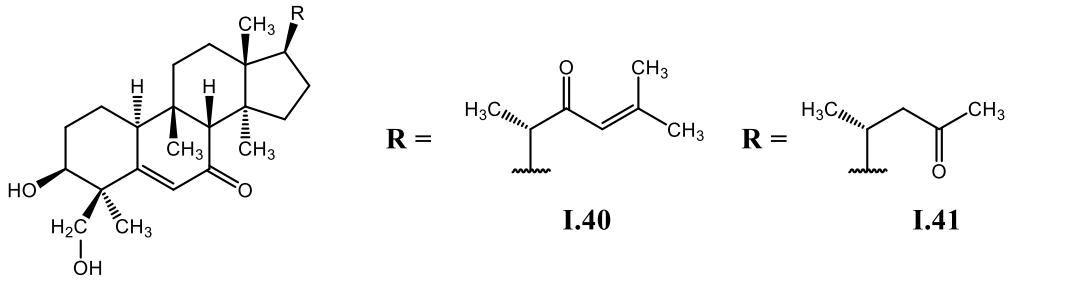

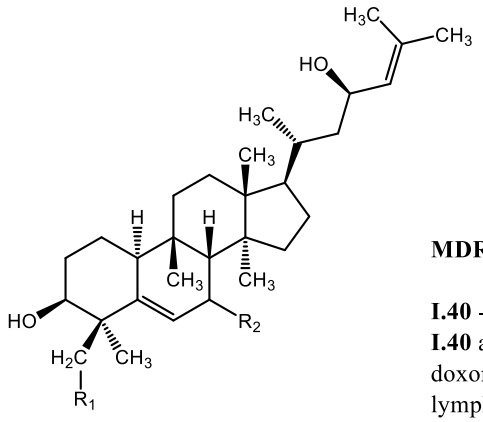

I.42. R_1 = OH, R_2 = OH
I.43. R_1 = OH, R_2 = OH
I.44. R_1 = H, R_2 = OMe
I.45. R_1 = H, R_2 = =O

MDR reversal ability (Ramalhete et al., 2016):

I.40 - I.45 as strong P-gp efflux modulators at 20 μM;
I.40 and **I.42** revealed synergism and strong synergism with doxorubicin on human MDR1-gene transfected mouse T-lymphoma cells (L5178Y-MDR).

Figure 1.19. Triterpenes with a cucurbitane scaffold.

Flavonoids are another class of secondary metabolites that have proven to possess a large number of biological effects, namely anti-oxidant, anti-inflammatory, antitumor and anti-viral activities, among others (Nijveldt et al., 2001). They are biosynthesized through the phenylpropanoid pathway by converting phenylalanine into 4-coumaroyl-CoA that enters to the flavonoid biosynthesis pathway. Following, while chalcone synthase synthetizes the initial chalcone scaffold that precede flavonoids, the final steps of flavonoid synthesis involve a group of enzymes, (isomerases, reductases, hydroxylases and dioxygenases) that modify the basic flavonoid skeleton, thus originating the different flavonoid subclasses (**Figure 1.20**). This basic flavonoid skeleton can have numerous substituents, but the most common are hydroxyl groups at the 4', 5, and 7 positions. Posterior modifications by specific tranferases can also modify the flavonoid backbone with sugars, methyl groups and/or acyl moieties that alter their solubility, reactivity and interaction with cellular targets (Falcone Ferreyra et al., 2012).

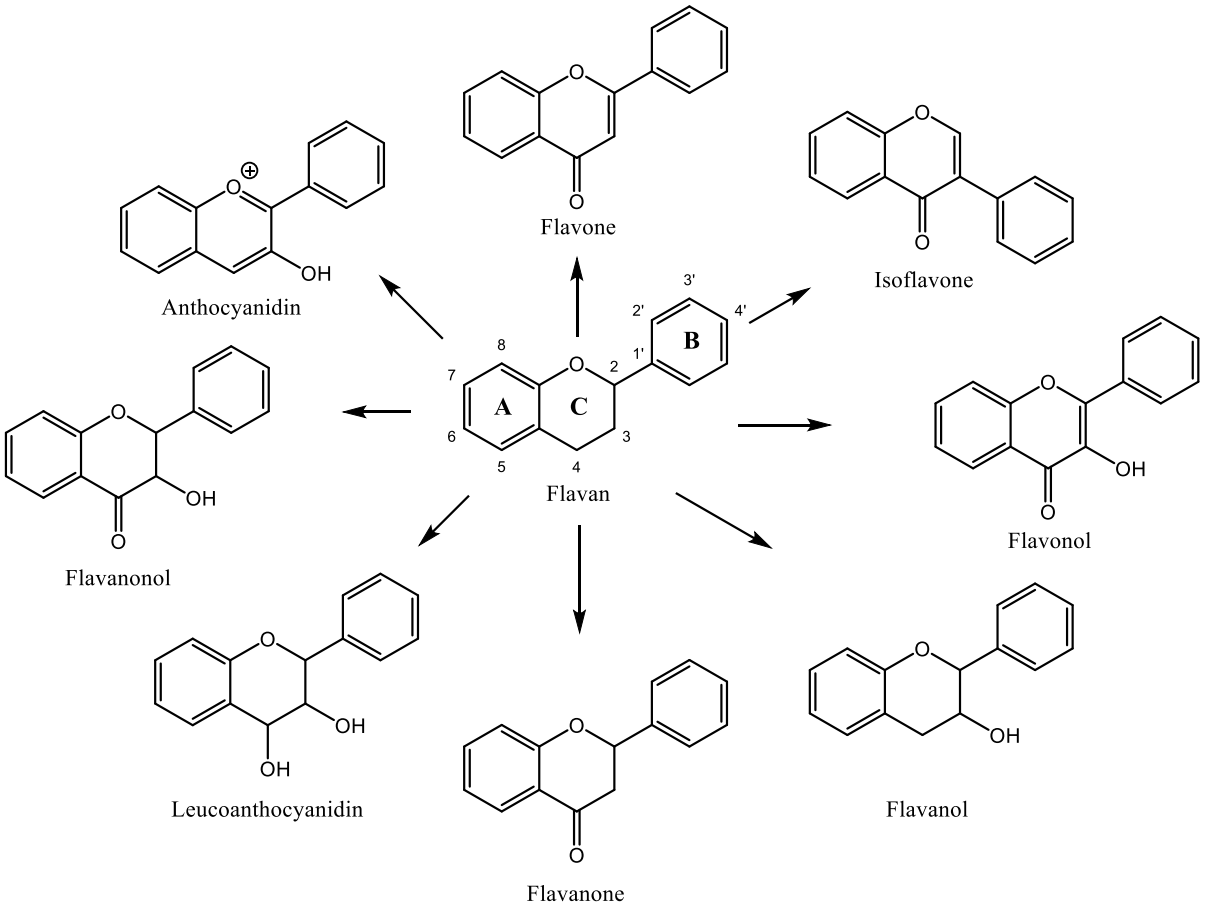

Figure 1.20. Chemical classifications and core structures of flavonoids (adapted from Eid et al., 2015).

Regarding its MDR reversal activities, while quercetin was one of the first flavonoids identified as a P-gp competitive modulator for Hoechst 33342 (H33342) efflux (Shapiro and Ling, 1997a), the interaction of flavonoids in a vicinal ATP- and steroid-binding region within the cytosolic domain of P-gp was additionally proposed as a different MDR reversal mechanism (Conseil et al., 1998). Flavonoids also presented promising results as MRP1 efflux inhibitors, with prenyl, geranyl or lavandulyl groups at C-8 (Bobrowska-Hägerstrand et al., 2003) or hydroxyl substitutions at C-3'/C-4' (Yoshimura et al., 2009) being important for the observed inhibitory activity. In BCRP, flavonoids as genistein and naringenin showed to competitively inhibit BCRP-mediated efflux, without measurable effects on P-gp or MRP1 (Boumendjel et al., 2011; Imai et al., 2004; Pick et al., 2011). Furthermore, flavonoids and their phase II metabolites (e.g. sulfates or glucuronides) were also found to act as organic anion transporters (OATP) inhibitors (Miron et al., 2017). Thus, flavonoids can provide suitable building blocks for the development of novel MDR reversal agents, acting on the most important ABC transporters often overexpressed in cancer.

1.4. Computational studies as useful tools for understanding ABC efflux transporters

Computational techniques are becoming valuable tools to better understand not only the structure-activity relationships by which some molecules are able to modulate efflux by ABC transporters, but also to unveil which structural determinants in the efflux pumps architecture that are intimately related with the efflux process itself. Thus, studies on the molecular recognition of substrates by P-gp and how they are translocated from the cell is of the utmost importance in order to better design new selective and potent P-gp efflux modulators (Ferreira et al., 2015b).

1.4.1. Ligand-based studies in P-glycoprotein substrates and modulators

Ligand-based studies are performed to gain insights about which structural features on a given set of molecules are related with its biological activity in a given target. From these studies, initial structure-activity relationships (SAR) studies can be used to guide chemical derivatization studies towards more potent compounds or, alternatively, to understand which chemical features potentiates and which ones are deleterious for the required biological activity.

1.4.1.1. Structure-activity relationship (SAR) studies

Regarding P-gp modulation, the first SAR studies not only pointed out lipid solubility at physiological pH, cationic charge and molar refractivity but also identified the spatial disposition of two aromatic planar rings and the presence of a basic nitrogen atom as the most important features for the biological activity of reserpine analogues (**Figure 1.21**) (Pearce et al., 1989; Zamora et al., 1988).

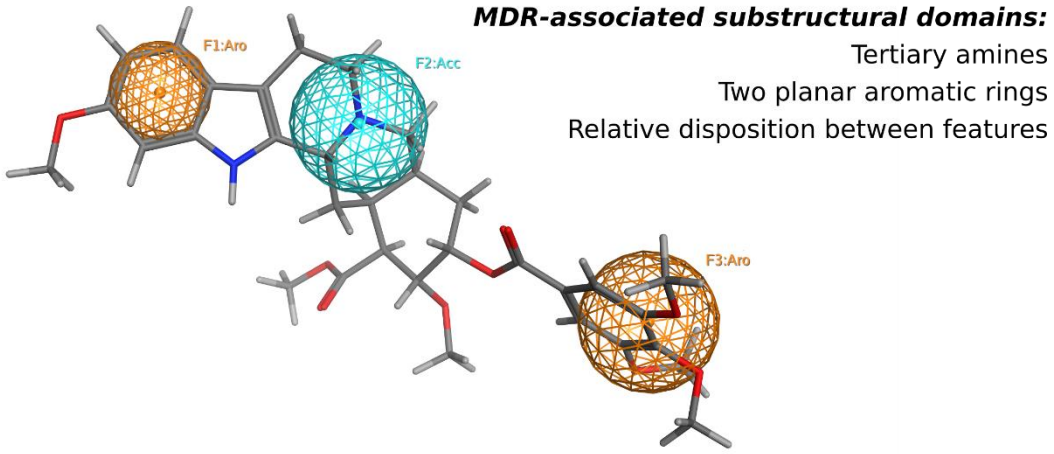

Figure 1.21. Representation of the reserpine-derived pharmacophore (adapted from Pearce et al., 1989; Zamora et al., 1988).

More recently, studies identified new chemical moieties intimately related with P-gp modulation capability. For instance, while a pharmacophore comprising one hydrogen-bond acceptor (HBA) and two large hydrophobic regions (HYD) together with an optimal molecular shape was a key requisite in the identification of P-gp inhibitors (Broccatelli et al., 2011), aromatic groups and/or hydrophobic ring substructures were found to be more common in inhibitors than in substrates (Klepsch et al., 2014); tertiary aliphatic amines, alkylaryl ethers and aromatic amines were prevalent in inhibitors (Poongavanam et al., 2012); and large, branched structure with biphenyl, naphthalene or aromatic nitrogen-containing heterocycles were identified as key features in increasing the inhibitory activity towards P-gp (Prachayasittikul et al., 2017). However, as other structural features as hydrophobicity, presence of HBA and amino groups have been ambiguously attributed to both substrates and inhibitors, all of the above features must be included in a general drug recognition pattern by P-gp, with efflux and inhibition capability being determined by other factors as lipid bilayer partitioning and/or affinity towards the transporter (Ferreira et al., 2015b). In the following

section, ligand-based studies on diterpenic compounds will be presented as a way to uphold which chemical modifications are related with greater potency towards P-gp efflux modulation.

1.4.1.2. SAR and QSAR studies on diterpenic compounds

One of the first studies to describe structure-activity relationships in diterpenes was the development of a 4-point pharmacophore from macrocyclic diterpenes isolated from several *Euphorbia* species. This pharmacophore not only was able to detect all molecules in-house (macrocyclic and polycyclic diterpenes, triterpene-type cucurbitacins) but also about 84% of all P-gp modulators published in scientific literature (**Figure 1.22**). Moreover, the importance of hydrophobic, aromatic and hydrogen-bond acceptor moieties were found to be correlated with the biological activities of diterpenes (Ferreira et al., 2011). Furthermore, another study by the same authors allowed the identification of a fifth pharmacophoric point (aromatic) that, when added to the previously developed pharmacophore, corroborated the supporting current knowledge on the importance of aromatic rings for P-gp modulation activity (Reis et al., 2012).

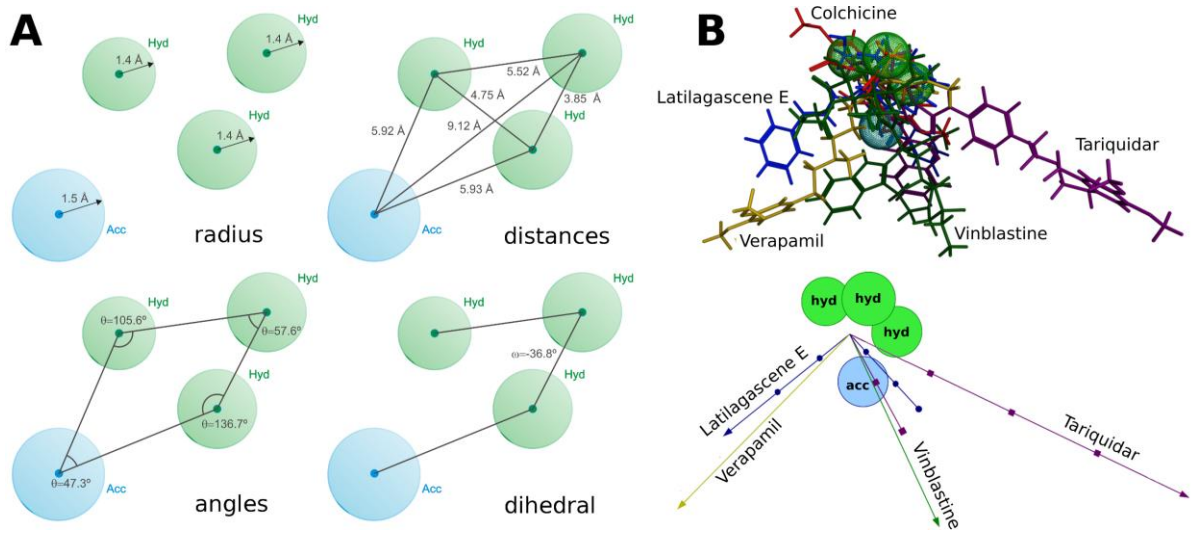

Figure 1.22. (A) Proposed 4-point pharmacophore (distances, angles, and dihedrals are represented); (B) Lowest RMSD conformations and alignment diagram for verapamil (yellow), tariquidar (purple), vinblastine (green) and latilagascene E (blue), in agreement with the developed pharmacophore (adapted from Ferreira et al., 2011).

From a similar subset of compounds, Sousa et al. also developed a quantitative SAR (QSAR) model towards the identification of the most relevant features in macrocyclic diterpenes that were related with their biological activity. Thus, from the obtained QSAR equation the increase of lipophilicity and number of atoms with positive charges together with

the decrease of conjugated systems would be important modifications to increase the activity of such compounds (Sousa et al., 2013).

Deriving structure-activity relationships from synthetized libraries of compounds is another approach to better understand which chemical modifications are important for improving biological activity. Toward that end and by grouping all compounds through *k*-means clustering and performing a linear regression analysis, the activity of a small library of Jolkinol D derivatives was found to be intimately related with its octanol/water partition coefficient (log*P*), solvent accessible area (SAS), the size of the ester side chain and with the presence of aromatic moieties at position C-3. Oppositely, long hydrophobic acyl side chains were found to decrease the compounds activity (Reis et al., 2013). Jiao and co-workers also developed a new library comprising 37 new acylated and epoxide derivatives from *Euphorbia* factor L_3, from which an identification of the key characteristics for MDR reversal activity was performed. Again, a strong correlation with log*P* and molecular weight (MW) was observed. Interestingly, while a bulky aromatic group at position C-3 seemed to enhance activity, the presence of two aromatic groups simultaneously at positions C-3 and C-5 impairs its activity against P-gp, thus suggesting a relationship between aromatic substituents and steric/electrostatic effects (Jiao et al., 2015).

A diterpenic library was also studied by Zhu and co-workers comprising not only isolated jatrophanes from *Euphorbia tithymaloides* but also analogues designed by esterification, hydrolysis, hydrogenation and epoxidation. Quite interestingly, all derivatives containing a double bond at positions Δ^2 or Δ^3, hydroxylation at the positions C-5, C-7 and C-9 and epoxidation at Δ^{12} showed a significant decrease in its P-gp reversal activity. Oppositely, benzyl groups at position C-3, acyl groups at position C-12 and a rare C-5/C-13 oxygen linkage strongly favored the activity of the compounds (**Figure 1.23A**) (Zhu et al., 2016). Recently, *in silico* approaches were also used to assess which structural features could be correlated with the biological activity displayed by a small library of epoxiboetirane A derivatives. In both L5178Y and Colo320 cell lines a significant correlation was found between activity and molecular descriptors containing information about the overall conformation and charge distribution within the diterpene scaffold. Moreover, a new pharmacophoric model derived from molecular interaction fields revealed, in agreement with previous studies, that *ortho*- or *meta*-substituted benzyl rings at position 3 are favorable for the activity. Interestingly, sterically-hindered structures as *p*-phenylbenzyl moieties, amantadine or activated 5-membered

heterocyclic rings as furan or thiophene were detrimental for the activity, most particularly when located at C-3 (**Figure 1.23B**) (Baptista et al., 2016).

Thus, and taken all into account, the activity of macrocyclic diterpenes can be enhanced by several mechanisms, but notwithstanding the presence of a benzyl moiety at C-3, branched or not, and an optimal log*P* to facilitate membrane partition seemed to be the key determinants for enhancing the affinity of such compounds towards P-gp.

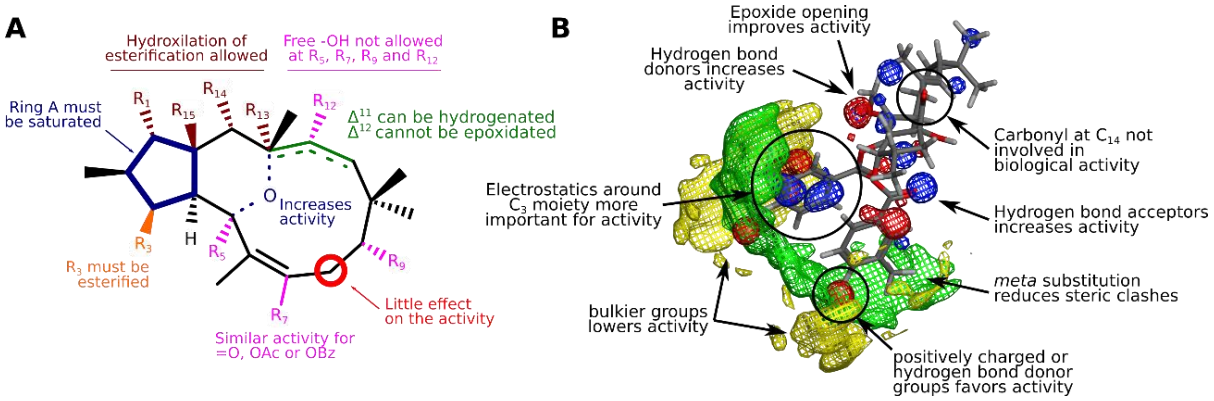

Figure 1.23. (A) Structure-activity relationship (SAR) of jatrophane diterpenes on P-gp inhibition; (B), Pharmacophoric hypothesis for epoxylathyrane derivatives. Green and yellow contours identify areas where steric bulk is positively or negatively correlated with biological activity. Red/blue contours identify areas where positively charged/hydrogen bond donor or negatively charged/hydrogen bond acceptor substituents are positively correlated with biological activity (adapted from Zhu et al., 2016; Baptista et al., 2016).

1.4.2. Structure-based studies in ABC transporters: unveiling its efflux mechanism

Until the publication of the first crystallographic murine P-gp structure in 2009 (Aller et al., 2009), all structure-based studies on ABC efflux transporters used either the *Staphylococcus aureus* Sav1866 (Dawson and Locher, 2007, 2006) structure or human P-gp homology models based on the Sav1866 (Becker et al., 2009; Globisch et al., 2008) or MalK (O'Mara and Tieleman, 2007) crystallographic data. Although with low homology with P-gp (15.8 % and 12.9% for TMD1 and TMD2, respectively), it was considered a suitable template for comparative modeling due to the presence of many common inter-linking domains in both Sav1866 and P-gp (Dawson and Locher, 2006; Rosenberg et al., 2005). Such templates were further used to evaluate drug-protein interactions either by assessing modes of binding, specific location or molecule's orientations within the drug-binding pocket (through molecular docking)

or by screening large databases of compounds in order to identify possible new scaffolds from which new potent and selective P-gp modulators could be derived (by virtual screening) (Anderson, 2003). At the same time, crystallographic structures also allowed studies on the dynamic behavior of the transporter itself. By means of molecular dynamics, insights on the ATP-driven mechanism by which P-gp operates, possible conformational pathways related with drug efflux, drug recognition and binding, translocation mechanism and structural relationships with the surrounding lipid bilayer (Ferreira et al., 2015b) were obtained. In the following sections, some of the most relevant studies concerning *in silico* approaches in the study of P-glycoprotein will be addressed.

1.4.2.1. Molecular Docking

Some of the first attempts to map possible drug-binding sites within the transmembrane drug-binding pocket were performed with homology models, using the prokaryotic crystallographic structures as template for modeling the human P-gp transporter. For instance, Globish and co-workers aimed for the identification of drug-binding sites by using specific algorithms for pocket and site detection. Herein, three distinct drug-binding sites were identified in a large binding pocket, one located at the membrane-cytosol interface and other two at the transmembrane domains. Moreover, residues from transmembrane helices (TMH) 2/3, TMH4/5, TMH 8/9 and TMH 10/11 were also found to be involved in drug binding and recognition at the first binding site, some of which experimentally demonstrated by *in situ* labeling or cross-linking studies (Globisch et al., 2008). From four P-gp homology models obtained in two distinct catalytic states, Becker *et al.* performed molecular docking using known P-gp binders (verapamil, rhodamine B, colchicine and vinblastine) to assess if the central cavity was able to accommodate all ligands and to identify any drug-binding sites and the corresponding residues. Interestingly, and in agreement with the above study, all ligands interacted with residues that had been experimentally identified to that particular ligand. Furthermore, for colchicine and verapamil at least two locations were identified as being its most probable drug-binding sites (Becker et al., 2009).

Already with the murine crystallographic data published, Tarcsay *et al.* aimed for a more thorough identification of drug-binding sites within P-gp. The internal cavity was mapped, for the first time, as a mainly hydrophobic cavity in agreement with experimental evidences at date. Again, by using several known molecules that bind P-gp, several residues were identified from its induced-fit binding mode. Nonetheless, with this model no difference between active and

inactive molecules could be found in several *virtual screening* attempts (Tarcsay and Keserű, 2011). Thus, while the polyspecificity of P-gp could be mostly explained by its large drug-binding pocket being able to accommodate several structurally unrelated drugs (in all studies), a clear definition on the most relevant drug-binding sites and their relationship with the experimental evidences by Shapiro *et al.* on H33342, R123 and LDS-751 was still required to fully understand drug recognition and binding by P-gp.

Molecular docking studies were also used to predict either the binding sites or binding poses for several compounds isolated from natural sources, as an attempt to explain and rationalize the biological activities encountered. Reis et al. performed molecular docking studies in a series of jatrophane and lathyrane diterpenes to identify that these compounds bind P-gp at a similar location than verapamil, corresponding to the intersection between QZ59-SSS and QZ59-RRR binding sites (**Figure 1.24A**) (Reis et al., 2012).

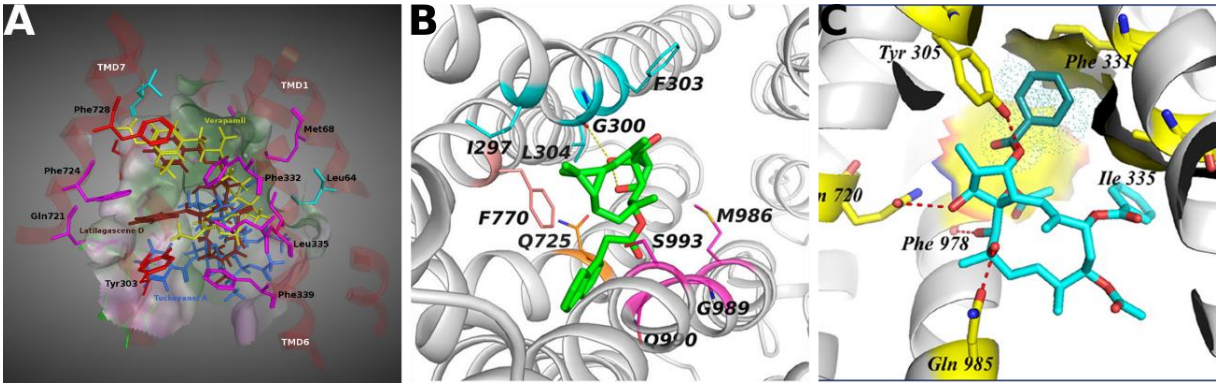

Figure 1.24. (A) Docking studies on several diterpenoids in murine P-gp model; (B) Binding mode of 5-(1-naphthylacetyloxy)-lathyra-6(17),12-dien-3,15-diol-14-one in a human homology P-gp model; (C) binding pose of 9,15-fiacetoxy-3,7-dibenzoyloxy-1,13,14-trihydroxyjatropha-5*E*-ene within a human homology P-gp model (adapted from Reis et al., 2012; Jiao et al., 2015; Zhu et al., 2016).

Similarly, Jiao et al. performed docking studies on P-gp with lathyrol diterpenes derivatives to find that residues in TMH5-8 and TMH12 were involved in drug binding mainly through hydrophobic interactions (**Figure 1.24B**) (Jiao et al., 2015) and Zhou and co-workers docked miltirinone, an abietane-type diterpene, in both a murine and human P-gp models to identify Phe974 (Phe978 in human P-gp) as a key residue that interacts via π-π stacking with rings B and C in miltirinone. Finally, the most promising jatrophane-type diterpene identified by Zhu et al. from *Euphorbia tithymaloides* was found to dock next to several polar (Gln720, Gln985), hydrophobic (Ile335) and aromatic (Phe978, Tyr305, Phe331) residues in a murine P-gp model, in close agreement with the previous studies (**Figure 1.24C**) (Zhu et al., 2016).

1.4.2.2. Molecular Dynamics

ABC transporters are characterized by the high structural flexibility (Ward et al., 2007, 2013; Wen et al., 2013; Wollmann et al., 2005) that allows these proteins to alternate between an inward- (high affinity) and outward-facing (low affinity) conformations during its efflux cycle. Unfortunately, crystallographic structures cannot encompass this functional dynamic, and although providing important information on its structural organization, they only sample a limited range of conformational snapshots that cannot be used directly to understand its whole dynamic behavior. Moreover, structural artifacts introduced by the crystallization process itself, as the removal of the protein from its natural lipid environment (Caffrey, 2003), along with their low crystallographic resolution (Biggin and Bond, 2008; Kleywegt, 2000) may impair the utilization of such templates in structure-based drug design studies. Therefore, *in silico* studies using molecular dynamics are a powerful tool that can be used to evaluate the structural stability of a given structure, to further refine the crystallographic data or to gain new insights on the dynamic behavior of a protein in its natural environment (Brunger and Adams, 2012; Burnley et al., 2012; Fan and Mark, 2003).

By using the available P-gp crystallographic structures so far, new insights on its dynamic behavior have provided new and valuable data that allowed current researchers to better understand the efflux cycle. One of the first MD studies using the murine crystallographic data was performed by Ferreira et al. in an attempt to evaluate the structural stability of the transporter. In this particular study, it was found that both the membrane and the 'linker' sections had a strong impact on the stability of the transporter: while a 1-palmitoyl-2-oleoyl-*sn*-glycero-3-phosphocholine (POPC) membrane stabilized the transmembrane section of the transporter by minimizing its hydrophobic mismatch, the addition of a modeled 'linker' section, absent in the murine crystallographic structure, was able to stabilize the insertion angle of the whole transporter even in a thinner dimiristoyl-*sn*-glycero-3-phosphocholine (DMPC) membrane (Ferreira et al., 2012). These results were also supported by a human homology P-gp model that, although simulated without the linker, showed increased structural stability due to the presence of the lipid membrane and also cholate molecules between NBDs (O'Mara and Mark, 2012). In both studies, either the 'linker' or the cholate molecules seem to absorb stronger NBD motions that could disturb the structural architecture of the transporter, thus contributing for its increased stability (Ferreira et al., 2013a). Moreover, it was also found that the dynamic behavior of the transporter is altered in the presence of a substrate within the 'entrance' gate,

shifting its normal motion patterns into efflux-related motions (**Figure 1.25**) (Ferreira et al., 2012).

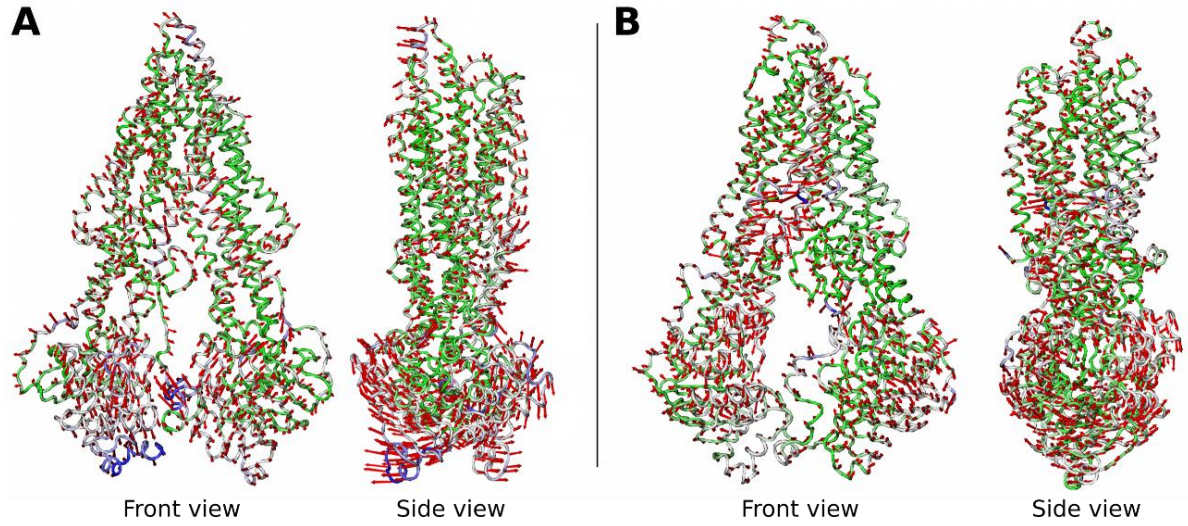

Figure 1.25. Normal motion patterns displayed by the ABC transporter P-glycoprotein (A) in the absence of substrates and (B) in the presence of a substrate at the TM helices 10-12 portal (adapted from Ferreira et al., 2012).

The conformational changes by which P-gp can shift from the inward- to the outward-facing state were also explored by Wise, using targeted MD to drive P-gp (opened inwards) into a similar conformation that of Sav1866 (opened outwards). Herein, it was demonstrated that both NBDs engage a concerted rotation that increases the distance of the extracellular halves of the TMDs while decreasing the NBD distance until the canonical dimer is formed. Interestingly, as the contacts between the TMH's intracellular coupling helices (ICH) and NBDs are maintained (especially with ICH2 and ICH4), these specific motifs were classified as having a determinant role in the TMH reorganization and, ultimately, allowing the extracellular widening of the drug-binding pocket (DBP) (Chang et al., 2013; Pajeva et al., 2013; Wise, 2012). In addition, studies concerning the role of ATP in the efflux process also clarified that while binding of the ATP is sufficient to drive the formation of the canonical dimer by inducing smaller NBD-NBD distances and promoting dimerization by shifting the equilibrium among all possible combinations rather than driving the whole process (Rosenberg et al., 2001; Wen et al., 2013), ATP hydrolysis is required to reset the transporter into its initial state (George and Jones, 2013; Oliveira et al., 2010). For P-gp, as both NBDs are catalytically active, an alternate model involving a 'tightly bound' (occluded) ATP and a 'loose' ATP molecule at the opposite NBD (Siarheyeva et al., 2010) is currently the most accepted model for the ATP-driven

mechanism (**Figure 1.26**). Remarkably, one of the latest crystallographic structures published (CFTR, ABCC7) displayed for the first time an asymmetric opening of the nucleotide-binding domains (Zhang and Chen, 2016), which seem to corroborate the *Constant Contact* model proposed by George and Jones (George and Jones, 2013, 2012) as the main mechanism by which the canonical dimer may be formed (although in P-gp this mechanism is expected to occur alternatively in both competent ATP-binding sites).

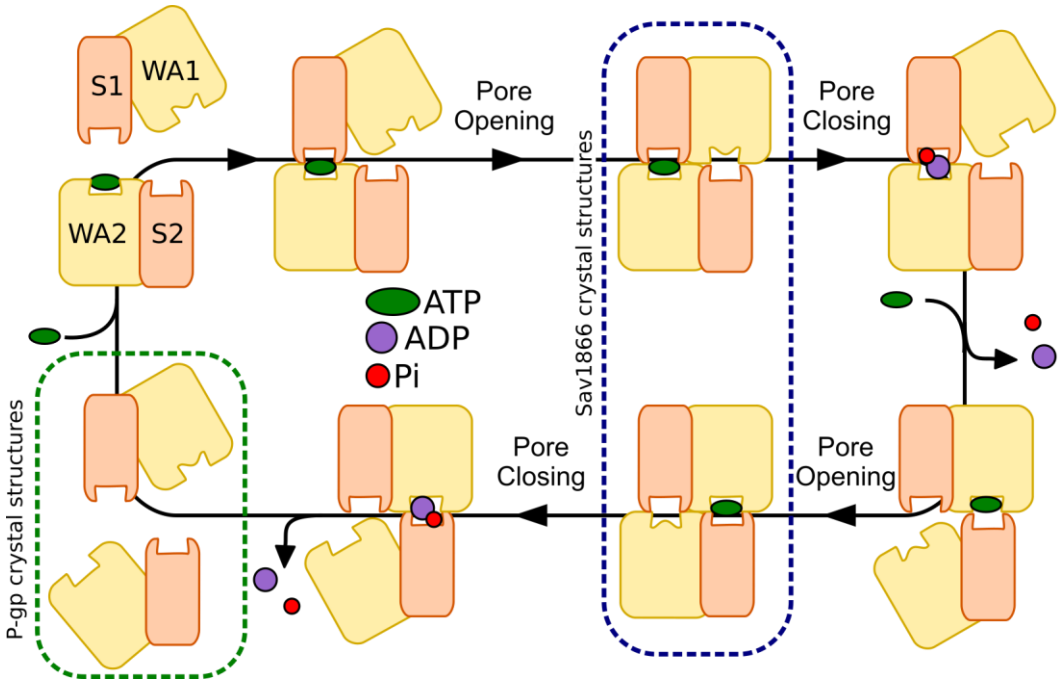

Figure 1.26. Hypothetical model for the ATP catalytic cycle, according the *Constant Contact* model for both ATP-binding competent NBDs. The ATP-binding pocket is formed by Walker A motifs of NBD1 (WA1) and NBD2 (WA2) with the signature motifs of the opposite NBD2 (S2) and NBD1 (S1). Pore opening/closing refers to the outward-facing structure, dashed lines refer to the known crystallographic structures (green, inward-facing; blue, outward-facing) (adapted from Ferreira et al., 2015).

Regarding substrate transport, the postulated "dual pseudosymmetrical solute translocation pathways" proposed by Parveen *et al.* (Parveen et al., 2011) regarding drug efflux was evaluated by McCormick and co-workers to find that both daunorubicin and verapamil, but not pyrophosphate methyl ester, showed a vectorial movement along the *z* axis (perpendicular to the membrane plane) from the inside (cytoplasmic) surface of the drug-binding pocket into the outside (extracellular), while P-gp was shifting from the inward- to the outward-facing state by targeted MD. Even if docked in non-optimal position within P-gp, both drugs could still be transported towards the extracellular space during the targeted MD simulated efflux cycles. Surprisingly, while for the high-affinity modulator tariquidar such motion was not observed for

a position outside the drug-binding pocket, when already inside the pocket at non-optimal docking positions it could be transported in a similar way as verapamil. Ultimately, as both drugs were shown to have distinct binding locations and residue contacts along the simulations, at least two distinct drug transport pathways could be inferred from which drugs are translocated during the efflux cycle (McCormick et al., 2015).

Chapter 2

Objectives

2. Objectives

Drug resistance to the anticancer drugs currently in use threats to severely compromise the success of cancer chemotherapy. One of the most significant mechanism results from the over-expression of efflux pumps that contributes to the decrease of the intracellular concentration of the drug by acting as extrusion pumps. Moreover, and despite the several theoretical and experimental studies performed in order to understand P-gp´s structure-function relationships, lack of substrate specificity and characteristics of the drug-binding sites, no efflux modulator become clinically available so far.

Euphorbia species have been used in traditional medicine to treat cancer, tumors and warts and are a valuable source for novel scaffolds due to the unusual diversity of chemical constituents, including a wide range of structurally unique macrocyclic diterpene polyesters that have revealed to be strong P-gp efflux inhibitors. Other secondary metabolites as triterpenes, sterols or flavonoids were also proved to possess variable MDR reversal properties.

Therefore, the main goals of this project are a) to obtain new MDR reversers in cancer cells by specifically targeting ABC transporters and b) to obtain new insights on the initial steps of the efflux mechanism by P-gp through new structure-based *in silico* studies.

It was carried out through three main approaches:

i) **Phytochemical studies**, through the isolation of macrocyclic diterpenes, diterpenic lactones, triterpenes and flavonoids compounds from *Euphorbia pedroi*;

ii) **Molecular derivatization of isolated compounds**, when isolated in large amounts, in order to increase its selectivity and potency as P-gp modulators. The MDR reversal properties in other efflux pumps (MRP1, BCRP) will also be studied. Towards that end, from helioscopinolide E (**15**) and naringenin (**17**) two libraries of *ent*-abietane (**20**-**24**) and flavanone (**25**-**71**) derivatives were obtained by chemical derivatization and evaluated as MDR reversal agents;

iii) **Computational studies** i) of the interaction profiles between molecules and Pgp in Pgp-lipid bilayer systems, by obtaining new quantitative structure-activity relationships (QSAR) and ii) novel insights on the initial steps of the efflux mechanism through molecular dynamics (MD) and molecular docking studies.

Chapter 3

Phytochemical research on *Euphorbia pedroi*.

Results and Discussion

3. Structure elucidation of isolated compounds

Three new macrocyclic diterpenes of the lathyrane- (**8**, **11**) and jatrophane-type (**9**) and a new polycyclic diterpene (**13**), together with a new steroid (**6**) were isolated from the methanol extract of *Euphorbia pedroi*. Other known macrocyclic and polycyclic diterpenes were also isolated: jolkinol D (**7**), piscatoriol A (**10**), 15β-acetoxy-3β-hydroxylathyra-5,6-epoxi-12*E*-en-14-one (**12**), helioscopinolides B (**14**) and E (**15**) and *ent*-13*R*-hydroxy-3,14-dioxo-16-atisene (**16**). In addition, cycloart-25-ene-3β,24-diol (**3**), cycloart-23-ene-3β,25-diol (**4**), 7,11-dioxo-obtusifoliol (**5**) and two flavonoids, naringenin (**17**) and quercetin (**18**) were additionally identified. Their structures were characterized by spectroscopic methods mainly 1D- (^{1}H, ^{13}C) and 2D-NMR (DEPT, COSY, HMBC, HMQC and NOESY) experiments and by comparison with literature data.

Furthermore, as reasonable amounts of helioscopinolide E (**15**) and naringenin (**17**) were isolated, a small library of *ent*-abietane derivatives (**19**-**24**) and a larger one containing flavanone derivatives (**25**-**71**) were obtained by the chemical modification of compounds **15** and **17** to allow the identification of new structure-activity relationships able to identify which chemical features are intimately correlated with the experimentally determined MDR reversal activities (**Chapter 4**).

3.1. Lathyrane-type macrocyclic diterpenes

3.1.1. Pedrodione A, 15β-acetoxy-3β-hydroxylathyra-6(17),12*E*-dien-5,14-dione

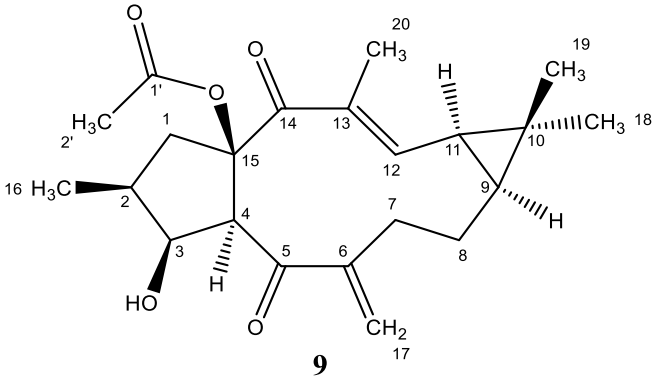

9

Compound **9,** named pedrodione A, is a new compound obtained as an amorphous white powder with $[\alpha]_D^{20}$ + 189.0° (*c* 0.1, $CHCl_3$). Its IR spectrum showed the presence of hydroxyl (3446 cm^{-1}) and carbonyl groups (1737 and 1716 cm^{-1}). The low resolution ESI-MS spectrum provided one molecular ion peak at *m/z* 398 $[M + H + Na]^+$. Its molecular formula, $C_{22}H_{30}O_5$, was deduced from its ESI-HRMS spectrum, which showed a sodium adduct ion peak at *m/z* 397.1988 $[M + Na]^+$ (calcd. for $C_{22}H_{30}NaO_5$, 397.1985), corresponding to eight degrees of unsaturation. The ^{1}H-NMR spectrum of **9** (**Table 3.1**) displayed signals for five methyl groups: two singlets corresponding to tertiary methyl groups (δ_H 0.99 and 1.15), a doublet from a secondary methyl at δ_H 1.11 (*d*, *J* = 6.7 Hz), one acetyl (δ_H 2.00) and one vinylic methyl group (δ_H 1.78). The ^{1}H-NMR spectrum also displayed signals that could be assigned to three diastereotopic methylene groups [δ_H 3.47 (*dd*, *J* = 13.4, 7.5 Hz) and 1.72 (m); δ_H 3.02 (*dd*, *J* = 13.1, 4.8 Hz) and 2.04 (*m*); δ_H 2.03 (*m*) and 1.54 (*m*)], two methines [δ_H 3.37 (*d*, *J* = 3.0 Hz); 1.38 (*dd*, *J* = 11.1, 8.2 Hz)] and one oxymethine (δ_H 4.19, *br t*, *J* = 3.0 Hz). Furthermore, vinylic NMR signals from a trisubstituted double bond at δ_H 6.20 (*d*, *J* = 11.1) and a terminal double bond as two broad singlets (δ_H 5.84 and 5.64) were also observed. The ^{13}C-NMR and DEPT (**Table 3.1**) spectra displayed twenty-two carbon signals, corresponding to five methyl groups, four methylenes (including one sp^2 at δ_C 127.5), six methines (including an oxygenated one at δ_C 78.4 and one sp^2 at 146.6) and seven quaternary carbons (three carbonyl groups at δ_C 201.6, 195.1 and 169.7 and two olefinic carbons at δ_C 149.5 and 133.2).

From the above data, a macrocyclic diterpene was assumed, with the presence of a quaternary carbon at δ_C 25.0 suggesting a lathyrane-type scaffold. When compared with similar compounds such as piscatoriol B, with a hydroxyl at C-5, the relative downfield signal found for H-4 (δ_H 3.37), that resonate at $\delta_{H\text{-}4} \approx 2.43$ in piscatoriol B (Reis et al., 2014b), suggested the existence of an additional sp^2 oxygenated group at C-5. Moreover, the H-3 signal resonance at lower fields (δ_H 4.19) also suggests the presence of an intramolecular hydrogen bond, possibly between the hydroxyl at C-3 and a carbonyl group at C-5. Further structural details obtained from 2D-NMR experiments (COSY, HMBC, HMQC and NOESY) allowed an unambiguous assignment of all carbon signals (**Table 3.1**, **Figure 3.1**).

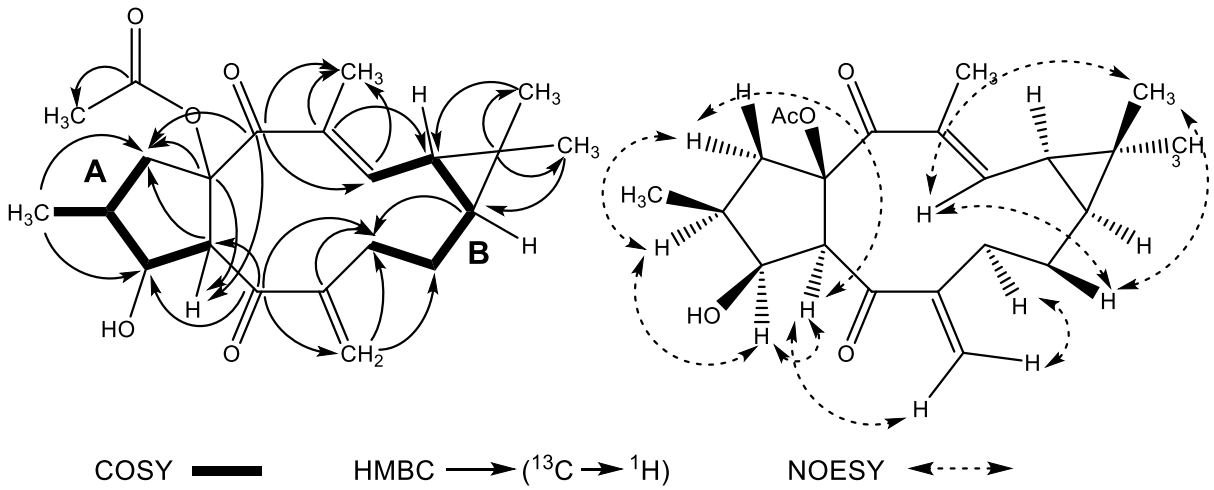

Figure 3.1. Key COSY, HMBC and NOESY correlations for pedrodione A (**9**). ^{1}H spin systems (A-B) and respective connections by main heteronuclear $^2J_{C\text{-}H}$ and $^3J_{C\text{-}H}$ correlations.

The ^{1}H-^{1}H COSY experiment allowed the identification of two key fragments (A-B) that were further interconnected through heteronuclear $^2J_{C\text{-}H}$ and $^3J_{C\text{-}H}$ correlations retrieved from the HMBC spectrum. While the HMBC correlations between Me-20 (δ_H 1.78) and the carbon signal at δ_C 195.1 placed the corresponding carbonyl group at position C-14, the $^2J_{C\text{-}H}$ and $^3J_{C\text{-}H}$ correlations between the diastereotopic proton at δ_H 3.47 (H-1α) and the carbon signals at δ_C 92.3 (C-15) and δ_C 195.1 (C-14) corroborated these assignments. Furthermore, the HMBC correlations between the olefinic exocyclic protons H-17a (δ_H 5.64), H-17b (δ_H 5.84) and the methine signal at δ_H 3.37 (H-4) with the carbon signal at δ_C 201.6 located the second carbonyl function at C-5. This was further confirmed through the observation of HMBC correlations between H-3 (δ_H 4.19) and H-7α (δ_H 3.02) with C-5 (δ_C 201.6). Finally, $^2J_{C\text{-}H}$ and $^3J_{C\text{-}H}$ correlations between the methyl groups Me-18 (δ_H 1.15) and Me-19 (δ_H 0.99), the

quaternary carbon signal at δ_C 25.0 (C-10) and the two methines at δ_H 1.08 (H-9) and δ_H 1.38 (H-11) clearly identified the location of the *geminal* methyl groups at the cyclopropane ring, in agreement with the expected features of a lathyrane-type diterpene.

Table 3.1. ^{1}H, ^{13}C-NMR and DEPT spectra [$CDCl_3$, δ (ppm), (*J*, Hz)] of pedrodione A (**9**).

Position	^{1}H	^{13}C	DEPT	Position	^{1}H	^{13}C	DEPT
1α	3.47 *dd* (13.4, 7.5)	45.1	CH_2	**11**	1.38 *dd* (11.1, 8.2)	29.2	CH
1β	1.72, *m*			**12**	6.20, *d* (11.1)	146.6	CH
2	1.94, *m*	40.3	CH	**13**	--	133.2	C
3	4.19, *br t* (3.0)	78.4	CH	**14**	--	195.1	C
4	3.37, *d* (3.0)	53.3	CH	**15**	--	92.3	C
5	--	201.6	C	**16**	1.11, *d* (6.7)	13.0	CH_3
6	--	149.5	C	**17a**	5.64, *br s*	127.5	CH_2
7α	2.04, *m*[a]	32.6	CH_2	**17b**	5.84, *br s*		
7β	3.02 *dd* (13.1, 4.8)			**18**	1.15, *s*	28.8	CH_3
8α	2.03, *m*[a]	22.0	CH_2	**19**	0.99, *s*	16.4	CH_3
8β	1.54, *m*			**20**	1.78, *s*	12.7	CH_3
9	1.08, *m*[a]	34.7	CH	**1'**	--	169.7	C
10	--	25.0	C	**2'**	2.00, *s*	21.6	CH_3

[a] signals partially overlapped.

The stereochemical orientation of the protons were further obtained from the NOESY spectrum. The α-orientation of H-4 was taken for biogenetic reasons. Herein, NOE correlations between H-1α/H-2/H-3/H-4 agreed with the α-orientation of these protons. Furthermore, NOE cross peaks between H-17a/H-4 and H-17b/H-7β suggested an orientation of the terminal double bond towards the α-plane of the molecule, further corroborated by the identification of NOE correlations between H-8β/H-12/H-19. It is also worth noticing that the above proposed orientation of the $\Delta^{6,17}$ double bond places the carbonyl group at C-5 in an optimal position for the formation of an intramolecular hydrogen-bond (HB) between the hydroxyl group at C-3, as previously suggested (**Figure 3.2)**.

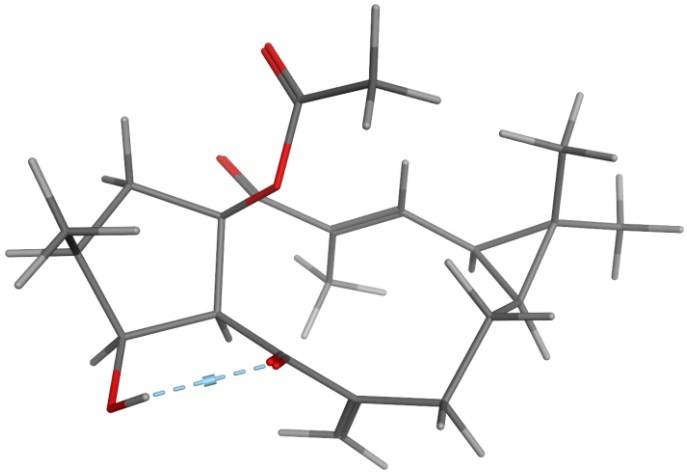

Figure 3.2. Energy minimized structure for pedrodione A (**9**). Intramolecular hydrogen-bonds are depicted in light blue. Minimization was made in MOE software using the AMBER10:ETH force field, according to the semi-empiric Hamiltonian PM3 (available in MOPAC).

From the above data, compound **9** was identified as a functional isomer of piscatoriol B, isolated from *Euphorbia piscatoria* (Reis et al., 2014), only differing in the oxidation status at C-5 by having a carbonyl instead of a hydroxyl group. It should be noticed that the existence of two α,β-unsaturated ketone systems is highly unusual, but nonetheless it could still be found in literature a similar diterpenic compound, isolated from *Euphorbia kansuensis*. This compound, ekanpenoid A, is a norditerpene that also has a carbonyl group at C-5, but in which the terminal double bond $\Delta^{6,17}$ is replaced by an endocyclic bond at C-6 while lacking the acetoxy moiety at C-15 (Zhang et al., 2013).

3.1.2. Pedrodiol, 15β-acetoxy-6(17),12*E*-dien-3β,5α-dihydroxylathyra-14-one

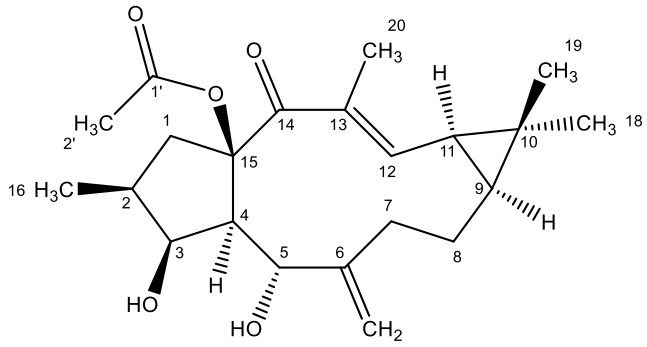

12

Compound **12**, named pedrodiol, is a new compound that was isolated as an amorphous white powder with $[\alpha]_D^{20}$ + 90.6° (*c* 0.1, $CHCl_3$). From the IR spectrum, it could be identified the presence of hydroxyl (3481 cm^{-1}) and carbonyl (1741 and 1649 cm^{-1}) groups. While from the ESI-MS a molecular ion peak at *m/z* 377 $[M + H]^+$ could be identified, from the ESI-HRMS spectrum a molecular formula of $C_{22}H_{32}O_5$ could be determined from the protonated molecular ion at *m/z* 377.2324 $[M + H]^+$ (calcd. for $C_{22}H_{33}O_5$, 377.2323), corresponding to the presence of seven degrees of unsaturation. The ^{1}H- and ^{13}C-NMR spectra revealed signals similar to the ones reported for piscatoriol B (Reis et al., 2014b) (**Table 3.2**). Accordingly, four tertiary methyl groups (δ_H 1.07, 1.15, 1.70 and 2.06), one secondary methyl group [δ_H 1.08, *d* (*J* = 8.2 Hz)], three diastereotopic methylene groups and four methine groups were identified from the ^{1}H-NMR experiment. The ^{1}H-NMR spectrum also revealed the presence of vinylic protons in a trisubstituted double bond at δ_H 6.33 (*d*, *J* = 11.2 Hz) and in a terminal exocyclic double bond at δ_H 4.75 and 4.95 (both as broad singlets). In the ^{13}C-NMR spectrum, five methyl groups, four methylenes (with one sp^2 at δ_C 113.4), six methines (two oxygenated at δ_C 66.8 and 79.6 and one sp^2 at 145.4) and seven quaternary carbons (including two carbonyls at δ_C 197.2 and 169.9 and two olefinic carbons at δ_C 148.3 and 133.7) could also be identified.

From the above ^{1}H- and ^{13}C-NMR data, a macrocyclic lathyrane-type similar to piscatoriol B was assumed. However, important differences were found in the calculated optical rotation ($[\alpha]_D^{20}$ + 90.6° vs. $[\alpha]_D^{26}$ – 103.0° for piscatoriol B [*c* 0.1, $CHCl_3$]) and in the spectroscopic data for the H-5 signal in the ^{1}H-NMR spectrum. To that matter, the comparison of signal multiplicity and the corresponding $J_{4\text{-}5}$ coupling constant values for pedrodiol (**12**, δ_H 4.81, *t*, *J* = 8.0 Hz) vs. piscatoriol B (δ_H 4.81, *bs*) suggested an α-oriented hydroxyl group at

position C-5. Therefore, aiming for the unambiguous assignment of all chemical shifts, detailed structural details were obtained from two-dimensional NMR data (COSY, HMBC, HMQC and NOESY) (**Figure 3.3**).

Both ^{1}H-^{1}H COSY and HMBC experiments clearly assigned the position of the carbonyl at C-14, the oxymethine groups at C-3 and C-5 and the double bonds at $\Delta^{6,17}$ (exocyclic) and C-11 (endocyclic, conjugated), in agreement with the assignments reported for piscatoriol B (Reis et al., 2014b). By observing the NOESY spectrum, the absence of NOE cross peaks between H-4 and H-5 agrees with an α-orientation of the hydroxyl group at C-5.

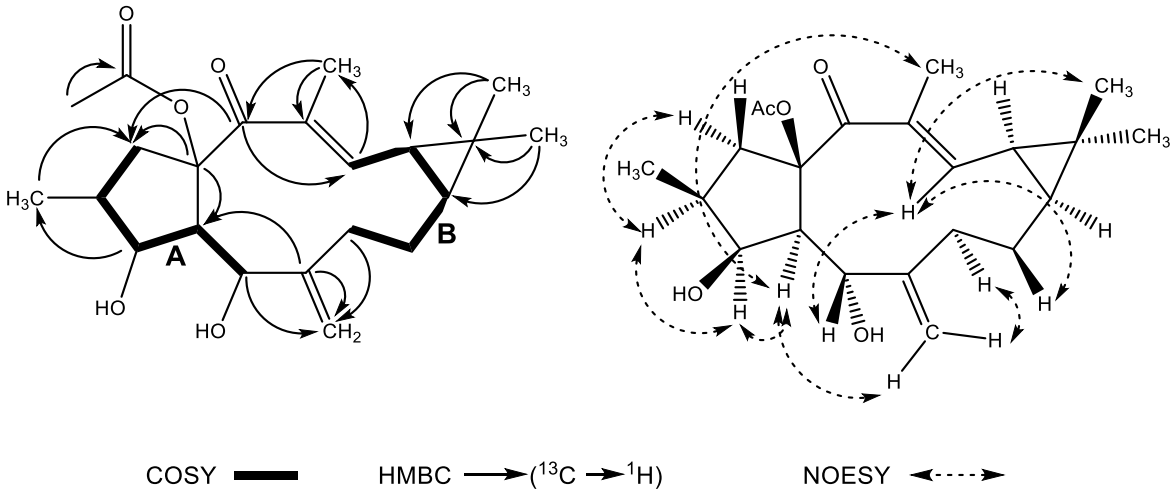

Figure 3.3. Key COSY, HMBC and NOESY correlations for pedrodiol (**12**). ^{1}H spin systems (A-B) and respective connections by main heteronuclear $^{2}J_{C\text{-}H}$ and $^{3}J_{C\text{-}H}$ HMBC correlations.

Furthermore, the NOE correlations between H-1α/H-2/H-3/H-4, the observation of NOE cross peaks between H-12 and H-5/H-8β/H-19 and between H-4/H-20 corroborated the proposed stereochemistry. As in pedrodione A (**9**), the α-orientation of the hydroxyl group at C-5 enables the formation of intramolecular hydrogen-bonds with the hydroxyl group at C-3 (**Figure 3.4**), observed as a broadening of the H-3 (double doublet) and H-5 (triplet) signals.

Table 3.2. ^{1}H-, ^{13}C- NMR and DEPT [$CDCl_3$, δ (ppm) mult (*J*, Hz)] spectra of pedrodiol (**12**) and piscatoriol A (**11**).

	pedrodiol (12)			piscatoriol A (11)		
Position	**^{1}H**	**^{13}C**	**DEPT**	**^{1}H**	**^{13}C**	**DEPT**
1α	3.39 *dd* (13.7, 7.9)	47.3	CH_2	3.32, *dd* (13.5, 7.6)	47.4	CH_2
1β	1.70, *m*			1.70, *m*		
2	2.09, *m*	37.8	CH	2.04, *m*[a]	37.8	CH
3	4.34, *dd* (3.5, 3.1)	79.6	CH	4.34, *t* (3.1)	79.7	CH
4	2.43, *dd* (8.0, 3.5)	54.2	CH	2.11, *dd* (6.2, 3.1)[a]	54.7	CH
5	4.81, *t* (8.0)	66.8	CH	5.37, *d* (6.2)	65.8	CH
6	--	148.3	C	--	135.6	C
7α	2.14, *m*	35.5	CH_2	5.25, *dd* (11.1, 6.2)	126.7	CH
7β	2.72 *dd* (13.4, 5.4)					
8α	2.01, *m*	22.1	CH_2	2.35, *m*[a]	23.9	CH_2
8β	1.58, *m*			2.39, *m*[a]		
9	1.09, *m*[a]	34.6	CH	1.25, *m*[a]	31.9	CH
10	--	24.8	C	--	25.5	C
11	1.37 *dd* (11.2, 8.2)	28.2	CH	1.42, *dd* (11.2, 8.8)	27.9	CH
12	6.33, *d* (11.2)	145.4	CH	6.44, *d* (11.2)	142.6	CH
13	--	133.7	C	--	133.6	C
14	--	197.2	C	--	197.9	C
15	--	92.8	C	--	92.7	C
16	1.08, *d* (8.2)	13.5	CH_3	1.07, *d* (6.8)	13.4	CH_3
17α	4.95, *br s*	113.4	CH_2	1.65, *s*	17.8	CH_3
17β	4.75, *br s*					
18	1.15, *s*	29.1	CH_3	1.23, *s*	28.8	CH_3
19	1.07, *s*	16.7	CH_3	1.16, *s*	17.0	CH_3
20	1.70, *s*	12.6	CH_3	1.75, *s*	12.2	CH_3
1'	--	169.9	C	--	170.1	C
2'	2.06, *s*	22.0	CH_3	2.09, *s*	22.2	CH_3

[a] signals partially overlapped.

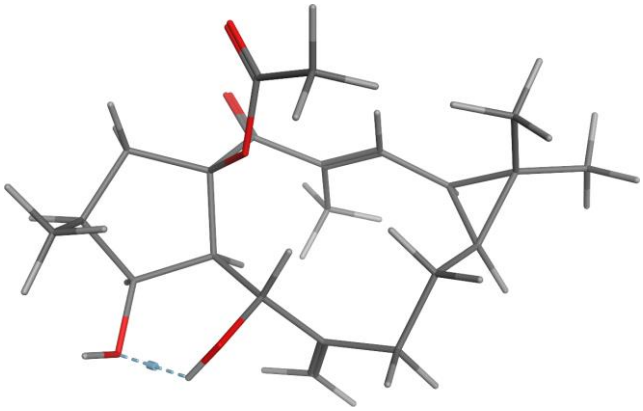

Figure 3.4. Energy minimized structure for pedrodiol (**12**). Intramolecular hydrogen-bonds are depicted in light blue. Minimization was made in MOE software using the AMBER10:ETH force field, according to the semi-empiric Hamiltonian PM3 (available in MOPAC).

Consequently, compound **12** was identified as an epimer of piscatoriol B (Reis et al., 2014b), only differing in the α-orientation of the hydroxyl group at C-5, and as a functional isomer of pedrodione A in which the carbonyl group at C-5 is replaced by a hydroxyl group.

3.1.3. Piscatoriol A, 15β-acetoxy-6*Z*,12*E*-dien-3β,5α-dihydroxylathyra-14-one

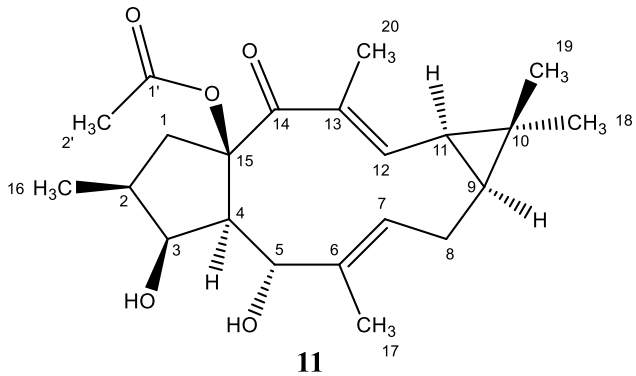

11

Compound **11** was identified as piscatoriol A, based on the comparison of the spectroscopic data obtained for compound **11** with pedrodiol (**12**) and other data available in literature. Piscatoriol A was isolated as a white powder with $[\alpha]_D^{20}$ - 68.6° (*c* 0.1, $CHCl_3$). From the IR spectrum the presence of a hydroxyl (3319 cm^{-1}) and carbonyl groups (1747 cm^{-1}) were suggested, and the and low-resolution ESI-MS mass spectrum allowed the identification of a protonated molecule peak at *m/z* 377 $[M + H]^+$.

Following, by comparison of the ^{1}H- and ^{13}C-NMR data with those found for pedrodiol (**12**, **Table 3.2**), the main difference was the absence of signals for the $\Delta^{6,17}$ exocyclic double bond and the presence of an olefinic proton at δ_H 5.25 (*dd*, *J* = 11.1, 5.4 Hz) at C-7. Instead, an endocyclic double bond between C-6 and C-7 (δ_C 135.6 and 126.7, respectively) and a vinylic methyl group (Me-17, δ_H 1.65, δ_C 17.8) were found in that location. Furthermore, the deshielding of the oxymethine proton H-5 (δ_H 5.37; $\Delta\delta_H$ = + 0.56 ppm) and of the diastereotopic protons H-8α (δ_H 2.35, *m*; $\Delta\delta_H$ = + 0.35) and H-8β (δ_H 2.39, *m;* $\Delta\delta_H$ = + 0.81), together with the shielding of C-6 ($\Delta\delta_C$ = – 23.3), corroborated the presence of the double bond at Δ^6. Moreover, from the ^{13}C-NMR and HMBC experiments a conjugated carbonyl (δ_C 197.9), a trisubstituted double bond (δ_C 142.6, 133.6) and two oxymethines (δ_C 79.7 and 65.8) were also assigned to C-14, C-12/C-13, C-3 and C-5, respectively and allowed the identification of compound **11** as piscatoriol A, a lathyrane-type diterpene previously isolated from the aerial parts of *Euphorbia piscatoria* (Reis et al., 2014b).

3.1.4. Jolkinol D, 15β-acetoxy-3β-hydroxylathyra-5E,12*E*-dien-14-one

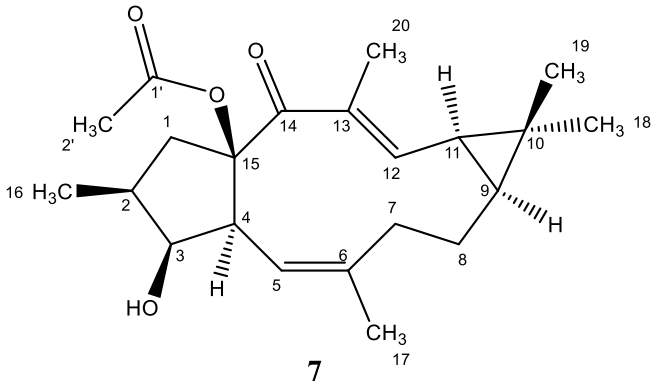

7

Compound **7** was isolated as white crystals with $[\alpha]_D^{20}$ of + 42.6° (*c* 0.1, $CHCl_3$). While the IR experiment suggested the presence of an hydroxyl (3475 cm^{-1}), one ester (1745 cm^{-1}) and a conjugated ketone (1645 cm^{-1}), from the ESI-MS spectrum a protonated molecule peak at *m/z* 361 $[M + H]^+$ was recorded. From the ^{1}H- and ^{13}C-NMR spectra (**Table 3.3**), compound **7** was identified as jolkinol D due to the presence of two olefinic methyl groups (δ_H 1.45 and 1.83; δ_C 21.0 and 12.4), two vinylic protons (δ_H 5.66 and 6.64; δ_C 119.5 and 146.6), two olefinic quaternary carbons (δ_C 143.1 and 132.2), one of which conjugated with a carbonyl (δ_C 195.3), and one oxymethine group (δ_H 3.90; δ_C 80.0). Furthermore, from the NMR experiments the presence of an acetoxy group (δ_H 2.01, *s*; δ_C 21.7 and 169.8) and a quaternary carbon at δ_C 24.5

corroborated the presence of a lathyrane-type macrocyclic diterpenic scaffold. At the end, from the 2D spectroscopic data (COSY, HMQC and HMBC) and by comparison with previously published literature, the identification of compound **7** as jolkinol D, isolated from *Euphorbia jolkini* Boiss (Reis et al., 2014b; Uemura et al., 1977), was confirmed.

3.1.5. Jolkinol D epoxide, 15β-acetoxy-3β-hydroxylathyra-5,6-epoxi-12*E*-en-14-one

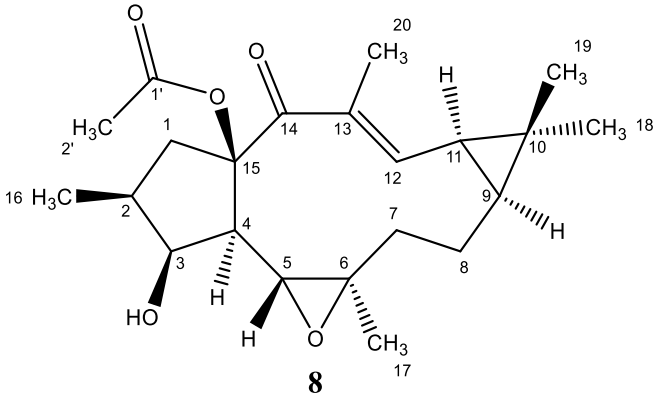

8

Compound **8**, isolated as an amorphous white powder with $[\alpha]_D^{20}$ – 10.0° (*c* 0.1, $CHCl_3$), was identified as the epoxidated derivative of jolkinol D by comparing its spectroscopic data with those obtained for compound **7**. Whereas the low-resolution mass ESI-MS spectrum revealed a protonated molecule peak at *m/z* 377 $[M + H]^+$, the IR experiment suggested the existence of a hydroxyl (3365 cm^{-1}) and carbonyl (1747 cm^{-1}) groups. Although the ^1H and ^{13}C-NMR spectra were quite similar to the NMR data obtained for jolkinol D (**7**), a close inspection revealed that the main difference between compounds **7** and **8** was a replacement of the Δ^5 double bond (δ_C 119.5 and 143.1) by a oxymethine (δ_H 3.51; δ_C 58.1) and a quaternary carbon (63.8 ppm), suggesting an epoxidation of the double bond (**Table 3.3**). Furthermore, the presence of an oxygenated methine (δ_C 78.5; δ_H 4.08 ppm), and an α,β-unsaturated system (δ_C 195.5; δ_H 6.92, δ_C 143.8, 134.5) was also found.

Thus, by comparing the above results with the data published in literature, compound **8** was identified as 15β-acetoxy-3β-hydroxylathyr-5,6-epoxi-12*E*-en-14-one, first isolated from the ethanolic extract of *Euphorbia micractina* roots (Tian et al., 2011).

Table 3.3. ^{1}H and ^{13}C NMR [$CDCl_3$, δ (ppm), mult, *J* (Hz)] spectra of jolkinol D (**7**) and jolkinol D epoxide (**8**).

	jolkinol D (7)		**jolkinol D epoxide (8)**	
Position	**^{1}H**	**^{13}C**	**^{1}H**	**^{13}C**
1α	3.49, *dd* (14.0, 8.1)	44.0	3.46, *dd* (13.5, 7.5)	44.9
1β	1.50, *dd* (14.0)		1.64, *br t* (13.5)	
2	2.02, *m*	39.2	1.94, *m*	38.3
3	3.90, *dd* (8.0, 4.0)	80.0	4.08, *dt* (7.0, 3.5)	78.5
4	2.38, *dd* (10.8, 4.0)	52.7	1.50, *dd* (9.5, 3.5)	51.9
5	5.66, *d* (10.8)	119.5	3.51, *d* (9.5)	58.1
6	--	143.1	--	63.8
7α	2.57, *d* (13.3)	36.8	2.03, *m*	38.7
7β	1.78, *td* (13.3, 2.0)		1.54, *m*	
8α	2.20, *dd* (14.4, 2.0)	28.4	2.10, *m*	23.2
8β	1.56, *m*		1.51, *m*[a]	
9	1.06, *m*	34.2	1.13, *dd* (8.0, 3.2)	33.8
10	--	24.5	--	26.1
11	1.39, *dd* (11.2, 8.3)	29.7	1.51, *dd* (11.1, 8.0)	29.7
12	6.64, *d* (11.2)	146.6	6.92, *d* (11.1)	143.8
13	--	132.2	--	134.5
14	--	195.3	--	195.5
15	--	95.3	--	91.9
16	1.07, *d* (6.7)	13.8	1.08, *d* (5.7)	13.2
17	1.45, *s*	21.0	1.17, *s*	20.0
18	1.17, *s*	29.3	1.20, *s*	28.9
19	1.04, *s*	16.4	1.07, *s*	16.4
20	1.83, *s*	12.4	1.86, *br s*	12.4
1'	--	169.8	--	169.8
2'	2.01, *s*	21.7	2.07, *s*	21.3

[a] signals partially overlapped.

3.2. Jatrophane-type macrocyclic diterpenes

3.2.1. Pedrodione B, 3β,5*α*,15β-triacetoxyjatropha-6(17),11*E*-dien-9,14-dione

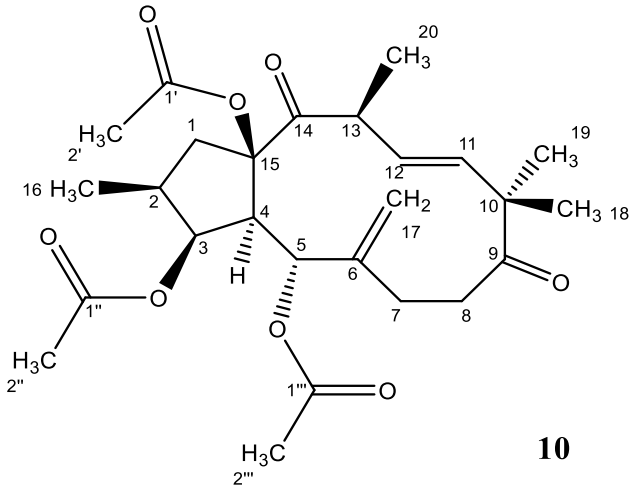

10

Compound **10** is a new compound that was named pedrodione B, and was isolated as a white powder with $[\alpha]_D^{20}$ + 95.6° (*c* 0.1, $CHCl_3$). From the ESI-MS mass spectrum, a protonated molecule peak at *m/z* 477 $[M + H]^+$ was identified. Furthermore, from the high resolution ESI-HRMS a molecular formula of $C_{26}H_{36}O_8$ was obtained from a sodium adduct ion peak at *m/z* 499.2303 $[M + Na]^+$ (calcd. for $C_{26}H_{36}O_8$, 499.2302) and corresponding to nine degrees of unsaturation. The IR spectrum additionally suggested the presence of multiple carbonyl groups (υ_{max} 1741 and 1705 cm^{-1}).

The analysis of the ^{1}H-RMN spectrum (**Table 3.4**) allowed the identification of seven methyl groups: three acetyl groups (δ_H 1.95, 2.05 and 2.16), two tertiary (δ_H 1.19, 1.21) and two doublets from secondary methyls at δ_H 1.00 (6.5 Hz) and δ_H 1.35 (6.6 Hz); and two oxymethines at δ_H 5.58 (*t*, *J* = 4.0 Hz) and δ_H 5.75 (*d*, *J* = 10.0 Hz). Furthermore, vinylic NMR signals from a disubstituted double bond [δ_H 5.59 (*d*, *J* = 10.5) and 5.72 (*t*, *J* = 10.5)] and two broad singlets from a terminal double bond (δ_H 4.87 and 5.18) were also observed.

The ^{13}C-NMR and DEPT experiments (**Table 3.4**) identified the presence of twenty-six carbons corresponding to seven methyl groups (three of which in an acetoxy moiety: δ_C 20.7, 20.9 and 21.3), four methylene groups (including one sp^2 at δ_C 116.1), two oxymethines at δ_C 72.3 and 76.7, two methines and seven quaternary carbons, from which two ketones (δ_C 203.7

and 212.4), three carbonyl esters (δ_C 169.2, 169.4 and 170.4) and one olefinic carbon (δ_C 141.4) could be identified. The absence of a characteristic C-10 signal usually resonating at ≈ 25.0 ppm in lathyranes suggested the presence of a jatrophane-type skeleton. To further assign all carbon signals and to elucidate the most relevant structural details, 2D spectroscopic data from COSY, HMQC, HMBC and NOESY experiments were used (**Table 3.3**, **Figure 3.5**).

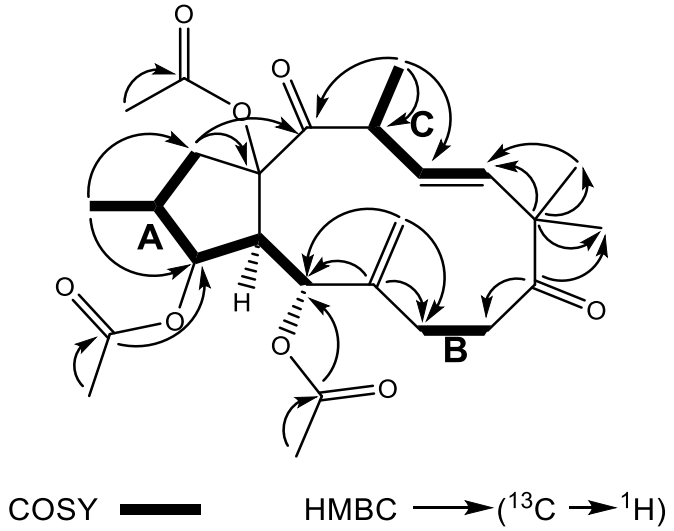

Figure 3.5. Key COSY and HMBC for pedrodione B (**10**). ^{1}H spin systems (A-B) and respective connections by main heteronuclear $^{2}J_{C\text{-}H}$ and $^{3}J_{C\text{-}H}$ HMBC correlations.

While from the ^{1}H-^{1}H COSY spectrum three spin systems could be identified (A-B-C), HMBC correlations between the olefinic protons H-17a and H-17b with C-5, C-6 and C-7 located the exocyclic double bond at $\Delta^{6,17}$, preferentially in an *endo*-type conformation (as shown by the characteristic $J_{4,5}$ = 10.0 Hz). By the analysis of existent literature, the macrocyclic ring may adopt two main conformations: *endo*- and *exo*-type, which can be identified through the $J_{4,5}$ value and some NOESY correlations (Appendino et al., 1998). Accordingly, in the *endo*-type conformation the exomethylene is perpendicular to the main plane of the molecule and H-4/H-5 have an antiperiplanar relationship, displayed as $J_{4,5}$ = 9 – 11 Hz. The observed nuclear Overhauser effects for this kind of conformation are H-5/H-17a and H-17b/H-7; oppositely, in the *exo*-type conformation, the exomethylene is in the plane of the molecule, which is further characterized by lower values (0 – 3 Hz) for the $J_{4,5}$ coupling constant due to the almost orthogonal position of H-4 and H-5 (Appendino et al., 1998).

Following, HMBC correlations between the tertiary methyl groups at δ_H 1.19 and 1.12 with the carbonyl at δ_C 203.7, the olefinic carbon at δ_C 132.3 and the quaternary carbon at δ_C

50.6 placed the second carbonyl at C-9 and the disubstituted double bond between C-11 and C-12. Although the oxidation of C-9 is rare in lathyranes, in jatrophanes it is relatively common either as a free (Wan et al., 2016) or esterified hydroxyls (Reis et al., 2015) or as a carbonyl (Appendino et al., 1998; Wan et al., 2016). Further correlations between the Me-20/C-14 and H-1α/C-15/C-14 corroborated the location of the second carbonyl at C-14. Additionally, the presence of HMBC $^{3}J_{C\text{-}H}$ correlations between the oxymethine protons H-3 and H-5 with the ester moieties δ_C 169.2 and δ_C 169.4, respectively, and its absence for the third ester (δ_C 170.4), provided evidence for the location of the acetoxy groups at C-3, C-5 and C-15.

Table 3.4. ^{1}H-, ^{13}C-NMR and DEPT [$CDCl_3$, δ (ppm), *J* (Hz)] data for pedrodione B (**10**)

Position	^{1}H	^{13}C	DEPT	Position	^{1}H	^{13}C	DEPT
1α	2.83, *dd* (13.4, 7.5)	44.8	CH_2	**13**	3.31, *dq* (10.0, 6.6)	133.2	CH
1β	2.11, *m*			**14**	--	212.4	C
2	2.30, *m*	38.7	CH	**15**	--	90.7	C
3	5.58, *t* (4.0)	76.7	CH	**16**	1.00, *d* (6.5)	13.8	CH_3
4	2.66, *dd* (10.0, 4.0)	49.4	CH	**17a**	5.18, *br s*	116.1	CH_2
5	5.75, *d* (10.0)	72.3	CH	**17b**	4.87, *br s*		
6	--	141.4	C	**18**	1.21, *s*	23.3[a]	CH_3
7α	2.11, *m*	25.1	CH_2	**19**	1.19, *s*	23.3[a]	CH_3
7β	1.77, *dd* (17.0, 11.0)			**20**	1.35, *d* (6.6)	20.1	CH_3
8α	2.59, *td* (11.0, 9.0)	34.4	CH_2	**1'**	--	170.4	C
8β	2.23, *td* (11.0, 9.0)			**2'**	2.05, *s*	20.7	CH_3
9	--	203.7	C	**1"**	--	169.2	C
10	--	50.6	C	**2"**	2.16, *s*	21.3	CH_3
11	5.59, *d* (10.5)	132.3	CH	**1"'**	--	169.4	C
12	5.72, *d* (11.1)	135.0	CH	**2"'**	1.95, *s*	20.9	CH_3

The stereochemistry of compound **10** was deduced from the NOESY experiment (**Figure 3.6**). The α-orientation of H-4 was considered based on biogenetic reasons (Appendino et al., 1998). Herein, strong NOE cross peaks between H-17a/H-5 and H-17b/H-7α/H-7β supported the β-orientation of H-5, thus being close to the exomethylene (as expected for an *endo*-type conformation of the exocyclic double bond) and antiperiplanar regarding H-4, in accordance with the large value observed for the $J_{4,5}$ coupling constant (10.0 Hz). The α-

orientation of H-13 was also confirmed through the observation of NOE correlations with H-1α, H-3, H-4 and H-11.

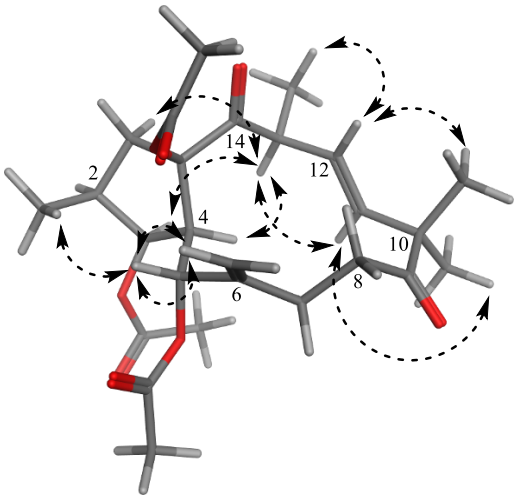

Figure 3.6. Key NOESY correlations for pedrodione B (**10**). The energy minimized structure was obtained in MOE software using the AMBER10:ETH force field, according to the semi-empiric Hamiltonian PM3 (available in MOPAC).

From the above data, compound **10** was identified as 3β,5α,15β-triacetoxyjatropha-6(17),11*E*-dien-9,14-dione. The comparison of the above data with those reported for 3,5,7,15-tetracetoxy-9,14-dioxojatropha-6(17),11*E*-diene, firstly isolated from an acetone extract of *Euphorbia peplus* (Wan et al., 2016), allowed the identification of pedrodione B, in which the acetoxy moiety at C-7 is replaced by a methylene group. It is also worth noticing that jatrophane-type diterpenes lacking the oxymethine function at C-7 are unusual (Vasas and Hohmann, 2014) but other jatrophanes as guyonianins D-E (El-Bassuony, 2007; Hegazy et al., 2010) or Esulatin J (Vasas et al., 2011) are reported in literature.

3.3. Diterpenes with a polycyclic scaffold

3.3.1. Pedrolide

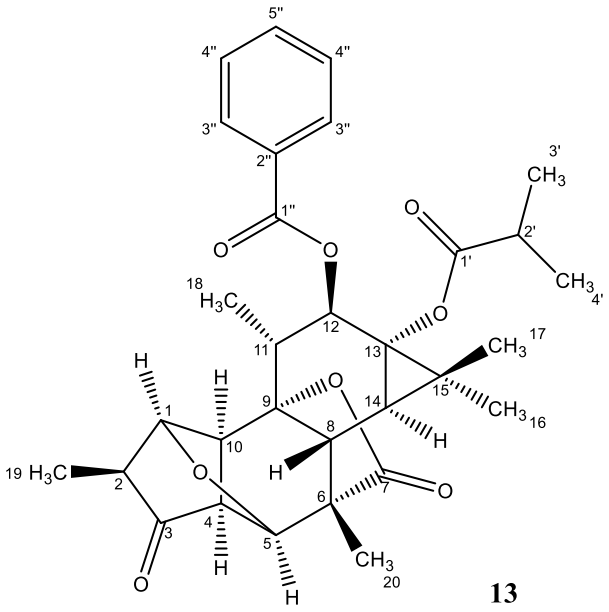

13

Compound **13** is a new compound, isolated as a pale white powder with $[\alpha]_D^{20}$ of + 75.4° (*c* 0.1, $CHCl_3$). While from the IR experiment two carbonyl groups were identified (1750, 1701 cm^{-1}), the low molecular ESI-MS spectrum revealed the presence of a protonated molecule peak at *m/z* 537 $[M + H]^+$. From the ESI-HRMS spectrum, the identification of a sodium adduct ion peak at *m/z* 559.2096 $[M + Na]^+$ allowed us to infer a molecular formula of $C_{31}H_{36}O_8$, along with a degree of unsaturation (DoU) of fourteen.

From the ^{1}H-NMR spectrum (**Table 3.5**) were identified seven methyl groups: three tertiaries (δ_H 1.12, 1.25 and 1.45), four secondaries at δ_H 1.10 (7.0 Hz), 1.12 (7.0 Hz), 1.18 (6.7 Hz) and 1.25 (6.7 Hz); and fifteen methines, five of which aromatic (δ_H 7.44, 7.55 and 8.02) and one oxymethine (δ_H 5.95). Furthermore, the relative downfield signal and the multiplicity of the methine at δ_H 2.54 (*h*, 7.0 Hz) also suggested the presence of an isobutyrate ester. The ^{13}C-NMR and DEPT experiments revealed the presence of thirty-one carbons: seven methyl groups, fifteen methines, five of which aromatic [δ_C 128.5 (2), 129.8 (2) and 132.8], an oxygenated one (δ_C 80.1) and two others slightly downfield (δ_C 55.6 and 63.1) suggesting the presence of an epoxide. Nine quaternary methyls were also identified, including one saturated ketone (δ_C 212.2), two esters (δ_C 166.3 and 177.3) and two oxygenated carbons (δ_C 88.5 and

66.4). Therefore, 2D-NMR experiments (COSY, HMQC, HMBC and NOESY) were performed to further assign all carbon signals and to elucidate the relevant structural details (**Figure 3.7**).

Table 3.5. ^{1}H-, ^{13}C-NMR and DEPT [$CDCl_3$, δ (ppm), mult, *J* (Hz)] spectra of pedrolide (**13**)

Position	^{1}H	^{13}C	DEPT	Position	^{1}H	^{13}C	DEPT
1	2.61, *bs* [a]	63.1	CH	**16**	1.12, *s*	23.2	CH_3
2	2.39, *dq* (6.7, 4.7)	45.0	CH	**17**	1.45, *s*	18.0	CH_3
3	--	212.2	C	**18**	1.18, *d* (7.0)	13.8	CH_3
4	3.03, *dd* (4.7, 2.4)	50.1	CH	**19**	1.25, *d* (6.7) [a]	12.4	CH_3
5	2.63, *d* (4.7) [a]	55.6	CH	**20**	1.25, *s* [a]	17.4	CH_3
6	--	45.6	C	**1'**	--	177.3	C
7	--	176.8	C	**2'**	2.54, *h* (7.0)	33.8	CH
8	1.75, *d* (5.5)	51.0	CH	**3'**	1.10, *d* (7.0)	18.9	CH_3
9	--	88.5	C	**4'**	1.12, *d* (7.0)	19.1	CH_3
10	2.44, *bs*	46.7	CH	**1"**	--	166.3	C
11	1.80, *dq* (8.2, 7.0)	43.4	CH	**2"**	--	130.9	C
12	5.95, *d* (8.2)	80.1	CH	**3"**	8.02, *dd* (7.3, 1.4)	129.8	CH
13	--	66.4	C	**4"**	7.44, *td* (7.3, 1.4)	128.5	CH
14	0.96, *d* (5.5)	28.2	CH	**5"**	7.55, *td* (7.3, 1.4)	132.8	CH
15	--	30.3	C				

[a] signals partially overlapped

From the ^{1}H-^{1}H COSY experiment, three spin-spin systems (A-C) were found. Following, HMBC cross peaks identified between H-8 and C-6/C-8/C-14 ($^{2}J_{C\text{-}H}$) or C-5/C-10/C-11 ($^{3}J_{C\text{-}H}$) elucidated the position of the correspondent carbons and cross correlations between H-12/C-13, H-14/C-13/C15, Me-16/C-13/C-14/C-15 and Me-17/C-13/C-15 acknowledged the position of a cyclopropane ring. The position of the benzoate ester at C-12 was established by a $^{3}J_{C\text{-}H}$ cross correlation between H-12 (δ_H 5.95) and the benzoate carbonyl carbon (δ_C 166.3). The absence of any HMBC correlations of the carbonyl (δ_C 179.6) of the isobutyrate ester function indicated that was attached to a quaternary carbon (C-13). Furthermore, the location of the ether bridge was found to be located between C-1 (δ_C 63.1) and C-5 (δ_C 55.6)

The correlations found between the methyl Me-19 and C-2/C-1/C-3 located the carbonyl group at C-3 and, together with the above data, allowed us to infer a tigliane-type scaffold. However, as no C-6/C-7 double bond was found in this molecule, a closer analysis of the HMBC correlations observed for H-5 and H-8 indicated the occurrence of a rearrangement involving C-6 and C-7. To that matter, the presence of an exocyclic ester function at C-7 could be explained by a Pinacol rearrangement, in which the epoxidation of the typical $\Delta^{6,7}$ led to the formation of a vicinal diol that, upon loss of a water molecule, rearranges in order to establish a C-6/C-8 bond, creating an aldehyde at C-7 that is further oxidized to a carboxylic acid (**Figure 3.8**). Furthermore, the absence of an intense IR band for either a free carboxylic acid or hydroxyl groups also suggests the presence of a lactone, most likely with C-9. To our knowledge, this is the first time that such C-6/C-7/C-8 rearrangement is observed in tiglianes, but nonetheless is known that i) ingenanes can reorganize to tiglianes by a retro-pinacol rearrangement at C-10/C-11 (Appendino et al., 1999) and ii) phorbobutanone-20-monoacetate was synthesized from phorbol-20-monoacetate by a similar rearrangement in positions C-12 and C-13 (Bartsch and Hecker, 1969).

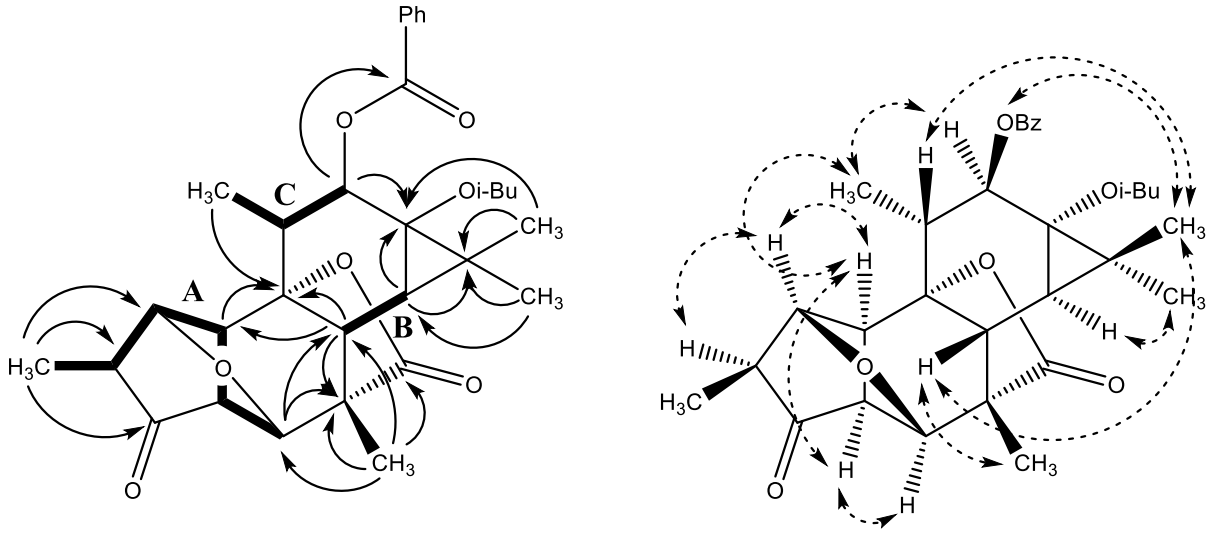

Figure 3.7. Key COSY, HMBC and NOESY for pedrolide (**13**). ^{1}H spin systems (A-B-C) and respective connections by main heteronuclear $^{2}J_{C\text{-}H}$ and $^{3}J_{C\text{-}H}$ HMBC correlations.

The stereochemistry of pedrolide (**13**) was obtained through NOESY experiments. As all tiglianes isolated to date possess H-8β, OH-9α and H-10α, these orientations were assumed unless stated otherwise. Herein, the NOE cross peaks between H-8/H-17/H-20 corroborated its β-orientation and cross correlations between H-1/H-2, H-4/H-5, H-5/H-10 and H-1/Me-18

supported its α-orientation. Furthermore, from the observed NOE correlations between H-12/Me-18 and Me-17/H-3", an α-orientation for the methyl Me-18 and a β-orientation of the benzoate ester were inferred.

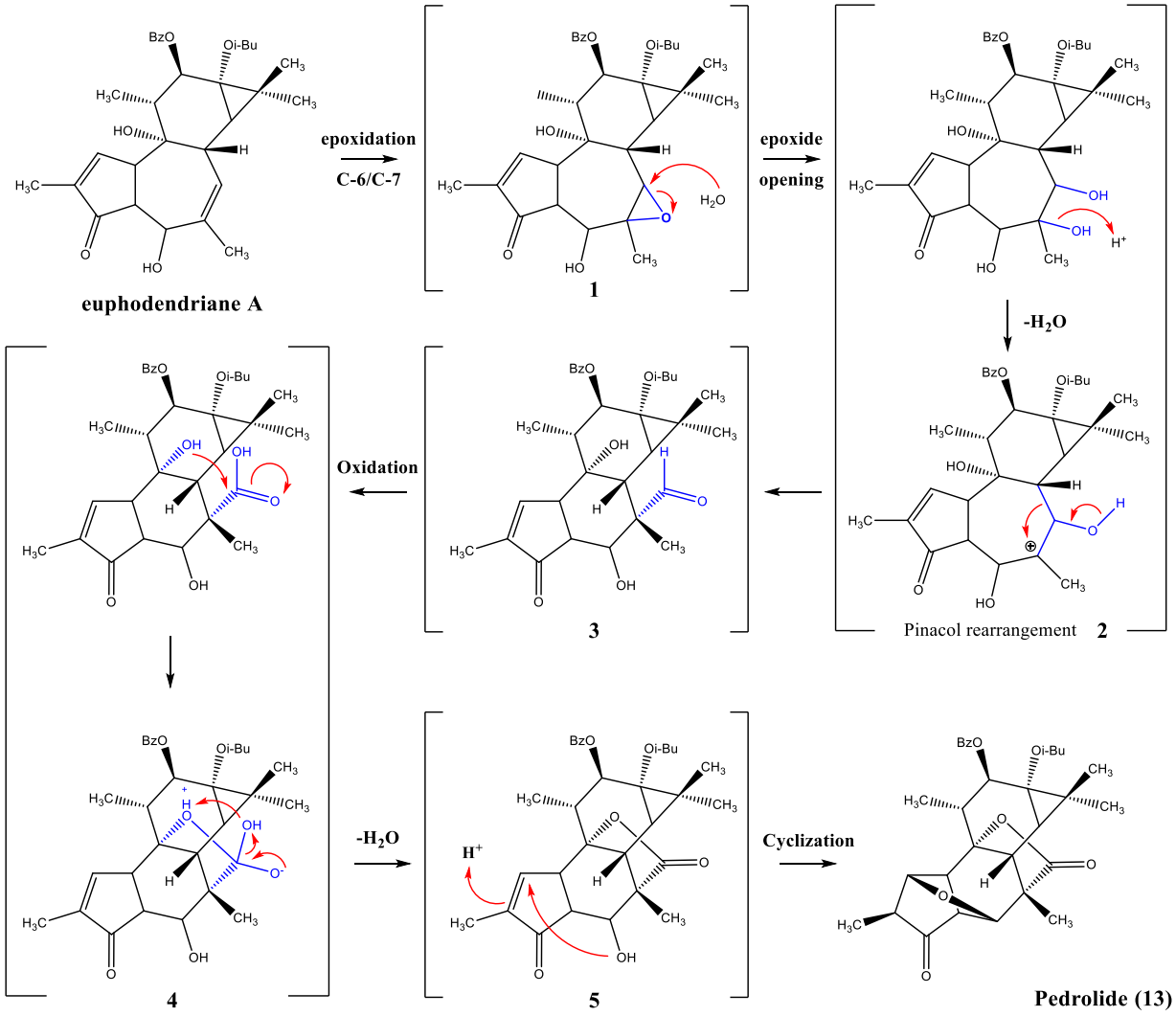

Figure 3.8. Possible biogenetic pathway for **13** from the known compound euphodendriane A.

Thus, compound **13** was identified as a rearranged tigliane derivative from euphodendriane A (**Figure 3.9**), in which a pinacol rearrangement at C-6/C-7 induces the formation of an exocyclic carboxylic acid and followed by intramolecular cyclization to yield a lactone upon loss of a water molecule. Following, an intramolecular Michael-type addition of the hydroxyl at C-5 to the position C-1 yields the ether bridge. Further studies are currently undergoing, in an attempt to obtain a crystallographic structure to further support the observed structural features, but nonetheless another rearranged tigliane was recently reported as having

a 5/5/6/3 fused ring system, hypothetically through an intramolecular Michael addition to a α,β-unsaturated aldehyde intermediate (Wang et al., 2017).

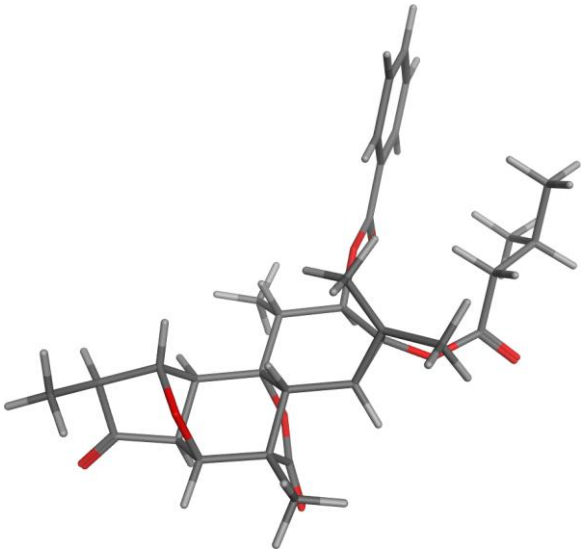

Figure 3.9. Energy minimized structure for pedrolide (**13**). Minimization was made in MOE software using the AMBER10:ETH force field, according to the semi-empiric Hamiltonian PM3 (available in MOPAC).

3.3.2. *ent*-13*R*-hydroxy-3,14-dioxo-16-atisene

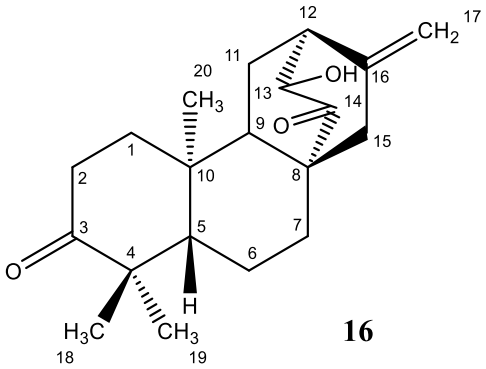

16

Compound **16** was identified as *ent*-13*R*-hydroxy-3,14-dioxo-16-atisene (Lal et al., 1989) based on its physical and spectroscopic data. It was isolated as white needles with $[\alpha]_D^{20}$ + 47.6° (*c* 0.1, $CHCl_3$). The IR spectrum revealed the presence of a hydroxyl (3419 cm^{-1}) and two carbonyl groups (1724, 1703 cm^{-1}) and the low-resolution ESI-MS a protonated molecule peak at *m/z* 317 $[M + H]^+$, in agreement with the molecular formula $C_{20}H_{28}O_3$. From the ^1H- and ^{13}C-NMR spectra, twenty carbon signals were identified, including two carbonyls (δ_C 216.2, 218.2), one exocyclic double bond (δ_H 4.88, 5.02; δ_C 142.2, 111.2), one oxymethine (δ_H 3.88; δ_C 75.2) and

three tertiary methyl groups (δ_H 0.84, 1.02 and 1.08). Furthermore, six methylenes, two methines and three quaternary carbons were also observed (**Table 3.6**).

Table 3.6. ^{1}H-, ^{13}C-NMR and DEPT [$CDCl_3$, δ (ppm), *J* (Hz)] spectra for compound **16**.

	***ent*-13R-hydroxy-3,14-dioxo-16-atisene (16)**		
Position	**^{1}H**	**^{13}C**	**DEPT**
1α	1.86, *ddd* (13.5, 6.4, 3.2)	36.8	CH_2
1β	1.38, *td* (13.4, 5.5)		
2α	2.54, *ddd* (15.9, 13.2, 6.4)	34.2	CH_2
2β	2.35, *dd* (5.5, 3.2)		
3	--	216.2	C
4	--	47.6	C
5	1.30, *dd* (3.5, 2.0)	55.2	CH
6α	1.53, *dd* (9.0, 3.5)	20.1	CH_2
6β	1.49, *ddd* (9.0, 3.5, 2.0)		
7α	2.40, *dt* (9.0, 3.5)	30.5	CH_2
7β	1.00, *m*		
8	--	47.4	C
9	1.65, *dd* (11.2, 4.8)	51.2	CH
10	--	37.7	C
11α	2.01, *ddd* (14.5, 11.2, 2.8)	25.4	CH_2
11β	1.75, *ddd* (14.5, 5.4, 2.8)		
12	2.81, *dd* (5.4, 2.8)	44.8	CH
13	3.88, *s*	75.2	CH
14	--	218.2	C
15	2.32, *br s*	43.8	CH_2
16	--	142.4	C
17α	5.02, *s*	111.2	CH_2
17β	4.88, *s*		
18	1.08, *s*	26.3	CH_3
19	1.02, *s*	22.0	CH_3
20	0.84, *s*	13.9	CH_3

However, the above ^{1}H- and ^{13}C-NMR data were consistent with two compounds already reported in literature, *ent*-13*R*-hydroxy-3,14-dioxo-16-atisene (Lal et al., 1989) and

antiquorin (Zhi-Da et al., 1989) that only differ in the configuration at C-5. Hence, from the NOESY experiment the observation of strong NOE cross peaks between H-5 and H-6β/H-9/Me-18 clarified the β-orientation of H-5. Moreover, additional NOE correlations between H-13/Me-20 located the hydroxyketone bridge in an α-position against the mean plane of the molecule. Therefore, from the spectroscopic data compound **16** could be identified as *ent*-13*R*-hydroxy-3,14-dioxo-16-atisene, isolated from the heartwood of *Euphorbia fidjiana* Boiss (Lal et al., 1989).

3.3.3. Helioscopinolide B

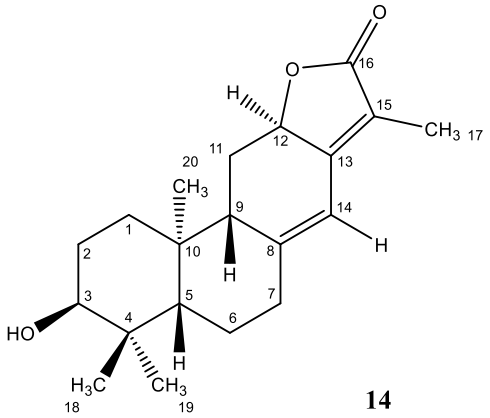

14

Compound **14**, identified as helioscopinolide B, was isolated as a colorless oil with $[\alpha]_D^{20}$ + 302.8° (*c* 0.1, $CHCl_3$). While the IR spectrum suggested the presence of a double bonf (1666 cm^{-1}), a carbonyl (1732 cm^{-1}) and a hydroxyl function (3479 cm^{-1}), the ESI-MS low resolution mass spectrum revealed a protonated molecular ion peak at *m/z* 317 $[M + H]^+$. From the ^1H- and ^{13}C-NMR experiments, one conjugated carbonyl (δ_C 175.5), two double bonds, a tetrasubstituted (δ_C 117.1 and 155.7) and a trisubstituted (δ_C 114.1 and 150.3) with one olefinic proton (δ_H 6.32, *s*), one vinylic methyl (δ_H 1.79; δ_C 28.8) and two oxymethines (δ_H 3.45, 4.85; δ_C 75.5, 76.1) were observed. Furthermore, three tertiary methyl groups, five diastereotopic methylenes, two methines and three quaternary carbons were further identified (**Table 3.7**). By comparing the above spectroscopic data with the one reported for *ent*-abietane lactones, compound **14** could be further identified as helioscopinolide B, isolated from *Euphorbia helioscopica* (Borghi et al., 1991; Crespi-Perellino et al., 1996).

Table 3.7. ^{1}H and ^{13}C-NMR [$CDCl_3$, δ (ppm), *J* (Hz)] spectra for helioscopinolide B (**14**) and helioscopinolide E (**15**).

	Helioscopinolide B (14)		Helioscopinolide E (15)	
Position	**^{1}H**	**^{13}C**	**^{1}H**	**^{13}C**
1α	1.92, *m*	32.2	2.17, *ddd* (10.4, 6.4, 3.5)	37.5
1β	1.66, *m*[a]		1.59, *m*	
2α	1.95, *m*	25.8	2.63, *ddd* (15.7, 12.6, 6.0)	34.5
2β	1.64, *m*		2.45, *ddd* (15.7, 6.0, 3.5)	
3	3.45, *br s*	75.5	--	215.7
4	--	37.8	--	47.6
5	1.62, *m*[a]	48.3	1.64, *m*	54.8
6α	1.72, *m*	23.4	1.80, *m*	24.7
6β	1.38, *ddd* (13.3, 12.3, 3.3)		1.53, *m*	
7α	2.48, *br d* (13.7)	37.1	2.50, *m*[a]	36.7
7β	2.20, *td* (14.3, 13.7, 4.1)		2.22, *m*[a]	
8	--	152.3	--	150.3
9	2.28, *br d* (8.4)	51.6	2.25, *d* (8.3)	50.7
10	--	41.1	--	41.0
11α	2.54, *dd* (13.5, 6.0)	27.5	2.50, *m*[a]	27.9
11β	1.47, *dd* (13.3, 5.0)		1.53, *m*	
12	4.85, *dd* (13.0, 5.0)	76.1	4.87, *dd* (13.3, 5.8)	75.8
13	--	156.3	--	155.7
14	6.24, *s*	114.1	6.32, *s*	114.8
15	--	116.3	--	117.1
16	--	175.5	--	175.2
17	1.79, *s*	28.8	1.11, *s*	26.2
18	0.96, *s*	22.3	1.04, *s*	21.5
19	0.84, *s*	16.8	1.17, *s*	16.0
20	0.93, *s*	8.3	1.83, *br s*	8.1

[a] signals partially overlapped.

3.3.4. Helioscopinolide E

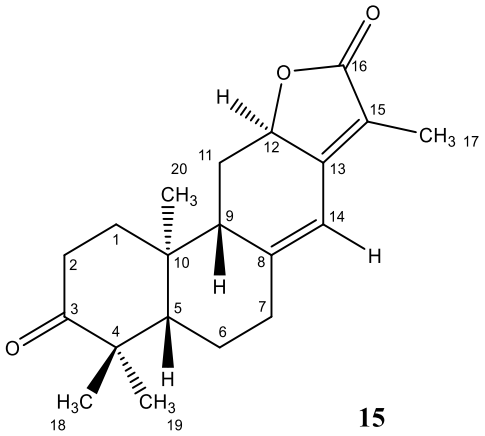

15

Compound **15** was identified as helioscopinolide E by comparison of the physical and spectroscopic data with the results obtained for the previously isolated helioscopinolide B (**14**). It was isolated as white needles with $[\alpha]_D^{20}$ + 353° (*c* 0.1, $CHCl_3$), and while in the IR spectrum the hydroxyl absortion band was replaced by a carbonyl (1724 cm^{-1}), in the ESI-MS experiment the identification of a protonated molecular ion peak at *m/z* 315 $[M + H]^+$ again suggested that one of the oxymethine moieties in compound **14** was replaced by a carbonyl, in agreement with a molecular formula of $C_{20}H_{26}O_3$. This structural feature was also observed in the ^1H- and ^{13}C-NMR spectra, being identified a carbonyl group at C-3 (δ_C 215.7) instead of an oxygenated methine group (**Table 3.7**), which induced a paramagnetic effect at positions C-1 ($\Delta\delta_C$ = + 5.3), C-2 ($\Delta\delta_C$ = + 8.7) and C-4 ($\Delta\delta_C$ = + 9.8). Therefore, compound **15** was acknowledged as helioscopinolide E.

3.3.5. Preparation of helioscopinolide E oxime derivatives

As helioscopinolide E (**15**) was obtained in a reasonable amount (239 mg), a small library of *ent*-abietane derivatives was built by chemical derivatization of the ketone (C=O) moiety. According to literature, the presence of nitrogen atoms and aromatic rings are characterized as key features for the P-gp efflux modulation (Suzuki et al., 1997; Zamora et al., 1988). Thus, the rationale for the chemical derivatization of compound **15** was the introduction of nitrogen-containing and aromatic moieties able to potentiate the MDR reversal capabilities of the compounds.

Reaction between **15** and hydroxylamine hydrochloride (**Scheme 3.1**, **i**) yielded the corresponding helioscopinolide oxime (C=N-OH, **19**). The subsequent acylation of the oxime with acyl anhydrides or chlorides (**Scheme 3.1**, **ii**) yielded five new compounds (**20**-**24**).

The imine at C-3 in compound **19** was confirmed by the analysis of the ^{1}H- and ^{13}C-NMR spectra, in which a strong diamagnetic effect on the C-3 (δ_C 215.7 → 166.3, $\Delta\delta_C$ = – 48.9) and smaller diamagnetic effects at C-2 (δ_C 34.5 → 17.7, $\Delta\delta_C$ = – 16.8) and C-4 (δ_C 47.6 → 41.4 ppm, $\Delta\delta_C$ = – 6.2) corroborated the substitution of the carbonyl moiety by the corresponding imine. A diamagnetic effect on the protons H-2α (δ_H 3.26 → 2.63 ppm, $\Delta\delta_H$ = – 0.63) and H-2β (2.45 → 2.08 ppm, $\Delta\delta_H$ = – 0.37) was also observed.

Scheme 3.1. Preparation of helioscopinolide E (**15**) derivatives (**20**–**24**).[a]

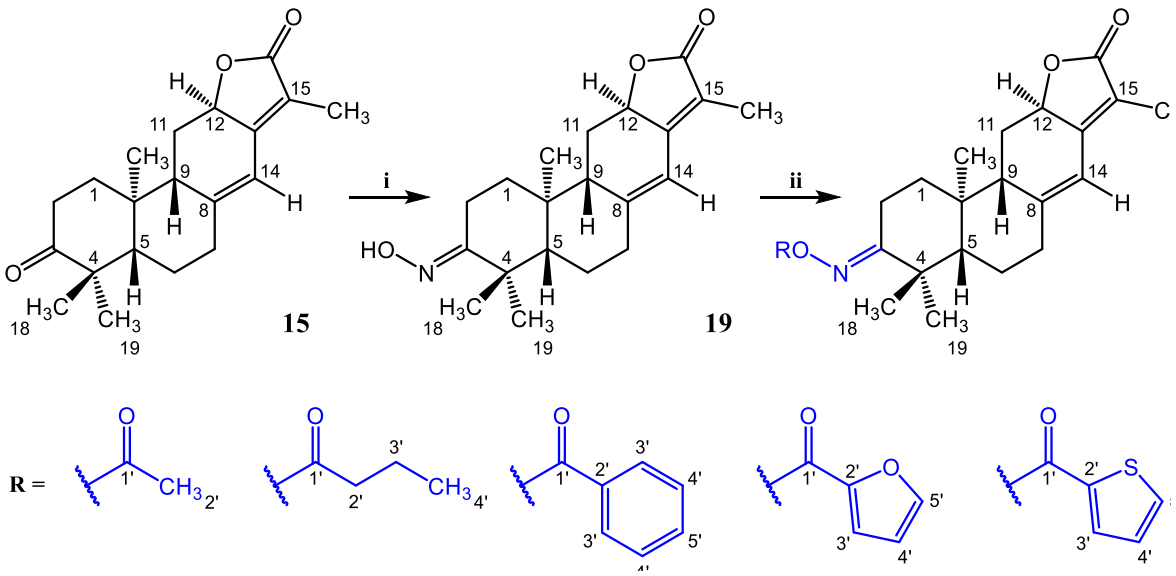

[a] Reagents and conditions: (i) $NH_2OH.HCl$ (5 eq.) in pyridine, rt, overnight; (ii) 3.0 eq. anhydride and acyl chlorides, rt, 6-12 h.

Following, the reaction of helioscopinolide oxime (**19**) with acetic anhydride (**20**), butyryl chloride (**21**), benzoyl chloride (**22**), furan-2-carbonyl chloride (**23**) and tiofene-2-carbonyl chloride (**24**) yielded five new compounds. In the ^{13}C-NMR spectra, these reactions were verified to occur by observing the appearance of a new signal corresponding to the carbonyl of the ester linkage ($\Delta\delta_C \approx$ 171.0 – 175.0) along with small paramagnetic shifts ($\Delta\delta_C$ = + 3.2 – 8.8) of the imine carbon at C-3 (**Tables 3.8 and 3.9**).

Table 3.8. ^{1}H-NMR [$CDCl_3$, δ (ppm), *J* (Hz)] spectra for *ent*-abietane derivatives **19-24.**

Position	19	20	21	22	23	24
2α	3.26, *ddd*	3.13, *dt*	3.11, *dt*	3.27, *dt*	3.24, *dt*	3.23, *dt*
2β	2.08, *m*	2.31, *ddd*	2.51, *dd*	2.47, *ddd*	2.43, *ddd*	2.45, *ddd*
9	2.20, *d*	2.20, *d*	2.21, *d*	2.25, *d*	2.23, *d*	2.23, *d*
12	4.88, *dd*	4.86, *dd*	4.86, *dd*	4.89, *ddd*	4.88, *ddd*	4.87, *dd*
14	6.31, *s*	6.31, *s*	6.31, *s*	6.32, *s*	6.32, *s*	6.33, *s*
17	1.83, *d*	1.83, *d*	1.83, *d*	1.86, *d*	1.84, *d*	1.83, *s*
18	1.09, *s*	1.15, *s*	1.15, *s*	1.24, *s*	1.21, *s*	1.22, *s*
19	1.20, *s*	1.29, *s*	1.30, *s*	1.41, *s*	1.37, *s*	1.37, *s*
20	1.04, *s*	1.04, *s*	1.04, *s*	1.09, *s*	1.07, *s*	1.07, *s*
2'	--	2.18, *s*	2.41, *t*	--	--	--
3'	--	--	1.72, *h*	8.07, *d*	7.25, *dd*	7.60, *dd*
4'	--	--	0.99, *t*	7.49, *t*	6.54, *dd*	7.15, *dd*
5'	--	--	--	7.61, *t*	7.62, *dd*	7.88, *dd*

Table 3.9. ^{13}C-NMR [$CDCl_3$, δ (ppm)] data for *ent*-abietane derivatives **19-24.**

Position	19	20	21	22	23	24
2	17.7	20.0	20.4	20.5	20.4	20.4
3	166.3	169.5	173.7	175.0	175.1	174.8
4	41.4	41.6	41.8	41.9	41.9	41.8
10	40.6	41.2	41.2	41.2	41.2	41.2
18	24.2	20.1	23.4	23.5	23.5	23.5
19	27.6	27.5	27.6	27.6	27.6	27.6
1'	--	171.7	171.7	164.3	166.7	160.1
2'	--	19.9	35.1	130.2	132.2	132.2
3'	--	--	18.5	129.5	132.8	132.7
4'	--	--	13.9	128.7	128.0	128.0
5'	--	--	--	133.3	134.0	133.9

3.4. Steroids

3.4.1. Spiropedroxodiol, 3,7-dihydroxy-7(8→9)*abeo*-ergosta-24(28)-en-8-one

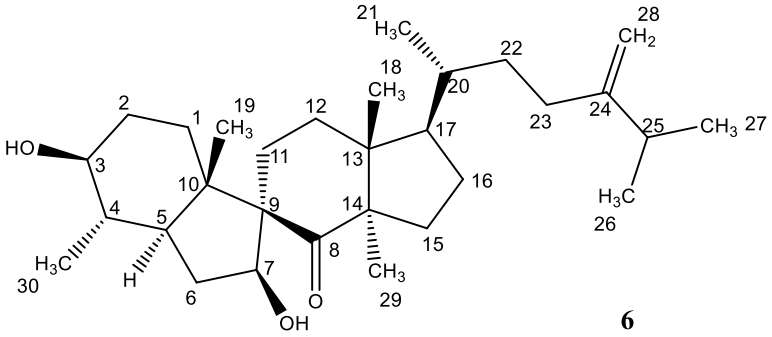

6

Compound **6** is a new compound, which was isolated as a colorless oil with $[\alpha]_D^{20}$ + 12.0° (*c* 0.1, $CHCl_3$). From its IR spectrum, characteristic absorption bands corresponding to hydroxyl (3383 cm^{-1}) and a carbonyl (1691 cm^{-1}) were observed. From the low resolution ESI-MS spectrum a protonated molecular ion at *m/z* 459 $[M + H]^+$ was identified. Furthermore, a sodium adduct ion peak at *m/z* 481.3655 $[M + Na]^+$ (calcd. for $C_{30}H_{50}NaO_3$, 481.3652) was observed in the ESI-HRMS spectrum, from which a molecular formula of $C_{31}H_{36}O_8$ and a DoU of six were inferred. The ^{1}H-NMR spectrum revealed the presence of seven methyl groups, three tertiary (δ_H 0.66, 1.20, 1.47); and four secondary at δ_H 0.94 (*J* = 5.6 Hz), 0.96 (*J* = 5.4 Hz), 1.01 (*J* = 6.8 Hz) and 1.03 (*J* = 6.8 Hz). Furthermore, a terminal double bond (δ_H 4.65 and 4.72) and two oxymethines (δ_H 3.04, 4.34) were additionally found. From the ^{13}C-NMR and DEPT experiments, thirty carbons could be found: seven methyl groups, ten methylene units (including one sp^2 at δ_C 106.3), seven methine groups (including two oxygenated methines at δ_C 77.4 and 80.6) and six quaternary carbons, which included one carbonyl (δ_C 215.2) and one olefinic (δ_C 156.7).

Although pointing to a tetracyclic triterpene skeleton, the ^{13}C-NMR spectrum suggested the presence of a *spiro* rearrangement by the presence of a quaternary carbon at δ_C 64.2, similar to the resonance value reported for C-9 of spiroterpenoids as spiroinonotsuoxodiol and 3,7-dihydroxy-4,14-dimethyl-7(8→9)*abeo*-cholestan-8-one, isolated from *Inonotis obliquos* and *Euphorbia officinalis*, respectively (Daoubi et al., 2007; Handa et al., 2010). Further structural details were obtained from 2D-NMR experiments (COSY, HMBC, HMQC and NOESY) that allowed an unambiguous assignment of all carbon signals (**Figure 3.10, Table 3.10**).

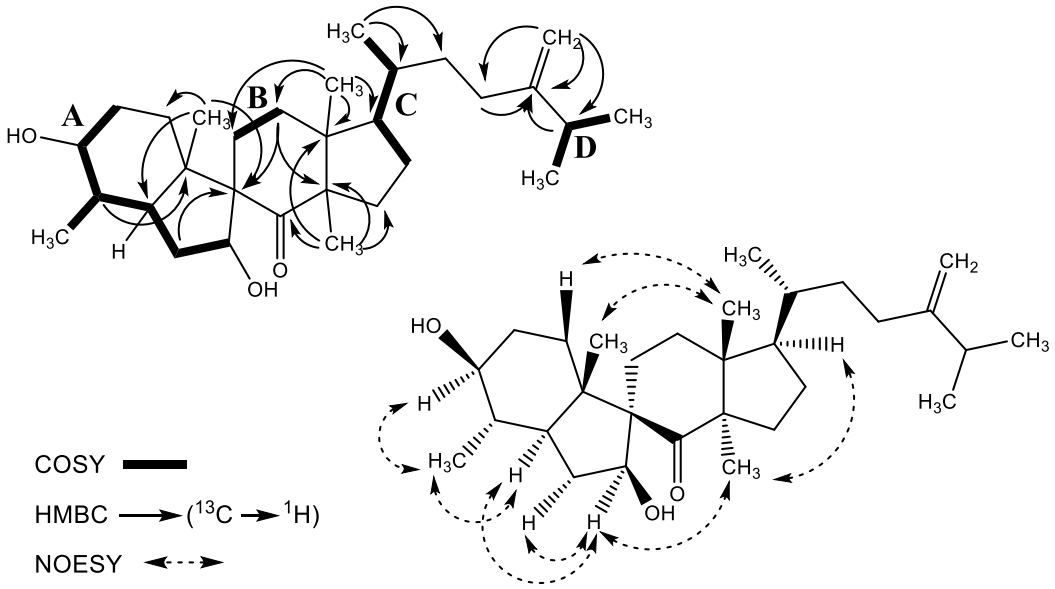

Figure 3.10. Key COSY, HMBC and main NOESY correlations for spiropedroxodiol (**6**). ^{1}H spin systems (A-B) and respective connections by main heteronuclear $^{2}J_{C\text{-}H}$ and $^{3}J_{C\text{-}H}$ HMBC correlations.

Herein, the ^{1}H-^{1}H COSY experiments identified four key fragments (**A**-**D**), which were additionally connected by $^{2}J_{C\text{-}H}$ and $^{3}J_{C\text{-}H}$ HMBC correlations. While in the ^{1}H-^{1}H COSY, H-7 correlated with H-6α and H-6β, in the HMBC experiment the correlations between Me-19 and the carbon signals C-1/C-5/C-9 and between H-6α/H-6β and C-5/C-7/C-9 corroborated the presence of a quaternary carbon at C-9. Moreover, correlations of i) Me-18 with C-11/C-12/C-13/C-14/C-17 and ii) Me-29 with the two quaternary carbons C-13/C-14, a ketone at C-8 and a methylene group at C-15 clarified the position of the ketone and further corroborated the existence of a *spiro* skeleton. The position of both hydroxyl groups at C-3 and C-7 was also found to agree with the data reported in literature for spiroinonotsuoxodiol (δ_C 79.7, C-3; δ_C 80.6, C-7) and 3,7-dihydroxy-4,14-dimethyl-7(8→9)-*abeo*-cholestan-8-one (δ_C 77.2, C-3; δ_C 80.4, C-7). Furthermore, while NOE cross peaks between Me-18/Me-19/H-1α suggested a β-orientation of both methyls, nuclear Overhauser correlations between H-6α/H-7/Me-29/H-17 and H-3/Me-30/H-5/H-6α corroborated the α-orientation of these protons and the β-orientation of the hydroxyl groups at C-3 and C-5. In this particular case, the spectroscopic data do not seem to support the existence of any intramolecular hydrogen-bond between the hydroxyl at C-7 and the carbonyl at C-8, as it can be seen in **Figure 3.11**.

Table 3.10. ^{1}H-, ^{13}C-NMR and DEPT [$CDCl_3$, δ (ppm), *J* (Hz)] data of spiropedroxodiol (**6**).

Position	^{1}H	^{13}C	DEPT	Position	^{1}H	^{13}C	DEPT
1α	2.00, *m*[a]	30.3	CH_2	**16α**	1.96, *m*[a]	27.2	CH_2
1β	1.60, *m*[a]			**16β**	1.33, *m*[a]		
2α	1.98, *m*[a]	28.8	CH_2	**17**	1.67, *m*[a]	50.3	CH
2β	1.41, *m*[a]			**18**	0.66, *s*	16.6	CH_3
3	3.04, *ddd* (12.0, 9.5, 5.3)	77.4	CH	**19**	1.47, *s*	18.6	CH_3
4	1.66, *m*[a]	38.3	CH	**20**	1.40, *m*[a]	35.8	CH
5	1.22, *m*[a]	48.3	CH	**21**	0.94, *d* (5.5)	18.9	CH_3
6α	1.39, *dt* (13.3, 3.4)	37.9	CH_2	**22α**	1.58, *m*	34.9	CH_2
6β	2.39, *dt* (13.3, 7.6)			**22β**	1.15, *m*		
7	4.34, *dd* (8.0, 3.4)	80.6	CH_2	**23α**	2.13, *t* (4.0)	31.4	CH_2
8	--	215.2	C	**23β**	1.92, *d* (4.0)		
9	--	65.2	C	**24**	--	156.7	C
10	--	47.8	C	**25**	2.22, *h* (6.8)	33.9	CH
11α	2.02, *m*[a]	30.3	CH_2	**26**	1.03, *d* (6.8)	22.1	CH_3
11β	1.60, *m*[a]			**27**	1.01, *d* (6.8)	22.0	CH_3
12α	2.07, *m*	30.9	CH_2	**28a**	4.72, *s*	106.3	CH_2
12β	1.74, *m*			**28b**	4.65, *s*		
13	--	48.3	C	**29**	1.20, *s*	19.7	CH_3
14	--	61.1	C	**30**	0.96, *d* (5.5)	16.3	CH_3
15α	1.88, *m*	29.7	CH_2				
15β	1.25, *m*[a]						

[a] signals partially overlapped.

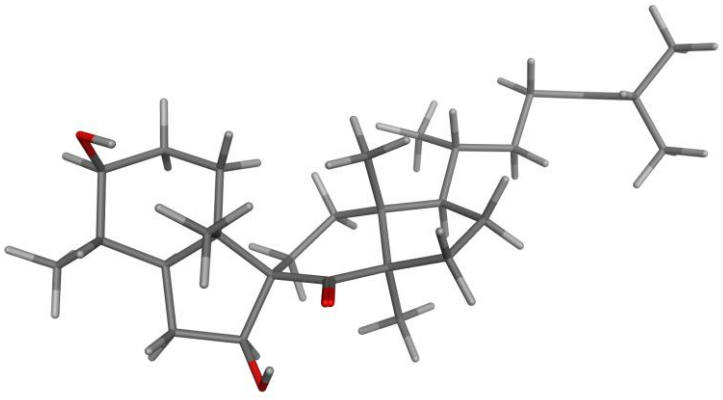

Figure 3.11. Energy minimized structure for spiropedroxodiol (**6**), obtained in MOE software using the AMBER10:ETH force field, according to the semi-empiric Hamiltonian PM3 (available in MOPAC).

3.4.2. 7,11-dioxo-obtusifoliol, 3β-hydroxy-4α,14α-dimethyl-5α-ergosta-8,24(28)-dien-7,11-dione

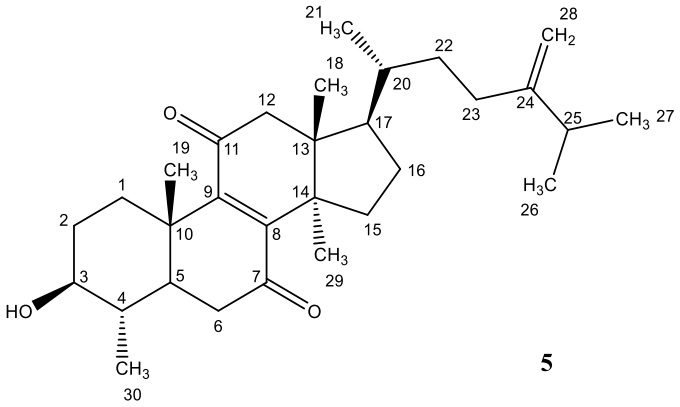

5

Compound **5**, $[\alpha]_D^{20}$ + 94.2° (*c* 0.1, $CHCl_3$), was isolated as a yellowish powder and identified as 7,11-dioxo-obtusifoliol. From the IR spectrum, a conjugated carbonyl (1674 cm^{-1}) and one hydroxyl (3367 cm^{-1}) groups were identified. Additionally, the low-resolution ESI-MS experiment revealed a protonated molecular ion peak at *m/z* 455 $[M + H]^+$, in agreement with the molecular formula $C_{30}H_{46}O_3$. By comparing the ^{1}H- and ^{13}C-NMR spectra to those obtained for compound **6**, a tetracyclic scaffold was inferred. The ^{13}C-NMR spectrum provided evidence for the presence of a conjugated system, instead of the *spiro* scaffold of compound **6**. In addition, the presence of two conjugated carbonyls (δ_C 201.8 and 202.8) and a tetrasubstituted double bond (δ_C 151.4 and 151.6) suggested the presence of a double conjugated enone system. Moreover, from the ^{1}H- and ^{13}C-NMR data, it was also identified one terminal double bond (δ_H 4.66 and 4.72; δ_C 156.6 and 106.3) and three secondary methyl groups (**Table 3.11**), suggesting a similar side chain to that of compound **6**. Thus, and by comparison with literature data, compound **5** was identified as 7,11-dioxo-obtusifoliol, previously isolated from the whole herb of *Euphorbia chamaesyce* (Tanaka et al., 1999).

Table 3.11. ^{1}H-, ^{13}C-NMR and DEPT [$CDCl_3$, δ (ppm), *J* (Hz)] spectroscopic data of 7,11-dioxo-obtusifoliol (**5**).

Position	^{1}H	^{13}C	DEPT	Position	^{1}H	^{13}C	DEPT
1α	2.84, *dt* (13.8, 3.9)	33.4	CH_2	**16α**	2.01, *m*[a]	27.5	CH_2
1β	1.16, *m*[a]			**16β**	1.36, *m*		
2α	1.85, *dd* (9.4, 5.1)	31.0	CH_2	**17**	1.70, *m*	49.2	CH
2β	1.59, *m*[a]			**18**	0.82, *s*	16.9	CH_3
3	3.13, *ddd* (11.1, 9.4, 5.1)	75.5	CH	**19**	1.30, *s*	16.6	CH_3
4	1.49, *m*[a]	38.3	CH	**20**	1.41, *m*	36.3	CH
5	1.47, *m*[a]	47.3	CH	**21**	0.92, *d* (6.4)	18.7	CH_3
6α	2.51, *dd* (15.5, 2.8)	38.4	CH_2	**22α**	1.59, *m*[a]	34.8	CH_2
6β	2.39, *dt* (16.3, 15.5)			**22β**	1.16, *m*[a]		
7	--	201.8	C	**23α**	2.13, *m*	31.3	CH_2
8	--	151.4	C	**23β**	1.87, *m*		
9	--	151.6	C	**24**	--	156.6	C
10	--	38.8	C	**25**	2.24, *h* (6.8)	33.9	CH
11	--	202.8		**26**	1.02, *d* (6.8)[a]	22.0	CH_3
12α	2.77, *d* (16.0)	51.8	CH_2	**27**	1.02, *d* (6.8)[a]	22.1	CH_3
12β	2.63, *d* (16.0)			**28a**	4.72, *s*	106.3	CH_2
13	--	49.1		**28b**	4.66, *s*		
14	--	47.6	C	**29**	1.20, *s*	26.1	CH_3
15α	2.10, *m*[a]	32.2	C	**30**	1.01, *d* (6.1)	14.9	CH_3
15β	1.88, *m*						

[a] signals partially overlapped.

3.4.3. β-sitostenone, (24*R*)-stigmast-4-en-3-one

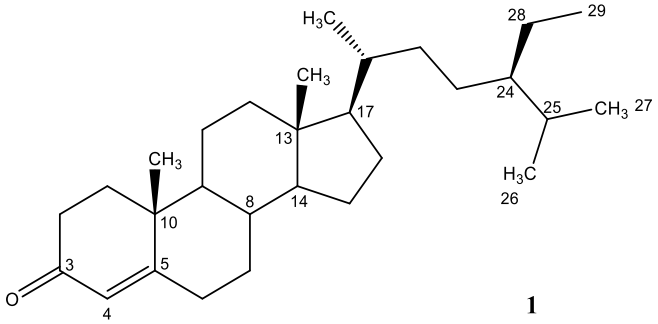

1

Compound **1** was isolated as a white amorphous powder with $[\alpha]_D^{20}$ + 57.4° (*c* 0.1, $CHCl_3$) and further identified as β-sitostenone (Gaspar and das Neves, 1993; Gopalakrishnan et al., 1990). Accordingly, the ESI-MS spectrum revealed a protonated molecular ion peak at *m/z* 413 $[M + H]^+$, which corresponds to a molecular formula of $C_{29}H_{48}O$, and the IR experiment revealed the presence of a conjugated carbonyl (1732 cm^{-1}). From the ^1H- and ^{13}C-NMR data (**Table 3.12**), one vinylic proton and six methyl groups, one of which as a triplet (Me-29, *J* = 7.5 Hz), corroborated the identification of compound **1** as β-sitostenone.

Table 3.12. ^1H-, ^{13}C-NMR and DEPT data [$CDCl_3$, δ (ppm), *J* (Hz)] for β-sitostenone (**1**).

Position	^1H	^{13}C	DEPT
2α	2.41, *dd* (14.1, 4.6)	34.0	CH_2
2β	1.68, *m*		
3	--	199.8	C
4	5.71, *s*	132.8	CH
5	--	171.9	C
18	0.70, *s*	12.1	CH_3
19	1.17, *s*	17.5	CH_3
21	0.91, *d* (6.4)	18.8	CH_3
26	0.82, *d* (8.4)	20.0	CH_3
27	0.80, *d* (8.4)	19.1	CH_3
29	0.83, *t* (7.5)	12.1	CH_3

[a] signals partially overlapped.

3.5. Tetracyclic and pentacyclic triterpenes

3.5.1. Oleanolic acid, 3β-hydroxyolean-12-en-28-oic acid

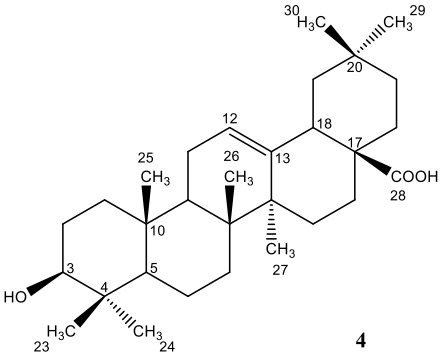

4

Compound **2**, oleanolic acid, was isolated as a white powder with $[\alpha]_D^{20}$ + 104.4° (*c* 0.1, $CHCl_3$). The IR spectrum revealed the presence of a hydroxyl (3423 cm^{-1}) and a carboxylic acid group (1680 and 1271 cm^{-1}). The ESI-MS spectrum showed a molecular ion peak at *m/z* 457 $[M + H]^+$, in agreement with the molecular formula $C_{30}H_{48}O_3$. From the ^1H and ^{13}C-NMR data (**Table 3.13**), a quaternary carbon at δ_C 183.5, a trisubstituted double bond (δ_C 122.6, 143.6) and one olefinic proton (δ_H 5.27) were identified. Furthermore, the presence of an oxymethine at δ_C 79.0 and δ_H 3.21 also confirmed the existence of a hydroxyl group. Thus, compound **2** was identified as oleanolic acid, a pentacyclic diterpene (Huang and Liou, 1997; Ragasa and Lim, 2005).

Table 3.13. ^1H-, ^{13}C-NMR and DEPT data [$CDCl_3$, δ (ppm), mult, *J* (Hz)] of oleanolic acid (**2**).

Position	^1H	^{13}C	DEPT
3	3.21, *dd* (11.0, 4.2)	79.0	CH
5	0.74, *t*, (9.9)	55.7	CH
12	5.27, *t*, (4.1)	122.6	CH
13	--	143.6	C
18	2.81, *dd*, (13.9, 3.7)	40.9	CH
23	0.98, *s*	28.0	CH_3
24	0.74, *s*	15.6	CH_3
25	0.91, *s*	15.3	CH_3
26	0.77, *s*	17.1	CH_3
27	1.13, *s*	25.9	CH_3
28	--	183.5	C
29	0.92, *s*	33.1	CH_3
30	0.90, *s*	23.6	CH_3

3.5.2. Cycloart-25-en-3β,24-diol

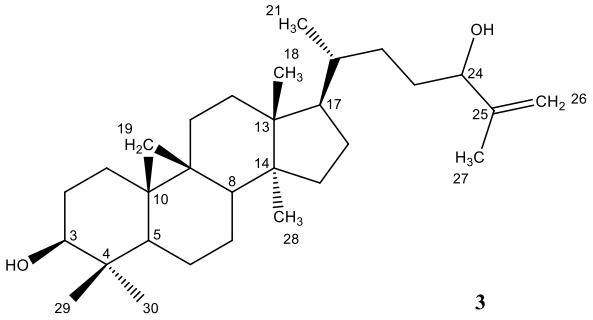

3

Compound **3**, identified as cycloart-25-en-3β,24-diol, was isolated as a white powder with $[\alpha]_D^{20}$ of + 30.6° (*c* 0.1, $CHCl_3$). From the IR spectrum, the presence of hydroxyl (3445 cm^{-1}) was inferred. Furthermore, from the low-resolution ESI-MS spectrum a molecular ion peak at *m/z* 443 $[M + H]^+$ agreed with the molecular formula found in literature for compound **3**, $C_{30}H_{50}O_2$. From the analysis of the ^{1}H- and ^{13}C-NMR data (**Table 3.14**) it was possible to confirm the presence of a terminal double bond (δ_H 4.83, 4.93; δ_C, 147.9, 111.1) and to additionally identify the presence of two oxymethines at δ_C 76.5 and 78.9. Furthermore, the characteristic ^{1}H-NMR signals of the cyclopropane ring at δ_H 0.54 *d* (*J* = 3.5 Hz) and 0.33 *d* (*J* = 3.9 Hz) allowed the identification of this compound as the triterpene cycloart-25-en-3β,24-diol (Anjaneyulu et al., 1985; Della Greca et al., 1994).

3.5.3. Cycloart-23-en-3β,25-diol

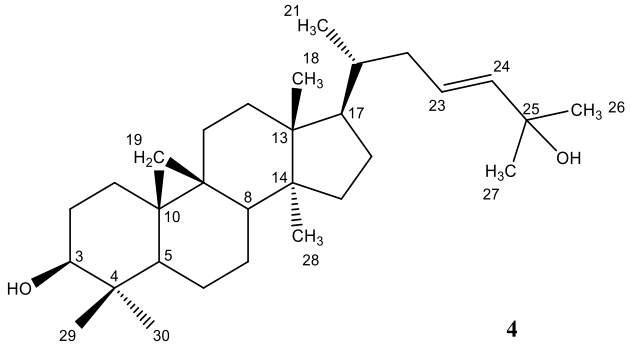

4

Compound **4**, identified as cycloart-23-en-3β,25-diol, was obtained as a white powder with $[\alpha]_D^{20}$ of + 24.6° (*c* 0.1, $CHCl_3$). The comparison of the obtained NMR data with those obtained for compound **3** suggested a cycloartane-type scaffold. While the IR spectrum indicated the presence of a hydroxyl group (3446 cm^{-1}), the ESI-MS experiment showed a molecular ion

peak at *m/z* 443 $[M + H]^+$, in agreement with the molecular formula $C_{30}H_{50}O_2$. Comparison the ^{1}H- and ^{13}C-NMR data (**Table 3.14**) of compound **4** with those of **3** provided evidence for a cycloartane with a different side chain, having compound **4** a disubstituted double bond at Δ^{23} (δ_H 5.60; δ_C 139.3 and 125.6) and a tertiary hydroxyl at C-25 (δ_C 77.5). Thus, by comparing the physical and spectroscopic data with literature, compound **4** was identified as cicloart-23-en-3β,25-diol (de Pascual Teresa et al., 1987; Smith-Kielland et al., 1996).

Table 3.14. ^{1}H- and ^{13}C-NMR [$CDCl_3$, δ (ppm), mult, *J* (Hz)] data of cycloart-25-en-3β,24-diol (**3**) and cycloart-23-en-3β,25-diol (**4**).

cycloart-25-ene-3β,24-diol (3)			**cycloart-23-ene-3β,25-diol (4)**		
Position	**^{1}H**	**^{13}C**	**Position**	**^{1}H**	**^{13}C**
3	3.28, *dd* (10.4, 4.1)	78.9	**3**	3.28, *dd* (10.9, 4.4)	78.8
18	0.96, *s*	18.2	**18**	0.96, *s*	18.1
19α	0.54, *d* (3.7)	30.0	**19α**	0.55, *d* (4.0)	29.9
19β	0.33, *d* (3.7)		**19β**	0.33, *d* (4.0)	
21	0.87, *d* (5.5)	18.4	**21**	0.86, *d* (6.4)	18.3
24	4.02, *t* (6.2)	76.5	**23**	5.60, *br s*	139.3
25	--	147.9	**24**	5.60, *br s*	125.6
26α	4.83, *br s*	111.1	**25**	--	77.5
26β	4.93, *d* (0.5)		**26**	1.31, *br s*	28.1
27	1.72, *s*	17.7	**27**	1.31, *br s*	30.4
28	0.80, *s*	19.4	**28**	0.88, *s*	21.1
29	0.96, *s*	14.2	**29**	0.96, *s*	14.0
30	0.88, *s*	25.6	**30**	0.81, *s*	25.4

3.6. Flavonoids

3.6.1. Naringenin and quercetin

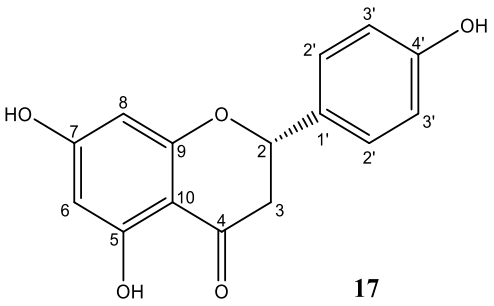

17 **18**

The well-known flavonoids naringenin (**17**) and quercetin (**18)** were isolated from the more polar fractions and identified through their ^{1}H- and ^{13}C-NMR data (**Table 3.15**). While naringenin (**17**) is classified as flavanone due to the presence of a methylene group at C-3 (δ_C 42.6; δ_H 2.60, 3.02), flavanols as quercetin (**18**) possess a double bond between positions C-2 and C-3 (δ_C 147.8 and 135.8, respectively) and additional hydroxyl groups at position C-3 and C-3' (δ_C 145.1).

The hydroxyl positions in ring A were assumed to be at position 5 and 7, due to the aromatic signals at δ_H 5.83 – 6.40 with small coupling constants (J_{meta} ~ 1-2 Hz). Regarding the oxygenation pattern in ring B, while in naringenin the protons H-2'/H-3' were present as doublets (**Table 3.15**) with *ortho* coupling constants ($J_{2',3'}$= 8.4 Hz) in agreement with a *para*-substitution pattern, in quercetin the presence of an aromatic proton (δ_H 7.54) with two coupling constants ($J_{6',5'}$= 8.5 Hz and $J_{6',2'}$ = 1.6 Hz) indicated coupling with protons located in *ortho* (H-5') and *meta* (H-2') positions. Accordingly, H-5' (δ_H 6.88) appeared in the ^{1}H-NMR spectrum as a doublet with a $J_{5',6'}$ = 8.5 Hz (*ortho* coupling) and H-2' (δ_H 7.67) as a doublet with a *meta* coupling constant ($J_{2',6'}$ = 1.6 Hz).

3.6.2. Preparation of naringenin derivatives

Flavonoids are among a multitude of compounds have already been described as efflux modulators (Ferreira et al., 2014), inhibiting all major contributors in MDR, namely BCRP (Cooray et al., 2004; Imai et al., 2004; Pick et al., 2011), MRP1 (Bobrowska-Hägerstrand et al., 2003; Yoshimura et al., 2009) and P-gp (Conseil et al., 1998; Hadjeri et al., 2003). They can be

classified in flavonoids (2-phenylchromen-4-one), isoflavonoids (3-phenylchromen-4-one) or neoflavonoids (4-phenylcoumarine) (Nijveldt et al., 2001; Ross and Kasum, 2002), and are an important and abundant class of molecules with antioxidant, anti-inflammatory, or antiproliferative effects (Pick et al., 2011).

Table 3.15. ^{1}H- and ^{13}C-NMR [δ (ppm), mult, *J* (Hz)] data of compounds **17** and **18**.

	Naringenin (17)[a]		**Quercetin (18)[a]**	
Position	**^{1}H**	**^{13}C**	**^{1}H**	**^{13}C**
2	5.23, *dd* (13.0, 3.0)	79.0	--	147.8
3α	3.02, *dd* (17.1, 13.0)	42.6	--	135.8
3β	2.60, *dd* (17.1, 3.0)			
4	--	196.4	--	175.9
5	--	163.4	--	160.8
6	5.83, *s*[b]	95.7	6.40, *d* (1.1)	98.2
7	--	166.9	--	164.0
8	5.83, *s*[b]	94.8	6.18, *d* (1.1)	93.4
9	--	164.0	--	156.2
10	--	101.9	--	103.1
1'	--	129.6	--	122.0
2'	7.23, *d* (8.4)	127.7	7.67, *d* (1.6)	115.7
3'	6.76, *d* (8.4)	114.9	--	145.1
4'	--	157.8	--	146.8
5'	--	--	6.88, *d* (8.5)	115.1
6'	--	--	7.54, *dd* (8.5, 1.6)	120.1

[a] Naringenin, Methanol-D_4; Quercetin in DMSO-D_6; [b] signals partially overlapped.

As a large amount of naringenin was isolated, chemical modifications on the chromone scaffold were undertaken as an attempt to improve the MDR reversal effects of naringenin in P-gp.

To generate a diverse pool of naringenin derivatives, methylation of the phenolic hydroxyls by dimethylsulphate (**Schemes 3.2 and 3.4**, **i**) was initially performed to yield sakuranetin (**46**) and 4'-methoxysakuranetin (**47**) as building blocks (Kim et al., 2007). In these cases, while new signals in the ^{1}H- and ^{13}C-NMR experiments were found for each methoxy group at C-7 (δ_H 3.85; δ_C 56.2 ppm) and C-4' (δ_H 3.86; δ_C 55.6 ppm), small paramagnetic shifts

were also observed in the carbon signals at C-7 and C-10 ($\Delta\delta_C$ + 1.9 ppm) for sakuranetin and at C-4' ($\Delta\delta_C$ = + 3.1 ppm) and C-1' ($\Delta\delta_C$ = + 2.2 ppm) for the dimethoxy derivative.

Thus, while the reactivity of the carbonyl at C-4 was used to synthesize hydrazones (**Scheme 3.2**, **ii**), azines (**Scheme 3.3**, **ii**) and carbohydrazides (**Scheme 3.4**, **ii**), other nitrogen-containing derivatives were obtained by reacting naringenin with *N*,*N*-dimethyl thiosemicarbazide (**Scheme 3.5**, **i**), through a Mannich-type reaction at C-6 and C-8 (**Scheme 3.5**, **ii**) or by alkylation of sakuranetin with epichlorohydrin at position C-4' (**64**) followed by reaction with the desired amine to yield the correspondent propanolamines (**Scheme 3.6**).

Scheme 3.2. Preparation of hydrazones (**25-28, 46-51**).[a]

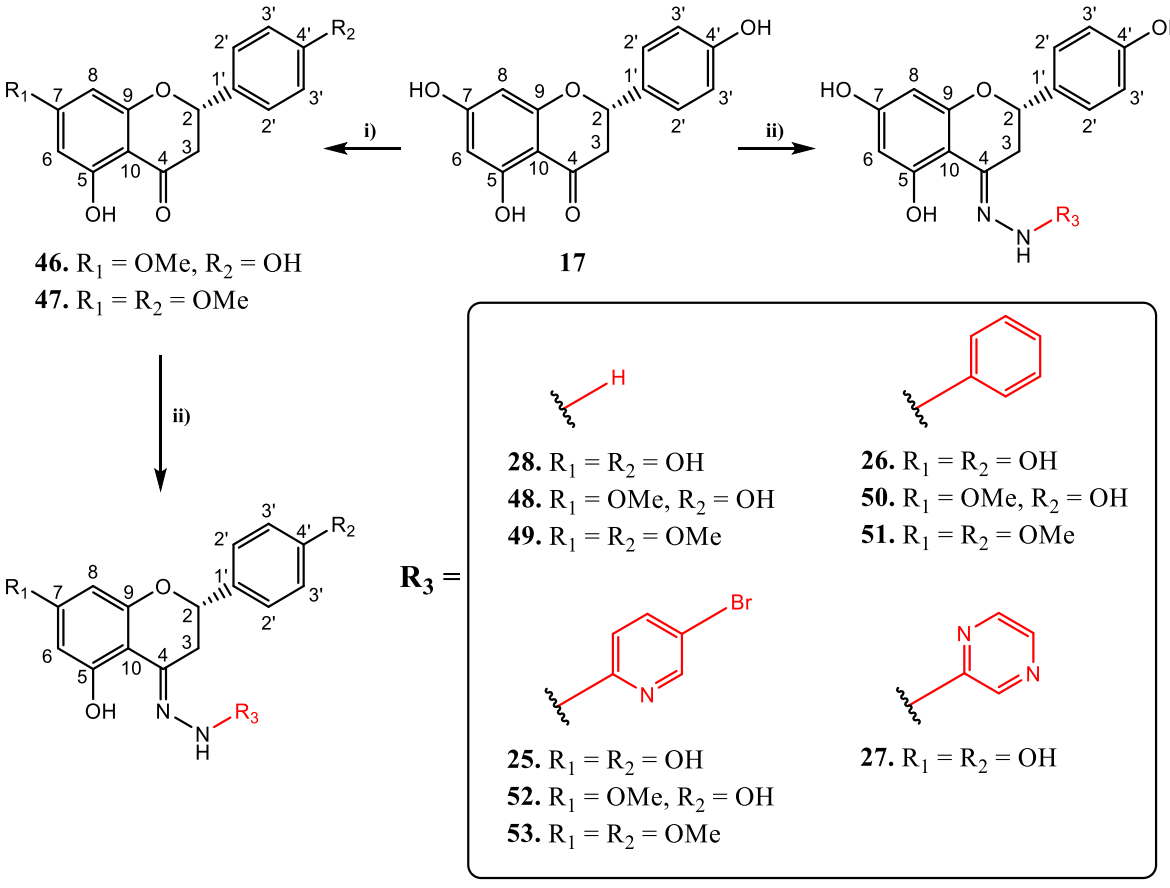

[a] Reagents and conditions: (i) DMS (1 eq.) and K_2CO_3 (1 eq.) in acetone, 50 °C, 12 h; (ii) 2.0 eq. hydrazine (R-NH-NH_2) in ethanol, reflux, 12-48 h.

Scheme 3.3. Preparation of azines (**29-36**).[a]

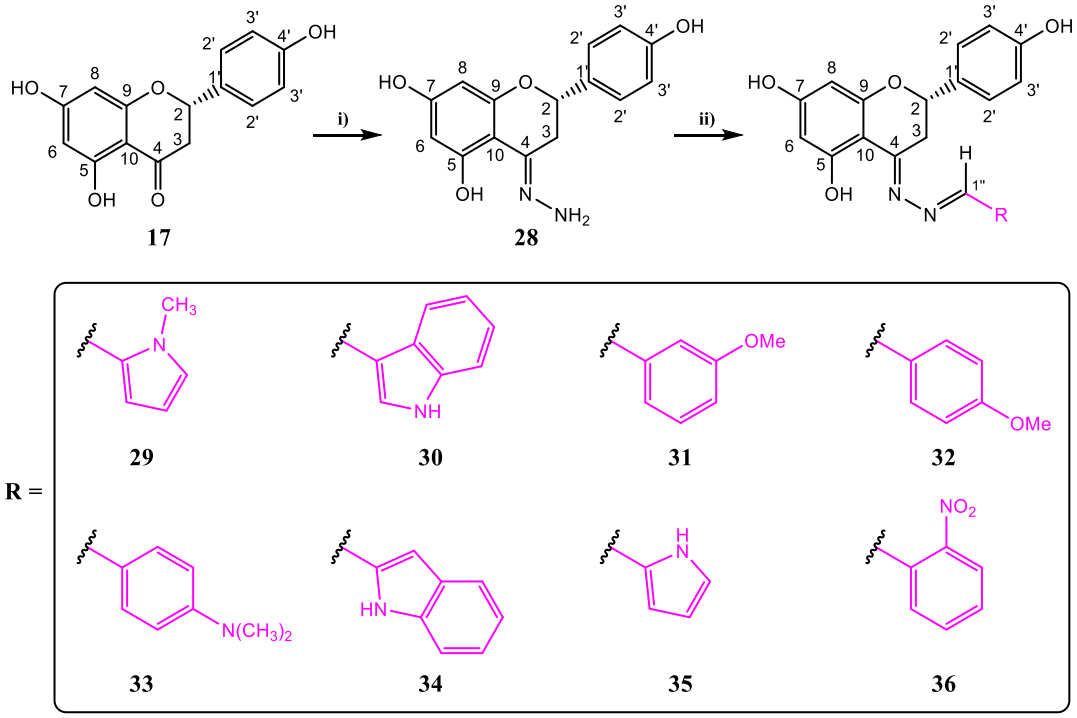

[a] Reagents and conditions: (i) hydrazine monohydrate (5 eq.) in ethanol, reflux, 24 h; (ii) 1.0 eq. aldehyde (R-COH) in ethanol, catalytic acid, reflux, 6-12 h.

After the reaction with hydrazines or hydrazides, and in addition to the new ^{1}H- and ^{13}C-NMR signal from the new substituents, strong diamagnetic shifts in the ^{13}C-NMR signal at C-4 were also identified. In substituted hydrazones (**Scheme 3.2**, **25-27** and **50-52)** in which the aromatic ring is directly attached to the hydrazone (C=N-NH-Ar), the shift was $\Delta\delta_C$ = – 46.8 - 50.8. Quite interestingly, in unsubstituted hydrazones (C=NH-NH_2, **28**, **48**, **49**) the observed shift was smaller ($\Delta\delta_C$ = – 35.4 - 36.0). In azines (**Scheme 3.3**), bearing an extra methylene moiety (C=N-N=CH-R), the diamagnetic shifts registered at C-4 were similar to those reported for unsubstituted hydrazones ($\Delta\delta_C$ = – 29.1 - 32.4), ranging from δ_C 164.0 in compound **30** up to δ_C 167.3 in compound **31**. Finally, if having a carbohydrazide moiety (C=N-NH-CO-R, **Scheme 3.4**), the diamagnetic shifts were found to have values in-between those above reported ($\Delta\delta_C$ = – 38.5 - 45.6), ranging from δ_C 150.8 (compound **63**) to δ_C 157.9 (compound **42**). Regarding the stereochemistry at position C-2, as the energetic barrier for naringenin enantiomerrization is lower at basic (pH 9-11) than at neutral (pH 7) or acidic (pH 2) conditions, no significant epimerization was considered to occur at the reactional conditions employed (Wisturba et al., 2006).

Scheme 3.4. Preparation of carbohydrazides (**37, 38, 40-42, 54-63**).[a]

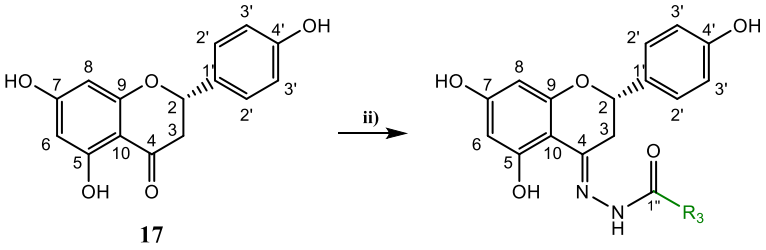

46. R_1 = OMe, R_2 = OH
47. R_1 = R_2 = OMe

R_3 =

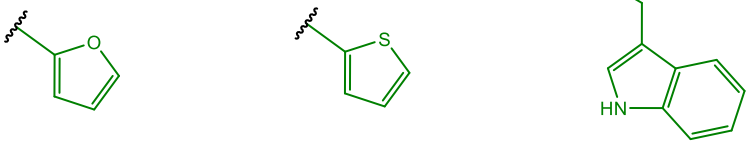

38. R_1 = R_2 = OH
54. R_1 = OMe, R_2 = OH
55. R_1 = R_2 = OMe

37. R_1 = R_2 = OH
56. R_1 = OMe, R_2 = OH

40. R_1 = R_2 = OH
62. R_1 = OMe, R_2 = OH
63. R_1 = R_2 = OMe

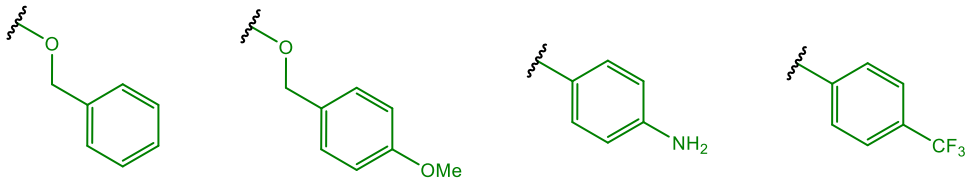

41. R_1 = R_2 = OH
60. R_1 = OMe, R_2 = OH
61. R_1 = R_2 = OMe

42. R_1 = R_2 = OH

57. R_1 = OMe, R_2 = OH
58. R_1 = R_2 = OMe

59. R_1 = OMe, R_2 = OH

[a] Reagents and conditions: (i) DMS (1 eq.) and K_2CO_3 (1 eq.) in acetone, 50 °C, 12 h; (ii) 2.0 eq. hydrazide (R-CO-NH-NH_2) in ethanol, reflux, 12-80 h.

A thiosemicarbazone (**Scheme 3.5**, **i**) was also prepared by reacting naringenin (**17**) with *N*,*N*-dimethylthiosemicarbazide. Herein, the presence of a thioketone (C=S) decreased the magnitude of the diamagnetic effect ($\Delta\delta_C$ = – 33.0) to a value (δ_C = 163.4) similar to those observed for azines. In compounds **43-45**, prepared by a Mannich-type reaction between

naringenin (**17**), formaldehyde and primary or secondary amines (**Scheme 3.5**, **ii**), the introduction of a single substituent at position C-6 induced a strong paramagnetic shift of C-6 carbon signal ($\Delta\delta_C$ = + 27.6 – 33.4), but when both positions C-6 and C-8 are substituted the deshielding effect is smaller, as observed by the slightly downfield carbon signals (δ_C = 115.7 and 114.6; $\Delta\delta_C$ = +20.0 and 18.9, for C-6 and C-8, respectively). Despite this large variation at C-4, similar diamagnetic shifts were registered in positions C-3 ($\Delta\delta_C$ = - 8.6 – 11.8 ppm) and C-10 ($\Delta\delta_C$ = - 0.8 – 3.7 ppm) for compound **28-63** compounds.

Scheme 3.5. Preparation of thiosemicarbazone (**39**) and Mannich-type (**43-45**) naringenin derivatives.[a]

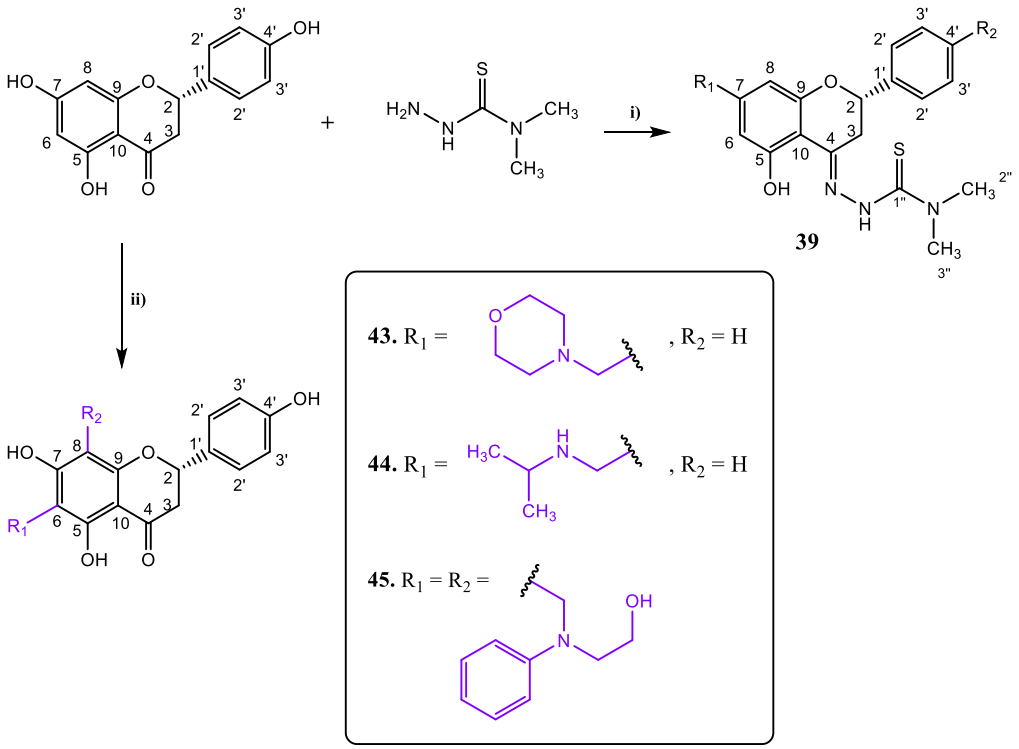

[a] Reagents and conditions: (i) *N*,*N*-dimethylthiosemicarbazone (2 eq.) in ethanol, reflux, overnight; (ii) 1.5 eq. formaldehyde and 1.0 eq. amine in MeOH/DMF (15:1), 50 °C, 2-12 h.

Regarding the ^{1}H-NMR data, and by comparison with compound **17**, hydrazones (**25-27, 50-53**) induced diamagnetic effects on proton signals H-2 and H-3α ($\Delta\delta_H$ = –0.22 to –0.30) and a paramagnetic effect on H-3β ($\Delta\delta_H \approx$ + 0.60). In both azines (**29-36**) and carbohydrazides (**37, 38, 40-42, 54-53**), while the observed diamagnetic effects on H-2 ($\Delta\delta_H$ = 0 to – 0.25) and H-3α ($\Delta\delta_H$ = +0.08 to –0.32) are smaller, the paramagnetic effect on H-3β signal tend to increase in carbohydrazides ($\Delta\delta_H$ = + 0.44 – 0.82) and azines ($\Delta\delta_H$ = + 0.92 – 1.44). Thus, and from the

above ^{1}H- and ^{13}C-NMR data obtained, an *anti* (E) configuration for the C-4 imine is inferred, based on previous literature on the stereochemistry of flavanone hydrazones and oximes in which was determined that, if the substituent is to be located near the α-carbon (C-3), the ^{13}C-NMR signal of this carbon atom will display an upfield shift by 12 –15 ppm (δ_C 42.6 in naringenin against δ_C 30.8 – 34.0 in derivatives, $\Delta\delta_C$ –8.6 to –11.8) and the proton signal a variable downfield shift (Janzsó, 1985; Janzsó et al., 1967).

Another attempt in the development of novel P-gp efflux modulators from naringenin was attempted by the introduction of secondary and tertiary amines in the position 4'. This approach was based on early studies by Chiba and co-workers (Chiba et al., 1997, 1996, 1995) in which nitrogen atoms were incorporated into the class IC antiarrhythmic agent propafenone to obtain compounds able to re-sensitize P-gp expressing human T-lymphoblastoid CCRF-CEM cells. Thus, after methylation of naringenin at position C-7 (**Scheme 3.2**, **i**), a similar methodology was undertaken by reacting sakuranetin (**46**) with epichlorohydrin at position C-4' to yield compound **64** (**Scheme 3.6, i**), followed by treatment with the desired amine to obtain the correspondent propanolamines (**Scheme 3.6**, **ii**, compounds **66**-**69**). Other derivatives were prepared by reaction of **64** with indole (**70**) or thiophenol (**71**). Herein, sakuranetin (**46**) was chosen over naringenin (**17**) to avoid polyalkyations and to speed up the separation processes.

Scheme 3.6. Preparation of 4'-alkylated sakuranetin derivatives (**64**-**71**).[a]

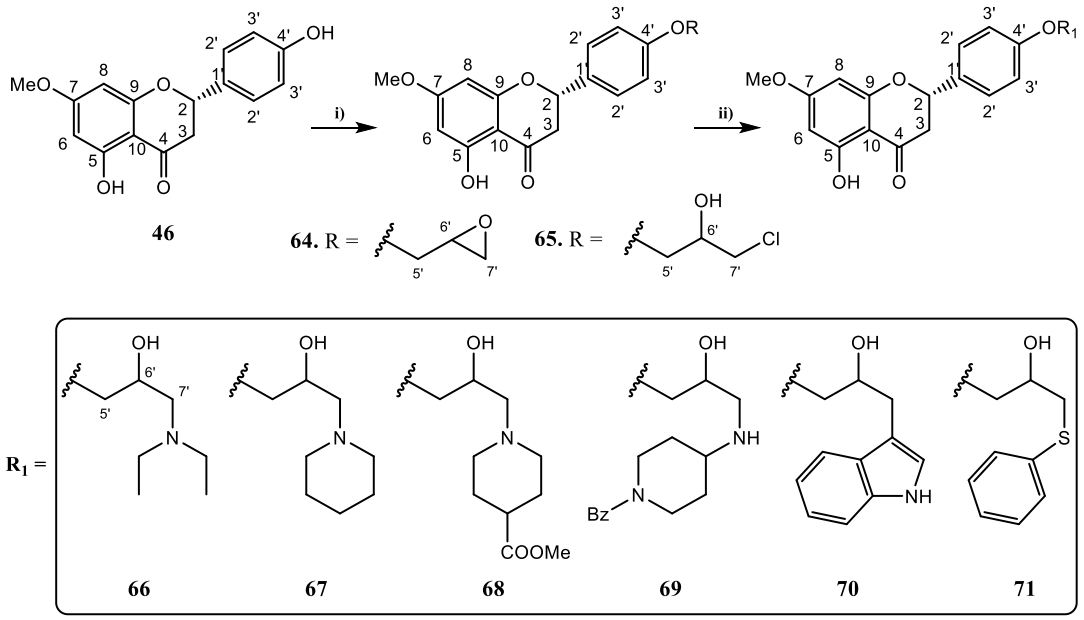

[a] Reagents and conditions: (i) 1.5 eq. epichlorohydrin in ethanol, 1.1 eq. NaOH, reflux, overnight; (ii) 1.0 eq. desired amine in MeOH, H^+, reflux, 24-48 h.

The introduction of the oxyran-2-yl moiety of **64** was confirmed by the appearance of three additional signals in the ^{13}C-NMR spectra, corresponding to one oxymethylene linked to the oxygen at C-4' (δ_C 70.2) and two other carbon signals (δ_C 44.4 and 50.6) from the oxyrane ring, together with a small paramagnetic shift of carbon signal at position C-4' ($\Delta\delta_C$ = + 0.6 – 1.2). A secondary product, 4'-(3-chloro-2-hydroxypropoxy)-sakuranetin (**Scheme 3.6**, **65**), was also obtained as a side reaction in which the nucleophilic opening of the oxyrane ring is preferred to the SN_2 attack to the carbon lined to the chloride. Herein, the opening of the epoxide ring induces a strong paramagnetic effect on the oxymethine group ($\Delta\delta_H$ = 4.22; δ_C 70.0), also deshielding the methylene group linked to the halogen.

After the reaction of **64** or **65** with the desired amine, along with the new signals corresponding to the added substituents, paramagnetic effects in the ^{13}C-NMR signals in positions C-6' ($\Delta\delta_C$ = + 13.7 – 19.5) and C-7' ($\Delta\delta_C$ = + 2.4 – 16.9) were also observable due to the epoxide opening and to the coupling of the nitrogen atom to position C-7' of the oxyran-2-yl moiety. However, while in ^{1}H-NMR the oxymethine at C-6' was found upfield ($\Delta\delta_H$ = – 0.64 - 0.88), the methylene at C-7' was found to be slightly upfield in **66**-**68** ($\Delta\delta_H$ = – 0.19 - 0.63) and downfield in compounds **69**-**71** ($\Delta\delta_H$ = + 0.98 - 1.14).

Chapter 4

Biological studies.

Results and Discussion

4. Evaluation of the MDR reversal activity

For all compounds, a thorough assessment of their anti-MDR activity was undertaken to obtain the most important relationships between structural features and the biological effects observed on MDR reversal. Towards that end, the cytotoxicity and antiproliferative effects of all compounds (**1-71)** were assessed in mouse *MDR1*-transfected T-lymphoma (L5178Y-MDR) cell line and its parental (L5178Y-PAR) cell line. Furthermore, the isolated compounds **1**-**16** were also tested in human adenocarcinoma MDR cells (Colo320), its parental cell line (Colo205) and in murine (NIH/3T3) and human (MRC-5) embryonic fibroblast cell lines. Their ability to modulate P-gp efflux was assessed using the L5178Y-MDR (**1-71**) and Colo320 (**1-16**) cell lines through the rhodamine-123 (R123) accumulation assay. Finally, drug combination assays were performed for the strongest modulators on the L5178Y-MDR cell line (**6**, **9**, **10**, **12**, **13**, **22**, **60**, **69**), thus evaluating their effect in combination with the known anticancer drug doxorubicin.

As flavonoids are also described to be active as efflux modulators in other ABC transporters as MRP1 and BCRP, the cytotoxicity of naringenin (**17**) and several derivatives (**25-45**) were also assessed in parental baby hamster kidney (BHK21-PAR), mouse embryonic fibroblasts (NIH/3T3-PAR), human embryonic kidney (HEK293-PAR) and in the correspondent resistant counterparts (MRP1, BHK21-MDR; P-gp, NIH/3T3-MDR; and BCRP, HEK293-MDR) cell lines. The efflux modulation ability of compounds **17** and **25-45** were also assessed by measuring the intracellular accumulation of calcein-AM (MRP1), rhodamine-123 (P-gp) or mitoxantrone (BCRP), and verapamil (5 μM, MRP1), elacridar (5 μM, P-gp) and Ko143 (1 μM, BCRP) were used to define the fluorescence linked to 100% of efflux inhibition.

4.1. Anti-proliferative and cytotoxic activity of compounds 1-16

The anti-proliferative and cytotoxic activities of compounds **1**-**16** were evaluated. (**Tables 4.1**-**4.4**). Herein, the thiazolyl blue tetrazolium bromide (MTT) assay, a colorimetric assay in which the viability of the cells is calculated from the amount of reduced dye (formazan) that is formed by the cellular nicotinamide adenine dinucleotide phosphatase (NADPH) oxidoreductase enzymes. Due to the number of cells per well in each assay (6000 vs. 10000 for anti-proliferative and cytotoxic assays, respectively), while in the first case cell proliferation is allowed for longer time due to a lower cell confluency, in the second case cell growth is greatly

impaired due to the higher cell confluency. Therefore, the reduced cellular growth can be related with the ability of a given compound to inhibit cell proliferation (anti-proliferative assays) or to induce cellular death (cytotoxicity assay) in 50% of the total population (Berridge et al., 1996; Mosmann, 1983).

Table 4.1. Anti-proliferative activity of compounds **1-16** on mouse T-lymphoma (L5178Y-PAR and L5178Y-MDR) cells.

Compound	**L5178Y-PAR IC_{50} (μM ± SD)**	**L5178Y-MDR IC_{50} (μM ± SD)**	**SI**
β-sitostenone (**1**)	32.50 ± 1.04	37.91 ± 1.06	1.17
oleanolic acid (**2**)	40.55 ± 1.06	25.71 ± 1.08	0.63
cycloart-23-ene-3β,25-diol (**3**)	22.59 ± 1.03	26.41 ± 1.04	1.17
cycloart-25-ene-3β,24-diol (**4**)	15.40 ± 1.08	35.19 ± 1.12	2.28
7,11-dioxo-obtusifoliol (**5**)	18.26 ± 1.07	57.82 ± 1.11	3.16
spiropedroxodiol (**6**)	13.94 ± 1.06	21.89 ± 1.07	1.57
jolkinol D (**7**)	50.01 ± 1.04	39.28 ± 1.06	0.78
jolkinol D epoxide (**8**)	> 100	> 100	--
pedrodione A **(9)**	0.395 ± 1.01	0.335 ± 1.02	0.84
pedrodione B (**10**)	50.51 ± 1.04	50.45 ± 1.07	1.00
piscatoriol A (**11**)	42.36 ± 1.05	37.81 ± 1.04	0.89
pedrodiol (**12**)	37.27 ± 1.05	40.56 ± 1.10	1.09
pedrolide (**13**)	48.49 ± 1.02	41.97 ± 1.04	0.86
helioscopinolide B (**14**)	40.55 ± 1.06	25.71 ± 1.08	0.63
helioscopinolide E (**15**)	24.40 ± 1.05	29.19 ± 1.05	1.20
ent-13*R*-hydroxy-3,14-dioxo-16-atisene (**16**)	40.98 ± 1.05	38.50 ± 1.08	0.94
DMSO (1%)	> 100	> 100	--

Values of IC_{50} are the mean ± standard deviation of four independent experiments. Selectivity index (SI) = IC_{50} MDR cells / IC_{50} PAR cells.

Table 4.2. Anti-proliferative activity of compounds **1-16** on human adenocarcinoma (Colo205 and Colo320) cells.

Compound	**Colo205** IC_{50} **(μM ± SD)**	**Colo320** IC_{50} **(μM ± SD)**	**SI**
β-sitostenone (**1**)	55.41 ± 1.03	42.51 ± 1.03	0.77
oleanolic acid (**2**)	> 100	75.48 ± 1,03	0.11
cycloart-23-ene-3β,25-diol (**3**)	15.19 ± 1.05	25.96 ± 1.03	1.71
cycloart-25-ene-3β,24-diol (**4**)	16.87 ± 1.15	55.76 ± 1.03	3.07
7,11-dioxo-obtusifoliol (**5**)	17.95 ± 1.05	> 100	12.48
spiropedroxodiol (**6**)	6.788 ± 1.04	23.84 ± 3.20	3.51
jolkinol D (**7**)	> 100	> 100	0.89
jolkinol D epoxide (**8**)	> 100	64.52 ± 1.15	0.50
pedrodione A **(9)**	0.267 ± 1.04	0.306 ± 1.05	1.14
pedrodione B (**10**)	> 100	n.d.	--
piscatoriol A (**11**)	60.75 ± 1.78	67.87 ± 1.03	1.12
pedrodiol (**12**)	> 100	54.50 ± 1.03	0.50
pedrolide (**13**)	74.68 ± 1.09	> 100	1.50
helioscopinolide B (**14**)	> 100	> 100	23.27
helioscopinolide E (**15**)	> 100	57.39 ± 1.08	0.48
ent-13*R*-hydroxy-3,14-dioxo-16-atisene (**16**)	> 100	> 100	1.81
DMSO (1%)	> 100	> 100	--

Values of IC_{50} are the mean ± standard deviation of four independent experiments. Selectivity index (SI) = IC_{50} Colo320 cells / IC_{50} Colo205 cells.

Table 4.3. Cytotoxic activity (μM ± SD) of compounds **1**-**16** on mouse T-lymphoma (L5178Y-PAR and L5178Y-MDR) and murine embryonic fibroblasts (NIH/3T3) cells.

Compound	**L5178Y-PAR IC_{50} (μM ± SD)**	**L5178Y-MDR IC_{50} (μM ± SD)**	**SI**	**NIH/3T3 IC_{50} (μM ± SD)**
β-sitostenone (**1**)	80.91 ± 1.08	97.20 ± 1.06	1.20	> 100
oleanolic acid (**2**)	91.97 ± 1.05	> 100	1.28	> 100
cycloart-23-ene-3β,25-diol (**3**)	49.44 ± 1.03	71.63 ± 1.18	1.45	52.26 ± 1.10
cycloart-25-ene-3β,24-diol (**4**)	90.65 ± 1.09	65.57 ± 1.03	0.72	> 100
7,11-dioxo-obtusifoliol (**5**)	> 100	> 100	--	> 100
spiropedroxodiol (**6**)	42.27 ± 1.03	46.81 ± 1.08	1.11	56.96 ± 1.05
jolkinol D (**7**)	98.90 ± 1.12	> 100	1.43	> 100
jolkinol D epoxide (**8**)	> 100	> 100	--	> 100
pedrodione A (**9**)	0.430 ± 1.02	0.259 ± 1.05	0.60	4.200 ± 1.08
pedrodione B (**10**)	> 100	> 100	--	> 100
piscatoriol A (**11**)	75.20 ± 1.11	60.50 ± 1.06	0.80	> 100
pedrodiol (**12**)	57.61 ± 1.11	53.53 ± 1.10	0.93	> 100
pedrolide (**13**)	> 100	86.39 ± 1.13	0.67	> 100
helioscopinolide B (**14**)	90.65 ± 1.09	> 100	1.16	> 100
helioscopinolide E (**15**)	32.92 ± 1.08	> 100	3.62	> 100
ent-13*R*-hydroxy-3,14-dioxo-16-atisene (**16**)	> 100	> 100	--	> 100
DMSO (1%)	> 100	> 100	--	> 100

Values of IC_{50} are the mean ± standard deviation of four independent experiments. Selectivity index (SI) = IC_{50} MDR cells / IC_{50} PAR cells.

Table 4.4. Cytotoxic activity (μM ± SD) of compounds **1-16** on human adenocarcinoma (Colo205 and Colo320) and human embryonic fibroblasts (MRC-5) cell lines.

Compound	Colo205 IC_{50} (μM ± SD)	Colo320 IC_{50} (μM ± SD)	SI	MRC-5 IC_{50} (μM ± SD)
β-sitostenone (**1**)	46.59 ± 1.04	21.31 ± 1.07	0.46	77.68 ± 1.05
oleanolic acid (**2**)	> 100	> 100	--	> 100
cycloart-23-ene-3β,25-diol (**3**)	16.70 ± 1.07	31.57 ± 1.07	1.89	12.87 ± 1.08
cycloart-25-ene-3β,24-diol (**4**)	49.78 ± 1.11	48.51 ± 1.14	0.97	14.78 ± 1.09
7,11-dioxo-obtusifoliol (**5**)	89.27 ± 1.17	> 100	1.35	> 100
spiropedroxodiol (**6**)	16.79 ± 1.07	27.70 ± 1.04	1.65	64.63 ± 1.05
jolkinol D (**7**)	> 100	> 100	--	> 100
jolkinol D epoxide (**8**)	> 100	> 100	--	> 100
pedrodione A **(9)**	0.635 ± 1.03	0.822 ± 1.05	1.30	2.060 ± 1.05
pedrodione B (**10**)	> 100	> 100	--	> 100
piscatoriol A (**11**)	72.10 ± 1.10	> 100	1.76	> 100
pedrodiol (**12**)	76.81 ± 1.09	> 100	1.45	> 100
pedrolide (**13**)	86.39 ± 1.13	> 100	2.31	> 100
helioscopinolide B (**14**)	> 100	> 100	--	> 100
helioscopinolide E (**15**)	> 100	> 100	--	> 100
ent-13*R*-hydroxy-3,14-dioxo-16-atisene (**16**)	> 100	> 100	--	> 100
DMSO (1%)	> 100	> 100	--	> 100

Values of IC_{50} are the mean ± standard deviation of four independent experiments. Selectivity index (SI) = IC_{50} Colo320 cells / IC_{50} Colo205 cells.

As can be observed, pedrodione A (**9**) showed the strongest anti-proliferative (< 0.5 μM) and cytotoxic effects (< 1 μM) in all tested cancer cell lines (**Tables 4.1-4.4**). This compound presents two α,β-unsaturated ketones (at C-5 and C-14), which can act as strong electrophiles

(β-carbons, C-12 and C-17) when in the presence of nucleophiles as proteins or DNA. Indeed, this rare structural feature was recently reported for a similar norlathyrane diterpene (ekanpenoid A) with an *in vitro* moderate cytotoxic (IC_{50} of 14.8 – 32.1 μM) (Zhang et al., 2013). However, while in the latter compound the carbonyl at C-5 is conjugated with an endocyclic double bond at $\Delta^{6,7}$, in compound **9** the exocyclic double bond $\Delta^{6,17}$ (**Figure 4.1**) is expected to favor nucleophilic attacks due to the formation of more stable adducts (Kalia et al., 2016; Zhang et al., 2008). For the remaining molecules, none revealed significant activity in MDR-resistant cells when compared with the parental ones (Tables **4.1**-**4.4**). However, other compounds also showed an increased anti-proliferative activity towards MDR-resistant Colo320 (**2**, **8**, **12** and **15**) and in L5178Y-MDR (**2**, **7**, **9**, **11**, **13** and **14**) cell lines when compared with the parental cells. As referred above, pedrodione A (**9**) was found to be highly cytotoxic in cancer cell lines, but while in mouse L5178Y-MDR and human adenocarcinoma Colo320 the IC_{50} values ranged from 0.259 ± 1.05 μM and 0.822 ± 1.05 μM, in normal cell lines these values were higher by almost three-fold (2.060 ± 1.05 μM) or six-fold (4.200 ± 1.08 μM) in NIH-3T3 and MRC-5 cells, respectively.

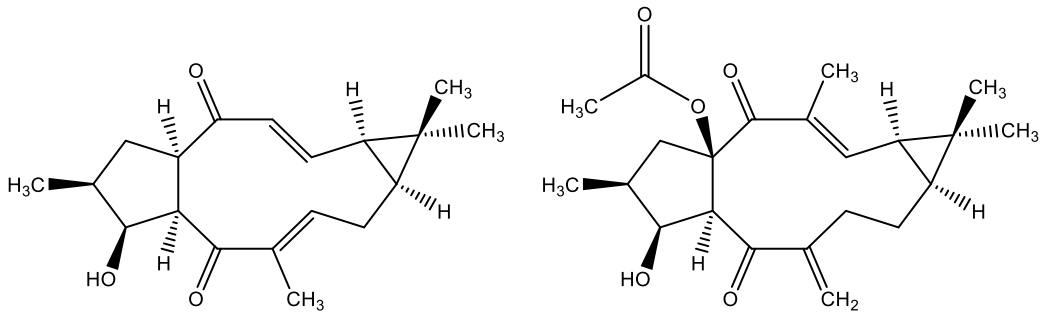

Figure 4.1. Rare macrocyclic lathyrane-type diterpenes with two α,β-conjugated ketone systems at C-5 and C-14.

4.2. Modulation of P-glycoprotein efflux by compounds 1-16

Compounds **1**-**16** were tested at 2.0 and 20 μM to assess their ability as P-gp efflux modulators through the R123 accumulation assay. During sample preparation and the flow cytometry assay, toxicity effects could be excluded due to the absence of significant changes on size (FSC) and granularity (SSC) of cell population (data not shown). In L5178Y-MDR cells, an active compound was defined as having a FAR > 1.0. If greater than 10, the compound was classified as a strong MDR reversal agent (Reis et al., 2014a).

Table 4.5. Effect of isolated compounds (**1**-**16**) on P-gp mediated R123 efflux, in *MDR1*-transfected mouse T-lymphoma (L5178Y-MDR) cells.

Compound	Concentration (μM)	Fluorescence Activity Ratio (FAR)	
		L5178Y-MDR	Colo320
β-sitostenone **(1)**	2.0	2.51	0.97
	20	22.56	1.34
oleanolic acid **(2)**	2.0	1.06	2.10
	20	1.70	4.71
cycloart-23-ene-3β,25-diol **(3)**	2.0	10.68	1.26
	20	67.05	3.45
cycloart-25-ene-3β,24-diol **(4)**	2.0	5.91	0.77
	20	43.58	5.91
7,11-dioxo-obtusifoliol **(5)**	2.0	6.14	1.09
	20	30.68	1.84
spiropedroxodiol **(6)**	0.2	43.75	1.68
	2.0	54.38	2.27
	20	96.02	8.00
jolkinol D **(7)**	2.0	1.73	1.08
	20	2.03	1.18
jolkinol D epoxide **(8)**	2.0	0.81	0.67
	20	4.21	0.94
pedrodione A **(9)**	0.2	1.72	n.d.
	2.0	19.13	1.52
	20	38.74	5.53
pedrodione B **(10)**	2.0	1.68	1.13
	20	5.80	1.91
piscatoriol A **(11)**	2.0	4.63	2.35
	20	36.09	6.20
pedrodiol **(12)**	2.0	1.19	1.08
	20	16.43	3.56
pedrolide **(13)**	2.0	1.87	1.64
	20	16.04	5.36
helioscopinolide B **(14)**	2.0	1.70	1.73
	20	8.18	6.78
helioscopinolide E **(15)**	2.0	1.84	0.44
	20	10.23	0.98
ent-13*R*-hydroxy-3,14-dioxo-16-atisene **(16)**	2.0	2.20	1.35
	20	4.41	1.19
Verapamil	20	9.66	4.10
Tariquidar	0.5	58.83	8.88
DMSO	2%	1.01	0.79

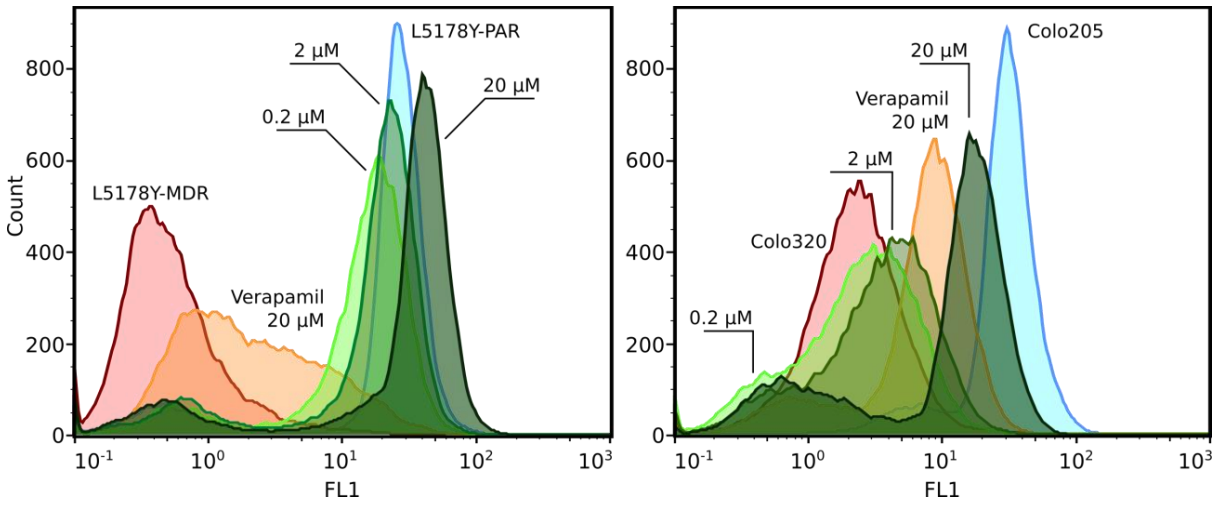

Figure 4.2. Flow cytometry histograms on R123 accumulation assay for spiropedroxodiol (**6**) at 0.2, 2.0 and 20 µM in chemo-resistant L5178Y-MDR and parental L5178Y-PAR (left) and human adenocarcinoma resistant Colo320 and parental Colo205 (right) cell lines.

As shown in **Table 4.5**, spiropedroxodiol (**6**) was the most active compound displaying a remarkable P-gp efflux modulation even at low concentrations as 0.2 µM in both L5178Y-MDR (FAR = 43.75) and Colo320 (FAR = 1.68) cell lines (**Figure 4.2**). It is also worth noticing that the two cycloartanes **(3-4)** and 7,11-dioxo-obtusifoliol (**5**) also showed a good profile for P-gp efflux modulation at both 2.0 µM (**3**, FAR 10.68; **4**, FAR 5.91; **5**, FAR 6.14) and 20 µM (**3**, FAR 67.05; **4**, FAR 43.58; **5**, FAR 30.68). Regarding the set of diterpenes (**7-16**), only pedrodione A (**9**) revealed to be a strong P-gp modulator at 2 µM (FAR, 19.13), being able to slightly reverse MDR at concentrations as low as 0.2 µM (FAR, 1.78). Interestingly, both compounds **6** and **9** revealed higher cytotoxicities in both cancer cell lines (L5178Y-MDR and Colo320) when compared with normal cell lines (NIH/3T3 and MRC-5), thus configuring new scaffolds that can be further modified to increase their activity and selectivity towards P-gp modulation. All other compounds were found to be weak P-gp efflux modulators in both L5178Y-MDR and Colo320 cell lines.

4.3. Anti-proliferative and cytotoxic activity of *ent*-abietane and flavonoid derivatives

Two small libraries were built by chemical derivatization of helioscopinolide E (**15**) and naringenin (**17**), previously mentioned as isolated from *Euphorbia pedroi* in large amounts. In literature, as the presence of nitrogen atoms and aromatic rings are characterized as key features

for the P-gp efflux modulation, the common rationale for the chemical derivatization of helioscopinolide E (**15**) and naringenin (**17**) was the introduction of nitrogen atoms and aromatic moieties to potentiate the MDR reversing capabilities of the compounds. In the following sections, the results refer to L5178Y-MDR cells unless stated otherwise.

4.3.1. MDR reversal activities of helioscopinolide E derivatives

4.3.1.1. Anti-proliferative and cytotoxic activities of compounds 19-24

When analyzing the synthesized derivatives (**19-24**), and while no significant change was observed regarding the cytotoxic or anti-proliferative activities (IC_{50} > 10 μM), it is worth noticing that, for the oxime (**19,** IC_{50} 25.05 ± 1.05 μM, SI 0.91) and compound (**20**, IC_{50} 38.04 ± 1.04 μM, SI 0.85), higher anti-proliferative activities were found in the L5178Y-MDR cell line (**Tables 4.6 and 4.7**). Regarding cytotoxicity, and although more cytotoxic than the parent compound **14** (IC_{50} > 100 μM) and the oxime (**19**, 66.41 ± 1.08 μM), only compounds **20** (15.10 ± 1.15 μM, SI 0.34) and **21** (22.75 ± 1.16 μM, SI 0.37) revealed an increased cytotoxicity towards the resistant L5178Y-MDR cell line.

4.3.1.2. Modulation of rhodamine-123 efflux by compounds 19-24

After evaluating the ability to reverse R123 efflux by P-gp (**Table 4.8**), only the oxime (**19**) was inactive at the lowest concentration tested (2.0 μM). In general, the ability to modulate P-gp by compounds **20-24** (FAR values between 1.09 – 3.02 at 2.0 μM) was improved when compared with helioscopinolide E (FAR 1.84), especially at the higher concentration tested (20 μM, FAR 7.09 – 56.37). However, while short aliphatic chains or unsubstituted phenyl rings seemed beneficial for the biological activity of compounds **20** (2.0 μM, FAR 3.02; 20 μM, FAR 38.64**)** and **22** (2.0 μM, FAR 5.78; 20 μM, FAR 56.37), longer aliphatic sidechains (**22**) (2.0 μM, FAR 1.36; 20 μM, FAR 10.38) or five-membered heterocyclic rings (as thiophenes, less for furans) seem to be deleterious for the P-gp efflux modulation capability.

Table 4.6. Cytotoxic activity of helioscopinolide E (**15**) derivatives (**19-24**) on mouse T-lymphoma (L5178Y-PAR and L5178Y-MDR) cells.

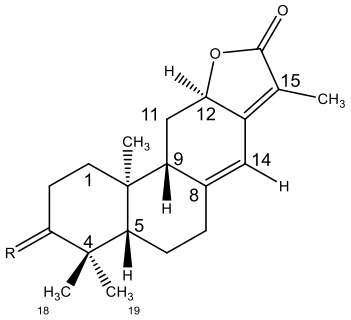

Compound		Cytotoxicity / µM ± SD		
		L5178Y-PAR	L5178Y-MDR	SI
15	helioscopinolide E	32.92 ± 1.08	> 100	3.62
19	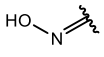	49.86 ± 1.09	66.41 ± 1.08	1.33
20	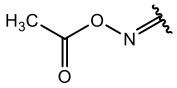	43.90 ± 1.07	15.10 ± 1.15	0.34
21	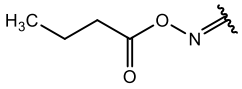	61.28 ± 1.07	22.75 ± 1.16	0.37
22	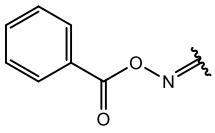	50.13 ± 1.05	58.58 ± 1.07	1.17
23	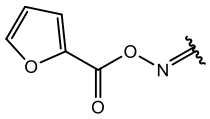	48.10 ± 1.06	69.51 ± 1.06	1.45
24	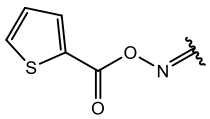	89.30 ± 1.13	117.0 ± 1.18	1.31

Table 4.7. Anti-proliferative activity of helioscopinolide E (**15**) derivatives (**19**-**24**) on mouse T-lymphoma (L5178Y-PAR and L5178Y-MDR) cells.

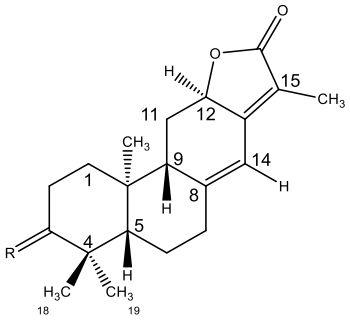

Compound		Antiproliferative activity / μM ± SD		
		L5178Y-PAR	L5178Y-MDR	SI
15	helioscopinolide E	24.40 ± 1.05	29.19 ± 1.05	1.20
19	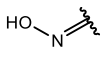	27.52 ± 1.07	25.05 ± 1.05	0.91
20	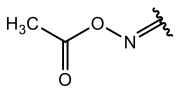	44.52 ± 1.01	38.04 ± 1.04	0.85
21	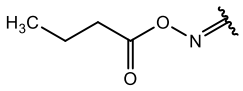	22.67 ± 1.03	21.72 ± 1.06	0.96
22	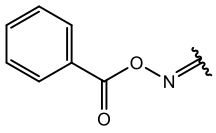	30.81 ± 1.05	31.31 ± 1.05	1.00
23	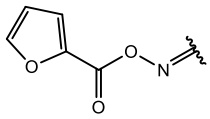	33.68 ± 1.06	32.80 ± 1.08	0.97
24	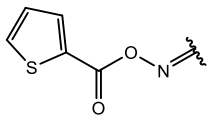	56.19 ± 1.04	40.07 ± 1.05	0.71

Table 4.8. Effect of helioscopinolide E (**15**) derivatives (**19**-**24**) on P-gp mediated R123 efflux, in *MDR1*-transfected mouse T-lymphoma (L5178Y-MDR) cells.

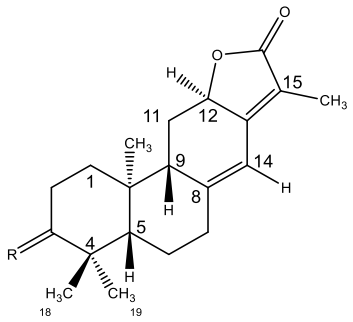

Compound		log*P* [a]	Fluorescence Activity Ratio (FAR)	
			2.0 µM	20 µM
15	helioscopinolide E	3.91	1.84	10.23
19	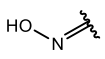	3.92	0.96	4.88
20	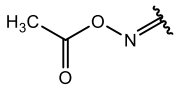	4.06	3.02	38.64
21	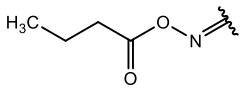	5.21	1.36	10.38
22	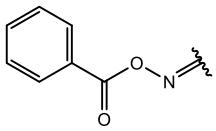	6.12	5.78	56.37
23	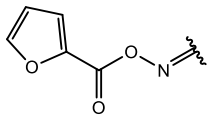	5.18	2.10	40.69
24	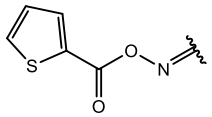	6.03	1.09	7.09
DMSO (2%)		--	1.01	

[a] calculated in MarvinSketch v17.2.27.0

Interestingly, the presence of a hydrogen-bond donor in the oxime (**19**) was deleterious for the MDR activity but the corresponding acylation restored and improved the MDR reversal

activity (**20**-**24**). However, as longer aliphatic sidechains did not contribute to further increase the reversal activity (**21**) and the obtained results suggest that electronic effects (i.e. electron density around the acyl substituent) seem to be one of the major determinants for the activity of helioscopinolide E derivatives (compounds **22**-**24**), a suitable approach for further studies on these compounds may involve the synthesis of new derivatives bearing phenyl rings with different substitution patterns or heterocyclic rings as pyridines or pyrazines.

4.3.2. MDR reversal activities of naringenin derivatives

As a large amount of the flavonoid naringenin (**17**) was isolated, chemical modifications on the chromone scaffold were undertaken as an attempt to improve the P-gp-mediated MDR reversal effects of naringenin. Thus, naringenin was initially methylated with dimethylsulphate to yield 7-methoxy-naringenin (sakuranetin) (**46**) and 4',7-dimethoxy-naringenin (**47**) that, together with naringenin, were suitable building blocks for further chemical derivatization.

4.3.2.1. Anti-proliferative and cytotoxic activities of naringenin derivatives

In general, most of the nitrogen-containing derivatives (**25**-**31, 37**-**41, 46**-**63**) except compounds **26**, **39, 40, 50** and **57** (5 out of 30) were found to have lower anti-proliferative activities (IC_{50} 0.550 – 39.90 μM) when compared with naringenin (**17**) (42.77 ± 1.07 μM) in L5178Y-MDR cell line. However, it did not increase their selectivity towards MDR resistant cells. It is also possible to infer that, when compared with unmethylated derivatives (IC_{50}, 12.17 – 252.4 μM), the methylation of the hydroxyl groups at positions C-7 (IC_{50}, 1.852 – 66.40 μM) and C-4' (IC_{50}, 0.796 – 44.36 μM) generally increases the anti-proliferative activity in resistant cells (an example can be found in **Table 4.9**). More interestingly, the reaction with hydrazine alone was enough to decrease by three-, four- or two-fold the IC_{50} for the anti-proliferative activity of compounds **28** (15.2 ± 1.04 μM), **48** (8.03 ± 1.13 μM) and **49** (11.2 ± 1.09 μM) in L1578Y-MDR cells when compared with **17** (IC_{50}, 42.7 ± 1.07 μM), **46** (IC_{50}, 34.4 ± 1.08 μM) and **47** (IC_{50}, 22.6 ± 1.78 μM).

While no relevant cytotoxicity was found for the large majority of naringenin derivatives (data not shown), it is worth noticing that i) unlike the results obtained for the anti-proliferative effect, dimethylated compounds at C-7 and C-4' are more cytotoxic (IC_{50} ranging from 1.321 to 10.73 μM) than the monomethylated ones at C-7 (IC_{50}, 11.78 to 54.95 μM) or the

unmethylated (IC_{50}, 44.96 to > 100 μM) in resistant cells. Such examples are shown in **Table 4.10**, in which the selectivity towards L5178Y-MDR cells increases with methylation with the IC_{50} values decreasing from 217.7 ± 2.73 μM in compound **41** (unmethylated) to 54.9 ± 1.17 μM (7-OMe) and 7.25 ± 1.36 μM (4',7-OMe) in compounds **60** and **61** respectively (selectivity index < 0.1 for compound **61**). However, there are some cases the methylation of the hydroxyl group at C-7 has almost no effect in L5178Y-MDR cells, as for compounds **40** (IC_{50}, 45.0 ± 1.10 μM) and **62** (IC_{50}, 49.3 ± 1.06 μM), but again decreasing in the dimethylated derivative (**63**, IC_{50} 7.47 ± 1.11 μM).

Table 4.9. Effect on anti-proliferative activity by methylation of the hydroxyls at position C-7 and C-4' for naringenin (**17**), sakuranetin (**46**), 4'-methoxysakuranetin **(47**) and the correspondent hydrazones (**28, 48, 49**).

	Antiproliferative activity / μM ± SD				
Compound	**L5178Y (PAR)**	**L5178Y (MDR)**	**Compound**	**L5178Y (PAR)**	**L5178Y (MDR)**
17	52.5 ± 1.06	42.7 ± 1.07	**28**	5.58 ± 1.05	15.2 ± 1.04
46 – 7-OMe	41.6 ± 1.13	34.4 ± 1.08	**48** – 7-OMe	5.52 ± 1.07	8.03 ± 1.13
47 – 4',7-OMe	41.6 ± 1.08	22.6 ± 1.78	**49** – 4',7-OMe	5.88 ± 1.07	11.2 ± 1.09

Table 4.10. Effect on cytotoxic activity by methylation of the hydroxyls at position C-7 and C-4' for derivatives bearing a benzoyloxy (**41**, **60**, **61**) and a 3-indolacetyl (**40**, **62**, **63**) substituent.

	Cytotoxic activity / μM ± SD				
Compound	**L5178Y (PAR)**	**L5178Y (MDR)**	**Compound**	**L5178Y (PAR)**	**L5178Y (MDR)**
41	50.4 ± 1.53	> 100	**40**	72.6 ± 1.04	45.0 ± 1.10
60 – 7-OMe	63.8 ± 1.16	54.9 ± 1.17	**62** – 7-OMe	25.3 ± 1.06	49.3 ± 1.06
61 – 4',7-OMe	> 100	7.25 ± 1.36	**63** – 4',7-OMe	8.61 ± 1.11	7.47 ± 1.11

4.3.2.2. Modulation of rhodamine-123 efflux by compounds 25-63

The ability of naringenin derivatives (**25-63**) to modulate P-gp was also assessed on the L5178Y-MDR resistant cell line but, unlike the above described activities, methylation of

naringenin (**46**-**47**) or substitution of the ketone by an hydrazone (=N-NH_2) moiety (**48**-**49**) did not significantly improved the activity at 2.0 μM. Nevertheless, it is clear from data in **Table 4.11** that methylation of C-7 and C-4' generally improved the activity of compounds and that unsubstituted phenyl rings (**50**, **51**, **60**), heterocyclic rings (**27**, **52**-**53**) and indoles (**62**-**63**) improved the MDR-reversal activity of the compounds.

Table 4.11. Effect of naringenin derivatives (**25**-**31**, **37**-**63**) on P-gp mediated R123 efflux, in *MDR1*-transfected murine T-lymphoma (L5178Y-MDR) cells.

	Fluorescence activity ratio (FAR)			**Fluorescence activity ratio (FAR)**	
Compound	**2.0 μM**	**20 μM**	**Compound**	**2.0 μM**	**20 μM**
17	0.72	0.72	**28**	0.72	3.13
46	1.06	1.32	**48**	1.26	15.60
47	1.03	1.36	**49**	0.85	1.06
Hydrazones (C=N-NH-R)			**Carbohydrazides (C=N-NH-CO-R)**		
25	1.08	26.80	**37**	0.92	1.13
26	1.16	4.86	**38**	0.86	0.94
27	1.65	47.00	**40**	1.00	2.48
50	1.16	40.31	**41**	0.76	8.80
51	1.80	13.79	**54**	1.28	11.08
52	2.10	64.70	**55**	2.24	18.47
53	10.67	30.54	**56**	1.39	1.54
Azines (C=N-N=CH-R)			**57**	0.96	1.10
29	0.64	6.54	**58**	1.32	18.88
30	0.95	17.71	**59**	0.83	2.55
31	0.78	13.58	**60**	4.14	67.24
Thiosemicarbazone (C=N-NH-CS-NR_2)			**61**	0.94	1.13
39	2.17	23.04	**62**	1.12	40.64
DMSO (2%)	1.01		**63**	2.47	26.93

Herein, while compound **53** was found to be the most active at the lowest concentration (2.0 μM, FAR 10.67), most of the compounds were found to be moderate (FAR 1.10 – 8.80) or strong (FAR 11.08 – 64.70) P-gp modulators at the highest concentration (20 μM). Additionally, compounds **39** (thiosemicarbazone), **50** and **52** (7-methoxyhydrazone), **60** (7-methoxycarbohydrazide) and **63** (4',7-dimethoxycarbohydrazides) also showed to be good P-gp efflux modulators at both concentrations tested. Therefore, the methylation of the naringenin hydroxyl groups at C-7 and C-4', together with the introduction of nitrogen atoms and aromatic rings at position C-4, can configure a suitable approach for the development of novel efflux modulations. Moreover, by using different flavonoids with different substitution patterns, further studies will be conducted towards the optimization of the benzopyran-4-one skeleton as a novel generation of MDR reversal agents.

4.3.3. MDR reversal activities of 4'-OH alkylated naringenin derivatives

4.3.3.1. Anti-proliferative and cytotoxic activities of compounds 64-71

The alkylation of the hydroxyl group at C-4' with epichlorohydrin and further reaction with primary or secondary amines to yield propanolamines was inspired on early studies, in which a significative improvement of benzophenone- and propafenone-type compounds towards P-gp inhibition was achieved (Chiba et al., 1997; Cramer et al., 2007; Jabeen et al., 2012). However, and to our knowledge, such approach has never been attempted for increasing the potency of flavonoids as P-gp efflux modulators. Thus, a new series of nitrogen-containing derivatives was planned based on the flavanone scaffold, taking advantage of the large amount of naringenin isolated from *E. pedroi* (**17**). However, sakuranetin (**46**) was found to be a more suitable building block: while allowing a greater control over the reaction (avoiding polyalkylations), the methylation of the hydroxyl group at C-7 was also found to improve the anti-proliferative and cytotoxic activities of the derivatives previously synthetized (**46**-**63**).

As expected, and when compared with sakuranetin (**46**), all derivatives (**64**-**71**) but **65** showed increased anti-proliferative activities towards both parental and resistant mouse lymphoma cells but only compounds **66** (IC_{50}, 9.14 ± 1.06 μM)**, 67** (IC_{50}, 7.33 ± 1.07 μM) and **71** (IC_{50}, 3.64 ± 1.06 μM) showed an IC_{50} below 10 μM (**Table 4.12**). Regarding the cytotoxic

activities in the same cells, all compounds were non-cytotoxic (IC_{50} > 10 μM) at the tested concentrations (**Table 4.12**). No selectivity towards the resistant cell line was observed.

Table 4.12. Cytotoxic and anti-proliferative activity of naringenin derivatives (**64-71**) on mouse T-lymphoma (L5178Y-PAR and L5178Y-MDR) cells.

	Citotoxicity / μM ± SD			Anti-proliferative / μM ± SD		
Compound	**L5178Y-PAR**	**L5178Y-MDR**	**SI**	**L5178Y-PAR**	**L5178Y-MDR**	**SI**
46	> 100	> 100	--	41.6 ± 1.13	34.4 ± 1.08	1.21
64	60.1 ± 1.04	84.2 ± 1.14	1.40	28.9 ± 1.05	25.1 ± 1.06	0.87
65	> 100	> 100	--	47.7 ± 1.19	70.6 ± 1.30	1.48
66	14.3 ± 1.07	16.6 ± 1.12	1.16	6.84 ± 1.07	9.14 ± 1.06	1.34
67	9.33 ± 1.10	17.4 ± 1.31	1.87	6.63 ± 1.06	7.33 ± 1.07	1.11
68	15.9 ± 1.09	47.9 ± 1.08	3.02	25.0 ± 1.10	31.0 ± 1.05	1.24
69	12.9 ± 1.02	17.9 ± 1.77	1.39	16.7 ± 1.14	20.6 ± 1.08	1.23
70	76.4 ± 1.19	96.3 ± 1.03	1.26	27.2 ± 1.15	30.0 ± 1.12	1.10
71	16.3 ± 1.07	25.3 ± 1.05	1.55	4.13 ± 1.14	3.64 ± 1.06	0.88

4.3.3.2. Modulation of rhodamine-123 efflux by compounds 64-71

As can be observed in **Table 4.13**, the alkylation reaction of the hydroxyl group at C-4' yielded compounds (**64-71**) with better efflux modulation properties than naringenin (**17**) or sakuranetin (**46**). However, only with the propanolamine derivatives (**66-69**) the activity was strongly increased at 2.0 μM, with FAR values ranging from 3.08 (**67**) up to 18.70 (**69**), again lowering in the presence of indol (**70**) or thiophenol (**71**) substituents. Herein, through the analysis of log*P* and pKa, two of the most important physico-chemical properties that are directly related with the ability to modulate P-gp efflux (Chiba et al., 1997; Zamora et al., 1988), it is possible to verify that while the MDR reversal activity at lower concentrations seems to be correlated with the presence of a nitrogen (**66-68**), the presence of both a nitrogen together with an additional aromatic moiety (**69**) seems to further improve the potency of the P-gp efflux modulator (FAR 18.70 at 2.0 μM). To better understand the main features that contributed for the increased reversal activity showed by compound **69**, the pKa distribution profile for the

secondary and tertiary amino groups and molecular docking studies were further analyzed (**Figure 4.3**).

Table 4.13. Effect of naringenin derivatives (**64-71**) on P-gp mediated R123 efflux, in *MDR1*-transfected mouse T-lymphoma (L5178Y-MDR) cells.

Compound	Chemical properties		Fluorescence Activity Ratio (FAR)	
	log*P* [a]	pKa (amine)[a]	2.0 µM	20 µM
Sakuranetin (46)	2.98	--	1.06	1.32
64	2.97	--	1.17	1.83
65	3.16	--	1.33	13.30
66	3.23	9.36	4.06	36.25
67	3.37	9.06	3.08	30.76
68	2.73	7.83	8.01	43.68
69	3.88	9.67; 7.01	18.70	62.09
70	4.61	17.32	0.86	6.65
71	4.67	---	0.92	12.78
DMSO (2%)			1.01	

[a] calculated in MarvinSketch v17.2.27.0

From the macrospecies distribution in **Figure 4.3A**, it is possible to verify that, while only considering the secondary and tertiary amines, compound **69** has at physiological pH a net charge that can be +1 or +2. Although a positively charged nitrogen is described as important for the activity, the diffusion of highly charged molecules into the lipid membrane becomes impaired. However, and as previously demonstrated for tariquidar (Ferreira et al., 2015c), compound **69** i) is expected to adopt a more elongated conformation where the flavanone core penetrates the membrane while the protonated benzylpiperidine moiety remains close to the phosphates and deprotonates through a phosphate-assisted reaction, or ii) adopts a more compact conformation (as seen in **Figure 4.3B**) where the protonated amine is packed close to the ring B of the flavanone scaffold in order to efficiently disperse the excess of positive charge (Ottiger et al., 2009; Palit et al., 1971) thus increasing membrane permeation.

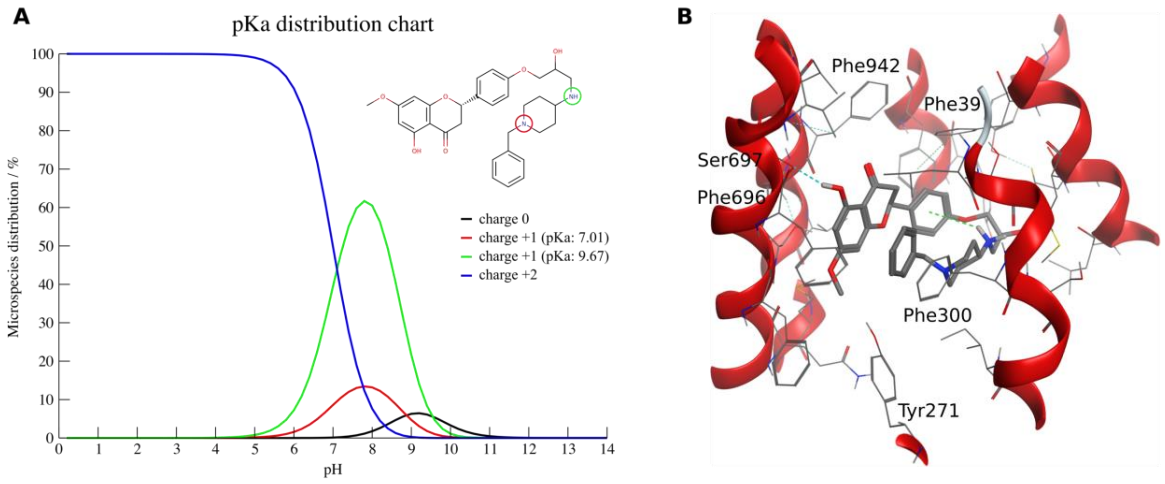

Figure 4.3. (A) Microspecies distribution percentages for nitrogen-containing groups as a function of pH. Default parameters (tautomerization, resonance effects and 0.1 mol/L ionic strength) were used while estimating pKa in MarvinSketch (B) top-ranked docking pose of compound **69** in the internal drug-binding of the refined murine P-gp model.

4.4. Drug Combination Assays

For all new compounds (**6**, **9**, **10**, **12** and **13**) and for the derivatives of helioscopinolide E (**22**) and naringenin (**60**, **69**) with the highest MDR reversal activities *in vitro*, their effect in the cytotoxic activity of doxorubicin, one of the most used anticancer drugs in chemotherapy and a known P-gp substrate, was also assessed through a drug combination assay. The extent of interaction between doxorubicin and a given compound was calculated by the combination index (CI) as suggested by Chou (**Table 4.14**). Herein, compounds **9**, **13, 22** and **69** showed a strong synergism, greatly enhancing the cytotoxicity of doxorubicin in resistant L5178Y-MDR cells.

Table 4.14. Interaction type between compounds **6**, **9**, **10**, **12**, **13**, **22**, **60** and **69** with doxorubicin on L5178Y-MDR cells.

Compound	ratio [a]	CI ± SD [b]	Interaction
6	6 : 1	0.872 ± 0.182	slight synergism
9	1 : 8	0.977 ± 0.095	additive effect
10	50 : 1	0.298 ± 0.102	strong synergism
12	50 : 1	0.424 ± 0.116	synergism
13	50 : 1	0.144 ± 0.026	strong synergism
22	25 : 1	0.152 ± 0.013	strong synergism
60	6 : 1	3.768 ± 0.878	strong antagonism
69	25 : 1	0.108 ± 0.025	strong synergism

[a] Data are shown as the best combination ratio between compounds and doxorubicin. [b] Combination index (CI) values are represented as the mean of three CI values calculated from different drug ratios ± standard deviation (SD) of the mean, for an inhibitory concentration of 50% (IC_{50}). 0.1 < CI < 0.3, strong synergism; 0.85 < CI < 0.9, slight synergism; 0.9 < CI < 1.1, additive effect; 3.3 < CI < 10, strong antagonism.

4.5. MDR reversal activities of compounds 25-45 in other cell lines

4.5.1 Cytotoxicity assays of compounds 25-45 in P-gp, MRP1 and BCRP

The cytotoxicity of compounds **25-45** was determined using a MTT colorimetric assay (Berridge et al., 1996; Mosmann, 1983) in cell lines overexpressing MRP1 (BHK-21) and BCRP (HEK-293). A cell line overexpressing P-gp (NIH/3T3) was also assessed. While most of the hydrazones, azines and carbohydrazides were found to be non-cytotoxic at the concentrations tested (IC_{50} > 50 μM) in P-gp, BCRP and MRP1-overexpressing cell lines (**Table 4.15**), compounds **25**, **29**, **30**, **33** and **34** showed a significant cytotoxic activity in both BHK21 parental and MDR cells (IC_{50} < 10 μM). Compound **3**, obtained by reacting **1** with phenylhydrazine, was the only derivative that showed an increased selectivity (RR, 0.39) for the resistant BHK21 cell line (IC_{50} 31.65 vs 12.36 μM, respectively). Other modifications as the ones obtained by a Mannich-type coupling reaction, had no impact on the cytotoxicity of compounds **43-44** towards the tested cell lines (**Table 4.15**). From the above results, it may be

deduced that the presence of nitrogen-containing heterocyclic rings as pyrrole, pyridine or indole strongly increased the cytotoxic activity of compounds (**25**, **30**, **33** and **34**, IC_{50} values between 1.02 and 13.4 μM) towards both parental and MRP1-overexpressing cell lines.

4.5.2 Fluorescent dye efflux inhibition in P-gp, MRP1 and BCRP

The ability of compounds **25**-**45** to modulate drug efflux by MRP1, P-gp and BCRP was also assessed on the same cell lines by comparing the fluorescence linked to a given percentage of inhibition in MDR cells overexpressing each one of the transporters. Hence, verapamil (35 μM), elacridar (5 μM) and Ko143 (1μM) were used to determine the fluorescence linked to 100 % of inhibition for MRP1, P-gp and BCRP, respectively. The results are depicted in **Figure 4.4**.

As can be observed hydrazones (**25**, **26**) and azines (**29**-**36**) displayed an interesting activity pattern in BCRP-overexpressing HEK-293 cells (efflux inhibition up to 72.97 %). Azines **29**, **31**, **33** and **26** (C=N-N=CH-R_2) displayed the highest activities in HEK293-MDR cell lines, ranging from 64.10 ± 1.17 % inhibition in compound **31** up to 72.97 ± 5.91 % inhibition in compound **33**. Interestingly, while activated pyrroles (**29**, **35**) and phenyl rings (**26**, **31**-**33** and **36**) improved the MDR activity towards BCRP, other substituents as pyrazino (**27**), indoles (**30**, **34**) or carbohydrazides bearing an aromatic moiety (**37**, **38**, and **40**-**42**) were detrimental for the activity. As can be further observed, only by replacing the carbonyl by an hydrazone (as in compound **28**) a two-fold increase in the BCRP efflux inhibition was obtained when compared with naringenin (46.70 ± 15.96 % vs. 26.63 ± 0.11 %). Regarding P-gp, no compound was active in NIH/3T3-MDR cells.

It is also worth noticing that while **35** (BCRP, 53.5 ± 14.2; MRP1, 56.3 ± 14.4 %), **36** (BCRP, 71.1 ± 0.89; MRP1, 45.1 ± 3.60 %) and **39** (BCRP, 43.6 ± 1.74; MRP1, 21.6 ± 4.63 %), are the only compounds that retained some degree of inhibition in both BCRP and MRP1 pumps the presence of activated five-membered ring thiophene (**37**) or furan (**38**) completely abolished its MDR reversal activity. Oppositely, in azines pyrroles still displayed some activity in both pumps (**29**, MRP1: 28.7 ± 13.2 %, BCRP: 69.7 ± 5.07 %; **35**, MRP1: 56.3 ± 14.4 %, BCRP: 53.5 ± 14.2 %).

Table 4.15. Cytotoxic activity of naringenin (**17**) and derivatives **25**−**45** on ABCC1- (BHK21), ABCB1- (NIH/3T3) and ABCG2-transfected (HEK293) and parental cell lines.

Compound	BHK21		NIH/3T3		HEK293	
	PAR [a]	MDR [a]	PAR [a]	MDR [b]	PAR [a]	MDR [a]
17	89.3 ± 3.78	67.7 ± 4.38	107.4 ± 4.62	91.3 ± 8.42	65.4 ± 29.5	85.6 ± 9.80
25	3.44 ± 0.31	13.4 ± 2.28	n.d.	n.d.	55.8 ± 15.9	49.5 ± 7.50
26	31.6 ± 0.96	12.4 ± 3.79	n.d.	n.d.	109.3 ± 20.3	95.1 ± 8.40
27	32.7 ± 2.18	49.3 ± 4.15	89.7 ± 17.9	76.9 ± 5.94	100.7 ± 25.6	82.6 ± 6.00
28	85.8 ± 7.33	99.5 ± 3.62	103.2 ± 4.45	93.3 ± 11.7	69.4 ± 31.9	105.8 ± 3.90
29	11.1 ± 1.19	15.9 ± 4.86	n.d.	n.d.	97.4 ± 16.4	106.5 ± 13.3
30	3.85 ± 0.61	7.99 ± 1.17	97.0 ± 30.7	75.1 ± 4.33	81.4 ± 19.4	90.8 ± 8.40
31	45.3 ± 2.88	45.5 ± 4.41	99.8 ± 2.70	81.4 ± 7.16	71.4 ± 10.4	119.5 ± 13.6
32	38.9 ± 4.29	54.7 ± 2.16	89.5 ± 19.5	73.4 ± 2.66	71.1 ± 6.80	117.2 ± 7.60
33	1.02 ± 0.24	4.77 ± 0.55	101.2 ± 5.72	103.3 ± 3.34	95.6 ± 19.5	109.3 ± 11.1
34	1.58 ± 0.25	5.31 ± 1.21	107.5 ± 9.56	93.3 ± 3.29	63.2 ± 22.5	98.2 ± 11.3
35	45.9 ± 1.02	40.3 ± 10.3	99.3 ± 18.2	86.1 ± 8.20	95.6 ± 24.6	103.2 ± 10.8
36	22.7 ± 3.11	55.6 ± 7.43	100.0 ± 7.02	127.0 ± 7.89	70.5 ± 8.90	78.2 ± 9.70
37	10.8 ± 0.31	45.0 ± 3.02	95.7 ± 4.73	92.3 ± 6.69	73.1 ± 27.8	103.8 ± 9.90
38	19.1 ± 0.55	41.8 ± 6.37	94.0 ± 5.94	84.1 ± 18.7	106.5 ± 8.30	111.1 ± 12.0
39	87.3 ± 5.57	89.9 ± 1.76	102.5 ± 9.53	90.7 ± 8.99	103.2 ± 23.9	99.6 ± 21.3
40	5.31 ± 1.66	98.6 ± 3.96	95.1 ± 8.29	83.5 ± 5.89	60.7 ± 14.1	111.5 ± 11.7
41	37.0 ± 7.92	49.3 ± 6.05	101.8 ± 8.07	93.8 ± 23.8	63.4 ± 7.50	102.5 ± 11.7
42	30.5 ± 1.39	50.5 ± 4.00	105.5 ± 9.21	95.8 ± 11.2	76.1 ± 14.3	118.7 ± 7.00
43	97.2 ± 0.95	101.3 ± 3.81	100.8 ± 11.7	89.9 ± 0.41	92.6 ± 18.6	122.7 ± 4.00
44	102.9 ± 1.45	100.1 ± 3.68	102.6 ± 12.4	101.0 ± 3.29	108.9 ± 28.0	82.9 ± 14.4
45	99.0 ± 2.57	122.6 ± 8.59	107.0 ± 6.42	95.8 ± 9.54	111.8 ± 23.8	116.7 ± 14.0

[a] Results are expressed in % cell viability, calculated as the difference in absorbance between test wells and medium control wells; [b] Relative Resistance ratio (RR) was calculated as the ratio between % cell viability for MDR and PAR cells. Values of RR < 0.5 are depicted in green and RR > 1.5 in red; n.d., not determined.

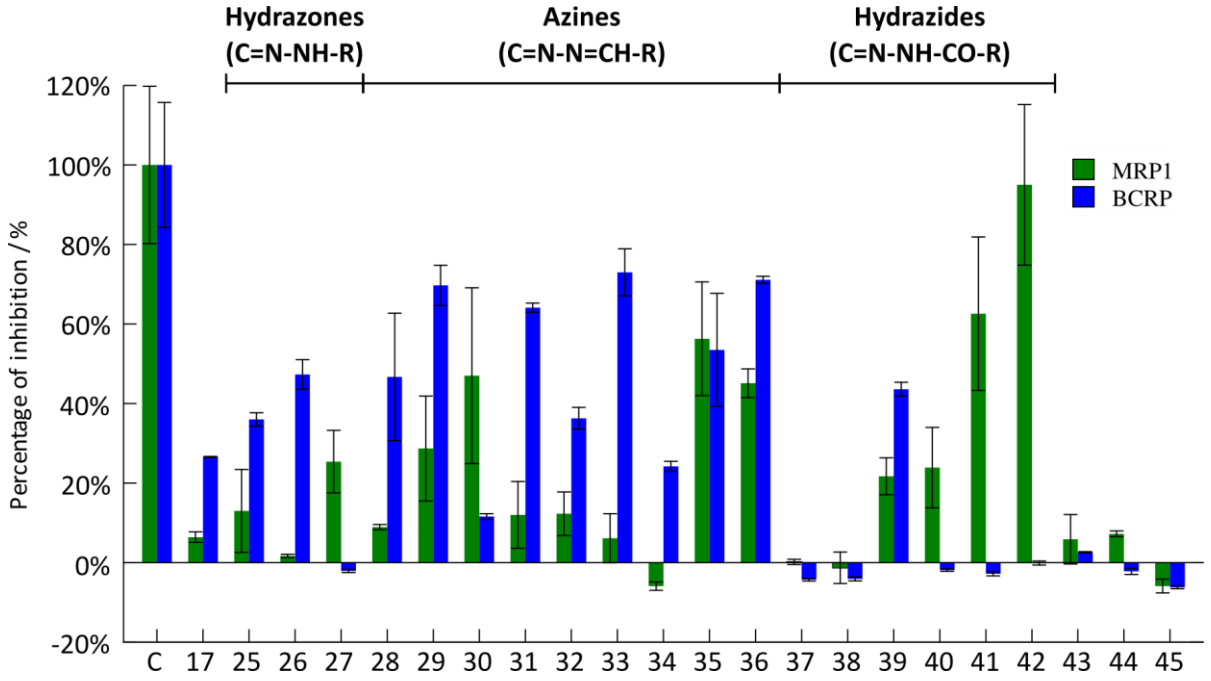

Figure 4.4. Inhibition percentage for MRP1 and BCRP (20 μM). Control refers to verapamil (5 μM, MRP1) and Ko143 (1 μM, BCRP) and were used to determine the fluorescence linked to 100% of efflux inhibition.

Thus, a pre-requisite for an efficient BCRP modulation by azines may arise from the decreased flexibility of the whole scaffold, in which the resonance between the flavanone scaffold and the aromatic substituent through the C=N-N=C framework (Ramakrishnan et al., 2015) restrains the spatial position of the substituent in a given orientation. For carbohydrazides the presence of a carbonyl (**37, 38** and **40-42**) and/or an extra methylene unit (**40-42**) does not allow the extension of conjugation between the substituent and the flavanone scaffold. However, it cannot also be excluded that steric effects (compounds **29** vs. **35** and **31** vs. **32**), hydrophobicity (compound **32** vs. **33** and **36**) or substitution patterns (compounds **32** vs. **31** and **33**) may also influence the BCRP inhibitory activity.

In the MRP1-overexpressing BHK21 cell line, some compounds were also found to be active, although in a lesser extension than for BCRP. Compounds **41** and **42** showed the highest activity with 62.6 ± 19.3 % and 95.0 ± 20.2 % inhibition of calcein-AM (cAM) efflux, respectively. Hydrazone **30** (indol-3-yl) and azines **35** (pyrrol-2-yl) and **36** (2-nitrophenyl) were also found to be moderate MRP1 efflux modulators, achieving ~50% inhibition of cAM efflux. Oppositely, compounds **26**, **31-34**, **36**, **37** and **43-45** showed little or none activity as MRP inhibitors. Thus, and opposite to the previously observed for BCRP, carbohydrazides are

preferred efflux modulators for MRP1, with the spatial position of the substituent and ring substitution pattern having also an important role on the reported biological activities. This can be inferred by comparing compounds **34** (indol-2-yl, -5.88 ± 1.06 %) and **30** (indol-3-yl, 47.0 ± 22.1 %) or compounds **32** (4-methoxyphenyl, 12.3 ± 5.47 %) and **42** (4-methoxybenzoyloxy, 95.0 ± 20.2 %). Finally, for compounds **25**-**27** with a shorter hydrazone bridge, the MRP1 inhibition activity was severely decreased or neglectable. Interestingly, while compounds **35** and **36** could act as dual BCRP/MRP1 moderate efflux modulators (**35**, MRP1: 56.3 ± 14.4 %, BCRP: 53.5 ± 14.2 %; **36**, MRP1: 45.1 ± 3.60 %, BCRP: 71.1 ± 5.91 %), compounds **28**, **31** and **33** were better BCRP inhibitors and compounds **27**, **30** and **40**-**42** almost exclusively modulated MRP1. The identification of such scaffolds, able to selectively modulate each pump or capable of a simultaneous blockade of BCRP and MRP1, provides new insights on the development of new MDR modulators and allows further quantitative structure-activity relationships (QSAR) studies.

Other studies have also clarified flavonoids as inhibitors of the major contributors for MDR. While for MRP1 *N*-substituted carboxamide chromone derivatives were proved to be potent and selective inhibitors of MRP1 with almost no effect on other pumps (Obreque-Balboa et al., 2016), in BCRP flavonoids as genistein and naringenin showed to competitively inhibit BCRP-mediated efflux, with no effect on P-gp or MRP1, with such activities being enhanced due to the presence of an hydroxyl group in position 5 and a double bond between positions 2 and 3 (Boumendjel et al., 2011; Pick et al., 2011). In addition, the number of nitrogen atoms, the aromaticity and the presence of fused aromatic heterocycles also seem to favor BCRP inhibition (Ferreira et al., 2015b; Michaelis et al., 2014; Montanari and Ecker, 2015).

4.5.3. Structure-activity relationship (SAR) studies on MRP1 and BCRP efflux modulators

Aiming for new insights on the specific interaction modes of the most active molecules with BCRP or MRP1, two pharmacophoric hypothesis were built (**Figure 4.5**). For BCRP, a 7-point pharmacophore comprising one aromatic (Ar), one hydrophobic or aromatic (H/A), one hydrogen-bond acceptor (Ac), one hydrogen-bond donor (Do) and three Exclusion Volumes (Ex) was obtained. While detecting all the most active molecules within the dataset (5/5, true positives), filters all non-active compounds (8/8, 100% true negatives) and the large majority

of low-activity compounds (4/9) (**Table 4.16**). Moreover, while ring B of the flavanone scaffold does not seem to be important for BCRP efflux modulation, hydrogen-bond donor and acceptor groups at position 5 and 7 respectively are identified as crucial for the activity, in agreement with published literature (Pick et al., 2011). Finally, this pharmacophore is also able to detect Fumitremorgin C and Ko143, two of the most potent BCRP modulators available.

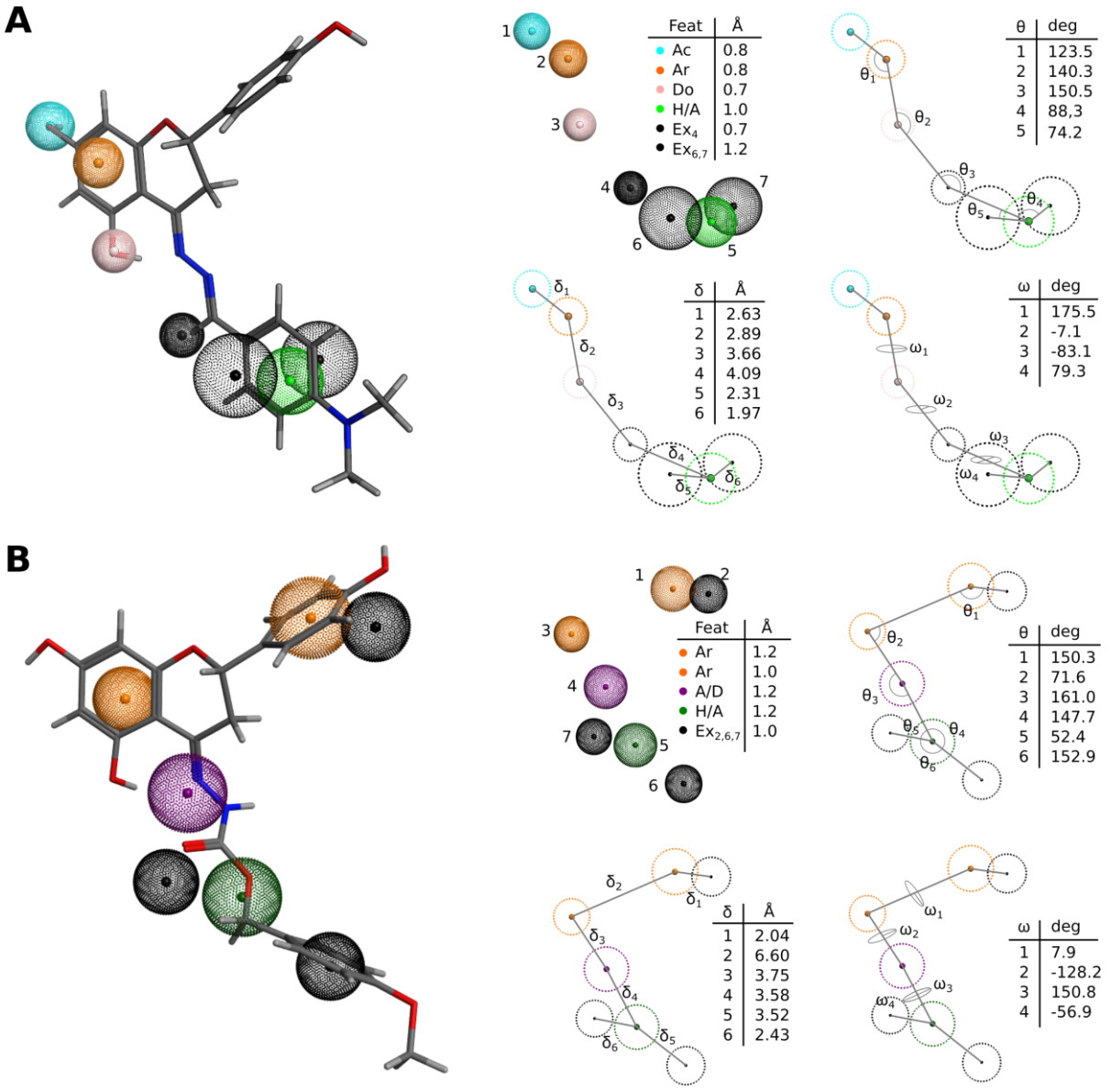

Figure 4.5. Pharmacophoric hypothesis for A) BCRP and B) MRP1 specific modulators. Measurement of distances, angles and dihedrals on the developed pharmacophores are also depicted.

Oppositely to BCRP, MRP1 efflux modulation does not seem to involve the presence of hydrogen-bond groups at positions 5 and 7, instead requiring the presence of ring B. In this seven-point pharmacophore, with two aromatic (Ar), one hydrogen-bond acceptor/donor (A/D),

one hydrophobic or aromatic (H/A) and three volume exclusion (Ex) features were identified (c.f. **Figure 4.5**). Herein, ring B must be kept spatially constrained to a given position by an additional exclusion volume (Ex_2) while other two ($Ex_{6,7}$) exclusion features around the hydrazide substituents to improve the accuracy of the pharmacophore. As such, all the most active MRP1 modulators (2/3, 66% positives) were detected while filtering all the inactive ones (0/3, 100% negatives). For low-activity compounds (**Table 4.16**), a detection rate of 38% (6/16) was observed.

Table 4.16. Distribution percentages of the detected molecules for MRP1 and BCRP.[a]

	MRP1 (% of inhibition)			**BCRP (% of inhibition)**		
	Pos	**0 < x < 50%**	**Neg**	**Pos**	**0 < x < 50%**	**Neg**
detected	2	6	3	5	4	8
total	3	16	3	5	9	8
d/t ratio	66%	38%	100%	100%	44%	100%

[a] Pos, positives; Neg, negatives; d/t ratio, detection percentage (number of detected molecules over total number of molecules within the category).

Interestingly, in both cases only by spatially restraining the orientation of chemical features within the flavanone scaffold a good selectivity towards the most active molecules was achieved. In BCRP, the co-planarity of the substituent with the flavanone scaffold was the major feature driving selectivity towards hydrazones and azines (**25-36**), meaning that this substituent may be in a specific pocket buried within the BCRP structure, involved in π-π interactions with aromatic residues as phenylalanine or tyrosine. Regarding MRP1, the spatial disposition of the exclusion volume (Ex) features towards both ring B and the substituent allows us to infer that, and unlike BCRP, an out-of-plane conformation of both features is important to maximize interactions, through π-π stacking, between both features and aromatic sidechains in MRP1.Therefore, and in order to thoroughly characterize the interactions in both efflux pumps, a molecular docking study on recently published bovine MRP1 crystallographic structure (Johnson and Chen, 2017) and human BCRP homology model (Ferreira et al., 2017a), developed in-house, was also performed (**Figure 4.6**).

The drug-binding pocket in BCRP is characterized as "surface groove", located immediately next to a cholesterol-recognition aminoacid consensus (CRAC) domain and with

regions of distinct polarities (Ferreira et al., 2017a). Herein, molecular docking revealed that the most active compounds bind to the center of the groove, with the flavanone scaffold in close proximity of hydrophobic residues in TM helix 4 (Leu513-Ala528) and TM helix 5 (Val534-Thr542) where fumitremorgin C (FMC), a known BCRP modulator, also binds (**Figure 4.6A**). Interestingly, while ring B is found to be buried in a small hydrophobic pocket formed by Val516, Phe545 and Pro574, the hydrazone substituent is found in another hydrophobic pocket involved in π-π stacking with Phe515 and dipole-dipole interactions with Met541. Interestingly, both residues are located next to three CRAC domains where cholesterol was also found to bind in molecular dynamics (MD) simulations (Ferreira et al., 2017a).

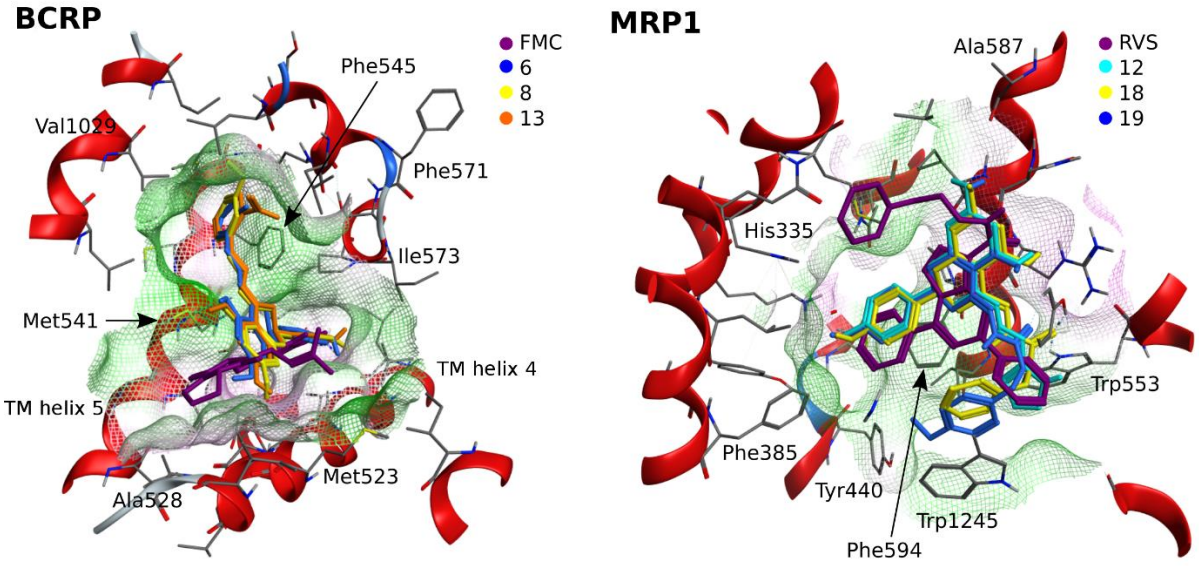

Figure 4.6. Docking poses for the most active compounds in BCRP and MRP1. Reference inhibitors as fumitremorgin C (FMC) and Reversan (RVS) were docked for comparison purposes. Drug-binding sites are drawn as molecular surfaces (green, hydrophobic; pink, polar).

The above docking results agree with the previously developed BCRP pharmacophore, in which the two exclusion volumes located next to the hydrazone substituent ($Ex_{6,7}$, **Figure 4.6A**) assure a proper orientation of the aromatic ring towards π-π interactions with the Phe571 aromatic sidechain. Moreover, and as ring B was not found to be essential for the activity, BCRP modulation due to hydrazones is expected to be due to i) competition with its natural substrates or ii) competition with cholesterol for the CRAC domains, having this an immediate effect by lowering the activity of the pump. Therefore, a feasible approach for further

optimization of the flavanone scaffold will involve chemical modifications of ring B to improve the potency and selectivity of hydrazones towards BCRP.

Most recently, the publication of the bovine MRP1, with 91% identity toward human MRP1, enables its utilization in new structure-based medicinal chemistry studies to identify probable drug-binding sites and interaction modes (Johnson and Chen, 2017). Herein, the LTC_4-bound MRP1 structure (PDBID: 5UJA) was used as template for molecular docking to better understand structure-activity relationships with the observed biological activity. Herein, the most active compounds towards MRP1 (**35**, **41**-**42**) were found to dock in a small cleft located at the top of the internal drug-binding pocket, in close proximity to the LTC_4-bound co-crystallized substrate and interacting with residues from TM helices 6, 10, 11 and 17. Furthermore, while ring B was found to participate in π-π interactions with Phe594, the hydrazide substituent of compounds **41** and **42** were able to also interact through π-π stacking with Trp1245 due to the longer hydrazide linker. In addition, the carbonyl moiety also allowed hydrogen-bonds with residues Trp553 (**36**, **42**-**43**), Arg593 and Tyr1242 (**41**). As in BCRP, one of the most potent MDR1 modulators, Reversan (Burkhart et al., 2009; Obreque-Balboa et al., 2016), docked in the same location (**Figure 4.6B**) and adopted a similar conformation in which one of the aromatic rings stacks with Phe594 while the other remained close to Trp1245 and the morpholine moiety in a hydrophilic pocket, interacting by hydrogen-bonding with Gln377 and Leu1237.

The predicted docking poses for MRP1 are in a good agreement with the herein developed pharmacophore. Due to the extra methylene unit in compounds **41** and **42**, the hydrazide linker is longer and allows the phenyl ring to easily adopt the required "out-of-plane" conformation to better interact with Trp1245. It was also observed that i) in the absence of aromatic substituents, CH-π interactions between methyl or methylene groups and aromatic residues can be present, and that ii) hydrogen-bonds can also be found between the hydrazide moiety (C=N-NH-CO-R) and hydrogen-bond donors as Trp553, Arg593 or Tyr1242. Moreover, the interaction between ring B and Phe594 clarifies the importance of this aromatic moiety, with the small exclusion volume (Ex_2) close to the 4'-hydroxyl being important for a proper orientation of ring B towards the aromatic sidechain of Phe594. Taking all together, chemical modifications at position 7, as methylation or acylation of the hydroxyl group, could be suitable approaches to further improve the potency of naringenin carbohydrazides towards MRP1.

Chapter 5

In silico studies on P-glycoprotein efflux mechanism. Results and Discussion

5. *In silico* studies of ABC efflux pumps

Despite the large knowledge obtained from experimental data regarding ABC transporters, the efflux mechanism by which they efflux drugs out of the cell is still obscure. Especially relevant in the identification of drugs as substrates or modulators, experimental techniques are often unable to thoroughly characterize the number of drug-binding sites, binding modes or the complete efflux mechanism. Nonetheless, and specifically for P-glycoprotein, the evidences provided by such techniques were determinant for the identification, through ligand-based studies (Ferreira et al., 2015b), of the chemical features related with the ability of a given chemical class to behave as substrate or modulator and allowing significant advances on the design of molecules to act as potent efflux modulators. Herein, the importance of aromatic features (Suzuki et al., 1997), the presence of nitrogen atoms (Ecker et al., 1999; Pearce et al., 1989) or the spatial relationship through QSAR studies were used to distinguish substrates from modulators (Ferreira et al., 2011; Sousa et al., 2013; Srivastava et al., 2016), to classify molecule classes into P-gp substrates or non-substrates (Klepsch et al., 2014; Prachayasittikul et al., 2016) or to predict the activity of newly synthesized derivatives towards more potent efflux modulators (Baptista et al., 2016; Srivastava et al., 2016; Yang et al., 2015).

To date, no efflux modulator has been used clinically for reversing the MDR phenotype in cancers, or even passed phase III clinical trials. Even *third generation* modulators as tariquidar or zosuquidar, able to block P-gp efflux at the nanomolar range, failed to succeed *in vivo* due to increased cellular toxicity or reduced efficacy (Ferreira et al., 2015b). Thus, it is also important to thoroughly understand the specific basis of the efflux mechanism through a comprehensive study of P-gp's structural features. Towards that end a refined P-gp model (Ferreira et al., 2012), obtained through molecular dynamics (MD) studies from the murine P-gp crystallographic structure published in 2009 (Aller et al., 2009), provided new insights on the structural stability of this ABC transporter. Briefly, both the lipid membrane and the "linker", a short polypeptidic sequence missing in the original crystallographic data, were found to be important for the structural stability of the transporter. Regarding the lipid membrane, while 1-palmitoyl-2-oleoyl-phosphatidyl choline (POPC) was found to stabilize the transmembrane domains (TMD) by reducing the correspondent hydrophobic mismatch with the membrane, the "linker" had a distinct effect on the transporters' insertion angle, stabilizing the

protein even when inserted in a short-chain dimyristoyl-phosphatidylcholine (DMPC) membrane (Ferreira et al., 2012).

The development of the above P-gp model was a crucial step for elaborating further studies, aiming for a better comprehension of the structural details that can be involved in drug efflux. Therefore, studies involving structural details, identification and characterization of drug-binding sites, efflux mechanisms or drug-transporter interactions were performed to better understand not only the transporter itself, but also which key points are important during the efflux mechanism. Therefore, by studying the structural dynamics of the transporter, new insights can potentially be used to develop more potent and selective modulators to be used as MDR reversers suitable to be co-administered with anticancer drugs in multidrug-resistant cancers.

5.1. The "linker" (residues 627-684) function in P-glycoprotein

While already known to be important for drug transport and ATPase activity of the pump (Hrycyna et al., 1998; Sato et al., 2009), other studies described this sequence as important for P-gp expression and cell trafficking (Rao et al., 2006), ubiquitination (Kölling and Losko, 1997) or actin motor pathways (Chan et al., 2005; Georges, 2007). From a previous paper, the "linker" was also found to be important for the structural stability of the transporter, having a strong positive effect by stabilizing the tilt angle of P-gp in DMPC, being the hydrophobic mismatch compensated by the increase in the total thickness of the membrane. When in POPC, the insertion of the "linker" (**Figure 5.1**) decreased NBD-NBD distance variations and fluctuations between the two domains.

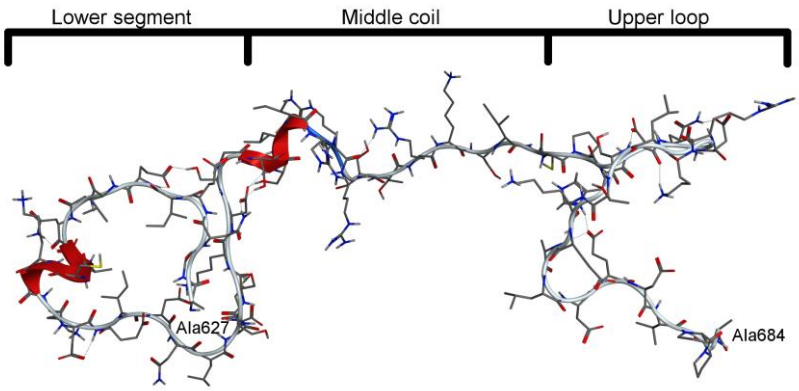

Figure 5.1. Linker's secondary structure after the 100 ns production run, showing the two α-helices, the N-terminal Ala627 and C-terminal Ala684 residues (Ferreira et al., 2013a).

These findings support the fact that the presence of the linker sequence and the membrane are, indeed, essential to the stabilization of the whole structure, and led to further studies aiming for a thorough characterization of the "linker" role in P-gp stabilization.

5.1.1. Structural and functional analysis of the "linker"

From the amino acid sequence, a more detailed analysis of the linker by PredictProtein™ server (Rost et al., 2004), estimates that more than 85% of the residues are exposed with only 10.5% probability for helix/strand formation, being in accordance with previous predictions used to build the linker and with other previous results (Ferreira et al., 2012). In addition, three favorable hot spots for protein-protein binding were identified, located next to highly conserved sequences on ABC transporters that could be involved, specifically for P-gp, in its structural stability.

The role of the "linker" became apparent since the first MD simulations using the published and correctly protonated crystallographic structure. While a 33% increase in the distance between the NBDs centers of mass was observed in simulations without a membrane, the insertion of P-gp in a lipid bilayer without adding the linker was not sufficient to correct this issue. Herein, the NBD distance in the *x* axis (*xy* axis are coplanar to the membrane plane) still increased even when inserted in a DMPC membrane, together with a tilt in the protein's insertion angle as a way to compensate the existent hydrophobic mismatch between the transporter and the membrane. With POPC this shift was not observed and distance variations

were mainly observed in the *y* axis, which can be linked to the normal motion patterns identified for this transporter.

Following the insertion of the linker, the NBD fluctuations were greatly reduced (**Figure 5.2A**) and, for DMPC and POPC bilayers, the insertion angle and NBD distance remained unaffected. Interestingly, only after a 30 ns MD run, the hydrophobic mismatch between P-gp and DMPC membrane was compensated through a 5.2% increase in bilayer thickness, increasing membrane curvature and shifting the NBD2 spatial position. In the 100 ns production run with POPC membrane, no hydrophobic mismatch or membrane curvature was observed and the previously identified P-gp motion patterns were still identified in the *y* axis, mainly due to the NBD pendular/rotational movements previously described (Ferreira et al., 2012). In addition, the RMSF profile obtained from the 100 ns production run (**Figure 5.2B**) identified two major fluctuation areas between aminoacids 632-643 and 654-663, appearing to be intimately related with the two small helices packed between both NBDs.

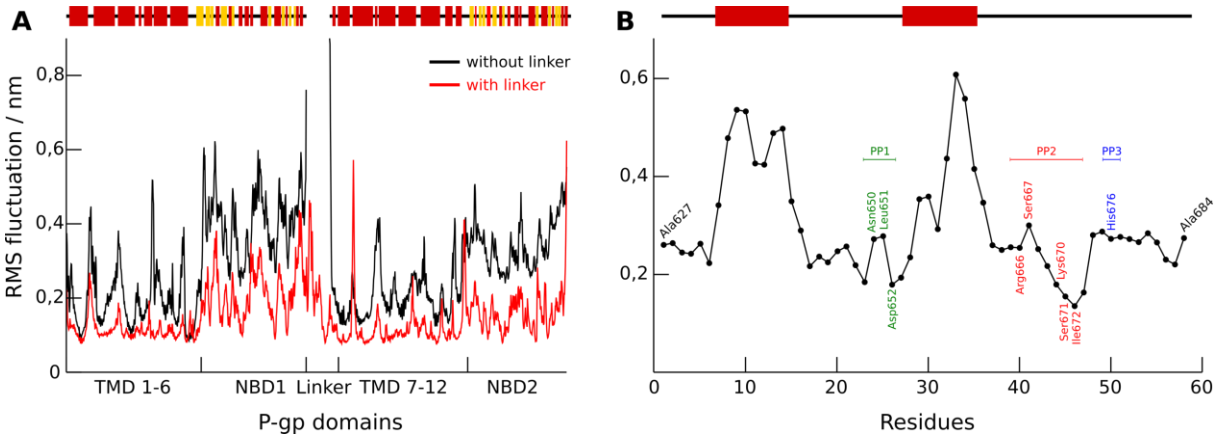

Figure 5.2. (A) Root Mean Square Fluctuations (RMSF) of the α-carbon for the P-gp domains, in the absence (black) or presence of linker (red), on a POPC Membrane (Ferreira et al., 2012); (B) RMSF for linker residues (α-carbons) from the 100 ns run, with the protein-protein contact residues identified by PredictProtein server (Ferreira et al., 2013a). A scheme of the secondary structure is displayed at the top, with α-helices in red, β-sheets in yellow and coils as a black line.

While the first one (residues 632-643) shows some of the characteristics of an ideal α-helix (radius 0.23 ± 0.01 nm, twist 98 ± 5 degrees and rise of 0.15 ± 0.02 nm), the second one (residues 654-663) displays a severe change in the secondary structure, shifting from an α-helix into a π-helix during about half of the 100 ns run. This type of structure is rarely seen in proteins, but is frequently associated to the formation or stabilization of a specific binding sites (Weaver, 2000). The rate of formation/distortion of these two helices, particularly the second one, could

be also related with P-gp normal motion patterns and specifically with the linker's 'damper' function, acting as two flexible springs absorbing large motions and stabilizing the cytoplasmic domains of the transporter.

The importance of the predicted protein-protein hot spots was initially assessed by comparing the P-gp contact maps before (crystallographic structure with the linker, prior to the energy minimization and refinement protocol) and after the 100 ns production run. It is possible to verify that the number of initial contacts only involved linker residues between Leu637-Ala649 but, at the end of the simulation, a 67.4% increase was registered due to the formation of new contacts mainly involving residues Ile648-Asp652, Arg666-Lys670 and Cys673-Asp679.

It is expected that the existence of protein-protein contact surfaces near the NBD2 ATP-binding site are involved in the stabilization of the structure, defining the ATP-binding pocket outer boundaries and contributing to the affinity of ATP towards NBD2. A different function is, however, expected from the linker's upper loop (**Figure 5.1**) protein-protein contact surface, as it impairs access to the internal drug-binding pocket from the cytoplasm. Additionally, and since it defines the lower boundary of the pocket, it is expected to be also directly involved in substrate recognition by R- and H-sites (Shapiro and Ling, 1997b). Therefore, and as shown by several studies (Hrycyna et al., 1998; Sato et al., 2009), the upper loop's position stability will affect the volume of the internal cavity and possible interactions with molecules at the substrate-binding sites.

From the three protein-protein interaction hot spots identified by PredictProtein server, the first one (PP1) is located after the first small α-helix, near Walker A (GSSGCGKS) and H-loop (IVIAH) motifs. As these conserved sequences are involved in the ATP binding pocket formation and ATP-dependent switch, and considering that the "linker" sequence was proved important for ATP binding and hydrolysis, it is possible that the magnitude and number of residues involved in the interaction between PP1/NBD2 can affect not only the ATP binding pocket formation but also the orientation and accessibility of the catalytic residue in NBD2 towards ATP.

The next predicted contact surface (PP2) includes the first amino acids of the middle coil, connecting the lower segment and the upper loop. The high variation in the middle coil RMSD during the 100 ns run (Ferreira et al., 2012) was particularly interesting because it could suggest the formation and breaking of a contact point contributing to the NBD2 stability. As

these residues are located next to the outer NBD2 helices, PP2 was thought to also contribute as an additional stabilizing anchor point to favour ATP binding and hydrolysis. Finally, and unlike PP1 and PP2, a single residue was identified as a third preferred contact point (His676, PP3) that interacted almost exclusively with linker residues. Based on his location (far from NBD2 and at the beginning of the upper loop) and since it defines the lower boundary of the internal drug-binding pocket, this contact point must be involved in the stabilization of the linker's upper loop by interacting with residues in the transmembrane helices (TMH), directly affecting the molecule's recognition by the substrate-binding H and R-sites hypothetically localized near the inner leaflet of the lipid bilayer.

5.1.2. Detailed "linker" contact analysis

5.1.2.1 Lower segment (residues 648-652)

After the preliminary linker equilibration and POPC insertion, the number of contacts and amino acids involved in the PP1 hotspot interactions were assessed. All the predicted contacts by the online server were already established, but additional contacts were found between Ile648/Arg1233 and Asp649/His1232. In addition, while all PP1 residues interacted with H-loop and C-terminal residues of NBD2, residue Asp652 is the only one simultaneously interacting with Walker A (Ser1071 and Ser1072) and H-loop (His1232) motifs. Hydrogen-bonds were found between residue pairs Asp649/His1232, Asn650/Val1273 and Asp652/Ser1072. Having performed the initial identification of the residues possibly involved in PP1 contacts with NBD2, the stability of this contact surface was evaluated throughout the production run.

A first approach was made through the evaluation of the minimum distances between the previously identified residue pairs. It was clear that the distance between Asp649/His1232 and Asp652/Ser1071, Asp652/Ser1072 and Asp652/His1232 were stable throughout all simulation while Ile648/Arg1233 and Asn650/Ala1275 distances increased after the first 30-40 ns. For Leu651, the distances with His1232 and Met1270 were shorter and more stable than the ones registered with Val1273 or Ala1275. Following, non-bonded interactions (hydrogen-bonds, HBs) between linker residues and NBD2 conserved motifs were studied because they can be one of the reasons for the PP1 stability. Despite the major number of HBs detected is between peptides, water-mediated HBs can also participate in the protein stabilization.

However, according to the Luzar and Chandler kinetics (Luzar, 2000; Luzar and Chandler, 1996), these peptide-water interactions are weaker when compared with peptide-peptide HB and can be ignored. Oppositely, HB involving aspartic acid residues (Asp649 and Asp652) seems to be the most stable, thus having a greater contribution for NBD2 stabilization. Using Luzar's intermittent HB correlation function (Luzar, 2000; van der Spoel et al., 2006), the dynamics of the formation and breaking of hydrogen-bonds for all contact surfaces could be analyzed with additional detail.

For PP1 (**Table 5.1**), the weaker initial Ile648/Arg1233 interaction was substituted by a stronger Asp649/Arg1233 contact and the interactions established between Asp649/His1232 (H-loop) and Asp652/Ser1072 (Walker A motif) showed the highest average number of HBs per time unit. However, Asp652/Cys1074 and Asp652/His1232 displayed the larger HB lifetime although with a lower average number of HBs per time unit than Asp652/Ser1072. Therefore, aspartic acid residues Asp649 and Asp652 seem to have a central role in the interaction with NBD2, creating an anchor point that not only stabilizes the NBD1/NBD2 distance but also provides a more defined boundary of the ATP-binding site.

Table 5.1. Physical properties of the hydrogen-bonds between PP1 and NBD2 (τ, lifetime of bond formation; ΔG, HB formation energy; $\langle N_{HB} \rangle$, average number of HB) (van der Spoel et al., 2006).

Residue				
PP1	**NBD2**	**τ / ps**	**ΔG / kJ.mol^{-1}**	**$\langle N_{HB} \rangle$**
Ile648	Arg1233	41.7	-14.0	0.03
Asp649	His1232	119.5	-16.7	1.21
	Arg1233	49.1	-14.4	0.25
Asn650	Ala1275	131.0	-16.9	0.56
Asp652	Ser1071	472.2	-20.2	0.64
	Ser1072	209.7	-18.1	1.66
	Gly1073	991.4	-22.0	0.43
	Cys1074	2443.4	-24.3	0.27
	His1232	2020.6	-23.8	0.10

Additionally, and despite the loss of hydrogen-bonds between Ile648/Arg1233, a new hydrophobic contact point with the C-terminal residues Val1273 and Ala1275 was formed to

avoid the more hydrophilic aqueous environment. Curiously, and despite the relative stability in the minimum distance for residues Leu651/His1232 and Leu651/Met1270, no evidence of HBs were found, mainly due to an unfavourable orientation of the amino and carbonyl groups towards His1232 and Met1270.

5.1.2.2 Middle coil (residues 666-672)

As predicted for PP2 (**Figure 5.2B**), the main interactions were between linker residues Arg666, Ser667 or Lys670 with residues at D-loop (Ser1204), Q-loop (Glu1119) and *Signature* (Leu1176 and Lys1181) motifs. Interestingly, by the analysis of the 100 ns production run, no meaningful interactions were found between "linker" residues Ser671 and Ile672 with residues in the conserved motifs. Instead, Thr668 appears to be involved in protein-protein contacts with Q-loop and Signature motifs whereas Arg699 seems to interact with a Thr1174, a non-conserved residue.

After the first 20 ns, and when compared with PP1, the variations in the residues minimum distances are smaller and within 2 nm. However, only Thr668 and Lys670 seem to have the most stable distances, whereas Arg666/Ser1204, Ser667/Glu1119 and Thr668/Glu1119 are more irregular. As this contact spot is located immediately after the second α-helix, the NBD2 rotational motion pattern can affect the length of this surface, widening when NBD2 is closer and forcing the second helix to shift from an α-helix to a π-helix to better absorb NBD2 motions. This can be inferred by overlapping the Lys670 minimum distances with the changes in the second helix radius/twist, with residue pairs being at their minimum distance when the π-helix is formed (between 30 and 60 ns). In the absence of the linker, NBD2 rotates more freely around the 'ball-and-socket' joint formed by ICH4 and NBD2. With the linker, PP1 seems to be essential to maintain an ideal distance between NBDs (around 3 nm) while PP2 creates an additional anchor point, increasing the stability of the NBDs and favouring the linker's damper function by transferring the residue fluctuations into the linker's α-helices.

As previously, the physical properties of the HBs established between residues were thoroughly analysed thoroughly. By the analysis of **Table 5.2**, showing some HB physical properties of the PP2 hot spot, is possible to identify the HBs between Thr668/Leu1176 (*Signature* motif) as the most frequent and the second most stable. Herein, Lys670/Thr1174 exhibits the strongest binding energy and establishes of a very stable hydrogen bond with an extremely long lifetime between the lysine amino group and threonine carbonyl group, both in

the mainchain. A deeper analysis revealed that the simultaneous HB interactions between Arg669/Thr1174 sidechains and Thr668/Leu1179 induces an optimal distance between Lys670 and Thr1174 backbones that favors the extremely long HB between Lys670 and Thr1174. Moreover, this assumption is corroborated by the observation that, when both pairs Thr668/Leu1179 and Lys670/Thr1174 interact, a small transient β-sheet is formed. Interestingly, PP2 only shows three interactions below -20 kJ.mol^{-1} involving three different amino acids, whereas in PP1, a single aminoacid (Asp652) registered 4 hydrogen-bonds with lower binding energies. As such, it seems that interactions between Thr668/Leu1176 and Lys670/Thr1174 have a central role in the creation of a wider HB network ranging from Arg666/Ser1204 (D-loop) to Lys670/Val1174 (before *Signature* motif).

Table 5.2. Physical properties of the hydrogen-bonds between PP2 and NBD2 (τ, lifetime of bond formation; ΔG, HB formation energy; $\langle N_{HB} \rangle$, average number of HB).

Residue				
PP2	**NBD2**	**τ / ps**	**ΔG / kJ.mol^{-1}**	**$\langle N_{HB} \rangle$**
Arg666	Ser1204	276.5	-18.8	0.15
Ser667	Glu1119	59.4	-14.9	0.04
	Glu1175	473.0	-20.2	0.24
Thr668	Glu1119	177.6	-17.7	0.30
	Leu1176	922.8	-21.8	1.28
	Lys1181	24.2	-12.7	0.002
Arg669	Thr1174	19.9	-12.2	0.06
Lys670	Asp1124	102.0	-16.3	0.44
	Val1169	208.4	-18.1	0.39
	Thr1174	13386.0	-28.6	0.78

5.1.2.3. Upper loop (residues 673-690)

In the upper loop of the linker, His676 was pointed out by the online server as a possible residue involved in protein-protein contacts. Since through the simulation analysis we additionally found stable contacts between residues Cys673/Glu255 (in TMH4), the aminoacids from Cys673 to Glu690 were also evaluated to assess its importance for the upper loop's stability. Thus, a more thorough examination of this sequence allowed us to further exclude other residues from this analysis, as their hydrogen-bond acceptor groups are oriented towards

water molecules. Only residues Thr684/Asp177, Thr684/Ser180, Lys685/Asp177 and Lys685/Ser180 (belonging to TMH3) and Asp689/Thr816, Glu690/Thr816, Asp689/Arg817 and Glu690/Arg817 (residues from TMH9) were found to establish HBs with TMH residues.

One of the unique characteristic features of this contact surface is the fact by which HBs are almost exclusively found to be between sidechains, which allow a greater fluctuation throughout the production run. It is also possible to identify Cys673/Glu255, His676/Glu690, His676/Asn820 and Lys685/Asp177 as the ones having a more stable minimum distance, leading us to predict the formation of HBs between these residue pairs. Another interesting characteristic of the PP3 hot spot is the relatively stable position near the interface of the bilayer's inner leaflet. This cannot be solely due to His676 because most of the interactions are related with the stabilization of the upper loop through HBs with Ser693, Glu686 and Glu690, also belonging to the linker. Oppositelly, the position of this structure is sustained due to Thr684/Asp177, Thr684/Ser180, Lys685/Asp177, Asp689/Arg817 and Glu690/Thr816 interactions.

As expected, from the analysis of the HB characteristics (**Table 5.3**), the HB with lowest binding energies are between His676/Ser683 (within the linker) and His676/Asn820 (in TMH9), with the latter having a much larger average number of HBs per time unit. Residue pairs Thr684/Asp177 and Lys685/Asp177, not predicted by the online server but detected by visual inspection as a possible anchor point between the linker and TMH3, also had relatively high lifetimes and energies, which are indicative of a relatively stable contact zone. The other detected HBs seem to contribute to increase the upper loop's stability through the creation of an efficient HB network able to crosslink both P-gp halves. Therefore, although not participating in the stabilization of the nucleotide-binding domains, the linker's upper loop noticeably defines a stable lower boundary for the internal drug-binding pocket, probably being part of the substrate-binding H- and R-sites.

Table 5.3. Physical properties of the hydrogen-bonds between PP3 and TM helices 3, 4 and 9 (τ, lifetime of bond formation; ΔG, HB formation energy; $\langle N_{HB} \rangle$, average number of HB).

Residue				
PP3	**TMH**	**τ / ps**	**ΔG / kJ.mol^{-1}**	**$\langle N_{HB} \rangle$**
Cys673	Glu255	125.0	-16.8	1.05
His676	Ser683	800.0	-21.5	0.21

	Glu686	90.7	-16.0	0.03
	Glu690	39.2	-13.9	1.24
	Asn820	951.8	-21.9	0.96
Thr684	Asp177	356.6	-19.4	1.27
	Ser180	158.2	-17.4	0.06
Lys685	Asp177	500.6	-20.3	0.71
Asp689	Arg817	69.4	-15.3	0.17
Glu690	Thr816	159.2	-17.4	0.29

5.2. Identification and characterization of the drug-binding sites

5.2.1. Identification of possible drug-binding sites

From literature, many published studies identified three major drug-binding sites in P-gp, based on experiments with verapamil (gold-standard modulator), Hoechst 33342 and Rhodamine-123 (substrates). Two of them were named H-site and R-site by Shapiro and Ling (Shapiro et al., 1997; Shapiro and Ling, 1998) after identifying Hoechst 33342 and Rhodamine-123 as preferential substrates for each, respectively. Additionally, they also suggested that both could interact in a positively cooperative manner, thus affecting the substrate efflux (Shapiro and Ling, 1997b).

In our study (Ferreira et al., 2013b), the whole internal drug-binding pocket was defined as the docking box. The nine best ranked docking poses obtained for verapamil, Rhodamine-123 (R123) and Hoechst 33342 (H33342) outlined two out of three major drug-binding sites (**Figure 5.3**). Herein, verapamil was found in two major locations, with four poses (-7.6 to -7.4 kcal.mol^{-1}) close to the outer leaflet of the lipid bilayer and five docking poses in a lower location, next to the inner leaflet interface, with binding energies ranging from -7.6 to -7.3 kcal.mol^{-1}. Interestingly, the site identified at the top of the cavity— hereafter named M-site— had been already described from a murine P-gp structure with two co-crystallized modulators (QZ59-SSS and QZ59-RRR) (Aller et al., 2009). As verapamil is described in literature as

substrate (Cabrera et al., 2006; Wang et al., 2003; Xue et al., 2004) and modulator (Tsuruo et al., 1981; Wang et al., 2003; Wiese and Pajeva, 2001), and assuming that the lower location detected next to cytoplasmic interface is a substrate binding site, the identical binding energies at both sites provided a glimpse on the promiscuous behavior of verapamil. In addition, the docking poses of R123 were also found in both locations with equal binding energies of -9.2 kcal.mol^{-1}. This finding supports the cytoplasmic inner leaflet C-terminal position as a substrate-binding site, described in literature as the location where R123 interacts— R-site. Therefore, verapamil and Rhodamine-123 poses allowed a first insight about the boundaries of the R-site (**Figure 5.3**).

For H33349, however, almost all the top-ranked docking poses were found at the assigned R-site (-10.5 kcal.mol^{-1}), with only two poses registered at the N-terminal halve in a symmetrical location, although with lower binding energy (-9.0 kcal.mol^{-1}, **Figure 5.3**). This result alone did not allow a positive identification of the remaining site– the H-site– location but agrees with several studies corroborating the H-site location in the N-terminal domain. Pajeva *et al.* identified two possible locations for the H-site next to TMH5 and TMH11 (Pajeva et al., 2004), based on a pharmacophore model of Hoechst 33342. Loo and Clarke, through cysteine scanning mutagenesis (Loo and Clarke, 2002, 2001, 2000), showed that TMHs 6, 9 and 12 were part of the R-site while TMHs 2, 3, 4, 10 and 11 delimited the H-site. Both studies are consistent with our R-site assignment and, therefore, its symmetrical position located next to TMDs 2, 3, 4, 10 and 11 could be assigned as the H-site. In addition, Sharom and co-workers mapped H-site 10-14 Å below the membrane surface (Qu and Sharom, 2002), also locating LDS-751 binding site closer to the cytoplasmic membrane/water interface regarding the Hoechst 33342 binding site (Lugo and Sharom, 2005). In our study, and for the identified substrate-binding sites, the assigned H-site is indeed more deeply buried in the cytoplasmic leaflet of the membrane (2.4 Å for the water/lipid interface against 0.5 Å mapped for the R-site).

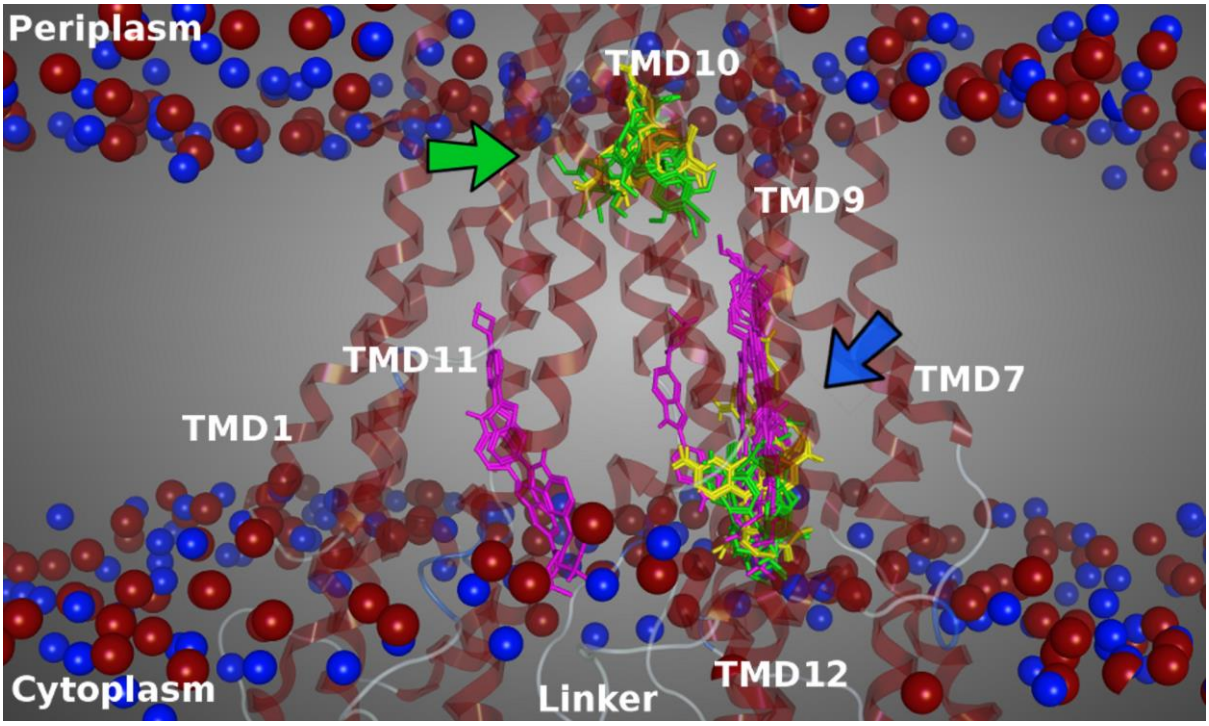

Figure 5.3. Best ranked docking poses for verapamil (green), Rhodamine-123 (yellow) and Hoechst 33342 (pink), allowing the M-site (green arrow) and R-site (blue arrow) assignments. Phosphate (red) and nitrogen (blue) atoms of lipid headgroups are also represented to assess the relative position of the lipid membrane (Ferreira et al., 2013b).

Another way to validate the assignment of H and R-sites is to analyse docking poses for additional molecules as anthracyclines (Shapiro and Ling, 1997b) and LDS-751, described to preferably bind to the R-site (Shapiro and Ling, 1998), quercetin and colchicine as specific binders to the H-site (Shapiro and Ling, 1997b) and vinblastine, actinomycin D and etoposide in both sites (Shapiro and Ling, 1997b). Our docking study showed, for LDS-751 (**Figure 5.4**), docking poses at the assigned R-site (top-ranked pose, -8.1 kcal.mol^{-1}) and H-site (-7.9 kcal.mol^{-1}), but also at M-site (-7.8 kcal.mol^{-1}). For antracyclines (daunorubicin and doxorubicin), the top-ranked docking poses were found at the assigned R-site (**Figure 5.4**) with binding energies lower than -10 kcal.mol^{-1}.

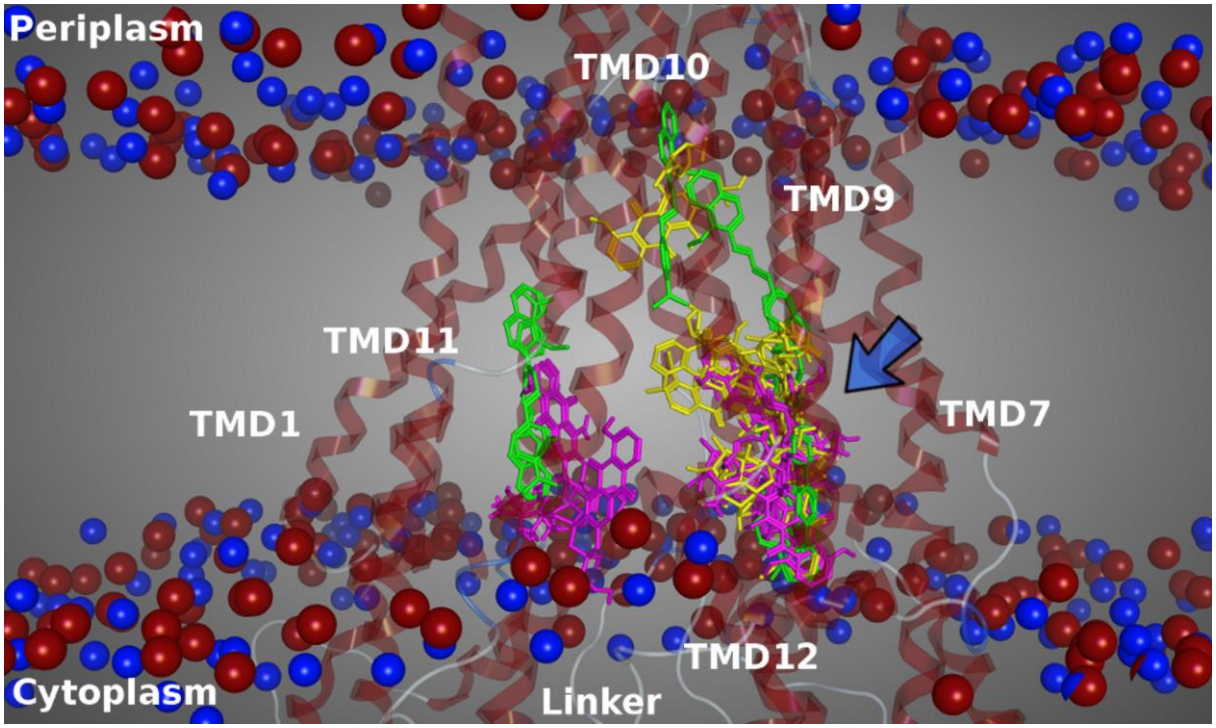

Figure 5.4. Best ranked docking poses for LDS-751 (green), daunorubicin (yellow) and doxorubicin (pink). The R-site is identified by a blue arrow. Phosphate (red) and nitrogen (blue) atoms of lipid headgroups are also represented to assess the relative position of the lipid membrane (Ferreira et al., 2013b).

Although daunorubicin almost exclusively docked at the R-site (only 1 pose registered at M-site with -8.8 kcal.mol^{-1}), doxorubicin displayed three poses at H-site, with affinities ranging from -9.4 to -9.2 kcal.mol^{-1}. Since H33342 and doxorubicin docked in both H and R-sites within the standard error reported for VINA (2.85 kcal.mol^{-1}) (Trott and Olson, 2010), this does not allow to discriminate between sites. However, the global results are in accordance with previous experimental findings which claimed that molecules interacting at H-site will positively affect the efflux from R-site and vice-versa. From the above results and for H33342, low doxorubicin concentrations may effectively stimulate the efflux from the H-site translocation pathway, whereas at higher concentrations the competition between both molecules increases and efflux is impaired, as demonstrated by Shapiro and Ling (Shapiro and Ling, 1997b). Finally, while etoposide was also found at both (with ΔG of -10.0 and -9.5 kcal.mol^{-1} for R- and H-sites respectively), vinblastine (-8.6 kcal.mol^{-1}) and actinomycin D (-11.2 kcal.mol^{-1}) top-ranked poses were found at the assigned H-site (**Figure 5.5**). Hence, the symmetrical positions in which these molecules docked (near the inner leaflet interface) strongly corroborate our H- and R-sites assignment hereby proposed.

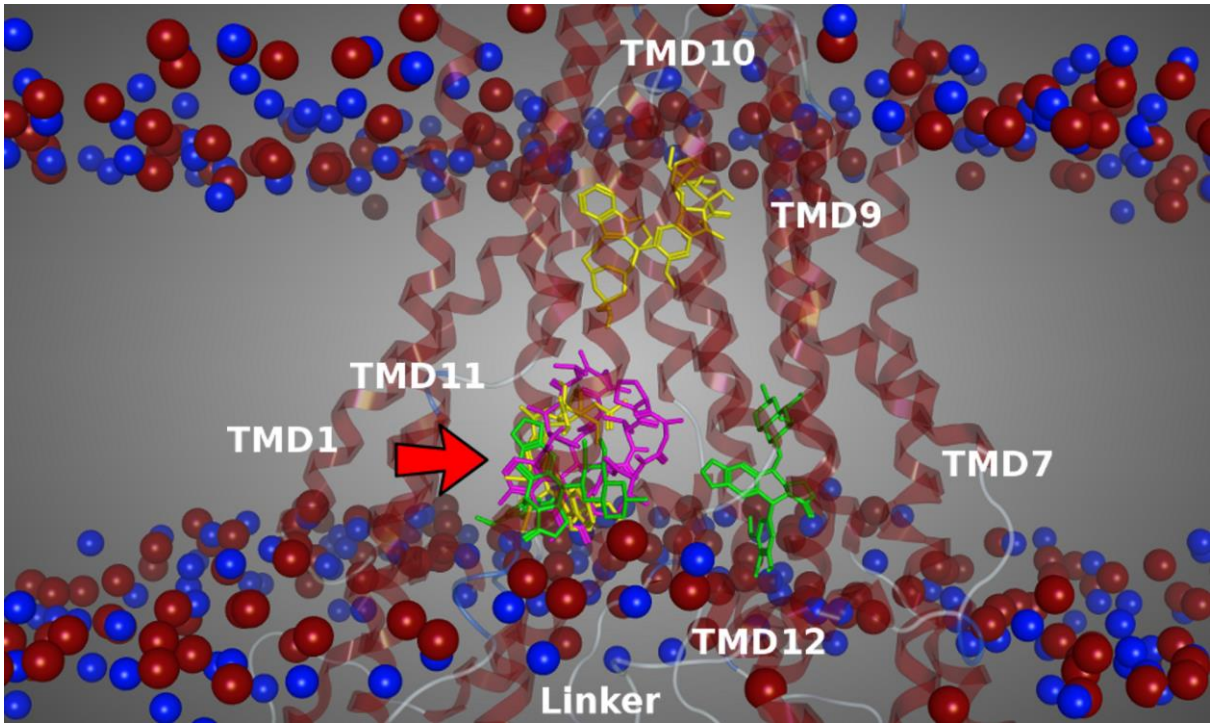

Figure 5.5. Docking poses for etoposide (green), vinblastine (yellow) and actinomycin D (pink). H-site is identified by a red arrow. Phosphate (red) and nitrogen (blue) atoms of lipid headgroups are also represented to assess the relative position of the lipid membrane (Ferreira et al., 2013b).

Quercetin and colchicine, on the other hand, did not docked preferentially at the assigned H-site, instead being found at M-site and R-site with similar binding energies (difference of 0.3 kcal.mol^{-1} between sites). Although different from previously reported results (Shapiro and Ling, 1997b), the docking results are in accordance with several experimental results in which colchicine was showed to protect residues in TMH6 and TMH12 (belonging to R-site) from dibromobimane labelling (Loo and Clarke, 2001, 1999). Quercetin and also colchicine also compete with [^{3}H]-azidopine for P-gp labelling, a substrate proved to interact in a similar location as calcium channel blockers like verapamil (Safa et al., 1987; Shapiro and Ling, 1997a) and different from cyclosporine A or vinblastine (Tamai and Safa, 1991). In addition, the large number of cellular targets and the type of phospholipid and protein/phospholipid ratio can also bias results obtained with quercetin (Shapiro and Ling, 1997a). Therefore, it is not clear that quercetin and colchicine bind preferentially at the H-site or if their influence in R123 efflux can be exerted by other mechanism.

Based on the above data, a question remains: how can these results explain the Rhodamine-123 efflux increase in the presence of colchicine and quercetin and simultaneously

affect Hoechst efflux? A direct competition between Rhodamine-123, quercetin and colchicine may favor R123 efflux by displacing colchicine and quercetin into the alternative H-site pathway, having as consequence an impairment of H33342 efflux. However, another suitable response can be found in an early proposed mini-pharmacokinetic system (Didziapetris et al., 2003), in which essential pre-requisites for any P-gp substrate are molecular weight (MW) > 400 and a Lipinski number of acceptors (LA) ≥ 8. While none of the considered molecules (Rhodamine-123, quercetin or colchicine) fully comply with these specifications, the combined properties of such small molecules may have a positive influence in the stimulation of drug efflux at one of the translocation pathways. All the above data thoroughly supports the logical assignment of three major drug-binding sites within P-gp's drug-binding pocket, corroborating the earlier identification by Aller *et al.* of a modulator-binding site (M-site) and, for the first time to our knowledge, assigning the substrate-binding H-site and R-site to specific locations within the internal cavity.

5.2.2. Characterization of the drug-binding sites

After the identification of three major drug-binding sites (DBS) at the P-gp's internal pocket, a thoughtful characterization of the lining residues, volume and polarity followed. One of the first noticeable differences between M-site and H/R drug-binding sites is the aminoacid composition (**Table 5.4**). At the M-site, 33% of residues have aromatic sidechains (namely phenylalanine and tyrosine) against 15 ± 1% in the H and R-sites. Although the number of hydrophobic residues is similar in all sites (40 ± 1%), polar residues are more predominant at the H and R-sites (44 ± 1% against 27% in M-site). This asymmetry in residues distribution, already described in 2009 (Aller et al., 2009), has a direct effect in the DBS mean polarities with calculated values of + 0.24 for the M-site, + 0.32 for R-site and + 0.33 for H-site. The analysis also revealed that three residues in the linker's upper loop are common to H and R-sites, thus supporting the importance of this structure for the structural recognition of substrates (Hrycyna et al., 1998).

Since several other residues are also common to both substrate-binding sites (**Table 5.4**), this structural finding can be a link to the positively cooperative assumption by Shapiro and Ling. Moreover, while M-site registers an increased percentage of aromatic and hydrophobic residues (phenylalanine, valine, methionine and tyrosine), residue distribution between H- and R-sites are similar, presenting an increased prevalence of more polar

aminoacids such as glutamines or glycines at the R-site, and cysteine or triptophane only found at H-site. Serines and leucines, however, show similar distributions throughout the three sites. Therefore, it is tempting to explain that affinity differences towards drug molecules between H and R-sites are due to this asymmetry in residues distribution.

Table 5.4. Mapped residues for each drug-binding site.[a]

M-site (*n* = 33)			**R-site (*n* = 49)**			**H-site (*n* = 45)**		
His60	Val327	Ser729	Ala229	Ala344	Gly774	*His60*	Gly187	Lys677
Leu64	Leu328	Val732	Thr236	*Ser345*	Glu778	*Val121*	Met188	Leu678
Met67	Thr329	*Gln942*	Asp237	*Pro346*	Ala819	Leu122	Phe190	Leu875
Met68	Phe332	Met945	Leu240	*Glu349*	Gln820	Ala125	Gln191	Ser876
Phe71	Ser333	*Tyr946*	His241	Gln674	Val821	Gln128	His241	Leu880
Gly72	*Ile336*	Tyr949	Ile289	Asn675	Lys822	Val129	*Ser340*	Ala897
Thr75	*Phe339*	Leu971	Asn292	*Arg676*	Gly823	Trp132	*Val341*	Lys930
Tyr113	*Gln721*	Phe974	Met295	Asn717	Gly985	Cys133	*Gln343*	Phe934
Val121	*Phe724*	Ser975	Gly296	Leu720	Gln986	Asn179	*Ser345*	Phe938
Tyr303	Ser725	Val978	Phe299	*Gln721*	Ser988	Glu180	*Pro346*	Ser939
Gln326	Phe728	Met982	Leu300	*Phe724*	Ser989	Gly181	Asn347	*Gln942*
			Ile336	Ser762	Phe990	Ile182	*Glu349*	Ala943
			Phe339	Thr765	Ala991	Gly183	Ala350	*Tyr946*
			Ser340	Phe766	Pro992	Asp184	Ala351	*Asp993*
			Val341	Gln769	*Asp993*	Ile186	*Arg676*	Lys996
			Gly342	Glu770				
			Gln343	Phe773				

[a] Residues in *italic* are common to at least two DBS, and underlined residues are part of the linker sequence.

For instance, H-site have a higher percentage of charged residues (lysine, histidine and glutamic acid residues), whereas R-site have a higher number of glycines, glutamines and prolines (non-ionizable residues). Interestingly, no threonines and tyrosines are found in H- and R-sites, respectively.

For all three DBS, individual volumes were also calculated by probing the internal space with EPOS^{BP}. A mean volume of 1300 ± 300 Å^3 was estimated for M-site, whereas the calculated mean volume for both substrate-binding sites were considerably higher, 1900 ± 500 and 2200 ± 600 Å^3 for R and H-sites (30% and 39% higher, respectively). A graphical representation of the Molecular Surface (MS) for M-site (**Figure 5.6**, top left) shows a 'bell-shaped' structure at the top of the DBP, opening directly into the internal cavity. The

correspondent Electrostatic Map (EM – **Figure 5.6**, top right) revealed a hydrophobic surface, with π electrons from aromatic rings arising as contact surfaces with an electron-donating potential and four extra electron-acceptor surfaces found near hydroxyl and amino groups of residues Gln326, Gln721, Ser725 and Tyr946. For R-site, a 'pouch-shaped' like cavity was observed (**Figure 5.6**, middle left), with its entrance delimited by polar residues (Ser340, Arg676, Gln721, Ser988 and Ser989) and with two aromatic residues (Phe339 and Phe756) additionally contributing for a hydrophobic region next to the pocket entrance. The EM shows an increased proportion of charged surfaces (**Figure 6.6**, middle right), with electron-donating carbonyl and hydroxyl groups of residues Gln769, Ser988, Ser989 and Phe990 spanning through a wide surface, further extended by the aromatic sidechain of residue Phe773. On the contrary, Arg676 and Gln721 have electron-accepting characteristics and are located next to the cavity entrance.

Interestingly, for H-site, the most noticeable feature is the direct access from the 'entrance-gate' between TMH10/12. Hence, in this study H-site is much more accessible to any molecule that leaves the inner leaflet into the DBP (**Figure 5.6**, bottom left). The cavity surface is much more hydrophobic when compared with R-site, having a hydrophobic cleft ranging residues Val129, Trp132, Phe934 and Phe938. Towards the R-site, a more polar cleft extends through TMH3, from residue Asn179 to Gly181, ending at Ser340 (common with R-site). The EM (**Figure 5.6**, bottom right) shows a more positively charged domain formed by residue Arg676 (linker) and Lys996 (TMH12) against two negative contact points, formed by Glu180 (TMH3), Ser939 and Gln942 (TMH11).

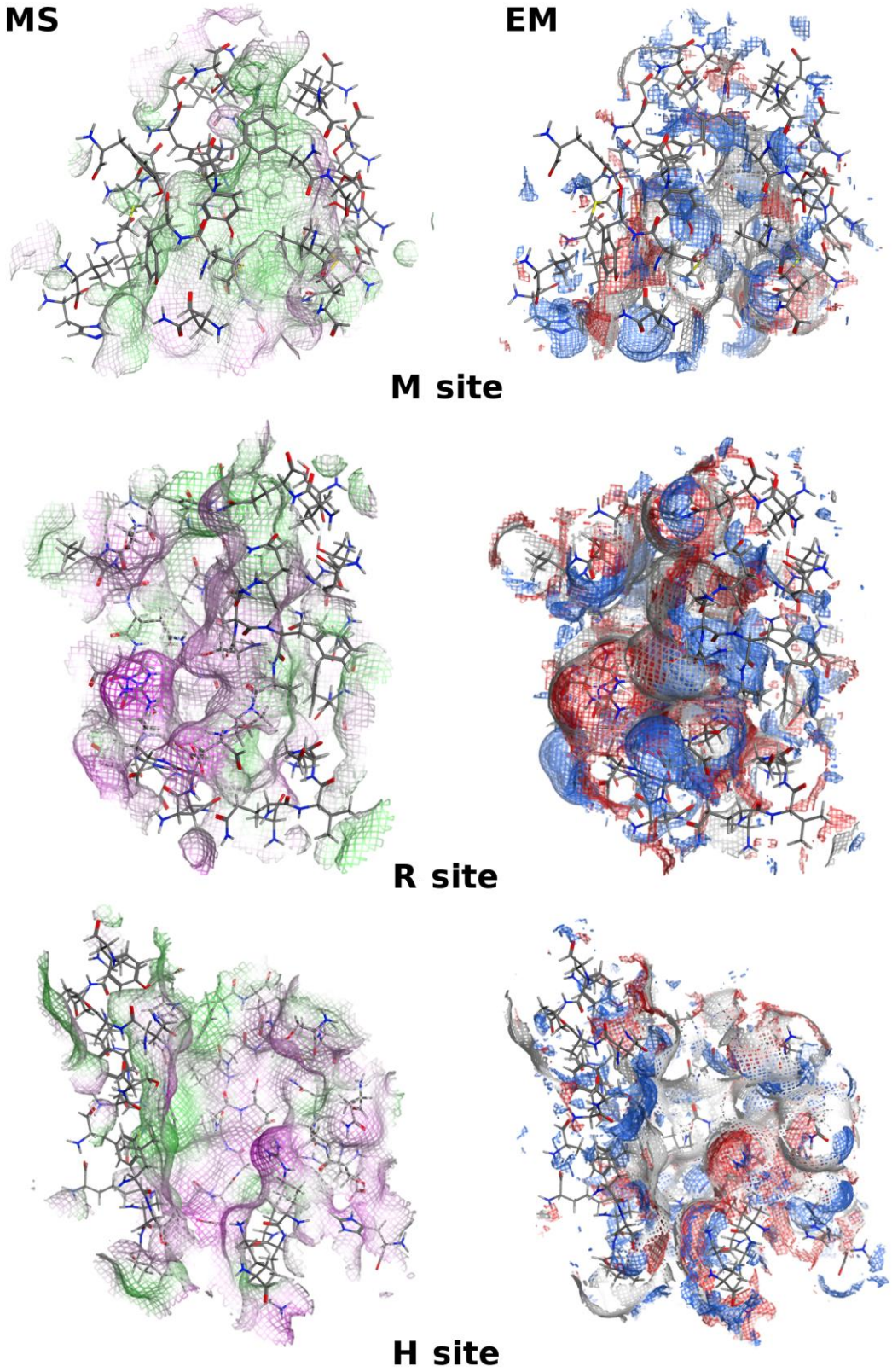

Figure 5.6. Graphical representation of the Molecular Surface (MS— green, hydrophobic and pink, polar) and Electrostatic Map (EM— blue, electron donor; grey, neutral and red, electron acceptor) for the identified drug-binding sites (Ferreira et al., 2013b).

The statement that only H-site is directly accessible from the lipid bilayer must be considered with caution. Many studies clarified that P-gp efflux tends to occur in an alternate way, with NBD1 and NBD2 hydrolyzing ATP in a sequential mode at different points of the efflux cycle (Callaghan et al., 2006; Martin et al., 2000; Senior et al., 1995; Siarheyeva et al., 2010). Our previous study (Ferreira et al., 2012) showed that NBD2 can more easily accept an ATP molecule. However, it is possible that this configuration would change when NBD1 is the one involved in nucleotide hydrolysis, shifting the 'entrance gate' to the gap between TMH 4/6 and creating a direct access into the R-site. Indeed, a recent study identified intrinsic local structural asymmetries at the NBDs, when P-gp is at a transition state, with the occlusion of nucleotide occurring in one NBD at a time and taking turns in hydrolysis. In addition, an intrinsic catalytic preference for one of the NBDs was also suggested, being required one ATP for closing the intracellular side and a second ATP for pushing P-gp into the outward-facing conformation (Verhalen et al., 2017). Therefore, for each NBD a pseudo-symmetric drug efflux pathway may exist (Parveen et al., 2011), starting in each substrate-binding site (R and H), but even the specific characteristics herein identified for R- and H-sites could change accordingly.

5.2.3. Development of a classification scheme for substrates and modulators

Having positively identified and characterized the three drug-binding sites within the P-gp internal cavity, we carried out further docking studies with molecules classified as substrates (*n* = 32), modulators (*n* = 19), efflux probes (*n* = 10) and phospholipids (*n* = 7) (Polli et al., 2001; Rautio et al., 2006). At this point, it is imperative to define the concept of P-gp efflux modulation. Experimentally, the modulation ability is evaluated through several experimental methods such as cell monolayer efflux studies (digoxin, calcein-AM, prazosin, vinblastine or colchicine) (Rautio et al., 2006), calcein-AM efflux inhibition (Polli et al., 2001), drug-stimulated ATPase quantification (Polli et al., 2001) and R123 accumulation assays (Reis et al., 2012, 2013). The affinity of probe substrates for drug-binding sites in P-gp affects the outcome, for any evaluated molecule. An example is the experimentally determined effect of daunorubicin and colchicine on R123 efflux. In our study, daunorubicin has a low binding free energy (-10.2 kcal.mol^{-1}) which may favor a direct competition with R123 (-9.2 kcal.mol^{-1}) for the R-site and, consequently, decrease the R123 efflux rate in a concentration-dependent manner. For colchicine, with a higher ΔG (-8.4 kcal.mol^{-1}), the competition for R-site favors R123, displacing colchicine into the alternative translocation pathway and decreasing H33342

efflux (as observed experimentally) (Shapiro and Ling, 1997b). This model can also explain the modulation observed by actinomycin D (-11.2 kcal.mol^{-1}), in which a direct competition for H-site will reduce Hoechst 33342 efflux, displacing it to the R-site translocation pathway and increasing the competition of Hoechst 33342 with R123. For etoposide, with lower binding free energies for both sites than Rhodamine-123 (-10.0 and -9.5 kcal.mol-1 for R and H-sites, respectively), both translocation pathways would be directly affected.

Other possible way to modulate P-gp efflux is through allosteric influence of a given molecule at M-site, recently characterized as a central modulator drug-binding site (Aller et al., 2009; Gutmann et al., 2010). Many molecules found in literature are simultaneously described as substrates and modulators, and even proven substrates as vinblastine seem to behave as efflux modulators for colchicine/digoxin (Rautio et al., 2006) and R123 (Wang et al., 2001). Moreover, vinblastine is also able of self-modulation (IC_{50} of 89.7 μM) (Rautio et al., 2006). Herein, Shapiro and Ling demonstrated experimentally that vinblastine can indeed inhibit the efflux of R123 and H33342 (Shapiro and Ling, 1997b), providing an explanation based on equal affinities for both H and R-sites. However, according to our results, a different proposal can be suggested. Vinblastine's top-ranked poses were found at H-site and M-site. Unlike etoposide and actinomycin D, the poses at M-site were found to allow the formation of hydrogen-bonds and non-bonded interactions between both halves of P-gp, i.e. cross interactions. The number, type and distribution of these cross interactions between both halves can have an impact on conformational changes following ATP binding, impairing P-gp opening and modulating drug efflux. Another example is verapamil, a molecule ambiguously identified as modulator and substrate. In our previous work (Ferreira et al., 2012), we characterized verapamil as a modulator, in an intermediate level between substrates and inhibitors. In the present study, verapamil top-ranked poses at M- and R-site have the same energy (-7.6 kcal.mol^{-1}), not allowing a direct identification as modulator or substrate. However, the analysis of the interaction pattern between both halves at M-site identified a high capability for cross interaction formation, thus supporting verapamil as a modulator rather than a substrate and corroborating our previous findings.

The above described insights allowed a simpler interpretation of some aspects of P-gp's efflux process. For instance, in the experimental methodologies, the cellular line is selected with caution whereas probe molecules are frequently selected based solely on their efflux ability by P-gp. In addition, it seems that some molecules frequently characterized as substrates (e.g.

vinblastine, paclitaxel, and ritonavir) also have some modulatory ability. The present docking results identified the formation of hydrogen-bond and non-bonded interactions between both halves of P-gp, exclusively at the M-site, as a possible explanation for the modulation effect of some molecules. These findings were the basis for an alternative classification, based on docking binding energies and cross interaction capability at the M-site. This classification, not depending on the use of probes, allows a better clarification of the preferred interaction sites and the molecules ability to compete for substrate-binding sites or to establish cross interactions between both halves (**Figure 5.7**).

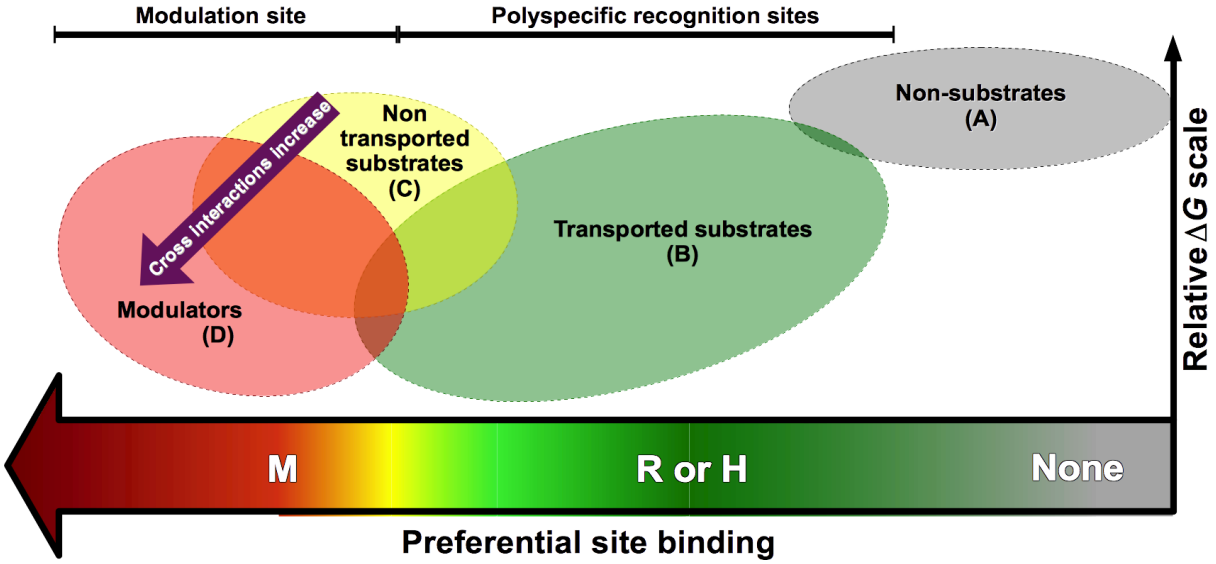

Figure 5.7. Classification scheme for P-gp substrates and modulators (Ferreira et al., 2013b).

The above classification scheme comprises four main categories:

(A) *Non-substrates*, molecules with an estimated binding energy higher than -7.0 kcal.mol^{-1} (not likely to interact with P-gp).

(B) *Transported substrates*, molecules with increased preference (lower ΔG) for substrate-binding H- and R-sites and, if any docking pose at the M-site, displaying weak cross interaction capabilities;

(C) *Non-transported substrates*, molecules with a slightly higher preference for M-site rather than H- and R-sites, yet with weak cross interaction abilities;

(D) *Modulators*, molecules with lower ΔG and increased preference for the M-site, also able to establish moderate to strong cross interaction effects;

The definition of modulator or inhibitor remains unclear throughout the literature. As fully competitive inhibition of P-gp transport is yet to be achieved, the herein developed classification scheme aims to clarify the molecules affinity towards the substrate-binding sites (ability to be effluxed i.e. *transported substrates*), against other molecules that have a weak (*non-transported substrates*) or strong (*modulators*) impact on P-gp efflux due to their cross-interaction capability.

5.2.4. Classification of P-glycoprotein substrates

Using this classification, a thorough analysis of the above databases was performed. For modulators, fourteen molecules (74%, ΔG from -7.9 to -11.2 kcal.mol^{-1}) had the top-ranked pose at the M-site and only five (26%, -7.9 to -11.1 kcal.mol^{-1}) at the substrate-binding sites. This seems to reveal an increased preference of most modulators towards a more hydrophobic drug-binding site (Ferreira et al., 2012). In substrates, the top-ranked docking poses for 20 molecules (63%) were effectively found in substrate-binding sites, 8 (25%) were observed at M-site and 4 (12%) had identical binding energies for M, H or R-sites. Regarding probes group, 5 molecules (50%) had their top-ranked docking pose in R-site, 2 (20%) in M-site and 3 (30%) showed the same binding affinity for SBSs and M-site. Interestingly, for lipids, the binding energies registered were all above -7.0 kcal.mol^{-1} except for cholesterol. Therefore, and according to the classification scheme they cannot be considered substrates for P-gp. For additional information on the molecules in each group, please refer to the published paper (Ferreira et al., 2013b).

5.2.4.1. Non-substrates (A)

To define possible non-substrates, an empirical cut-off value was established at values greater or equal to -7.0 kcal.mol^{-1}. Thus, and from their top-ranked binding poses, diphenhydramine (-7.0 kcal.mol^{-1}), trimethoprim (-6.7 kcal.mol^{-1}) and chloroquine (-6.4 kcal.mol^{-1}) were classified as *non-substrates*. According to several studies, while the first two are unambiguously classified as non-substrates (Chen et al., 2003; Romiti et al., 2002), chloroquine is described to partially reverse MDR without significant inhibition of P-gp photolabeling (Akiyama et al., 1988). Due to the high binding energy found in this study, it's conceivable that chloroquine may act in a different target (Vezmar and Georges, 1998) rather than P-gp.

5.2.4.2. Transported substrates (B)

Nine molecules, including doxorubicin, etoposide and Hoechst 33342, were found to dock exclusively in both SBSs with binding affinities between -10.5 and -9.0 kcal.mol^{-1}. Daunorubicin, progesterone and LDS-751 additionally had at least one pose at the M-site, however with a weak cross interaction capability. Methotrexate (MTX), frequently referred in literature as a non-substrate (Polli et al., 2001; Rautio et al., 2006), docked exclusively at the R-site with a binding energy of -8.6 kcal.mol^{-1}. However, it is known that this molecule has an active carrier-mediated influx that allows the accumulation of MTX within the cell but, in carrier-deficient cells, MTX was shown to be actively effluxed by P-gp (Akiyama et al., 1988; Chen et al., 2003; Romiti et al., 2002).

Cyclosporine A, found exclusively at the H-site, is referred as a potent inhibitor with IC_{50} values ranging from 1.4 to 6.2 μM (Rautio et al., 2006). In this study, cyclosporine A registered a binding energy higher than most substrates (-7.9 kcal.mol^{-1}). However, cyclosporine A is also the molecule with the highest molecular volume (1721 Å^3, calculated with MOE). When considering the earlier calculated volumes for M, R and H-sites, the only site in which cyclosporine A may fit is the H-site, and in our model cyclosporine fully occupies the whole site and part of the entrance gate. For the case of large molecules, and based on our docking findings, P-gp inhibition can also be achieved through a non-specific "bulk" mechanism, by which the "entrance gate" or the internal drug-binding pocket of P-gp becomes blocked. Actinomycin D, in a similar way as cyclosporine, is also a large molecule (1645 Å^3) that is only found at H-site (-11.2 kcal.mol^{-1}) and may also act through this unspecific mechanism.

5.2.4.3. Non-transported substrates (C)

Six molecules were identified, all showing lower binding energies for M-site between -9.1 kcal.mol^{-1} (itraconazole) and -7.9 kcal.mol^{-1} (QZ59-RRR) when compared with *transported substrates* (A). Interestingly, QZ59-RRR (IC_{50} = 4.8 μM) showed a weaker cross interaction effect when compared with QZ59-SSS (IC_{50} = 1.2 μM) (Aller et al., 2009). For mefloquine enantiomers (IC_{50} = 1-10 μM) (Gifford et al., 1998), (–)-mefloquine also had a weak cross interaction effect when compared to (+)-mefloquine, in accordance with at least one experimental study that showed higher activity for the latter (Pham et al., 2000). Interestingly,

no stereospecific effect was observed for flupentixol enantiomers, thus corroborating their similar activity (IC_{50} = 24 and 25 μM for isomers *Z* and *E*, respectively) (Ford et al., 1990).

Although colchicine is considered a P-gp substrate, several experimental studies showed some degree of modulatory activity in many cell lines, with an IC_{50} ranging from 89 μM (Ekins et al., 2002a, 2002b) to 230 μM (Melchior et al., 2012). According to our model, this can be explained due to a weak cross interaction capability displayed by colchicine when interacting at the M-site. Itraconazole, with identical binding energies for H-site and M-site and a moderate cross interaction capability, shows an increased efflux modulation capability (IC_{50}= 1.6 μM) (Kurosawa et al., 1996; Wang et al., 2002). It is interesting to note that for this class, with the exception of QZ59 molecule, the activity increases with log*P*.

5.2.4.4. Modulators (D)

This group comprises 8 molecules with binding affinities ranging from -7.9 to -11.5 kcal.mol^{-1} at the M-site. Laniquidar (EC_{50} of 510 nM) (van Zuylen et al., 2002, 2000), latilagascene D (IC_{50} unknown) (Duarte et al., 2007) and zosuquidar (IC_{50} 60 nM) (Dantzig et al., 1996), are some of the most potent P-gp modulators included in this group. Midazolam (IC_{50} 10 μM, -9.1 kcal.mol^{-1}) (Ekins et al., 2002a, 2002b), QB13 (IC_{50} 1.0 μM, -8 9 kcal.mol^{-1}) (Kondratov et al., 2001) and (S)-methadone (IC_{50} 7.5 μM, -7.9 kcal.mol^{-1}) (Störmer et al., 2001) were also included in this group in despite of their lowest activity. Regarding paclitaxel, its inclusion in this group was due to the lowest binding energy registered in this study (-11.5 kcal.mol^{-1}) and strong cross interaction capability when at the M-site. Although frequently referred as a substrate, several studies identified this molecule as a potential modulator on several cell lines (IC_{50} from 1.2 to 54 μM) (Ekins et al., 2002a; Melchior et al., 2012; Wang et al., 2001). In addition, the inhibition potential of the taxane scaffold was demonstrated through the utilization of a library of noncytotoxic taxane-based reversal agents (tRAs), in which doxorubicin and mitoxantrone efflux were strongly modulated in P-gp, MRP1 and BCRP (Brooks et al., 2003), or through the utilization of simplified "non-natural" taxanes as P-gp inhibitors (IC_{50} of 7.2 μM) (Castagnolo et al., 2010). Amprenavir (IC_{50} of 8.6 μM) (Storch et al., 2007) is also able to establish strong cross interactions between both halves of P-gp, but with a higher binding energy at M-site (-8.9 kcal.mol^{-1}) and similar binding energies for the R-site top-ranked pose (-8.5 kcal.mol^{-1}). Interestingly, the multidrug-reversal activity of several anti-retrovirals was evaluated by docking against the crystallographic murine P-gp structure. The conclusion was

that ritonavir (IC_{50} of 1.29 μM) (Storch et al., 2007) is a more potent P-gp inhibitor than amprenavir (Zha et al., 2013), achieving a lower Glide SP docking score. Herein, ritonavir also obtained lower M-site binding energies, when compared with amprenavir.

5.2.4.5. Intersections between main groups A-D

Twenty-four molecules (35%), however, could not be included in any of the above groups due to small differences in binding energies between all three sites. Although no conclusive identification as substrate or modulator could be achieved, the calculated cross interaction capabilities for poses located at the modulator site poses may provide clues for the modulation capability of these molecules. Our study shows that cross interaction capability tends to increase from *transported substrates* (A) to *non-transported substrates* (B), associated with a progressive shift of the top-ranked binding pose from the SBSs to the M-site (lower ΔG values). From *non-transported substrates* (B) to *modulators* (C), the cross-interaction capability increases inversely with the binding free energy at M-site, thus strengthening the protein-ligand interactions and increasing the modulation ability.

The above data strongly suggests that P-gp efflux modulation can be achieved through i) direct competition with molecules at SBSs, ii) by restraining efflux-related conformational changes at M-site or iii) through both mechanisms. As already seen for ritonavir and amprenavir, a more detailed analysis of the QZ59 isomers and tariquidar docking can further clarify on this issue. While QZ59-RRR only docks at H-site and M-site with a relatively high binding energy (-7.9 and -7.5 kcal.mol^{-1} respectively), QZ59-SSS is found at both SBSs and M-site (ΔG ranging from -8.4 kcal.mol^{-1} at M-site to -8.7 kcal.mol^{-1} at R-site). Although the QZ59-SSS modulation capability could be explained by a high M-site cross interaction capability, a more thorough analysis of QZ59-SSS top-ranked binding pose at R-site revealed a strong interaction with Ser989. The serine oxygen sits at the centre of the macrocycle ring, establishing CH-π interactions with each of the three five-membered rings and allowing hydrogen-bonds between the hydroxyl group and the aromatic nitrogens. In addition, HBs with Gln689 and Gln954 were also found to occur. This suggests that QZ59-SSS was anchored to this point and restrained the access to the R-site. QZ59-RRR, however, was not found in this location and could not impair access to the R-site. A similar conclusion was taken from tariquidar docking results, able to dock all three sites with one of the lowest binding energies within this study (-10.6 kcal.mol^{-1} for M and R-sites and -10.1 kcal.mol^{-1} for H-site). In

addition, it also seems capable of establishing strong cross interactions between both halves at M-site. Therefore, and based on the lowest IC_{50} experimental value (20-145 nM) (Mistry et al., 2001; Sterz et al., 2009), its plausible that tariquidar can impair P-gp efflux through the blockage of both translocation pathways (direct competition) but also by P-gp conformational alterations due to ATP binding and hydrolysis. Quite recently, a study by Loo and Clarke corroborated these findings and described tariquidar binding site within the transmembrane (TM) segments, at the interface between the two P-gp halves, in a very good agreement with the herein reported results (Tip W. Loo and Clarke, 2015).

5.2.4.6. Probes

Molecules frequently used as efflux probes were also tested, namely digoxin, R123 and calcein-AM. For digoxin (-10.9 kcal.mol^{-1}) and R123 (-9.2 kcal.mol^{-1}), the calculated binding energies are identical for M- and R-sites, being the main difference the cross-interaction capability, stronger in digoxin than R123. For calcein-AM, the ΔG of M- and H-sites is also similar (-8.0 and -7.9 kcal.mol^{-1}), but a strong cross interaction capability gives to this molecule some degree of efflux modulation capability. As these molecules are used to determine P-gp efflux, it was expected that they should be found with lower binding energies at substrate-binding sites. However, several experimental studies demonstrated some degree of efflux modulation by digoxin or its metabolites (Gozalpour et al., 2013; Melchior et al., 2012) or competition between digoxin and verapamil for drug-binding sites (Funakoshi et al., 2003; Rebbeor and Senior, 1998). For rhodamine derivatives, an inhibitory potential was also demonstrated (Gannon et al., 2009). Hence, we additionally docked the most common digoxin metabolites (digoxigenin, bis- and mono-digitoxoside), rhodamine derivatives with inhibitory potency and the hydrolysed metabolite from calcein-AM (Tenopoulou et al., 2007) in order to clarify the effect of these molecules on P-gp.

The results obtained were quite surprising. For digoxin metabolites, while digoxigenin was still found at both sites, the bis- and mono-digitoxosides docked exclusively at the R-site with binding energies of -11.5 and -10.2 kcal.mol^{-1} respectively (*transported substrates*— class B). In addition, the cross interaction ability of digoxigenin at M-site it is lower than digoxin, in accordance with previoulsy published results (Melchior et al., 2012). For calcein, the top-ranked binding pose was found not in H-site as Calcein-AM but at R-site with -8.5 kcal.mol^{-1}. The best ranked calcein docking pose found at M-site also displayed a reduced cross interaction

ability regarding calcein-AM, thus being a worse modulator. As this molecule is ionized at physiological pH, lipid partitioning and the access to P-gp's internal DBP becomes severely impaired. However, it is not to be excluded some degree of efflux by P-gp at high concentrations. For rhodamine, we found that the substitution of the heteroatom in the xanthylium core by sulphur (1-S) decreases the binding energy at R-site in a larger extent than M-site (1.0 against 0.2 kcal.mol^{-1}, respectively) and increases its cross interaction capability (modulator, class D), in a very good agreement with previous results (Gannon et al., 2009). When two additional rhodamine derivatives were docked (2-S and 31-S), the binding energies were lower than R123 and the cross-interaction capability at the M-site further increased. These findings are of great importance since they highlight the necessity for an adequate selection of probe substrates for P-gp efflux assays and uphold many interesting questions about the influence of probe metabolites in P-gp efflux assays.

5.2.4.7. Lipids

Several lipid molecules were also tested in order to assess the ability of P-gp as a lipid flippase suggested in several studies (Eckford and Sharom, 2005; Higgins and Gottesman, 1992; Sharom et al., 2005). However, none of the tested molecules could be classified as a P-gp substrate, all with binding energies higher than -7.0 kcal.mol^{-1}. Only cholesterol displayed binding energies like R123 (-9.5 kcal.mol^{-1} for R-site), therefore identified as a substrate (Garrigues et al., 2002).

5.3. Studies on drug permeation into the drug-binding pocket

Previous P-gp working models suggest that the presence of a membrane is mandatory for efflux to occur (Ferreira et al., 2015a), and although a different model have been proposed in which the membrane would be unnecessary (Altenberg et al., 1994), additional studies proved that only in the presence of a membrane P-gp retains its ATPase function and the ability to transport drugs (Urbatsch and Senior, 1995). Furthermore, it was demonstrated that P-gp ATPase function is intimately dependent on membrane composition, with different lipid types and/or membrane components having a strong influence on the ATP binding, hydrolysis, and drug efflux rates (Romsicki and Sharom, 1999, 1998). While P-gp seems to transport drugs that mainly build-up in the membrane (Siarheyeva et al., 2006) according to their octanol-water

partition coefficients (Eytan et al., 1996; Eytan and Kuchel, 1999), other studies demonstrated that the efflux only occurs from the cytoplasmic leaflet through two distinct translocation pathways, identified for both H and R-sites and presumably located in a water-filled internal cavity located within the transmembrane domains (Parveen et al., 2011).

Interestingly, the internal cavity was accessible from both the cytoplasm or lipid bilayer through two "entrance gates" located between transmembrane helices 4/6 and 10/12, a characteristic that was maintained in all the P-gp crystallographic structures published so far (Esser et al., 2017; Ferreira et al., 2015b; Verhalen et al., 2017). However, since the peptide sequence linking the *N*-terminal and the *C*-terminal domains (linker sequence) was missing in all crystallographic structures, the direct accessibility of the internal drug-binding pocket from the cytoplasm (Altenberg et al., 1994) was still not able to be confirmed experimentally through X-ray crystallography.

According to our previous results (Ferreira et al., 2013b, 2012), this access is only possible from the cytoplasmic leaflet of the membrane and through the only fully open "entrance gate", located between TMH 10/12. Therefore, MD simulations were used to study the thermodynamic process of drug permeation from bulk water to the internal drug-binding pocket of P-gp. To that matter, steered MD simulations were performed in which a substrate (colchicine) or a modulator (tariquidar) (**Figure 5.8**) was pulled from the entrance gate to the hydrophobic core of the lipid bilayer or into the P-gp drug-binding pocket.

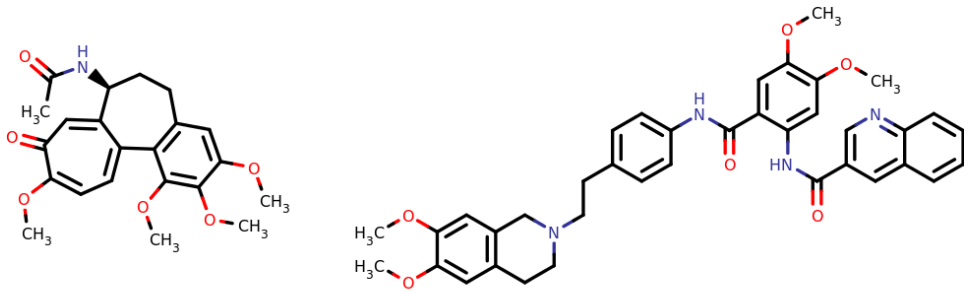

Figure 5.8. Chemical structures of colchicine (substrate) and tariquidar (modulator) (Ferreira et al., 2015c).

Colchicine and tariquidar molecules (neutral forms) were inserted at the entrance gate as previously described for vinblastine (Ferreira et al., 2012). In each case, both molecules were pulled away from the entrance gate along the axes parallel to the bilayer over 10 ns (pocket) or 15 ns (bilayer), using an harmonic potential with a spring constant of 1000 kJ.mol^{-1}.nm^{-2} and a

pull rate of 0.15 nm.ns^{-1}. These trajectories were the starting points for defining a reaction coordinate used in the umbrella sampling technique, with fifty-two or fifty-eight umbrella windows and a mean width of 0.7 Å (total distance: colchicine– 3.9 nm; tariquidar– 4.2 nm). In each window, 20 ns of MD was performed, for a total umbrella sampling simulation over 2 μs. Analysis of results was performed through the weighted histogram analysis method (WHAM) (Hub et al., 2010). The free-energy profiles obtained show that both colchicine and tariquidar enter the internal drug-binding pocket through a spontaneous process (**Figure 5.9**).

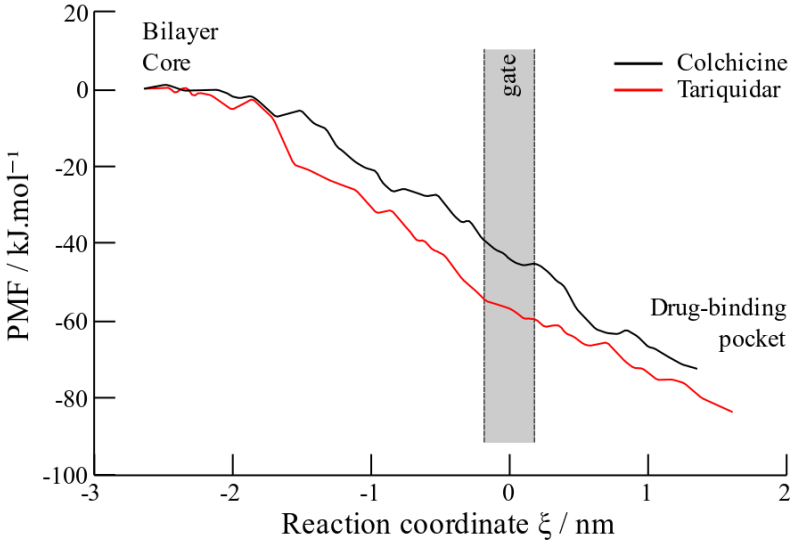

Figure 5.9. Potential of mean force (PMF) energetic profile for colchicine and tariquidar translocation from the membrane into the drug binding pocket. The grey shading represents the average radius of the TM helices at the entrance gate ($\xi = 0$) (Ferreira et al., 2015c).

When analyzing the reaction coordinate, it is possible to identify that, at distances far from the protein ($\xi > -2$ nm), no change in free energy occurs and it can be considered that at such distances i) the bulk lipid hydrophobic environment is the main influence on the behavior of the molecules and ii) the presence of the P-gp is not felt. Then, the free energy decreases steadily with the colchicine slope remaining unchanged until it reaches the entrance gate. However, the slope of the tariquidar PMF is steeper at the beginning ($-2 < \xi < -1.5$ nm), having the same slope as for colchicine afterwards. The initial steep decrease on tariquidar slope was observed to be due to a conformational change of tariquidar where the quinoline-3-carboxamide moiety shifted from a parallel to a perpendicular orientation regarding the POPC acyl chains, inducing a more packed conformation and having a positive impact on the motion of tariquidar between the hydrophobic lipid chains (colchicine is unable of this transition between an

elongated to a compact conformation; c.f. **Figure 5.8**). Interestingly, the stabilization energy due to the conformational change of tariquidar gained at this step is roughly maintained along the reaction coordinate.

With both molecules already located at the entrance gate (grey shading), the energetic difference between them is $\Delta\Delta G$ = 12.8 kJ.mol^{-1} (-44.3 vs. -57.1 kJ.mol^{-1} for colchicine and tariquidar respectively). Immediately after crossing the gate, colchicine reorientates, allowing the formation of transient hydrogen-bonds with Ser340 and Gln343 (TMH6) and favoring a better interaction between colchicine and P-gp. The crossing of the gate by the molecules could be foreseen as a bottleneck in the pathway to the DBP because this is a location acting as an interface between the lipid environment and the protein/water environment. Interestingly, the data show no activation energy barrier for any of the molecules when crossing the gate. At the end, the calculated free energies for drug permeation from the bilayer core to the drug-binding pocket were ΔG = -72.4 kJ.mol^{-1} for colchicine and ΔG = -79.0 kJ.mol^{-1} for tariquidar, with a $\Delta\Delta G$ = 6.6 kJ.mol^{-1} between both molecules.

It was already determined that P-gp reorganizes the surrounding lipid environment up to a 15-20 nm radius around the protein (Oleinikov et al., 2006), inducing a more ordered state that may promote drug efflux, while others showed that P-gp has a large destabilizing effect on the surrounding lipid environment, preventing up to 375 ± 197 lipids to undergo phase transition (Romsicki and Sharom, 1997). The lower limit of this lipid estimate is close to the size of our MD box (6 nm radius around the protein). However, the lipids are expected to shield the influence of P-gp on drug-like molecules inside the membrane. From **Figure 5.9**, the real impact on the free energy due to the P-gp starts at about 4.25 nm. This lipid organization will have an impact on the molecules conformations when located at the hydrophobic membrane core. As observed for tariquidar, changes in the orientation of some moieties induce more packed conformations that facilitate drug translocation to the P-gp drug-binding pocket. These results show a spontaneous route for drug entrance from the hydrophobic membrane core (hydrophobic tail region of the cytoplasmic leaflet) into the internal drug-binding pocket, through the "entrance gate" located between TM helices 10 and 12 and in agreement with both *flippase* and *vacuum cleaner* models.

The herein reported results can be additionally linked to those obtained by Oliveira *et al.* for Sav1866 and McCormick *et al.* for human P-gp homology models. While in the first

study it was shown that doxorubicin interaction energy profile is downhill inside Sav1866 drug-binding pocket to the extracellular side along the transmembrane pore (Oliveira et al., 2011), in the latter a vectorial movement of the drug along the *z* axes, dominated by non-polar and aromatic interactions, from the inside surface of the membrane to the outside surface of the membrane was observed for daunorubicin, verapamil and tariquidar (McCormick et al., 2015). Together, these results allow us to conclude that P-glycoprotein can indeed extract drugs from the cytoplasmic leaflet of the membrane through a gate and transporting them to outside of the cell. However, it is worth noticing that, for the last step to occur (molecule leaving the DBP), ATP hydrolysis is required to promote conformational changes (Verhalen et al., 2017) that shifts the drug-binding sites from high-affinity to low-affinity states (Callaghan et al., 2012) promoting drug release from the drug-binding sites into the extracellular medium.

During the translocation of the molecules from the hydrophobic membrane core into the DBP, differences regarding colchicine and tariquidar interaction with P-gp were also observed. Colchicine seems to interact preferentially with polar residues, namely Asn835 (TMH9) and Ser988/Tyr994 (TMH12) when at the entrance gate and with Ser340/Gln343 (TMH6) and Ala991/Tyr994 (TMH12) inside the pocket. However, while still in the hydrophobic membrane core, tariquidar interacts with Phe693 and Trp694 (TMH7), aromatic residues that are in direct contact with the phospholipids. Contacts with Asn835, Asn838 (TMH9) and Tyr994 (TMH12) are observable as tariquidar approaches the "entrance gate", followed by contacts with Val984, Val987, Ser988, Ala991 and Pro992 (TMH12) while entering the pocket. Inside the DBP, tariquidar interacts with all residue types (hydrophobic, polar and aromatic). Interestingly, tariquidar but not colchicine also interacts with the charged linker residue Arg676, which may also account for the lower ΔG energies registered inside the pocket.

Furthermore, and to provide additional evidences that would characterize the drug permeation to the DBP for these two molecules, the energetic profile for drug permeation from the bulk water into the hydrophobic membrane core (in the absence of P-gp) was also calculated. **Figure 5.10** shows that colchicine and tariquidar permeation into the hydrophobic membrane core is energetically favorable. For tariquidar, the protonation of its tertiary nitrogen (p*Ka* 8.2) favors a more elongated structure that allows the quinoline-3-carboxamide moiety to enter the membrane while the protonated tetrahydro-isoquinoline moiety remains near the phosphate headgroups. Then, phosphate-assisted deprotonation of the tertiary nitrogen occurs (Sandén et al., 2010) to allow neutral tariquidar to enter the membrane.

At the membrane hydrophobic core, the free energy minima for both colchicine and tariquidar is found to be located below the phosphate headgroups (colchicine) or between the lipid acyl chains of the cytoplasmic leaflet (tariquidar). As the "entrance gate" is also found to open to the cytoplasmic leaflet (Oleinikov et al., 2006), this allows a more direct access to the drug-binding pocket for both molecules.

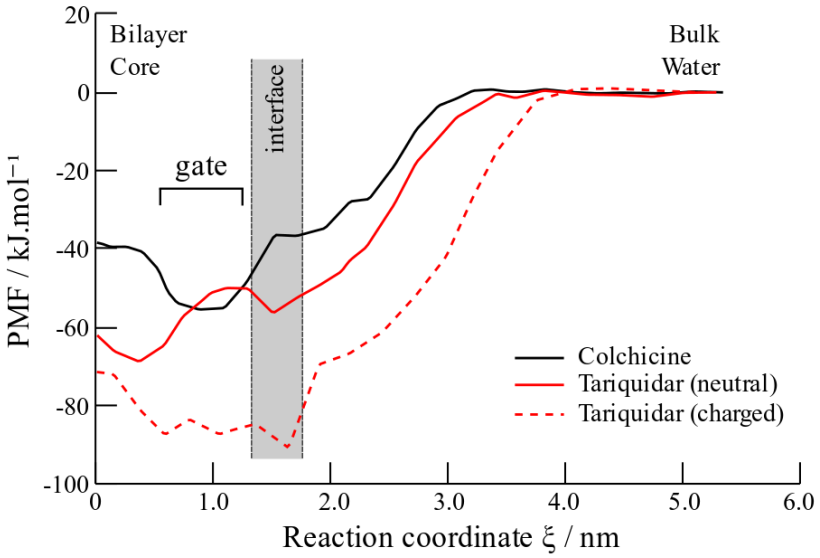

Figure 5.10. Potential of mean force (PMF) energetic profile for colchicine and tariquidar permeation from bulk water into the hydrophobic membrane core in the absence of P-gp. The grey shading represents an estimation of the headgroup thickness in the POPC membrane (Ferreira et al., 2015c).

At approximately 2 nm from the entrance gate (**Figure 5.9**, ξ = -2 nm) both molecules are driven to approach P-gp through a favorable downhill energetic pathway while entering the internal drug-binding pocket. Inside, molecules interact in one (or more) of three identified drug-binding sites (Aller et al., 2009; Ferreira et al., 2013b; Shapiro and Ling, 1997b), inducing conformational changes that favors ATP binding and hydrolysis (Ambudkar et al., 2006; Sauna and Ambudkar, 2007; Sharom, 1997; Verhalen et al., 2017). Thus, while shifting from the inward- to the outward-facing structure, the affinity of the drug-binding sites decreases (Gutmann et al., 2010) and drugs are released to the extracellular medium, following an overall downhill energetic pathway as shown by other groups (McCormick et al., 2015; Oliveira et al., 2011).

5.4. Role of drug adsorption at the surface of P-glycoprotein and at the membrane interface

To be able to reach the drug-binding sites, any molecule must first diffuse into the lipid bilayer to gain access to one of the 'entrance' gates located between TM helices 4/6 or 10/12 (Aller et al., 2009; Ferreira et al., 2015c, 2012). Recently, a physical model was proposed by which mechanical interactions between drugs and lipid membranes could directly affect efflux (Rauch et al., 2013). More specifically, changes on membranes' biophysical properties due to drug adsorption are expected to have an impact on P-gp dependent efflux through a non-linear effect. While drug permeation towards the lipid bilayer initiates with its adsorption at the water/lipid interface, followed by drug diffusion into the membranes' inner leaflet, mechanical changes in the membrane due to drug adsorption/permeation may also have an impact of some degree on P-gp efflux. Moreover, it is also expected to occur drug adsorption to the cytoplasmic nucleotide-binding domains, and such phenomenon might also have an impact in the ATP-driven rigid-body motions that drive conformational changes towards substrate efflux.

Although the previous study by Rauch *et al.* only considered drug-membrane interactions, drug-protein interactions must also occur as a step-by-step addition dependent on law of mass action, in accordance with the thermodynamics of adsorption of small molecules by proteins (Harrold and Pethica, 1958; Kuznetsov et al., 1975). Thus, as the NBDs account for almost all P-gp's solvent accessible area, it can be expected that this stepwise adsorption could have some degree of impact on the rigid-body motions that initiate efflux, depending on the number of adsorbed molecules and their physicochemical properties.

To better investigate these phenomena, a series of MD runs comprising twelve small molecules are described, eleven of which are frequently characterized as *non-substrates* (n = 3), *substrates* (n = 5) and *modulators* (n = 3). Adenosine triphosphate (ATP) was also evaluated as the natural substrate for the ATP-binding site, located at the canonical dimer interface. The main objectives were, for the first time, to evaluate the free energies of adsorption for molecules of the different groups by identifying the amino acid residues more frequently involved in drug adsorption and to identify mechanical alterations in the bilayers' physical properties derived from drug adsorption at the lipid-water interface.

5.4.1. Free energy calculations

The free energy of adsorption for several classes of molecules (**Figure 5.11**) towards the protein surface and lipid-water interface was assessed. From **Figure 5.12** it is possible to observe that, in all classes, molecule adsorption is an energetically favorable process. To this matter, the lowest energies were found for ATP in both protein (-9.6 ± 0.6 kJ.mol^{-1}) and membrane (-12.4 ± 1.6 kJ.mol^{-1}) interfaces. However, this can be explained by its negative charge (net charge of -4) that promotes electrostatic interactions with positively charged lysines, arginines or choline moieties, as in POPC. However, a statistically significant difference could be found between ATP and all classes but *modulators* ($p < 0.05$).

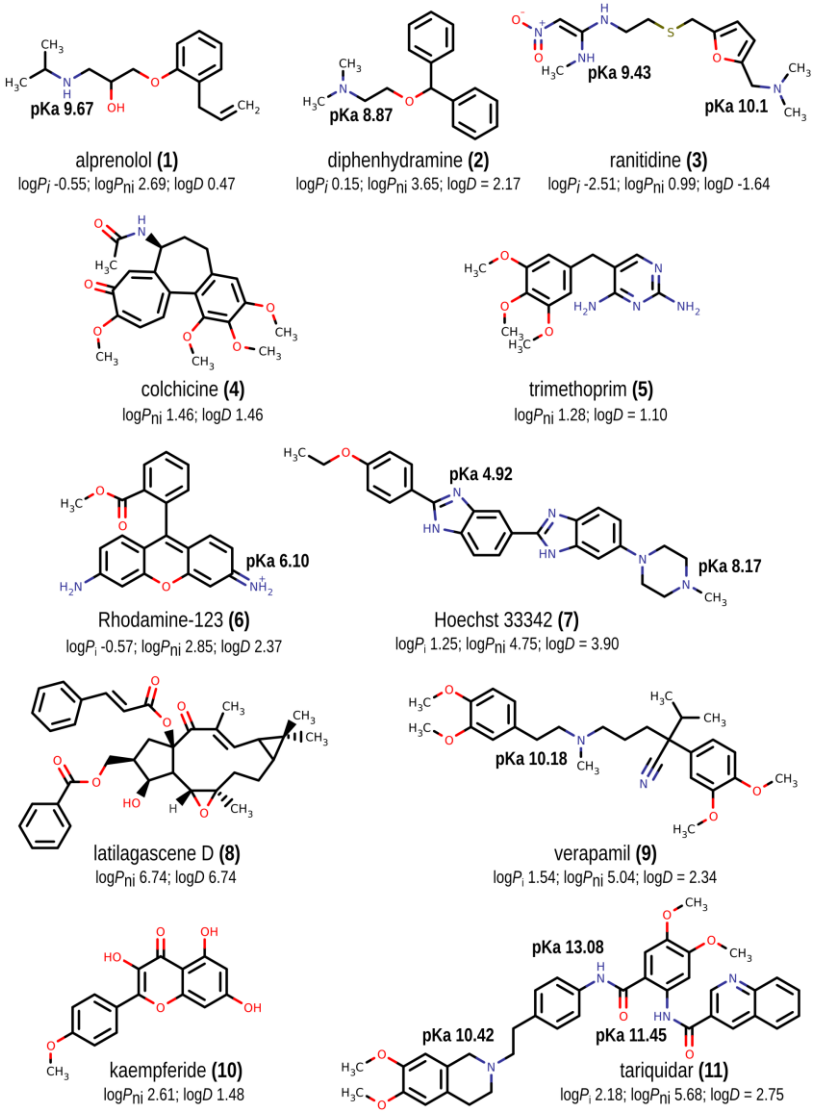

Figure 5.11. Chemical structures of the molecules used in the molecular dynamics simulations, with pK_a of the ionizable groups, log*P* and log*D* (Ferreira et al., 2015d).

Interestingly, *modulators* free energies of adsorption were found to be the lowest among the evaluated classes, with ΔG_{ads} ranging from -8.8 ± 0.8 kJ.mol^{-1} up to -9.9 ± 0.5 kJ.mol^{-1} and showing a statistically significant difference from *substrates* and *non-substrates* for protein adsorption ($p < 0.05$). For *substrates* and *non-substrates*, the free energies of binding to each interface were higher than *modulators* but still favourable, as shown in **Figure 5.12** i.e. the for *substrates* were of -7.1 ± 0.4 kJ.mol^{-1} and -8.9 ± 0.8 kJ.mol^{-1} for the protein and lipid interfaces, whereas for *non-substrates* the calculated energies for each interface were -6.0 ± 1.0 and -9.1 ± 2.7 kJ.mol^{-1} respectively.

The adsorption energies towards the lipid-water interface are always more favorable than the ones reported for protein-water interface, suggesting that the adsorption to the lipid bilayer is the primary mode of action for these molecules, in comparison to the adsorption towards P-gp. Moreover, the energetic difference between both interfaces seem to increase from *modulators* (~1.1 kJ.mol^{-1}) to *substrates* (~1.8 kJ.mol^{-1}) and *non-substrates* (~3.1 kJ.mol^{-1}). It is also worth noticing that drug adsorption to both structures showed different behaviors. When considering molecule adsorption to the protein-water interface, a higher number of molecules are found for both substrates and modulators when compared with *non-substrates*. Regarding the lipid interface, a close inspection of the *z* coordinate evolution over time, representing the molecules' path, showed that in few cases (~10%) a transient adsorption of the molecule to the lipid bilayer first occurs before it becomes fully adsorbed.

Oppositely, the molecules' adsorption to the protein occurs almost immediately after the first contact. In this study, smaller molecules as trimethoprim, diphenhydramine or alprenolol were found to be inserted between the lipid headgroups. However, only kaempferide and diphenhydramine showed full permeation into the inner leaflet of the membrane, with kaempferide additionally showing spontaneous flip-flop movement between both membrane leaflets, in agreement with experimental evidences for related molecules (Rooney et al., 1979; Saija et al., 1995). In addition, it is also known that a wide range of flavonoids bind to vicinal ATP- and steroid-binding sites (Conseil et al., 1998), modulating efflux by impairing ATP binding. Thus, the high adsorption rates observed for kaempferide may be a possible explanation for its modulating activity, not only at the ATP-binding site but also by changing the biophysical properties of membranes.

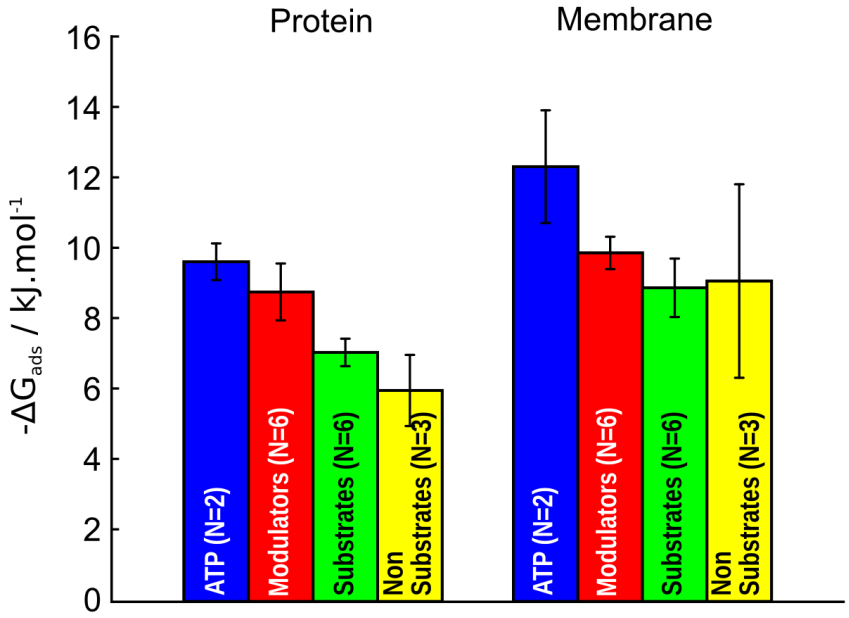

Figure 5.12. Free energies of adsorption (mean ± SE) for the different classes at protein-water or membrane-water interface. Statistical significance was determined by comparing the different classes with multiple *t*-tests ($p < 0.05$) (Ferreira et al., 2015d).

Since several experimental studies clearly demonstrated that molecules may interact with P-gp and induce ATPase activity without significant efflux (Doan et al., 2002; Polli et al., 2001; Rautio et al., 2006), this led us to suppose that a different mechanism, unrelated with substrate competition or passive permeation rates, may also be involved in efflux modulation. In this mechanism, drug adsorption at the surface of NBDs may be able to disturb the mass/charge balance between both domains, affecting the normal motion patterns that drive conformational changes during the efflux cycle. This agrees with the observations by Litman *et al.* showing that the intrinsic affinity of some drugs for the cytoplasmic P-gp surface is four-fold higher than at the other side of the membrane (Litman et al., 2003). Moreover, Äänismaa *et al.* also concluded that, at sufficiently high drug concentrations, the P-gp ATPase works in an enthalpy-driven manner probably due to the loss of residual motion of the transporter (Äänismaa et al., 2008).

As suggested by the calculated adsorption energies, NBDs may also participate in the efflux process by increasing the concentration in the surrounding environment, displacing molecules from the bulk water environment into the water shell next to their surface, which may indirectly enhance membrane permeation. In addition, drug adsorption may also affect the normal motion patterns. This effect may respond to changes in the surrounding environment,

with the magnitude of such changes intimately related with the physicochemical properties of the adsorbed molecules.

5.4.2. Protein interaction profile

We thoroughly investigated all interactions between individual molecules that effectively adsorbed to the protein (**Table 5.5**) or to the lipid bilayer.

Table 5.5. Contacts and hydrogen-bond statistics for each class of molecules.

	Interaction type						
	Contacts [a]				**Hydrogen-bonds** [b]		
Classes	‹N_{NB}›	ARO (%)	HYD (%)	POL (%)	‹N_{HB}›	‹τ› (ps)	ΔG_{HB} (kJ.mol^{-1})
non-substrates	7.8	13.7	23.4	62.8	0.47	1035	-20.9
substrates	8.6	10.8	33.6	55.6	0.85	1631	-22.4
modulators	16.6[c]	9.7	26.8	63.5	1.09	1481	-22.3
ATP	11.1	12.3	16.3	71.4	2.82[d]	2351[e]	-23.9[d]

[a], ‹N_{NB}›, average number of non-bonded interactions; ARO, interaction with aromatic residues; HYD, interaction with hydrophobic residues; POL, interaction with polar residues; [b], ‹N_{HB}›, average number of hydrogen-bonds per time frame; ‹τ›, mean hydrogen bond lifetime; ΔG_{HB}, HB formation energy in kJ.mol^{-1}. Statistical significance was determined by comparing classes with multiple *t*-tests ([c], $p < 0.05$ with *non-substrates* and *substrates*; [d], $p < 0.05$ with *non-substrates*; [e], $p < 0.05$ with all classes).

While for membrane adsorption electrostatic interactions play a major role due to the charged phosphate and choline moieties at its interface, protein adsorption seems to be not only dependent on charged residues (e.g. glutamate, aspartate, lysine, arginine) residues but also on hydrogen-bond donor residues such as glutamine and asparagine. Interestingly, all classes seem to preferentially interact with residues with additional methylene units (-CH_2-) like glutamate and glutamine (against aspartate and asparagine) or even longer sidechains as in arginine and lysine (with two and three additional –CH_2- units respectively). In addition, from **Table 5.5** a sustainable increase in the total number of interactions occurs from *non-substrates* toward *modulators.*

Regarding protein contacts, *substrates* interaction pattern is higher for hydrophobic residues and lower for polar residues, when compared with the other classes. Oppositely, *modulators* interaction with aromatic residues is always lower when compared with the remaining classes, leading us to assume that polar interactions have a greater importance for

the molecules included in this class. As expected, ATP interacts mainly through electrostatic and/or hydrogen bond interactions and higher contact frequencies with polar residues were effectively observed throughout the simulation time.

For hydrogen bond (HB) capability, the mean number of hydrogen-bonds per time frame also increased from *non-substrates* (0.47) to *modulators* (1.09) and while *non-substrates* have the highest HB formation energies (ΔG_{HB}, -20.9 kJ.mol^{-1}), all the remaining classes have similar energies around -22.3 ± 0.1 kJ.mol^{-1}. However, higher hydrogen bond lifetimes are registered for *substrates* (1631 ps) when compared with *modulators* (1481 ps) and even higher than for *non-substrates* (1035 ps). Finally, ATP registered the highest number of HB per time frame (2.82) and HB lifetimes (2351 ps) and the lowest ΔG_{HB} values (-23.9 kJ.mol^{-1}).

The electrostatic contribution to drug adsorption was also assessed by comparing the relative interaction free energies between neutral and charged molecules with P-gp, during the last 10 ns of each simulation. In this case, since P-glycoprotein is a transmembrane protein, a correction to the polar solvation energy was corrected by applying an implicit membrane correction with ion-accessibility and dielectric maps incorporating the membrane environment. Thus, by setting the dielectric slab constant to 2.0, the corrected polar solvation energies can be used as input with *g_mmpbsa* tool available for GROMACS (Kumari et al., 2014).

From the obtained energies by the above method, two distinct behaviours were observed. While *non-substrates* interaction energies were similar within the group, for both *substrates* and *modulators* the interaction energy decreased almost linearly with increasing molecular size, in agreement other published reports.(Abad-Zapatero, 2007; García-Sosa et al., 2010) Thus, an efficiency index (EI) was calculated by dividing each interaction energy by the molecules' molecular weight (MW) to assess possible differences between charged and neutral molecules. From **Table 5.6**, it is possible to conclude that charged molecules have higher efficiency indexes when compared with neutral ones, implying that electrostatic interactions, together with hydrogen bonding, are important for drug adsorption.

Based on the findings described above, as small molecules' adsorption to the protein surface seem to be highly influenced by electrostatics and hydrogen bonding, these interactions can be significant in defining the strength of the adsorption by increasing molecules' residence time at the protein surface and contributing for a greater stabilization of the ligand-protein complex.

Table 5.6. Comparison between neutral and charged molecules on protein adsorption

Efficiency Index (EI) *				
non-substrates (charged)	*substrates (neutral)*	*substrates (charged)*	*modulators (neutral)*	*modulators (charged)*
0.22 ± 0.06 [b]	0.07 ± 0.02 [a]	0.17 ± 0.04	0.06 ± 0.02 [a]	0.15 ± 0.03

* Statistical significance was determined with *t*-Tests ([a], $p < 0.05$ between charged and neutral molecules within the same class; [b], $p < 0.05$ with all groups except *charged substrates*).

Moreover, as many molecules are found to be simultaneously adsorbed to the protein surface, changes on the mass/charge relation between nucleotide-binding domains (NBDs) may be susceptible to perturb the proteins residual motion patterns, as previously suggested (Äänismaa et al., 2008). Additionally, by generating spatial distribution maps, adsorption preferences on specific regions around NBDs were also evaluated for all classes (**Figure 5.13**).

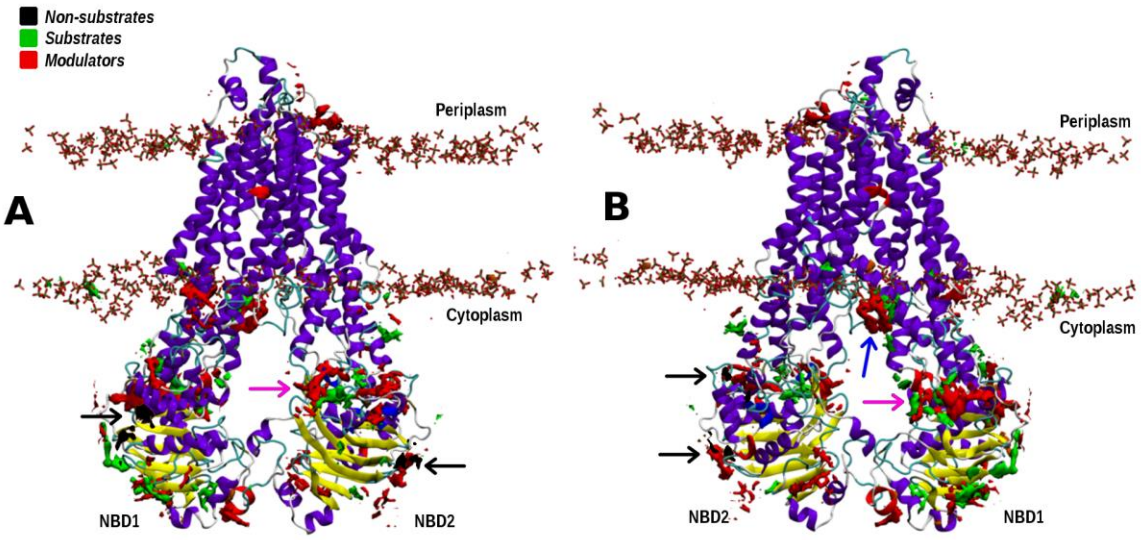

Figure 5.13. Spatial distribution maps for the different classes. A. Front view; B, Back view. Isosurfaces represent a probability greater than 50% of molecules to be in that region. Phosphate groups are also represented to assess lipid-water interface boundaries (Ferreira et al., 2015d).

It is worth noticing that while *non-substrates* are characterized by weak population densities around the protein, most of which located on coil motifs next to α-helix or β-sheet motifs (black arrows), all other classes show higher densities next to both NBDs, with *substrates* achieving higher densities next to β-sheets and modulators around α-helices and coils. Interestingly, both *substrates* and *modulators* show increased densities around both

TMD-NBD interfaces (pink arrows), next to intracellular helices (ICHs) thought to mediate the transmission to the transmembrane domains of conformational changes triggered by ATP binding/hydrolysis. Moreover, higher densities were also found for *substrates* and *modulators* at the lipid-water interface (blue arrow), next to one of the hypothetical 'entrance gate' located between TMHs 4 and 6.

From the above spatial distribution maps, the adsorption of molecules to these specific locations is expected to disrupt the transmission of normal motions, induced by ATP binding, to the transmembrane domains (TMD-NBD interfaces) or may promote drug permeation into the membrane (when at the lipid-water interface next to 'entrance gates'). To our knowledge, other studies have also identified the TMD-NBD interface as a possible interaction region for substrates (Kim et al., 2010; Pajeva et al., 2013; Subramanian, 2015). In addition, these results are also in agreement with recently published studies not only in P-gp (Ferreira et al., 2017b; Subramanian et al., 2015) but also in other ABC transporters (Johnson and Chen, 2017; Liu et al., 2017), thus providing new perspectives on using the TMD-NBD interface as an interesting drugable domain for the development of new specific efflux modulators (Ferreira et al., 2017b).

5.4.3. Internal cavity volumes

In a previous paper we also demonstrated that a better helix repacking due to membrane and linker insertion were important for stabilizing the volume of the internal drug-binding pocket around 4000 Å^3 (Ferreira et al., 2012). As the above results indicate that drug adsorption occurs in specific locations that may affect residual motion patterns, to evaluate the impact that drug adsorption may have on helix repacking of the transmembrane domains, we monitored the internal cavity volume throughout the simulation time (**Figure 5.14**) to allow a better comparison of the volume variations associated to each class.

In the presence of ATP, the volume distribution is almost identical to the values registered for the *apo* structure, supporting the fact that ATP adsorption either to the membrane or to the protein surface was not able to induce significant alterations in the TMH packing. However, with *non-substrates* the volume distribution is shifted towards lower volumes (2100 - 4000 Å^3 vs. 2900 – 5600 A^3 in *apo* system). In this case, as the number of molecules adsorbed to the lipid-water interface is higher than to the protein-water interface, it seems that changes in the volume of the internal drug-binding pocket are a response to modifications in membrane

properties rather than protein motions. Indeed, visual inspection of the systems verified that the large majority of the adsorbed molecules were located below the choline moiety, next to the phosphate groups.

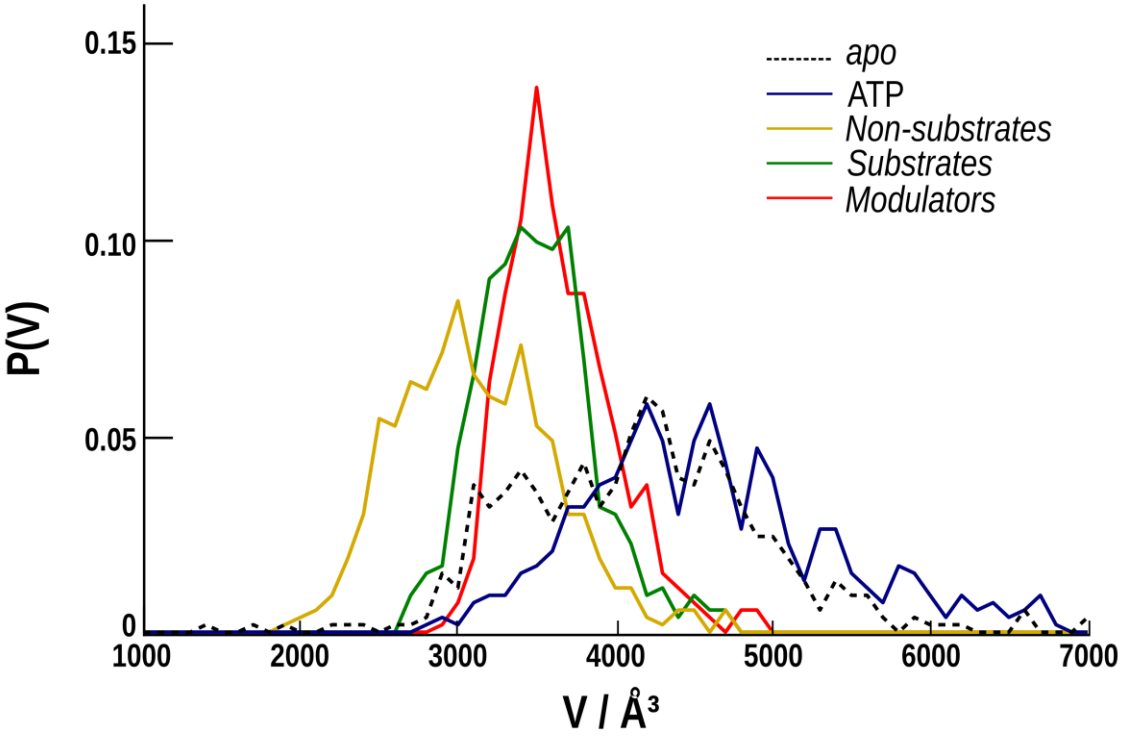

Figure 5.14. Normalized internal cavity volume distributions for the apo structure and the different classes (Ferreira et al., 2015d).

Similarly, *substrates* and *modulators* also shift down volumes regarding the *apo* system, although in a lesser extent. However, they both narrow down the calculated volume distributions to values with maximum probabilities around 3400 - 3500 Å³ (2700 - 4700 Å³ and 2900 - 4900 Å³ interval, respectively). Herein, data suggests that *substrates* and *modulators* induce a more efficient TMD reorientation/repacking, distinct from the one induced by *non-substrates*, that can be due to the previously reported interactions with the ICHs at the TMD-NBD interface and enhanced communication between both domains. As already suggested (Ferreira et al., 2017b, 2015b), these data support the hypothesis that targeting the TMD-NBD interface with small molecules able to decouple TMD-NBD motions would affect the coordinated NBD-TMD motions the same way as mutations in the ICH do (Kwan and Gros, 1998; Loo and Clarke, 2013; Loo and Clarke, 2015).

5.4.4. Membrane biophysics

Since Rauch *et al.* suggested that mechanical alterations of the lipid bilayer may have a direct impact on P-gp efflux through a non-linear effect, we also aimed for the evaluation on the effects of drug adsorption on the biophysical properties of the membrane. No statistically relevant changes were found for standard properties like lateral diffusion, acyl chain order parameters and membrane densities (assessed by *g_msd*, *g_order* and *g_density* tools respectively). Hence, as drug adsorption to membranes are described to induce alterations in the area per lipid (A_L) and membrane thickness (D_{HH}), these properties were additionally calculated for each adsorbed molecule and the results are summarized in **Figure 5.15**.

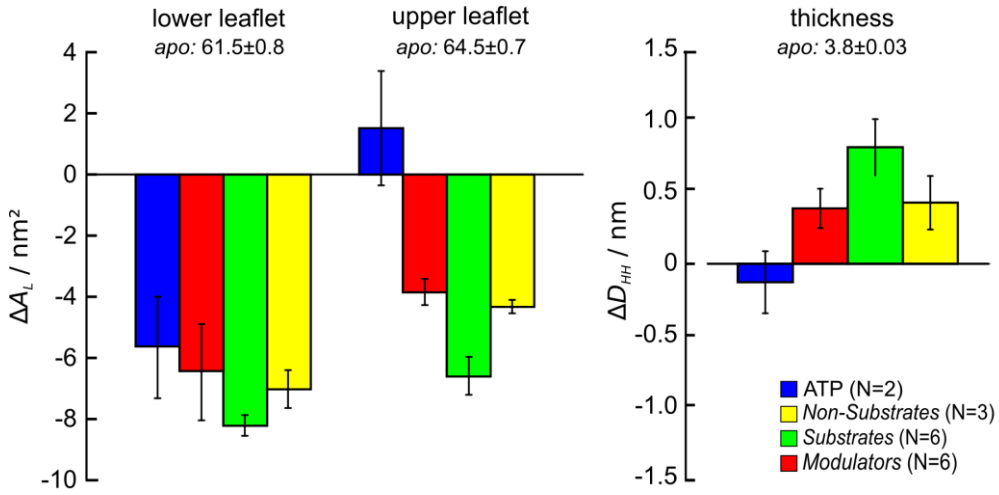

Figure 5.15. Area per lipid ($\Delta A_L \pm$ SE) and thickness ($\Delta D_{HH} \pm$ SE) variations for each class (Ferreira et al., 2015d).

We found that, although no correlation was found between changes in the total area per lipid and the number of adsorbed molecules, adsorbed molecules induce a decrease in A_L values in a 3 nm radius around its geometrical center. To this matter, all classes decreased A_L values similarly in both the inner (in a greater extent) and outer leaflets, with minimum values being registered for *substrates* (53.2 Å² and 54.8 Å² for the lower and upper leaflets respectively). As neither charge nor molecular weight seem to affect drug adsorption to the lipid-water interface, the data corroborate the fact by which drug adsorption to membranes is unspecific. However, the decrease of A_L together with a slight increase in membrane thickness suggests that lipids become more tightly packed, similarly to what is observed in lipid-ordered domains where P-gp is found to be highly active (Ferreira et al., 2015a; Lu et al., 2001; Romsicki and Sharom, 1999).

The ability of substrates and inhibitors to modify ATPase activity was proved to be higher in the liquid-ordered phase, with lipids tightly packed with cholesterol (Meyer dos Santos et al., 2007) but still having lateral motility comparable to the liquid-crystalline phase (Modok et al., 2004). In addition, large transmembrane P-gp domains are also thought to mediate its association to lipid rafts and to enhance affinity towards cholesterol-enriched domains (Bretscher and Munro, 1993; Scheiffele et al., 1997). Thus, if drug adsorption can assist, at least partially, in the formation of such liquid-ordered domains, optimal P-gp activity would be promoted (Oleinikov et al., 2006; Romsicki and Sharom, 1997).

As P-gp is a multi-helical transmembrane protein with large membrane-spawning domains, membrane deformation to accommodate hydrophobic mismatches is also expected to occur. However, instead of analyzing the protein effect on membrane deformation, we used the Continuum-Molecular Dynamics (CTMD) approach to quantify energetic changes on the membrane biophysics due to drug adsorption (Mondal et al., 2011). Thus, the contributions of the membrane deformation energy penalty (ΔG_{def}) and residual hydrophobic exposure energy penalty (ΔG_{res}) were calculated for all classes and compared with the *apo* system (**Figure 5.16**).

Quite surprisingly, only diphenhydramine (*non-substrate*) and kaempferide (*modulator*) increase the energy penalty due to membrane deformation (ΔG_{def}), which may contribute to a destabilizing effect of the transporter (**Table 5.7**). Interestingly, only in these systems was observed drug permeation into the hydrophobic membrane core. Thus, the increase of the ΔG_{def} energetic penalty may be correlated with the fact that diphenhydramine and kaempferide were able to fully permeate into the membrane hydrophobic core and with the number of molecules (at least three) that entered the membrane. While other molecules as ranitidine (*non-substrate*), R123, trimethoprim (*substrates*) and tariquidar (*modulator*) seem to have a minimal impact on membrane deformation, all the remaining molecules alleviate the hydrophobic mismatch, with values ranging from -1.44 k_BT for verapamil up to -3.14 k_BT in Hoechst 33342 (both *substrates*).

These results, along with the result obtained from A_L and D_{HH}, reinforces the fact that by inducing a more ordered state the energy penalty associated with membrane deformation decreases due to a better compensation of hydrophobic mismatches. Therefore, drug adsorption to the lipid-water interface may assist the formation of such domains, with implications on the efflux activity of the transporter.

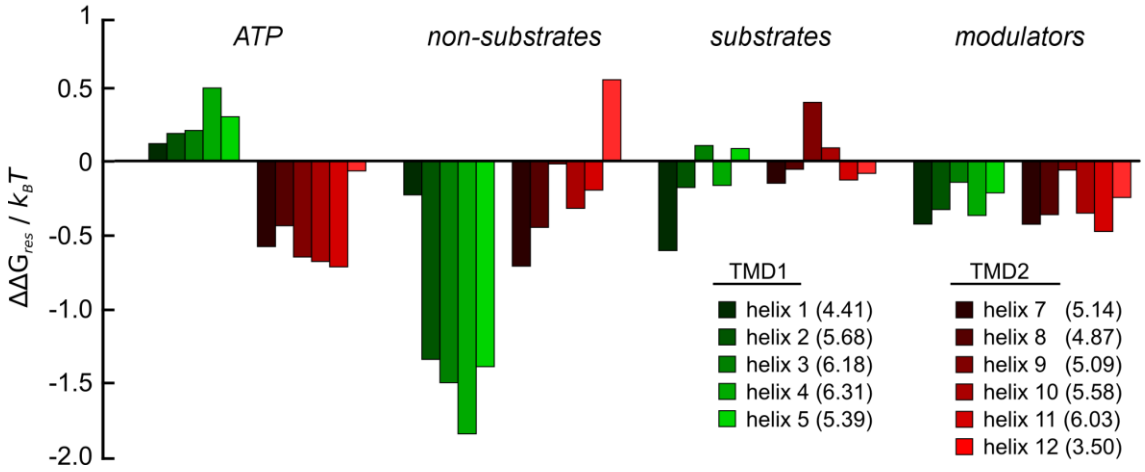

Figure 5.16. Changes in the residual hydrophobic exposure energy penalty ($\Delta\Delta G_{res}$) for each class compared with the apo system (under parenthesis in k_BT units). TMD1, N-terminal transmembrane domain; TMD2, C-terminal transmembrane domain. Residue exposure for helix 6 in TMD1 was undetermined (no exposed residues to the bilayer).

Table 5.7. Membrane deformation energy penalty (ΔG_{def}).

	Energetic Penalty (k_BT)				
non-substrates		*substrates*		*modulators*	
alprenolol	-1.86	colchicine	-2.09	latilagascene D	-2.15
diphenhydramine	1.77	Hoechst 33342	-3.14	kaempferide	2.09
ranitidine	-1.00	Rhodamine-123	-0.03	tariquidar	-0.05
		trimethoprim	-0.70		
		verapamil	-1.44		

In addition to the above described effect, drug adsorption to either protein-water and lipid-water interface may also contribute to change not only the pattern of membrane deformation but also the residual hydrophobic exposure of residues located at the end of each transmembrane domains. Similar to the results reported for rhodopsin and 5-HT_{2A} receptors (Mondal et al., 2011; Shan et al., 2011), P-gp also reveal radially asymmetric deformations around each TMD. Regarding hydrophobic residue exposure, a striking difference emerges between classes. While ATP seem to asymmetrically change the hydrophobic exposure of both *N*-terminal and *C*-terminal domains, both *non-substrates* and *modulators* seem to stabilize the protein by reducing the energetic penalty in both halves. However, this effect is much more pronounced in TMD1 for *non-substrates* whereas in *modulators* the same effect is similarly distributed by all transmembrane helices. Interestingly, *substrates* do not show this behavior, having a negligible effect on all transmembrane domains except TM helices 1 (decreasing exposure) and 9 (increasing exposure). The above data support the fact that mechanical

alterations can indeed be induced by drug adsorption to the lipid bilayer interface (with or without permeation) but also to the cytoplasmic domains of P-gp. Nonetheless, such changes heavily depend on the physico-chemical characteristics of molecules, lipid composition and number of adsorbed molecules. Moreover, it is not totally clear if the observed membrane changes are due solely to drug adsorption at the lipid-water interface or if drug adsorption at the protein-water interface also contributes for changes in the bilayer.

Chapter 6

Conclusions

6. Conclusions

The main goals of this work were to isolate and characterize new MDR reversers in cancer cells by specifically targeting ABC transporters, and to obtain new insights on the initial steps of the efflux mechanism by P-gp through novel ligand-based and structure-based *in silico* approaches.

The phytochemical study of *E. pedroi* yielded four new terpenoids (**Figure 6.1**): three macrocyclic diterpenes, two lathyranes, pedrodione A (**9**) and pedrodiol (**12**) and one jatrophane, pedrodione B (**10**); and one tigliane, pedrolide (**13**), presenting an unusual scaffold that may derive from a pinacol rearrangement at C-6/C-7 followed by the formation of a lactone with the hydroxyl at C-9. Furthermore, one new steroid with a *spiro* scaffold, spiropedroxodiol (**6**), was also characterized. The following known diterpenic compounds were also isolated: jolkinol D (**7**), piscatoriol A (**11**), 15-acetoxy-5,6-epoxylathyra-12*E*-en-3-hydroxy-14-dione (**8**), helioscopinolide B (**14**), helioscopinolide E (**15**) and *ent*-13*R*-hydroxy-3,14-dioxo-16-atisene (**16**). From helioscopinolide E (**15**) and naringenin (**17**), isolated in large amounts from *E. pedroi*, two libraries comprising six *ent*-abietane (**19**-**24**) and 46 flavanone (**25**-**71**) derivatives were also prepared. All chemical structures were deduced from physical and spectroscopic data (IR, MS, ^{1}H-, ^{13}C-NMR) and their potential as MDR reversal agents was assessed by exploring their ability to modulate P-gp efflux.

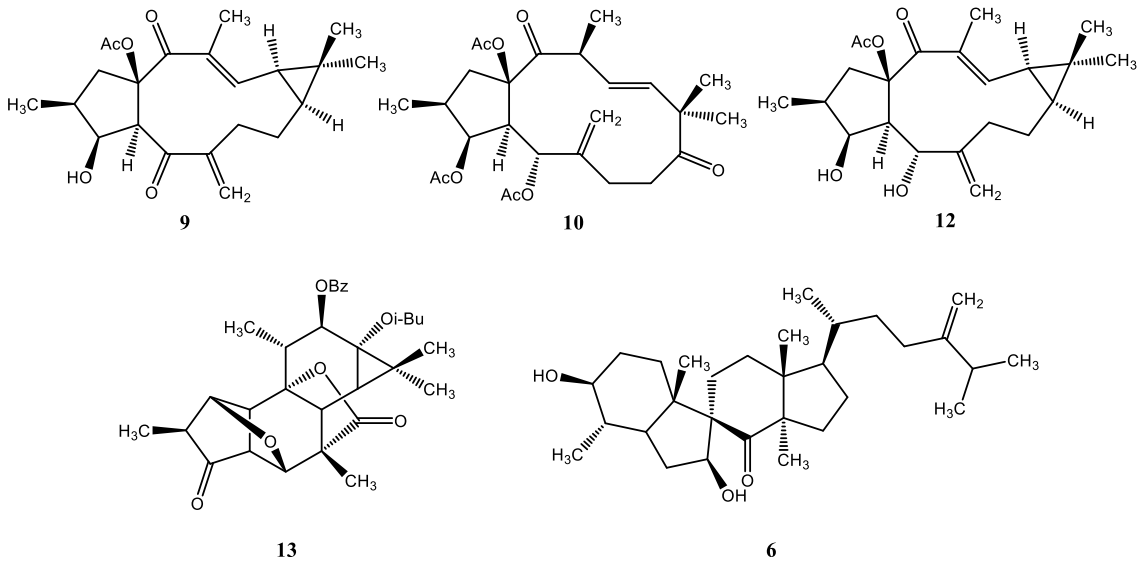

The MDR reversal activity of compounds **1**-**16** was assessed in L5178Y-MDR and Colo320 cell models. All compounds showed a variable degree of P-gp modulation, with

spiropedroxodiol (**6**) and pedrodione A (**9**) being the most potent ones. Furthermore, the high cytotoxicity and anti-proliferative effects showed by pedrodione A (**9**) in cancer cells identifies it as a possible lead compound in the 'pipeline' for the development of novel MDR reversers. In addition, pedrodione B (**10**) and pedrolide (**13**) also synergistically enhanced the anti-proliferative activity of doxorubicin (combination indexes < 0.5).

Helioscopinolide E (**15**) and naringenin (**17**) derivatives were also assessed as P-gp efflux modulators. Concerning the *ent*-abietane scaffold the acetylation (**20**) or benzoylation (**22**) of helioscopinolide E oxime **19** (C=N-OH) was sufficient to increase the potency of the derivatives towards the L5178Y-MDR cells.

In the flavanone scaffold, important structure-activity relationships were obtained from the synthetized derivatives: while the methylation of the phenolic hydroxyl at position C-7 was found to be important for the MDR reversal activity, the synthesis of hydrazones (C=N-NH-R; **25**-**28**, **48**-**53**), azines (C=N-N=CH-R; **29**-**36**) and carbohydrazides (C=N-NH-CO-R; **37**, **38**, **40**-**42**, **54**-**63**) at position C-4 greatly enhanced the P-gp efflux modulation (at 20 µM). Furthermore, the alkylation of the hydroxyl group at C-4' with epichlorohydrin (**62**, **63**) followed by the reaction with amines to yield propanolamines (**64**-**69**) greatly improved their anti-MDR activities even at lower concentrations as 2.0 µM.

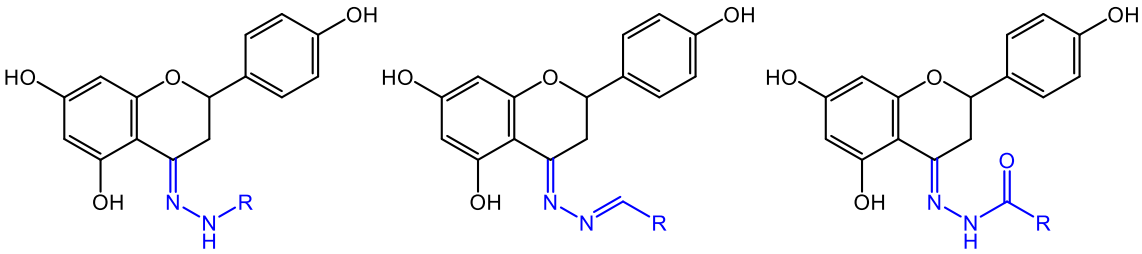

Hydrazones **Azines** **Carbohydrazides**

Therefore, and in agreement with previously published literature, the introduction of nitrogen atoms and aromatic moieties is a successful approach to enhance the potency of flavanones towards P-gp.

In addition to the studies described above, several flavanone derivatives (**25**-**45**) were also assessed as MDR reversers in MDR-related efflux pumps from the ABC superfamily, namely the BCRP and MRP1. Herein, azines (**31**-**36**) were found to be more effective efflux modulators in BCRP-overexpressing HEK293 cells while carbohydrazides (**40**-**42**) displayed a

highly selective profile as MRP1 efflux modulators in MRP1-overexpressing BHK21 cells. Interestingly, while compounds **36** and **37** were found to be moderately active as efflux modulators in both BCRP and MRP1, the thiosemicarbazone derivative **39** was found to be the only compound to act as efflux modulator in BCRP and MRP1 (when at 20 μM) but also in P-gp (L5178Y-MDR cells). However, when tested in P-gp overexpressing NIH/3T3 cells, no compound could modulate P-gp efflux. Nonetheless, a proof of concept that flavanones can be used as useful building blocks for the development of either selective, dual or triple efflux modulators is herein provided for the first time.

Regarding *in silico* studies, we analyzed in detail some of the characteristics predicted for the 'linker' and which role they play in combination with the remaining structure. The results confirm a previous observation that the linker acts as a 'damper' between both NBDs, stabilizing the cytosolic portion of the transporter. Moreover, the formation of specific contact surfaces explains why this structure is important, not only for the formation of the ATP binding pocket (thus affecting ATP binding and hydrolysis) but also affecting the substrate recognition by the substrate-binding sites.

In addition to the site determined by Aller *et al.* two additional drug-binding sites were identified. These sites, hereby characterized for the first time, were assigned as substrate-binding H- and R-sites identified by Shapiro and Ling based on the docking poses of verapamil, R123 and Hoechst 33342 and supported by experimental results (locating them near the inner leaflet interface). A third site with modulatory characteristics, already described, was also mapped at the top of the drug-binding pocket, next to the outer leaflet of the lipid bilayer– M site. The assignment of the above substrate-binding sites was assessed through docking of additional molecules as LDS-751 and antracyclines (R-site), quercetin and colchicine (H-site) or actinomycin D, vinblastine and etoposide (both). The results corroborated the previous assignment. Furthermore, it was possible to identify the lining residues for each site and, consequently, to assess several characteristics as mean volume, polarity and residues distribution.

A new classification scheme was developed, in which the cross-interaction capability shown by several molecules at the M site was a key feature to distinguish substrates from modulators. The properties of the most common efflux probes and their metabolites were also assessed, being identified modulatory properties in several of the evaluated molecules which

has implications in the interpretation of the different efflux assay results. Lipid molecules were also evaluated, but the binding energy registered classifies them as non-substrates. The cross-interaction capability offers, for the first time, a suitable explanation for the modulation capability associated to molecules frequently classified as substrates, as indinavir, ritonavir, reserpine, colchicine or vinblastine.

The evaluation of drug permeation from the bulk water environment into the internal drug-binding pocket was also determined to be an energetically favorable, spontaneous process for all stages (drug permeation, drug DBP entry and drug release after ATP hydrolysis) but one (ATP-driven conformational changes). Thus, P-glycoprotein seems to function as a "facilitator" that bypasses drug flip-flop between membrane leaflets, allowing drugs to pass from the cytoplasmic leaflet directly into the extracellular medium. However, for drug release to occur, P-gp must shift the binding affinities in drug-binding sites from high- to low-affinities, with such conformational changes intimately related with ATP binding and hydrolysis at the nucleotide-binding domains.

The calculation of the free energies of adsorption of several molecules towards the protein and lipid bilayer was also important to clarify the impact of this physical phenomenon on the transporter. It was determined that molecules belonging to the *modulators* group were characterized by lower adsorption energies towards nucleotide-binding domains of P-gp and lipid bilayer and, when compared with *non-substrates* and *substrates*, this difference was calculated to be statistically significant for protein adsorption. Protein-ligand interactions identified polar residues with the ability to induce the formation of hydrogen bond networks or to participate in electrostatic interactions as the most important factors for drug adsorption.

Our study also revealed differences in density distribution of molecules around the cytoplasmic NBDs, with lower population densities for *non-substrates* when compared with the remaining classes. In the latter, while *substrates* show higher densities around β-sheet motifs, *modulators* revealed higher densities in both α-helices and coil motifs. However, both classes revealed higher spatial distributions in locations around the TMD-NBD interfaces and at the lipid interface next to the 'entrance gate' located between TM helices 4 and 6. If adsorbed to these regions, especially at the TMD-NBD interface, normal motion patterns are expected to change due to alterations in how coordinated motion following ATP binding are transmitted to the transmembrane domains.

On the other hand, molecule adsorption to the lipid bilayer is also expected to change the biophysical behavior of the membrane through a nonlinear effect. For small molecules having hydrogen-bond acceptor and donor capability, as colchicine, kaempferide or trimethoprim, simultaneous interactions with multiple phospholipids are expected to decrease membrane fluidity, as also described in another study. Herein, all molecules induced a decrease in the calculated area per lipid (A_L) in both leaflets, additionally increasing membrane thickness (D_{HH}) in a lesser extent, which suggests the formation of more liquid-ordered patches around P-gp. Thus, these combined effects would further increase the formation of liquid-ordered domains around P-gp, stimulating the efflux activity proportionally to the number of adsorbed molecules.

At the end, the conjoined efforts of phytochemical, computational and biological approaches were able to obtain valuable information towards the development of novel efflux modulators. While the identification of novel terpenoids able to reverse MDR was important for increasing the pool of available scaffolds, the structural modification of the *ent*-abietane and flavanone scaffolds provided new information about the structure-activity relationships linked with efflux modulation in P-gp, MRP1 and BCRP, the most important "efflux triad" involved in the MDR onset in cancer. Thus, while compounds **6**, **8**, **9**, **53** and **69** could be used as lead compounds for developing novel efflux modulators for P-gp, compounds **29**, **33** and **36** (BCRP) and **41**-**42** (MRP1) can be used for searching more selective efflux modulators for other ABC transporters. Furthermore, our *in silico* results clarified the most important aspects related with the efflux mechanism by P-gp, aiming for the development of selective modulators able to achieve clinical usage.

Chapter 7

Material and Methods

7. Material and Methods

7.1. Chemistry

7.1.1. General experimental procedures

Optical rotations were obtained in a Perkin Elmer 241 polarimeter, with a 10-cm path length quartz cell at a temperature of 20 ºC (maintained constant by a water bath) and all samples were dissolved in spectroscopy grade $CHCl_3$ or MeOH. Infrared spectra were determined on an Shimadzu Affinity-1 FTIR spectrophotometer using NaCl pellets.

Low resolution mass spectrometry (ESI-MS) was performed on a Triple Quadrupole mass spectrometer (Micromass Quattro Micro API, Waters) and high-resolution mass spectra were obtained on a FTICR-MS Apex Ultra 7T instrument (Brüker Daltonics). NMR spectra were recorded on a Bruker 400 (^{1}H 400 MHz, ^{13}C 101 MHz) and on a Bruker 300 (^{1}H 300 MHz, ^{13}C 75 MHz) Ultra-Shield instruments, with all ^{1}H and ^{13}C shifts expressed in δ (ppm) and referenced to the solvent used. Coupling constants *J* were expressed in hertz (Hz) and all spectra were assigned using the appropriate COSY, DEPT, HMQC and HMBC sequences.

Column chromatography was performed using Silicagel 60 (0.040-0.063 mm, Merck 1.09385.9025) or CombiFlash systems (RediSep®R*f*, Teledyne-Isco) using standard (SiO_2) or reversed-phase (C18) prepacked columns. Analytical and preparative thin-layer chromatography was performed using pre-coated SiO_2 plates (Merck 1.05554.9025) and 20 x 20 cm Silicagel 60 GF_{254}-coated glass plates (Merck 1.07730.9025), respectively. Visualization was done under UV light (λ 254 and 366 nm) and by revealing them with sulfuric acid/methanol (1:1) followed by heating.

High-pressure liquid chromatography (HPLC) was performed on a Merck-Hitachi system with UV detection. For analytical and semi-preparative HPLC, Merck LiChrospher 100 RP-18 columns were used (analytical, 5 μm; 125 x 4 mm; semi-preparative, 10 μm, 250 x 10 mm) with mixtures of MeOH/H_2O and ACN/H_2O as mobile phases.

7.1.2. Phytochemical study of Euphorbia pedroi

7.1.2.1. Plant Material

Euphorbia pedroi Molero & Rovira was collected at the Parque Natural da Arrábida (June 2011) and identified by the plant taxonomist Dr. Teresa Vasconcelos, of Instituto Superior de Agronomia, Universidade de Lisboa. A voucher specimen (nº LISI-06/2011) has been deposited at the herbarium of Instituto Superior de Agronomia.

7.1.2.2. Extraction and isolation

The air-dried powdered aerial parts (17.8 Kg) was exhaustively extracted with methanol (10 × 12.5 L) at room temperature (**Figure 7.1**). The solvent was evaporated under vacuum (at 40 °C) from the crude extract to yield a 3.33 kg residue. Following, the residue was resuspended in MeOH–H_2O solution (1:1) and sequentially extracted with *n*-hexane (3 × 0.3 L) and ethyl acetate (EtOAc, 10 × 12.5 L). The EtOAc soluble fraction was dried with sodium sulphate and evaporated under vacuum to obtain a residue (901 g) that was chromatographed over SiO_2 (6.5 Kg), using as eluents mixtures of *n*-hexane–EtOAc (1:0 to 0:1) and EtOAc–MeOH (1:0 to 5:1). According to differences in composition as indicated by TLC, 10 crude fractions were obtained (Fractions A–L, **Table 7.1**). As from the crude fraction **E** a white precipitate was readily obtained, the mother liquor was further designated as fraction **F**. The other fractions (**D** and **G**) were also selected due to their TLC profiles (**Figure 7.1**).

Table 7.1. Fractions obtained from the EtOAc soluble fraction of *Euphorbia pedroi*.

		Eluents (v/v)	
Fraction	**Amount (g)**	***n*-hexane–EtOAc**	**EtOAc–MeOH**
A	2.76	100:0 to 90:10	--
B	3.90	90:10 to 70:30	--
C	0.90	70:30 to 65:35	--
D	2.71	65:35 to 55:45	--
E	1.35	55:45 to 45:55	--
F	9.21	55:45 to 45:55	--
G	24.8	45:55 to 40:60	--
H	15.4	40:60 to 20:80	--
I-K	41.7	20:80 to 0:100	100:0 to 95:5
L	52.9	--	95:5 to 70:30

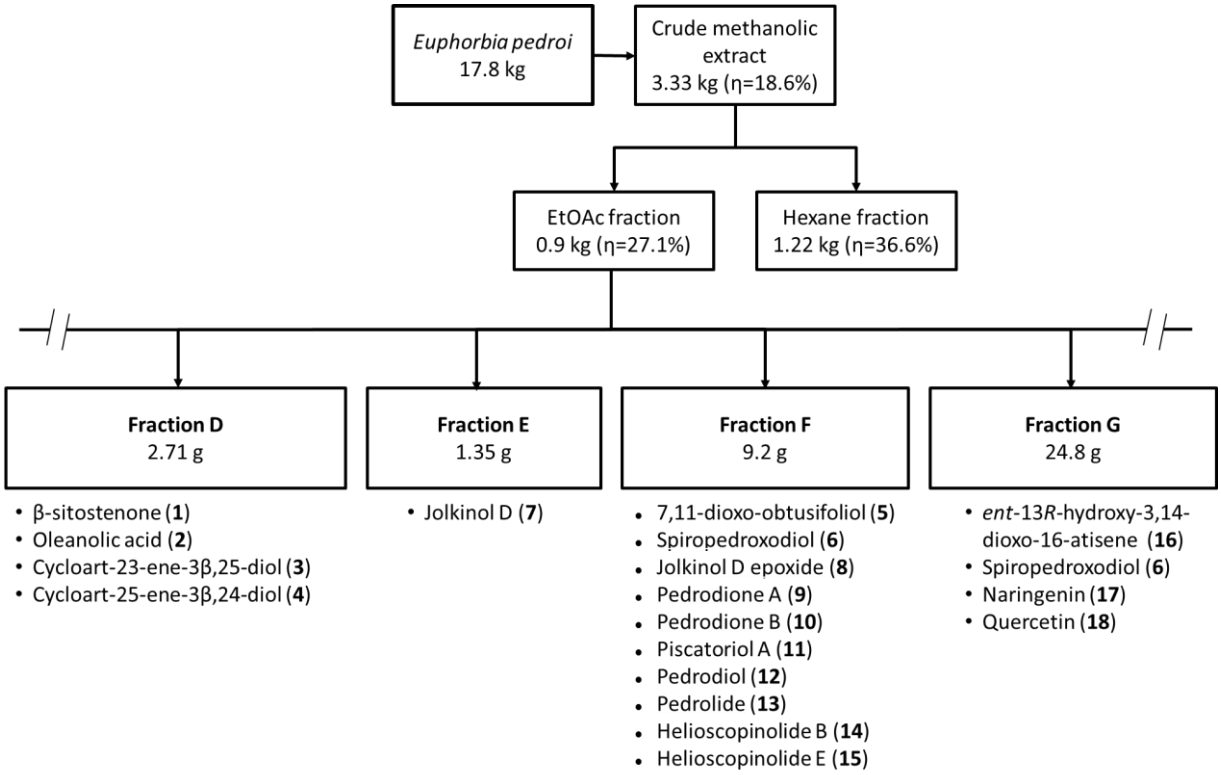

Figure 7.1. Study of *Euphorbia pedroi*: extraction, isolation procedures and identified compounds from fractions D-G.

7.1.2.3. Study of fraction D

The whole fraction **D** (2.71 g) was further processed through column chromatography (110 g SiO_2) with *n*-hexane–EtOAc (100:0 to 70:30, used in increased gradients of 10%, 500 mL each) and CH_2Cl_2–MeOH (100:0 to 90:10, 200 mL each), originating 9 subfractions (**D1**-**D9**). Subfraction **D4** (338 mg) was again chromatographed by column chromatography (15 g SiO_2) with *n*-hexane–EtOAc (100:00 to 80:20, 500 mL each) to obtain five subfractions (**D4A**-**D4E**), with the known steroid β-sitostenone (**1**, 15 mg) being isolated from **D4B** subfraction by preparative TLC, using dichloromethane as eluent. Similarly, **D5** and **D6** fractions were joined into one single subfraction (**D5/6**) and separated through column chromatography (60 g SiO_2) using *n*-hexane–EtOAc as mobile phase, from 100:0 to 70:30 with increasing gradients of 10 %), to obtain 4 subfractions (**D5/6A**-**D5/6D**). Two known triterpenic cycloartanes were isolated: while cycloart-25-ene-3β,24-diol (**3**, 56 mg) was isolated from subfraction **D5/6C** through a column chromatography (190 mg, 15 g SiO_2), with CH_2Cl_2–Acetone (100:0 to 80:20) as mobile phase, the related compound cycloart-23-ene-3β,25-diol (**4**, 13 mg) was isolated from subfraction **D5/6D** in the CombiFlash system, using standard columns (501 mg, 12 g SiO_2

prepacked column, RediSep®R*f*, TeleDyne Isco) and CH_2Cl_2–acetone as eluent (100:0 to 80:20, 18 mL.min^{-1} with an increasing gradient of 2%) followed by a preparative TLC using CH_2Cl_2:MeOH 1% as mobile phase.

β-sitostenone, (24*R*)-stigmast-4-ene-3-one (**1**):

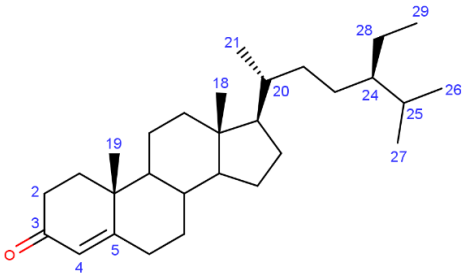

White amorphous powder;

$[\alpha]_D^{20}$ + 57.4 ° (*c* 0.1, $CHCl_3$); lit. $[\alpha]_D^{20}$ + 81.3 °;

IR ν_{max} (CH_2Cl_2) 2957, 2933, 2870, 1732, 1674, 1616, 1464, 1379, 1267 cm^{-1};

ESI-MS *m/z* (positive mode): 413 $[M + H]^+$;

^{1}H-NMR (400 MHz, $CDCl_3$): δ 5.71 (1H, *s*, H-4), 2.41 (1H, *dd*, *J* = 4.5 Hz, H-2α), 2.37 (1H, *dd*, *J* = 4.5 Hz, H-2β), 1.64 (1H, *m*, H-25), 1.32 (1H, *m*, H-20), 1.22 (2H, *m*, H-28), 1.17 (3H, *s*, H-19), 0.91 (1H, *d*, *J* = 6.4 Hz, H-21), 0.83 (3H, *t*, *J* = 7.5, H-29), 0.82 (3H, *d*, *J* = 7.4 Hz, H-26), 0.80 (3H, *d*, *J* = 7.4 Hz, H-27), 0.70 (3H, *s*, H-18) ppm;

^{13}C-NMR (101 MHz, $CDCl_3$): δ 199.8 (C-3), 171.88, (C-5), 123.8 (C-4), 45.9 (C-24), 36.2 (C-20), 34.0 (C-2), 28.3 (C-25), 23.2 (C-28), 19.9 (C-26), 19.1 (C-27), 18.8 (C-21), 17.5 (C-19), 12.1 (C-28, C-29).

Cycloart-25-ene-3β,24-diol (**3**):

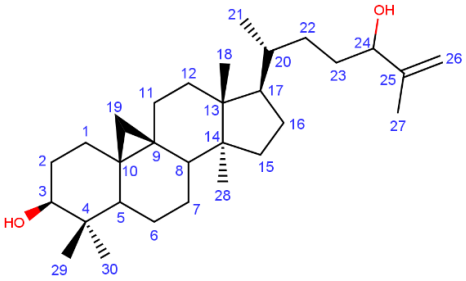

White powder;

$[\alpha]_D^{20}$ + 24.6 ° (*c* 0.1, $CHCl_3$); lit. $[\alpha]_D^{20}$ + 44.0 ° (*c* 0.2, $CHCl_3$);

IR ν_{max} (CH_2Cl_2) 3446, 3419, 2964, 2872, 1689, 1656, 1618, 1458, 1375 cm^{-1};

ESI-MS *m/z* (positive mode): 443 $[M + H]^+$;

^{1}H-NMR (400 MHz, $CDCl_3$): δ 4.93 (1H, *d*, *J* = 0.5 Hz, H-26β), 4.83 (1H, *br s*, H-26α), 4.02 (1H, *t*, *J* = 6.2 Hz, H-24), 3.28 (1H, *dd*, *J* = 10.4, 4.1 Hz, H-3), 1.72 (3H, *s*, H-27), 0.96 (6H, *s*, H-18, H-29), 0.88 (3H, *s*, H-30), 0.87 (3H, *d*, *J* = 5.5 Hz, H-21), 0.80 (3H, *s*, H-28), 0.54 (1H, *d*, *J* = 3.7 Hz, H-19α), 0.33 (1H, *d*, *J* = 3.7 Hz, H-19β) ppm;

^{13}C-NMR (101 MHz, $CDCl_3$): δ 111.1 (C-26), 78.9 (C-3), 76.5 (C-24), 30.0 (C-19), 25.6 (C-30), 19.4 (C-28), 18.4 (C-21), 18.2 (C-18), 17.7 (C-27), 14.2 (C-29).

Cycloart-23-ene-3β,25-diol (**4**):

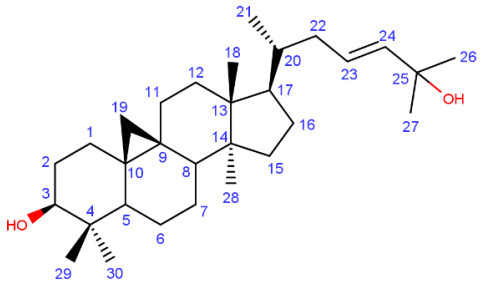

White powder;

$[\alpha]_D^{20}$ + 30.6 ° (*c* 0.1, $CHCl_3$); lit. $[\alpha]_D^{20}$ + 43.6 ° (*c* 0.22, $CHCl_3$);

IR ν_{max} (CH_2Cl_2) 3445, 3421, 2949, 2924, 2870, 1697, 1452, 1375 cm^{-1};

ESI-MS *m/z* (positive mode): 443 $[M + H]^+$;

^{1}H-NMR (400 MHz, $CDCl_3$): δ 5.60 (2H, *br s*, H-23, H-24), 3.28 (1H, *dd*, *J* = 10.9, 4.4 Hz, H-3), 2.17 (1H, *dd*, *J* = 14.3, 3.5 Hz, H-22α), 1.75 (1H, *dd*, *J* = 7.3, 3.5 Hz, H-22β), 1.44 (1H, *m*, H-20), 1.31 (6H, *br s*, H-26, H-27), 0.96 (6H, *s*, H-18, H-29), 0.88 (3H, *s*, H-28), 0.86 (3H, *d*, *J* = 6.4 Hz, H-21), 0.81 (3H, *s*, H-30), 0.55 (1H, *d*, *J* = 4.0 Hz, H-19α), 0.33 (1H, *d*, *J* = 4.0 Hz, H-19β) ppm;

^{13}C-NMR (101 MHz, $CDCl_3$): δ 139.3 (C-24), 125.6 (C-23), 78.8 (C-3), 52.0 (C-17), 39.0 (C-22), 36.4 (C-20), 35.7 (C-12), 32.9 (C-15), 31.9 (C-1), 30.4 (C-19), 30.0 (C-16), 29.9 (C-26), 28.1 (C-7), 26.4 (C-2), 26.0 (C-10), 25.4 (C-30), 21.1 (C-6), 20.0 (C-9), 19.3 (C-28), 14.2 (C-29).

7.1.2.4. Study of fractions E and F

Jolkinol D was obtained by crystallization from *n*-hexane–EtOAc eluted directly from the main column, and therefore designated as fraction **E** (**7**, 1.35 g). The mother liquid (hereby designated fraction **F**) was fractionated through column chromatography (9.2 g, 500 g SiO_2) using *n*-hexane–EtOAc (100:0 to 30:70, gradient of 10% in 500 mL portions) as eluents, originating 12 subfractions (**F1-F12**).

Subfraction 5 (**F5**) was first separated in Combiflash (587 mg, 43 g prepacked C-18 column, RediSep®R*f*, Teledyne Isco) with MeOH–H_2O as mobile phase (0:100 to 100:0, increasing gradient of 10%, 10 $mL.min^{-1}$) to obtain 5 distinct subfractions (**F5A-F5E**). After evaluation by analytical TLC, subfraction E (**F5E**) was chosen to be further processed by

Combiflash (137.6 mg, 12 g prepacked SiO_2 column, RediSep®R*f*, Teledyne Isco) using a CH_2Cl–MeOH gradient (100:0 to 80:20, 2% increments with an 8 mL.min^{-1} flow). Following, by sequential preparative TLCs (*n*-hexane–Acetone 60:40; *n*-hexane–EtOAc 80:20) the compound 7,11-dioxo-obtusifoliol (**5**, 6 mg) was able to be obtained as a white powder.

From subfraction 6 (**F6**), a white precipitate was readily obtained from *n*-hexane–EtOAc and identified as oleanolic acid (**2**, 17 mg), a pentacyclic triterpene. Following, the mother liquid was fractionated through by chromatography (1.35g, 60 g SiO_2), using as eluents *n*-hexane–EtOAc (100:0 to 0:100) and EtOAc–MeOH (100:0 to 70:30). From the obtained 4 subfractions (**F6A-F6D**), subfraction B (**F6B**) was further separated on a CombiFlash system (443 mg, 12 g prepacked SiO_2 column, RediSep®R*f*, Teledyne Isco) using as eluents *n*-hexane–EtOAc (100:0 to 50:50, 12 mL.min^{-1} with increasing gradients of 5%). While piscatoriol A (**10**, 6 mg) was isolated by crystallization from *n*-hexane–EtOAc, pedrodiol (**11**, 7 mg) and 15β-acetoxy-3β-hydroxylathyra-5,6-epoxi-12*E*-dien-14-one (**12**, 5 mg) were obtained after purification by HPLC using standard conditions.

Similarly, subfraction C (**F6C**) was separated in a CombiFlash system (378 mg, 12 g prepacked SiO_2 column, RediSep®R*f*, Teledyne Isco) using the same eluting conditions as described for **F6B**, allowing the isolation of pedrodione A (**8**, 7 mg) by crystallization from *n*-hexane–EtOAc. The mother liquid was further separated in Combiflash (100 mg, 43 g prepacked C-18 column, RediSep®R*f*, Teledyne Isco) with MeOH–H_2O as mobile phase (0:100 to 100:0, increasing gradient of 10%, 10 mL.min^{-1}). At the end, pedrodione B (**9**, 8 mg) was isolated after purification by preparative TLC (3 runs, *n*-hexane–acetone, 80:20).

Subfraction 7 (**F7**) was separated by reverse-phase chromathography in Combiflash (412 mg, 43 g prepacked C-18 column, RediSep®R*f*, Teledyne Isco) with MeOH–H_2O as mobile phase (0:100 to 100:0, increasing gradient of 10%, 10 mL.min^{-1}) and 11 subfractions (**F7A**-**F7L**) were obtained. While from subfraction D (**F7D**) *ent*-13*R*-hydroxy-3,14-dioxo-16-atisene (**16**, 10 mg) was obtained through a Combiflash chromatography (36 mg, 4 g prepacked SiO_2, RediSep®R*f*, Teledyne Isco) using CH_2Cl_2–acetone (100:0 to 80:20, 5% gradient increase at 8 mL.min^{-1}), from subfraction G (**F7G**) helioscopinolide B (**14**, 51 mg) was obtained by preparative TLC using *n*-hexane–acetone (80:20) as eluent. Piscatoriol A (**10**) was also isolated in this subfraction (9 mg).

From subfraction **F8**, helioscopinolide E (**15**, 239 mg) was obtained by crystallization from *n*-hexane–EtOAc. Following, the mother liquid was separated by chromatography in Combiflash (1.33 g, 24 g prepacked SiO_2 column) with *n*-hexane–EtOAc as mobile phase (100:0 to 0:100), giving rise to four subfractions (**F8A-F8D**). Subfraction C (**F8C**) was further separated by reverse phase chromatography in Combiflash (1000 mg, 43 g prepacked C-18 column, RediSep®R*f*, Teledyne Isco) with MeOH–H_2O as eluent (0:100 to 100:0), followed by a column chromathography in Combiflash (656 mg, 12 g prepacked SiO_2 column, RediSep®R*f*, Teledyne Isco) with *n*-hexane–CH_2Cl_2 (100:0 to 0:100) and CH_2Cl_2–MeOH (100:0 to 90:10) and preparative TLC (*n*-hexane–isopropanol 90:10) to obtain pedrolide (**13**, 5 mg). From subfraction D (**F8D**), standard column chromatography (100 mg, 10 g SiO_2) was performed in order to purify and obtain the compound spiropedroxodiol (**6**, 6 mg).

Oleanolic acid, 3β-hydroxyolean-12-en-28-oic acid (**2**):

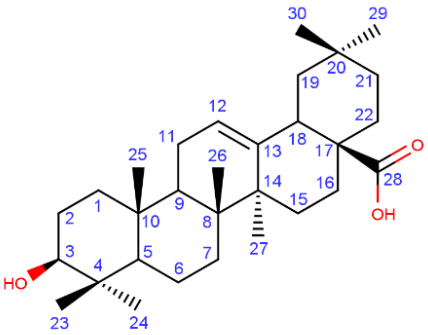

White powder;

$[\alpha]_D^{20}$ + 104.4 ° (*c* 0.1, $CHCl_3$); lit. $[\alpha]_D^{20}$ + 64.6° (*c* 0.27, $CHCl_3$);

IR ν_{max} (CH_2Cl_2) 3423, 2958, 2870, 1680, 1271 cm^{-1};

ESI-MS *m/z* (positive mode): 457 $[M + H]^+$;

^{1}H-NMR (400 MHz, $CDCl_3$): δ 5.27 (1H, *t*, *J* = 4.1 Hz, H-12), 3.21 (1H, *dd*, *J* = 11.0, 4.2 Hz, H-3), 2.81 (1H, *dd*, *J* = 13.9, 3.7 Hz, H-18), 0.98 (3H, *s*, H-23), 1.13 (3H, *s*, H-27), 0.92 (3H, *s*, H-29), 0.91 (3H, *s*, H-25), 0.90 (3H, *s*, H-30), 0.77 (3H, *s*, H-26), 0.74 (3H, *s*, H-24), 0.74 (1H, *br d*, *J* = 9.9 Hz, H-5) ppm;

^{13}C-NMR (101 MHz, $CDCl_3$): δ 183.5 (C-28), 143.6 (C-13), 122.6 (C-12), 79.0 (C-3), 55.7 (C-5), 47.6 (C-9), 46.5 (C-17), 45.9 (C-19), 41.6 (C-14), 40.9 (C-18), 39.2 (C-8), 38.7 (C-4), 38.4 (C-1), 37.1 (C-10), 33.1 (C-7, C-29), 32.6 (C-21), 32.4 (C-22), 30.7 (C-20), 28.0 (C-23), 27.7 (C-2), 27.6 (C-15), 26.0 (C-27), 23.6 (C-30), 23.4 (C-16), 22.9 (C-11), 18.3 (C-6), 17.1 (C-26), 15.6 (C-24), 15.3 (C-25).

7,11-dioxo-obtusifoliol, 3β-hydroxy-4α,14α-dimethyl-5α-ergosta-8,24(28)-dien-7,11-dione (**5**):

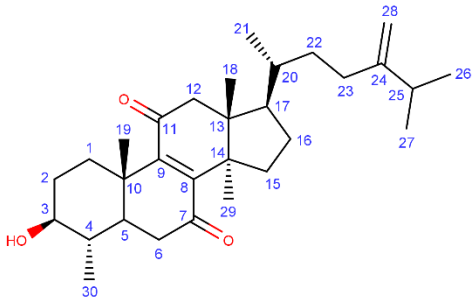

White powder;

$[\alpha]_D^{20}$ + 94.2 ° (*c* 0.1, $CHCl_3$); lit. $[\alpha]_D^{23}$ + 102 ° (*c* 0.92, $CHCl_3$)

IR ν_{max} (CH_2Cl_2) 3367, 2960, 2928, 2870, 1674, 1643, 1458, 1377 cm^{-1};

ESI-MS *m/z* (positive mode): 455 $[M + H]^+$;

^{1}H-NMR (400 MHz, $CDCl_3$): δ 4.72 (1H, *br s*, H-28α), 4.66 (1H, *br s*, H-28β), 3.13 (1H, *ddd*, *J* = 11.1, 9.4, 5.1 Hz, H-3), 2.84 (1H, *dt*, *J* = 13.8, 3.9 Hz, H-1α), 2.77 (1H, *d*, *J* = 16.0 Hz, H-12α), 2.63 (1H, *d*, *J* = 16.0 Hz, H-12β), 2.51 (1H, *dd*, *J* = 15.5, 2.8 Hz, H-6α), 2.30 (1H, *dd*, *J* = 16.3, 15.5 Hz, H-6β), 2.24 (1H, *m*, H-25), 2.11 (1H, *m*, H-23α), 2.10 (1H, *m*, H-15α), 2.01 (1H, *m*, H-16α), 1.88 (1H, *m*, H-15β), 1.87 (1H, *m*, H-23β), 1.85 (1H, *dd*, *J* = 9.4, 5.1 Hz, H-2α), 1.70 (1H, *m*, H-17), 1.59 (2H, *m*¸ H-2β, H-22α), 1.49 (1H, *m*, H-4), 1.47 (1H, *m*, H-5), 1.41 (1H, *m*, H-20), 1.36 (1H, *m*, H-16β), 1.30 (3H, *s*, H-19), 1.20 (3H, *s*, H-29), 1.16 (2H, *m*, H-1β, H-22β), 1.02 (6H, *d*, *J* = 6.8 Hz, H-26, H-27), 1.01 (3H, *d*, *J* = 6.1 Hz, H-30), 0.92 (3H, *d*, *J* = 6.4 Hz, H-21), 0.82 (3H, *s*, H-18) ppm;

^{13}C-NMR (101 MHz, $CDCl_3$): δ 202.8 (C-11), 201.8 (C-7), 156.6 (C-24), 151.6 (C-9), 151.4 (C-8), 106.3 (C-28), 75.5 (C-3), 51.8 (C-12), 49.2 (C-17), 49.1 (C-13), 47.6 (C-14), 47.3 (C-5), 38.8 (C-10), 38.4 (C-6), 38.3 (C-4), 36.3 (C-20), 34.8 (C-22), 33.9 (C-25), 33.4 (C-1), 32.2 (C-15), 31.3 (C-23), 31.0 (C-2), 27.5 (C-16), 26.1 (C-29), 22.1 (C-27), 22.0 (C-26), 18.7 (C-21), 16.9 (C-18), 16.58 (C-19), 14.9 (C-30).

Spiropedroxodiol, (3S,7S,9R)-3,7-dihydroxy-7(8→9)-*abeo*-ergosta-24(28)-en-8-one (**6**):

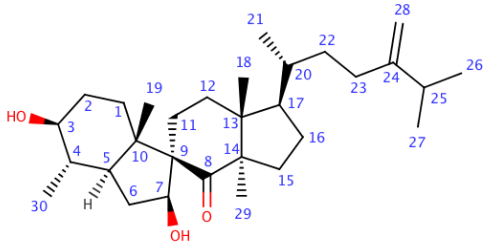

Colorless oil;

$[\alpha]_D^{20}$ + 12.0 ° (*c* 0.1, $CHCl_3$);

IR ν_{max} (CH_2Cl_2) 3364, 1691, 1658, 1456, 1379 cm^{-1};

ESI-MS *m/z*: 459 $[M + H]^+$;

ESI-HRMS *m/z* 481.3655 $[M + Na]^+$ (calcd. for $C_{30}H_{50}NaO_3$, 481.3652);

^{1}H-NMR (300 MHz, $CDCl_3$): δ 4.72 (1H, *s*, H-28α), 4.65 (1H, *d*, *J* = 1.5 Hz, H-28β), 4.34 (1H, *dd*, *J* = 8.0, 3.4 Hz, H-7), 3.04 (1H, *ddd*, *J* = 12.0, 9.5, 5.3 Hz, H-3), 2.39 (1H, *dt*, *J* = 13.3, 7.6 Hz, H-6α), 2.22 (1H, *h*, *J* = 6.8 Hz, H-25), 2.13 (1H, *br t*, *J* = 4.0 Hz, H-23α), 2.07 (1H, *br d*, *J* = 4.5 Hz, H-12α), 2.02 (1H, *m*, H-11α), 2.00-1.98 (2H, *m*, H-1α, H-2α), 1.96 (1H, *m*, H-16α), 1.92 (1H, *br d*, *J* = 4.5 Hz, H-23β), 1.88 (1H, *m*, H-15α), 1.74 (1H, *m*, H-12β), 1.67 (1H, *m*, H-17), 1.66 (1H, *d*, *J* = 12.0 Hz, H-4) 1.60 (2H, *m*, H1-β, H-11β), 1.58 (1H, *m*, H-22α), 1.47 (3H, *s*, H-19), 1.41 (2H, *m*, H-2β, H-20), 1.39 (1H, *dt*, *J* = 13.3, 3.4 Hz, H-6β), 1.33 (1H, *m*, H-16β), 1.25 (1H, *m*, H-15β), 1.22 (1H, *m*, H-5), 1-20 (3H, *s*, H-29), 1.15 (1H, *m*, H-22β), 1.03 (3H, *d*, *J* = 6.8 Hz, H-26), 1.01 (3H, *d*, *J* = 6.8 Hz, H-27), 0.96 (3H, *d*, *J* = 5.4 Hz, H-30), 0.94 (3H, *d*, *J* = 5.6 Hz, H-21), 0.66 (3H, *s*, H-18) ppm;

^{13}C-NMR (75 MHz, $CDCl_3$): δ 215.2 (C-8), 156.7 (C-24), 106.3 (C-28), 80.6 (C-7), 77.4 (C-3), 64.2 (C-9), 61.1 (C-14), 50.3 (C-17), 48.3 (C-13), 48.3 (C-5), 47.8 (C-10), 38.3 (C-4), 37.9 (C-6), 35.8 (C-20), 34.9 (C-22), 33.9 (C-25), 31.4 (C-23), 30.9 (C-12), 30.3 (C-1), 30.3 (C-11), 29.7 (C-15), 28.8 (C-2), 27.2 (C-16), 22.1 (C-26), 22.0 (C-27) ,19.7 (C-29), 18.9 (C-21), 18.6 (C-19), 16.6 (C-18), 16.3 (C-30) ppm.

Jolkinol D, 15β-acetoxy-3β-hydroxylathyra-5*E*,12*E*-dien-14-one (**7**):

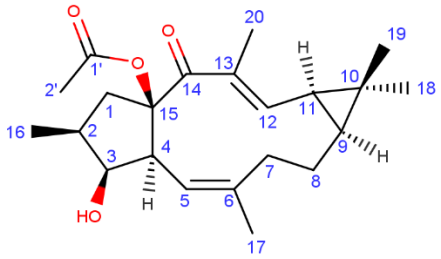

White crystals;

M.p. 187-189 ºC (*n*-hexane–EtOAc);

$[\alpha]_D^{20}$ + 42.6 ° (*c* 0.1, $CHCl_3$); lit. $[\alpha]_D^{24}$ + 20° (*c* 0.52, $CHCl_3$);

IR ν_{max} (CH_2Cl_2) 3475, 2947, 2921, 1872, 1736, 1645, 1612, 1454, 1367, 1265, 1244 cm^{-1};

ESI-MS *m/z* (positive mode): 361 $[M + H]^+$;

^{1}H-NMR (400 MHz, $CDCl_3$): δ 6.64 (1H, *d*, *J* = 11.2 Hz, H-12), 5.66 (1H, *d*, *J* = 10.8 Hz, H-5), 3.90 (1H, *dd*, *J* = 8.0, 4.0 Hz, H-3), 3.49 (1H, *dd*, *J* = 14.0, 8.1 Hz, H-1α), 2.57 (1H, *d*, *J* = 13.3 Hz, H-7α), 2.38 (1H, *dd*, *J* = 10.8, 4.0 Hz, H-4), 2.20 (1H, *dd*, *J* = 14.4, 2.0 Hz, H-8α), 2.02 (1H, *m*, H-2), 2.01 (3H, *s*, H-2'), 1.83 (3H, *s*, H-20), 1.78 (1H, *td*, *J* = 13.3, 2.0 Hz, H-7β), 1.56 (1H, *m*, H-8β), 1.50 (1H, *d*, *J* = 14.0, 4.7 Hz, H-2β), 1.45 (3H, *s*, H-17), 1.39 (1H, *dd*, *J* = 11.2, 8.3 Hz, H-11), 1.17 (3H, *s*, H-18), 1.07 (3H, *d*, *J* = 6.7 Hz, H-16), 1.06 (1H, *m*, H-9), 1.04 (3H, *s*, H-19) ppm;

^{13}C-NMR (101 MHz, $CDCl_3$): δ 195.3 (C-14), 169.8 (C-1'), 146.6 (C-12), 143.1 (C-6), 132.2 (C-13), 119.5 (C-5), 95.3 (C-15), 80.0 (C-3), 53.6 (C-4), 44.0 (C-1), 39.2 (C-2), 36.8 (C-7), 34.2 (C-9), 29.7 (C-11), 29.3 (C-18), 28.3 (C-8), 24.5 (CC-10), 21.7 (C-2'), 20.9 (C-17), 16.4 (C-19), 13.8 (C-16), 12.4 (C-20).

Jolkinol D epoxide, 15β-acetoxy-3β-hydroxylathyra-5,6-epoxi-12*E*-dien-14-one (**8**):

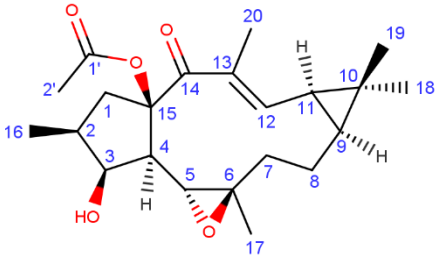

White powder;

$[\alpha]_D^{20}$ – 10 ° (*c* 0.1, $CHCl_3$); lit. $[\alpha]_D^{24}$ – 41.4° (*c* 0.15, MeOH);

IR ν_{max} (CH_2Cl_2) 3365, 2930, 2872, 2854, 1743, 1454, 1207 cm^{-1};

ESI-MS *m/z* (positive mode): 377 $[M + H]^+$;

^{1}H-NMR (300 MHz, $CDCl_3$): δ 6.92 (1H, *d*, *J* = 11.1 Hz, H-12), 4.08 (1H, *dd*, *J* = 6.9, 3.5 Hz, H-3), 3.51 (1H, *d*, *J* = 9.5 Hz, H-5), 3.46 (1H, *dd*, *J* = 13.6, 7.5 Hz, H-1α), 2.10 (1H, *br s*, H-8α), 2.07 (3H, *s*, H-2'), 2.03 (1H, *m*, H-7α), 1.94 (1H, *m*, H-2), 1.86 (3H, *br s*, H-20), 1.64 (1H, *br t*, *J* = 13.5 Hz, H-1β), 1.54 (1H, *m*, H-7β), 1.51 (2H, *m*, H-8β, H-11), 1.50 (1H, *dd*, *J* = 9.2, 3.5 Hz, H-4), 1.20 (3H, *s*, H-18), 1.17 (3H, *s*, H-17), 1.13 (1H, *dd*, *J* = 8.0, 3.2 Hz, H-9), 1.08 (3H, *d*, *J* = 5.7 Hz, H-16), 1.07 (3H, *s*, H-19) ppm;

^{13}C-NMR (75 MHz, $CDCl_3$): δ 195.3 (C-14), 169.8 (C-1'), 143.5 (C-12), 134.5 (C-13), 91.9 (C-15), 78.6 (C-3), 63.8 (C-6), 57.9 (C-5), 51.9 (C-4), 44.8 (C-1), 38.7 (C-7), 38.2 (C-2), 33.9 (C-9), 29.8 (C-11), 28.9 (C-18), 26.1 (C-10), 23.2 (C-8), 21.3 (C-2'), 19.7 (C-17), 16.1 (C-19), 13.0 (C-16), 12.3 (C-20).

Pedrodione A, 15β-acetoxy-3β-hydroxylathyra-6(17),12E-dien-5,14-dione (**9**):

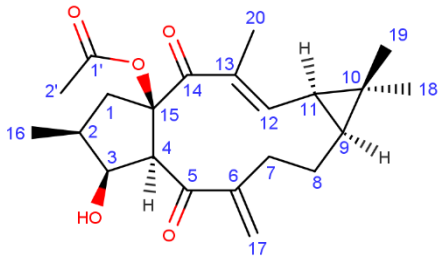

White powder;

$[\alpha]_D^{20}$ + 189 ° (*c* 0.1, $CHCl_3$);

IR ν_{max} (CH_2Cl_2) 3446, 2955, 2924, 2852, 1737, 1716, 1651, 1456 cm^{-1};

ESI-MS *m/z* (positive mode): 398 $[M + H + Na]^+$;

ESI-HRMS *m/z* 397.19883 $[M + Na]^+$ (calcd. for $C_{22}H_{30}NaO_5$, 397.19854);

^{1}H-NMR (300 MHz, $CDCl_3$): δ 6.20 (1H, *d*, *J* = 11.1 Hz, H-12), 5.84 (1H, *br s*, H-17α), 5.64 (1H, *br s*, H-17β), 4.19 (1H, *br t*, *J* = 3.0 Hz, H-3), 3.47 (1H, *dd*, *J* = 13.4, 7.5 Hz, H-1α), 3.37 (1H, *d*, *J* = 3.0 Hz, H-4), 3.02 (1H, *dd*, *J* = 13.1, 4.8 Hz, H-7α), 2.04 (1H, *m*, H-7β), 2.03 (1H, *m*, H-8α), 2.00 (3H, *s*, H-2'), 1.94 (1H, *m*, H-2), 1.78 (3H, *s*, H-20), 1.72 (1H, *br t*, *J* = 13.4 Hz, H-1β), 1.54 (1H, *m*, H-8β), 1.38 (1H, *dd*, *J* = 11.1, 8.2 Hz, H-11), 1.15 (3H, *s*, H-18), 1.11 (3H, *d*, J = 6.7 Hz, H-16), 1.08 (1H, *m*, H-9), 0.99 (3H, *s*, H-19) ppm;

^{13}C-NMR (75 MHz, $CDCl_3$): δ 201.6 (C-5), 195.1 (C-14), 169.7 (C-1'), 149.5 (C-6), 146.6 (C-12), 133.3 (C-13), 127.5 (C-17), 92.3 (C-15), 78.4 (C-3), 53.3 (C-4), 45.1 (C-1), 40.3 (C-2), 34.7 (C-9), 29.2 (C-11), 32.6 (C-7), 28.8 (C-18), 25.0 (C-10), 22.0 (C-8), 21.6 (C-2'), 16.4 (C-19), 13.0 (C-16), 12.7 (C-20) ppm.

Pedrodione B, 3β,5α,15β-triacetoxyjatropha-6(17),12*E*-dien-9,14-dione (**10**):

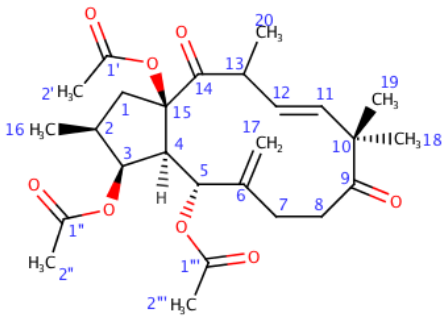

White powder;

$[\alpha]_D^{20}$ + 95.6 ° (*c* 0.1, $CHCl_3$);

IR ν_{max} (CH_2Cl_2) 2972, 2935, 2875, 1741, 1705, 1456, 1437, 1371 cm^{-1};

ESI-MS *m/z* (positive mode): 477 $[M + H]^+$;

ESI-HRMS *m/z* 499.2303 $[M + Na]^+$ (calcd. for $C_{26}H_{36}NaO_8$, 499.2303);

^{1}H-NMR (300 MHz, $CDCl_3$): δ 5.75 (1H, *d*, *J* = 10.0 Hz, H-5), 5.72 (1H, *t*, *J* = 10.5 Hz, H-12), 5.59 (1H, *d*, *J* = 10.5 Hz, H-11), 5.58 (1H, *dd*, *J* = 5.7, 4.0 Hz, H-3), 5.18 (1H, *s*, H-17α), 4.87 (1H, *s*, H-17β), 3.31 (1H, *dq*, *J* = 13.3, 6.6 Hz, H-13), 2.83 (1H, *dd*, *J* = 15.5, 8.0 Hz, H-1α), 2.66 (1H, *dd*, *J* = 10.0, 4.0 Hz, H-4), 2.59 (1H, *td*, *J* = 11.0, 9.0 Hz, H-8α), 2.30 (1H, *m*, H-2), 2.23 (1H, *td*, *J* = 11.0, 9.0 Hz, H-8β), 2.16 (3H, *s*, H-2"), 2.11 (2H, *m*, H-1β, H-7α), 2.05 (3H, *s*, H-2'), 1.95 (3H, *s*, H-2"'), 1.77 (1H, *dt*, *J* = 17.0, 11.1 Hz, H-7β), 1.35 (3H, *d*, *J* = 6.6 Hz, H-20), 1.21 (3H, *s*, H-18), 1.19 (3H, *s*, H-19), 1.00 (3H, *d*, *J* = 6.5 Hz, H-16) ppm;

^{13}C-NMR (75 MHz, $CDCl_3$): δ 212.4 (C-9), 203.7 (C-14), 170.4 (C-1'), 169.4 (C-2"'), 169.2 (C-2"), 141.4 (C-6), 135.0 (C-11), 132.3 (C-12), 116.1 (C-17), 90.7 (C-15), 76.7 (C-3), 72.3

(C-5), 50.6 (C-10), 49.4 (C-4), 44.8 (C-1), 43.8 (C-13), 38.7 (C-2), 34.4 (C-8), 25.1 (C-7), 23.3 (C-18, C-19), 21.3 (C-2"), 20.9 (C-2"'), 20.7 (C-2'), 20.1 (C-20), 13.8 (C-16) ppm.

Piscatoriol A, 15β-acetoxy-6*Z*,12*E*-dien-3β,5α-dihydroxylathyra-14-one (**11**):

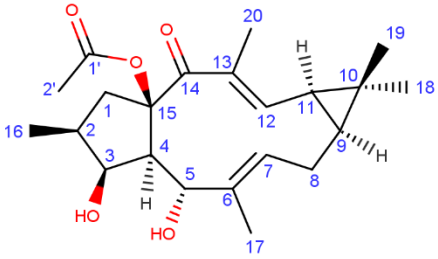

White prismatic crystals;

M.p. 255 – 257 ºC;

$[\alpha]_D^{20}$ - 68.6 ° (*c* 0.1, $CHCl_3$); lit. $[\alpha]_D^{20}$ – 43.2 ° (*c* 0.1, $CHCl_3$);

IR ν_{max} (CH_2Cl_2) 3319, 2947, 2928, 2872, 1747, 1647, 1624, 1234 cm^{-1};

ESI-MS *m/z* (positive mode): 377 $[M + H]^+$;

^{1}H-NMR (300 MHz, $CDCl_3$): δ 6.44 (1H, *d*, *J* = 11.2 Hz, H-12), 5.37 (1H, *d*, *J* = 6.2 Hz, H-5), 5.25 (1H, *dd*, *J* = 11.1, 5.4 Hz, H-7), 4.34 (1H, *t*, *J* = 3.1 Hz, H-3), 3.32 (1H, *dd*, *J* = 13.5, 7.6 Hz, H-1α), 2.37 (1H, *m*, H-8β), 2.34 (1H, *m*, H-8α), 2.10 (1H, *m*, H-4), 2.09 (3H, *s*, H-2'), 2.04 (1H, *m*, H-2), 1.75 (3H, *s*, H-20), 1.70 (1H, *m*, H-1β), 1.65 (3H, *s*, H-17), 1.42 (1H, *dd*, *J* = 11.2, 8.8 Hz, H-11), 1.25 (1H, *m*, H-9), 1.23 (3H, *s*, H-18), 1.16 (3H, *s*, H-19), 1.07 (3H, *d*, *J* = 6.8 Hz, H-16) ppm;

^{13}C-NMR (101 MHz, $CDCl_3$): δ 197.9 (C-14), 170.1 (C-1'), 142.6 (C-12), 135.5 (C-6), 133.6 (C-13), 126.7 (C-7), 92.7 (C-15), 79.7 (C-3), 65.8 (C-5), 54.7 (C-4), 47.4 (C-1), 37.8 (C-2), 31.9 (C-9), 28.8 (C-19), 27.9 (C-11), 25.5 (C-10), 23.9 (C-8), 22.2 (C-2'), 17.8 (C-17), 17.0 (C-18), 13.5 (C-16), 12.2 (C-20) ppm, in accordance with the published literature (Reis et al., 2014b).

Pedrodiol, 15β-acetoxy-6(17),12*E*-dien-3β,5α-dihydroxylathyra-14-one (**12**):

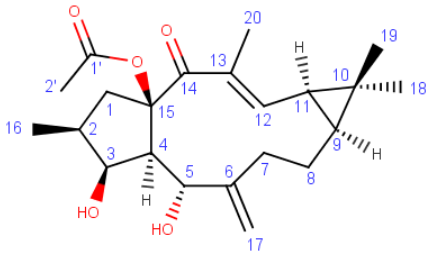

White powder;

$[\alpha]_D^{20}$ + 90.6 ° (*c* 0.1, $CHCl_3$);

IR ν_{max} (CH_2Cl_2) 3421, 2955, 2926, 2875, 1741, 1726, 16469, 1620, 1452, 1369 cm^{-1};

ESI-MS *m/z* (positive mode): 377 $[M + H]^+$;

ESI-HRMS *m/z* 377.2324 $[M + H]^+$ (calcd. for $C_{22}H_{33}O_5$, 377.2324);

^{1}H-NMR (300 MHz, $CDCl_3$): δ 6.33 (1H, *d*, *J* = 11.2 Hz, H-12), 4.95 (1H, *s*, H-17α), 4.81 (1H, *t*, *J* = 8.0 Hz, H-5), 4.75 (1H, *s*, H-17β), 4.34 (1H, *q*, *J* = 3.5 Hz, H-3), 3.39 (1H, *dd*, *J* = 13.7, 7.9 Hz, H-1α), 2.72 (1H, *dd*, *J* = 13.4, 5.4 Hz, H-7α), 2.43 (1H, *dd*, *J* = 8.0, 3.5 Hz, H-4), 2.14 (1H, *m*, H-7β), 2.09 (1H, *m*, H-2), 2.06 (3H, *s*, H-2'), 2.01 (1H, *m*, H-8α), 1.70 (4H, *m*, H-1β, H-20), 1.58 (1H, *m*, H-8β), 1.37 (1H, *dd*, *J* = 11.2, 8.2 Hz, H-11), 1.15 (3H, s, H-18), 1.09 (1H, *m*, H-9), 1.08 (3H, *d*, *J* = 8.2 Hz, H-16), 1.07 (3H, *s*, H-19) ppm;

^{13}C-NMR (75 MHz, $CDCl_3$): δ 197.2 (C-14), 169.9 (C-1'), 148.3 (C-6), 145.4 (C-12), 133.7 (C-13), 113.4 (C-17), 92.8 (C-15), 79.6 (C-3), 66.8 (C-5), 54.2 (C-4), 47.3 (C-1), 37.5 (C-2), 35.5 (C-7), 34.6 (C-9), 29.1 (C-19), 28.2 (C-11), 24.8 (C-10), 22.1 (C-8), 22.0 (C-2'), 16.7 (C-18), 13.5 (C-16), 12.6 (C-20) ppm.

Pedrolide (**13**):

Pale white powder;

$[\alpha]_D^{20}$ + 75.4 ° (*c* 0.1, $CHCl_3$);

IR ν_{max} (CH_2Cl_2) 2980, 2930, 2870, 1750, 1722, 1458 cm^{-1};

ESI-MS *m/z* (positive mode): 537 $[M + H]^+$;

ESI-HRMS *m/z* 559.2096 $[M + Na]^+$ (calcd. for $C_{31}H_{36}NaO_8$, 559.2302);

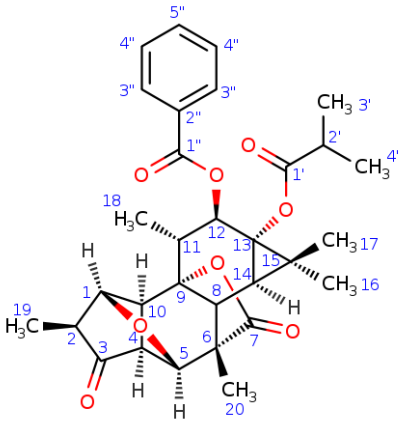

^{1}H-NMR (300 MHz, $CDCl_3$): δ 8.02 (2H, *dd*, *J* = 7.0, 1.4 Hz, H-3"), 7.55 (2H, *td*, *J* = 7.0, 1.4 Hz, H-5"), 7.44 (2H, *dd*, *J* = 7.2, 1.4 Hz, H-4"), 5.95 (1H, *d*, *J* = 8.0 Hz, H-12), 3.03 (1H, *q*, *J* = 4.7, 2.4 Hz, H-4), 2.63 (1H, *d*, *J* = 4.7 Hz, H-5), 2.61 (1H, *bd*, H-3), 2.54 (1H, *h*, *J* = 7.0 Hz, H-2'), 2.44 (1H, *d*, *J* = 2.4 Hz, H-10), 2.39 (1H, *qd*, *J* = 7.0, 4.7 Hz, H-2), 1.45 (3H, *s*, H-17), 1.25 (3H, *d*, *J* = 7.0 Hz, H-16), 1.25 (3H, *s*, H-20), 1.80 (1H, *dq*, *J* = 8.0, 6.7 Hz, H-11), 1.75 (1H, *br d*, *J* = 5.5 Hz, H-8), 1.12 (3H, *d*, *J* = 7.0 Hz, H-3'), 1.12 (3H, *s*, H-17), 1.10 (3H, *d*, *J* = 7.0 Hz, H-4'), 1.18 (3H, *d*, *J* = 6.7 Hz, H-18), 0.96 (1H, *d*, *J* = 5.5 Hz, H-14) ppm;

^{13}C-NMR (75 MHz, $CDCl_3$): δ 212.18 (C-3), 177.3 (C-1'), 176.8 (C-1), 166.3 (C-1"), 132.8 (C-5"), 131.0 (C-2"), 129.8 (C-3"), 128.5 (C-4"), 88.5 (C-9), 80.1 (C-12), 66.4 (C-13), 63.2 (C-1), 55.6 (C-5), 51.0 (C-8), 50.1 (C-4), 46.7 (C-10), 45.6 (C-6), 43.4 (C-11), 33.8 (C-2'), 30.3

(C-15), 28.2 (C-14), 23.2 (C-17), 19.1 (C-3'), 18.9 (C-4'), 18.0 (C-20), 17.4 (C-19), 13.8 (C-18), 12.4 (C-16) ppm.

Helioscopinolide B (**14**):

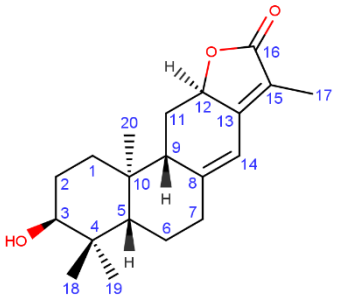

Colorless oil;

$[\alpha]_D^{20}$ + 302.8 ° (*c* 0.1, $CHCl_3$); lit. $[\alpha]_D^{20}$ + 154.0 ° (*c* 0.74, $CHCl_3$);

IR ν_{max} (CH_2Cl_2) 3462, 2951, 2926, 2872, 1747, 1666, 1608, 1456, 1386 cm^{-1};

ESI-MS *m/z* (positive mode): 317 $[M + H]^+$;

^{1}H-NMR (300 MHz, $CDCl_3$): δ 6.24 (1H, *s*, H-14), 4.85 (1H, *dd*, *J* = 13.0, 5.0 Hz, H-12), 3.45 (1H, *br s*, H-3), 2.54 (1H, *dd*, *J* = 13.5, 6.0 Hz, H-11α), 2.48 (1H, *br d*, *J* = 13.7 Hz, H-7α), 2.28 (1H, *br d*, *J* = 8.4 Hz, H-9), 2.20 (1H, *ddd*, *J* = 14.3, 13.7, 4.1 Hz, H-7β), 1.95 – 1.92 (2H, *m*, H-1α, H-2α), 1.79 (3H, *s*, H-17), 1.66 (2H, *m*, H-1β, H-2β), 1.62 (1H, *m*, H-5), 1.72 (1H, *m*, H-6α), 1.47 (1H, *dd*, *J* = 13.3, 5.0 Hz, H-11β), 1.38 (1H, *ddd*, *J* = 13.3, 12.3, 3.3 Hz, H-6β), 0.96 (3H, *s*, H-19), 0.93 (3H, *s*, H-20), 0.84 (3H, *s*, H-18) ppm;

^{13}C-NMR (75 MHz, $CDCl_3$): δ 175.5 (C-16), 156.3 (C-13), 152.3 (C-8), 116.3 (C-15), 114.1 (C-14), 76.2 (C-12), 75.5 (C-3), 51.6 (C-9), 48.3 (C-5), 41.1 (C-10), 37.8 (C-4), 37.1 (C-7), 32.2 (C-1), 28.8 (C-20), 27.5 (C-2), 25.8 (C-11), 23.4 (C-6), 22.3 (C-18), 16.8 (C-20), 8.2 (C-17) ppm.

Helioscopinolide E (**15**):

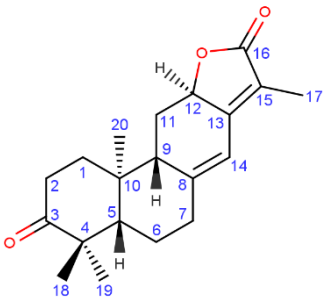

White powder;

$[\alpha]_D^{20}$ + 353 ° (*c* 0.1, $CHCl_3$); lit. $[\alpha]_D^{20}$ + 283.2 ° (*c* 0.74, $CHCl_3$);

IR ν_{max} (CH_2Cl_2) 2960, 2931, 2870, 1724, 1655, 1458, 1363 cm^{-1};

ESI-MS *m/z* (positive mode): 315 $[M + H]^+$;

^{1}H-NMR (300 MHz, $CDCl_3$): δ 6.32 (1H, *s*, H-14), 4.87 (1H, *dd*, *J* = 13.3, 5.8 Hz, H-12), 2.63 (1H, *ddd*, *J* = 15.7, 12.6, 6.0 Hz, H-2α), 2.50 (2H, *m*, H-7α, H-11α), 2.45 (1H, *ddd*, *J* = 15.7, 6.0, 3.5 Hz, H-2β), 2.25 (1H, *d*, *J* = 8.3 Hz, H-9), 2.22 (1H, *m*, H-7β), 2.17 (1H, *ddd*, J = 10.4,

6.4, 3.5 Hz, H-1α), 1.83 (3H, *s*, H-17), 1.80 (1H, *m*, H-6α), 1.64 (1H, *m*, H-5), 1.59 (1H, *m*, H-1β), 1.53 (2H, *m*, H-6β, H-11β), 1.11 (3H, *s*¸ H-20), 1.07 (3H, *s*, H-19), 1.04 (3H, *s*, H-18) ppm;

^{13}C-NMR (75 MHz, $CDCl_3$): δ 215.7 (C-3), 175.2 (C-16), 155.6 (C-13), 150.3 (C-8), 117.1 (C-15), 114.4 (C-14), 75.6 (C-12), 54.8 (C-5), 50.7 (C-9), 47.6 (C-4), 37.5 (C-1), 36.7 (C-7), 41.0 (C-10), 34.5 (C-2), 27.9 (C-11), 26.2 (C-18), 24.7 (C-6), 21.5 (C-18), 16.0 (C-20), 8.1 (C-17) ppm.

***ent*-13*R*-hydroxy-3,14-dioxo-16-atisene** (**16**):

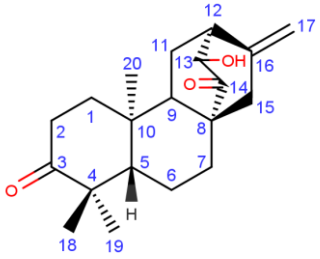

White needles;

M.p. 177 – 179 ºC;

$[\alpha]_D^{20}$ + 47.6 ° (*c* 0.1, $CHCl_3$); lit. $[\alpha]_D^{20}$ + 44.0 ° (*c* 0.03, $CHCl_3$);

IR ν_{max} (CH_2Cl_2) 3419, 2970, 2941, 2872, 1724, 1722, 1458, 1438, 1387 cm^{-1};

ESI-MS *m/z* (positive mode): 317 $[M + H]^+$;

^{1}H-NMR (300 MHz, $CDCl_3$): δ 5.02 (1H, *s*, H-17α), 4.88 (1H, *s*, H-17β), 3.88 (1H, *s*, H-13), 2.81 (1H, *dd*, *J* = 5.4, 2.8 Hz, H-12), 2.54 (1H, *ddd*, *J* = 15.9, 13.2, 6.4 Hz, H-2α), 2.40 (1H, *dt*, *J* = 13.5, 3.4 Hz, H-7α), 2.35 (1H, *dd*, *J* = 5.4, 3.3 Hz, H-2β), 2.32 (2H, *m*, H-15), 2.01 (1H, *ddd*, *J* = 14.9, 11.6, 3.8 Hz, H-11α), 1.86 (1H, *ddd*, *J* = 13.5, 6.4, 3.2 Hz, H-1β), 1.75 (1H, *ddd*, *J* = 14.2, 6.4, 2.5 Hz, H-11β), 1.65 (1H, *dd*, *J* = 11.2, 4.8 Hz, H-9), 1.53 (1H, *dd*, *J* = 9.0, 3.5 Hz, H-6α), 1.49 (1H, *dd*, *J* = 8.9, 3.3 Hz, H-6β), 1.33-1.28 (1H, *m*, H-5), 1.38 (1H, *td*, *J* = 13.4, 5.6 Hz, H-1β),1.08 (3H, *s*, H-18), 1.00 (3H, s, H-19), 0.99-0.91 (1H, *m*, H-7β), 0.84 (3H, *s*, H-20) ppm;

^{13}C-NMR (75 MHz, $CDCl_3$): δ 218.2 (C-14), 216.2 (C-3), 143.3 (C-16), 111.2 (C-17), 75.2 (C-13), 55.2 (C-5), 51.2 (C-9), 47.6 (C-4), 47.4 (C-8), 44.8 (C-12), 43.8 (C-15), 37.7 (C-10), 36.8 (C-1), 34.2 (C-2), 30.5 (C-7), 26.3 (C-18), 25.4 (C-11), 22.0 (C-19), 20.1 (C-6), 13.9 (C-20) ppm.

7.1.2.5. Study of fraction G

From fraction **G** (24.7 g), and taking advantage of the different solubility of flavonoids in organic solvents (Chebil et al., 2007), the whole fraction was suspended in acetonitrile and,

after filtration, naringenin (**18**, ~ 15 g) was obtained in a large amount in the filtrate. The remaining residue was separated by Combiflash (5 g sample, 48 g SiO_2 prepacked columns, RediSep®R*f*, TeleDyne Isco) using *n*-hexane–EtOAc as eluents (100:0 to 0:100, increasing gradient of 10%, 12 mL.min^{-1}) to afford 9 subfraction (**G1**-**G9**). Based on the chromatographic profile obtained by analytical TLC, subfraction **G3** was further chosen to be studied. Thus, a standard column chromatography was performed (300 mg, 5 g SiO_2) using CH_2Cl_2–MeOH as mobile phase (100:0 to 80:20, 2% gradient increase, 100 mL each) to afford 6 new subfractions (**G3A**-**G3F**). While quercetin (**18**, 20 mg) was obtained through a preparative TLC from subfraction **G3B** using *n*-hexane–acetone (70:30) as mobile phase, spiropedroxodiol (**17**, 22.3 mg) and *ent*-13*R*-hydroxy-3,14-dioxo-16-atisene (**17**, 77 mg) were further obtained in different subfractions.

Naringenin (**17**):

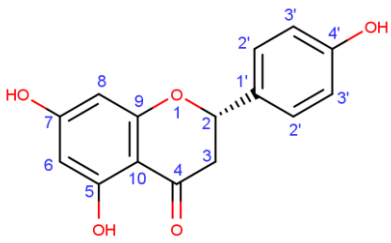

Pale yellow powder;

$[\alpha]_D^{20}$ – 18 ° (*c* 0.1, MeOH);

IR ν_{max} (MeOH) 3387, 1643, 1554, 1454, 1338, 1271 cm^{-1};

ESI-MS *m/z* (positive mode): 273 $[M + H]^+$;

^{1}H-NMR (300 MHz, Methanol-D$_4$): δ 7.23 (2H, *d*, *J* = 8.4 Hz, H-2'), 6.76 (2H, *d*, *J* = 8.4 Hz, H-3'), 5.83 (2H, *s*, H-6, H-8), 5.23 (1H, *dd*, *J* = 13.0, 3.0 Hz, H-2), 3.02 (1H, *dd*, *J* = 17.1, 13.0 Hz, H-3α), 2.60 (1H, *dd*, *J* = 17.1, 3.0 Hz, H-1β) ppm;

^{13}C-NMR (75 MHz, Methanol-D$_4$): δ 196.4 (C-4), 166.9 (C-7), 164.0 (C-5), 163.4 (C-9), 157.8 (C-4'), 129.6 (C-1'), 127.7 (C-2'), 114.9 (C-3'), 101.9 (C-10), 95.7 (C-6), 94.8 (C-8), 79.0 (C-2), 42.6 (C-3) ppm.

Quercetin (**18**):

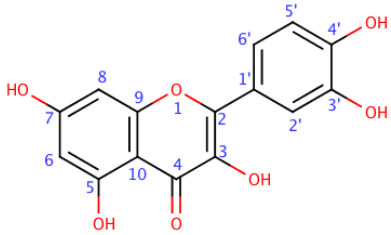

Dark yellow powder;

IR ν_{max} (MeOH) 3406, 1645, 1633, 1317, 1203 cm^{-1};

ESI-MS *m/z* (positive mode): 303 $[M + H]^+$;

^{1}H-NMR (300 MHz, DMSO-D$_6$): δ 7.67 (1H, *d*, *J* = 1.6 Hz, H-2'), 7.54 (1H, *dd*, *J* = 8.5, 1.6 Hz, H-6'), 6.88 (1H, *d*, *J* = 8.5 Hz, H-5'), 6.40 (1H, *d*, *J* = 1.2 Hz, H-8), 6.18 (1H, *d*, *J* = 1.1 Hz, H-6) ppm;

^{13}C-NMR (75 MHz, DMSO-D$_6$): δ 175.9 (C-4), 164.0 (C-7), 160.8 (C-5), 156.2 (C-9), 147.8 (C-2), 146.8 (C-4'), 135.8 (C-3), 145.1 (C-3'), 122.0 (C-1'), 120.1 (C-6'), 115.7 (C-2'), 115.1 (C-5'), 103.1 (C-10), 98.2 (C-8), 93.4 (C-6) ppm.

7.2. Generation of a small library of helioscopinolide E derivatives

7.2.1. Synthesis of helioscopinolide E oxime

To 250 mg (1 eq.) of helioscopinolide E (**15**) dissolved in dry pyridine (2.5 mL) was added 276.2 mg (5 eq.) of hydroxylamine hydrochloride. The mixture was then stirred at room temperature overnight until the reaction was complete (as seen by analytical TLC, mobile phase *n*-hexane–EtOAc, 70:30). The reaction was evaporated under reduced pressure and purified by column chromathography using *n*-hexane–EtOAc (100:0 to 50:50) until recovery of the reaction product.

Helioscopinolide E oxime (**19**):

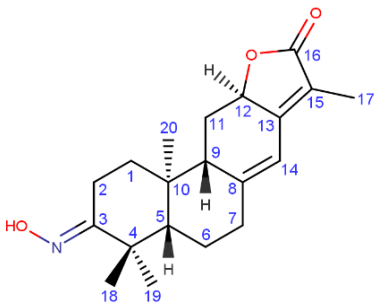

Amorphous white powder, 95 %;

ESI-MS (positive mode): *m/z* 330 $[M + H]^+$;

^{1}H-NMR (400 MHz, CDCl$_3$): δ 6.31 (1H, *s*, H-14), 4.88 (1H, *dd*, *J* = 12.7, 5.5 Hz, H-12), 3.26 (1H, *ddd*, *J* = 14.8, 4.6, 3.3 Hz, H-2α), 2.57 (1H, *d*, *J* = 5.7 Hz, H-7α), 2.53 (1H, *d*, *J* = 5.9 Hz, H-7β), 2.26-2.12 (2H, H-1α, H-11α), 2.20 (1H, *d*, *J* = 8.4 Hz, H-9), 2.08 (1H, *m*, H-2β), 1.95-1.83 (1H, *m*, H-6α), 1.83 (3H, *d*, *J* = 1.6 Hz, H-17), 1.56-1.52 (1H, *m*, H-5), 1.52-1.43 (1H, *m*, H-6β, H-11β), 1.33 (1H, *dt*, *J* = 12.7, 4.6 Hz, H-1β), 1.20 (3H, *s*¸ H-19), 1.09 (3H, *s*, H-18), 1.04 (3H, *s*, H-20) ppm;

^{13}C-NMR (101 MHz, CDCl$_3$): 175.2 (C-16), 166.3 (C-3), 155.9 (C-13), 150.9 (C-8), 117.0 (C-15), 114.6 (C-14), 75.9 (C-12), 55.2 (C-5), 51.2 (C-9), 41.4 (C-4), 40.6 (C-10), 37.4 (C-1), 36.8

(C-7), 27.8 (C-11), 27.6 (C-19), 24.2 (C-18), 23.1 (C-6), 17.7 (C-2), 16.6 (C-20), 8.5 (C-17) ppm.

7.2.2. General procedure for helioscopinolide E oxime derivatives

To 50 mg (1 eq.) of **19** dissolved in dry pyridine (2.0 mL) was added 3 eq. of the desired acyl chloride. The mixture was then stirred at room temperature until the reaction was complete, as seem by analytical TLC, mobile phase *n*-hexane–EtOAc, 70:30). The reaction was then stopped, evaporated under reduced pressure (40 °C) and purified by column chromatography using *n*-hexane–EtOAc (100:0 to 50:50) to yield the desired compounds.

Helioscopinolide oxime acetate (**20**):

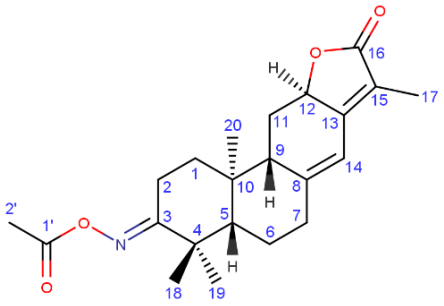

Amorphous white powder, 75.3 %;

ESI-MS (positive mode): *m/z* 372 $[M + H]^+$;

^{1}H-NMR (400 MHz, $CDCl_3$): δ 6.31 (1H, *s*, H-14), 4.86 (1H, *dd*, *J* = 13.5, 6.0 Hz, H-12), 3.13 (1H, *dt*, *J* = 15.1, 4.3 Hz, H-2α), 2.58-2.53 (2H, *m*, H-7α, H-7β), 2.51 (1H, *dd*, *J* = 13.2, 5.5 Hz, H-11α), 2.31 (1H, *ddd*, *J* = 15.1, 13.2, 5.3 Hz, H-2β), 2.20 (1H, *d*, *J* = 8.4 Hz, H-9), 2.18 (3H, *s*, H-2'), 2.07 (1H, *ddd*, J = 13.6, 4.4 Hz, H-1α), 1.94-1.86 (1H, *m*, H-6α), 1.83 (3H, *d*, *J* = 1.6 Hz, H-17), 1.55 (1H, *m*, H-5), 1.53-1.47 (1H, *m*, H-6β, H-11β), 1.39 (1H, *dt*, *J* = 13.1, 4.9 Hz, H-1β), 1.29 (3H, *s*¸ H-19), 1.15 (3H, *s*, H-18), 1.04 (3H, *s*, H-20) ppm;

^{13}C-NMR (101 MHz, $CDCl_3$): 175.2 (C-16), 171.7 (C-1'), 169.5 (C-3), 155.7 (C-13), 150.4 (C-8), 117.1 (C-15), 114.8 (C-14), 75.8 (C-12), 55.2 (C-5), 51.0 (C-9), 41.6 (C-4), 41.2 (C-10), 37.6 (C-1), 36.7 (C-7), 27.8 (C-11), 27.5 (C-19), 24.1 (C-6), 20.1 (C-18), 20.0 (C-2), 19.9 (C-2'), 16.7 (C-20), 8.5 (C-17) ppm.

Helioscopinolide oxime butanoate (**21**):

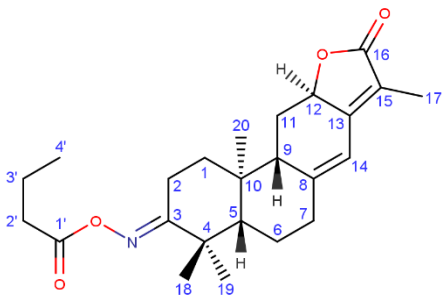

Amorphous white powder, 58.0 %;

ESI-MS (positive mode): *m/z* 400 $[M + H]^+$;

^{1}H-NMR (400 MHz, $CDCl_3$): δ 6.31 (1H, *s*, H-14), 4.86 (1H, *ddd*, *J* = 13.4, 6.2, 1.8 Hz, H-12), 3.11 (1H, *dt*, *J* =

15.1, 4.5 Hz, H-2α), 2.58-2.53 (2H, *m*, H-7α, H-7β), 2.51 (1H, *dd*, *J* = 13.6, 6.0 Hz, H-2β), 2.41 (2H, *t*, *J* = 7.4 Hz, H-2'), 2.31 (1H, *ddd*, *J* = 15.1, 13.0, 5.3 Hz, H-11β), 2.21 (1H, *d*, *J* = 8.1 Hz, H-9), 2.06 (1H, *ddd*, J = 13.1, 4.7 Hz, H-1α), 1.94 (1H, *m*, H-6α), 1.83 (3H, *d*, *J* = 1.6 Hz, H-17), 1.72 (2H, *h*, *J* = 7.4 Hz, H-3'), 1.60 (1H, *m*, H-5), 1.62-1.53 (2H, *m*, H-6β, H-11β), 1.45 (1H, *dt*, *J* = 13.4, 4.1 Hz, H-1β), 1.30 (3H, *s*¸ H-19), 1.15 (3H, *s*, H-18), 1.04 (3H, *s*, H-20), 0.99 (3H, *t*, *J* = 7.4 Hz, H-4') ppm;

^{13}C-NMR (101 MHz, $CDCl_3$): 175.2 (C-16), 173.7 (C-2), 171.7 (C-1'), 155.7 (C-13), 150.5 (C-8), 117.1 (C-15), 114.8 (C-14), 75.8 (C-12), 55.2 (C-5), 51.0 (C-9), 41.8 (C-4), 41.2 (C-10), 37.6 (C-1), 36.7 (C-7), 35.1 (C-2'), 27.8 (C-11), 27.6 (C-19), 24.1 (C-6), 23.4 (C-18), 20.4 (C-2), 18.5 (C-3'), 16.7 (C-20), 13.9 (C-4'), 8.5 (C-17) ppm.

Helioscopinolide oxime benzoate (**22**):

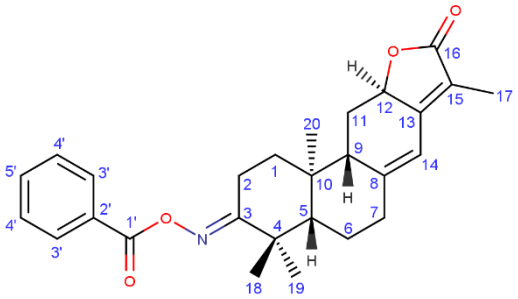

Amorphous white powder, 70.0 %;

ESI-MS (positive mode): *m/z* 434 $[M + H]^+$;

^{1}H-NMR (400 MHz, $CDCl_3$): δ 8.07 (2H, *d*, *J* = 7.1, H-3'), 7.61 (1H, *t*, *J* = 7.4 Hz, 4'-OMe), 7.49 (2H, *t*, *J* = 7.5 Hz, H-4'), 6.32 5(1H, *s*, H-14), 4.89 (1H, *ddd*, *J* = 13.6, 6.2, 1.8 Hz, H-12), 3.27 (1H, *dt*, *J* = 15.2, 4.4 Hz, H-2α), 2.63-2.54 (2H, *m*, H-7α, H-7β), 2.64-2.47 (1H, *m*, H-11α), 2.47 (1H, *ddd*, *J* = 15.1, 12.8, 5.7 Hz, H-2β), 2.25 (1H, *br d*, *J* = 8.1 Hz, H-9), 2.13 (1H, *ddd*, J = 13.1, 4.8 Hz, H-1α), 2.02-1.89 (1H, *m*, H-6α), 1.86 (3H, *d*, *J* = 1.6 Hz, H-17), 1.60 (1H, *m*, H-5), 1.60-1.54 (2H, *m*, H-6β, H-11β), 1.45 (1H, *dt*, *J* = 13.4, 4.3 Hz, H-1β), 1.41 (3H, *s*¸ H-19), 1.24 (3H, *s*, H-18), 1.09 (3H, *s*, H-20) ppm;

^{13}C-NMR (101 MHz, $CDCl_3$): 175.2 (C-16), 175.0 (C-2), 164.3 (C-1'), 155.7 (C-13), 150.5 (C-8), 133.3 (4'-OMe), 130.2 (C-2'), 129.5 (C-3'), 128.7 (C-4'), 117.1 (C-15), 114.8 (C-14), 75.8 (C-12), 55.2 (C-5), 51.0 (C-9), 41.9 (C-4), 41.2 (C-10), 37.6 (C-1), 36.7 (C-7), 27.8 (C-11), 27.6 (C-19), 24.1 (C-6), 23.5 (C-18), 20.5 (C-2), 16.7 (C-20), 8.5 (C-17) ppm.

Helioscopinolide oxime furoate (**23**):

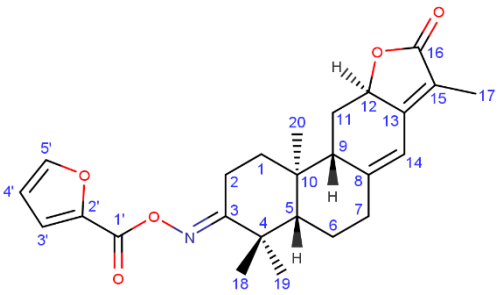

Amorphous white powder, 61.0 %;

ESI-MS (positive mode): *m/z* 424 $[M + H]^+$;

^{1}H-NMR (400 MHz, $CDCl_3$): δ 7.62 (1H, *dd*, *J* = 1.8, 0.8 Hz, H-5'), 7.25 (1H, *dd*, *J* = 3.5, 0.9 Hz, H-3'), 6.54 (1H, *dd*, *J* = 3.5, 1.7 Hz, H-4'), 6.32 (1H, *s*, H-14), 4.88 (1H, *ddd*, *J* = 13.3, 6.2, 1.8 Hz, H-12), 3.24 (1H, *dt*, *J* = 15.1, 4.5 Hz, H-2α), 2.60-2.56 (2H, *m*, H-7α, H-7β), 2.52-2.48 (1H, *m*, H-11α), 2.43 (1H, *ddd*, *J* = 15.1, 13.2, 5.6 Hz, H-2β), 2.23 (1H, *br d*, *J* = 8.2 Hz, H-9), 2.11 (1H, *ddd*, J = 12.9, 4.6, 0.6 Hz, H-1α), 1.97-1.89 (1H, *m*, H-6α), 1.84 (3H, *d*, *J* = 1.6 Hz, H-17), 1.60 (1H, *dd*, *J* = 8.6, 6.9 Hz, H-5), 1.62-1.54 (2H, *m*, H-6β, H-11β), 1.45 (1H, *dt*, *J* = 13.3, 5.2 Hz, H-1β), 1.37 (3H, *s*, H-19), 1.21 (3H, *s*, H-18), 1.07 (3H, *s*, H-20) ppm;

^{13}C-NMR (101 MHz, $CDCl_3$): 175.2 (C-16), 175.1 (C-2), 166.7 (C-1'), 155.7 (C-13), 150.4 (C-8), 134.0 (4'-OMe), 132.8 (C-3'), 132.2 (C-2'), 128.0 (C-4'), 117.1 (C-15), 114.8 (C-14), 75.8 (C-12), 55.2 (C-5), 51.0 (C-9), 41.9 (C-4), 41.2 (C-10), 37.6 (C-1), 36.6 (C-7), 27.8 (C-11), 27.6 (C-19), 24.1 (C-6), 23.5 (C-18), 20.4 (C-2), 16.7 (C-20), 8.5 (C-17) ppm.

Helioscopinolide oxime thiophenate (**24**):

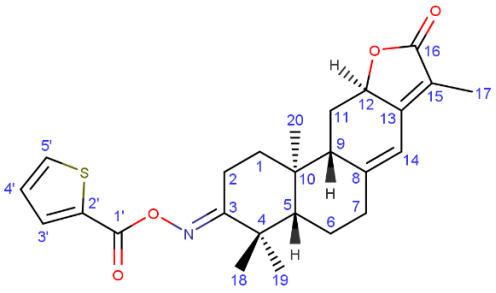

Amorphous white powder, 72.0 %;

ESI-MS (positive mode): *m/z* 440 $[M + H]^+$;

^{1}H-NMR (400 MHz, $CDCl_3$): δ 7.88 (1H, *dd*, *J* = 3.8, 1.3 Hz, H-5'), 7.60 (1H, *dd*, *J* = 5.0, 1.3 Hz, H-3'), 7.15 (1H, *dd*, *J* = 5.0, 3.7 Hz, H-4'), 6.33 (1H, *s*, H-14), 4.87 (1H, *dd*, *J* = 13.1, 5.2 Hz, H-12), 3.23 (1H, *dt*, *J* = 15.1, 5.3 Hz, H-2α), 2.58-2.54 (2H, *m*, H-7α, H-7β), 2.55-2.47 (1H, *m*, H-11α), 2.45 (1H, *ddd*, *J* = 15.1, 13.1, 5.3 Hz, H-2β), 2.23 (1H, *br d*, *J* = 8.1 Hz, H-9), 2.13 (1H, *ddd*, *J* = 13.1, 4.6 Hz, H-1α), 1.96-1.84 (1H, *m*, H-6α), 1.83 (3H, *s*, H-17), 1.60 (1H, *dd*, *J* = 8.0, 5.5 Hz, H-5), 1.60-1.54 (2H, *m*, H-6β, H-11β), 1.45 (1H, *dt*, *J* = 13.4, 5.9 Hz, H-1β), 1.37 (3H, *s*¸ H-19), 1.22 (3H, *s*, H-18), 1.07 (3H, *s*, H-20) ppm;

^{13}C-NMR (101 MHz, $CDCl_3$): δ 175.2 (C-16), 174.8 (C-2), 160.0 (C-1'), 155.7 (C-13), 150.4 (C-8), 134.0 (4'-OMe), 132.8 (C-3'), 132.2 (C-2'), 128.0 (C-4'), 117.1 (C-15), 114.8 (C-14),

75.8 (C-12), 55.2 (C-5), 51.0 (C-9), 41.8 (C-4), 41.2 (C-10), 37.6 (C-1), 36.6 (C-7), 27.8 (C-11), 27.6 (C-19), 24.0 (C-6), 23.5 (C-18), 20.4 (C-2), 16.7 (C-20), 8.5 (C-17) ppm.

7.3. Generation of a small library of naringenin derivatives

7.3.1. General preparation of naringenin hydrazones

7.3.1.1. Reaction between naringenin and hydrazines

To 1 eq. of naringenin (**17**) dissolved in ethanol was added 2 eq. of the desired hydrazine (NH_2-NH-R) and 0.01 eq. of 10% acetic acid in ethanol. Following, the mixture was stirred under N_2, at room temperature, until the total disappearance of the starting compound (by TLC). Then, the solvent was evaporated, the residue extracted with ethyl acetate, dried (with Na_2SO_4) and further purified by preparative TLC (CH_2Cl_2–MeOH 98:2) to obtain the corresponding hydrazone (C=N-NH-R).

4',5,7-trihydroxybenzopyran-4-(5-bromopyridin-2-yl)-hydrazone (**25**):

To 100 mg (0.370 mmol) of naringenin (**1**) dissolved in ethanol was added 139.1 mg (0.740 mmol) of 5-bromo-2-hydrazinepyridine, and the mixture was kept stirring under reflux for 24 h. Following, after evaporation of the solvent the product was purified by a column chromatography using CH_2Cl_2–acetone (100:0 to 80:20) to obtain 98 mg (0.221 mmol, 59.7% yield) of **25** as a brown amorphous powder.

ESI-MS (positive mode): *m/z* 443 $[M + H]^+$;

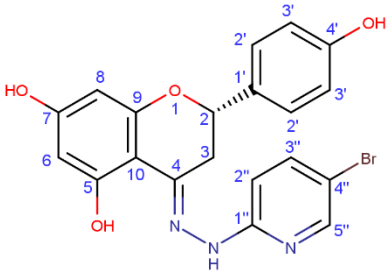

^{1}H-NMR (300 MHz, Methanol-D$_4$): δ 8.15 (1H, *d*, *J* = 2.4 Hz, H-5"), 7.71 (1H, *dd*, *J* = 9.0, 2.5 Hz, H-3"), 7.31 (2H, *d*, *J* = 8.5 Hz, H-2'), 6.81 (3H, *m*, H-3', H-2"), 5.96 (1H, *dd*, *J* = 2.4, 0.8 Hz, H-8), 5.90 (1H, *dd*, *J* = 2.4, 0.8 Hz, H-6), 5.00 (1H, *dd*, *J* = 12.2, 3.1 Hz, H-2), 3.22 (1H, *dd*, *J* = 16.8, 3.1 Hz, H-3β), 2.79 (1H, *dd*, *J* = 16.8, 12.2 Hz, H-3α) ppm;

^{13}C NMR (75 MHz, Methanol-D$_4$): δ 161.9 (C-7), 161.3 (C-5), 160.1 (C-9), 158.8 (C-4'), 156.7 (C-5"), 149.8 (C-1"), 149.6 (C-4), 141.7 (C-3"), 132.0 (C-1'), 128.9 (C-2'), 116.3 (C-3'), 110.6 (C-4"), 109.7 (C-2"), 100.2 (C-10), 97.8 (C-6), 96.4 (C-8, 77.9 (C-2), 33.1 (C-3) ppm.

4',5,7-trihydroxybenzopyran-4-phenylhydrazone (**26**):

Naringenin (100 mg, 0.370 mmol) was dissolved in ethanol in a round-bottomed flask. Following, 59.4 mg (0.550 mmol, 54 μM) of phenylhydrazine was added and a catalytic amount of acetic acid. The mixture was allowed to reflux overnight under constant stirring. After evaporation of the solvent, the product was purified by a column chromatography using CH_2Cl_2–MeOH (100:0 to 95:5) to obtain compound **26** (60 mg, 0.167 mmol) as an amorphous orange-brownish powder, yield 45.0%.

ESI-MS (positive mode): *m/z* 363 $[M + H]^+$;

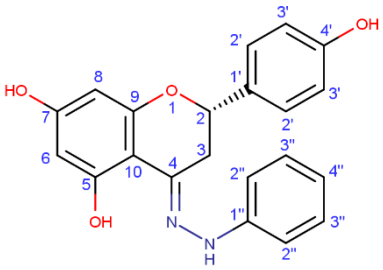

^{1}H-NMR (300 MHz, Methanol-D$_4$): δ 7.31 (2H, *d*, *J* = 8.4 Hz, H-2'), 7.19 (2H, *d*, *J* = 7.8 Hz, H-3"), 6.97 (2H, *d*, *J* = 7.8 Hz, H-2"), 6.82 (2H, *d*, *J* = 8.4 Hz, H-3'), 6.77 (1H, *d*, *J* = 7.8 Hz, H-4"), 6.00 (1H, *d*, *J* = 2.3 Hz, H-8), 5.93 (1H, *d*, *J* = 2.3 Hz, H-6), 4.94 (1H, *dd*, *J* = 12.0, 2.6 Hz, H-2), 3.20 (1H, *dd*, *J* = 16.8, 2.6 Hz, H-3β), 2.72 (1H, *dd*, *J* = 16.8, 12.0 Hz, H-3α) ppm;

^{13}C NMR (75 MHz, Methanol-D$_4$): δ 160.9 (C-7), 160.7 (C-5), 159.6 (C-9), 158.6 (C-4'), 146.8 (C-1"), 146.4 (C-4), 132.2 (C-1'), 130.2 (C-3"), 128.8(C-2'), 120.9 (C-4"), 116.1 (C-3'), 113.6 (C-2"), 100.6 (C-10), 97.9 (C-6), 96.1 (C-8), 77.8 (C-2), 32.8 (C-3) ppm.

4',5,7-trihydroxybenzopyran-4-(pyrazin-2-yl)-hydrazone (**27**):

To 100 mg (0.370 mmol) of naringenin was added 81.5 mg (0.740 mmol) of 2-hydrazinopyrazine and a catalytic amount of acid. After 24 h under constant stirring and reflux, the solvent was evaporated and the residue purified by column chromatography using CH_2Cl_2–MeOH (100:0 to 90:10) to obtain 68 mg (0.1855 mmol, 50.1% yield) of **27** an amorphous, brownish powder.

ESI-MS (positive mode): *m/z* 404 $[M + H + K]^+$;

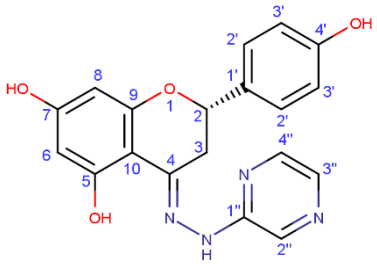

^{1}H-NMR (300 MHz, DMSO-D$_6$): δ 8.14 (1H, *d*, *J* = 1.5 Hz, H-2"), 8.07 (1H, *dd*, *J* = 2.7, 1.5 Hz, H-3"), 7.87 (1H, *d*, *J* = 2.7 Hz, H-4"), 7.25 (2H, *br d*, *J* = 8.6 Hz, H-2'), 6.72 (2H, *br d*, *J* = 8.6 Hz, H-3'), 5.83 (1H, *d*, *J* = 2.2 Hz, H-8), 5.77 (1H,

d, *J* = 2.2 Hz, H-6), 5.01 (1H, *dd*, *J* = 12.0, 3.0 Hz, H-2), 3.20 (1H, *dd*, *J* = 17.0, 3.0 Hz, H-3β), 2.80 (1H, *dd*, *J* = 17.0, 12.0 Hz, H-3α) ppm;

^{13}C NMR (75 MHz, DMSO-D$_6$): δ 160.4 (C-7), 159.9 (C-5), 158.3 (C-9), 157.6 (C-4'), 151.8 (C-1"), 148.1 (C-4), 142.3 (C-3"), 134.9 (C-4"), 132.0 (C-2"), 130.0 (C-1'), 128.2 (C-2'), 115.2 (C-3'), 98.7 (C-10), 96.8 (C-6), 95.0 (C-8), 76.0 (C-2), 33.1 (C-3) ppm.

7.3.1.2. Preparation of naringenin hydrazone (28).

To naringenin (**17**, 400 mg, 1.469 mmol) was dissolved in a solution of hydrazine monohydrate (2 mL, 63.7 mmol) and was kept stirring 24 h at 50 ºC, under N_2. The mixture was evaporated, and the residue was purified by column chromatography (*n*-hexane–EtOAc, 100:0 to 0:100) to afford 29 mg (1.024 mmol, 70% yield) of *4',5,7-trihydroxybenzopyran-4-hydrazone* (**28**) as an amorphous orange powder.

ESI-MS (positive mode): *m/z* 328 $[M + H + ACN]^+$;

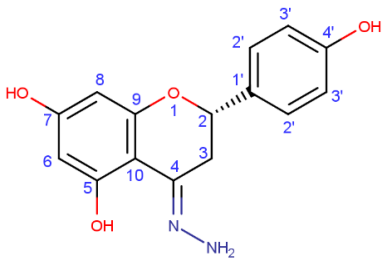

^{1}H-NMR (300 MHz, Methanol-D$_4$): *δ* 7.24 (2H, *d*, *J* = 8.5 Hz, H-2'), 6.77 (2H, *d*, *J* = 8.5 Hz, H-3'), 5.88 (2H, *s*, H-6, H-8), 4.98 (1H, *dd*, *J* = 12.3, 2.9 Hz, H-2), 3.52 (1H, *dd*, *J* = 17.3, 2.9 Hz, H-3β), 2.74 (1H, *dd*, *J* = 17.3, 12.3 Hz, H-3α) ppm;

^{13}C NMR (75 MHz, Methanol-D$_4$): *δ* 166.9 (C-7), 163.9 (C-5), 163.6 (C-9), 161.6 (C-4), 158.7 (C-4'), 131.9 (C-1'), 128.8 (C-2'), 116.2 (C-3'), 99.9 (C-10), 97.6 (C-6), 96.2 (C-8), 78.4 (C-2), 33.1 (C-3) ppm.

7.3.1.3. Preparation of compounds 29-36.

Following, to 1 eq. of **28** in ethanol was added 1.5 eq. of the desired aldehyde. The mixture was kept stirring, under N_2, at 50 ºC until no starting product is detectable by TLC. After evaporation of the solvent under vacuum (at 40 ºC), the residue was extracted with ethyl acetate, dried with sodium sulphate and purified by preparative TLC (CH_2Cl_2–MeOH 99:1 to 95:5) to obtain the desired azine (C=N-N=CH-R_2).

4',5,7-trihydroxybenzopyran-4-(*N*-methylpyrrol-2-yl)-azine (29):

To 50 mg (0.175 mmol) of naringenin hydrazone (**28**) dissolved in ethanol was added 38 mg (0.350 mmol) of *N*-methyl-2-pyrrolecarboxaldehyde. After keeping the mixture stirring under reflux for 80 h, the solvent was evaporated under reduced pressure and the product was purified by a preparative TLC using CH_2Cl_2–acetone (80:20) to recover 36 mg (0.095 mmol, 54.5% yield) of **29** an amorphous green powder.

ESI-MS (positive mode): *m/z* 378 $[M + H]^+$;

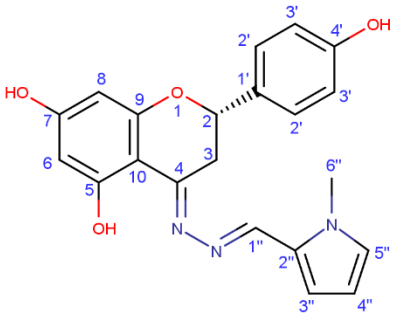

^{1}H-NMR (300 MHz, Acetone-D$_6$): δ 8.45 (1H, *s*, H-1"), 7.39 (2H, *d*, *J* = 8.4 Hz, H-2'), 6.96 (1H, *t*, *J* = 2.5 Hz, H-4"), 6.89 (2H, *d*, *J* = 8.4 Hz, H-3'), 6.68 (1H, *dd*, *J* = 3.9, 2.5 Hz, H-3"), 6.15 (1H, *dd*, *J* = 3.9, 2.5 Hz, H-5"), 6.02 (1H, *d*, *J* = 2.3 Hz, H-8), 5.96 (1H, *d*, *J* = 2.3 Hz, H-6), 5.14 (1H, *dd*, *J* = 12.2, 3.1 Hz, H-2), 3.92 (3H, *s*, Me-6"), 3.77 (1H, *dd*, *J* = 17.4, 3.1 Hz, H-3β), 3.03 (1H, *dd*, *J* = 17.4, 12.2 Hz, H-3α) ppm;

^{13}C NMR (75 MHz, Acetone-D$_6$): δ 164.6 (C-4), 163.5 (C-7), 163.1 (C-5), 161.1 (C-9), 158.4 (C-4'), 151.5 (C-1"), 131.8 (C-1'), 130.5 (C-4"), 128.9 (C-2'), 128.6 (C-2"), 119.3 (C-3"), 116.1 (C-3'), 109.7 (C-5"), 100.0 (C-10), 97.4 (C-6), 95.8 (C-8), 78.0 (C-2), 37.3 (C-6"), 33.6 (C-3) ppm.

4',5,7-trihydroxybenzopyran-4-(indol-3-yl)-azine (30):

To 50 mg (0.175 mmol) of compound **28** dissolved in ethanol was added 50.75 mg (0.350 mmol) of indole-3-carboxaldehyde. The mixture was kept stirring under reflux for 96 h, the solvent was evaporated under reduced pressure and the product was further purified by means of column chromatography, using CH_2Cl_2–acetone (100:0 to 90:10), and recovering 70 mg (0.169 mmol, 97.1% yield) of compound **30** as an amorphous brown powder.

ESI-MS (positive mode): *m/z* 414 $[M + H]^+$;

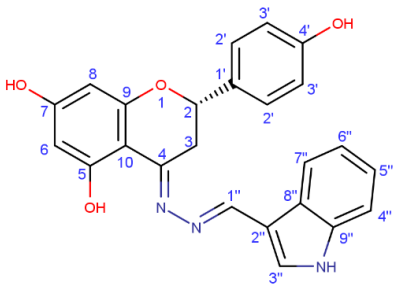

^{1}H-NMR (300 MHz, Methanol-D$_4$): δ 8.66 (1H, *s*, H-3"), 8.15 (1H, *d*, *J* = 7.7 Hz, H-7"), 7.67 (1H, *s*, H-1"), 7.41 (1H, *d*, *J* = 8.0 Hz, H-4"), 7.30 (2H, *d*, *J* = 8.5 Hz, H-2'), 7.19 (1H, *t*, *J* = 7.2 Hz, H-5"), 7.11 (1H, *t*, *J* = 7.0 Hz, H-6"), 6.83

(1H, *d*, *J* = 8.5 Hz, H-3'), 5.97 (1H, *d*, *J* = 2.3 Hz, H-6), 5.91 (1H, *d*, *J* = 2.2 Hz, H-8), 5.03 (1H, *dd*, *J* = 12.2, 3.0 Hz, H-2), 3.89 (1H, *dd*, *J* = 17.2, 3.0 Hz, H-3β), 2.99 (1H, *dd*, *J* = 17.2, 12.2 Hz, H-3α) ppm;

^{13}C NMR (75 MHz, Methanol-D$_4$): δ 164.0 (C-4), 163.5 (C-7), 163.4 (C-5), 161.4 (C-9), 158.7 (C-4'), 156.3 (C-3"), 139.0 (C-9"), 133.2 (C-1"), 132.2 (C-1'), 129.0 (C-2'), 126.1 (C-2"), 124.2 (C-5"), 123.3 (C-7"), 122.2 (C-6"), 116.3 (C-3'), 114.2 (C-8"), 112.7 (C-4"), 100.3 (C-10), 97.6 (C-6), 96.1 (C-8), 78.7 (C-2), 34.0 (C-3) ppm.

4',5,7-trihydroxybenzopyran-4-(3-methoxybenzyl)-azine (**31**):

To 40 mg (0.140 mmol) of compound **28** dissolved in ethanol was added 38.1 mg (0.280 mmol) of 3-methoxy benzaldehyde and a catalytic amount of acid. The mixture was kept stirring under reflux for 21 h, the solvent was evaporated under reduced pressure and the product was further purified by means of preparative TLC using CH_2Cl_2–acetone (90:10) to yield 13 mg (0.033 mmol, 13.3%) of **31** as an amorphous brown powder.

ESI-MS (positive mode): *m/z* 405 $[M + H]^+$;

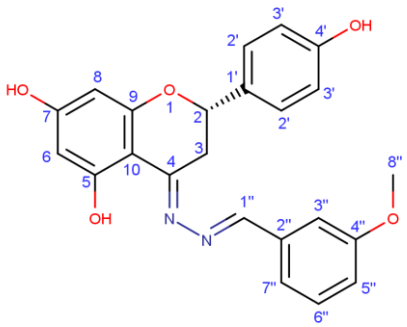

^{1}H-NMR (300 MHz, Acetone-D$_6$): δ 8.57 (1H, *s*, H-1"), 7.45 (1H, *d*, *J* = 6.9 Hz, H-7"), 7.44 (1H, *s*, H-3"), 7.41 (1H, *d*, *J* = 8.5 Hz, H-2'), 7.37 (1H, *t*, *J* = 6.9 Hz, H-6"), 7.05 (1H, *m*, H-5"), 6.02 (2H, *d*, *J* = 8.5 Hz, H-3'), 5.98 (1H, *d*, *J* = 2.3 Hz, H-6), 5.98 (1H, *d*, *J* = 2.3 Hz, H-8), 5.19 (1H, *dd*, *J* = 12.3, 3.0 Hz, H-2), 3.91 (1H, *dd*, *J* = 17.4, 3.0 Hz, H-3β), 3.82 (3H, *s*, Me-8"), 3.05 (1H, *dd*, *J* = 17.4, 12.3 Hz, H-3α) ppm;

^{13}C NMR (75 MHz, Acetone-D$_6$): δ 167.3 (C-4), 164.2 (C-7), 163.8 (C-5), 163.5 (C-9), 161.7 (C-4"), 158.6 (C-4'), 158.5 (C-1"), 136.8 (C-2"), 131.6 (C-1'), 130.8 (C-6"), 129.0 (C-2'), 122.0 (C-7"), 117.9 (C-5"), 116.1 (C-3'), 113.8 (C-3"), 99.8 (C-10), 97.45 (C-6), 96.0 (C-8), 55.6 (C-8"), 78.06 (C-2), 33.4 (C-3) ppm.

4',5,7-trihydroxybenzopyran-4-(4-methoxybenzyl)-azine (32):

To a solution of compound **28** (50 mg, 0.175 mmol) in ethanol (5 mL) it was added *p*-anisaldehyde (21 μL, 0.175 mmol). Then, it was added to the mixture a catalytic amount of acid. The mixture was kept stirring under N_2, at 50 ºC, during 10 h. The residue was purified

by column chromatography using *n*-hexane–EtOAc (100:0 to 0:100) and preparative TLC with CH_2Cl_2/MeOH (90:10) to afford 38 mg of compound **32**, an amorphous yellow powder (0.0937 mmol, 53.5 % yield).

ESI-MS (negative mode): *m/z* 403 $[M - H]^-$;

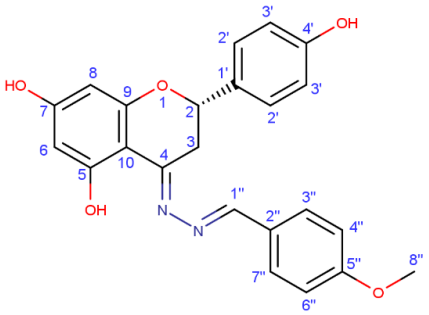

^{1}H-NMR (300 MHz, Methanol-D$_4$): δ 8.49 (1H, *s*, H-1”), 7.70 (2H, *d*, *J* = 8.6 Hz, H-3’), 7.29 (2H, *d*, *J* = 8.4 Hz, H-2’), 6.93 (2H, *d*, *J* = 8.6 Hz, H-4”), 6.86 (2H, *d*, *J* = 8.4 Hz, H-3”), 5.89 (1H, *d*, *J* = 2.2 Hz, H-8), 5.85 (1H, *d*, *J* = 2.2 Hz, H-6), 5.00 (1H, *dd*, *J* = 12.0, 3.1 Hz, H-2), 3.82 (1H, *dd*, *J* = 17.1, 3.1 Hz, H-3β), 3.80 (3H, *s*, Me-6”), 2.90 (1H, *dd*, *J* = 17.1, 12.0 Hz, H-3α) ppm;

^{13}C NMR (75 MHz, Methanol-D$_4$): δ 166.5 (C-4), 164.2 (C-5”), 163.7 (C-7), 163.6 (C5), 161.9 (C-9), 159.7 (C-1”), 158.8 (C-4’), 132.0 (C-2”), 131.9 (C-1’), 129.0 (C-2’), 128.3 (C-3”), 116.3 (C-4”), 115.3 (C-3’), 100.0 (C-10), 97.7 (C-6), 96.3 (C-8), 78.6 (C-2), 55.9 (Me-6”), 33.9 (C-3) ppm.

4’,5,7-trihydroxybenzopyran-4-(4-*N*,*N*-dimethylaminobenzyl)-azine (**33**):

To a solution of naringenin hydrazone (**28**, 50 mg, 0.175 mmol) in 5 mL of ethanol was added 36.06 mg of 4-(dimethylamino) benzaldehyde (0.175 mmol). The mixture was kept stirring, under N_2, overnight at room temperature. The reside was then purified by column chromatography (*n*-hexane–EtOAc, 100:0 to 0:100) and preparative TLC with *n*-hexane–EtOAc (1:1) resulting in 52 mg of compound **33** as an amorphous yellow powder (0.125 mmol, 71.4% yield).

ESI-MS (negative mode): *m/z* 478 $[M + K - 2H]^-$;

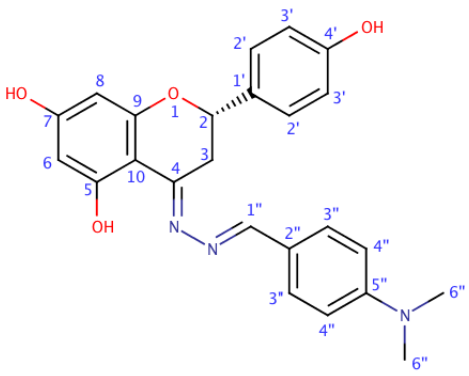

^{1}H-NMR (300 MHz, Methanol-D$_4$): δ 8.35 (1H, *s*, H-1”), 7.66 (2H, *d*, *J* = 9.0 Hz, H-4”), 7.34 (2H, *d*, *J* = 8.5 Hz, H-3’), 6.84 (2H, *d*, *J* = 8.5 Hz, H-2’), 6.76 (2H, *d*, *J* = 9.0 Hz, H-3”), 5.93 (1H, *d*, *J* = 2.3 Hz, H-8), 5.91 (1H, *d*, *J* = 2.3 Hz, H-6), 5.07 (1H, *dd*, *J* = 12.3, 2.9 Hz, H-2), 3.88 (1H, *dd*, *J* = 17.4, 2.9 Hz, H-3β), 3.03

(6H, *s*, Me-6”), 2.94 (1H, *dd*, *J* = 17.4, 12.3 Hz, H-3α) ppm;

^{13}C NMR (75 MHz, Methanol-D$_4$): δ 166.0 (C-4), 163.5 (C-7), 162.6 (C-5), 163.7 (C-9), 160.5 (C-1”), 158.8 (C-4’, C-5”), 132.2 (C-1’), 131.1 (C-3”), 129.3 (C-3”), 128.9 (C-2’), 128.1 (C-2”), 116.3 (C-3’), 112.8 (C-4”), 100.4 (C-10), 97.3 (C-6), 93.1 (C-8), 78.7 (C-2), 40.3 (Me-6”), 32.5 (C-3) ppm.

4’,5,7-trihydroxybenzopyran-4-(indol-2-yl)-azine (34):

To a solution of naringenin hydrazone (**28**, 50 mg, 0.175 mmol) in ethanol (5 mL) was added 25.3 mg of 3H-indole-2-carbaldehyde (0.175 mmol). Then, it was added a catalytic amount of acid and the mixture was kept stirring under N_2, overnight, at room temperature. It was purified the residue by column chromatography (*n*-hexane–EtOAc, 100:0 to 0:100) resulting in 39 mg of compound **11** as an amorphous yellow powder (0.0938 mmol, yield 53.6%).

ESI-MS (negative mode): *m/z* 413 [M - H]$^-$;

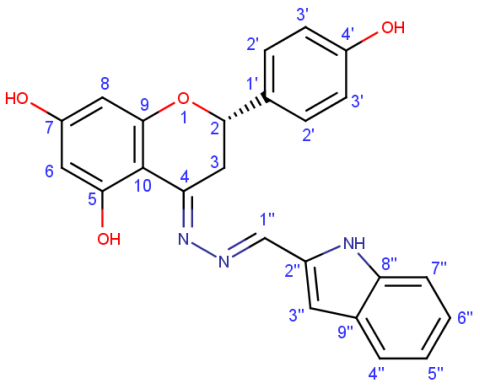

^{1}H-NMR (300 MHz, Methanol-D$_4$): δ 8.41 (1H, *s*, H-1”), 7.54 (1H, *d*, *J* = 7.6 Hz, H-7”), 7.36 (1H, *d*, *J* = 7.6 Hz, H-4”), 7.29 (2H, *d*, *J* = 8.5 Hz, H-2’), 7.18 (1H, *t*, *J* = 7.6 Hz, H-6”), 7.01 (1H, *t*, *J* = 7.6 Hz, H-5”), 6.82 (1H, *s*, H-3”), 6.81 (2H, *d*, *J* = 8.5 Hz, H-3’), 5.99 (1H, *d*, *J* = 2.3 Hz, H-6), 5.94 (1H, *d*, *J* = 2.3 Hz, H-8), 5.01 (1H, *dd*, *J* = 12.6, 3.0 Hz, H-2), 4.01 (1H, *dd*, *J* = 18.0, 3.0 Hz, H-3β), 2.90 (1H, *dd*, *J* = 18.0, 12.6 Hz, H-3α) ppm;

^{13}C NMR (75 MHz, Methanol-D$_4$): δ 167.0 (C-4), 164.1 (C-7), 163.6 (C-5), 161.9 (C-9), 158.7 (C-4’), 151.1 (C-1”), 139.8 (C-8”), 134.6 (C-2”), 132.1 (C-1’), 129.5 (C-9”), 129.0 (C-2’), 125.4 (C-6”), 122.4 (C-4”), 120.9 (C-5”), 116.2 (C-3’), 112.7 (C-7”), 110.6 (C-3”), 100.2 (C-10), 97.7 (C-6), 96.3 (C-8), 78.7 (C-2), 33.9 (C-3) ppm.

4’,5,7-trihydroxybenzopyran-4-(pyrrol-2-yl)-azine (35):

To a solution of compound **28** (50 mg, 0.175 mmol) in ethanol (5 mL) it was added 16.6 mg of pyrrole-2-carboxaldehyde (0.175 mmol). The mixture was kept stirring under N_2, during 6 h, at room temperature. The reside was then purified by column chromatography (*n*-hexane–EtOAc, 1:0 to 0:1) to yield 53 mg of compound **35**, an amorphous yellow powder (0.147 mmol, 84.0%).

ESI-MS (negative mode): *m/z* 362 $[M - H]^-$;

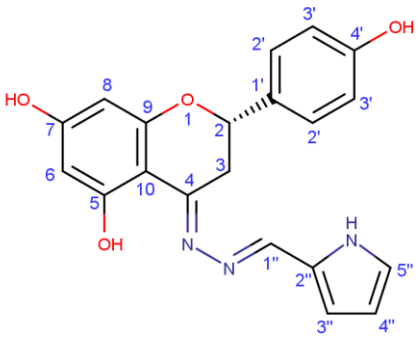

^{1}H-NMR (300 MHz, Methanol-D$_4$): *δ* 8.29 (1H, *s*, H-1”), 7.35 (2H, *d*, *J* = 8.5 Hz, H-2’), 6.95 (1H, *t*, *J* = 2.1 Hz, H-4”), 6.83 (2H, *d*, *J* = 8.6 Hz, H-3’), 6.61 (1H, *dd*, *J* = 3.6, 1.4 Hz, H-3”), 6.21 (1H, *dd*, *J* = 3.6, 2.6 Hz, H-5”), 5.95 (1H, *d*, *J* = 2.3 Hz, H-8), 5.92 (1H, *d*, *J* = 2.3 Hz, H-6), 5.07 (1H, *dd*, *J* = 12.3, 2.8 Hz, H-2), 4.98 (1H, *dd*, *J* = 18.5, 3.0 Hz, H-3β), 2.94 (1H, *dd*, *J* = 18.5, 12.3 Hz, H-3α) ppm;

^{13}C-NMR (75 MHz, Methanol-D$_4$): *δ* 165.1 (C-4), 163.6 (C-7), 163.4 (C-5), 161.6 (C-9), 158.8 (C-4’), 150.8 (C-1”), 132.2 (C-1’), 129.1 (C-2”), 129.0 (C-2’), 124.6 (C-4”), 117.3 (C-3”), 116.2 (C-3’), 110.9 (C-5”), 100.2 (C-10), 97.6 (C-6), 96.2 (C-8), 78.9 (C-2), 33.9 (C-3) ppm.

4’,5,7-trihydroxybenzopyran-4-(2-nitrobenzyl)azine (36):

40 mg (0.140 mmol) of **28** and 42.3 mg (0.280 mmol) of 2-nitrobenzaldehyde were dissolved in ethanol, and a catalytic amount of acid was added to the mixture. After stirring under reflux for 48 h, the solvent was evaporated under reduced pressure and the product was purified by column chromatography using CH_2Cl_2–acetone (100:0 to 90:10) to yield 15 mg (0.035 mmol, 25.0%) of compound **36** an amorphous yellow powder.

ESI-MS (positive mode): m/z 419 $[M + H]^+$;

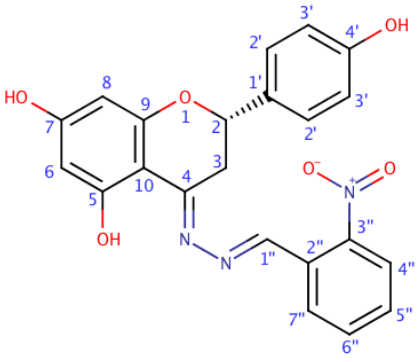

^{1}H-NMR (300 MHz, Acetone-D$_6$): δ 8.94 (1H, *s*, H-1”), 8.24 (1H, *dd*, *J* = 7.7, 1.7 Hz, H-7”), 8.07 (1H, *dd*, *J* = 7.7, 1.7 Hz, H-4”), 7.81 (1H, *td*, *J* = 7.7, 1.7 Hz, H-6”), 7.76 (1H, *dd*, *J* = 7.7, 1.7 Hz, H-5”), 7.42 (2H, *d*, *J* = 8.5 Hz, H-2’), 6.91 (2H, *d*, *J* = 8.5 Hz, H-3’), 6.03 (1H, *d*, *J* = 2.3 Hz, H-8), 5.99 (1H, *d*, *J* = 2.3 Hz, H-6), 5.23 (1H, *dd*, *J* = 12.3, 3.0 Hz, H-2), 3.91 (1H, *dd*, *J* = 12.3, 3.0 Hz, H-3β), 3.11 (1H, *dd*, *J* = 17.4, 12.3 Hz, H-3α) ppm;

^{13}C-NMR (75 MHz, Acetone-D$_6$): δ 169.3 (C-4), 162.4 (C-7), 161.6 (C-9), 160.9 (C-5), 157.3 (C-4’), 155.3 (C-1”), 149.7 (C-3”), 134.2 (C-6”), 132.4 (C-5”) 131.5 (C-1’), 130.5 (C-7”), 129.0

(C-2'), 126.0 (C-3"), 121.0 (C-5"), 115.8 (C-3'), 102.3 (C-10), 99.8 (C-6), 96.2 (C-8), 77.9 (C-2), 32.3 (C-3) ppm.

7.3.2. General preparation of naringenin carbohydrazides.

Naringenin (**17**, 1 eq.) was dissolved in a proper amount of ethanol, under stirring at room temperature. Following, the desired hydrazide (2 eq.) and a catalytic amount of acid (10% acetic acid in ethanol, 0.01 eq) were added and the mixture was kept stirring under N_2 overnight, at room temperature. The reaction was followed by TLC and, upon completion, the solvent was evaporated under vacuum at 40 ºC, the residue extracted with ethyl acetate and dried with Na_2SO_4. After evaporation of the solvent, the residue was further purified by preparative TLC to obtain the desired product (R_1=N-NH-C[=O]-R_2).

4',5,7-trihydroxybenzopyran-4-(tiophen-2-yl)-carbohydrazide (**37**):

To 5 ml ethanol was added 100 mg (0.370 mmol) of naringenin (**17**), 78.2 mg (0.550 mmol) of 2-tiophene carboxylic acid hydrazide and a catalytic amount of acid. After 24 h under constant stirring and reflux, the solvent was evaporated and the residue purified by column chromatography using CH_2Cl_2–MeOH (100:0 to 90:10) to obtain 72 mg (0.381 mmol, 53.4% yield) of **37** as an amorphous yellowish powder.

ESI-MS (positive mode): *m/z* 397 $[M + H]^+$;

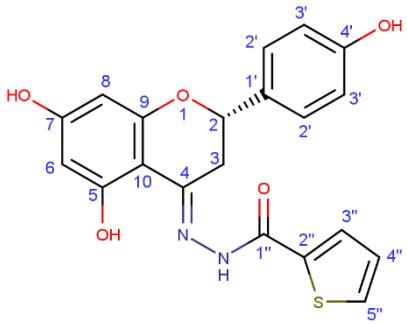

^{1}H-NMR (300 MHz, Acetone-D$_6$): δ 7.86 (1H, *dd*, *J* = 3.8, 0.7 Hz, H-5"), 7.76 (1H, *dd*, *J* = 5.0, 3.8 Hz, H-4"), 7.76 (1H, *dd*, *J* = 5.0, 0.7 Hz, H-3"), 7.40 (2H, *d*, *J* = 8.5 Hz, H-2'), 6.91 (2H, *d*, *J* = 8.5 Hz, H-3"), 6.03 (1H, *d*, *J* = 2.3 Hz, H-8), 5.97 (1H, *d*, *J* = 2.3 Hz, H-6), 5.13 (1H, *dd*, *J* = 12.4, 2.7 Hz, H-2), 3.42 (1H, *dd*, *J* = 16.9, 2.7 Hz, H-3β), 2.93 (1H, *dd*, *J* = 16.9, 12.4 Hz, H-3α) ppm;

^{13}C-NMR (75 MHz, Acetone-D$_6$): δ 162.5 (C-7), 162.4 (C-1"), 160.6 (C-5), 158.6 (C-9, C-4'), 155.1 (C-4), 138.6 (C-2"), 132.3 (C-5"), 131.0 (C-1'), 129.9 (C-3"), 128.9 (C-2'), 128.6 (C-4"), 116.3 (C-3'), 99.7 (C-10), 97.8 (C-8), 95.8 (C-6), 77.4 (C-2), 33.1 (C-3) ppm.

4',5,7-trihydroxybenzopyran-4-(furan-2-yl)-carbohydrazide (**38**):

To 100 mg (0.370 mmol) of naringenin (**17**) dissolved in ethanol was added 93.6 mg (0.750 mmol) of 2-furan carboxylic acid hydrazide and a catalytic amount of acid. After keeping the mixture stirring under reflux for 36 h, the solvent was evaporated under reduced pressure and the product was purified by column chromatography using CH_2Cl_2–MeOH (100:0 to 95:5) to yield 27 mg (0.073 mmol, 20.0%) of **38** as an amorphous brown powder.

ESI-MS (positive mode): *m/z* 381 $[M + H]^+$;

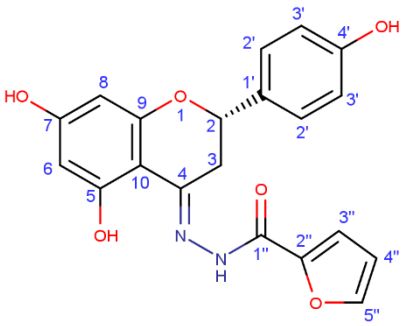

^{1}H-NMR (300 MHz, DMSO-D$_6$): δ 7.90 (1H, *d*, *J* = 1.5 Hz, H-5"), 7.32 (1H, *d*, *J* = 8.6 Hz, H-2'), 7.31 (1H, *d*, *J* = 3.0 Hz, H-3"), 6.79 (1H, *d*, *J* = 8.6 Hz, H-3'), 6.68 (1H, *dd*, *J* = 3.0, 1.5 Hz, H-4"), 5.92 (1H, *d*, *J* = 2.3 Hz, H-8), 5.86 (1H, *d*, *J* = 2.3 Hz, H-6), 5.08 (1H, *dd*, *J* = 12.3, 2.9 Hz, H-2), 3.35 (1H, *dd*, *J* = 12.3, 2.9 Hz, H-3β), 2.95 (1H, *dd*, *J* = 17.1, 12.3 Hz, H-3α) ppm;

^{13}C-NMR (75 MHz, DMSO-D$_6$): δ 161.7 (C-7), 161.6 (C-5), 159.2 (C-1"), 159.0 (C-9), 157.6 (C-4'), 155.4 (C-4), 146.4 (C-2"), 146.0 (C-5"), 129.8 (C-1'), 128.2 (C-2'), 115.3 (C-3"), 115.2 (C-3"), 112.1 (C-4"), 98.2 (C-10), 96.8 (C-8), 94.9 (C-6), 76.1 (C-2), 33.3 (C-3) ppm.

4',5,7-trihydroxybenzopyran-4-(*N*,*N*-dimethyl)-thiosemicarbazone (39):

To 100 mg (0.370 mmol) of naringenin (**17**) dissolved in ethanol was added 87.4 mg (0.740 mmol) of *N*,*N*-dimethylthiosemicarbazide, and the mixture was kept stirring under reflux for 24 h under mildly acidic conditions. Following, after evaporation of the solvent the product was purified by a column chromatography using *n*-hexane–EtOAc (100:0 to 50:50) to yield 54 mg (0.143 mmol, 38.8%) of compound **39** as an amorphous, yellow powder.

ESI-MS (positive mode): *m/z* 413 $[M + H + K]^+$;

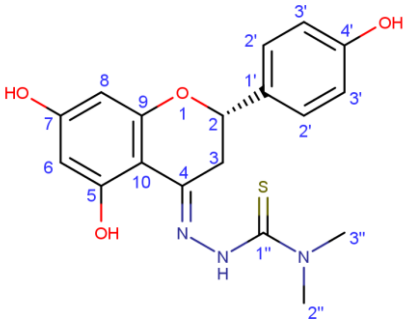

^{1}H-NMR (300 MHz, Acetone-D$_6$): δ 7.35 (1H, *d*, *J* = 8.5 Hz, H-2'), 6.87 (1H, *d*, *J* = 8.5 Hz, H-3'), 6.00 (1H, *d*, *J* = 2.2 Hz, H-8), 5.95 (1H, *d*, *J* = 2.2 Hz, H-6), 5.09 (1H, *dd*, *J* = 12.2, 3.0 Hz, H-2), 3.66 (1H, *dd*, *J* = 17.3, 3.0 Hz, H-3β), 2.83 (1H, *dd*, *J* = 17.3, 12.2 Hz, H-3α), 2.05 (3H, *s*, Me-2"), 2.00 (3H, *s*, Me-3") ppm;

^{13}C-NMR (75 MHz, Acetone-D$_6$): δ 165.5 (C-1"), 163.7 (C-7), 163.4 (C-4), 163.1 (C-5), 161.22 (C-9), 158.4 (C-4'), 131.7 (C-1'), 128.8 (C-2'), 116.1 (C-3'), 99.8 (C-10), 97.3 (C-6), 95.7 (C-8), 77.9 (C-2), 33.0 (C-3), 25.4 (C-3"), 18.5 (C-2") ppm.

4',5,7-trihydroxybenzopyran-4-(indol-3-yl)-acetohydrazide (40):

To 100 mg (0.370 mmol) of naringenin (**17**) previously dissolved in ethanol was added 138.9 mg (0.750 mmol) of indole-3-acetic hydrazide. After keeping the mixture stirring under reflux for 60 h in mildly acidic conditions, the solvent was evaporated under reduced pressure at 40 ºC and the product was purified by column chromatography using CH_2Cl_2–acetone (100:0 to 90:10) and preparative TLC (CH_2Cl_2–MeOH, 95:5) to yield 68 mg (0.153 mmol, 41.5%) of an amorphous brown powder.

ESI-MS (positive mode): *m/z* 444 $[M + H]^+$;

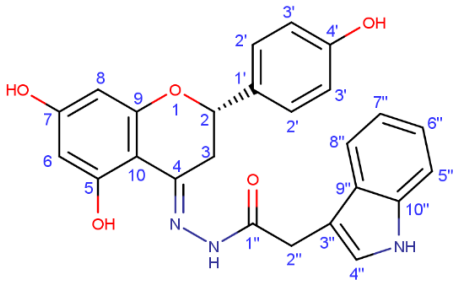

^{1}H-NMR (300 MHz, DMSO-D$_6$): δ 7.58 (1H, *d*, *J* = 7.8 Hz, H-8"), 7.33 (1H, *d*, *J* = 7.8 Hz, H-5"), 7.32 (2H, *d*, *J* = 8.6 Hz, H-2'), 7.23 (1H, *d*, *J* = 2.1 Hz, H-4"), 7.05 (1H, *td*, *J* = 7.8, 0.8 Hz, H-6"), 6.96 (1H, *td*, *J* = 7.8, 0.8 Hz, H-7"), 6.81 (2H, *d*, *J* = 8.6 Hz, H-3'), 5.90 (1H, *d*, *J* = 2.2 Hz, H-8), 5.89 (1H, *d*, *J* = 2.2 Hz, H-6), 5.17 (1H, *dd*, *J* = 12.1, 3.0 Hz, H-2), 3.55 (2H, *br s*, H-2"), 3.32 (1H, *dd*, *J* = 15.5, 3.0 Hz, H-3β), 3.10 (1H, *dd*, *J* = 15.5, 12.1 Hz, H-3α) ppm;

^{13}C-NMR (75 MHz, DMSO-D$_6$): δ 169.9 (C-1"), 162.9 (C-7), 162.2 (C-5), 160.0 (C-9), 157.7 (C-4'), 156.3 (C-4), 136.1 (C-10"), 129.6 (C-1'), 128.3 (C-2'), 127.2 (C-9"), 123.9 (C-4"), 121.0 (C-6"), 118.8 (C-8"), 118.4 (C-7"), 115.3 (C-3'), 108.8 (C-3"), 99.6 (C-10), 96.6 (C-6), 95.3 (C-8), 76.6 (C-2), 30.8 (C-3), 30.6 (C-2") ppm.

4',5,7-trihydroxybenzopyran-4-(benzoyloxy)-formohydrazide (41):

To 100 mg (0.370 mmol) of compound **17**, dissolved in ethanol, was added 123.0 mg (0.740 mmol) of benzyl carbazate. After keeping the mixture stirring under reflux for 36 h, the evaporation of the solvent yielded a residue that was further purified column chromatography using CH_2Cl_2–MeOH (100:0 to 90:10). At the end, 83 mg (0.205 mmol, 55.3% yield) of compound **41** was obtained as a pale white amorphous powder.

ESI-MS (positive mode): *m/z* 421 $[M + H]^+$;

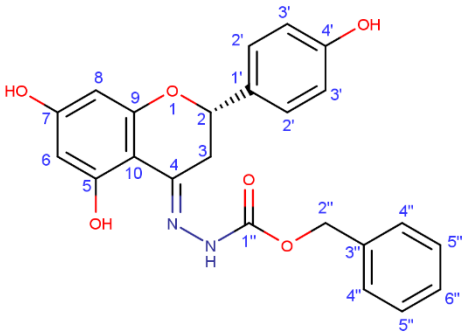

^{1}H-NMR (300 MHz, Methanol-D$_6$): δ 7.23-7.43 (7H, *m*, H-2', H-4", H-5", H-6"), 6.81 (1H, *d*, *J* = 8.5 Hz, H-3"), 5.96 (1H, *d*, *J* = 2.2 Hz, H-8), 5.90 (1H, *d*, *J* = 2.2 Hz, H-6), 5.20 (2H, *br s*, H-2"), 4.96 (1H, *dd*, *J* = 12.2, 3.0 Hz, H-2), 3.08 (1H, *dd*, *J* = 16.9, 3.0 Hz, H-3β), 2.70 (1H, *dd*, *J* = 16.9, 12.2 Hz, H-3α) ppm;

^{13}C-NMR (75 MHz, Methanol-D$_6$): δ 172.8 (C-1"), 162.4 (C-7), 161.8 (C-5), 160.6 (C-9), 158.8 (C-4'), 156.2 (C-4), 137.6 (C-3"), 131.8 (C-1'), 130.2 (C-5"), 129.8 (C-6"), 129.5 (C-2', C-4"), 116.2 (C-3'), 99.8 (C-10), 97.9 (C-6), 96.8 (C-8), 77.8 (C-2), 66.9 (C-2"), 33.1 (C-3) ppm.

4',5,7-trihydroxybenzopyran-4-(methoxybenzoyloxy)-formohydrazide (42):

Naringenin (100 mg, 0.370 mmol) was dissolved in EtOH (5 mL), at room temperature. Then, it was added 4-methoxybenzylcarbazate (72.1 mg, 0.367 mmol) and 50 µL of a ethanolic solution of 10% acetic acid. The mixture was kept stirring under N_2 overnight, at room temperature. The mixture was purified by column chromatography, using *n*-hexane–EtOAc, 100:0 to 0:100) as mobile phase to afford 64 mg of compound **42**, an amorphous yellow powder (0.142 mmol, 77% yield).

ESI-MS (negative mode): *m/z* 449 $[M - H]^-$;

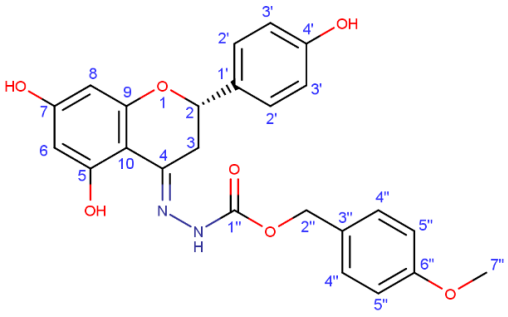

^{1}H-NMR (300 MHz, Methanol-D$_6$): δ 7.35 (2H, *d*, *J* = 8.7 Hz, H-4"), 7.28 (2H, *d*, *J* = 8.5 Hz, H-2'), 6.94 (2H, *d*, *J* = 8.7 Hz, H-5"), 6.79 (2H, *d*, *J* = 8.5 Hz, H-3'), 5.89 (1H, *d*, *J* = 2.2 Hz, H-6), 5.85 (1H,

d, *J* = 2.2 Hz, H-8), 5.12 (2H, *br s*, H-2"), 5.04 (1H, *dd*, *J* = 12.0, 3.0 Hz, H-2), 3.75 (3H, *s*, Me-7"), 3.21 (1H, *dd*, *J* = 17.4, 3.0 Hz, H-3β), 2.76 (1H, *dd*, *J* = 17.4, 12.0 Hz, H-3α) ppm;

^{13}C-NMR (75 MHz, Methanol-D$_6$): δ 161.3 (C-7), 160.6 (C-5), 160.3 (C-9), 159.7 (C-6"), 159.0 (C-4), 157.9 (C-4'), 154.4 (C-1"), 130.5 (C-1'), 130.2 (C-4"), 128.7 (C-2'), 115.5 (C-3'), 114.3 (C-5"), 98.6 (C-10), 97.2 (C-6), 95.4 (C-8), 76.1 (C-2), 66.6 (C-2"), 55.6 (C-7"), 32.1 (C-3) ppm.

7.3.3. General preparation of derivatives (43-45) by a Mannich-type coupling reaction

To 1 eq. of naringenin (**17**) in methanol and dimethylformamide (15:1) at room temperature was added, dropwise, a methanolic solution of formaldehyde (1.5 eq.) and the desired amine (1 eq.). The mixture was kept stirring under N_2 at 50 ºC until the reaction was complete (monitored by analytical TLC). Following, the solvent was evaporated under reduced pressure and separated by preparative TLC to afford the desired product.

Naringenin 6-(*N*-morpholinomethyl) (**43**):

Naringenin (**1**, 50 mg, 0.184 mmol) was dissolved in MeOH (15 mL) and DMF (1 mL) at 50 ºC. Then, it was added to the stirring solution, dropwise, the formaldehyde solution (36.5% in MeOH; 14 µL, 0.276 mmol) and morpholine (15.9 µL, 0.184 mmol). After, the solution was kept stirring under N_2 at 50 ºC for 2 h. The mixture was evaporated under vacuum and separated by preparative TLC (CH_2Cl_2–MeOH, 80:20) to afford 43 mg of compound **43** as an amorphous yellow powder (0.116 mmol, yield 62.9%).

ESI-MS (negative mode): *m/z* 370 $[M - H]^-$;

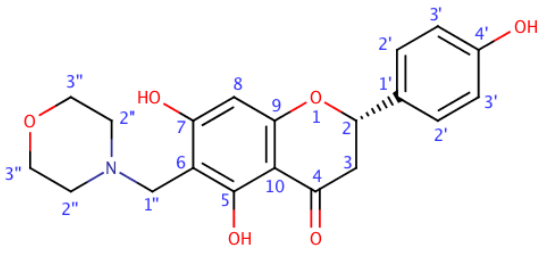

^{1}H-NMR (300 MHz, Methanol-D$_6$): δ 7.25 (2H, *d*, *J* = 8.5 Hz, H-2'), 6.76 (2H, *d*, *J* = 8.5 Hz, H-3'), 5.81 (1H, *s*, H-8), 5.25 (1H, *dd*, *J* = 12.7, 2.8 Hz, H-2), 3.75 (2H, *s*, H-1"), 3.69 (2H, *br t*, *J* = 4.8 Hz, H-3"), 3.03 (1H, *dd*, *J* = 17.2, 12.7 Hz, H-3α), 2.67 (2H, *br t*, *J* = 4.8 Hz, H-2"), 2.61 (1H, *dd*, *J* = 17.2, 2.8 Hz, H-3β) ppm;

^{13}C-NMR (75 MHz, Methanol-D$_6$): δ 197.8 (C-4), 173.3 (C-7), 163.5 (C-5), 163.3 (C-9), 159.3 (C-4'), 131.1 (C-1'), 129.1 (C-6), 116.4 (C-2'), 116.3 (C-3'), 101.3 (C-10), 97.0 (C-8), 80.3 (C-2), 67.1 (C-3"), 53.7 (C-2"), 53.0 (C-1"), 43.9 (C-3) ppm.

Naringenin 6-(N-isopropylaminomethyl) (**44**):

To a solution of **1** (50 mg, 0.184 mmol) in MeOH (15 mL) and DMF (1 mL) at room temperature was added, dropwise, the formaldehyde solution (36.5% in MeOH; 14 µL, 0.276 mmol) and isopropylamine (28.6 µL, 0.275 mmol). After 2 h stirring under N_2 at room temperature, the mixture was evaporated and **44** was recovered by preparative TLC (CH_2Cl_2–MeOH, 90:10), yielding 19 mg as an amorphous yellow powder (0.055 mmol, 30% yield).

ESI-MS (negative mode): *m/z* 342 $[M - H]^-$;

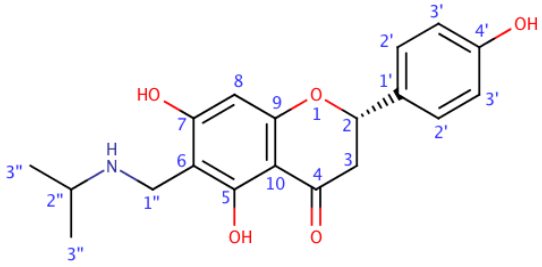

^{1}H-NMR (400 MHz, Methanol-D$_6$): δ 7.26 (2H, *d*, *J* = 9.0 Hz, H-2'), 6.77 (2H, *d*, *J* = 9.0 Hz, H-3'), 5.68 (1H, *s*, H-8), 5.20 (1H, *dd*, *J* = 12.5, 3.5 Hz, H-2), 4.05 (2H, *s*, H-1"), 3.28 (1H, *h*, *J* = 3.3 Hz, H-2"), 2.95 (1H, *dd*, *J* = 16.5, 12.5 Hz, H-3α), 2.61 (1H, *dd*, *J* = 16.5, 3.5 Hz, H-3β), 1.31 (6H, *d*, *J* = 3.0 Hz, H-3") ppm;

^{13}C-NMR (75 MHz, Methanol-D$_6$): δ 195.3 (C-4), 164.9 (C-7), 164.0 (C-5), 162.4 (C-9), 158.8 (C-4'), 131.6 (C-1'), 128.9 (C-2'), 116.2 (C-3'), 101.2 (C-10), 99.5 (C-8), 98.9 (C-6), 79.8 (C-2), 50.5 (C-2"), 43.6 (C-3), 39.9 (7-OMe), 19.5 (C-3") ppm.

6,8-bis{[(2-hydroxyethyl)(phenyl)amino]methyl}naringenin (**45**):

Naringenin (50 mg, 0.184 mmol) was dissolved in MeOH (15 mL) and DMF (1 mL) at 50ºC. After, it was added, dropwise, the formaldehyde solution (36.5% in MeOH; 14 µL, 0.276 mmol) and a solution of 2-anilinoethanol (34 µL, 0,275 mmol). The mixture was kept stirring overnight under N_2 and then was evaporated under vacuum. The mixture was separated by column chromatography (EtOAc–MeOH, 100:0 to 60:40) to afford 7 mg of an amorphous brown powder as compound **45** (0.013, 7% yield).

ESI-MS (negative mode): *m/z* 570 $[M - H]^-$;

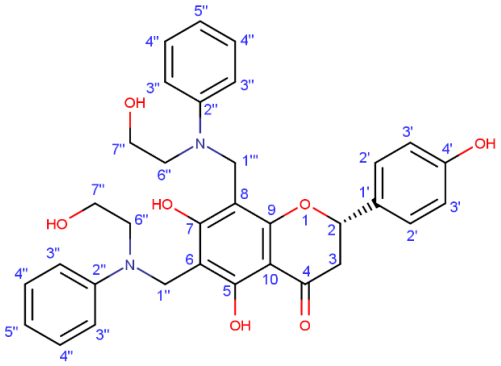

^{1}H-NMR (400 MHz, Methanol-D$_6$): δ 7.21 (2H, *d*, *J* = 8.5 Hz, H-2'), 6.77 (2H, *d*, *J* = 8.5 Hz, H-3'), 6.97 (6H, *m*, H-3", H-5"), 6.77 (2H, *d*, *J* = 8.4 Hz, H-3'), 6.53 (4H, *t*, *J* = 7.7 Hz, H-4"), 5.25 (1H, *dd*, *J* = 12.7, 3.0 Hz, H-2), 3.81 (2H, *s*, H-1"), 3.79 (2H, *s*, H-1"'), 3.67 (4H, *t*, *J* = 5.7 Hz, H-6"), 3.15 (2H, *t*, *J* = 5.7 Hz, H-7"), 3.03 (1H, *dd*, *J* = 17.2, 12.8 Hz, H-3α), 2.69 (1H, *dd*, *J* = 17.0, 3.1 Hz, H-3β) ppm;

^{13}C-NMR (75 MHz, Methanol-D$_6$): δ 196.5 (C-4), 166.3 (C-7), 165.6 (C-5), 164.5 (C-9), 158.8 (C-4'), 147.9 (C-2"), 147.0 (C-2"'), 131.3 (C-1'), 131.1 (C-4"), 130.0 (C-4"'), 128.9 (C-2'), 116.2 (C-3', C-5"), 115.7 (C-6), 114.6 (C-8), 114.5 (C-3"), 114.4 (C-3"'), 101.4 (C-10), 80.1 (C-2), 61.5 (C-7"), 47.6 (C-6"), 44.0 (C-3), 28.3 (C-1") ppm.

7.3.4. Methylation of naringenin (17) with dimethylsulphate

To compound **17** (1 eq.) in a proper amount of acetone, were added dimethyl sulfate (1.1 or 3 eq. for mono- or demethylation respectively) and potassium carbonate (K_2CO_3, 3 eq) while the mixture was kept in reflux (50 °C) overnight under constant stirring (Kim et al., 2007). The reaction was followed by TLC and, upon completion, the solvent was evaporated under vacuum at 40 °C, the residue extracted with ethyl acetate and dried with Na_2SO_4. After evaporation of the solvent, the residue was further purified by column chromatography (CH_2Cl_2: acetone 100:0 to 80:20) to obtain the desired products.

Sakuranetin (**46**):

Amorphous orange power, yield 76%;

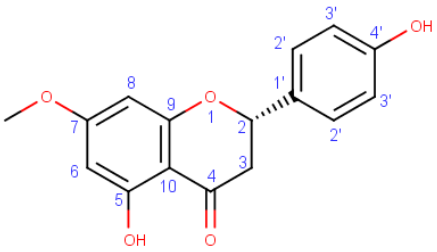

ESI-MS (positive mode): *m/z* 287 $[M + H]^+$;

^{1}H-NMR (300 MHz, Acetone-D$_6$): δ 7.40 (2H, *d*, *J* = 8.4 Hz, H-2'), 6.90 (2H, *d*, *J* = 8.4 Hz, H-3'), 6.04 (2H, *m*, H-6, H-8), 5.48 (1H, *dd*, *J* = 12.9, 3.0 Hz, H-2), 3.85 (3H, *s*, 7-OMe), 3.22 (1H, *dd*, *J* = 17.2, 12.9 Hz, H-3α), 2.75 (1H, *dd*, *J* = 17.2, 3.0 Hz, H-1β) ppm;

^{13}C-NMR (75 MHz, Acetone-D$_6$): δ 197.6 (C-4), 168.8 (C-7), 166.9 (C-5), 164.9 (C-9), 158.8 (C-4'), 130.5 (C-1'), 129.0 (C-2'), 116.1 (C-3'), 103.8 (C-10), 95.4 (C-8), 94.5 (C-6), 80.0 (C-2), 56.2 (7-OMe), 43.4 (C-3) ppm.

4'-methoxysakuranetin (**47**):

Amorphous dark orange power, yield 16%;

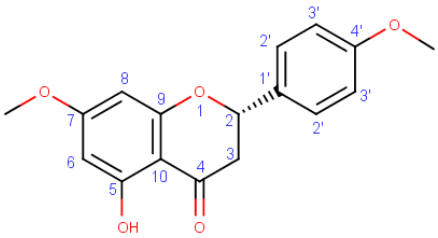

ESI-MS (positive mode): *m/z* 301 $[M + H]^+$;

^{1}H-NMR (300 MHz, Acetone-D$_6$): δ 7.49 (2H, *d*, *J* = 8.6 Hz, H-2'), 7.00 (2H, *d*, *J* = 8.6 Hz, H-3'), 6.05 (2H, *m*, H-6, H-8), 5.53 (1H, *dd*, *J* = 12.8, 3.0 Hz, H-2), 3.86 (3H, *s*, 4'-OMe), 3.83 (3H, *s*, 7-OMe), 3.22 (1H, *dd*, *J* = 17.2, 12.8 Hz, H-3α), 2.78 (1H, *dd*, *J* = 17.1, 3.0 Hz, H-3β) ppm;

^{13}C-NMR (75 MHz, Acetone-D$_6$): δ 197.5 (C-4), 168.8 (C-7), 165.0 (C-5), 164.1 (C-9), 160.9 (C-4'), 131.8 (C-1'), 128.9 (C-2'), 114.8 (C-3'), 103.7 (C-10), 95.5 (C-8), 94.6 (C-6), 79.8 (C-2), 56.2 (7-OMe), 55.6 (4'-OMe), 43.5 (C-3) ppm.

7.3.5. Synthesis of sakuranetin and 4'-methoxysakuranetin derivatives

Sakuranetin and 4'-methoxysakuranetin derivatives were prepared according to the methods previously described for naringenin hydrazones (Method A) and carbohydrazides: to 20 mg (1 eq.) of sakuranetin (**46**) or 4'-methoxysakuranetin (**47**) dissolved in ethanol was added 2 eq. of the desired hydrazine (NH_2-NH-R_2) or hydrazide (NH_2-NH-CO-R) and 0.01 eq. of 10% acetic acid in ethanol. Following, the mixture was stirred under N_2, at room temperature, until the total disappearance of the starting compound (by TLC). Then, the solvent was evaporated, the residue extracted with ethyl acetate, dried (with Na_2SO_4) and further purified by preparative TLC (CH_2Cl_2–MeOH 98:2) to obtain the corresponding hydrazone (C=N-NH-R).

Sakuranetin 4-hydrazone (**48**):

Amorphous dark orange power, yield 68 %;

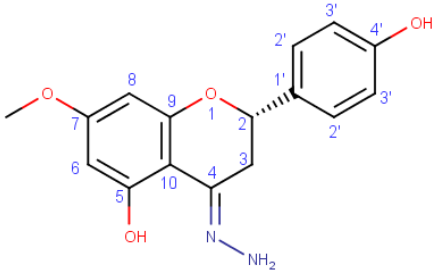

ESI-MS (positive mode): *m/z* 342 $[M + H + ACN]^+$;

^{1}H-NMR (300 MHz, DMSO-D$_6$): δ 7.30 (2H, *d*, *J* = 8.4 Hz, H-2'), 6.78 (2H, *d*, *J* = 8.5 Hz, H-3'), 6.07 (1H,

d, *J* = 2.2 Hz, H-6), 6.05 (1H, *d*, *J* = 2.2 Hz, H-8), 5.15 (1H, *dd*, *J* = 12.0, 2.6 Hz, H-2), 3.73 (3H, *s*, 7-OMe), 3.53 (1H, *dd*, *J* = 17.2, 2.8 Hz, H-3β), 2.94 (1H, *dd*, *J* = 17.2, 12.2 Hz, H-3α) ppm;

^{13}C-NMR (75 MHz, DMSO-D$_6$): δ 163.6 (C-7), 162.2 (C-4), 161.8 (C-5), 159.8 (C-9), 157.6 (C-4'), 129.6 (C-1'), 128.2 (C-2'), 115.2 (C-3'), 99.3 (C-10), 95.1 (C-6), 93.6 (C-8), 76.6 (C-2), 55.4 (7-OMe), 31.6 (C-3) ppm.

4'-methoxysakuranetin 4-hydrazone (**49**):

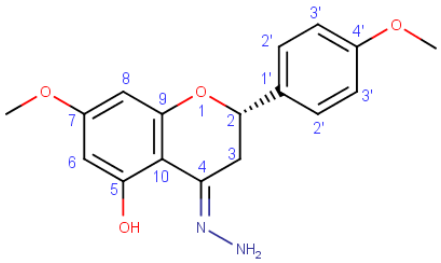

Amorphous dark orange power, yield 85 %;

ESI-MS (positive mode): *m/z* 355 $[M + H + ACN]^+$;

^{1}H-NMR (300 MHz, DMSO-D$_6$): δ 7.43 (2H, *d*, *J* = 8.7 Hz, H-2'), 6.96 (2H, *d*, *J* = 8.7 Hz, H-3'), 6.07 (2H, *q*, *J* = 2.4 Hz, H-6, H-8), 5.23 (1H, *dd*, *J* = 11.9, 3.0 Hz, H-2), 3.76 (3H, *s*, 4'-OMe), 3.73 (3H, *s*, 7-OMe), 3.54 (1H, *dd*, *J* = 17.3, 3.0 Hz, H-3β), 2.99 (1H, *dd*, *J* = 17.3, 11.9 Hz, H-3α) ppm;

^{13}C-NMR (75 MHz, DMSO-D$_6$): δ 164.0 (C-7), 162.2 (C-4), 162.0 (C-5), 160.1 (C-9), 159.7 (C-4'), 131.4 (C-1'), 128.2 (C-2'), 113.9 (C-3'), 99.4 (C-10), 95.1 (C-6), 93.6 (C-8), 76.0 (C-2), 55.5 (7-OMe), 55.2 (4'-OMe), 31.7 (C-3) ppm.

Sakuranetin 4-phenylhydrazone (**50**):

Sakuranetin (20 mg, 0.070 mmol) was dissolved in EtOH (2 mL), at room temperature. Then, it was added phenylhydrazine (11.4 mg, 0.105 mmol, 9.83 µL) and 50 µL of a ethanolic solution of 10% acetic acid. The mixture was kept overnight under N_2, reflux and constant stirring. The mixture was purified by preparative TLC using *n*-hexane–acetone, 70:30) as mobile phase to afford 19 mg of compound **50**, an amorphous yellow powder (0.049 mmol, 71% yield).

ESI-MS (positive mode): *m/z* 377 $[M + H]^+$;

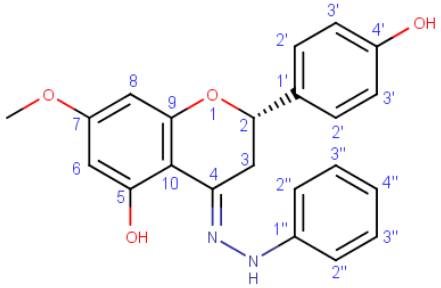

^{1}H-NMR (300 MHz, Acetone-D$_6$): δ 7.37 (2H, *d*, *J* = 8.6 Hz, H-2'), 7.24 (2H, *dd*, *J* = 8.6, 7.4 Hz, H-3"), 7.03 (2H, *dd*, *J* = 8.6, 1.0 Hz, H-2"), 6.88 (2H, *d*, *J* = 8.6 Hz, H-3'), 6.81 (1H, *td*, *J* = 7.4, 1.0 Hz, H-4"), 6.08 (1H, *d*, *J* = 2.5 Hz, H-8), 6.01 (1H, *d*, *J* = 2.5 Hz, H-6), 5.08 (1H, *dd*, *J*

= 12.1, 3.2 Hz, H-2), 3.73 (3H, *s*, 7-OMe), 3.26 (1H, *dd*, *J* = 16.8, 3.2 Hz, H-3β), 2.77 (1H, *dd*, *J* = 16.8, 12.1 Hz, H-1α) ppm;

^{13}C-NMR (75 MHz, Acetone-D$_6$): δ 162.8 (C-7), 160.7 (C-5), 159.1 (C-9), 158.5 (C-4'), 146.1 (C-1"), 145.6 (C-4), 132.0 (C-1'), 130.1 (C-2"), 128.8 (C-2'), 120.7 (C-4"), 116.1 (C-3'), 113.3 (C-3"), 101.0 (C-10), 96.2 (C-6), 94.5 (C-8), 77.4 (C-2), 55.6 (7-OMe), 32.6 (C-3) ppm.

4'-methoxysakuranetin 4-phenylhydrazone (**51**):

4'-methoxysakuranetin (20 mg, 0.066 mmol) was dissolved in EtOH (2 mL), at room temperature. Then, it was added phenylhydrazine (11.4 mg, 0.105 mmol, 9.83 µL) and 50 µL of an ethanolic solution of 10% acetic acid. The mixture was kept overnight under N_2, reflux and constant stirring. The mixture was purified by preparative TLC using *n*-hexane–EtOAc, 80:20) as mobile phase to afford 9 mg of compound **51**, an amorphous brown powder (0.024 mmol, 34% yield).

ESI-MS (positive mode): *m/z* 391 $[M + H]^+$;

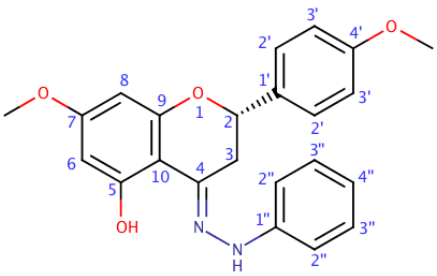

^{1}H-NMR (300 MHz, Acetone-D$_6$): δ 7.50 (2H, *d*, *J* = 8.6 Hz, H-2'), 7.28 (2H, *dd*, *J* = 8.6, 7.4 Hz, H-3"), 7.06 (2H, *dd*, *J* = 8.6, 1.1 Hz, H-2"), 7.01 (2H, *d*, *J* = 8.6 Hz, H-3'), 6.85 (1H, *td*, *J* = 7.4, 1.1 Hz, H-5"), 6.12 (1H, *d*, *J* = 2.5 Hz, H-8), 6.06 (1H, *d*, *J* = 2.4 Hz, H-6), 5.17 (1H, *dd*, *J* = 12.0, 3.1 Hz, H-2), 3.83 (3H, *s*, 4'-OMe), 3.78 (3H, *s*, 7-OMe), 3.32 (1H, *dd*, *J* = 16.8, 3.1 Hz, H-3β), 2.79 (1H, *dd*, *J* = 16.8, 12.0 Hz, H-1α) ppm;

^{13}C-NMR (75 MHz, Acetone-D$_6$): δ 162.8 (C-7), 160.8 (C-5), 160.7 (C-7), 159.0 (C-4'), 146.1 (C-1"), 145.6 (C-4), 133.1 (C-1'), 130.1 (C-2"), 128.7 (C-2'), 120.7 (C-4"), 114.7 (C-3'), 113.3 (C-3"), 101.1 (C-10), 96.3 (C-6), 94.5 (C-8), 77.2 (C-2), 55.7 (4'-OMe), 55.6 (7-OMe), 32.5 (C-3) ppm.

Sakuranetin 4-(5-bromopyridin-2-yl)hydrazone (**52**):

Sakuranetin (20 mg, 0.070 mmol) was dissolved in EtOH (2 mL), at room temperature. Then, it was added 5-bromopyridin-2-yl-hydrazine (19.7 mg, 0.105 mmol) and 50 µL of a ethanolic solution of 10% acetic acid. The mixture was kept overnight under N_2, reflux and constant stirring. The mixture was purified by preparative TLC using *n*-hexane–acetone, 70:30) as

mobile phase to afford 12 mg of compound **52**, an amorphous brown powder (0.026 mmol, 37% yield).

ESI-MS (positive mode): *m/z* 497 $[M + H + ACN]^+$;

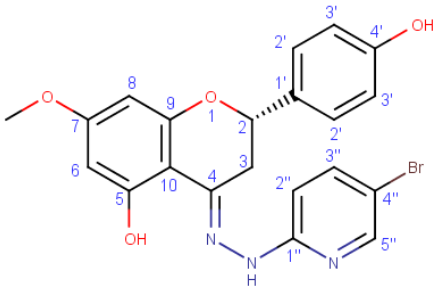

^{1}H-NMR (300 MHz, Acetone-D$_6$): δ 8.24 (1H, *d*, *J* = 2.4 Hz, H-5"), 7.82 (1H, *dd*, *J* = 8.5, 2.4 Hz, H-3"), 7.45 (1H, *d*, *J* = 8.5 Hz, H-2"), 7.41 (2H, *d*, *J* = 8.6 Hz, H-2'), 6.91 (2H, *d*, *J* = 8.6 Hz, H-3') 6.11 (1H, *d*, *J* = 2.5 Hz, H-8), 6.06 (1H, *d*, *J* = 2.5 Hz, H-6), 5.08 (1H, *dd*, *J* = 11.9, 3.4 Hz, H-2), 3.73 (3H, *s*, 7-OMe), 3.40 (1H, *dd*, *J* = 16.5, 3.4 Hz, H-3β), 2.94 (1H, *dd*, *J* = 16.5, 11.9 Hz, H-1α) ppm;

^{13}C-NMR (75 MHz, Acetone-D$_6$): δ 163.3 (C-7), 161.2 (C-5), 160.6 (C-9), 159.6 (C-4'), 155.4 (C-1"), 149.6 (C-5"), 145.6 (C-4), 141.2 (C-3"), 131.7 (C-1'), 128.8 (C-2'), 116.1 (C-4"), 116.0 (C-3'), 110.5 (C-2"), 100.4 (C-10), 96.4 (C-8), 94.5 (C-6), 77.4 (C-2), 55.7 (7-OMe), 32.6 (C-3) ppm.

4'-methoxysakuranetin 4-(5-bromopyridin-2-yl)hydrazone (**53**):

4-methoxyakuranetin (20 mg, 0.066 mmol) was dissolved in EtOH (2 mL), at room temperature. Then, it was added 5-bromopyridin-2-yl-hydrazine (19.7 mg, 0.105 mmol) and 50 µL of a ethanolic solution of 10% acetic acid. The mixture was kept during 46 h under N_2, reflux and constant stirring. The mixture was purified by preparative TLC using *n*-hexane–acetone, 70:30) as mobile phase to afford 8 mg of compound **53**, an amorphous yellow powder (0.017 mmol, 37% yield).

ESI-MS (positive mode): *m/z* 470 $[M + H]^+$;

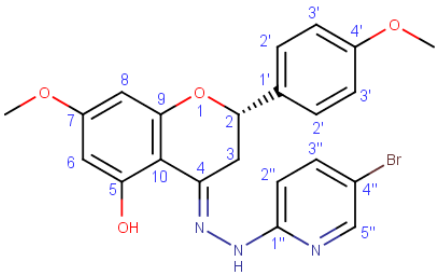

^{1}H-NMR (300 MHz, Acetone-D$_6$): δ 8.24 (1H, *d*, *J* = 2.4 Hz, H-5"), 7.82 (1H, *dd*, *J* = 8.8, 2.4 Hz, H-3"), 7.51 (2H, *d*, *J* = 8.8 Hz, H-2"), 7.01 (2H, *d*, *J* = 8.7 Hz, H-3'), 6.93 (1H, *d*, *J* = 8.7 Hz, H-2'), 6.12 (1H, *d*, J = 2.5 Hz, H-8), 6.07 (1H, *d*, J= 2.5 Hz, H-6), 5.20 (1H, dd, *J* = 12.5, 2.9 Hz,H-2), 3.83 (3H, *d*, *J* = 0.9 Hz, 4'-OMe), 3.78 ppm (3H, *s*, 7-OMe), 3.43 ppm (1H, *dd*, *J* = 16.6, 2.9 Hz, H-3β), 2.96 ppm (1H, *dd*, *J* = 16.6, 12.5 Hz, H-3α);

^{13}C-NMR (75 MHz, Acetone-D$_6$): δ 163.5 (C-7), 162.8 (C-5), 161.3 (C-4'), 160.9 (C-9), 156.6 (C-1"), 149.6 (C-5"), 148.9 (C-4), 141.6 (C-3"), 132.8 (C-1'), 128.8 (C-2'), 114.7 (C-3'), 109.2 (C-4"), 109.0 (C-2"), 100.9 (C-10), 95.5 (C-6), 94.6 (C-8), 77.2 (C-2), 55.7 (4'-OMe), 55.6 (7-OMe), 32.5 (C-3) ppm.

Sakuranetin 4-(furan-2-yl)-carbohydrazide (**54**):

Sakuranetin (20 mg, 0.070 mmol) was dissolved in EtOH (2 mL), at room temperature. Then, it was added 2-furoic hydrazide (13.2 mg, 0.105 mmol) and 50 µL of a ethanolic solution of 10% acetic acid. The mixture was kept overnight under N_2, reflux and constant stirring. The mixture was purified by preparative TLC using *n*-hexane–acetone, 40:60) as mobile phase to afford 11 mg of compound **54**, an amorphous orange brownish powder (0.029 mmol, 41% yield).

ESI-MS (positive mode): *m/z* 395 $[M + H]^+$;

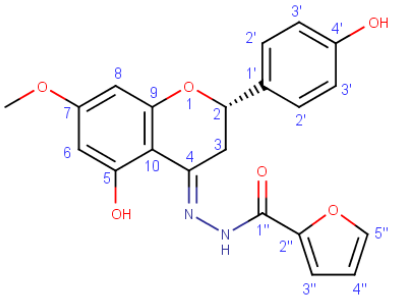

^{1}H-NMR (300 MHz, Acetone-D$_6$): δ 7.72 (1H, *d*, *J* = 1.6 Hz, H-5"), 7.40 (2H, *d*, *J* = 7.8 Hz, H-2'), 7.24 (1H, *br s*, H-3"), 6.91 (2H, *d*, *J* = 7.8 Hz, H-3'), 6.63 (1H, *br s*, H-4"), 6.10 (1H, *d*, *J* = 2.4 Hz, H-8), 6.04 (1H, *d*, *J* = 2.4 Hz, H-6), 5.16 (1H, *br d*, *J* = 13.5 Hz, H-2), 3.79 (3H, *s*, 7-OMe), 3.43 (1H, *br d*, *J* = 16.0 Hz, H-3β), 3.00 (1H, *dd*, *J* = 16.0, 13.5 Hz, H-3α) ppm;

^{13}C-NMR (75 MHz, Acetone-D$_6$): δ 164.4 (C-7), 163.6 (C-5), 162.3 (C-9), 158.6 (C-4'), 155.0 (C-4), 147.8 (C-1"), 147.2 (C-2"), 145.6 (C-5"), 131.4 (C-1'), 128.9 (C-2'), 116.1 (C-3'), 116.0 (C-3"), 112.9 (C-4"), 100.4 (C-10), 96.4 (C-8), 94.5 (C-6), 77.6 (C-2), 55.7 (7-OMe), 32.9 (C-3) ppm.

4'-methoxysakuranetin 4-(furan-2-yl)-carbohydrazide (**55**):

4'-methoxysakuranetin (20 mg, 0.066 mmol) was dissolved in EtOH (2 mL), at room temperature. Then, it was added 2-furoic hydrazide (13.2 mg, 0.105 mmol) and 50 µL of a ethanolic solution of 10% acetic acid. The mixture was kept for 25 h under N_2, reflux and constant stirring. The mixture was purified by preparative TLC using CH_2Cl_2–acetone, 95:5) as

mobile phase to afford 13 mg of compound **55**, an amorphous orange brownish powder (0.031 mmol, 45% yield).

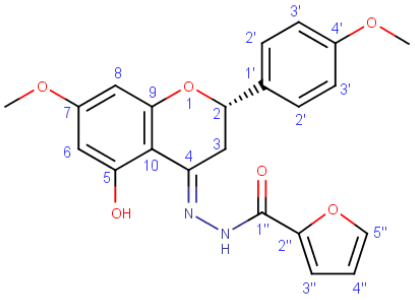

ESI-MS (positive mode): *m/z* 409 $[M + H]^+$;

^{1}H-NMR (300 MHz, Acetone-D$_6$): δ 7.72 (1H, *d*, *J* = 1.7 Hz, H-5"), 7.50 (2H, *d*, *J* = 8.6 Hz, H-2'), 7.23 (1H, *d*, *J* = 3.5 Hz, H-3"), 7.01 (2H, *d*, *J* = 8.6 Hz, H-3'), 6.63 (1H, *dd*, *J* = 2.8, 1.4 Hz, H-4"), 6.11 (1H, *d*, *J* = 2.5 Hz, H-8), 6.05 (1H, *d*, *J* = 2.5 Hz, H-6), 5.20 (1H, *dd*, *J* = 12.4, 1.4 Hz, H-2), 3.83 (3H, *s*, 4'-OMe), 3.79 (3H, *s*, 7-OMe), 3.45 (1H, *dd*, *J* = 16.5, 1.4 Hz, H-3β), 3.01 (1H, *dd*, *J* = 16.5, 12.4 Hz, H-3α) ppm;

^{13}C-NMR (75 MHz, Acetone-D$_6$): δ 164.4 (C-7), 162.3 (C-5), 160.8 (C-9), 160.3 (C-4'), 155.1 (C-4), 147.8 (C-1"), 146.8 (C-2"), 145.6 (C-5"), 132.6 (C-1'), 128.7 (C-2'), 116.1 (C-3"), 114.7 (C-3'), 112.9 (C-4"), 100.4 (C-10), 96.4 (C-8), 94.5 (C-6), 77.4 (C-2), 55.8 (4'-OMe), 55.6 (7-OMe), 32.9 (C-3) ppm.

Sakuranetin 4-(tiophen-2-yl)-carbohydrazide (**56**):

Sakuranetin (20 mg, 0.070 mmol) was dissolved in EtOH (2 mL), at room temperature. Then, it was added 2-thiophene-carboxyhydrazide (20 mg, 0.140 mmol) and 50 µL of a ethanolic solution of 10% acetic acid. The mixture was kept overnight under N_2, reflux and constant stirring. The mixture was purified by preparative TLC using *n*-hexane–acetone, 50:50) as mobile phase to afford 6 mg of compound **56**, an amorphous orange brownish powder (0.015 mmol, 21% yield).

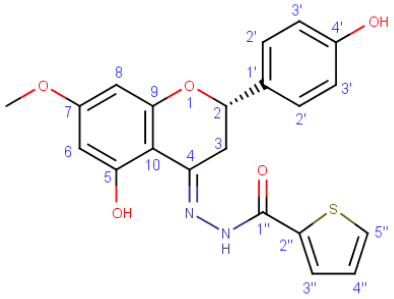

ESI-MS (positive mode): *m/z* 411 $[M + H]^+$;

^{1}H-NMR (300 MHz, Acetone-D$_6$): δ 7.87 (1H, *br s*, H-3"), 7.78 (1H, *d*, *J* = 4.9 Hz, H-5"), 7.41 (2H, *d*, *J* = 8.4 Hz, H-2'), 7.14 (1H, *br d*, *J* = 4.9 Hz, H-4"), 6.91 (2H, *d*, *J* = 8.4 Hz, H-3'), 6.11 (1H, *d*, *J* = 2.5 Hz, H-8), 6.04 (1H, *d*, *J* = 2.5 Hz, H-6), 5.16 (1H, *dd*, *J* = 12.0, 1.9 Hz, H-2), 3.79 (3H, *s*, 7-OMe), 3.44 (1H, *dd*, *J* = 16.5, 1.9 Hz, H-3β), 2.96 (1H, *dd*, *J* = 16.5, 12.0 Hz, H-1α) ppm;

^{13}C-NMR (75 MHz, Acetone-D$_6$): δ 164.8 (C-7), 162.4 (C-5), 160.6 (C-9), 158.6 (C-4'), 156.6 (C-4), 148.5 (C-1"), 140.6 (C-2"), 132.4 (C-5"), 131.5 (C-1'), 128.9 (C-2'), 128.6 (C-3"), 126.6

(C-4”), 116.1 (C-3’), 100.9 (C-10), 96.4 (C-8), 95.9 (C-6), 78.5 (C-2), 55.8 (7-OMe), 32.9 (C-3) ppm.

Sakuranetin 4-(*p*-aminophenyl)-carbohydrazide (**57**):

Sakuranetin (20 mg, 0.070 mmol) was dissolved in EtOH (2 mL), at room temperature. Then, it was added 4-aminophenyl-carboxyhydrazide (21.2 mg, 0.140 mmol) and 50 µL of a ethanolic solution of 10% acetic acid. The mixture was kept 68 h under N_2, reflux and constant stirring. The mixture was purified by preparative TLC using *n*-hexane–acetone, 60:40) as mobile phase to afford 6 mg of compound **57**, an amorphous orange brownish powder (0.014 mmol, 20% yield).

ESI-MS (positive mode): *m/z* 420 $[M + H]^+$;

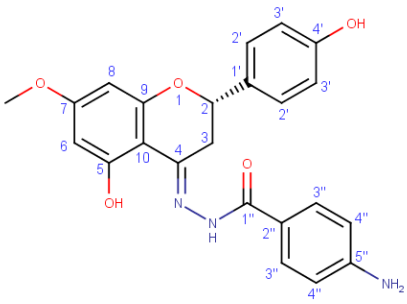

^{1}H-NMR (300 MHz, Acetone-D$_6$): δ 7.72 (2H, *d*, *J* = 8.1 Hz, H-3”), 7.40 (1H, *d*, *J* = 7.9 Hz, H-2’), 6.90 (2H, *d*, *J* = 8.0 Hz, H-3’), 6.67 (2H, *d*, *J* = 7.9 Hz, H-4”), 6.10 (1H, *d*, *J* = 2.4 Hz, H-6), 6.04 (1H, *d*, *J* = 2.4 Hz, H-8), 5.14 (1H, *br d*, *J* = 11.5 Hz, H-2), 3.78 (3H, *s*, 7-OMe), 3.44 (1H, *br d*, *J* = 16.4 Hz, H-3β), 3.01 (1H, *dd*, *J* = 16.4, 11.5 Hz, H-1α) ppm;

^{13}C-NMR (75 MHz, Acetone-D$_6$): δ 164.8 (C-1”), 163.9 (C-7), 162.2 (C-5), 160.2 (C-9), 158.6 (C-4’), 157.7 (C-4), 153.2 (C-5”), 131.6 (C-1’), 130.4 (C-3”), 128.9 (C-2’), 121.2 (C-2”), 116.1 (C-3’), 113.9 (C-4”), 100.6 (C-10), 96.3 (C-8), 94.3 (C-6), 77.6 (C-2), 55.7 (7-OMe), 32.8 (C-3) ppm.

4’-methoxysakuranetin 4-(*p*-aminophenyl)-carbohydrazide (**58**):

S4-methoxysakuranetin (20 mg, 0.066 mmol) was dissolved in EtOH (2 mL), at room temperature. Then, it was added 4-aminophenyl-carboxyhydrazide (21.2 mg, 0.140 mmol) and 50 µL of a ethanolic solution of 10% acetic acid. The mixture was kept 68 h under N_2, reflux and constant stirring. The mixture was purified by preparative TLC using *n*-hexane–acetone, 60:40) as mobile phase to afford 8 mg of compound **58**, an amorphous orange brownish powder (0.019 mmol, 27% yield).

ESI-MS (positive mode): *m/z* 434 $[M + H]^+$;

^{1}H-NMR (300 MHz, DMSO-D$_6$): δ 7.64 (2H, *d*, *J* = 8.5 Hz, H-3”), 7.46 (2H, *d*, *J* = 8.5 Hz, H-2’), 7.00 (2H, *d*, *J* = 8.5 Hz, H-3’), 6.57 (2H, *d*, *J* = 8.5 Hz, H-4”), 6.09 (1H, *d*, *J* = 2.4 Hz, H-8), 6.04 (1H, *d*, *J* = 2.4 Hz, H-6), 5.18 (1H, *dd*, *J* = 12.2, 2.2 Hz, H-2), 3.78 (3H, *s*, 4’-OMe), 3.73 (3H, *s*, 7-OMe), 3.48 (1H, *dd*, *J* = 17.0, 2.2 Hz, H-3β), 2.97 (1H, *dd*, *J* = 17.0, 12.2 Hz, H-1α) ppm;

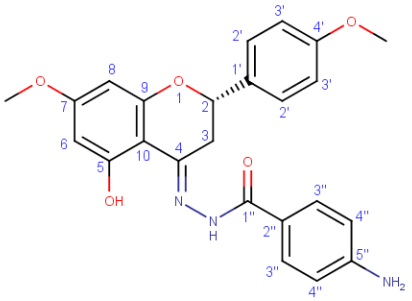

^{13}C-NMR (75 MHz, DMSO-D$_6$): δ 164.5 (C-7), 162.4 (C-1”), 160.6 (C-5), 159.4 (C-9), 158.7 (C-4’), 152.5 (C-4), 152.1 (C-5”), 131.5 (C-1’), 129.8 (C-3”), 128.1 (C-2’), 118.9 (C-2”), 113.0 (C-3’), 112.5 (C-4”), 99.6 (C-10), 95.4 (C-6), 93.5 (C-8), 76.0 (C-2), 55.3 (7-OMe), 55.2 (4’-OMe), 32.0 (C-2) ppm.

Sakuranetin 4-(*p*-trifluormethylphenyl)-carbohydrazide (**59**):

Sakuranetin (20 mg, 0.070 mmol) was dissolved in EtOH (2 mL), at room temperature. Then, it was added 4-trifluormethylphenyl-carboxyhydrazide (28.6 mg, 0.140 mmol) and 50 µL of a ethanolic solution of 10% acetic acid. The mixture was kept 48 h under N_2, reflux and constant stirring. The mixture was purified by preparative TLC using *n*-hexane–acetone, 60:40) as mobile phase to afford 12 mg of compound **59**, an amorphous orange brownish powder (0.025 mmol, 33% yield).

ESI-MS (positive mode): *m/z* 473 $[M + H]^+$;

^{1}H-NMR (300 MHz, Acetone-D$_6$): δ 8.07 (1H, *d*, *J* = 8.0 Hz, H-3”), 7.87 (1H, *d*, *J* = 8.0 Hz, H-4”), 7.34 (2H, *d*, *J* = 8.2 Hz, H-2’), 6.81 (2H, *d*, *J* = 8.2 Hz, H-3’), 6.11 (1H, *d*, *J* = 2.3 Hz, H-8), 6.06 (1H, *d*, *J* = 2.3 Hz, H-6), 5.14 (1H, *br d*, *J* = 13.0 Hz, H-2), 3.74 (3H, *s*, 7-OMe), 3.43 (1H, *br d*, *J* = 16.3 Hz, H-3β), 2.99 (1H, *dd*, *J* = 16.3, 13.0 Hz, H-1α) ppm;

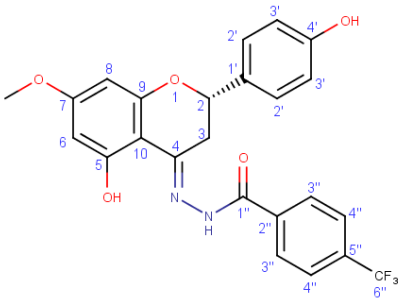

^{13}C-NMR (75 MHz, Acetone-D$_6$): δ 167.0 (C-1”), 163.1 (C-7), 161.0 (C-5), 159.3 (C-9), 157.7 (C-4’), 155.0 (C-4), 137.6 (C-2”), 132.1 (C-5”), 129.6 (C-1’), 129.1 (C-3”), 128.3 (C-2’), 125.4 (C-6”), 115.2 (C-3’), 99.3 (C-10), 95.5 (C-6), 93.7 (C-8), 76.4 (C-2), 55.4 (7-OMe), 32.3 (C-2) ppm.

Sakuranetin 4-(benzoyloxy)-formohydrazide (**60**):

Sakuranetin (20 mg, 0.070 mmol) was dissolved in EtOH (2 mL), at room temperature. Then, it was added benzyl carbazate (17.5 mg, 0.105 mmol) and 50 μL of a ethanolic solution of 10% acetic acid. The mixture was kept 25 h under N_2, reflux and constant stirring. The mixture was purified by preparative TLC using *n*-hexane–acetone, 60:40) as mobile phase to afford 29 mg of compound **60**, an amorphous orange brownish powder (0.066 mmol, 92% yield).

ESI-MS (positive mode): *m/z* 435 $[M + H]^+$;

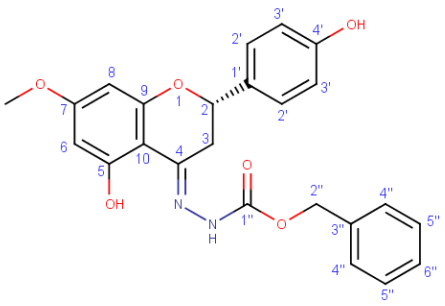

^{1}H-NMR (300 MHz, Acetone-D$_6$): δ 7.52-7.26 (7H, *m*, H-2', H-3", H-4", C-5"), 6.90 (2H, *d*, *J* = 8.4 Hz, H-3', 6.09 (1H, *d*, *J* = 2.5 Hz, H-8), 6.04 (1H, *d*, *J* = 2.4 Hz, H-6), 5.23 (2H, *s*, H-2"), 5.13 (1H, *dd*, *J* = 12.0, 2.6 Hz, H-2), 3.78 (3H, *s*, 7-OMe), 3.32 (1H, *dd*, *J* = 16.7, 2.6 Hz, H-3β), 2.86 (1H, *dd*, *J* = 16.7, 12.0 Hz, H-1α) ppm;

^{13}C-NMR (75 MHz, Acetone-D$_6$): δ 163.7 (C-7), 161.7 (C-9), 160.0 (C-5), 158.5 (C-1"), 151.8 (C-4'), 137.5 (C-3"), 131.5 (C-1'), 129.3 (C-4", C-5"), 129.0 (C-6"), 128.7 (C-2'), 116.1 (C-3'), 100.4 (C-10), 96.3 (C-8), 94.4 (C-6), 77.2 (C-2), 67.6 (C-2"), 55.7 (7-OMe), 32.5 (C-2) ppm.

4'methoxysakuranetin 4-(benzoyloxy)-formohydrazide (**61**):

4-methoxysakuranetin (20 mg, 0.066 mmol) was dissolved in EtOH (2 mL), at room temperature. Then, it was added benzyl carbazate (17.5 mg, 0.105 mmol) and 50 μL of a ethanolic solution of 10% acetic acid. The mixture was kept 48 h under N_2, reflux and constant stirring. The mixture was purified by preparative TLC using *n*-hexane–acetone, 60:40) as mobile phase to afford 14.9 mg of compound **61**, an amorphous orange brownish powder (0.032 mmol, 47% yield).

ESI-MS (positive mode): *m/z* 449 $[M + H]^+$;

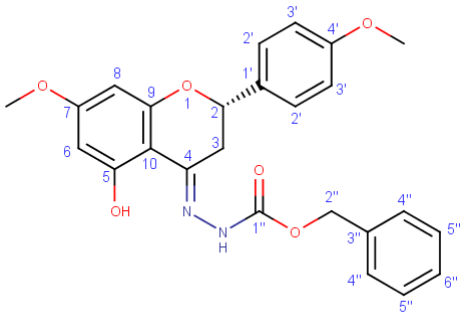

^{1}H-NMR (300 MHz, DMSO-D$_6$): δ 7.45-7.32 (7H, *m*, H-2', H-4", C-5", H-6"), 6.98 (2H, *d*, *J* = 8.7 Hz, H-3'), 6.07 (1H, *d*, *J* = 2.4 Hz, H-6), 6.05 (1H, *d*, *J* = 2.4 Hz, H-8), 5.21 (2H, *s*, H-2"), 5.17 (1H, *dd*, *J* = 12.0, 2.8 Hz, H-2), 3.77 (3H, *s*, 7-OMe), 3.72 (3H, *s*, 4'-OMe), 3.29 (1H, *dd*, *J* = 17.1, 2.8 Hz, H-3β), 2.84 (1H, *dd*, *J* = 17.1, 12.0 Hz, H-1α) ppm;

^{13}C-NMR (75 MHz, DMSO-D$_6$): δ 162.2 (C-7), 162.2 (C-5), 160.0 (C-9), 159.3 (C-4'), 158.3 (C-1"), 152.2 (C-4), 144.4 (C-3"), 131.6 (C-1'), 128.5 (C-2'), 128.4 (C-6"), 127.9 (C-4", C-5"), 113.8 (C-3'), 99.4 (C-10), 95.4 (C-8), 93.6 (C-6), 75.8 (C-2), 66.4 (C-2"), 55.3 (7-OMe), 55.1 (4'-OMe), 34.0 (C-2) ppm.

Sakuranetin 4-(1H-indol-3-yl)-acetohydrazide (**62**):

Sakuranetin (20 mg, 0.070 mmol) was dissolved in EtOH (2 mL), at room temperature. Then, it was added 3-indoleacetic acid hydrazide (26.5 mg, 0.140 mmol) and 50 μL of a ethanolic solution of 10% acetic acid. The mixture was kept 64 h under N_2, reflux and constant stirring. The mixture was purified by preparative TLC using *n*-hexane–EtOAc, 70:30) as mobile phase to afford 12.3 mg of compound **62**, an amorphous yellow powder (0.027 mmol, 38% yield).

ESI-MS (positive mode): *m/z* 458 $[M + H]^+$;

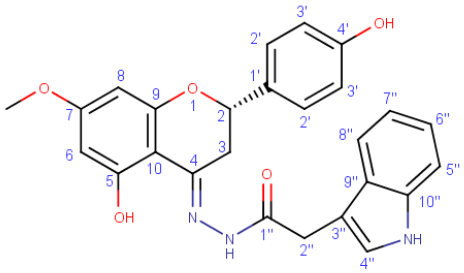

^{1}H-NMR (300 MHz, Acetone-D$_6$): δ 7.64 (1H, *d*, *J* = 7.5 Hz, H-8"), 7.37 (2H, *d*, *J* = 8.0 Hz, H-2'), 7.33 (1H, *d*, *J* = 7.5 Hz, H-5"), 7.30 (1H, *s*, H-4"), 7.08 (1H, *t*, *J* = 7.5 Hz, H-6"), 6.99 (1H, *t*, *J* = 7.5 Hz, H-7"), 6.89 (2H, *d*, *J* = 8.0 Hz, H-3'), 6.06 (1H, *d*, *J* = 2.5 Hz, H-8), 6.00 (1H, *d*, *J* = 2.5 Hz, H-6), 5.08 (1H, *br d*, *J* = 13.6 Hz, H-2), 3.80 (2H, *s*, H-2"), 3.76 (3H, *s*, 7-OMe), 3.15 (1H, *br d*, *J* = 16.0 Hz, H-3β), 2.75 (1H, *dd*, *J* = 16.0, 13.6 Hz, H-1α) ppm;

^{13}C-NMR (75 MHz, Acetone-D$_6$): δ 167.7 (C-7), 164.0 (C-1"), 162.1 (C-5), 160.2 (C-9), 158.6 (C-4'), 152.4 (C-4), 137.5 (C-10"), 131.4 (C-1'), 128.8 (C-2'), 128.4 (C-9"), 124.7 (C-4"),

122.2 (C-6”), 119.7 (C-8”), 119.6 (C-7”), 116.1 (C-3’), 112.2 (C-5”), 109.4 (C-3”), 100.4 (C-10), 96.3 (C-6), 94.4 (C-8), 77.4 (C-2), 55.7 (7-OMe), 32.8 (C-2), 32.2 (C-2”) ppm.

4’-methoxysakuranetin 4-(1H-indol-3-yl)-acetohydrazide (**63**):

4-methoxysakuranetin (20 mg, 0.066 mmol) was dissolved in EtOH (2 mL), at room temperature. Then, it was added 3-indoleacetic acid hydrazide (26.5 mg, 0.140 mmol) and 50 µL of a ethanolic solution of 10% acetic acid. The mixture was kept 64 h under N_2, reflux and constant stirring. The mixture was purified by preparative TLC using *n*-hexane–EtOAc, 50:50) as mobile phase to afford 11.1 mg of compound **63**, an amorphous yellow powder (0.024 mmol, 34% yield).

ESI-MS (positive mode): *m/z* 472 $[M + H]^+$;

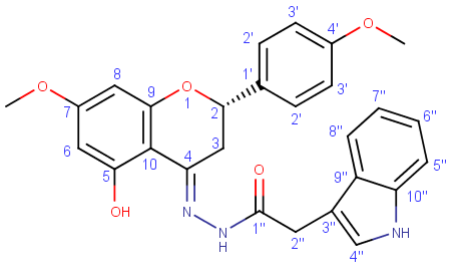

^{1}H-NMR (300 MHz, DMSO-D$_6$): δ 7.58 (1H, *br d*, *J* = 7.8 Hz, H-8”), 7.47 (2H, *d*, *J* = 8.5 Hz, H-2’), 7.34 (1H, *d*, *J* = 7.8 Hz, H-5”), 7.23 (1H, *br s*, H-4”), 7.06 (1H, *br t*, *J* = 7.8 Hz, H-6”), 7.00 (2H, *d*, *J* = 8.5 Hz, H-3’), 6.95 (1H, *br t*, *J* = 7.8 Hz, H-7”), 6.5 (1H, *d*, *J* = 2.2 Hz, H-8), 6.03 (1H, *d*, *J* = 2.2 Hz, H-6), 5.20 (1H, *br d*, *J* = 12.5 Hz, H-2), 3.78 (3H, *s*, 4’-OMe), 3.72 (2H, *s*, H-2”), 3.71 (3H, *s*, 7-OMe), 3.31 (1H, *br d*, *J* = 16.9 Hz, H-3β), 2.95 (1H, *dd*, *J* = 16.9, 12.5 Hz, H-3α) ppm;

^{13}C-NMR (75 MHz, DMSO-D$_6$): δ 167.5 (C-7), 167.4 (C-1”), 162.5 (C-5), 159.4 (C-9), 158.7 (C-4’), 150.8 (C-4), 136.1 (C-10”), 131.4 (C-1’), 128.1 (C-2’), 127.2 (C-9”), 123.9 (C-4”), 121.0 (C-6”), 118.7 (C-8”), 118.4 (C-7”), 113.9 (C-3’), 111.4 (C-5”), 108.3 (C-3”), 99.3 (C-10), 95.4 (C-6), 93.6 (C-8), 75.8 (C-2), 55.3 (4’-OMe), 55.2 (7-OMe), 32.7 (C-3), 30.7 (C-2”) ppm.

7.3.6 Synthesis of nitrogen-containing 4’-alkyl sakuranetin derivatives

7.3.6.1. Reaction of sakuranetin with epichlorohydrin

To 1 eq. of sakuranetin (7-methoxynaringenin, **46**) dissolved in ethanol was added 1.5 eq. of epichlorohydrin. Following, 1.1 eq. of NaOH (dissolved in ethanol) was added to the mixture and the reaction was refluxed overnight and evaporated to dryness under reduced pressure. The residue was then dissolved in ethyl acetate and washed twice with water. The organic layer was dried over Na_2SO_4 and after evaporation under reduced pressure was purified by column chromatography (CH_2Cl_2–acetone, 100:0 to 80:20, followed by CH_2Cl_2–MeOH 95:5 to 75:15) to obtain the desired products (**64** and **65**).

4'-(oxyran-3-yl)sakuranetin (**64**):

Amorphous yellow power, yield 75%;

ESI-MS (positive mode): *m/z* 379 $[M + K]^+$;

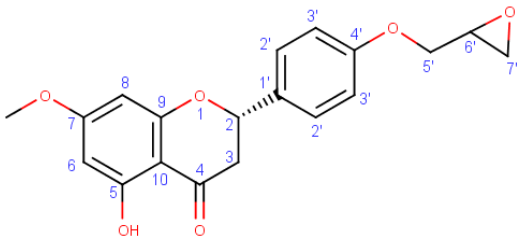

^{1}H-NMR (300 MHz, Acetone-D$_6$): δ 7.49 (2H, *d*, *J* = 8.7 Hz, H-2'), 7.03 (2H, *d*, *J* = 8.7 Hz, H-3'), 6.06 (1H, *d*, *J* = 2.3 Hz, H-6), 6.04 (1H, *d*, *J* = 2.3 Hz, H-8), 5.52 (1H, *dd*, *J* = 12.8, 3.1 Hz, H-2), 4.37 (1H, *dd*, *J* = 11.3, 3.7 Hz, H-5'α), 3.90 (1H, *dd*, *J* = 11.3, 6.4 Hz, H-5'β), 3.84 (3H, *s*, 7-OMe), 3.33 (1H, *ddt*, 6.4, 3.7, 2.6 Hz, H-6'), 3.21 (1H, *dd*, *J* = 17.1, 12.8 Hz, H-3α), 2.85 (1H, *dd*, *J* = 6.4, 3.7 Hz, H-7'α), 2.79 (1H, *dd*, *J* = 17.1, 3.1 Hz, H-3β), 2.72 (1H, *dd*, *J* = 6.4, 2.6 Hz, H-7'β) ppm;

^{13}C-NMR (75 MHz, Acetone-D$_6$): δ 197.5 (C-4), 168.9 (C-7), 165.0 (C-9), 164.1 (C-5), 160.0 (C-4'), 132.3 (C-1'), 129.0 (C-2'), 115.5 (C-3'), 103.8 (C-10), 95.5 (C-6), 94.6 (C-8), 79.8 (C-2), 70.2 (C-5'), 56.3 (7-OMe), 50.6 (C-6'), 44.4 (C-7'), 43.5 (C-3) ppm.

4'-(3-chloro-2-hydroxypropoxy) sakuranetin (**65**):

Amorphous yellow power, yield 25%;

ESI-MS (positive mode): *m/z* 416 $[M + H]^+$;

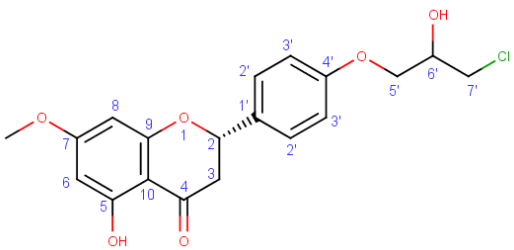

^{1}H-NMR (300 MHz, Acetone-D$_6$): δ 7.48 (2H, *d*, *J* = 8.5 Hz, H-2'), 7.03 (2H, *d*, *J* = 8.5 Hz, H-3'), 6.05 (1H, *d*, *J* = 2.3 Hz, H-6), 6.03 (1H, *d*, *J* = 2.3 Hz, H-8), 5.49 (1H, *dd*, *J* = 12.8, 3.1 Hz, H-2), 4.22 (1H, *p*, *J* = 5.2 Hz, H-6'), 4.13 (2H, *dd*, *J* = 5.2, 0.8 Hz, H-5'), 3.84 (3H, *s*, 7-OMe), 3.83 (1H, *dd*, *J* = 11.2, 5.2 Hz, H-7'α), 3.74 (1H, *dd*,

J = 11.2, 5.2, H-7'β), 3.18 (1H, *dd*, *J* = 17.1, 12.8 Hz, H-3α), 2.77 (1H, *dd*, *J* = 17.1, 3.1 Hz, H-3β) ppm;

^{13}C-NMR (75 MHz, Acetone-D$_6$): δ 197.4 (C-4), 168.8 (C-7), 164.9 (C-9), 164.0 (C-5), 159.9 (C-4'), 132.1 (C-1'), 128.8 (C-2'), 115.4 (C-3'), 103.7 (C-10), 95.5 (C-6), 94.6 (C-8), 79.7 (C-2), 70.4 (C-6'), 70.0 (C-5'), 56.2 (7-OMe), 47.1 (C-7'), 43.4 (C-3) ppm.

7.3.6.2. General preparation of compounds 66-71

Following, to 1 eq. of **64** dissolved in MeOH (3 mL) was added 1eq. of the chosen amine and a catalytic amount of acetic acid (0.01 eq). The mixture was stirred under reflux for 24-48 h. The reaction mixture was evaporated under vaccum (40 ºC) and extracted with ethyl acetate (3 x 50 mL). The organic layers were combined and dried (Na_2SO_4). The solvent was removed under vacuum at 40 ºC and the obtained residue was purified by preparative TLC.

4'-[3-(diethylamino)-2-hydroxypropoxy]-sakuranetin (**66**):

To 20 mg (0.058 mmol) of **64** dissolved in EtOH (3 mL) at room temperature was added diethylamine (8.5 mg, 0.115 mmol) and a catalytic amount of acetic acid. The mixture was kept under N_2 overnight, with reflux and constant stirring. After solvent evaporation and extraction with ethyl acetate, the residue was purified by preparative TLC using CH_2Cl_2–MeOH, 98:2) as mobile phase to afford 15 mg of compound **66**, an amorphous yellow powder (0.036 mmol, 63% yield).

$[\alpha]_D^{20}$ + 8.4 ° (*c* 0.1, MeOH);

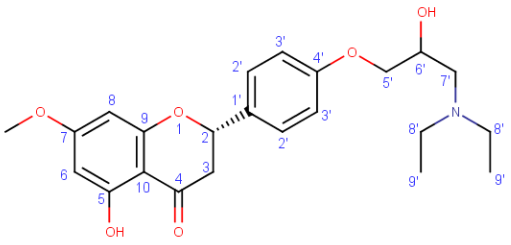

ESI-MS (positive mode): *m/z* 416 $[M + H]^+$;

^{1}H-NMR (300 MHz, Acetone-D$_6$: CDCl$_3$): δ 7.38 (2H, *d*, *J* = 8.8 Hz, H-2'), 6.94 (2H, *d*, *J* = 8.8 Hz, H-3'), 5.99 (1H, *d*, *J* = 2.4 Hz, H-6), 5.98 (1H, *d*, *J* = 2.4 Hz, H-8), 5.39 (1H, *dd*, *J* = 12.8, 3.0 Hz, H-2), 3.97 (3H, *m*, H-5', H-6'), 3.78 (3H, *s*, 7-OMe), 3.08 (1H, *dd*, *J* = 17.2, 12.8 Hz, H-3α), 2.73 (1H, *dd*, *J* = 17.2, 3.0 Hz, H-3β), 2.66-2.48 (6H, *m*, H-7', H-8'), 1.00 (6H, *t*, *J* = 7.1 Hz, H-9') ppm;

^{13}C-NMR (75 MHz, Acetone-D$_6$: CDCl$_3$): δ 196.4 (C-4), 168.1 (C-7), 164.3 (C-9), 163.3 (C-5), 159.6 (C-4'), 131.0 (C-1'), 128.0 (C-2'), 115.0 (C-3'), 103.2 (C-10), 95.0 (C-6), 94.1 (C-8),

79.2 (C-2), 71.0 (C-5'), 66.7 (C-6'), 55.7 (C-7'), 55.1 (7-OMe), 47.6 (C-8'), 43.4 (C-3), 12.0 (C-9') ppm.

4'-[2-hydroxy-3-(piperidin-1-yl)propoxy]-sakuranetin (**67**):

To 20 mg (0.058 mmol) of **64** dissolved in EtOH (3 mL) at room temperature was added piperidine (9.8 mg, 0.115 mmol) and a catalytic amount of acetic acid. The mixture was kept under N_2 overnight, with reflux and constant stirring. After solvent evaporation and extraction with ethyl acetate, the residue was purified by preparative TLC using CH_2Cl_2–MeOH, 98:2) as mobile phase to afford 15 mg of compound **67**, an amorphous yellow powder (0.036 mmol, 62% yield).

ESI-MS (positive mode): *m/z* 428 $[M + H]^+$;

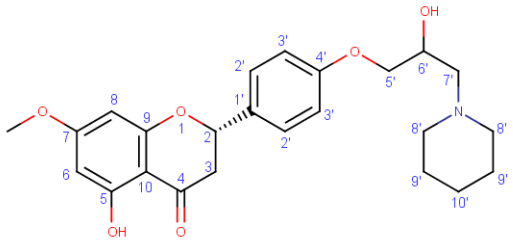

^{1}H-NMR (300 MHz, Acetone-D$_6$: CDCl$_3$): δ 7.37 (2H, *d*, *J* = 8.6 Hz, H-2'), 6.97 (2H, *d*, *J* = 8.6 Hz, H-3'), 6.07 (1H, *d*, *J* = 2.3 Hz, H-6), 6.04 (1H, *d*, *J* = 2.3 Hz, H-8), 5.36 (1H, *dd*, *J* = 13.0, 3.0 Hz, H-2), 4.08 (1H, *tdd*, *J* = 10.3, 6.7, 4.1 Hz, H-6'), 4.00 (1H, *m*, H-5'α), 3.99 (1H, *d*, *J* = 0.8 Hz, H-5'β), 3.80 (3H, *s*, 7-OMe), 3.04 (1H, *dd*, *J* = 17.2, 13.0 Hz, H-3α), 2.78 (1H, *dd*, *J* = 17.2, 3.0 Hz, H-3β), 2.49 (1H, *d*, *J* = 2.5 Hz, H-7'α), 2.47 (1H, *s*, H-7'β), 2.68-2.56 (2H, *m*, H-8'), 2.43-2.23 (2H, *m*, H-8'), 1.66-1.54 (4H, *m*, H-9'), 1.47 (2H, *h*, *J* = 5.7 Hz, H-10') ppm;

^{13}C-NMR (75 MHz, Acetone-D$_6$: CDCl$_3$): δ 196.2 (C-4), 168.1 (C-7), 164.2 (C-9), 163.0 (C-5), 159.4 (C-4'), 130.7 (C-1'), 127.8 (C-2'), 115.0 (C-3'), 103.3 (C-10), 95.2 (C-6), 94.4 (C-8), 79.1 (C-2), 70.7 (C-5'), 65.4 (C-6'), 55.8 (C-7'), 55.2 (7-OMe), 54.8 (C-8'), 43.3 (C-3), 26.2 (C-9'), 24.3 (C-10') ppm.

4'-[Methyl 2-hydroxy-(3-piperidine-4 carboxylate)propoxy]-sakuranetin (**68**):

To 20 mg (0.058 mmol) of **64** dissolved in EtOH (3 mL) at room temperature was added methyl 2-hydroxy-(3-piperidine-4 carboxylate (16.5 mg, 0.115 mmol) and a catalytic amount of acetic acid. The mixture was kept under N_2 overnight, with reflux and constant stirring. After solvent evaporation and extraction with ethyl acetate, the residue was purified by preparative TLC using CH_2Cl_2–MeOH, 95:5) as mobile phase to afford 14 mg of compound **68**, an amorphous yellow powder (0.031 mmol, 53% yield).

$[\alpha]_D^{20}$ – 7.0 ° (*c* 0.1, MeOH);

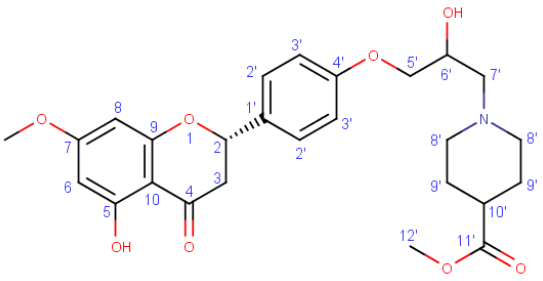

ESI-MS (positive mode): *m/z* 486 $[M + H]^+$;

^{1}H-NMR (300 MHz, Acetone-D$_6$: CDCl$_3$): δ 7.49 (2H, *d*, *J* = 8.6 Hz, H-2'), 7.02 (2H, *d*, *J* = 8.6 Hz, H-3'), 6.06 (1H, *d*, *J* = 2.3 Hz, H-6), 6.04 (1H, *d*, *J* = 2.3 Hz, H-8), 5.53 (1H, *dd*, *J* = 13.0, 3.0 Hz, H-2), 4.10 – 4.05 (3H, *m*, 4'-OMe, H-6'), 3.85 (3H, *s*, 7-OMe), 3.62 (3H, *s*, H-12'), 3.23 (1H, *dd*, *J* = 17.2, 13.0 Hz, H-3α), 2.78 (1H, *dd*, *J* = 17.2, 3.0 Hz, H-3β), 2.50 (1H, *dt*, *J* = 12.6, 5.5 Hz, H-7'α), 2.32 (1H, *m*, H-10'), 2.22 (1H, *td*, *J* = 11.4, 10.7, 2.3 Hz, H-7'β), 2.90 -2.80 (4H, *m*, H-8'), 1.86-1.79 (2H, *m*, H-9'α), 1.77-1.62 (2H, *m*, H-9'β) ppm;

^{13}C-NMR (75 MHz, Acetone-D$_6$: CDCl$_3$): δ 196.7 (C-4), 174.8 (C-11'), 167.8 (C-7), 164.1 (C-5), 163.2 (C-9), 161.5 (C-4'), 130.6 (C-1'), 128.1 (C-2'), 114.6 (C-3'), 102.8 (C-10), 94.6 (C-6), 93.7 (C-8), 79.0 (C-2), 71.1 (C-5'), 64.3 (C-6'), 61.6 (C-7'), 55.4 (7-OMe), 53.8 (C-8'), 42.3 (C-3), 40.6 (C-10'), 28.6 (C-9') ppm.

4'-(2-hydroxy-3-[(1-benzylpiperidin-4-yl)-amino]propoxy) sakuranetin (**69**):

To 20 mg (0.058 mmol) of **64** dissolved in EtOH (3 mL) at room temperature was added N-benzyl-4-aminopiperidine (21.9 mg, 0.115 mmol) and a catalytic amount of acetic acid. The mixture was kept under N_2 overnight, with reflux and constant stirring. After solvent evaporation and extraction with ethyl acetate, the residue was purified by preparative TLC using CH_2Cl_2–MeOH, 95:5) as mobile phase to afford 14 mg of compound **69**, an amorphous yellow powder (0.027 mmol, 46% yield).

$[\alpha]_D^{20}$ + 3.8 ° (*c* 0.1, MeOH);

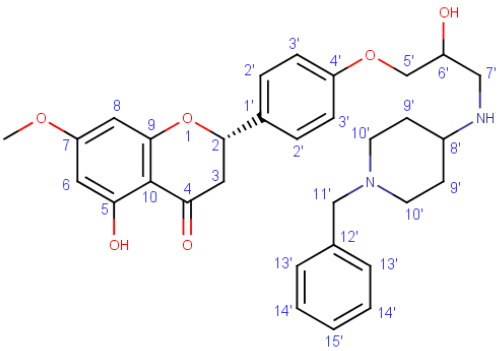

ESI-MS (positive mode): *m/z* 533 $[M + H]^+$;

^{1}H-NMR (300 MHz, Acetone-D$_6$:CDCl$_3$): δ 7.47 (2H, *d*, *J* = 8.6 Hz, H-2'), 7.40 – 7.18 (5H, *m*, H-13', H-14', H-15'), 7.02 (2H, *d*, *J* = 8.6 Hz, H-3'), 5.91 (1H, *d*, *J* = 2.4 Hz, H-6), 5.80 (1H, *d*, *J* = 2.4 Hz, H-8), 5.18 (1H, *dd*, *J* = 12.2, 2.9 Hz, H-2), 4.20 (1H, *dt*, *J* = 10.2, 5.2 Hz, H-6'), 4.14 (1H, *s*, H-5'α), 4.12 (1H, *d*, *J* = 0.9 Hz, H-5'β), 3.86 – 3.70 (3H, *m*, H-7', H-9'), 3.77 (3H, *s*, 7-OMe), 3.50 (2H, *s*, H-11'), 3.29 (1H, *dd*, *J* = 16.8, 2.9 Hz,

H-3β), 2.97 (1H, *dd*, *J* = 16.8, 12.2 Hz, H-3α), 2.85 - 2.67 (4H, *m*, H-10'), 1.98 - 1.56 (4H, *m*, H-9') ppm;

^{13}C-NMR (75 MHz, Acetone-D$_6$:CDCl$_3$): δ 169.9 (C-4), 165.9 (C-7), 165.8 (C-5), 160.7 (C-9), 159.8 (C-4'), 139.9 (C-12'), 133.2 (C-1'), 129.5 (C-13'), 129.0 (C-14'), 128.9 (C-2'), 127.7 (C-15'), 115.4 (C-3'), 101.3 (C-10), 96.3 (C-6), 92.4 (C-8), 77.7 (C-2), 70.4 (C-5'), 70.1 (C-6'), 55.6 (7-OMe), 55.5 (C-8'), 52.2 (C-10'), 47.1 (C-7'), 33.7 (C-9'), 33.5 (C-3) ppm.

4'-(2-hydroxy-3-[1H-indol-1-yl]-propoxy)sakuranetin (**70**):

To 20 mg (0.058 mmol) of **64** dissolved in EtOH (3 mL) at room temperature was added indole (21.9 mg, 0.115 mmol) and a catalytic amount of acetic acid. The mixture was kept under N_2 overnight, with reflux and constant stirring. After solvent evaporation and extraction with ethyl acetate, the residue was purified by preparative TLC using CH_2Cl_2–MeOH, 97:3) as mobile phase to afford 15 mg of compound **70**, an amorphous yellow powder (0.034 mmol, 58% yield).

ESI-MS (positive mode): *m/z* 482 $[M + Na]^+$;

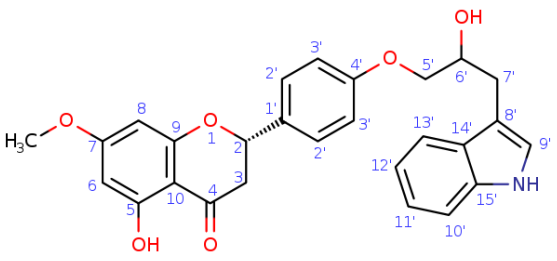

^{1}H-NMR (300 MHz, Acetone-D$_6$:CDCl$_3$): δ 7.56 (1H, *d*, *J* = 7.8 Hz, H-10'), 7.50 (2H, *d*, *J* = 8.7 Hz, H-2'), 7.42 (1H, *dd*, *J* = 7.0, 1.0 Hz, H-13'), 7.09 (1H, *td*, *J* = 7.0, 1.0 Hz, H-12'), 7.04 (2H, *d*, *J* = 8.7 Hz, H-3'), 7.04 (1H, *dd*, *J* = 7.0, 2.1 Hz, H-11'), 6.99 (1H, *td*, *J* = 7.0, 1.0 Hz, H-8'), 6.06 (1H, *d*, *J* = 2.3 Hz, H-6), 6.04 (1H, *d*, *J* = 2.5 Hz, H-8), 5.53 (1H, *dd*, *J* = 12.8, 3.0 Hz, H-2), 4.21 (1H, *h*, *J* = 5.0 Hz, H-6'), 4.14 (1H, *s*, H-5'α), 4.12 (1H, *d*, *J* = 0.9 Hz, H-5'β), 3.77 (2H, *m*, H-7'), 3.22 (1H, *dd*, *J* = 17.1, 12.8 Hz, H-3α), 2.79 (1H, *dd*, *J* = 17.1, 3.0 Hz, H-3β) ppm;

^{13}C-NMR (75 MHz, Acetone-D$_6$:CDCl$_3$): δ 197.4 (C-4), 168.8 (C-7), 165.0 (C-5), 164.1 (C-9), 160.0 (C-4'), 137.2 (C-14'), 132.2 (C-1'), 129.0 (C-15'), 128.9 (C-2'), 125.5 (C-9'), 122.0 (C-10'), 121.0 (C-12'), 119.8 (C-11'), 115.4 (C-3'), 112.1 (C-13'), 103.7 (C-10), 102.3 (C-8'), 95.4 (C-6), 94.6 (C-8), 79.8 (C-2), 70.4 (C-5'), 70.0 (C-6'), 56.2 (7-OMe), 47.1 (C-7'), 43.5 (C-3) ppm.

4'-(2-hydroxy-3-[phenylsulfanyl]propoxy) sakuranetin (**71**):

To 20 mg (0.058 mmol) of sakuranetin (**64**) dissolved in EtOH (3 mL) at room temperature was added indole (21.9 mg, 0.115 mmol) and a catalytic amount of acetic acid. The mixture was kept under N_2 overnight, with reflux and constant stirring. After solvent evaporation and extraction with ethyl acetate, the residue was purified by preparative TLC using CH_2Cl_2–MeOH, 97:3) as mobile phase to afford 24 mg of compound **71**, an amorphous white powder (0.053 mmol, 97% yield).

ESI-MS (positive mode): *m/z* 453 $[M + H]^+$;

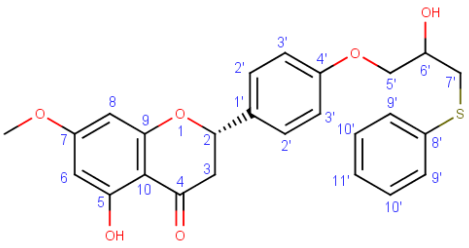

^{1}H-NMR (300 MHz, Acetone-D$_6$: CDCl$_3$): δ 7.55 (2H, *d*, *J* = 8.6 Hz, H-2'), 7.50 (2H, *dd*, *J* = 8.7, 2.1 Hz, H-9'), 7.38 (2H, *td*, *J* = 7.4, 1.6 Hz, H-10'), 7.29 (1H, *dd*, *J* = 7.3, 2.4 Hz, H-11'), 7.04 (2H, *d*, *J* = 8.8 Hz, H-3'), 6.06 (1H, *d*, *J* = 2.3 Hz, H-6), 6.05 (1H, *d*, *J* = 2.5 Hz, H-6), 5.53 (1H, *dd*, *J* = 12.8, 3.0 Hz, H-2), 4.20 (1H, *dq*, *J* = 9.0, 4.8, 4.1 Hz, H-6'), 4.14 (1H, *s*, H-5'α), 4.12 (1H, *d*, *J* = 1.0 Hz, H-5'β), 3.80 (2H, *dd*, *J* = 11.7, 5.3 Hz, H-7'), 3.22 (1H, *dd*, *J* = 17.1, 12.8 Hz, H-3α), 2.79 (1H, *dd*, *J* = 17.1, 3.0 Hz, H-3β) ppm;

^{13}C-NMR (75 MHz, Acetone-D$_6$: CDCl$_3$): δ 196.2 (C-4), 168.8 (C-7), 164.2 (C-9), 164.0 (C-5), 160.0 (C-4'), 137.3 (C-8'), 132.2 (C-1'), 130.2 (C-9'), 128.9 (C-10'), 128.3 (C-11'), 128.2 (C-2'), 115.2 (C-3'), 103.7 (C-10), 95.4 (C-6), 94.6 (C-8), 79.8 (C-2), 70.4 (C-5'), 70.0 (C-6'), 56.2 (7-OMe), 47.1 (C-7'), 43.4 (C-3) ppm.

7.4. Biological Studies

7.4.1. Reversal of multidrug-resistance mediated by P-glycoprotein

7.4.1.1. Cell lines and cultures.

L5178Y mouse T-lymphoma cell (ECACC cat. no. 87111908, U.S. FDA, Silver Springs, MD, USA) were transfected with the pHa *MDR1/A* retrovirus as previously described (Pastan et al., 1988). The *MDR1* overexpressing cell line was further selected by supplementing the growth medium with colchicine (60 ng/mL) in order to maintain the MDR phenotype expression. Both parental (L5178Y-PAR) and MDR (L5178Y-MDR) cells were cultivated in McCoy's 5A supplemented with 10% heat-inactivated horse serum, 100 U/L of L-glutamine and 100 mg/L of a penicillin-streptomycin mixture (Sigma-Aldrich Kft, Budapest, Hungary).

The human colon adenocarcinoma cell lines (Colo 205 parent and Colo 320/MDR-LRP expressing *MDR1*), ATCC-CCL-220.1 (Colo320) and ATCC-CCL-222 (Colo205) were purchased from LGC (Promochem, Teddington, England). The cells were cultured in RPMI 1640 growth medium, supplemented with 10% heat-inactivated fetal bovine serum, 2 mM L-glutamine, 1mM Na-pyruvate and 100 mM HEPES. Following, the semi-adherent human colon cancer cells were detached using 0.25% trypsin and 0.02% EDTA for 5 minutes at 37 ºC and incubated during 4 h in a humidified atmosphere (5% CO_2, 95% air) at the same temperature.

Mouse fibroblasts (NIH/3T3, ATCC® CRL-1658™) (Jainchill et al., 1969) and human fibroblasts (MRC-5, ATCC® CCL-171™, 18th population) (Jacobs et al., 1970) were cultivated in DMEM (GIBCO 52100-039) or EMEM (ATCC® 30-2003) respectively and supplemented with 10% heat-inactivated fetal bovine serum (Biowest, VWR International Kft, Debrecen, Hungary), 100 U/L of L-glutamine, 1% Na-pyruvate, 1% penicillin/streptomycin (Sigma-Aldrich Kft, Budapest, Hungary) and 0.1% nystatin (8.3 g/L in ethylene glycol). The adherent cells were detached using a combination of 0.25% trypsin and 0.02% EDTA for 5 minutes at 37 ºC. Before each cytotoxicity assay using this cell line, cells were seeded in untreated 96-well flat-bottom microtiter plates, following a 4-hour incubation period in a humidified atmosphere (5% CO_2, 95% air) at 37 °C. All cell lines were incubated in a humidified atmosphere (5% CO_2, 95% air) at 37 °C.

7.4.1.2. Anti-proliferative and cytotoxicity assays

The anti-proliferative and cytotoxicity of the compounds was assessed in a range of decreasing concentrations (2-fold dilutions) in several cell lines as follows:

- Cytotoxicity assays
  - Mouse T-lymphoma cell lines (L5178Y-PAR and L5178Y-MDR), all compounds;
  - Human colon adenocarcinoma (Colo205 and Colo320), mouse embryonic fibroblast (NIH/3T3) and human lung fibroblast (MRC-5) cell lines, compounds **1**-**16**;
- Anti-proliferative assays
  - Mouse T-lymphoma cell lines (L5178Y-PAR and L5178Y-MDR), all compounds;
  - Human colon adenocarcinoma (Colo205 and Colo320) cell lines, compounds **1**-**16**;

Compounds **1**-**16** were tested in quadruplicates (L5178Y and Colo cells) and all other in duplicates, with a maximum concentration of 100 μM. Then, cells were distributed into 96-well flat bottom microtiter plates at concentrations of 6 x 10^3 (anti-proliferative) or 1 x 10^4 (cytotoxicity) in 100 μM of medium were added to each well, with the exception of medium and cell control wells. For mouse and human fibroblasts, 10^4 cells were seeded in each well prior to the addition of the compounds.

The microtiter plates were then initially incubated for 72h (anti-proliferative) or 24h (citotoxicity), after which 20 μM of a 5 mg/mL MTT solution in phosphate-saline buffer (PBS) (thiazolyl blue tetrazolium bromide, Sigma-Aldrich Chemie GmbH, Steinheim, Germany) was added to each well and the plates were incubated by another 4 hours. Following, 100 μL of SDS (sodium dodecyl sulfate, 10% in 0.01 M HCl solution) was added to each well and incubated overnight at 37 °C. Cell growth was determined by measuring optical density (OD) at 550 nm (ref. 630 nm) in a Multiscan EX ELISA reader (Thermo Labsystems, Cheshire, WA, USA). The percentage of inhibition of cell growth was determined according to the equation

$$100 - \left[\frac{OD_{sample} - OD_{medium\ control}}{OD_{cell\ control} - OD_{medium\ control}}\right] \times 100 \quad , \quad (1).$$

The results were expressed as the mean ± SD, and the IC_{50} values were obtained by best fitting the dose-dependent inhibition curves independently in Libreoffice Calc and in GraphPad

Prism 5.03 for Windows software ("Graphpad Prism," 2015; Motulsky and Hristopoulos, 2004).

7.4.1.3. Rhodamine-123 accumulation assay

The cells were initially adjusted to a density of 2 x 10^6 /mL, resuspended in a serum-free McCoy's 5A medium (L5178Y cells) or RPM1 1640 (Colo cells) and distributed in 500 µL aliquots in Eppendorf centrifuge tubes. All test compounds were added at 2 and 20 µM, verapamil and tariquidar (positive controls, EGIS Pharmaceuticals PLC, Budapest, Hungary) at 20 and 0.5 µM respectively and DMSO at 2% as solvent control. The samples were incubated at room temperature for 10 min, after which 10 mL (5.2 µM final concentration) of Rhodamine-123 was added and further incubated for 20 min at 37 °C. The samples were washed twice, resuspended in 1 mL PBS and analyzed by flow cytometry (Partec CyFlow® Space instrument, Partec GmbH, Münster, Germany). Histograms were evaluated regarding mean fluorescence intensity (FL-1), standard deviation and both FSC and SSC parameters. The fluorescence activity ratio (FAR) was calculated as the quotient between FL-1 of treated/untreated resistant cell line (L5178Y-MDR, Colo320) over treated/untreated sensitive cell line (L5178Y-PAR, Colo205), according to the following equation

$$FAR = \frac{FL{-}1_{MDR\,treated} \Big/ FL{-}1_{MDR\,untreated}}{FL{-}1_{PAR\,treated} \Big/ FL{-}1_{PAR\,untreated}} \quad , \quad (2).$$

7.4.1.4. Drug combination assay

The combination studies were designed as suggested in the CalcuSyn software manual (http://www.biosoft.com), using a fixed ratio of the compounds across a concentration gradient. The dilution of doxorubicin was made in a horizontal direction (14.7 – 0.1 µM) while the dilutions of the MDR-reversal agents (at 2-fold of their IC_{50}'s) vertically in a microtiter plate to a final volume of 200 µL of medium per well. The cells were distributed into plates in a concentration of 2 x 10^5 /mL per well and were incubated for 48h, under standard conditions. Cell growth was determined after MTT staining, as previously described. Drug interactions were assessed according to Chou using the CalcuSyn v2.2 software (Chou, 2010). Each dose-response curve (individual agents as well as combinations) was fitted to a linear model using the median effect equation, in order to obtain the median effect value (thus corresponding to

the IC_{50}) and slope (m). Goodness-of-fit was assessed using the linear correlation coefficient *r* and only data with $r > 0.90$ was considered. The extent of interaction between drugs was expressed using the combination index (CI) for mutually exclusive drugs. A CI close to 1 indicates additivity; CI < 1 defines synergism and CI > 1 is related to antagonism.

7.4.2. Reversal of drug resistance mediated by P-gp, MRP1 and BCRP

7.4.2.1. Cell lines and cultures

Parental baby hamster kidney-21 (BHK21-PAR) and its resistant counterpart *ABCC1*-transfected (BHK21-MDR) (Chang et al., 1997) were cultivated in Dulbecco's Modified Eagle Medium F-12 (DMEM/F12: Gibco-Life Technologies, Saint Aubin, France). Parental mouse embryonic fibroblasts (NIH/3T3-PAR), human embryonic kidney (HEK293-PAR) and the corresponding *ABCB1*-transfected (NIH/3T3-MDR) (Pastan et al., 1988) and *ABCG2*-transfected with the pcDNA3.1 plasmid coding for the wild-type transporter (HEK293-MDR) resistant cell lines were obtained by culture in DMEM-High glucose medium supplemented with GlutaMAX™ (Gibco-Life Technologies). All cell lines were grown in a humidified atmosphere at 37 ºC in 5% CO_2 and supplemented with 5% heat-inactivated fetal bovine serum (FBS) and 1% of penicillin/streptomycin. In addition, and to selectively maintain the resistant cell lines, 200 μM methotrexate (BHK21-MDR), 60 ng/mL colchicine (NIH/3T3-MDR) or 750 μg/mL of G418 (Sigma Aldrich, HEK293-MDR) was added to the growth medium. Specifically, for HEK293-MDR the monoclonal cell line was obtained by Fluorescence-Activated Cell Sorting (FACS) using the phycoerythrin-coupled 5D3 antibody (Santa Cruz Biotech) as a native expression reporter.

7.4.2.2. Cytotoxicity assays

The cytotoxicity of the compounds was determined using a MTT colorimetric assay as reported in literature (Berridge et al., 1996; Mosmann, 1983). Briefly, BHK21, NIH/3T3 and HEK293 (PAR and MDR) cells were seeded into the 96-well plates at a density of 2×10^3 cells/well for a total growth medium volume of 100 μL and incubated overnight. Following, 100 μL of fresh medium containing sequential concentrations of compounds to be tested (dissolved in DMSO in a 0.5–100 μM concentration range) were added to each well while DMSO control was fixed at 0.5% (v/v). After 72 h incubation, 22 μL of MTT dye in PBS (5 mg/mL) were added to the

wells, the plates were incubated for an additional 4 h at 37 °C, and upon MTT removal, the formazan dye crystals were solubilized with 200 µL of DMSO/ethanol (1:1, v/v). The absorbance was measured using spectrophotometry at 570 nm and 690 nm as reference wavelength. The effect of each compound on cell viability in all cell lines was calculated as the difference in absorbance between test wells and medium control wells and the relative resistance ratio (RR) was calculated as the ratio between IC_{50} for resistant cells and IC_{50} for parental cells.

7.4.2.3. Inhibition tests of MDR pumps mediated drug efflux

Cells were seeded into 96-well plates at a density of 5×10^4 cells/well in 200 µL growth medium and incubated overnight. Following, growth medium was replaced with 100 µL fresh medium and cells were incubated 30 min at 37 °C in the presence of compounds **1**-**22** together with 0.5 µM rhodamine-123 (R123), 5 µM mitoxantrone (MX) and 0.2 µM calcein-AM (cAM) as fluorescent probes for P-gp, BCRP and MRP1, respectively, to a final concentration of DMSO 0.5% (v/v). Next, medium was removed, washed with 100 µL PBS, trypsinized 5 min at 37 °C with 25 µL trypsin and suspended with 175 µL ice-cold PBS with 2% BSA (Bovine Serum Albumin). Intracellular fluorescence was measured with a MacsQuant flow cytometer (Miltenyi Biotec) with, at least, 5.000 cells per run. While MX was excited at 635 nm and fluorescence emission recorded in a 655-730 nm window, R123 and cAM were excited at 488 nm and recorded in a 525-550 nm filter. The compound inhibition efficacy was estimated by using equation 3

$$\%\ inhibition = 100 \times \frac{MDR_{FA} - MDR_{FBG}}{MDR_{FE} - MDR_{FBG}} \quad , \quad (3).$$

where MDR_{FA} and MDR_{FBG} correspond to the intracellular fluorescence of the cells incubated with or withour fluorescent substrate, in the presence of each tested compound. MDR_{FE} correspond to fluorescence measurement in the presence of fluorescent substrate on control non-transfected cells. Assays were performed in triplicate.

7.5. Computational Studies

7.5.1. Molecular Dynamics (MD) studies

7.5.1.1. Initial structures

A system, comprising the whole P-gp transporter inserted in a 1-palmitoyl-2-oleoylphosphatidylcholine (POPC) lipid bilayer, solvated and neutralized with an adequate number of waters and counter-ions respectively (Ferreira et al., 2012), was the starting point for all MD studies. POPC force field parameterization was obtained from previous publications by Poger and co-workers (Poger et al., 2010; Poger and Mark, 2010). Ligand molecules were drawn in MarvinSketch (ChemAxon, 2012), parameterized according to the 53a6 (Oostenbrink et al., 2005, 2004) or 54a7 (Reif et al., 2012; Schmid et al., 2011) parameter sets of GROMOS96 (Bonvin et al., 2000; Chandrasekhar et al., 2005; Daura et al., 1998; Scott et al., 1999) force-field using the Automated Topology Builder (ATB) and Repository (Koziara et al., 2014; Malde et al., 2011) or PRODRG (Schüttelkopf and van Aalten, 2004) on-line servers and manually curated. Mülliken (Mulliken, 1955) or Merz-Kollman (Singh and Kollman, 1984) partial charges were assigned through *ab initio* calculations at the Hartree−Fock level of theory using the 6-31G basis set (Ditchfield et al., 1971; Hariharan and Pople, 1974, 1973; Hehre et al., 1972) with diffuse (neutral) or diffuse/polarization (charged molecules) functions (Clark et al., 1983; Frisch et al., 1984) in the Gaussian03 (Frisch et al., 2004) program. Visual Molecular Dynamics (VMD) (Humphrey et al., 1996) and Molecular Operating Environment (MOE) (Inc, 2015) software's were used for visual inspection and system manipulation.

7.5.1.2. Simulation Parameters

The GROMACS 4.6.x and 5.x simulation packages (Abraham et al., 2015; Berendsen et al., 1995; Hess et al., 2008; Lindahl et al., 2001; Páll et al., 2015; Pronk et al., 2013; Van Der Spoel et al., 2005) were used for the MD simulations. All simulations applied periodic boundary conditions (PBC) (Allen and Tildesley, 1987; van Gunsteren and Berendsen, 1990). Initial energy minimizations were performed using the steepest descent method. While *NVT* runs employed the Velocity-rescale (V-rescale) (Bussi et al., 2007) thermostat, *NpT* runs used the Nosé-Hoover (Hoover, 1985; Nosé and Klein, 1983) thermostat and the Parrinello-Rahman (Nosé and Klein, 1983; Parrinello, 1981) barostat for temperature (303 K) and pressure

coupling (1 bar), respectively. In the presence of membranes, the pressure equilibration was achieved through a semi-isotropic pressure coupling, with system compressibility defined as $4.5x10^{-5}$ bar^{-1} and initial box with dimensions *xyz* of 12.75 x 12.75 x 16.55 nm^3. Particle Mesh Ewald (PME) (Darden et al., 1993; Essmann et al., 1995) method with cubic interpolation and FFT grid spacing of 0.16 was used for long-range electrostatics, with identical short-range cut-off radius for electrostatic and van der Waals interactions (10 Å). Group-based or Verlet (Páll and Hess, 2013) cut-off schemes were applied for the calculation of non-bonded interactions on CPU and GPU respectively. SETTLE (Miyamoto and Kollman, 1992) (for water molecules) or LINCS (Hess, 2008; Hess et al., 1997) algorithms were used to constrain all bond lengths.

7.5.1.3. Steered Molecular Dynamics (sMD)

Two systems were built. For each system both colchicine and tariquidar molecules (neutral forms) were placed at the previously identified "entrance gate" located between transmembranar helices (TMH) 10 and 12 using a docking protocol available in MOE. Then, 10 runs of simulated annealing were performed, each one comprising six cycles with an iteration limit of 4000 at an initial temperature of 1000 K, after which the best ranked pose was chosen and converted into GROMOS96 format. Following, after a brief cycle of energy minimization in GROMACS, both molecules were pulled away from the 'entrance gate' along the axes, parallel to the bilayer plane, into the drug-binding pocket (for 10 ns) or into the hydrophobic membrane core (for 15 ns), using a spring constant of 1000 $kJ.mol^{-1}.nm^{-2}$ and a pull rate of 0.15 $nm.ns^{-1}$. In each case, molecules were pulled from its center of mass by using an umbrella potential along a vector in the *xy* plane between the reference group (P-gp) and one or more groups (colchicine and tariquidar molecules).

Other sMD runs were performed by pulling a molecule from the hydrophobic core of the lipid bilayer into the bulk water environment. Towards that end, colchicine and tariquidar were inserted in an equilibrated POPC membrane, solvated with an adequate number of water molecules. When in the presence of protonated tariquidar (+1 net charge), a chlorine ion was added to neutralize the global charge of the system. Following, the system was energy minimized and a 10 ps *NVT* equilibration run followed, above the POPC gel-fluid transition phase temperature (Leekumjorn and Sum, 2007), at 303 K. Following, both molecules were pulled during 20 ns and away from the lipid bilayer along the normal axis of the interface (*z*), using a spring constant of 500 $kJ.mol^{-1}.nm^{-2}$ and a pull rate of 0.25 $nm.ns^{-1}$. In each case,

molecules were pulled from its center of mass by using an umbrella potential along the vector *z* between the reference group (POPC membrane) and one or more groups (colchicine or tariquidar).

7.5.1.4. Adsorption Runs

In order to determine the free energy of adsorption of the molecules toward P-gp or lipid bilayer, four groups (Didziapetris et al., 2003; Polli et al., 2001; Rautio et al., 2006) were defined: alprenolol, diphenhydramine and ranitidine (*non-substrates*); verapamil, colchicine, Rhodamine-123, Hoechst 33342 and trimethoprim (*substrates*); latilagascene D, tariquidar and the flavonoid kaempferide (*modulators*). Colchicine, latilagascene D, kaempferide and trimethoprim were considered to be neutral at physiological pH (based on the pKa values of ionizable groups calculated in MarvinSketch) (ChemAxon, 2012). Another system solely comprising ATP adsorption was analyzed separately. In each system, sixteen molecules (~15 μM) were randomly placed in the bulk solvent around the cytoplasmic NBD domains and all water molecules within 2 Å were removed to avoid clashes. All systems were energy minimized followed by a 50 ns unrestricted *NpT* run. For sampling purposes, two (H33342 and tariquidar) and three (kaempferide) other systems were built. Finally, for comparison purposes, the *apo* system MD simulation described in a previous paper (Ferreira et al., 2012) was extended for an additional 50 ns.

7.5.2. Data analysis

7.5.2.1. General analysis

Root mean square deviation (RMSD), radius of gyration (GYR) and root mean square fluctuations (RMSF) were calculated with internal GROMACS routines. Hydrogen-bond and non-bonded interactions between molecules and protein residues were evaluated using *g_hbond* (van der Spoel et al., 2006) and *g_contacts* (Blau and Grubmuller, 2013) tools. Internal drug-binding pocket volume variations as a function of time [P(V) vs. *t*] were calculated using VOIDOO (Kleywegt and Jones, 1994) software with a 1.2 Å probe radius and a primary grid size of 0.7 Å and in-house python scripts. For each class of molecules, the P-gp pocket volume probability distribution was obtained by calculating the frequency that each instantaneous value felt in bins of size 100 $Å^3$. Principal Component analysis (PCA) for the evaluation of the

transporter's motion patterns was performed using the ProDy (Bahar et al., 2010; Bakan et al., 2011) software through the NMWiz plugin in VMD. Free energies of binding were calculated in *g_mmpbsa* (Baker et al., 2001; Kumari et al., 2014) with polar solvation energies corrected by generating ion-accessibility and dielectric maps incorporating membrane environment (dielectric slab constant is set to 2.0 using the *draw_membrane2* program, http://www.poissonboltzmann.org) through in-house python scripts. Area per lipid (A_L) and thickness (D_{HH}) were calculated with GridMAT-MD (Allen et al., 2009) or in-house developed python scripts.

7.5.2.2. Umbrella sampling

The trajectories obtained by sMD were used to define a reaction coordinate for the entrance of both molecules from the lipid bilayer into the internal drug-binding pocket. For colchicine and tariquidar, 52 (total distance: colchicine, 3.9 nm) or 58 (total distance: tariquidar, 4.2 nm) umbrella windows with a mean width of 0.7 Å were considered and, in each window, another 20 ns of MD was performed. For the lipid-water systems, 28 umbrella windows (reaction coordinate of 5.6 nm) with a mean width of 2 Å were considered and 10 ns MD was performed in each one. Analysis of results was done through the weighted histogram analysis method (WHAM) by using the *g_wham* (Hub et al., 2010) program available in GROMACS. Statistical errors were estimated using the bootstrap analysis technique by bootstraping new trajectories from Gaussian distributions with average and width taken from the respective histogram (b-hist, default method). The convergence of the PMF was assessed by generating PMFs with different sampling times (10, 12.5 and 15 ns for the protein-lipid system and 5, 6 and 7 ns for the lipid-water system respectively).

7.5.2.3. Adsorption runs

The trajectories of each molecule that adsorbed either to the NBD domains or the lipid-water interface were used to estimate the free energy of adsorption of the molecules, herein calculated from the probability of a given molecule to be found bound to i) the surface of the nucleotide-binding domains or ii) the lipid-water interface. For protein adsorption, the normalized probability density (P_i) was obtained with GROMACS tool *g_rdf* as a radial distribution function for the center of mass densities of a molecule A at a distance *r* around the closest atom in B, in this case the protein surface. Similarly, for lipid adsorption, and considering that the

lipid bilayer is similar to a flat surface where molecules adsorb, P_i was obtained in three steps. First, *g_traj* tool was used to extract the *z* coordinate for the center of mass of a given molecule as a function of time. Following, the probability distribution function for each molecule to be at a certain distance from the lipid bilayer was determined by first splitting the obtained plot in several bins (Δ_r = 0.05 Å) and calculating the frequency f_i of a molecule in each bin. Finally, from the positional probability p_i obtained from equation 3

$$p_i = \frac{f_i}{\sum f_i}, with\ \sum p_i = 1 \quad , \quad (3)$$

it was possible to calculate the normalized probability density P_i as the quotient between the positional probability (p_i) and bin width (Δ_r),

$$P_i = \frac{p_i}{\Delta r}\ , with\ \sum p_i . \Delta r = 1 \quad , \quad (4).$$

The calculated distributions for each adsorbed molecule were used to calculate the free energies of adsorption to the protein or to the lipid through the probability ratio method (Mezei, 1989; Raut et al., 2005). For each molecule considered, the relative free energy difference (ΔG_i) between two positions was calculated as the difference between the free energy in a given position (G_i) and of a reference state (G_0), which can be estimated by equation 5

$$\Delta G_i = G_i - G_0 = -RT . ln\left[\frac{P_i}{P_0}\right] \qquad (5),$$

where *R* is the ideal gas constant and *T* the absolute temperature (303 K). For the protein adsorption calculations, the reference state was obtained using the values in bulk water at 20 Å from the interfaces. When adsorption was fast, this cut-off was reduced to 10 Å due to lack of statistics for distances larger than this value (the molecules moved rapidly towards the interface with low probability to be found at larger distances). Finally, the overall free energy of adsorption (ΔG_{ads}) for a given molecule was calculated from the weighted sums of the relative free energies according to equation

$$\Delta G_{ads} = \int_{bin} P_i . \Delta G_i . \mathrm{d}r \approx \sum [P_i . \Delta G_i . \Delta r] \qquad (6).$$

For each class, the spatial distribution of molecules around P-gp was calculated with *g_spatial* tool, after centering the protein and removing its periodicity, rotational and translational motions.

Membrane leaflets are herein identified as upper and lower leaflets, with the lower leaflet being the one close to the nucleotide-binding domains (i.e. cytoplasmic leaflet). Membrane biophysics were characterized by means of area per lipid (A_L) and thickness (D_{HH}) and free energy calculations (ΔG_{def} and ΔG_{res}). A_L and D_{HH} were obtained from the last 10 ns of each trajectory when the large majority of the molecules were adsorbed to the membrane. This was accomplished by extracting a 6 x 6 nm² bilayer section around the geometrical center of each molecule, using in-house python scripts, in order to create suitable input files for GridMAT-MD calculations. Free-energy studies on membrane-deformation energy penalty (ΔG_{def}) and residual hydrophobic exposure energy penalty (ΔG_{res}) were calculated through the hybrid Continuum-Molecular Dynamics (CTMD) approach described in CTMD (Mondal et al., 2011; Shan et al., 2011) papers. Statistical results were performed using the Student's *T*-Test in Libreoffice Calc.

7.5.3. Molecular Docking studies

7.5.3.1. Docking studies

Molecular docking was performed in a previously published P-glycoprotein, derived from the original crystallographic data, comprising 100% identity between mouse and human structures for the residues inside the DBP. MarvinSketch was used for drawing structures. All ligands were exported to MOE, minimized with the MMFF94x (Halgren, 1999) force-field (adjusting hydrogen and lone pairs by default) and exported again as mol2 files in order to generate PDBQT files with AutoDockTools v1.5.6rc (Morris et al., 2009) for utilization in AutoDock VINA 1.1.2 (Trott and Olson, 2010) docking software. The binding location was defined by a docking box including the whole internal cavity defined by Aller *et al.* (Aller et al., 2009), centered at the DBP and with dimensions *xyz* of 35.25, 25.50 and 45.25 Å respectively (*xy* corresponds to the membrane plane). Due to the large search space volume (over 40.000 Å³), 'exhaustiveness' parameter was manually set to 50. Visual inspection of the docking poses was made in MOE to allow the identification of individual docking zones.

7.5.3.2. Identification of drug-binding pockets

As it was experimentally demonstrated that the H and R-sites are located next to the inner leaflet interface of the membrane bilayer, a cavity search was performed with EPOS^{BP} (Brady and

Stouten, 2000; Kohlbacher and Lenhof, 2000) software (default parameters) over the whole drug-binding pocket in an attempt to identify specific drug-binding sites that could be related with sucH-sites. Thus, each molecules' top-ranked pose in the previously identified binding zones was overlapped with the cavity search results (by EPOS^{BP}), allowing the identification of lining atoms (within a distance of 5 Å from the pocket probes) and mean pocket volumes/polarity calculations (ratio of the sum of N, O, and S atoms to the sum of N, O, S, and C atoms).

7.5.3.3. Pocket assignment

The identified drug-binding pockets were defined as substrate- or modulator-binding sites according to the molecules that preferentially docked in each location. Based on the information by Shapiro *et al.* and Lugo and Sharom (Lugo and Sharom, 2005; Shapiro et al., 1997; Shapiro and Ling, 1998, 1997b; Tang et al., 2004), the substrate-binding sites H and R were initially assigned from top ranked docking poses of H33342 and R123 respectively. Other experimentally assigned molecules were also used in DBS identification. In a similar way as in the studies by Loo and Clarke (Loo et al., 2003; Loo and Clarke, 2001), the modulator-binding (M) site was identified based on the interaction with verapamil (top-ranked docking poses).

References

Äänismaa, P., Gatlik-Landwojtowicz, E., Seelig, A., 2008. P-glycoprotein senses its substrates and the lateral membrane packing density: consequences for the catalytic cycle. *Biochemistry* **47**, 10197–10207.

Abad-Zapatero, C., 2007. Ligand efficiency indices for effective drug discovery. *Expert Opin Drug Discov* **2**, 469–488.

Abraham, M.J., Murtola, T., Schulz, R., Páll, S., Smith, J.C., Hess, B., Lindahl, E., 2015. GROMACS: High performance molecular simulations through multi-level parallelism from laptops to supercomputers. *SoftwareX* **1**–**2**, 19–25.

Akiyama, S., Cornwell, M.M., Kuwano, M., Pastan, I., Gottesman, M.M., 1988. Most drugs that reverse multidrug resistance also inhibit photoaffinity labeling of P-glycoprotein by a vinblastine analog. *Mol Pharmacol* **33**, 144–147.

Allen, M.P., Tildesley, D.J., 1987. *Computer Simulation of Liquids.* Oxford University Press, New York, NY.

Allen, W.J., Lemkul, J.A., Bevan, D.R., 2009. GridMAT-MD: a grid-based membrane analysis tool for use with molecular dynamics. *J Comput Chem* **30**, 1952–1958.

Aller, S.G., Yu, J., Ward, A., Weng, Y., Chittaboina, S., Zhuo, R., Harrell, P.M., Trinh, Y.T., Zhang, Q., Urbatsch, I.L., Chang, G., 2009. Structure of P-glycoprotein reveals a molecular basis for poly-specific drug binding. *Science* **323**, 1718–1722.

Allikmets, R., Schriml, L.M., Hutchinson, A., Romano-Spica, V., Dean, M., 1998. A human placenta-specific ATP-binding cassette gene (ABCP) on chromosome 4q22 that is involved in multidrug resistance. *Cancer Res* **58**, 5337–5339.

Altenberg, G.A., Vanoye, C.G., Horton, J.K., Reuss, L., Julie, K., 1994. Unidirectional fluxes of rhodamine 123 in multidrug-resistant cells: evidence against direct drug extrusion from the plasma membrane. *Proc Natl Acad Sci U S A* **91**, 4654–4657.

Ambudkar, S. V, Kim, I., Sauna, Z.E., 2006. The power of the pump: mechanisms of action of P-glycoprotein (ABCB1). *Eur J Pharm Sci* **27**, 392–400.

Anderson, A.C., 2003. The Process of Structure-Based Drug Design. *Chem Biol* **10**, 787–797.

Anjaneyulu, V., Rao, G.S., Connolly, J.D., 1985. Occurrence of 24-epimers of cycloart-25-ene-3β,24-diols in the stems of Euphorbia trigona. *Phytochemistry* **24**, 1610–1612.

Appendino, G., Jakupovic, S., Tron, G.C., Jakupovic, J., Milon, V., Ballero, M., 1998. Macrocyclic diterpenoids from Euphorbia semiperfoliata. *J Nat Prod* **61**, 749–756.

Appendino, G., Tron, G.C., Cravotto, G., Palmisano, G., Annunziata, R., Baj, G., Surico, N., 1999. Synthesis of Modified Ingenol Esters. *Eur J Org Chem* **1999**, 3413–3420.

Baguley, B.C., 2010. Multiple drug resistance mechanisms in cancer. *Mol Biotechnol* **46**, 308–316.

Bahar, I., Lezon, T.R., Bakan, A., Shrivastava, I.H., 2010. Normal mode analysis of biomolecular structures: functional mechanisms of membrane proteins. *Chem Rev* **110**, 1463–1497.

Bakan, A., Meireles, L.M., Bahar, I., 2011. ProDy: protein dynamics inferred from theory and experiments. *Bioinformatics* **27**, 1575–1577.

Baker, N.A., Sept, D., Joseph, S., Holst, M.J., McCammon, J.A., 2001. Electrostatics of nanosystems: Application to microtubules and the ribosome. *Proc Natl Acad Sci U S A* **98**, 10037–10041.

Baptista, R., Ferreira, R.J., dos Santos, D.J., Fernandes, M.X., Ferreira, M.-J.U., 2016. Optimizing the macrocyclic diterpenic core toward the reversal of multidrug resistance in cancer. *Future Med Chem* **8**, 629–645.

Barriault, L., 2016. Diterpenes, in: Zografos, A.L. (Ed.), *From Biosynthesis to Total Synthesis.* John Wiley & Sons, Inc, Hoboken, NJ, pp. 279–295.

Bartsch, H., Hecker, E., 1969. Zur Chemie des Phorbols, XII - Phorbobutanon. *Z Naturforsch B* **24**, 99–106.

Beck, W.T., Cirtain, M.C., Glover, C.J., Felsted, R.L., Safa, A.R., 1988. Effects of indole alkaloids on multidrug resistance and labeling of P-glycoprotein by a photoaffinity analog of vinblastine. *Biochem Biophys Res Commun* **153**, 959–966.

Becker, J., Depret, G., Van Bambeke, F., Tulkens, P.M., Prévost, M., van Bambeke, F., 2009. Molecular models of human P-glycoprotein in two different catalytic states. *BMC Struct Biol* **9**, 1–18.

Berendsen, H.J., van der Spoel, D., van Drunen, R., 1995. GROMACS: A message-passing parallel molecular dynamics implementation. *Comput Phys Commun* **91**, 43–56.

Berridge, M., Tan, A., McCoy, K., Wang, R., 1996. The biochemical and cellular basis of cell proliferation assays that use tetrazolium salts. *Biochemica* **4**, 4–9.

Biggin, P.C., Bond, P.J., 2008. Molecular dynamics simulations of membrane proteins. *Methods Mol Biol* **443**, 147–160.

Blau, C., Grubmuller, H., 2013. g_contacts: Fast contact search in bio-molecular ensemble data. *Comput Phys Commun* **184**, 2856–2859.

Bobrowska-Hägerstrand, M., Wróbel, A., Mrówczyńska, L., Söderström, T., Shirataki, Y., Motohashi, N., Molnár, J., Michalak, K., Hägerstrand, H., 2003. Flavonoids as inhibitors of MRP1-like efflux activity in human erythrocytes. A structure-activity relationship study. *Oncol Res* **13**, 463–469.

Bonvin, A.M., Mark, A.E., van Gunsteren, W.F., 2000. The GROMOS96 benchmarks for molecular simulation. *Comput Phys Commun* **128**, 550–557.

Borges-Walmsley, M.I., McKeegan, K.S., Walmsley, A.R., 2003. Structure and function of efflux pumps that confer resistance to drugs. *Biochem J* **376**, 313–338.

Borghi, D., Baumer, L., Ballabio, M., Arlandini, E., Perellino, N.C., Minghetti, A., Vincieri, F.F., 1991. Structure Elucidation of Helioscopinolides D and E from Euphorbia calyptrata Cell Cultures. *J Nat Prod* **54**, 1503–1508.

Boumendjel, A., Macalou, S., Valdameri, G., Pozza, A., Gauthier, C., Arnaud, O., Nicolle, E., Magnard, S., Falson, P., Terreux, R., Carrupt, P.-A., Payen, L., Di Pietro, A., 2011. Targeting the Multidrug ABCG2 Transporter with Flavonoidic Inhibitors: In Vitro Optimization and In Vivo Validation. *Curr Med Chem* **18**, 3387–3401.

Brady, G.P., Stouten, P.F., 2000. Fast prediction and visualization of protein binding pockets with PASS. *J Comput Aided Mol Des* **14**, 383–401.

Bretscher, M.S., Munro, S., 1993. Cholesterol and the Golgi apparatus. *Science* **261**, 1280–1281.

Brewer, F.K., Follit, C.A., Vogel, P.D., Wise, J.G., 2014. In Silico Screening for Inhibitors of P-Glycoprotein that Target the Nucleotide Binding Domains. *Mol Pharmacol* **86**, 716–726.

Broccatelli, F., Carosati, E., Neri, A., Frosini, M., Goracci, L., Oprea, T.I., Cruciani, G., 2011. A novel approach for predicting P-glycoprotein (ABCB1) inhibition using molecular interaction fields. *J Med Chem* **54**, 1740–1751.

Brooks, T.A., Minderman, H., O'Loughlin, K.L., Pera, P., Ojima, I., Baer, M.R., Bernacki, R.J., Brooks, T., 2003. Taxane-based reversal agents modulate drug resistance mediated by P-glycoprotein, multidrug resistance protein, and breast cancer resistance protein. *Mol Cancer Ther* **2**, 1195–1205.

Brunger, A.T., Adams, P.D., 2012. Refinement of X-ray Crystal Structures., in: Egelman, E.H. (Ed.), *Comprehensive Biophysics*. Elsevier Inc., pp. 105–115.

Burkhart, C.A., Watt, F., Murray, J., Pajic, M., Prokvolit, A., Xue, C., Flemming, C., Smith, J., Purmal, A., Isachenko, N., Komarov, P.G., Gurova, K. V., Sartorelli, A.C., Marshall, G.M., Norris, M.D., Gudkov, A. V., Haber, M., 2009. Small-molecule multidrug resistance-associated protein 1 inhibitor reversan increases the therapeutic index of chemotherapyin mouse models of neuroblastoma. *Cancer Res* **69**, 6573–6580.

Burnley, B.T., Afonine, P. V, Adams, P.D., Gros, P., 2012. Modelling dynamics in protein crystal structures by ensemble refinement. *Elife* **1**, e00311. doi:10.7554/eLife.00311

Bussi, G., Donadio, D., Parrinello, M., 2007. Canonical sampling through velocity rescaling. *J Chem Phys* **126**, 14101–14107.

Cabrera, M.A., González, I., Fernández, C., Navarro, C., Bermejo, M., 2006. A topological substructural approach for the prediction of P-glycoprotein substrates. *J Pharm Sci* **95**, 589–606.

Caffrey, M., 2003. Membrane protein crystallization. *J Struct Biol* **142**, 108–132.

Callaghan, R., Ford, R.C., Kerr, I.D., 2006. The translocation mechanism of P-glycoprotein. *FEBS Lett* **580**, 1056–1063.

Callaghan, R., George, A.M., Kerr, I.D., 2012. Molecular aspects of the translocation process by ABC proteins, in: *Comprehensive Biophysics*. Elsevier, pp. 145–173.

Castagnolo, D., Contemori, L., Maccari, G., Avramova, S.I., Neri, A., Sgaragli, G., Botta, M., 2010. From Taxuspine X to Structurally Simplified Taxanes with Remarkable P-Glycoprotein Inhibitory Activity. *ACS Med Chem Lett* **1**, 416–421.

Cen, J., Zhang, L., Liu, F., Zhang, F., Ji, B.-S., 2016. Long-Term Alteration of Reactive Oxygen Species Led to Multidrug Resistance in MCF-7 Cells. *Oxid Med Cell Longev* **2016**, 1–15.

Chan, W., Calderon, G., Swift, A.L., Moseley, J., Li, S., Hosoya, H., Arias, I.M., Ortiz, D.F., 2005. Myosin II regulatory light chain is required for trafficking of bile salt export protein to the apical membrane in Madin-Darby canine kidney cells. *J Biol Chem* **280**, 23741–23747.

Chandrasekhar, I., Bakowies, D., Glättli, A., Hünenberger, P., Pereira, C., van Gunsteren, W.F., 2005. Molecular dynamics simulation of lipid bilayers with GROMOS96: Application of surface tension. *Mol Simulat* **31**, 543–548.

Chang, S.-Y., Liu, F.-F., Dong, X.-Y., Sun, Y., 2013. Molecular insight into conformational transmission of human P-glycoprotein. *J Chem Phys* **139**, 225102. doi:10.1063/1.4832740

Chang, X.B., Hou, Y.X., Riordan, J.R., 1997. ATPase activity of purified multidrug resistance-associated protein. *J Biol Chem* **272**, 30962–30968.

Chartrain, M., Riond, J., Stennevin, A., Vandenberghe, I., Gomes, B., Lamant, L., Meyer, N., Gairin, J.E., Guilbaud, N., Annereau, J.P., 2012. Melanoma chemotherapy leads to the selection of ABCB5-expressing cells. *PLoS One* **7**, e36762. doi:10.1371/journal.pone.0036762

Chebil, L., Humeau, C., Anthoni, J., Dehez, F., Engasser, J.-M., Ghoul, M., 2007. Solubility of Flavonoids in Organic Solvents. *J Chem Eng Data* **52**, 1552–1556.

Chen, C.-K., Law, W.-C., Aalinkeel, R., Yu, Y., Nair, B., Wu, J., Mahajan, S., Reynolds, J.L., Li, Y., Lai, C.K., Tzanakakis, E.S., Schwartz, S. a, Prasad, P.N., Cheng, C., 2014. Biodegradable cationic polymeric nanocapsules for overcoming multidrug resistance and enabling drug-gene co-delivery to cancer cells. *Nanoscale* **6**, 1567–1572.

Chen, C., Hanson, E., Watson, J.W., Lee, J.S., 2003. P-glycoprotein limits the brain penetration of nonsedating but not sedating H1-antagonists. *Drug Metab Dispos* **31**, 312–318.

Chiba, P., Burghofer, S., Richter, E., Tell, B., Moser, A., Ecker, G., 1995. Synthesis, Pharmacologic Activity, and Structure-Activity Relationships of a Series of Propafenone-Related Modulators of Multidrug Resistance. *J Med Chem* **38**, 2789–2793.

Chiba, P., Ecker, G.F., Schmid, D., Drach, J., Tell, B., Goldenberg, S., Gekeler, V., 1996. Structural requirements for activity of propafenone-type modulators in P-glycoprotein-mediated multidrug resistance. *Mol Pharmacol* **49**, 1122–1130.

Chiba, P., Hitzler, M., Richter, E., Huber, M., Tmej, C., Giovagnoni, E., Ecker, G.F., 1997. Studies on Propafenone-type Modulators of Multidrug Resistance III: Variations on the Nitrogen. *Quant Struct-Act Relat* **16**, 361–366.

Chou, T.-C., 2010. Drug Combination Studies and Their Synergy Quantification Using the Chou-Talalay Method. *Cancer Res* **70**, 440–446.

Clark, T., Chandrasekhar, J., Spitznagel, G.W., Schleyer, P.V.R., 1983. Efficient diffuse function-augmented basis sets for anion calculations. III. The 3-21+G basis set for first-row elements, Li-F. *J Comput Chem* **4**, 294–301.

Clay, A.T., Lu, P., Sharom, F.J., 2015. Interaction of the P-glycoprotein Multidrug Transporter with Sterols. *Biochemistry* **54**, 6586-6597.

Cole, S.P., 2014a. Targeting Multidrug Resistance Protein 1 (MRP1, ABCC1): Past, Present, and Future. *Ann Rev Pharmacol Toxicol* **54**, 95–117.

Cole, S.P., 2014b. Multidrug Resistance Protein 1 (MRP1, ABCC1), a "Multitasking" ATP-binding Cassette (ABC) Transporter. *J Biol Chem* **289**, 30880–30888.

Cole, S.P., Bhardwaj, G., Gerlach, J.H., Mackie, J.E., Grant, C.E., Almquist, K.C., Stewart,

A.J., Kurz, E.U., Duncan, A.M., Deeley, R.G., 1992. Overexpression of a transporter gene in a multidrug-resistant human lung cancer cell line. *Science* **258**, 1650–1654.

Conseil, G.G., Baubichon-Cortay, H., Dayan, G., Jault, J.-M., Barron, D., Di Pietro, A., 1998. Flavonoids: A class of modulators with bifunctional interactions at vicinal ATP- and steroid-binding sites on mouse P-glycoprotein. *Proc Natl Acad Sci U S A* **95**, 9831–9836.

Cooray, H.C., Janvilisri, T., Van Veen, H.W., Hladky, S.B., Barrand, M.A., 2004. Interaction of the breast cancer resistance protein with plant polyphenols. *Biochem Biophys Res Commun* **317**, 269–275.

Cramer, J., Kopp, S., Bates, S.E., Chiba, P., Ecker, G.F., 2007. Multispecificity of drug transporters: probing inhibitor selectivity for the human drug efflux transporters ABCB1 and ABCG2. *ChemMedChem* **2**, 1783–1788.

Crespi-Perellino, N., Garofano, L., Arlandini, E., Pinciroli, V., Minghetti, A., Vincieri, F.F., Danieli, B., 1996. Identification of New Diterpenoids from Euphorbia calyptrata Cell Cultures. *J Nat Prod* **59**, 773–776.

da Silva, S.A.S., Agra, M. de F., Tavares, J.F., Da-Cunha, E.V.L., Barbosa-Filho, J.M., da Silva, M.S., 2010. Flavanones from aerial parts of Cordia globosa (Jacq.) Kunth, Boraginaceae. *Braz J Pharmacogn*. **20**, 682–685.

Dantzig, A.H., Shepard, R.L., Cao, J., Law, K.L., Ehlhardt, W.J., Baughman, T.M., Bumol, T.F., Starling, J.J., 1996. Reversal of P-glycoprotein-mediated multidrug resistance by a potent cyclopropyldibenzosuberane modulator, LY335979. *Cancer Res* **56**, 4171–4179.

Daoubi, M., Marquez, N., Mazoir, N., Benharref, A., Hernández-Galán, R., Muñoz, E., Collado, I.G., 2007. Isolation of new phenylacetylingol derivatives that reactivate HIV-1 latency and a novel spirotriterpenoid from Euphorbia officinarum latex. *Bioorgan Med Chem* **15**, 4577–4584.

Darden, T., York, D., Pedersen, L., 1993. Particle mesh Ewald: An N·log(N) method for Ewald sums in large systems. *J Chem Phys* **98**, 10089–10092.

Daura, X., Mark, A.E., Van Gunsteren, W.F., 1998. Parametrization of aliphatic CHn united atoms of GROMOS96 force field. *J Comput Chem* **19**, 535–547.

Dawson, R.J.P., Locher, K.P., 2007. Structure of the multidrug ABC transporter Sav1866 from Staphylococcus aureus in complex with AMP-PNP. *FEBS Lett* **581**, 935–938.

Dawson, R.J.P., Locher, K.P., 2006. Structure of a bacterial multidrug ABC transporter. *Nature* **443**, 180–185.

de Pascual Teresa, J., Urones, J.G., Marcos, I.S., Basabe, P., Cuadrado, M.. S., Fernandez Moro,

R., 1987. Triterpenes from Euphorbia broteri. *Phytochemistry* **26**, 1767–1776.

Della Greca, M., Fiorention, A., Monaco, P., Previtera, L., 1994. Cycloartane triterpenes from Juncus effusus. *Phytochemistry* **35**, 1017–1022.

Didziapetris, R., Japertas, P., Avdeef, A., Petrauskas, A., 2003. Classification analysis of P-glycoprotein substrate specificity. *J Drug Target* **11**, 391–406.

Ditchfield, R., Hehre, W.J., Pople, J.A., 1971. Self-Consistent Molecular-Orbital Methods. IX. An Extended Gaussian-Type Basis for Molecular-Orbital Studies of Organic Molecules. *J Chem Phys* **54**, 724–728.

Doan, K.M.M., Humphreys, J.E., Webster, L.O., Wring, S.A., Shampine, L.J., Serabjit-Singh, C.S., Adkison, K.K., Polli, J.W., 2002. Passive Permeability and P-Glycoprotein-Mediated Efflux Differentiate Central Nervous System (CNS) and Non-CNS Marketed Drugs. *J Pharmacol Exp Ther* **303**, 1029–1037.

Doyle, L.A., Yang, W., Abruzzo, L. V, Krogmann, T., Gao, Y., Rishi, A.K., Ross, D.D., 1998. A multidrug resistance transporter from human MCF-7 breast cancer cells. *Proc Natl Acad Sci U S A* **95**, 15665–15670.

Duarte, N., Ferreira, M.J.U., 2007. Lagaspholones A and B: Two new jatropholane-type diterpenes from euphorbia iagascae. *Org Lett* **9**, 489–492.

Duarte, N., Varga, A., Cherepnev, G., Radics, R., Molnár, J., Ferreira, M.-J.U., 2007. Apoptosis induction and modulation of P-glycoprotein mediated multidrug resistance by new macrocyclic lathyrane-type diterpenoids. *Bioorgan Med Chem* **15**, 546–554.

Ecker, G.F., Huber, M., Schmid, D., Chiba, P., 1999. The Importance of a Nitrogen Atom in Modulators of Multidrug Resistance. *Mol Pharmacol* **56**, 791–796.

Eckford, P.D.W., Sharom, F.J., 2005. The reconstituted P-glycoprotein multidrug transporter is a flippase for glucosylceramide and other simple glycosphingolipids. *Biochem J* **389**, 517–526.

Eid, S.Y., El-Readi, M.Z., Fatani, S.H., Eldin, E.E.M.N., Wink, M., 2015. Natural Products Modulate the Multifactorial Multidrug Resistance of Cancer. *Pharmacol Pharm* **6**, 146–176.

Ekins, S., Kim, R.B., Leake, B.F., Dantzig, A.H., Schuetz, E.G., Lan, L.-B., Yasuda, K., Shepard, R.L., Winter, M.A., Schuetz, J.D., Wikel, J.H., Wrighton, S.A., 2002a. Application of Three-Dimensional Quantitative Structure-Activity Relationships of P-Glycoprotein Inhibitors and Substrates. *Mol Pharmacol* **61**, 974–981.

Ekins, S., Kim, R.B., Leake, B.F., Dantzig, A.H., Schuetz, E.G., Lan, L.-B., Yasuda, K.,

Shepard, R.L., Winter, M.A., Schuetz, J.D., Wikel, J.H., Wrighton, S.A., 2002b. Three-Dimensional Quantitative Structure-Activity Relationships of Inhibitors of P-Glycoprotein. *Mol Pharmacol* **61**, 964–973.

El-Bassuony, A.A., 2007. Antibacterial activity of new polyester diterpenes from Euphorbia guyoniana. *Asian J Chem* **19**, 4553–4562.

Emmert, D., Campos, C.R., Ward, D., Lu, P., Namanja, H.A., Bohn, K., Miller, D.S., Sharom, F.J., Chmielewski, J., Hrycyna, C.A., 2014. Reversible dimers of the atypical antipsychotic quetiapine inhibit p-glycoprotein-mediated efflux in vitro with increased binding affinity and in situ at the blood-brain barrier. *ACS Chem Neurosci* **5**, 305–317.

Ernst, M., Grace, O.M., Saslis-Lagoudakis, C.H., Nilsson, N., Simonsen, H.T., Rønsted, N., 2015. Global medicinal uses of Euphorbia L. (Euphorbiaceae). *J Ethnofarmacol* **176**, 90–101.

Esser, L., Zhou, F., Pluchino, K.M., Shiloach, J., Ma, J., Tang, W.-K., Gutierrez, C., Zhang, A., Shukla, S., Madigan, J.P., Zhou, T., Kwong, P.D., Ambudkar, S. V., Gottesman, M.M., Xia, D., 2017. Structures of the Multidrug Transporter P-glycoprotein Reveal Asymmetric ATP Binding and the Mechanism of Polyspecificity. *J Biol Chem* **292**, 446–461.

Essmann, U., Perera, L., Berkowitz, M.L., Darden, T., Lee, H., Pedersen, L.G., 1995. A smooth particle mesh Ewald method. *J Chem Phys* **103**, 8577–8593.

Evans, F.J., Taylor, S.E., 1983. Pro-Inflammatory, *Tumour-Promoting and Anti-Tumour Diterpenes of the Plant Families Euphorbiaceae and Thymelaeaceae*. pp. 1–99.

Eytan, G.D., Kuchel, P.W., 1999. Mechanism of action of P-glycoprotein in relation to passive membrane permeation. *Int Rev Cytol* **190**, 175–250.

Eytan, G.D., Regev, R., Assaraf, Y.G., Oren, G., Assaraf, Y.G., Eytan, E.D., Regev, R., Oren, G., Assaraf, Y.G., 1996. The Role of Passive Transbilayer Drug Movement in Multidrug Resistance and Its Modulation. *J Biol Chem* **271**, 12897–12902.

Falcone Ferreyra, M.L., Rius, S.P., Casati, P., 2012. Flavonoids: biosynthesis, biological functions, and biotechnological applications. *Front Plant Sci* **3**, 222. doi:10.3389/ fpls.2012.00222

Fan, H., Mark, A.E., 2003. Relative stability of protein structures determined by X-ray crystallography or NMR spectroscopy: a molecular dynamics simulation study. *Proteins* **53**, 111–120.

Fantappiè, O., Sassoli, C., Tani, A., Nosi, D., Marchetti, S., Formigli, L., Mazzanti, R., 2015.

Mitochondria of a human multidrug-resistant hepatocellular carcinoma cell line constitutively express inducible nitric oxide synthase in the inner membrane. *J Cell Mol Med* **19**, 1410–1417.

Fei, D.-Q.Q., Dong, L.-L. Le, Qi, F.-M.M., Fan, G.-X.X., Li, H.-H.H., Li, Z.-Y.Y., Zhang, Z.-X.X., 2016. Euphorikanin A, a Diterpenoid Lactone with a Fused 5/6/7/3 Ring System from Euphorbia kansui. *Org Lett* **18**, 2844–2847.

Ferlay, J., Soerjomataram I, I., Dikshit, R., Eser, S., Mathers, C., Rebelo, M., Parkin, D.M., Forman D, D., Bray, F., 2015. Cancer incidence and mortality worldwide: sources, methods and major patterns in GLOBOCAN 2012. *Int J Cancer* **136**, E359-386.

Ferreira, M.-J.U., Duarte, N., Reis, M., Madureira, A.M., Molnár, J., 2014. Euphorbia and Momordica metabolites for overcoming multidrug resistance. *Phytochem Rev* **13**, 915–935.

Ferreira, R.J., Bonito, C.A., Cordeiro, M.N.D.S., Ferreira, M.-J.U., dos Santos, D.J.V.A., 2017a. Unveiling the ABCG2 transporter: insights from molecular dynamics simulations and molecular docking studies. *Sci Rep* (submitted).

Ferreira, R.J., Bonito, C.A., Ferreira, M.J.U., dos Santos, D.J.V.A., 2017b. About P-glycoprotein: a new drugable domain is emerging from structural data. *WIREs Comput Mol Sci* e1316 (in press). doi:10.1002/wcms.1316

Ferreira, R.J., dos Santos, D.J.V.A., Ferreira, M.-J.U., 2015a. P-glycoprotein and membrane roles in multidrug resistance. *Future Med Chem* **7**, 929–946.

Ferreira, R.J., dos Santos, D.J.V.A., Ferreira, M.J.U., Guedes, R.C., 2011. Toward a better pharmacophore description of P-glycoprotein modulators, based on macrocyclic diterpenes from Euphorbia species. *J Chem Inf Model* **51**, 1315–1324.

Ferreira, R.J., Ferreira, M.-J.U., dos Santos, D.J.V.A., 2015b. Reversing cancer multidrug resistance: insights into the efflux by ABC transports from in silico studies. *WIREs Comput Mol Sci* **5**, 27–55.

Ferreira, R.J., Ferreira, M.-J.U., dos Santos, D.J.V.A., 2015c. Do Drugs Have Access to the P-Glycoprotein Drug-Binding Pocket through Gates? *J Chem Theory Comput* **11**, 4525–4529.

Ferreira, R.J., Ferreira, M.-J.U., dos Santos, D.J.V.A., 2015d. Do adsorbed drugs onto P-glycoprotein influence its efflux capability? *Phys Chem Chem Phys* **17**, 22023–22034.

Ferreira, R.J., Ferreira, M.-J.U., dos Santos, D.J.V.A., 2013a. Assessing the Stabilization of P-Glycoprotein's Nucleotide-Binding Domains by the Linker, Using Molecular Dynamics. *Mol Inf* **32**, 529–540.

Ferreira, R.J., Ferreira, M.-J.U., dos Santos, D.J.V.A., 2013b. Molecular docking characterizes substrate-binding sites and efflux modulation mechanisms within P-glycoprotein. *J Chem Inf Model* **53**, 1747–1760.

Ferreira, R.J., Ferreira, M.-J.U., dos Santos, D.J.V.A., 2012. Insights on P-Glycoprotein's Efflux Mechanism Obtained by Molecular Dynamics Simulations. *J Chem Theory Comput* **8**, 1853–1864.

Follit, C.A., Brewer, F.K., Wise, J.G., Vogel, P.D., 2015. In silico identified targeted inhibitors of P-glycoprotein overcome multidrug resistance in human cancer cells in culture. *Pharmacol Res Perspect* **3**, e00170. doi:10.1002/prp2.170

Food and Drug Administration (FDA). Drug interaction studies—study design, data analysis, implications for dosing, and labeling recommendations; 2012. Available at: https://www.fda.gov/downloads/Drugs/GuidanceComplianceRegulatoryInformation/Guidances/UCM292362.pdf. (Accessed March 2017).

Ford, J.M., Bruggemann, E.P., Pastan, I., Gottesman, M.M., Hait, W.N., 1990. Cellular and biochemical characterization of thioxanthenes for reversal of multidrug resistance in human and murine cell lines. *Cancer Res* **50**, 1748–1756.

Ford, R.C., Kamis, A.B., Kerr, I.D., Callaghan, R., 2009. The ABC Transporters: Structural Insights into Drug Transport, in: Ecker, G., Chiba, P. (Eds.), *Transporters as Drug Carriers, Methods and Principles in Medicinal Chemistry*. Wiley-VCH Verlag GmbH & Co. KGaA, Weinheim, Germany, pp. 3–48.

Frank, N.Y., Margaryan, A., Huang, Y., Schatton, T., Waaga-Gasser, A.M., Gasser, M., Sayegh, M.H., Sadee, W., Frank, M.H., 2005. ABCB5-mediated doxorubicin transport and chemoresistance in human malignant melanoma. *Cancer Res* **65**, 4320–4333.

Frisch, M.J., Pople, J.A., Binkley, J.S., 1984. Self-consistent molecular orbital methods 25. Supplementary functions for Gaussian basis sets. *J Chem Phys* **80**, 3265–3269.

Frisch, M.J., Trucks, G.W., Schlegel, H.B., Scuseria, G.E., Robb, M.A., Cheeseman, J.R., Montgomery Jr., J.A., Vreven, T., Kudin, K.N., Burant, J.C., Millam, J.M., Iyengar, S.S., Tomasi, J., Barone, V., Mennucci, B., Cossi, M., Scalmani, G., Rega, N., Petersson, G.A., Nakatsuji, H., Hada, M., Ehara, M., Toyota, K., Fukuda, R., Hasegawa, J., Ishida, M., Nakajima, T., Honda, Y., Kitao, O., Nakai, H., Klene, M., Li, X., Knox, J.E., Hratchian, H.P., Cross, J.B., Bakken, V., Adamo, C., Jaramillo, J., Gomperts, R., Stratmann, R.E., Yazyev, O., Austin, A.J., Cammi, R., Pomelli, C., Ochterski, J.W., Ayala, P.Y., Morokuma, K., Voth, G.A., Salvador, P., Dannenberg, J.J., Zakrzewski, V.G., Dapprich, S., Daniels, A.D., Strain, M.C., Farkas, O., Malick, D.K., Rabuck, A.D., Raghavachari, K., Foresman, J.B., Ortiz, J. V., Cui, Q., Baboul, A.G., Clifford, S., Cioslowski, J., Stefanov, B.B., Liu, G., Liashenko, A., Piskorz, P., Komaromi, I., Martin, R.L., Fox, D.J.,

Keith, T., Al-Laham, M.A., Peng, C.Y., Nanayakkara, A., Challacombe, M., Gill, P.M.W., Johnson, B., Chen, W., Wong, M.W., Gonzalez, C., Pople, J.A., 2004. Gaussian 03, Revision D.01.

Funakoshi, S., Murakami, T., Yumoto, R., Kiribayashi, Y., Takano, M., 2003. Role of P-glycoprotein in pharmacokinetics and drug interactions of digoxin and beta-methyldigoxin in rats. *J Pharm Sci* **92**, 1455–1463.

Gannon, M.K., Holt, J.J., Bennett, S.M., Wetzel, B.R., Loo, T.W., Bartlett, M.C., Clarke, D.M., Sawada, G.A., Higgins, J.W., Tombline, G., Raub, T.J., Detty, M.R., 2009. Rhodamine inhibitors of P-glycoprotein: an amide/thioamide "switch" for ATPase activity. *J Med Chem* **52**, 3328–3341.

Gao, J., Aisa, H.A., 2017. Terpenoids from Euphorbia soongarica and Their Multidrug Resistance Reversal Activity. *J Nat Prod* **80**, 1767–1775.

Gao, Y., Shen, J.K., Choy, E., Zhang, Z., Mankin, H.J., Hornicek, F.J., Duan, Z., 2016. Pharmacokinetics and tolerability of NSC23925b, a novel P-glycoprotein inhibitor: preclinical study in mice and rats. *Sci Rep* **6**, 25659. doi:10.1038/srep25659

García-Sosa, A.T., Hetényi, C., Maran, U., 2010. Drug efficiency indices for improvement of molecular docking scoring functions. *J Comput Chem* **31**, 174–184.

Garrigues, A., Escargueil, A.E., Orlowski, S., 2002. The multidrug transporter, P-glycoprotein, actively mediates cholesterol redistribution in the cell membrane. *Proc Natl Acad Sci U S A* **99**, 10347–10352.

Gaspar, E.M.M., das Neves, H.J.C., 1993. Steroidal constituents from mature wheat straw. *Phytochemistry* **34**, 523–527.

George, A.M., Jones, P.M., 2013. An asymmetric post-hydrolysis state of the ABC transporter ATPase dimer. *PLoS One* **8**, e59854. doi:10.1371/journal.pone.0059854

George, A.M., Jones, P.M., 2012. Perspectives on the structure-function of ABC transporters: the Switch and Constant Contact models. *Prog Biophys Mol Biol* **109**, 95–107.

Georges, E., 2007. The P-glycoprotein (ABCB1) linker domain encodes high-affinity binding sequences to alpha- and beta-tubulins. *Biochemistry* **46**, 7337–7342.

Gifford, A.J., Kavallaris, M., Madafiglio, J., Matherly, L.H., Stewart, B.W., Haber, M., Norris, M.D., 1998. P-glycoprotein-mediated methotrexate resistance in CCRF-CEM sublines deficient in methotrexate accumulation due to a point mutation in the reduced folate carrier gene. *Int J Cancer* **78**, 176–181.

Gillet, J.-P., Gottesman, M.M., 2010. Mechanisms of multidrug resistance in cancer., in: Zhou,

J. (Ed.), *Methods in Molecular Biology*. Humana Press, pp. 47–76.

Globisch, C., Pajeva, I.K., Wiese, M., 2008. Identification of putative binding sites of P-glycoprotein based on its homology model. *ChemMedChem* **3**, 280–295.

Gong, Y., Duvvuri, M., Krise, J.P., 2003. Separate Roles for the Golgi Apparatus and Lysosomes in the Sequestration of Drugs in the Multidrug-resistant Human Leukemic Cell Line HL-60. *J Biol Chem* **278**, 50234–50239.

Gopalakrishnan, M., Narayanan, C.S., Grenz, M., 1990. Nonsaponifiable lipid constituents of cardamom. *J Agric Food Chem* **38**, 2133–2136.

Gottesman, M.M., 2002. Mechanisms of cancer drug resistance. *Annu Rev Med* **53**, 615–627.

Gottesman, M.M., Pastan, I.H., 2015. The Role of Multidrug Resistance Efflux Pumps in Cancer: Revisiting a JNCI Publication Exploring Expression of the MDR1 (P-glycoprotein) Gene. *J Natl Cancer Inst* **107**, djv222. doi:10.1093/jnci/djv222

Gozalpour, E., Wittgen, H.G.M., van den Heuvel, J.J.M.W., Greupink, R., Russel, F.G.M., Koenderink, J.B., 2013. Interaction of digitalis-like compounds with p-glycoprotein. *Toxicol Sci* **131**, 502–511.

Graf, G.A., Yu, L., Li, W.P., Gerard, R., Tuma, P.L., Cohen, J.C., Hobbs, H.H., 2003. ABCG5 and ABCG8 Are Obligate Heterodimers for Protein Trafficking and Biliary Cholesterol Excretion. *J Biol Chem* **278**, 48275–48282.

GraphPad Prism, version 5.00; GraphPad Software: San Diego, CA, U.S.; www.graphpad.com

Greenow, K., Clarke, A.R., 2012. Controlling the Stem Cell Compartment and Regeneration In Vivo: The Role of Pluripotency Pathways. *Physiol Rev* **92**, 75–99.

Gutmann, D.A.P., Ward, A., Urbatsch, I.L., Chang, G., van Veen, H.W., 2010. Understanding polyspecificity of multidrug ABC transporters: closing in on the gaps in ABCB1. *Trends Biochem Sci* **35**, 36–42.

Hadjeri, M., Barbier, M., Ronot, X., Mariotte, A.-M., Boumendjel, A., Boutonnat, J., 2003. Modulation of P-glycoprotein-mediated multidrug resistance by flavonoid derivatives and analogues. *J Med Chem* **46**, 2125–2131.

Halgren, T.A., 1999. MMFF VI. MMFF94s option for energy minimization studies. *J Comput Chem* **20**, 720–729.

Handa, N., Yamada, T., Tanaka, R., 2010. An unusual lanostane-type triterpenoid, spiroinonotsuoxodiol, and other triterpenoids from Inonotus obliquus. *Phytochemistry* **71**, 1774–1779.

Hariharan, P.C., Pople, J.A., 1974. Accuracy of AHn equilibrium geometries by single determinant molecular orbital theory. *Mol Phys* **27**, 209–214.

Hariharan, P.C., Pople, J.A., 1973. The influence of polarization functions on molecular orbital hydrogenation energies. *Theor. Chim. Acta* **28**, 213–222.

Harrold, S.P., Pethica, B.A., 1958. Thermodynamics of the adsorption of small molecules by proteins. *Trans Faraday Soc* **54**, 1876–1884.

Hegazy, M.E.F., Mohamed, A.E.H.H., Aoki, N., Ikeuchi, T., Ohta, E., Ohta, S., 2010. Bioactive jatrophane diterpenes from Euphorbia guyoniana. *Phytochemistry* **71**, 249–253.

Hehre, W.J., Ditchfield, R., Pople, J.A., 1972. Self—Consistent Molecular Orbital Methods. XII. Further Extensions of Gaussian—Type Basis Sets for Use in Molecular Orbital Studies of Organic Molecules. *J Chem Phys* **56**, 2257–2261.

Hess, B., 2008. P-LINCS: A Parallel Linear Constraint Solver for Molecular Simulation. *J Chem Theory Comput* **4**, 116–122.

Hess, B., Bekker, H., Berendsen, H.J., Fraaije, J.G.E.M., 1997. LINCS: A linear constraint solver for molecular simulations. *J Comput Chem* **18**, 1463–1472.

Hess, B., Kutzner, C., van der Spoel, D., Lindahl, E., 2008. GROMACS 4: Algorithms for Highly Efficient, Load-Balanced, and Scalable Molecular Simulation. *J Chem Theory Comput* **4**, 435–447.

Higgins, C.F., Gottesman, M.M., 1992. Is the multidrug transporter a flippase? *Trends Biochem Sci* **17**, 18–21.

Hiom, S.C., 2015. Diagnosing cancer earlier: reviewing the evidence for improving cancer survival. *Br J Cancer* **112**, S1–S5.

Höllt, V., Kouba, M., Dietel, M., Vogt, G., 1992. Stereoisomers of calcium antagonists which differ markedly in their potencies as calcium blockers are equally effective in modulating drug transport by P-glycoprotein. *Biochem Pharmacol* **43**, 2601–2608.

Hoover, W., 1985. Canonical dynamics: Equilibrium phase-space distributions. *Phys Rev A* **31**, 1695–1697.

Housman, G., Byler, S., Heerboth, S., Lapinska, K., Longacre, M., Snyder, N., Sarkar, S., 2014. Drug Resistance in Cancer: An Overview. *Cancers (Basel)* **6**, 1769–1792.

Hrycyna, C.A., Airan, L.E., Germann, U.A., Ambudkar, S. V, Pastan, I., Gottesman, M.M., 1998. Structural flexibility of the linker region of human P-glycoprotein permits ATP hydrolysis and drug transport. *Biochemistry* **37**, 13660–13673.

Huang, K.F., Liou, L.E., 1997. Constituents of Erythrina crista-galli. *Chinese Pharm. J.* **49**, 305–314.

Hub, J.S., de Groot, B.L., van der Spoel, D., 2010. g_wham—A Free Weighted Histogram Analysis Implementation Including Robust Error and Autocorrelation Estimates. *J Chem Theory Comput* **6**, 3713–3720.

Humphrey, W., Dalke, A., Schulten, K., 1996. VMD: visual molecular dynamics. *J Mol Graph* **14**, 33–38.

Hyafil, F., Vergely, C., Du Vignaud, P., Grand-Perret, T., 1993. In vitro and in vivo reversal of multidrug resistance by GF120918, an acridonecarboxamide derivative. *Cancer Res* **53**, 4595–602.

Imai, Y., Tsukahara, S., Asada, S., Sugimoto, Y., 2004. Phytoestrogens/flavonoids reverse breast cancer resistance protein/ABCG2-mediated multidrug resistance. **Cancer Res 64**, 4346–4352.

Molecular Operating Environment (MOE); Chemical Computing Group Inc., 1010 Sherbooke St. West, Suite #910, Montreal, QC, Canada, H3A 2R7, 2017.

Jabeen, I., Pleban, K., Rinner, U., Chiba, P., Ecker, G.F., 2012. Structure-activity relationships, ligand efficiency, and lipophilic efficiency profiles of benzophenone-type inhibitors of the multidrug transporter P-glycoprotein. *J Med Chem* **55**, 3261–3273.

Jacobs, J.P., Jones, C.M., Baille, J.P., 1970. Characteristics of a human diploid cell designated MRC-5. *Nature* **227**, 168–170.

Jainchill, J.L., Aaronson, S.A., Todaro, G.J., 1969. Murine sarcoma and leukemia viruses: assay using clonal lines of contact-inhibited mouse cells. *J Virol* **4**, 549–553.

Janzsó, G., 1985. Structure elucidation of N-substituted flavanone imines by 13C-NMR spectroscopy. *Acta Chim. Hungarica* **118**, 261–263.

Janzsó, G., Kállay, F., Koczor, I., Radics, L., 1967. Stereochemistry of 3-hydroxy- and 3-acetoxyflavanone oximes. *Tetrahedron* **23**, 3699–3704.

Jiao, W., Wan, Z., Chen, S., Lu, R., Chen, X., Fang, D., Wang, J., Pu, S., Huang, X., Gao, H., Shao, H., 2015. Lathyrol Diterpenes as Modulators of P-Glycoprotein Dependent Multidrug Resistance: Structure–Activity Relationship Studies on Euphorbia Factor L 3 Derivatives. *J Med Chem* **58**, 3720–3738.

Johnson, Z.L., Chen, J., 2017. Structural Basis of Substrate Recognition by the Multidrug Resistance Protein MRP1. *Cell* 1–11.

Juliano, R.L., Ling, V., 1976. A surface glycoprotein modulating drug permeability in Chinese hamster ovary cell mutants. *Biochim Biophys Acta* **455**, 152–162.

Kalia, D., Malekar, P. V., Parthasarathy, M., 2016. Exocyclic Olefinic Maleimides: Synthesis and Application for Stable and Thiol-Selective Bioconjugation. *Angew Chem Int Ed* **55**, 1432–1435.

Kawanobe, T., Kogure, S., Nakamura, S., Sato, M., Katayama, K., Mitsuhashi, J., Noguchi, K., Sugimoto, Y., 2012. Expression of human ABCB5 confers resistance to taxanes and anthracyclines. *Biochem Biophys Res Commun* **418**, 736–741.

Keniya, M. V, Holmes, A.R., Niimi, M., Lamping, E., Gillet, J.-P., Gottesman, M.M., Cannon, R.D., 2014. Drug Resistance Is Conferred on the Model Yeast Saccharomyces cerevisiae by Expression of Full-Length Melanoma-Associated Human ATP-Binding Cassette Transporter ABCB5. *Mol Pharmacol* **11**, 3452–3462.

Kim, J., Park, K.S., Lee, C., Chong, Y., 2007. Synthesis of a complete series of O-methyl analogues of naringenin and apigenin. *Bull Korean Chem Soc* **28**, 2527–2530.

Kim, J.Y., Henrichs, S., Bailly, A., Vincenzetti, V., Sovero, V., Mancuso, S., Pollmann, S., Kim, D., Geisler, M., Nam, H.G., 2010. Identification of an ABCB/P-glycoprotein-specific inhibitor of auxin transport by chemical genomics. *J Biol Chem* **285**, 23309–23317.

King, A.J., Brown, G.D., Gilday, A.D., Forestier, E., Larson, T.R., Graham, I.A., 2016. A Cytochrome P450-Mediated Intramolecular Carbon-Carbon Ring Closure in the Biosynthesis of Multidrug-Resistance-Reversing Lathyrane Diterpenoids. *ChemBioChem* **17**, 1593–1597.

King, A.J., Brown, G.D., Gilday, A.D., Larson, T.R., Graham, I. a, 2014. Production of bioactive diterpenoids in the euphorbiaceae depends on evolutionarily conserved gene clusters. *Plant Cell* **26**, 3286–3298.

Klepsch, F., Vasanthanathan, P., Ecker, G.F., 2014. Ligand and structure-based classification models for prediction of P-glycoprotein inhibitors. *J Chem Inf Model* **54**, 218–229.

Kleywegt, G.J., 2000. Validation of protein crystal structures. *Acta Crystallogr D Biol Crystallogr* **56**, 249–265.

Kleywegt, G.J., Jones, T.A., 1994. Detection, delineation, measurement and display of cavities in macromolecular structures. *Acta Crystallogr D Biol Crystallogr* **50**, 178–185.

Kobayashi, E., Iyer, A.K., Hornicek, F.J., Amiji, M.M., Duan, Z., 2013. Lipid-functionalized dextran nanosystems to overcome multidrug resistance in cancer: a pilot study. *Clin Orthop Relat Res* **471**, 915–925.

Kodan, A., Yamaguchi, T., Nakatsu, T., Sakiyama, K., Hipolito, C.J., Fujioka, A., Hirokane, R., Ikeguchi, K., Watanabe, B., Hiratake, J., Kimura, Y., Suga, H., Ueda, K., Kato, H., 2014. Structural basis for gating mechanisms of a eukaryotic P-glycoprotein homolog. *Proc Natl Acad Sci U S A* **111**, 4049–4054.

Kohlbacher, O., Lenhof, H.P., 2000. BALL--rapid software prototyping in computational molecular biology. Biochemicals Algorithms Library. *Bioinformatics* **16**, 815–824.

Kölling, R., Losko, S., 1997. The linker region of the ABC-transporter Ste6 mediates ubiquitination and fast turnover of the protein. *EMBO J* **16**, 2251–2261.

Kondratov, R. V, Komarov, P.G., Becker, Y., Ewenson, A., Gudkov, A. V, 2001. Small molecules that dramatically alter multidrug resistance phenotype by modulating the substrate specificity of P-glycoprotein. *Proc Natl Acad Sci U S A* **98**, 14078–14083.

Koziara, K.B., Stroet, M., Malde, A.K., Mark, A.E., 2014. Testing and validation of the Automated Topology Builder (ATB) version 2.0: prediction of hydration free enthalpies. *J Comput Aided Mol Des* **28**, 221–233.

Krawczyk, S., Baumert, C., Molnár, J., Ritter, C., Höpner, J., Kloft, C., Hilgeroth, A., 2015. Novel non-substrate modulators of the transmembrane efflux pump P-glycoprotein (ABCB1). *Med Chem Commun* **6**, 860-866.

Kuhnke, D., Jedlitschky, G., Grube, M., Krohn, M., Jucker, M., Mosyagin, I., Cascorbi, I., Walker, L.C., Kroemer, H.K., Warzok, R.W., Vogelgesang, S., 2007. MDR1-P-Glycoprotein (ABCB1) Mediates Transport of Alzheimer's amyloid-beta peptides - implications for the mechanisms of Abeta clearance at the blood-brain barrier. *Brain Pathol* **17**, 347–353.

Kumari, R., Kumar, R., Lynn, A., 2014. G-mmpbsa -A GROMACS tool for high-throughput MM-PBSA calculations. *J Chem Inf Model* **54**, 1951–1962.

Kurosawa, M., Okabe, M., Hara, N., Kawamura, K., Suzuki, S., Sakurada, K., Asaka, M., 1996. Reversal effect of itraconazole on adriamycin and etoposide resistance in human leukemia cells. *Ann Hematol* **72**, 17–21.

Kuznetsov, A.N., Ebert, B., Lassmann, G., Shapiro, A.B., 1975. Adsorption of small molecules to bovine serum albumin studied by the spin-probe method. *Biochim Biophys Acta* **379**, 139–146.

Kwan, T., Gros, P., 1998. Mutational analysis of the P-glycoprotein first intracellular loop and flanking transmembrane domains. *Biochemistry* **37**, 3337–3350.

Kwon, Y., Kamath, A. V, Morris, M.E., 1996. Inhibitors of P-glycoprotein-mediated daunomycin transport in rat liver canalicular membrane vesicles. *J Pharm Sci* **85**, 935–

939.

Lal, A.R., Cambie, R.C., Rutledge, P.S., Woodgate, P.D., Rickard, C.E.F., Clark, G.R., 1989. New oxidised ent-atisene diterpenes from Euphorbia fidjiana. *Tetrahedron Lett* **30**, 3205–3208.

Lam, F.C., Liu, R., Lu, P., Shapiro, A.B., Renoir, J.M., Sharom, F.J., Reiner, P.B., 2001. beta-Amyloid efflux mediated by p-glycoprotein. *J Neurochem* **76**, 1121–1128.

Leekumjorn, S., Sum, A.K., 2007. Molecular Characterization of Gel and Liquid-Crystalline Structures of Fully Hydrated POPC and POPE Bilayers. *J Phys Chem B* **111**, 6026–6033.

Leier, I., Jedlitschky, G., Buchholz, U., Cole, S.P., Deeley, R.G., Keppler, D., 1994. The MRP gene encodes an ATP-dependent export pump for leukotriene C4 and structurally related conjugates. *J Biol Chem* **269**, 27807–27810.

Lesterhuis, W.J., Rinaldi, C., Jones, A., Rozali, E.N., Dick, I.M., Khong, A., Boon, L., Robinson, B.W., Nowak, A.K., Bosco, A., Lake, R.A., 2015. Network analysis of immunotherapy-induced regressing tumours identifies novel synergistic drug combinations. *Sci Rep* **5**, 12298. doi:10.1038/srep12298

Li, X.-Q., Wang, L., Lei, Y., Hu, T., Zhang, F.-L., Cho, C.-H., To, K.K.W., 2015. Reversal of P-gp and BCRP-mediated MDR by Tariquidar derivatives. *Eur J Med Chem* **101**, 560–572.

Lindahl, E., Hess, B., van der Spoel, D., 2001. GROMACS 3.0: a package for molecular simulation and trajectory analysis. *J Mol Model* **7**, 306–317.

Litman, T., Skovsgaard, T., Stein, W.D., 2003. Pumping of drugs by P-glycoprotein: a two-step process? *J Pharmacol Exp Ther* **307**, 846–853.

Liu, F., Zhang, Z., Csanády, L., Gadsby, D.C., Chen, J., 2017. Molecular Structure of the Human CFTR Ion Channel. *Cell* **169**, 85–95.

Locher, K.P., 2009. Structure and mechanism of ATP-binding cassette transporters. Philos *Trans R Soc L. B Biol Sci* **364**, 239–245.

Loo, T.W., Bartlett, M.C., Clarke, D.M., 2003. Simultaneous binding of two different drugs in the binding pocket of the human multidrug resistance P-glycoprotein. *J Biol Chem* **278**, 39706–39710.

Loo, T.W., Clarke, D.M., 2015. Mapping the Binding Site of the Inhibitor Tariquidar That Stabilizes the First Transmembrane Domain of P-glycoprotein. *J Biol Chem* **290**, 29389–29401.

Loo, T.W., Clarke, D.M., 2015. The Transmission Interfaces Contribute Asymmetrically to the Assembly and Activity of Human P-glycoprotein. *J Biol Chem* **290**, 16954–16963.

Loo, T.W., Clarke, D.M., 2013. A Salt Bridge in Intracellular Loop 2 Is Essential for Folding of Human P-Glycoprotein. *Biochemistry* **52**, 3194–3196.

Loo, T.W., Clarke, D.M., 2002. Location of the rhodamine-binding site in the human multidrug resistance P-glycoprotein. *J Biol Chem* **277**, 44332–44338.

Loo, T.W., Clarke, D.M., 2001. Defining the drug-binding site in the human multidrug resistance P-glycoprotein using a methanethiosulfonate analog of verapamil, MTS-verapamil. *J Biol Chem* **276**, 14972–14979.

Loo, T.W., Clarke, D.M., 2000. Identification of residues within the drug-binding domain of the human multidrug resistance P-glycoprotein by cysteine-scanning mutagenesis and reaction with dibromobimane. *J Biol Chem* **275**, 39272–39278.

Loo, T.W., Clarke, D.M., 1999. Identification of residues in the drug-binding domain of human P-glycoprotein. Analysis of transmembrane segment 11 by cysteine-scanning mutagenesis and inhibition by dibromobimane. *J Biol Chem* **274**, 35388–35392.

Lu, P., Liu, R., Sharom, F.J., 2001. Drug transport by reconstituted P-glycoprotein in proteoliposomes. Effect of substrates and modulators, and dependence on bilayer phase state. *Eur J Biochem* **268**, 1687–1697.

Lugo, M.R., Sharom, F.J., 2005. Interaction of LDS-751 with P-glycoprotein and mapping of the location of the R drug binding site. *Biochemistry* **44**, 643–55.

Luo, D., Callari, R., Hamberger, B., Wubshet, S.G., Nielsen, M.T., Andersen-Ranberg, J., Hallström, B.M., Cozzi, F., Heider, H., Lindberg Møller, B., Staerk, D., Hamberger, B., 2016. Oxidation and cyclization of casbene in the biosynthesis of Euphorbia factors from mature seeds of Euphorbia lathyris L. *Proc Natl Acad Sci U S A* **113**, E5082–E5089.

Luzar, A., 2000. Resolving the hydrogen bond dynamics conundrum. *J Chem Phys* **113**, 10663–10675.

Luzar, A., Chandler, D., 1996. Hydrogen-bond kinetics in liquid water. *Nature* **379**, 55–57.

Madureira, A.M., Ferreira, M.-J.U., Gyémánt, N., Ugocsai, K., Ascenso, J.R., Abreu, P.M., Hohmann, J., Molnár, J., 2004. Rearranged jatrophane-type diterpenes from euphorbia species. Evaluation of their effects on the reversal of multidrug resistance. *Planta Med* **70**, 45–49.

Madureira, A.M., Gyémánt, N., Ascenso, J.R., Abreu, P.M., Molnár, J., Ferreira, M.-J.U., 2006. Euphoportlandols A and B, tetracylic diterpene polyesters from Euphorbia portlandica and their anti-MDR effects in cancer cells. *J Nat Prod* **69**, 950–953.

Malde, A.K., Zuo, L., Breeze, M., Stroet, M., Poger, D., Nair, P.C., Oostenbrink, C., Mark, A.E., 2011. An Automated Force Field Topology Builder (ATB) and Repository: Version 1.0. *J Chem Theory Comput* **7**, 4026–4037.

Martin, C., Berridge, G., Mistry, P., Higgins, C.F., Charlton, P., Callaghan, R., 2000. Drug Binding Sites on P-Glycoprotein Are Altered by ATP Binding Prior to Nucleotide Hydrolysis. *Biochemistry* **39**, 11901–11906.

Martin, C., Berridge, G., Mistry, P., Higgins, C.F., Charlton, P., Callaghan, R., 1999. The molecular interaction of the high affinity reversal agent XR9576 with P-glycoprotein. *Br J Pharmacol* **128**, 403–411.

MarvinSketch version 17.2.20. Chemaxon Ltd: Budapest, Hungary; www.chemaxon.com

McCormick, J.W., Vogel, P.D., Wise, J.G., 2015. Multiple Drug Transport Pathways through Human P-Glycoprotein. *Biochemistry* **54**, 4374–4390.

Meads, M.B., Gatenby, R.A., Dalton, W.S., 2009. Environment-mediated drug resistance: a major contributor to minimal residual disease. *Nat Rev Cancer* **9**, 665–674.

Mei, L., Zhu, G., Qiu, L., Wu, C., Chen, H., Liang, H., Cansiz, S., Lv, Y., Zhang, X., Tan, W., 2015. Self-assembled multifunctional DNA nanoflowers for the circumvention of multidrug resistance in targeted anticancer drug delivery. *Nano Res* **8**, 3447-3460.

Melchior, D.L., Sharom, F.J., Evers, R., Wright, G.E., Chu, J.W.K., Wright, S.E., Chu, X., Yabut, J., 2012. Determining P-glycoprotein-drug interactions: Evaluation of reconstituted P-glycoprotein in a liposomal system and LLC-MDR1 polarized cell monolayers. *J Pharmacol Toxicol Methods* **65**, 64–74.

Mercado-Lubo, R., Zhang, Y., Zhao, L., Rossi, K., Wu, X., Zou, Y., Castillo, A., Leonard, J., Bortell, R., Greiner, D.L., Shultz, L.D., Han, G., McCormick, B.A., 2016. A Salmonella nanoparticle mimic overcomes multidrug resistance in tumours. *Nat Comms* **7**, 12225. doi:10.1038/ncomms12225

Meyer dos Santos, S., Weber, C.-C., Franke, C., Müller, W.E., Eckert, G.P., 2007. Cholesterol: Coupling between membrane microenvironment and ABC transporter activity. *Biochem Biophys Res Commun* **354**, 216–221.

Mezei, M., 1989. Evaluation of the Adaptive Umbrella Sampling Method. *Mol Simulat* **3**, 301–313.

Michaelis, M., Rothweiler, F., Nerreter, T., Sharifi, M., Ghafourian, T., Cinatl, J., 2014. Karanjin interferes with ABCB1, ABCC1, and ABCG2. *J Pharm Pharm Sci* **17**, 92–105.

Miron, A., Aprotosoaie, A.C., Trifan, A., Xiao, J., 2017. Flavonoids as modulators of metabolic enzymes and drug transporters. *Ann N Y Acad Sci* **1398**, 152–167.

Mistry, P., Stewart, A.J., Dangerfield, W., Okiji, S., Liddle, C., Bootle, D., Plumb, J. a, Templeton, D., Charlton, P., 2001. In vitro and in vivo reversal of P-glycoprotein-mediated multidrug resistance by a novel potent modulator, XR9576. *Cancer Res* **61**, 749–758.

Miyake, K., Mickley, L., Litman, T., Zhan, Z., Robey, R., Cristensen, B., Brangi, M., Greenberger, L., Dean, M., Fojo, T., Bates, S.E., 1999. Molecular cloning of cDNAs which are highly overexpressed in mitoxantrone-resistant cells: demonstration of homology to ABC transport genes. *Cancer Res* **59**, 8–13.

Miyamoto, S., Kollman, P.A., 1992. Settle: An analytical version of the SHAKE and RATTLE algorithm for rigid water models. *J Comput Chem* **13**, 952–962.

Mo, W., Zhang, J.-T., 2012. Human ABCG2: structure, function, and its role in multidrug resistance. *Int J Biochem Mol Biol* **3**, 1–27.

Modok, S., Heyward, C., Callaghan, R., 2004. P-glycoprotein retains function when reconstituted into a sphingolipid- and cholesterol-rich environment. *J Lipid Res* **45**, 1910–1918.

Mondal, S., Khelashvili, G., Shan, J., Andersen, O.S., Weinstein, H., 2011. Quantitative modeling of membrane deformations by multihelical membrane proteins: application to G-protein coupled receptors. *Biophys J* **101**, 2092–2101.

Montanari, F., Ecker, G.F., 2015. Prediction of Drug-ABC Transporter Interaction - Recent Advances and Future Challenges. *Adv Drug Deliv Rev* **86**, 17-26.

Morris, G.M., Huey, R., Lindstrom, W., Sanner, M.F., Belew, R.K., Goodsell, D.S., Olson, A.J., 2009. AutoDock4 and AutoDockTools4: Automated docking with selective receptor flexibility. *J Comput Chem* **30**, 2785–2791.

Mosmann, T., 1983. Rapid colorimetric assay for cellular growth and survival: Application to proliferation and cytotoxicity assays. *J Immunol Methods* **65**, 55–63.

Motulsky, H., Hristopoulos, A., 2004. *Fitting Models to Biological Data Using Linear and Nonlinear Regression: A Practical Guide to Curve Fitting*. Oxford University Press, New York, USA.

Mulliken, R.S., 1955. Electronic Population Analysis on LCAO[Single Bond]MO Molecular Wave Functions. I. *J Chem Phys* **23**, 1833.

Murphy, G.F., Wilson, B.J., Girouard, S.D., Frank, N.Y., Frank, M.H., 2014. Stem cells and targeted approaches to melanoma cure. *Mol Asp Med* **39**, 33–49.

Nguyen, L. V, Vanner, R., Dirks, P., Eaves, C.J., 2012. Cancer stem cells: an evolving concept. *Nat Rev Cancer* **12**, 133–143.

Nijveldt, R.J., van Nood, E., van Hoorn, D.E., Boelens, P.G., van Norren, K., van Leeuwen, P.A., 2001. Flavonoids: a review of probable mechanisms of action and potential applications. *Am J Clin Nutr* **74**, 418–25.

Nosé, S., Klein, M.L., 1983. Constant pressure molecular dynamics for molecular systems. *Mol Phys* **50**, 1055–1076.

O'Mara, M.L., Mark, A.E., 2012. The Effect of Environment on the Structure of a Membrane Protein: P-Glycoprotein under Physiological Conditions. *J Chem Theory Comput* **8**, 3964–3976.

O'Mara, M.L., Tieleman, D.P., 2007. P-glycoprotein models of the apo and ATP-bound states based on homology with Sav1866 and MalK. *FEBS Lett* **581**, 4217–4222.

Obreque-Balboa, J.E., Sun, Q., Bernhardt, G., König, B., Buschauer, A., 2016. Flavonoid derivatives as selective ABCC1 modulators: Synthesis and functional characterization. *Eur J Med Chem* **109**, 124–133.

Oleinikov, V.A., Fleury, F., Ianoul, A., Zaitsev, S., Nabiev, I., 2006. P-glycoprotein effect on the properties of its natural lipid environment probed by Raman spectroscopy and Langmuir-Blodgett technique. *FEBS Lett* **580**, 4953–4958.

Oliveira, A.S., Baptista, A.M., Soares, C.M., 2011. Conformational changes induced by ATP-hydrolysis in an ABC transporter: a molecular dynamics study of the Sav1866 exporter. *Proteins* **79**, 1977–1990.

Oliveira, A.S.F., Baptista, A.M., Soares, C.M., 2010. Insights into the molecular mechanism of an ABC transporter: conformational changes in the NBD dimer of MJ0796. *J Phys Chem B* **114**, 5486–5496.

Oostenbrink, C., Soares, T. a., Van Der Vegt, N.F. a, Van Gunsteren, W.F., 2005. Validation of the 53A6 GROMOS force field. *Eur Biophys J* **34**, 273–284.

Oostenbrink, C., Villa, A., Mark, A.E., van Gunsteren, W.F., 2004. A biomolecular force field based on the free enthalpy of hydration and solvation: the GROMOS force-field parameter sets 53A5 and 53A6. *J Comput Chem* **25**, 1656–1676.

Orlowski, S., Martin, S., Escargueil, A., 2006. P-glycoprotein and “lipid rafts”: some ambiguous mutual relationships (floating on them, building them or meeting them by chance?). *Cell Mol Life Sci* **63**, 1038–1059.

Ottiger, P., Pfaffen, C., Leist, R., Leutwyler, S., Bachorz, R.A., Klopper, W., 2009. Strong N-H...pi hydrogen bonding in amide-benzene interactions. *J Phys Chem B* **113**, 2937–2943.

Pajeva, I.K., Globisch, C., Wiese, M., 2004. Structure-function relationships of multidrug resistance P-glycoprotein. *J Biol Chem* **47**, 2523–2533.

Pajeva, I.K., Hanl, M., Wiese, M., 2013. Protein contacts and ligand binding in the inward-facing model of human P-glycoprotein. *ChemMedChem* **8**, 748–762.

Palit, S.R., Mukherjee, S., De, S.K., 1971. N-H....pi hydrogen bonding. *J Phys Chem A* **75**, 2404–2405.

Páll, S., Abraham, M.J., Kutzner, C., Hess, B., Lindahl, E., 2015. Tackling Exascale Software Challenges in Molecular Dynamics Simulations with GROMACS, in: Markidis, S., Laure, E. (Eds.), *Solving Software Challenges for Exascale*. pp. 3–27.

Páll, S., Hess, B., 2013. A flexible algorithm for calculating pair interactions on SIMD architectures. *Comput Phys Commun* **184**, 2641–2650.

Palmeira, A., Sousa, E., Vasconcelos, H., Pinto, M., Fernandes, M.X., 2012a. Structure and ligand-based design of P-glycoprotein inhibitors: a historical perspective. *Curr Pharm Des*. **18**, 4197–4124.

Palmeira, A., Sousa, E., Vasconcelos, M.H., Pinto, M., 2012b. Three Decades of P-gp Inhibitors: Skimming Through Several Generations and Scaffolds. *Curr Med Chem* **19**, 1946–2025.

Parrinello, M., 1981. Polymorphic transitions in single crystals: A new molecular dynamics method. *J Appl Phys* **52**, 7182–7190

Parveen, Z., Stockner, T., Bentele, C., Pferschy, S., Kraupp, M., Freissmuth, M., Ecker, G.F., Chiba, P., 2011. Molecular dissection of dual pseudosymmetric solute translocation pathways in human P-glycoprotein. *Mol Pharmacol* **79**, 443–452.

Pastan, I., Gottesman, M.M., Ueda, K., Lovelace, E., Rutherford, A. V, Willingham, M.C., 1988. A retrovirus carrying an MDR1 cDNA confers multidrug resistance and polarized expression of P-glycoprotein in MDCK cells. *Proc Natl Acad Sci U S A* **85**, 4486–4490.

Pearce, H.L., Safa, A.R., Bach, N.J., Winter, M.A., Cirtain, M.C., Beck, W.T., 1989. Essential features of the P-glycoprotein pharmacophore as defined by a series of reserpine analogs that modulate multidrug resistance. *Proc Natl Acad Sci U S A* **86**, 5128–5132.

Peck, R.A., Hewett, J., Harding, M.W., Wang, Y.M., Chaturvedi, P.R., Bhatnagar, A., Ziessman, H., Atkins, F., Hawkins, M.J., 2001. Phase I and pharmacokinetic study of the novel MDR1 and MRP1 inhibitor biricodar administered alone and in combination with doxorubicin. *J Clin Oncol* **19**, 3130–3141.

Pham, Y.T., Régina, A., Farinotti, R., Couraud, P., Wainer, I.W., Roux, F., Gimenez, F., 2000. Interactions of racemic mefloquine and its enantiomers with P-glycoprotein in an immortalised rat brain capillary endothelial cell line, GPNT. *Biochim Biophys Acta* **1524**, 212–219.

Pick, A., Müller, H., Mayer, R., Haenisch, B., Pajeva, I.K., Weigt, M., Bönisch, H., Müller, C.E., Wiese, M., 2011. Structure-activity relationships of flavonoids as inhibitors of breast cancer resistance protein (BCRP). *Bioorgan Med Chem* **19**, 2090–2102.

Poger, D., Mark, A.E., 2010. On the Validation of Molecular Dynamics Simulations of Saturated and cis -Monounsaturated Phosphatidylcholine Lipid Bilayers: A Comparison with Experiment. *J Chem Theory Comput* **6**, 325–336.

Poger, D., Van Gunsteren, W.F., Mark, A.E., 2010. A new force field for simulating phosphatidylcholine bilayers. *J Comput Chem* **31**, 1117–1125.

Polli, J.W., Wring, S.A., Humphreys, J.E., Huang, L., Morgan, J.B., Webster, L.O., Serabjit-Singh, C.S., 2001. Rational use of in vitro P-glycoprotein assays in drug discovery. *J Pharmacol Exp Ther* **299**, 620–628.

Poongavanam, V., Haider, N., Ecker, G.F., 2012. Fingerprint-based in silico models for the prediction of P-glycoprotein substrates and inhibitors. *Bioorgan Med Chem* **20**, 5388–5395.

Prachayasittikul, V., Mandi, P., Prachayasittikul, S., Prachayasittikul, V., Nantasenamat, C., 2016. Exploring the chemical space of P-glycoprotein interacting compounds. Mini Rev Med Chem 16 (in press), http://www.eurekaselect.com/138630/article.

Prachayasittikul, V., Worachartcheewan, A., Toropova, A.P., Toropov, A.A., Schaduangrat, N., Prachayasittikul, V., Nantasenamat, C., 2017. Large-scale classification of P-glycoprotein inhibitors using SMILES-based descriptors. *SAR QSAR Env. Res* **28** 1–16.

Pronk, S., Páll, S., Schulz, R., Larsson, P., Bjelkmar, P., Apostolov, R., Shirts, M.R., Smith, J.C., Kasson, P.M., van der Spoel, D., Hess, B., Lindahl, E., 2013. GROMACS 4.5: a high-throughput and highly parallel open source molecular simulation toolkit. *Bioinformatics* **29**, 845–854.

Qiu, L., Qiao, M., Chen, Q., Tian, C., Long, M., Wang, M., Li, Z., Hu, W., Li, G., Cheng, L., Cheng, L., Hu, H., Zhao, X., Chen, D., 2014. Enhanced effect of pH-sensitive mixed copolymer micelles for overcoming multidrug resistance of doxorubicin. *Biomaterials* **35**, 9877–9887.

Qiu, L., Zheng, C., Zhao, Q., 2012. Mechanisms of drug resistance reversal in Dox-resistant MCF-7 cells by pH-responsive amphiphilic polyphosphazene containing diisopropylamino side groups. *Mol Pharm* **9**, 1109–1117.

Qu, Q., Sharom, F.J., 2002. Proximity of bound Hoechst 33342 to the ATPase catalytic sites places the drug binding site of P-glycoprotein within the cytoplasmic membrane leaflet. *Biochemistry* **41**, 4744–4752.

Ragasa, C.Y., Lim, K., 2005. Secondary Metabolites from Schefflera odorata Blanco. *Phil J. Sci* **134**, 63–67.

Rajagopal, A., 2003. Subcellular Localization and Activity of Multidrug Resistance Proteins. *Mol Biol Cell* **14**, 3389–3399.

Ramakrishnan, A., Chourasiya, S.S., Bharatam, P. V., 2015. Azine or hydrazone? The dilemma in amidinohydrazones. *RSC Adv* **5**, 55938–55947.

Rao, P.S., Mallya, K.B., Srivenugopal, K.S., Balaji, K.C., Rao, U.S., 2006. RNF2 interacts with the linker region of the human P-glycoprotein. *Int J Oncol* **29**, 1413–1419.

Rauch, C., Paine, S.W., Littlewood, P., 2013. Can long range mechanical interaction between drugs and membrane proteins define the notion of molecular promiscuity? Application to P-glycoprotein-mediated multidrug resistance (MDR). *Biochim Biophys Acta* **1830**, 5112–5118.

Raut, V.P., Agashe, M. a, Stuart, S.J., Latour, R.A., 2005. Molecular dynamics simulations of peptide-surface interactions. *Langmuir* **21**, 1629–1639.

Rautio, J., Humphreys, J.E., Webster, L.O., Balakrishnan, A., Keogh, J.P., Kunta, J.R., Serabjit-Singh, C.J., Polli, J.W., 2006. In vitro p-glycoprotein inhibition assays for assessment of clinical drug interaction potential of new drug candidates: a recommendation for probe substrates. *Drug Metab Dispos* **34**, 786–792.

Raviv, Y., Pollard, H.B., Bruggemann, E.P., Pastan, I., Gottesman, M.M., 1990. Photosensitized labeling of a functional multidrug transporter in living drug-resistant tumor cells. *J Biol Chem* **265**, 3975–3980.

Rebbeor, J.F., Senior, A.E., 1998. Effects of cardiovascular drugs on ATPase activity of P-glycoprotein in plasma membranes and in purified reconstituted form. *Biochim Biophys Acta* **1369**, 85–93.

Reif, M.M., Hünenberger, P.H., Oostenbrink, C., 2012. New Interaction Parameters for Charged Amino Acid Side Chains in the GROMOS Force Field. *J Chem Theory Comput* **8**, 3705–3723.

Reis, M.A., André, V., Duarte, M.T., Lage, H., Ferreira, M.-J.U., 2015. 12,17-Cyclojatrophane and Jatrophane Constituents of Euphorbia welwitschii. *J Nat Prod* **78**, 2684–2690.

Reis, M.A., Ferreira, R.J., Santos, M.M.M., dos Santos, D.J.V.A., Molnár, J., Ferreira, M.-J.U., 2013. Enhancing Macrocyclic Diterpenes as Multidrug-Resistance Reversers: Structure-Activity Studies on Jolkinol D Derivatives. *J Med Chem* **56**, 748–760.

Reis, M.A., Paterna, A., Ferreira, R.J., Lage, H., Ferreira, M.-J.U., 2014. Macrocyclic diterpenes resensitizing multidrug resistant phenotypes. *Bioorgan Med Chem* **22**, 3696–3702.

Reis, M., Ferreira, R.J., Serly, J., Duarte, N., Madureira, A.M., dos Santos, D.J.V.A., Molnár, J., Ferreira, M.-J.U., 2012. Colon Adenocarcinoma Multidrug Resistance Reverted by Euphorbia Diterpenes: Structure-Activity Relationships and Pharmacophore Modeling. *Anticancer Agents Med Chem* **12**, 1015–1024.

Reis, M., Paterna, A., Mónico, A., Molnar, J., Lage, H., Ferreira, M.-J., 2014. Diterpenes from Euphorbia piscatoria: Synergistic Interaction of Lathyranes with Doxorubicin on Resistant Cancer Cells. *Planta Med* **80**, 1739–1745.

Reymann, A., Looft, G., Woermann, C., Dietel, M., Erttmann, R., 1993. Reversal of multidrug resistance in Friend leukemia cells by dexniguldipine-HCl. *Cancer Chemother Pharmacol* **32**, 25–30.

Romiti, N., Tramonti, G., Chieli, E., 2002. Influence of Different Chemicals on MDR-1 P-Glycoprotein Expression and Activity in the HK-2 Proximal Tubular Cell Line. *Toxicol Appl Pharmacol* **183**, 83–91.

Romsicki, Y., Sharom, F.J., 1999. The membrane lipid environment modulates drug interactions with the P-glycoprotein multidrug transporter. *Biochemistry* **38**, 6887–6896.

Romsicki, Y., Sharom, F.J., 1998. The ATPase and ATP-binding functions of P-glycoprotein. Modulation by interaction with defined phospholipids. *Eur J Biochem* **256**, 170–178.

Romsicki, Y., Sharom, F.J., 1997. Interaction of P-glycoprotein with defined phospholipid bilayers: a differential scanning calorimetric study. *Biochemistry* **36**, 9807–9815.

Rooney, E.K., Gore, M.G., Lee, A.G., 1979. Interaction of antihistamines with lipid bilayers. *Biochem Pharmacol* **28**, 2199–2205.

Rosenberg, M.F., Callaghan, R., Modok, S., Higgins, C.F., Ford, R.C., 2005. Three-dimensional structure of P-glycoprotein: the transmembrane regions adopt an asymmetric configuration in the nucleotide-bound state. *J Biol Chem* **280**, 2857–2862.

Rosenberg, M.F., Velarde, G., Ford, R.C., Martin, C., Berridge, G., Kerr, I.D., Callaghan, R., Schmidlin, A., Wooding, C., Linton, K.J., Higgins, C.F., 2001. Repacking of the transmembrane domains of P-glycoprotein during the transport ATPase cycle. *EMBO J* **20**, 5615–5625.

Ross, J.A., Kasum, C.M., 2002. Dietary Flavonoids: Bioavailability, Metabolic Effects, and Safety. *Ann Rev Nutr* **22**, 19–34.

Rost, B., Yachdav, G., Liu, J., 2004. The PredictProtein server. *Nucleic Acids Res* **32**, W321-W326.

Safa, A.R., Glover, C.J., Sewell, J.L., Meyers, M.B., Biedler, J.L., Felsted, R.L., 1987. Identification of the multidrug resistance-related membrane glycoprotein as an acceptor for calcium channel blockers. *J Biol Chem* **262**, 7884–7888.

Saija, A., Bonina, F., Trombetta, D., Tomaino, A., Montenegro, L., Smeriglio, P., Castelli, F., 1995. Flavonoid-biomembrane interactions: A calorimetric study on dipalmitoyl phosphatidylcholine vesicles. *Int J Pharm* **124**, 1–8.

Sandén, T., Salomonsson, L., Brzezinski, P., Widengren, J., 2010. Surface-coupled proton exchange of a membrane-bound proton acceptor. *Proc Natl Acad Sci U S A* **107**, 4129–4134.

Sato, T., 2013. Unique Biosynthesis of Sesquarterpenes (C35 Terpenes). *Biosci Biotechnol Biochem* **77**, 1155–1159.

Sato, T., Kodan, A., Kimura, Y., Ueda, K., Nakatsu, T., Kato, H., 2009. Functional role of the linker region in purified human P-glycoprotein. *FEBS J* **276**, 3504–3516.

Sauna, Z.E., Ambudkar, S. V, 2007. About a switch: how P-glycoprotein (ABCB1) harnesses the energy of ATP binding and hydrolysis to do mechanical work. *Mol Cancer Ther* **6**, 13–23.

Scheiffele, P., Roth, M.G., Simons, K., 1997. Interaction of influenza virus haemagglutinin with sphingolipid-cholesterol membrane domains via its transmembrane domain. *EMBO J* **16**, 5501–5508.

Schmid, N., Eichenberger, A.P., Choutko, A., Riniker, S., Winger, M., Mark, A.E., van Gunsteren, W.F., 2011. Definition and testing of the GROMOS force-field versions 54A7 and 54B7. *Eur Biophys J* **40**, 843–856.

Schüttelkopf, A.W., van Aalten, D.M.F., 2004. PRODRG: a tool for high-throughput crystallography of protein-ligand complexes. *Acta Crystallogr D Biol Crystallogr* **60**, 1355–1363.

Scott, W.R., Hünenberger, P.H., Tironi, I.G., Mark, A.E., Billeter, S.R., Fennen, J., Torda, A.E., Huber, T., Krüger, P., van Gunsteren, W.F., 1999. The GROMOS Biomolecular Simulation Program Package. *J Phys Chem A* **103**, 3596–3607.

Seebacher, N.A., Lane, D.J.R., Jansson, P.J., Richardson, D.R., 2016. Glucose Modulation Induces Lysosome Formation and Increases Lysosomotropic Drug Sequestration via the P-Glycoprotein Drug Transporter. *J Biol Chem* **291**, 3796–3820.

Senior, A.E., Al-Shawi, M.K., Urbatsch, I.L., 1995. The catalytic cycle of P-glycoprotein. *FEBS Lett* **377**, 285–289.

Shahraki, O., Zargari, F., Edraki, N., Khoshneviszadeh, M., Firuzi, O., Miri, R., 2017. Molecular dynamics simulation and molecular docking studies of 1,4-Dihydropyridines as P-glycoprotein's allosteric inhibitors. J Biomol Struct Dyn 1–14 (in press). doi:10.1080/07391102.2016.1268976

Shan, J., Khelashvili, G., Mondal, S., Weinstein, H., 2011. Pharmacologically Distinct Ligands Induce Different States of 5-HT2AR and Trigger Different Membrane Remodeling: Implications For GPCR Oligomerization. *Biophys J* **100**, 254a. doi:10.1016/j.bpj.2010.12.1605

Shapiro, A.B., Corder, A.B., Ling, V., 1997. P-glycoprotein-mediated Hoechst 33342 transport out of the lipid bilayer. *Eur J Biochem* **250**, 115–121.

Shapiro, A.B., Fox, K., Lam, P., Ling, V., 2001. Stimulation of P-glycoprotein-mediated drug transport by prazosin and progesterone. *Eur J Biochem* **259**, 841–850.

Shapiro, A.B., Ling, V., 1998. Transport of LDS-751 from the cytoplasmic leaflet of the plasma membrane by the rhodamine-123-selective site of P-glycoprotein. *Eur J Biochem* **254**, 181–188.

Shapiro, A.B., Ling, V., 1997a. Effect of quercetin on Hoechst 33342 transport by purified and reconstituted P-glycoprotein. *Biochem Pharmacol* **53**, 587–596.

Shapiro, A.B., Ling, V., 1997b. Positively Cooperative Sites for Drug Transport by P-Glycoprotein with Distinct Drug Specificities. *Eur J Biochem* **250**, 130–137.

Sharom, F.J., 2011. The P-glycoprotein multidrug transporter. *Essays Biochem* **50**, 161–178.

Sharom, F.J., 1997. The P-glycoprotein Efflux Pump: How Does it Transport Drugs? *J Membr Biol* **160**, 161–175.

Sharom, F.J., Lugo, M.R., Eckford, P.D.W., 2005. New insights into the drug binding, transport and lipid flippase activities of the p-glycoprotein multidrug transporter. *J Bioenerg Biomembr* **37**, 481–487.

Shi, Q.-W., Su, X.-H., Kiyota, H., 2008. Chemical and Pharmacological Research of the Plants in Genus Euphorbia. *Chem Rev* **108**, 4295–4327.

Siarheyeva, A., Liu, R., Sharom, F.J., 2010. Characterization of an asymmetric occluded state of P-glycoprotein with two bound nucleotides: implications for catalysis. *J Biol Chem* **285**, 7575–7586.

Siarheyeva, A., Lopez, J.J., Glaubitz, C., 2006. Localization of multidrug transporter substrates within model membranes. *Biochemistry* **45**, 6203–6211.

Silva, M., Mundaca, J.M., Sammes, P.G., 1971. Flavonoid and triterpene constituents of Baccharis Rhomboidalis. *Phytochemistry* **10**, 1942–1943.

Simoff, I., Karlgren, M., Backlund, M., Lindström, A.-C., Gaugaz, F.Z., Matsson, P., Artursson, P., 2016. Complete Knockout of Endogenous Mdr1 (Abcb1) in MDCK Cells by CRISPR-Cas9. *J Pharm Sci* **105**, 1017–1021.

Singh, M.S., Lamprecht, A., 2014. Cargoing P-gp inhibitors via nanoparticle sensitizes tumor cells against doxorubicin. *Int J Pharm* **478**, 745-752.

Singh, U.C., Kollman, P.A., 1984. An approach to computing electrostatic charges for molecules. *J Comput Chem* **5**, 129–145.

Smith-Kielland, I., Dornish, J., Malterud, K., Hvistendahl, G., Rømming, C., Bøckmann, O., Kolsaker, P., Stenstrøm, Y., Nordal, A., 1996. Cytotoxic Triterpenoids from the Leaves of Euphorbia pulcherrima. *Planta Med* **62**, 322–325.

Somno, A., Anuchapreeda, S., Chruewkamlow, N., Pata, S., Kasinrerk, W., Chiampanichayakul, S., 2016. Involvement of CD147 on multidrug resistance through the regulation of P-glycoprotein expression in K562/ADR leukemic cell line. *Leuk Res Rep* **6**, 33–38.

Sousa, I.J., Ferreira, M.J.U., Molnár, J., Fernandes, M.X., 2013. QSAR studies of macrocyclic diterpenes with P-glycoprotein inhibitory activity. *Eur J Pharm Sci* **48**, 542–553.

Srivastava, S., Choudhary, B.S., Sharma, M., Malik, R., 2016. Pharmacophore modeling and 3D-QSAR studies of galloyl benzamides as potent P-gp inhibitors. *Med Chem Res* **25**, 1140–1147.

Sterz, K., Möllmann, L., Jacobs, A., Baumert, D., Wiese, M., 2009. Activators of P-glycoprotein: Structure-activity relationships and investigation of their mode of action. *ChemMedChem* **4**, 1897–1911.

Storch, C.H., Theile, D., Lindenmaier, H., Haefeli, W.E., Weiss, J., 2007. Comparison of the inhibitory activity of anti-HIV drugs on P-glycoprotein. *Biochem Pharmacol* **73**, 1573–1581.

Störmer, E., Perloff, M.D., von Moltke, L.L., Greenblatt, D.J., 2001. Methadone inhibits rhodamine123 transport in Caco-2 cells. *Drug Metab Dispos* **29**, 954–956.

Subramanian, N., 2015. *Understanding multidrug resistance: molecular dynamics studies of ligand recognition by P-glycoprotein.* The University of Queensland. doi:10.14264/uql.2015.1108

Subramanian, N., Condic-Jurkic, K., Mark, A.E., O'Mara, M.L., 2015. Identification of Possible Binding Sites for Morphine and Nicardipine on the Multidrug Transporter P-Glycoprotein Using Umbrella Sampling Techniques. *J Chem Inf Model* **55**, 1202–1217.

Suzuki, T., Fukazawa, N., San-nohe, K., 1997. Structure-Activity Relationship of Newly Synthesized Quinoline Derivatives for Reversal of Multidrug Resistance in Cancer. *J Med Chem* **40**, 2047–2052.

Tamai, I., Safa, A.R., 1991. Azidopine noncompetitively interacts with vinblastine and cyclosporin A binding to P-glycoprotein in multidrug resistant cells. *J Biol Chem* **266**, 16796–16800.

Tanaka, R., Kasubuchi, K., Kita, S., Matsunaga, S., 1999. Obtusifoliol and related steroids from the whole herb of Euphorbia chamaesyce. *Phytochemistry* **51**, 457–463.

Tang, F., Ouyang, H., Yang, J.Z., Borchardt, R.T., 2004. Bidirectional transport of rhodamine 123 and Hoechst 33342, fluorescence probes of the binding sites on P-glycoprotein, across MDCK-MDR1 cell monolayers. *J Pharm Sci* **93**, 1185–1194.

Tarcsay, Á., Keserű, G.M., 2011. Homology modeling and binding site assessment of the human P-glycoprotein. *Future Med Chem* **3**, 297–307.

Tarling, E.J., de Aguiar Vallim, T.Q., Edwards, P.A., 2013. Role of ABC transporters in lipid transport and human disease. *Trends Endocrinol Metab* **24**, 342–350.

Tenopoulou, M., Kurz, T., Doulias, P.-T., Galaris, D., Brunk, U.T., 2007. Does the calcein-AM method assay the total cellular "labile iron pool" or only a fraction of it? *Biochem J* **403**, 261–266.

Tholl, D., 2015. Biosynthesis and Biological Functions of Terpenoids in Plants, in: Schrader, J., Bohlmann, J. (Eds.), *Biotechnology of Isoprenoids*. Springer International Publishing, pp. 63–106.

Tian, Y., Xu, W., Zhu, C., Lin, S., Li, Y., Xiong, L., Wang, S., Wang, L., Yang, Y., Guo, Y., Sun, H., Wang, X., Shi, J., 2011. Lathyrane diterpenoids from the roots of Euphorbia micractina and their biological activities. *J Nat Prod* **74**, 1221–1229.

Trott, O., Olson, A.J., 2010. AutoDock Vina: improving the speed and accuracy of docking with a new scoring function, efficient optimization, and multithreading. *J Comput Chem* **31**, 455–461.

Tsuruo, T., Iida, H., Kitatani, Y., Yokota, K., Tsukagoshi, S., Sakurai, Y., 1984. Effects of quinidine and related compounds on cytotoxicity and cellular accumulation of vincristine and adriamycin in drug-resistant tumor cells. *Cancer Res* **44**, 4303–4307.

Tsuruo, T., Lida, H., Tsukagoshi, S., Sakurai, Y., 1981. Overcoming of Vincristine Resistance in P388 Leukemia in Vivo and in Vitro through Enhanced Cytotoxicity of Vincristine and Vinblastine by Verapamil. *Cancer Res* **41**, 1967–1972.

Twentyman, P.R., Bleehen, N.M., 1991. Resistance modification by PSC-833, a novel non-immunosuppressive cyclosporin A. *Eur J Cancer* **27**, 1639–1642.

Twentyman, P.R., Fox, N.E., White, D.J., 1987. Cyclosporin A and its analogues as modifiers of adriamycin and vincristine resistance in a multi-drug resistant human lung cancer cell line. *Br J Cancer* **56**, 55–57.

Uemura, D., Nakayama, Y., Nobuhara, Y., Katayama, T., Hirata, Y., 1977. The Structures of Diterpenes Isolated from Euphorbia Jolkini Boiss. *Tetrahedron Lett* **17**, 4593–4596.

Urbatsch, I.L., Senior, A.E., 1995. Effects of lipids on ATPase activity of purified Chinese hamster P-glycoprotein. *Arch Biochem Biophys* **316**, 135–140.

van Assema, D.M.E., Lubberink, M., Bauer, M., van der Flier, W.M., Schuit, R.C., Windhorst, A.D., Comans, E.F.I., Hoetjes, N.J., Tolboom, N., Langer, O., Müller, M., Scheltens, P., Lammertsma, A.A., van Berckel, B.N.M., 2012. Blood-brain barrier P-glycoprotein function in Alzheimer's disease. *Brain* **135**, 181–189.

van der Spoel, D., Lindahl, E., Hess, B., Groenhof, G., Mark, A.E., Berendsen, H.J., 2005. GROMACS: fast, flexible, and free. *J Comput Chem* **26**, 1701–1718.

van der Spoel, D., van Maaren, P.J., Larsson, P., Tîmneanu, N., 2006. Thermodynamics of hydrogen bonding in hydrophilic and hydrophobic media. *J Phys Chem B* **110**, 4393–4398.

van Gunsteren, W.F., Berendsen, H.J.C., 1990. Computer Simulation of Molecular Dynamics: Methodology, Applications, and Perspectives in Chemistry. *Angew Chem Int Ed* **29**, 992–1023.

van Zuylen, L., Sparreboom, A., van der Gaast, A., Nooter, K., Eskens, F. a L.M., Brouwer, E., Bol, C.J., de Vries, R., Palmer, P. a, Verweij, J., 2002. Disposition of docetaxel in the presence of P-glycoprotein inhibition by intravenous administration of R101933. *Eur J Cancer* **38**, 1090–1099.

van Zuylen, L., Sparreboom, A., van der Gaast, A., van der Burg, M.E., van Beurden, V., Bol, C.J., Woestenborghs, R., Palmer, P.A., Verweij, J., 2000. The orally administered P-glycoprotein inhibitor R101933 does not alter the plasma pharmacokinetics of docetaxel. *Clin Cancer Res* **6**, 1365–1371.

Vasas, A., Hohmann, J., 2014. Euphorbia Diterpenes: Isolation, Structure, Biological Activity, and Synthesis (2008-2012). *Chem Rev* **114**, 8579–8612.

Vasas, A., Sulyok, E., Rédei, D., Forgo, P., Szabó, P., Zupkó, I., Berényi, Á., Molnár, J., Hohmann, J., 2011. Jatrophane diterpenes from Euphorbia esula as antiproliferative agents and potent chemosensitizers to overcome multidrug resistance. *J Nat Prod* **74**, 1453–1461.

Verhalen, B., Dastvan, R., Thangapandian, S., Peskova, Y., Koteiche, H.A., Nakamoto, R.K., Tajkhorshid, E., Mchaourab, H.S., 2017. Energy transduction and alternating access of the mammalian ABC transporter P-glycoprotein. *Nature* **543**, 738–741.

Vezmar, M., Georges, E., 1998. Direct binding of chloroquine to the multidrug resistance protein (MRP): possible role for MRP in chloroquine drug transport and resistance in tumor cells. *Biochem Pharmacol* **56**, 733–742.

Wan, L.-S., Shao, L.-D., Fu, L., Xu, J., Zhu, G.-L., Peng, X.-R., Li, X.-N., Li, Y., Qiu, M.-H., 2016. One-Step Semisynthesis of a Segetane Diterpenoid from a Jatrophane Precursor via a Diels–Alder Reaction. *Org Lett* **18**, 496–499.

Wang, E., Casciano, C.N., Clement, R.P., Johnson, W.W., 2001. The farnesyl protein transferase inhibitor SCH66336 is a potent inhibitor of MDR1 product P-glycoprotein. *Cancer Res* **61**, 7525–7529.

Wang, E.J., Lew, K., Casciano, C.N., Clement, R.P., Johnson, W.W., 2002. Interaction of Common Azole Antifungals with P Glycoprotein. *Antimicrob Agents Chemother* **46**, 160–165.

Wang, L., Yang, J., Kong, L.-M., Deng, J., Xiong, Z., Huang, J., Luo, J., Yan, Y., Hu, Y., Li, X.-N., Li, Y., Zhao, Y., Huang, S.-X., 2017. Natural and Semisynthetic Tigliane Diterpenoids with New Carbon Skeletons from Euphorbia dracunculoides as a Wnt Signaling Pathway Inhibitor. *Org Lett* **19**, 3911-3914.

Wang, R.B., Kuo, C.L., Lien, L.L., Lien, E.J.-C., 2003. Structure-activity relationship: analyses of p-glycoprotein substrates and inhibitors. *J Clin Pharm Ther* **28**, 203–228.

Ward, A., Reyes, C.L., Yu, J., Roth, C.B., Chang, G., 2007. Flexibility in the ABC transporter MsbA: Alternating access with a twist. *Proc Natl Acad Sci U S A* **104**, 19005–19010.

Ward, A.B., Szewczyk, P., Grimard, V., Lee, C.-W., Martinez, L., Doshi, R., Caya, A., Villaluz, M., Pardon, E., Cregger, C., Swartz, D.J., Falson, P.G., Urbatsch, I.L., Govaerts, C., Steyaert, J., Chang, G., 2013. Structures of P-glycoprotein reveal its conformational flexibility and an epitope on the nucleotide-binding domain. *Proc Natl Acad Sci U S A* **110**, 13386–13391.

Weaver, T.M., 2000. The pi-helix translates structure into function. *Protein Sci* **9**, 201–206.

Wen, P.-C., Verhalen, B., Wilkens, S., Mchaourab, H.S., Tajkhorshid, E., 2013. On the origin of large flexibility of P-glycoprotein in the inward-facing state. *J Biol Chem* **288**, 19211–19220.

Wiese, M., Pajeva, I.K., 2001. Structure-activity relationships of multidrug resistance reversers. *Curr Med Chem* **8**, 685–713.

Wink, M. (Ed.), 2010. Functions and Biotechnology of Plant Secondary Metabolites. Wiley-Blackwell, Oxford, UK. doi:10.1002/9781444318876

Wise, J.G., 2012. Catalytic transitions in the human MDR1 P-glycoprotein drug binding sites. *Biochemistry* **51**, 5125–5141.

Wisturba, D., Trapp, O., Gel-Moreto, N., Galensa, R., Schurig, V, 2006. Stereoisomeric Separation of Flavanones and Flavanone-7-O-glycosides by Capillary Electrophoresis and Determination of Interconversion Barriers. *Anal Chem* **78**, 3424-3433.

Wollmann, J., Richter, M., Molnár, J., Hilgeroth, A., 2005. First insight into the symmetry and flexibility of membrane efflux pump P-glycoprotein by novel bifunctional modulators. *ChemBioChem* **6**, 1353–1356.

Wong, K., Briddon, S.J., Holliday, N.D., Kerr, I.D., 2016. Plasma membrane dynamics and tetrameric organisation of ABCG2 transporters in mammalian cells revealed by single particle imaging techniques. *Biochim Biophys Acta* **1863**, 19–29.

Xu, J., Liu, Y., Yang, Y., Bates, S.E., Zhang, J.-T., 2004. Characterization of oligomeric human

half-ABC transporter ATP-binding cassette G2. *J Biol Chem* **279**, 19781–19789.

Xue, Y., Yap, C.W., Sun, L.Z., Cao, Z.W., Wang, J.F., Chen, Y.Z., 2004. Prediction of P-glycoprotein substrates by a support vector machine approach. *J Chem Inf Comput Sci* **44**, 1497–1505.

Yamagishi, T., Sahni, S., Sharp, D.M., Arvind, A., Jansson, P.J., Richardson, D.R., 2013. P-glycoprotein mediates drug resistance via a novel mechanism involving lysosomal sequestration. *J Biol Chem* **288**, 31761–31771.

Yan, X.-J., Gong, L.-H., Zheng, F.-Y., Cheng, K.-J., Chen, Z.-S., Shi, Z., 2014. Triterpenoids as reversal agents for anticancer drug resistance treatment. *Drug Discov Today* **19**, 482–488.

Yang, M., Chen, J., Shi, X., Xu, L., Xi, Z., You, L., An, R., Wang, X., 2015. Development of in silico models for predicting P-Glycoprotein inhibitors based on a two-step approach for feature selection and its application to Chinese herbal medicine screening. *Mol Pharm* **12**, 3691-3713.

Yang, Y., Qiu, J.-G., Li, Y., Di, J.-M., Zhang, W.-J., Jiang, Q.-W., Zheng, D.-W., Chen, Y., Wei, M.-N., Huang, J.-R., Wang, K., Shi, Z., 2016. Targeting ABCB1-mediated tumor multidrug resistance by CRISPR/Cas9-based genome editing. *Am J Transl Res* **8**, 3986–3994.

Yoshimura, S., Kawano, K., Matsumura, R., Sugihara, N., Furuno, K., 2009. Inhibitory Effect of Flavonoids on the Efflux of -Acetyl 5-Aminosalicylic Acid Intracellularly Formed in Caco-2 Cells. *J Biomed Biotechnol* **2009**, 1–8.

Yu, Z., Pan, W., Li, N., Tang, B., 2016. A nuclear targeted dual-photosensitizer for drug-resistant cancer therapy with NIR activated multiple ROS. *Chem Sci* **7**, 4237–4244.

Zahreddine, H., Borden, K.L.B., 2013. Mechanisms and insights into drug resistance in cancer. *Front Pharmacol* **28**. doi:10.3389/fphar.2013.00028

Zamora, J.M., Pearce, H.L., Beck, W.T., 1988. Physical-chemical properties shared by compounds that modulate multidrug resistance in human leukemic cells. *Mol Pharmacol* **33**, 454–462.

Zeino, M., Paulsen, M.S., Zehl, M., Urban, E., Kopp, B., Efferth, T., 2015. Identification of new P-glycoprotein inhibitors derived from cardiotonic steroids. *Biochem Pharmacol* **93**, 11–24.

Zembruski, N.C.L., Nguyen, C.D.L., Theile, D., Ali, R.M.M., Herzog, M., Hofhaus, G., Heintz,

U., Burhenne, J., Haefeli, W.E., Weiss, J., 2013. Liposomal sphingomyelin influences the cellular lipid profile of human lymphoblastic leukemia cells without effect on P-glycoprotein activity. *Mol Pharm* **10**, 1020–1034.

Zha, W., Wang, G., Xu, W., Liu, X., Wang, Y., Zha, B.S., Shi, J., Zhao, Q., Gerk, P.M., Studer, E., Hylemon, P.B., Pandak, W.M., Zhou, H., 2013. Inhibition of P-Glycoprotein by HIV Protease Inhibitors Increases Intracellular Accumulation of Berberine in Murine and Human Macrophages. *PLoS One* **8**, e54349. doi:10.1371/journal.pone.0054349

Zhang, B.-B., Jiang, Q., Liao, Z.-X., Liu, C., Liu, S.-J., Ji, L.-J., Sun, H.-F., 2013. Norlathyrane Diterpenes from the Root of Euphorbia kansuensis. *Chem Biodivers* **10**, 1887–1893.

Zhang, Y.-K., Zhang, G.-N., Wang, Y.-J., Patel, B.A., Talele, T.T., Yang, D.-H., Chen, Z.-S., 2016. Bafetinib (INNO-406) reverses multidrug resistance by inhibiting the efflux function of ABCB1 and ABCG2 transporters. *Sci Rep* **6**, 25694. doi:10.1038/srep25694

Zhang, Z., Chen, J., 2016. Atomic Structure of the Cystic Fibrosis Transmembrane Conductance Regulator. *Cell* **167**, 1586–1597.

Zhang, Z.Q., Chow, R.K.K., Zhou, H.W., Li, J.L., Cheung, H.-Y., 2008. An ab initio study on the structure-cytotoxicity relationship of terpenoid lactones based on the Michael reaction between their pharmacophores and L-cysteine-methylester-1. *J Theor Comput Chem* **7**, 347–356.

Zhi-Da, M., Mizuno, M., Tanaka, T., Iinuma, M., Guang-Yi, X., Qing, H., 1989. A diterpene from Euphorbia antiquorum. *Phytochemistry* **28**, 553–555.

Zhu, J., Wang, R., Lou, L., Li, W., Tang, G., Bu, X., Yin, S., 2016. Jatrophane Diterpenoids as Modulators of P-Glycoprotein-Dependent Multidrug Resistance (MDR): Advances of Structure–Activity Relationships and Discovery of Promising MDR Reversal Agents. *J Med Chem* **59**, 6353–6369.

Zografos, A.L. (Ed.), 2016. *From Biosynthesis to Total Synthesis*. John Wiley & Sons, Inc, Hoboken, NJ.